CATALYSIS & PHOTOCATALYSIS EDITOR'S PICK 2021

EDITED BY: Bunsho Ohtani

PUBLISHED IN: Frontiers in Chemistry

frontiers Research Topics

ISSN 1664-8714
ISBN 978-2-88966-786-4
DOI 10.3389/978-2-88966-786-4

About Frontiers

Frontiers is more than just an open-access publisher of scholarly articles: it is a pioneering approach to the world of academia, radically improving the way scholarly research is managed. The grand vision of Frontiers is a world where all people have an equal opportunity to seek, share and generate knowledge. Frontiers provides immediate and permanent online open access to all its publications, but this alone is not enough to realize our grand goals.

Frontiers Journal Series

The Frontiers Journal Series is a multi-tier and interdisciplinary set of open-access, online journals, promising a paradigm shift from the current review, selection and dissemination processes in academic publishing. All Frontiers journals are driven by researchers for researchers; therefore, they constitute a service to the scholarly community. At the same time, the Frontiers Journal Series operates on a revolutionary invention, the tiered publishing system, initially addressing specific communities of scholars, and gradually climbing up to broader public understanding, thus serving the interests of the lay society, too.

Dedication to Quality

Each Frontiers article is a landmark of the highest quality, thanks to genuinely collaborative interactions between authors and review editors, who include some of the world's best academicians. Research must be certified by peers before entering a stream of knowledge that may eventually reach the public - and shape society; therefore, Frontiers only applies the most rigorous and unbiased reviews.
Frontiers revolutionizes research publishing by freely delivering the most outstanding research, evaluated with no bias from both the academic and social point of view. By applying the most advanced information technologies, Frontiers is catapulting scholarly publishing into a new generation.

What are Frontiers Research Topics?

Frontiers Research Topics are very popular trademarks of the Frontiers Journals Series: they are collections of at least ten articles, all centered on a particular subject. With their unique mix of varied contributions from Original Research to Review Articles, Frontiers Research Topics unify the most influential researchers, the latest key findings and historical advances in a hot research area! Find out more on how to host your own Frontiers Research Topic or contribute to one as an author by contacting the Frontiers Editorial Office: frontiersin.org/about/contact

CATALYSIS & PHOTOCATALYSIS EDITOR'S PICK 2021

Topic Editor:
Bunsho Ohtani, Hokkaido University, Japan

Citation: Ohtani, B., ed. (2021). Catalysis & Photocatalysis Editor's Pick 2021. Lausanne: Frontiers Media SA. doi: 10.3389/978-2-88966-786-4

Table of Contents

frontiers in Chemistry

ORIGINAL RESEARCH
published: 01 February 2019
doi: 10.3389/fchem.2019.00042

Synergistic Catalysis of Ruthenium Nanoparticles and Polyoxometalate Integrated Within Single UiO−66 Microcrystals for Boosting the Efficiency of Methyl Levulinate to γ-Valerolactone

Xiaoxiong Cai, Qionghao Xu, Gaomei Tu, Yanghe Fu, Fumin Zhang* and Weidong Zhu**

Key Laboratory of the Ministry of Education for Advanced Catalysis Materials, Institute of Physical Chemistry, Zhejiang Normal University, Jinhua, China

OPEN ACCESS

Edited by:
Wee-Jun Ong, Xiamen University Malaysia, Malaysia

Reviewed by:
Marek Majewski, Concordia University, Canada
Yangyang Liu, California State University, Los Angeles, United States

***Correspondence:**
Gaomei Tu
tugaomei@zjnu.cn
Fumin Zhang
zhangfumin@zjnu.edu.cn
Weidong Zhu
weidongzhu@zjnu.cn

Specialty section:
This article was submitted to Catalysis and Photocatalysis, a section of the journal Frontiers in Chemistry

Received: *31 October 2018*
Accepted: *15 January 2019*
Published: *01 February 2019*

Citation:
Cai X, Xu Q, Tu G, Fu Y, Zhang F and Zhu W (2019) Synergistic Catalysis of Ruthenium Nanoparticles and Polyoxometalate Integrated Within Single UiO−66 Microcrystals for Boosting the Efficiency of Methyl Levulinate to γ-Valerolactone. Front. Chem. 7:42. doi: 10.3389/fchem.2019.00042

The synthesis of heterogeneous cooperative catalysts in which two or more catalytically active components are spatially separated within a single material has generated considerable research efforts. The multiple functionalities of catalysts can significantly improve the efficiency of existing organic chemical transformations. Herein, we introduce ruthenium (Ru) nanoparticles (NPs) on the surfaces of a metal–organic framework pre-encapsulated with polyoxometalate silicotungstic acid (SiW) UiO−66 (University of Oslo [UiO]) and prepared a 2.0% Ru/11.7% SiW@UiO−66 porous hybrid using the impregnation method. The close synergistic effect of metal Ru NPs, SiW, and UiO-66 endow 2.0% Ru/11.7% SiW@UiO-66 with increased activity and stability for complete methyl levulinate (ML) conversion and exclusive γ-valerolactone (GVL) selectivity at mild conditions of 80°C and at a H_2 pressure of 0.5 MPa. Effectively, this serves as a model reaction for the upgrading of biomass and outperforms the performances of the constituent parts and that of the physical mixture (SiW + Ru/UiO−66). The highly dispersed Ru NPs act as active centers for hydrogenation, while the SiW molecules possess Brønsted acidic sites that cooperatively promote the subsequent lactonization of MHV to generate GVL, and the UiO−66 crystal accelerates the mass transportation facilitated by its own porous structure with a large surface area.

Keywords: upgrading of biomass, synergistic catalysis, metal–organic framework, polyoxometalate, γ-valerolactone

INTRODUCTION

Metal–organic frameworks (MOFs) are an emerging class of advanced functional materials that have generated tremendous research interest by virtue of their fascinating properties, such as the well-defined crystalline structures, large surface areas, tunable pore cavities, and abundant unsaturated metal sites in their scaffolds (Ma et al., 2009; Stock and Biswas, 2012; Furukawa et al., 2013; Chen et al., 2017; Jiao et al., 2017). Among the various MOFs, zirconium-based MOF UiO−66 (University of Oslo [UiO]), with a chemical formula of $Zr_6O_4(OH)_4(bdc)_6$ (bdc:

1,4-benzenedicarboxylate), is distinguished for its increased hydrothermal/chemical stability and good tolerance toward common organic solvents (Cavka et al., 2008; Kandiah et al., 2010). In addition, UiO−66 possesses a rigid three-dimensional cubic framework containing tetrahedral and octahedral cavities, with internal diameters that are approximately equal to 0.75 and 1.2 nm, respectively. These cavities are interconnected via microporous triangular pores with diameters of 0.6 nm, thus forming a high-porosity network. Thanks to these unique characteristics, the solid form of UiO−66 has been regarded as an ideal host matrix for encapsulation of metal nanoparticles (NPs) and guest molecules (Furukawa et al., 2014; Guo et al., 2014; Na et al., 2014; Yang et al., 2015a,b; Bai et al., 2016; Liu et al., 2016).

Production of biofuels and high-value biochemicals based on the utilization of biomass as starting feedstock has been identified as a sustainable strategy to mitigate the strong dependence on the rapidly diminishing fossil resources (Rojas-Buzo et al., 2018). Lignocellulosic biomass, including agricultural residues, wood, paper, and municipal solid waste, constitute the most abundant and biorenewable biomass on earth. Therefore, the transformation of lignocellulosic biomass to produce valuable biochemicals and biofuels has spurred intense efforts worldwide (Alonso et al., 2012; Zhang et al., 2017). Accordingly, γ-Valerolactone (GVL) is an intriguing platform molecule that originates from lignocellulosic biomass, and possesses tremendous potential for a variety of industrial applications (Serrano-Ruiz et al., 2011; Liguori et al., 2015; Zhang et al., 2016). GVL can be expediently generated via catalytic conversion of levulinic acid (LA) and its esters (Yan et al., 2015). Considering that LA is corrosive ($pKa = 4.59$) and that it easily induces the deactivation of catalysts owing to the leaching of active species, use of LA esters as starting reactants is a more advantageous option for biofuels and biochemical production (Wright and Palkovits, 2012). Considering methyl levulinate (ML) as an example, two steps are involved in the transformation of ML to GVL at relatively low-reaction temperatures: (a) the hydrogenation of ML to intermediate methyl-3-hydroxyvalerate (MHV), and (b) the successive transesterification of MHV to GVL, both of which are required to be catalyzed by metal NPs and acidic sites, respectively (Negahdar et al., 2017).

In the cohort of the various catalysts screened for the upgrade of LA and its esters to generate GVL (Du et al., 2011; Wright and Palkovits, 2012; Nadgeri et al., 2014; Tang et al., 2014; Ye et al., 2014; Kuwahara et al., 2015; Kadu et al., 2016; Winoto et al., 2016; Xiao et al., 2016; Albani et al., 2017; Hengst et al., 2017; Negahdar et al., 2017; Kondeboina et al., 2018; Li et al., 2018; Wang et al., 2018), precious metal ruthenium (Ru) NPs have been demonstrated to be the most active catalysts in liquid–phase catalytic reactions (Michel and Gallezot, 2015; Tan et al., 2015). Notably, the activation of the carbonyl group in the ML molecule by acid sites is the rate-determining step in the selective conversion of LA or ML to GVL. Thus, it has been reported that the conversion efficiency of LA or its esters could be enhanced over the Ru catalysts in the presence of the acid co-catalysts (Abdelrahman et al., 2014). For example, Galletti et al. evaluated the promotion effect of different solid acids on the Ru/C catalyst in the hydrogenation of LA to GVL, and found that the combination of Ru/C and resins Amberlyst A70 elicited the highest activity with a 99.9% GVL yield achieved at 70°C and at a H_2 pressure of 3 MPa over a period of 3 h (Galletti et al., 2012). Barbaro et al. prepared a supported Ru catalyst with sulfonated resin as the support, and measured a 99.8% GVL yield at 70°C and at a H_2 pressure of 0.5 MPa (Moreno-Marrodan and Barbaro, 2014). In our previous work, we reported the improved catalytic activity of Ru NPs supported on the acidified MOFs for the transformation of ML to GVL (Lin et al., 2017, 2018). These results manifest that the overall catalytic performance can be boosted considerably in the presence of the acid co-catalyst by significantly accelerating the sequential hydrogenation and lactonization steps in the upgrading process of LA and its esters.

Polyoxometalates (POMs) are a subset of anionic metal oxygen clusters of early transition metals that are extensively used as catalysts because of their facile tunable oxidation/redox and acid/base properties (Zeng et al., 2000; Du et al., 2014; Miras et al., 2014; Zhou et al., 2014; Zhang et al., 2015a,b; Buru et al., 2017, 2018). Using MOFs as the matrices to host POMs may elicit some benefits, such as the isolation of the POM molecules and the simultaneous improvement of substrate–POM accessibility (Miras et al., 2014; Zhang et al., 2015a,b; Buru et al., 2017, 2018). Notably, the cavities of UiO−66 are large enough to accommodate the POM molecules, while the apertures are small enough to prohibit the POM from leaching out of the pores. Based on the consideration of these facts, we report an approach that combines POM silicotungstic acid ($H_4SiW_{12}O_{40}{\cdot}xH_2O$, abbreviated as SiW), Ru NPs, and MOF, in a UiO−66-based hybrid material, Ru/SiW@UiO−66, with a significantly increased activity and selectivity in the upgrade of ML to GVL relative to each of the constituent components, or their physical mixture. Specifically, in the synthesized catalyst Ru/SiW@UiO−66, the Ru NPs, which are distributed on the external surface of the UiO−66 crystals, can catalyze the hydrogenation of ML to form MHV owing to their activities and role for hydrogen activation and dissociation. While the SiW molecules which possess Brønsted acidic sites, which are encapsulated within the cavities of UiO−66, promote the subsequent lactonization of MHV to generate GVL owing to their excellent dealcoholization properties. In a cooperative manner, the UiO−66 crystal accelerates mass transportation which is facilitated by its own porous structure with a large surface area. Thus, the metal/SiW bifunctionalities within a single MOF crystal are anticipated to boost the tandem hydrogenation–lactonization reaction via a highly efficient synergistic catalysis manner (**Scheme 1**). To the best of our knowledge, this is an initial report on the preparation of MOF-based metal/acid bifunctional catalysts, in which the metal NPs and acidic site are spatially separated on the outer and internal spaces of the MOF, respectively, and their application in the upgrading of biomass.

EXPERIMENTAL SECTION

Detailed information regarding the chemicals and methods can be found in Supporting Information.

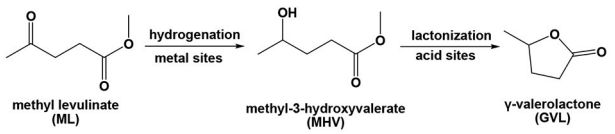

SCHEME 1 | Tandem hydrogenation–lactonization of ML used to yield GVL in the presence of a metal/acid bifunctional catalyst.

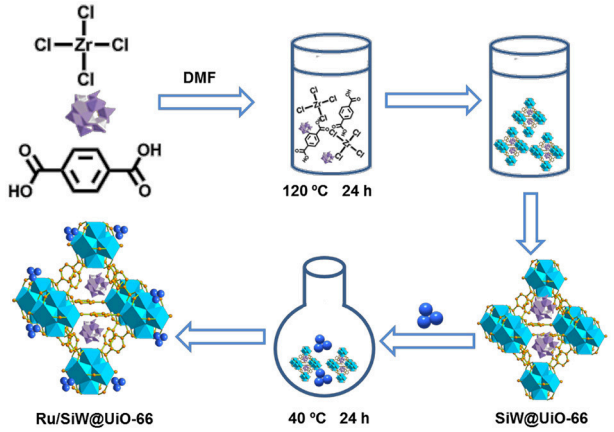

SCHEME 2 | Schematic showing the preparation procedure of the Ru/SiW@UiO−66 catalyst. Purple polyhedra: SiW, dark blue ball: Ru NPs, sky blue framework: UiO−66.

Catalyst Preparation

SiW@UiO−66

The UiO−66 crystals encapsulated SiW (SiW@UiO−66) which was synthesized by the one-pot hydrothermal method. In a typical synthesis, $ZrCl_4$ (0.233 g, 1.0 mmol), H_2BDC (0.166 g, 1.0 mmol), SiW (0.02 g, 6.95×10^{-3} mmol), and acetic acid (1 mL), were added to DMF (45 mL) during stirring to form a clear and colorless solution. After stirring for 30 min at 30°C, the solution was transferred into a Teflon-lined autoclave (100 mL) and was heated at 120°C for 24 h without stirring. The resulting white solid was collected by centrifugation and was washed with DMF and methanol three times. It was finally dried at 120°C for 12 h. For comparison, pure UiO−66 support was also synthesized following the same procedure as that described above but without the addition of SiW in the starting synthesis system.

Ru NPs

The Ru NPs were fabricated by a polyol reduction method (Zhao et al., 2016). In a typical procedure, 10.4 mg (0.5 mmol) $RuCl_3$, and 58.0 mg (0.001 mmol) PVP (Ru/PVP molar ratio: 50:1) were dissolved in EG (10 mL). The reaction mixture was ultrasonicated for 5 min at 25°C. Subsequently, the solution was degassed at 80°C for 30 min with the use of flowing Ar in a three-necked flask. The solution was then heated to 180°C under flux and was maintained for 2 h in an inert Ar atmosphere. When the reaction was complete, acetone was added into the solution at room temperature, and the resulting cloudy black suspension was subjected to a centrifuge. The precipitated Ru NPs were then separated, collected, and redispersed in 80 mL ethanol (0.6 mmol/L).

Ru/SiW@UiO−66

To prepare the Ru/SiW@UiO−66 catalyst, pre-dried SiW@UiO−66 (0.1 g) was dispersed in a Ru NPs ethanol solution (33 mL) that had been processed by ultrasound for 15 min. After stirring at 40°C for 12 h, the resulting solid was collected by centrifugation at 8,000 rpm for 5 min, and was then dried under vacuum at 120°C for 4 h. For comparison, Ru NPs supported a UiO−66 sample (referred to as Ru/UiO−66), which was also prepared using the same method as that described above.

Catalytic Activity Test

The catalytic upgrade of ML, a model compound of biomass, was performed in a Teflon-lined high-pressure reactor (50 mL, NS50–MP–LT–SS1–SV–BS, Anhui Kemi Machinery Technology Co. Ltd., Anhui, China) equipped with a gas inlet value and a sampling valve. The reactant ML (0.257 g, 1.98 mmol), pre-dried catalyst (50 mg, molar ratio of substrate to Ru NPs in the catalyst (S/C) was 200), and solvent H_2O (15 mL) were added into the reactor. Prior to the reaction, the reactor was flushed with hydrogen six times without stirring. Once the desired temperature was reached (80°C), 0.5 MPa of hydrogen was introduced into the reactor, and the suspension was vigorously stirred at the constant speed of 980 rpm. This was considered as the onset of the reaction. During the reaction interval, the liquid samples were withdrawn regularly from the reactor and were analyzed by a Shimadzu GC−2014 gas chromatography with a flame ionization detector, with the use of a DB−5 capillary column. Upon completion of the reaction, the reactor was cooled down naturally to room temperature and was depressurized carefully. For the recyclability test, the spent Ru/SiW@UiO−66 was recovered by filtration, washed with ethanol three times, dried at 120°C, and was then subjected to the subsequent reaction cycle.

RESULTS AND DISCUSSION

Catalyst Preparation and Characterization

Scheme 2 describes the preparation processes of the MOF-based metal/acid bifunctional hybrid by a facile two-step method. First, SiW molecules were confined within the UiO−66 cavities through the direct hydrothermal synthesis of UiO−66 in the presence of the preformed SiW. Subsequently, the pre-synthesized Ru NPs were loaded onto the external surfaces of the prepared SiW@UiO−66 by a conventional impregnation method. ICP–AES analyses revealed that the Ru and SiW contents within Ru/SiW@UiO−66 were 2.0 and 11.7% by weight, respectively (**Table 1**). These were very close to the nominal amounts added during the catalyst preparation procedure, thus implying that the *in-situ* encapsulation of SiW and subsequent immobilization of Ru NPs within the MOF was a feasible technique for catalyst preparation.

TABLE 1 | Physicochemical properties of various catalysts investigated in this study.

Catalyst	S_{BET}[a] m^2/g	V_{total}[b] cm^3/g	V_{micro}[c] cm^3/g	Acidity[d] mmol/g	SiW[e] %	Ru[f] %
UiO−66	1333	0.63	0.50	–	–	–
SiW@UiO−66	1200	0.54	0.44	–	–	–
Ru/UiO−66	1068	0.48	0.39	0.01	–	2.1
Ru/SiW@UiO-66	816	0.39	0.29	0.134	11.7	2.0
Spent Ru/SiW@UiO-66	811	0.39	0.29	0.131	11.6	1.9

[a]*BET specific area.*
[b]*Total pore volume.*
[c]*Microporous volume.*
[d]*Based on an acid–base titration method.*
[e,f]*Based on ICP–ASE analysis.*

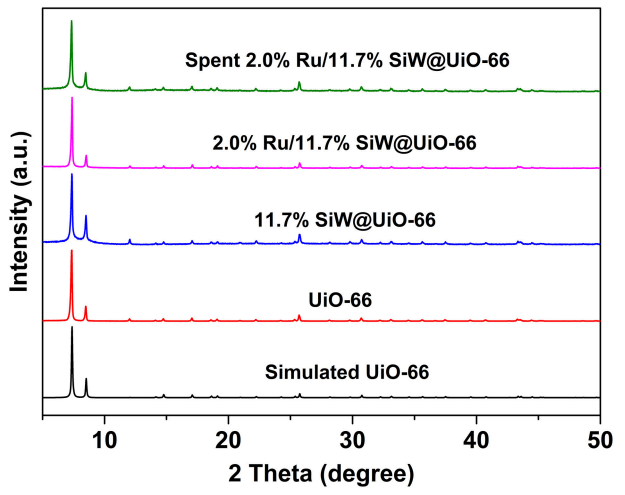

FIGURE 1 | XRD patterns of various tested samples.

TGA results demonstrate that the prepared MOF and corresponding catalysts were stable up to 500°C (**Figure S1** in Supporting Information). The XRD pattern of the synthesized UiO−66 support matches well the calculated pattern from crystal data (**Figure 1**) (Cavka et al., 2008; Kandiah et al., 2010). The crystal structure of 11.7% SiW@UiO−66, which remained almost unchanged compared to the prototype UiO−66, indicates that the addition of SiW molecules within UiO−66 hardly affected the crystalline structure of the pristine MOF (Yang et al., 2015b; Ullah et al., 2018). Moreover, no diffraction peaks associated with the SiW crystals were detected for 11.7% SiW@UiO−66, thus suggesting that the SiW nanoclusters were mainly confined within the MOF cavities. After the Ru NPs were introduced on SiW@UiO−66, the corresponding XRD pattern did not show any observable change probably owing to the very small Ru particle sizes and the low loading.

N_2 adsorption isotherms and the pore size distribution profiles of the various samples are shown in **Figure 2**. In addition, textural parameters as well as other physicochemical properties are summarized in **Table 1**. All the adsorption isotherms are type I curves according to the classification scheme of the International Union of Pure and Applied Chemistry, which verifies the inherit microporous structure of the prepared UiO−66-based samples (Cavka et al., 2008; Kandiah et al., 2010). Additionally, as listed in **Table 1**, the specific surface area (S_{BET}) and total pore volume (V_{total}) of UiO−66 are 1,333 m^2/g and 0.63 cm^3/g, respectively, which are much higher than the calculated value of perfect UiO−66 crystals, likely owing to missing linker defect sites that exist in the synthesized MOFs (Wu et al., 2013). As expected, both S_{BET} and V_{total} of SiW@UiO−66 decrease remarkably compared to the parent MOF. These changes are consistent with the SiW molecules incorporation in UiO−66. The pore size distribution of the various samples reveals two types of micropores: smaller pores with diameters in the range of 0.6–0.8 nm and larger pores in the range of 1.2–1.4 nm, thus confirming the presence of the two types of cages in these samples (Cavka et al., 2008; Kandiah et al., 2010; Ullah et al., 2018). After the Ru NPs were loaded onto SiW@UiO−66, the corresponding S_{BET} was remarkably reduced (816 m^2/g). Meanwhile, the V_{total} also decreased from 0.54 to 0.39 cm^3/g. The reductions in the surface area and pore volume were mainly attributed to the corresponding surface area and pore volume of SiW@UiO−66 which were occupied partially by the highly dispersed Ru NPs.

FTIR spectra have been used to analyze the bonding modes between UiO−66, SiW molecules, and Ru NPs (**Figure 3**). For SiW, the characteristic absorption peaks of the Keggin unit were detected at 974, 980, 922, and 810 cm^{-1}, and are attributed to the $v_{as}(Si–O_a)$, $v_{as}(W–O_d)$, $v_{as}(W–O_b-W)$, and $v_{as}(W–O_c-W)$, respectively (Rajkumar and Ranga Rao, 2008). The FTIR spectrum of SiW@UiO−66 contains nearly all the characteristic peaks of SiW and UiO−66 with minor shifts for some bands, probably because of the confinement effect of the cavities of the UiO−66 matrix on the guest SiW molecules (Yang et al., 2015b; Ullah et al., 2018). Notably, the FTIR features associated with the SiW Keggin structure are well-preserved in the range of 800–1,000 cm^{-1} for the 2.0% Ru/11.7% SiW@UiO−66 sample (curve d in **Figure 3**).

Surface chemical composition and valence state of the various elements in the hybrid are characterized by the XPS technique. The Zr 3d spectrum can be deconvoluted into two peaks centered at 185.3 and 182.9 eV (**Figure 4A**), which are related to the electron binding energies of Zr 3d3/2 and Zr 3d5/2, respectively, similar to that of the pristine UiO−66 (Cavka et al., 2008). The

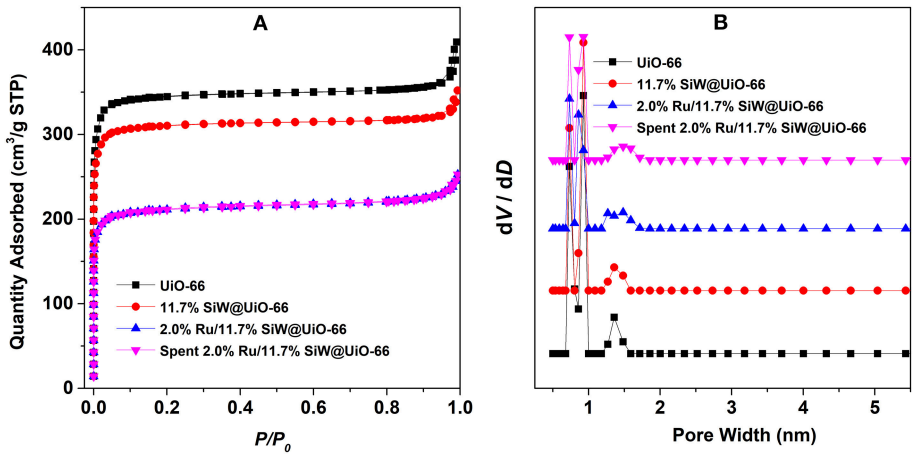

FIGURE 2 | N_2 adsorption isotherms at −196°C **(A)** and the corresponding pore size distribution plots **(B)** of the various tested samples.

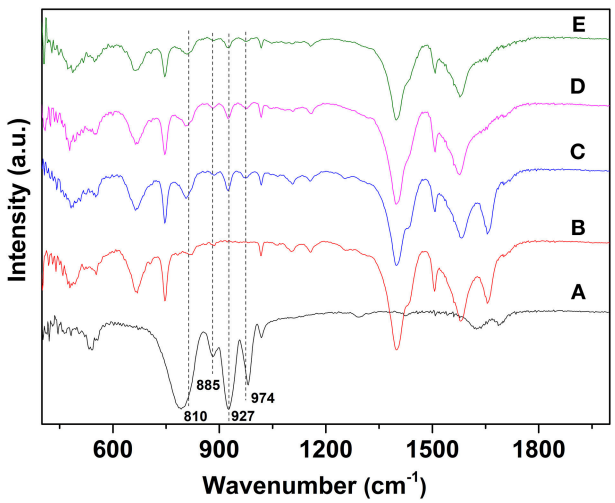

FIGURE 3 | FTIR spectra of SiW **(A)**, UiO−66 **(B)**, 11.7% SiW@UiO−66 **(C)**, 2.0% Ru/11.7% SiW@UiO−66 **(D)**, and the used 2.0% Ru/11.7% SiW@UiO−66 catalyst **(E)**.

peak for Si 2p in the Keggin structure of SiW was observed at 102.3 eV (**Figure 4B**) (Berry et al., 2009). For the tungsten species, two different chemical states were observed. The spin–orbit doublet with binding energies of 35.8 and 37.9 eV for W 4f7/2 and W 4f5/2, which account for ∼70% of the total spectral area (**Figure 4C**). These values are typical for the presence of W^{6+}, which is ascribed to SiW in the Keggin structure in the hybrid (Berry et al., 2009). A second doublet at 31.0 and 32.4 eV accounts for the remaining area, thus representing the partial decomposition of SiW within the MOF and the formation of an oxide of type WO_x in which W has an oxidation state lower than VI (Berry et al., 2009). Moreover, the sample exhibited Ru 3p bands at ca. 461.6 and 483.8 eV, which are the characteristic of zero-valent Ru species (**Figure 4D**).

The SEM image indicates that the pristine UiO−66 possesses well-defined octahedral microcrystals with an average crystal diameter of 150∼200 nm (**Figure S2**). In the presence of SiW, the morphology of SiW@UiO−66 crystallites tends to be in the form of spherical particles, with the crystallite diameters of SiW@UiO−66 being very close to those of the UiO−66 (**Figure S2**). The shape evolutions are assumed to be originated from the binding of metal ions and SiW anions (Yang and Wang, 2018). As expected, both the size and morphology of Ru/UiO−66 and Ru/SiW@UiO−66 are almost the same as those for the supports (**Figure S2**). The TEM images demonstrate that the Ru NPs with a uniform size of 1.5–4 nm were highly distributed on both the surface of the UiO−66 and SiW@UiO−66 supports, as shown in **Figure 5**, **Figure S3**. The further EDX mapping also verified that the Zr, Ru, Si, W and were highly distributed within UiO-66 (**Figure S4**). The content of Brønsted acid sites in the SiW@UiO−66 samples were measured to be 0.134 mmol/g (**Table 1**). Even though the coordination of unsaturated Zr^{4+} sites within UiO−66 may serve as acidic sites (Cavka et al., 2008; Kandiah et al., 2010), their strengths are exceedingly weaker than those of the SiW sites. Thus, the measured acidity can be mainly attributed to the Brønsted acidic SiW sites confined within the UiO−66 frameworks. Therefore, the combined results of XRD, N_2 adsorption, FTIR, XPS, SEM, TEM, and acid capacity measurements, confirm that the bifunctional 2.0% Ru/11.7% SiW@UiO−66 hybrid has been successfully prepared via the facile approach.

Catalytic Studies

The composition, structure, and morphology of the 2.0% Ru/11.7% SiW@UiO−66 hybrid implies that it may be suitably used as an efficient bifunctional catalyst. Correspondingly, we evaluated its catalytic properties in the transformation of ML to GVL under mild reaction conditions using water as a green solvent. The influence of the reaction temperature on the reactant and product distribution was studied and the results were compared in **Figure 6**. Obviously, both the hydrogenation and

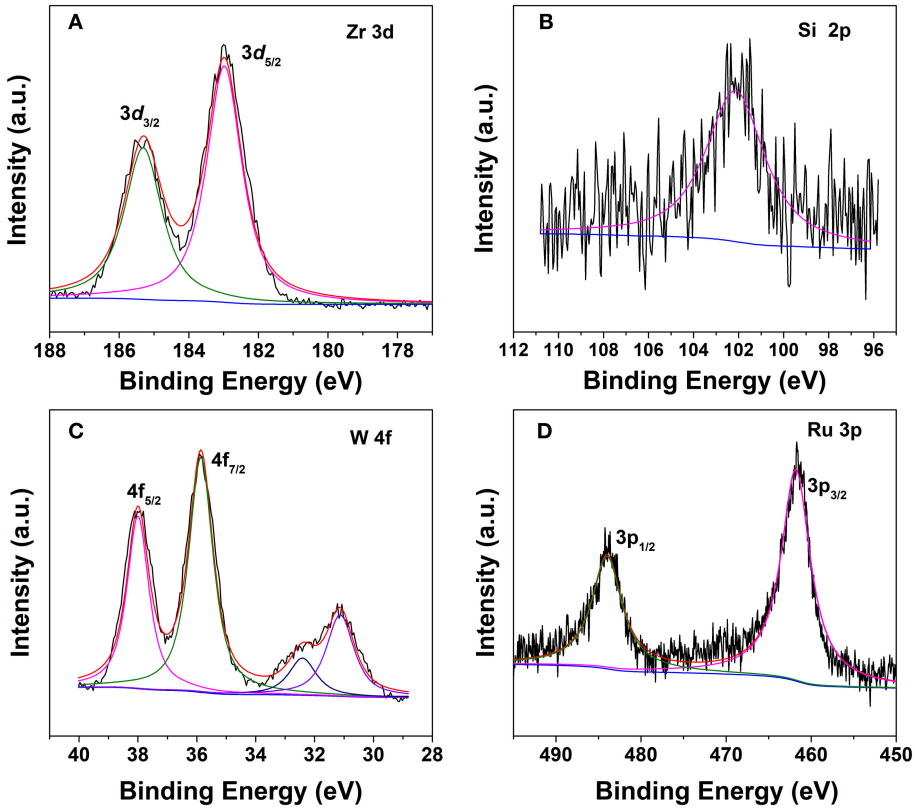

FIGURE 4 | XPS spectra of 2.0% Ru/11.7% SiW@UiO−66. **(A)** Zr, **(B)** Si, **(C)** W, and **(D)** Ru.

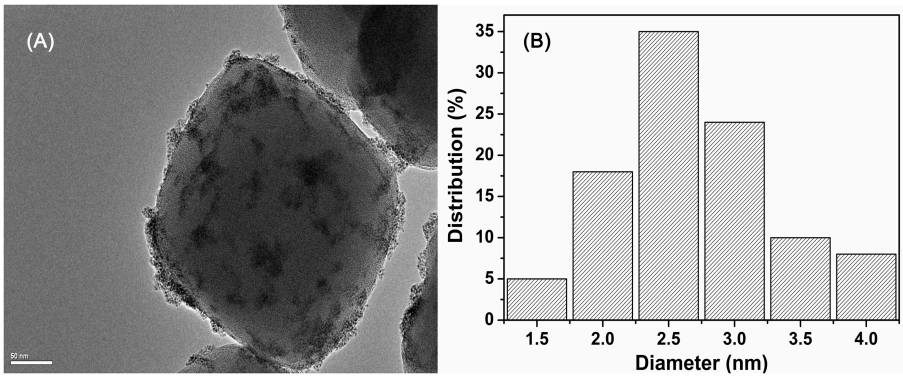

FIGURE 5 | TEM image of 2.0% Ru/11.7% SiW@UiO−66 **(A)** and the corresponding size distribution plot of Ru NPs **(B)**.

the subsequent lactonization steps for the transformation of ML to GVL were significantly influenced by the reaction temperature, and MHV was produced as the intermediate. Furthermore, a stoichiometric equivalent amount of methanol to GVL was also obtained. As expected, both the conversion rate of ML and the generation rate of GVL were slow at 60°C. When the temperature increased to 100°C, the transformation rate increased distinctly. When ML was completely consumed, the concentration of MHV decreased gradually with a marginal increase in the GVL yield, thus indicating that the hydrogenation of ML to yield MHV was much easier than the transesterification of MHV to GVL at low temperatures (Lin et al., 2018). These results confirm that conversion of ML to GVL is a tandem reaction, and requires both metal and acid functionalities to work cooperatively (Nadgeri et al., 2014; Kuwahara et al., 2015). The transformation of the intermediate MHV to yield the final GVL product is probably the rate controlling step in this tandem reaction (Negahdar et al., 2017). Moreover, if **Figure 6B** is considered as an

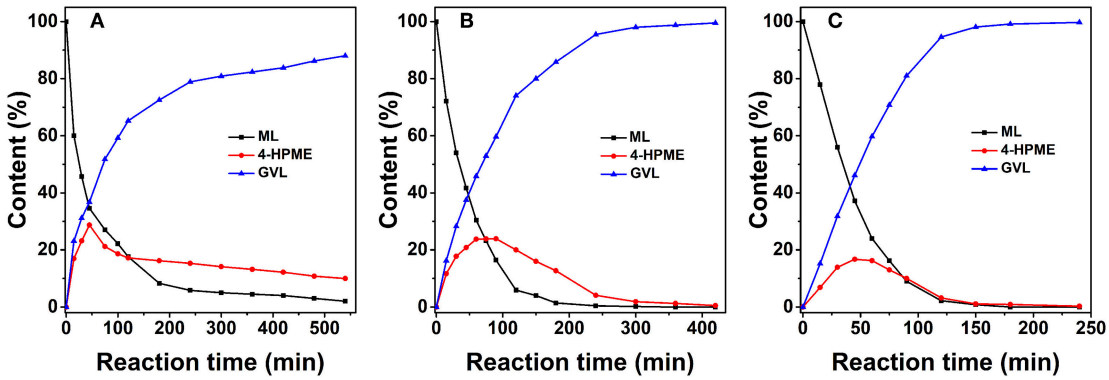

FIGURE 6 | Concentration evolution profiles of ML, MHV, and GVL vs. time for 2.0% Ru/11.7% SiW@UiO−66 at 60°C **(A)**, 80°C **(B)**, and 100°C **(C)**. Reaction conditions: 0.257 g of ML, 50 mg of catalyst, 15 mL of H_2O, and a H_2 pressure of 0.5 MPa.

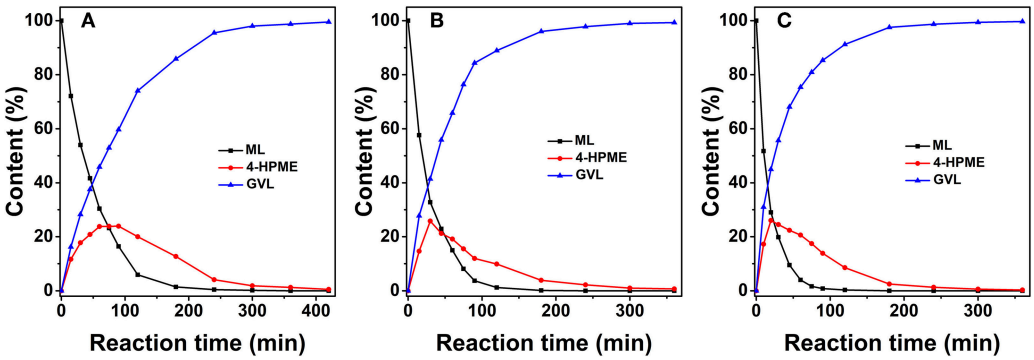

FIGURE 7 | Concentration evolution profiles of ML, MHV, and GVL vs. time over 2.0% Ru/11.7% SiW@UiO−66 at a H_2 pressure of 0.5 MPa **(A)**, 1.0 MPa **(B)**, and 1.5 MPa **(C)**. Reaction conditions: 0.257 g of ML, 50 mg of catalyst, 15 mL of H_2O, and a temperature of 80°C.

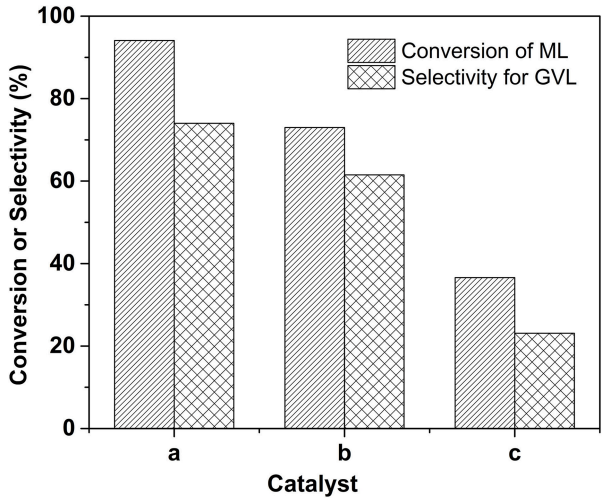

FIGURE 8 | Comparison of conversion and selectivity for various catalysts. Reaction conditions: 0.257 g of ML, 50 mg of 2.0% Ru/11.7% SiW@UiO−66 for case a; 5 mg of SiW + 50 mg of 2.0% Ru/UiO−66 for case b; 50 mg of 2.0% Ru/UiO−66 for case c, 15 mL of H_2O, 80°C, 0.5 MPa H_2, during a 120 min reaction period.

example, the transformation is shown to be accompanied by a rapid decrease in the concentration of ML and an increase in MHV in the first 75 min. As the reaction progressed, the intramolecular de-alcoholization of MHV to GVL proceeded rapidly. These results consistently prove that the ML-to-GVL over the 2.0% Ru/11.7% SiW@UiO−66 catalyst followed the procedure shown in **Scheme 1**. Importantly, it should be stated that 100% ML conversion with exclusive selectivity for GVL were achieved over the 2.0% Ru/11.7% SiW@UiO−66 catalyst within 360 min when the reaction was performed at 80°C and at a hydrogen pressure of 0.5 MPa. Additionally, no further by-product was formed even when the reaction time was extended to 520 min.

The influence of the H_2 pressure on the reactant and product distributions as a function of reaction time over 2.0% Ru/11.7% SiW@UiO−66 is presented in **Figure 7**. As expected, the dissolved hydrogen in the reaction solution would increase when the H_2 pressure in the reactor increases. Therefore, the hydrogenation of ML to MHV would be remarkably enhanced. Moreover, the lactonization of MHV to GVL is proportional with respect to the concentration of MHV, and can be accelerated by the Brønsted acid sites in the catalyst (Hao et al., 2018). Therefore,

the overall catalytic activity and selectivity of ML to GVL was essentially improved as the H_2 pressure increased.

To demonstrate the indispensable role of acid sites incorporated within the catalyst, the concentration evolution profiles over two controlled catalysts were also monitored under the identical reaction conditions, as displayed in **Figures S5,S6**. Overall, the catalytic activities over these two catalysts are lower than that of the 2.0% Ru/11.7% SiW@UiO−66 catalyst. For a more intuitive comparison, the catalytic results over 2.0% Ru/11.7% SiW@UiO−66, 2.0% Ru/UiO−66, and physical mixture of SiW and 2.0% Ru/UiO−66 under 80°C and 0.5 MP H_2 pressure for a duration of 120 min were extracted (**Figure 8**). Notably, in the presence of 2.0% Ru/11.7% SiW@UiO−66, satisfactory results for the sequential hydrogenation and the subsequent lactonization reaction were achieved, with a 94.1% conversion of ML and a 74% selectivity for the GVL product. In contrast, in the presence of the 2.0% Ru/UiO−66 catalyst, a rather low catalytic activity and selectivity were obtained when the reaction was performed under the same conditions. This is probably owing to the lower acid content of the UiO−66 as compared to that of the SiW@UiO−66 support (see **Table 1**). It has been reported that the Brønsted acid sites were likely used to cooperatively catalyze sequential hydrogenation and lactonization with the active metal counterpart (Lin et al., 2017). To test this hypothesis, the native 2.0% Ru/UiO−66 was physically mixed with SiW that contained Brønsted acid sites. This reaction elicited moderate improvement regarding the ML-to-GVL activity compared to 2.0% Ru/11.7% SiW@UiO−66. We deduced that the (1) Brønsted acid sites that originated from the SiW molecules were efficient for C–O scission and could dramatically accelerate the transesterification of MHV to generate GVL, and (2) the acids sites should be in close proximity to metal sites for synergetic catalysis. In addition to the activation of the lactonization step, the Brønsted acid sites also likely contributed to the promotion of ML hydrogenation, thus confirming that 2.0% Ru/11.7% SiW@UiO−66 improved the activity in the upgrade of ML to GVL based on a bifunctional way.

Furthermore, representative results for catalytic conversion of ML to GVL by heterogeneous catalysts reported in the literature were compared with our catalyst, and these data were listed in **Table S1**. Due to the different reaction conditions for these works, it is difficult to compare the catalytic activity directly. Considering that the catalytic reaction was performed under a relative mild condition in the current study, and the 2.0% Ru/11.7% SiW@UiO-66 catalyst exhibited a relatively higher catalytic performance, the comparison tentative demonstrates that the developed catalyst is among the best of candidates ever reported on Ru-based heterogeneous catalysts as far as we know.

To elucidate the efficiency of 2.0% Ru/11.7% SiW@UiO−66 as a bifunctional catalyst, kinetic studies were performed when the internal and external transport limitations were eliminated according to a similar procedure described in our previous work (Lin et al., 2018). As demonstrated in **Figure 9**, the evolution of reactant concentrations at the evaluated temperatures can be best fitted using the following equations,

$$\frac{dC_{ML}}{dt} = -k_1 C_{ML} \quad (1)$$

$$\frac{dC_{MHV}}{dt} = k_1 C_{ML} - k_2 C_{MHV} \quad (2)$$

$$\frac{dC_{GVL}}{dt} = k_2 C_{MHV} \quad (3)$$

where C_i represents the concentration of the component and $k_i$is the reaction rate coefficient. As listed in **Table 2**, the rate constant of the lactonization step is smaller than that of the hydrogenation step, thus indicating that lactonization is the rate-determining step and controls the overall reaction rate. Subsequently, the activation energy barrier is calculated according to the Arrhenius equation: $k = A \times \exp(-Ea/RT)$ (k: the aforementioned reaction rate coefficient, A: pre-exponential

TABLE 2 | Kinetic parameters of 2.0% Ru/11.7% SiW@UiO−66 in the upgrade of ML to GVL.

T (°C)	40	60	80	*Ea* (KJ/mol)	R^2
k_1 (10^{-2}/min)	2.78	4.85	8.60	26.1	0.99
k_2 (10^{-2}/min)	0.95	2.60	7.85	48.8	0.99

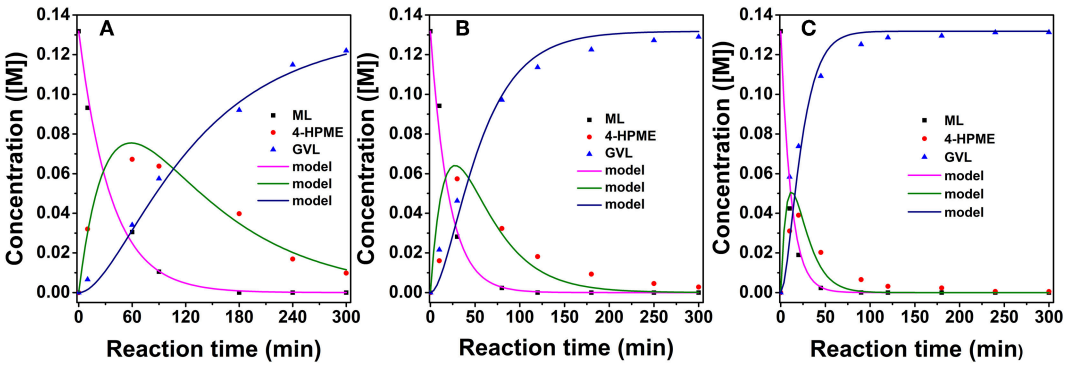

FIGURE 9 | Experimental data fitting at 40°C **(A)**, 60°C **(B)**, and 80°C **(C)** for 2.0% Ru/11.7% SiW@UiO−66. Reaction conditions: 0.257 g of ML, 50 mg of catalyst, 15 mL of H_2O, and an H_2 pressure of 2.0 MPa.

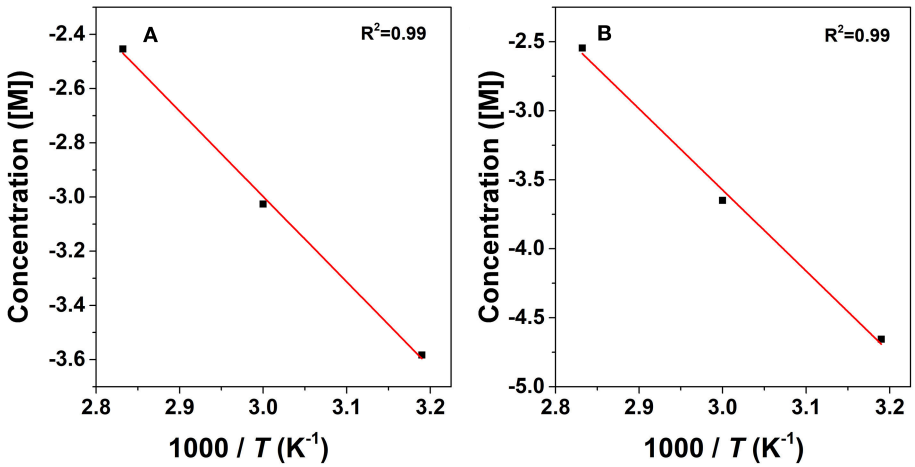

FIGURE 10 | Arrhenius plots for the conversion of ML to GVL: hydrogenation step **(A)** and transesterification step **(B)**.

factor, *Ea*: activation energy, *R*: gas constant, and *T*: reaction temperature). **Figure 10** shows the linear regression of ln*k* vs. 1/*T* for which the estimated slope is –*Ea/R*. The estimated activation energy for hydrogenation is 26.1 kJ/mol and that for lactonization is 48.8 kJ/mol (**Table 2**), which are much lower than the previously reported values for the aqueous hydrogenation of ML to GVL over Ru/C (41 kJ/mol for the hydrogenation and 50 kJ/mol for the lactonization) (Negahdar et al., 2017). This further indicates the advantages of integrating metal and acid sites within single MOF nanocrocrystals, that is, upon the intrinsic cooperation of the active sites, the energy barrier is reduced, thus facilitating the catalytic conversion of ML into GVL.

The durability of the prepared 2.0% Ru/11.7% SiW@UiO−66 was further evaluated. As shown in **Figure 11**, both ML conversion and GVL selectivity were well-maintained after the catalyst was repetitively used for five successive cycles, thus demonstrating its excellent reusability capacity. Regarding the recovered catalyst, no changes in the crystalline structure, composition, or textural properties, have been noted as compared to the fresh one (**Figures 1**–**3**, **Figure S7**), thus confirming its excellent stability. Moreover, based on the ICP–AES and TEM results of the catalyst after usage (**Figure S8**), 2.0% Ru/11.7% SiW@UiO−66 exhibited good resistance to the leaching and sintering of POM species and Ru NPs, which was probably due to the fact that SiW molecules were well-confined by the MOF cavities and Ru NPs embedded and stabilized by the local defect sites of UiO−66 (Miras et al., 2014). These results indicate that the developed 2.0% Ru/11.7% SiW@UiO−66 may be a promising catalyst for other reactions that require both metal and acid sites to work cooperatively.

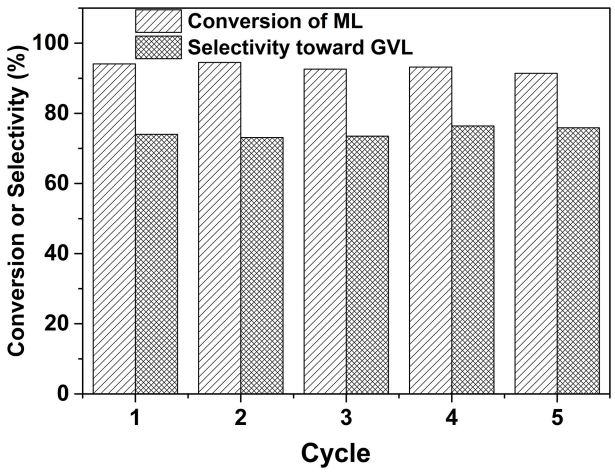

FIGURE 11 | Durability test of 2.0% Ru/11.7% SiW@UiO−66 for the conversion of ML to GVL. Reaction conditions: 0.257 g of ML, 50 mg of catalyst, 15 mL of H_2O, 80°C, an H_2 pressure of 0.5 MPa H_2, within a reaction period of 120 min.

CONCLUSIONS

In summary, we designed and prepared a MOF-based metal and acid bifunctional hybrid as an efficient heterogeneous catalyst for the upgrade of ML to produce valuable GVL under mild reaction conditions. The developed 2.0% Ru/11.7% SiW@UiO−66 catalyst exhibited high catalytic activity and high selectivity in the successive hydrogenation and lactonization steps, and it was proved that it could be repeatedly used for five times without any loss in activity and selectivity. The increased catalytic performance of the 2.0% Ru/11.7% SiW@UiO−66 catalyst was principally originated in the cooperative effect between the Ru NPs and Brønsted acid sites. These sites were appropriately spatially separated within a single UiO−66 crystal, and provided the active sites where the hybrid could catalyze the hydrogenation of ML to produce the intermediate MHV and the successive intramolecular de-alcoholization to form GVL. A kinetics study further demonstrated that the encapsulation of the SiW molecules within the UiO−66 cavities was favorable for

the hydrogenation and lactonization stepsa property likely to be attributed to their Brønsted acidity properties.

AUTHOR CONTRIBUTIONS

XC conceived the idea, proposed the strategy, designed and performed the experiment, analyzed the results, and wrote the manuscript. QX and YF helped with the catalyst evaluation and corresponding data analysis and discussions. GT, FZ, and WZ supervised the project, helped design the experiments, evaluated the data, and wrote the manuscript. The results of the manuscript were discussed by all authors.

ACKNOWLEDGMENTS

Financial supports from the National Natural Science Foundation of China (No. 21576243), and Zhejiang Provincial Natural Science Foundation of China (Nos. LY18B060006 and LY18B030006) are appreciated greatly.

SUPPLEMENTARY MATERIAL

The Supplementary Material for this article can be found online at: https://www.frontiersin.org/articles/10.3389/fchem.2019.00042/full#supplementary-material

REFERENCES

Abdelrahman, O. A., Heyden, A., and Bond, J. Q. (2014). Analysis of kinetics and reaction pathways in the aqueous-phase hydrogenation of levulinic acid to form γ-valerolactone over Ru/C. *ACS Catal.* 4, 1171–1181. doi: 10.1021/cs401177p

Albani, D., Li, Q., Vilé, G., Mitchell, S., Almora-Barrios, N., Witte, P. T., et al. (2017). Interfacial acidity in ligand-modified ruthenium nanoparticles boosts the hydrogenation of levulinic acid to γ-valerolactone. *Green Chem.* 19, 2361–2370. doi: 10.1039/C6GC02586B

Alonso, D. M., Wettstein, S. G., and Dumesic, J. A. (2012). Bimetallic catalysts for upgrading of biomass to fuels and chemicals. *Chem. Soc. Rev.* 41, 8075–8098. doi: 10.1039/c2cs35188a

Bai, Y., Dou, Y., Xie, L. H., Rutledge, W., Li, J. R., and Zhou, H. C. (2016). Zr-based metal-organic frameworks: design, synthesis, structure, and applications. *Chem. Soc. Rev.* 45, 2327–2367. doi: 10.1039/C5CS00837A

Berry, F. J., Derrick, G. R., Marco, J. F., and Mortimer, M. (2009). Silica-supported silicotungstic acid: a study by X-ray photoelectron spectroscopy. *Mater. Chem. Phys.* 114, 1000–1003. doi: 10.1016/j.matchemphys.2008.11.003

Buru, C. T., Li, P., Mehdi, B. L., Dohnalkova, A., Platero-Prats, A. E., Browning, N. D., et al. (2017). Adsorption of a catalytically accessible polyoxometalate in a mesoporous channel-type metal–organic framework. *Chem. Mater.* 29, 5174–5181. doi: 10.1021/acs.chemmater.7b00750

Buru, C. T., Platero-Prats, A. E., Chica, D. G., Kanatzidis, M. G., Chapman, K. W., and Farha, O. K. (2018). Thermally induced migration of a polyoxometalate within a metal–organic framework and its catalytic effects. *J. Mater. Chem. A* 6, 7389–7394. doi: 10.1039/C8TA02562B

Cavka, J. H., Jakobsen, S., Olsbye, U., Guillou, N., Lamberti, C., Bordiga, S., et al. (2008). A new zirconium inorganic building brick forming metal organic frameworks with exceptional stability. *J. Am. Chem. Soc.* 130, 13850–13851. doi: 10.1021/ja8057953

Chen, L., Luque, R., and Li, Y. (2017). Controllable design of tunable nanostructures inside metal-organic frameworks. *Chem. Soc. Rev.* 46, 4614–4630. doi: 10.1039/C6CS00537C

Du, D. Y., Qin, J. S., Li, S. L., Su, Z. M., and Lan, Y. Q. (2014). Recent advances in porous polyoxometalate-based metal–organic framework materials. *Chem. Soc. Rev.* 43, 4615–4632. doi: 10.1039/C3CS60404G

Du, X. L., Bi, Q. Y., Liu, Y. M., Cao, Y., and Fan, K. N. (2011). Conversion of biomass-derived levulinate and formate esters into γ-valerolactone over supported gold catalysts. *ChemSusChem* 4, 1838–1843. doi: 10.1002/cssc.201100483

Furukawa, H., Cordova, K. E., O'Keeffe, M., and Yaghi, O. M. (2013). The chemistry and applications of metal-organic frameworks. *Science* 341:1230444. doi: 10.1126/science.1230444

Furukawa, H., Gándara, F., Zhang, Y. B., Jiang, J., Queen, W. L., Hudson, M. R., et al. (2014). Water adsorption in porous metal-organic frameworks and related materials. *J. Am. Chem. Soc.* 136, 4369–4381. doi: 10.1021/ja500330a

Galletti, A. M. R., Antonetti, C., and De Luise, V., Martinelli, M. (2012). A sustainable process for the production of γ-valerolactone by hydrogenation of biomass-derived levulinic acid. *Green Chem.* 14, 688–694. doi: 10.1039/c2gc15872h

Guo, Z. Y., Xiao, C. X., Maligal-Ganesh, R. V., Zhou, L., Goh, T. W., Li, X. L., et al. (2014). Pt Nanoclusters confined within metal organic framework cavities for chemoselective cinnamaldehyde hydrogenation. *ACS Catal.* 4, 1340–1348. doi: 10.1021/cs400982n

Hao, P., Schwartz, D. K., and Medlin, J. W. (2018). Phosphonic acid promotion of supported Pd catalysts for low temperature vanillin hydrodeoxygenation in ethanol. *Appl. Catal. A Gen.* 561, 1–6. doi: 10.1016/j.apcata.2018.05.008

Hengst, K., Ligthart, D. A. J. M., Doronkin, D. E., Walter, K. M., Kleist, W., Hensen, E. J. M., et al. (2017). Continuous synthesis of γ-valerolactone in a trickle-bed reactor over supported nickel catalysts. *Ind. Eng. Chem. Res.* 56, 2680–2689. doi: 10.1021/acs.iecr.6b03493

Jiao, L., Wang, Y., Jiang, H. L., and Xu, Q. (2017). Metal-organic frameworks as platforms for catalytic applications. *Adv. Mater.* 30:e1703663. doi: 10.1002/adma.201703663

Kadu, B. S., Hengne, A. M., Biradar, N. S., Rode, C. V., and Chikate, R. C. (2016). Reductive cyclization of levulinic acid to γ-valerolactone over non-noble bimetallic nanocomposite. *Ind. Eng. Chem. Res.* 55, 13032–13039. doi: 10.1021/acs.iecr.6b03900

Kandiah, M., Nilsen, M. H., Usseglio, S., Jakobsen, S., Olsbye, U., Tilset, M., et al. (2010). Synthesis and stability of tagged UiO-66 Zr-MOFs. *Chem. Mater.* 22, 6632–6640. doi: 10.1021/cm102601v

Kondeboina, M., Enumula, S. S., Gurram, V. R. B., Chada, R. R., Burri, D. R., and Kamaraju, S. R. R. (2018). Selective hydrogenation of biomass-derived ethyl levulinate to γ-valerolactone over supported Co catalysts in continuous process at atmospheric pressure. *J. Ind. Eng. Chem.* 61, 227–235. doi: 10.1016/j.jiec.2017.12.020

Kuwahara, Y., Magatani, Y., and Yamashita, H. (2015). Ru nanoparticles confined in Zr-containing spherical mesoporous silica containers for hydrogenation of levulinic acid and its esters into γ-valerolactone at ambient conditions. *Catal. Today* 258, 262–269. doi: 10.1016/j.cattod.2015.01.015

Li, F., Li, Z., France, L. J., Mu, J., Song, C., Chen, Y., et al. (2018). Highly efficient transfer hydrogenation of levulinate esters to γ-valerolactone over basic zirconium carbonate. *Ind. Eng. Chem. Res.* 57, 10126–10136. doi: 10.1021/acs.iecr.8b00712

Liguori, F., Moreno-Marrodan, C., and Barbaro, P. (2015). Environmentally friendly synthesis of γ-valerolactone by direct catalytic conversion of renewable sources. *ACS Catal.* 5, 1882–1894. doi: 10.1021/cs501922e

Lin, Z., Cai, X., Fu, Y., Zhu, W., and Zhang, F. (2017). Cascade catalytic hydrogenation-cyclization of methyl levulinate to form γ-valerolactone over Ru nanoparticles supported on a sulfonic acid-functionalized UiO-66 catalyst. *RSC Adv.* 7, 44082–44088. doi: 10.1039/C7RA06293A

Lin, Z., Luo, M., Zhang, Y., Wu, X., Fu, Y., Zhang, F., et al. (2018). Coupling Ru nanoparticles and sulfonic acid moieties on single MIL-101 microcrystals for upgrading methyl levulinate into γ-valerolactone. *Appl. Catal. A Gen.* 563, 54–63. doi: 10.1016/j.apcata.2018.06.027

Liu, H., Chang, L., Bai, C., Chen, L., Luque, R., and Li, Y. (2016). Controllable encapsulation of "clean" metal clusters within mofs through

kinetic modulation: towards advanced heterogeneous nanocatalysts. *Angew. Chem. Int. Ed.* 55, 5019–5023. doi: 10.1002/anie.201511009

Ma, L., Abney, C., and Lin, W. (2009). Enantioselective catalysis with homochiral metal-organic frameworks. *Chem. Soc. Rev.* 38, 1248–1256. doi: 10.1039/b807083k

Michel, C., and Gallezot, P. (2015). Why is ruthenium an efficient catalyst for the aqueous-phase hydrogenation of biosourced carbonyl compounds? *ACS Catal.* 5, 4130–4132. doi: 10.1021/acscatal.5b00707

Miras, H. N., Vilà-Nadal, L., and Cronin, L. (2014). Polyoxometalate based open-frameworks (POM-OFs). *Chem. Soc. Rev.* 43, 5679–5699. doi: 10.1039/C4CS00097H

Moreno-Marrodan, C., and Barbaro, P. (2014). Energy efficient continuous production of γ-valerolactone by bifunctional metal/acid catalysis in one pot. *Green Chem.* 16, 3434–3438. doi: 10.1039/c4gc00298a

Na, K., Choi, K. M., Yaghi, O. M., and Somorjai, G. A. (2014). Metal nanocrystals embedded in single nanocrystals of MOFs give unusual selectivity as heterogeneous catalysts. *NANO Lett.* 14, 5979–5983. doi: 10.1021/nl503007h

Nadgeri, J. M., Hiyoshi, N., Yamaguchi, A., Sato, O., and Shirai, M. (2014). Liquid phase hydrogenation of methyl levulinate over the mixture of supported ruthenium catalyst and zeolite in water. *Appl. Catal. A Gen.* 470, 215–220. doi: 10.1016/j.apcata.2013.10.059

Negahdar, L., Al-Shaal, M. G., Holzhäuser, F. J., and Palkovits, R. (2017). Kinetic analysis of the catalytic hydrogenation of alkyl levulinates to γ-valerolactone. *Chem. Eng. Sci.* 158, 545–551. doi: 10.1016/j.ces.2016.11.007

Rajkumar, T., and Ranga Rao, G. (2008). Synthesis and characterization of hybrid molecular material prepared by ionic liquid and silicotungstic acid. *Mater. Chem. Phys.* 112, 853–857. doi: 10.1016/j.matchemphys.2008.06.046

Rojas-Buzo, S., García-García, P., Corma, A. (2018). Catalytic transfer hydrogenation of biomass-derived carbonyls over hafnium-based metal-organic frameworks. *ChemSusChem* 11, 432–438. doi: 10.1002/cssc.201701708

Serrano-Ruiz, J. C., Luque, R., and Sepúlveda-Escribano, A. (2011). Transformations of biomass-derived platform molecules: from high added-value chemicals to fuels via aqueous-phase processing. *Chem. Soc. Rev.* 40, 5266–5281. doi: 10.1039/c1cs15131b

Stock, N., and Biswas, S. (2012). Synthesis of metal-organic frameworks (MOFs): routes to various MOF topologies, morphologies, and composites. *Chem. Rev.* 112, 933–969. doi: 10.1021/cr200304e

Tan, J., Cui, J., Deng, T., Cui, X., Ding, G., Zhu, Y., et al. (2015). Water-promoted hydrogenation of levulinic acid to γ-valerolactone on supported ruthenium catalyst. *ChemCatChem* 7, 508–512. doi: 10.1002/cctc.201402834

Tang, X., Chen, H., Hu, L., Hao, W., Sun, Y., Zeng, X., et al. (2014). Conversion of biomass to γ-valerolactone by catalytic transfer hydrogenation of ethyl levulinate over metal hydroxides. *Appl. Catal. B Environ.* 147, 827–834. doi: 10.1016/j.apcatb.2013.10.021

Ullah, L., Zhao, G., Xu, Z., He, H., Usman, M., and Zhang, S. (2018). 12-Tungstophosphoric acid niched in Zr-based metal-organic framework: a stable and efficient catalyst for Friedel-Crafts acylation. *Sci. China Chem.* 61, 402–411. doi: 10.1007/s11426-017-9182-0

Wang, Y., Rong, Z., Wang, Y., Wang, T., Du, Q., Wang, Y., et al. (2018). Graphene-based metal/acid bifunctional catalyst for the conversion of levulinic acid to γ-valerolactone. *ACS Sustain. Chem. Eng.* 5, 1538–1548. doi: 10.1021/acssuschemeng.6b02244

Winoto, H. P., Ahn, B. S., and Jae, J. (2016). Production of γ-valerolactone from furfural by a single-step process using Sn-Al-Beta zeolites: optimizing the catalyst acid properties and process conditions. *J. Ind. Eng. Chem.* 40, 62–71. doi: 10.1016/j.jiec.2016.06.007

Wright, W. R., and Palkovits, R. (2012). Development of heterogeneous catalysts for the conversion of levulinic acid to γ-valerolactone. *ChemSusChem* 5, 1657–1667. doi: 10.1002/cssc.201200111

Wu, H., Chua, Y. S., Krungleviciute, V., Tyagi, M., Chen, P., Yildirim, T., et al. (2013). Unusual and highly tunable missing-linker defects in zirconium metal–organic framework UiO-66 and their important effects on gas adsorption. *J. Am. Chem. Soc.* 135, 10525–10532. doi: 10.1021/ja404514r

Xiao, C., Goh, T. W., Qi, Z., Goes, S., Brashler, K., Perez, C., et al. (2016). Conversion of levulinic acid to γ-valerolactone over few-layer graphene-supported ruthenium catalysts. *ACS Catal.* 6, 593–599. doi: 10.1021/acscatal.5b02673

Yan, K., Yang, Y., Chai, J., and Lu, Y. (2015). Catalytic reactions of γ-valerolactone: a platform to fuels and value-added chemicals. *Appl. Catal. B Environ.* 179, 292–304. doi: 10.1016/j.apcatb.2015.04.030

Yang, D., Odoh, S. O., Wang, T. C., Farha, O. K., Hupp, J. T., Cramer, C. J., et al. (2015a). Metal-organic framework nodes as nearly ideal supports for molecular catalysts: NU-1000-and UiO-66-supported iridium complexes. *J. Am. Chem. Soc.* 137, 7391–7396. doi: 10.1021/jacs.5b02956

Yang, H., and Wang, X. (2018). Secondary-component incorporated hollow MOFs and derivatives for catalytic and energy-related applications. *Adv. Mater.* doi: 10.1002/adma.201800743. [Epub ahead of print].

Yang, X. L., Qiao, L. M., and Dai, W. L. (2015b). Phosphotungstic acid encapsulated in metal-organic framework UiO-66: An effective catalyst for the selective oxidation of cyclopentene to glutaraldehyde. *Micropor. Mesopor. Mater.* 211, 73–81. doi: 10.1016/j.micromeso.2015.02.035

Ye, F., Zhang, D., Xue, T., Wang, Y., and Guan, Y. (2014). Enhanced hydrogenation of ethyl levulinate by Pd-AC doped with Nb_2O_5. *Green Chem.* 16, 3951–3957. doi: 10.1039/C4GC00972J

Zeng, H., Newkome, G. R., and Hill, C. L. (2000). Poly (polyoxometalate) dendrimers: molecular prototypes of new catalytic materials. *Angew. Chem. Int. Ed.* 39, 1771–1774. doi: 10.1002/(SICI)1521-3773(20000515)39:10<1771::AID-ANIE1771>3.0.CO;2-D

Zhang, F., Jin, Y., Shi, J., Zhong, Y., Zhu, W., and El-Shall, M. S. (2015a). Polyoxometalates confined in the mesoporous cages of metal–organic framework MIL-100(Fe): efficient heterogeneous catalysts for esterification and acetalization reactions. *Chem. Eng. J.* 269, 236–244. doi: 10.1016/j.cej.2015.01.092

Zhang, W., Meng, T., Tang, J., Zhuang, W., Zhou, Y., and Wang, J. (2017). Direct synthesis of 2,5-diformylfuran from carbohydrates using high-silica MOR zeolite-supported isolated vanadium species. *ACS Sustain. Chem. Eng.* 5, 10029–10037. doi: 10.1021/acssuschemeng.7b02002

Zhang, X., Wilson, K., and Lee, A. F. (2016). Heterogeneously catalyzed hydrothermal processing of C_5-C_6 sugars. *Chem. Rev.* 116, 12328–12368. doi: 10.1021/acs.chemrev.6b00311

Zhang, Z. M., Zhang, T., Wang, C., Lin, Z., Long, L. S., and Lin, W. (2015b). Photosensitizing metal-organic framework enabling visible-light-driven proton reduction by a Wells-Dawson-type polyoxometalate. *J. Am. Chem. Soc.* 137, 3197–3200. doi: 10.1021/jacs.5b00075

Zhao, M., Yuan, K., Wang, Y., Li, G., Guo, J., Gu, L., et al. (2016). Metal-organic frameworks as selectivity regulators for hydrogenation reactions. *Nature* 539:76. doi: 10.1038/nature19763

Zhou, Y., Chen, G., Long, Z., and Wang, J. (2014). Recent advances in polyoxometalate-based heterogeneous catalytic materials for liquid-phase organic transformations. *RSC Adv.* 4, 42092–42113. doi: 10.1039/C4RA05175K

Conflict of Interest Statement: The authors declare that the research was conducted in the absence of any commercial or financial relationships that could be construed as a potential conflict of interest.

frontiers in Chemistry

REVIEW
published: 14 May 2019
doi: 10.3389/fchem.2019.00296

Gold-Catalyzed Homogeneous (Cyclo)Isomerization Reactions

Marta Marín-Luna, Olalla Nieto Faza and Carlos Silva López**

Departamento de Química Orgánica, Universidade de Vigo, Vigo, Spain

Gold is currently one of the most used metals in organometallic catalysis. The ability of gold to activate unsaturated groups in different modes, together with its tolerance to a wide range of functional groups and reaction conditions, turns gold-based complexes into efficient and highly sought after catalysts. Natural products and relevant compounds with biological and pharmaceutical activity are often characterized by complex molecular structures. (Cyclo)isomerization reactions are often a useful strategy for the generation of this molecular complexity from synthetically accessible reactants. In this review, we collect the most recent contributions in which gold(I)- and/or gold(III)-catalysts mediate intramolecular (cyclo)isomerization transformations of unsaturated species, which commonly feature allene or alkyne motifs, and organize them depending on the substrate and the reaction type.

Keywords: gold, catalysis, isomerization, allenes, 1, *n*-enynes, 1, *n*-diynes

OPEN ACCESS

Edited by:
Hadi Nur,
University of Technology Malaysia, Malaysia

Reviewed by:
Pedro Almendros,
Spanish National Research Council (CSIC), Spain
Tomoo Mizugaki,
Osaka University, Japan

****Correspondence:***
Marta Marín-Luna
mmarin@uvigo.es
Carlos Silva López
carlos.silva@uvigo.es

Specialty section:
This article was submitted to Catalysis and Photocatalysis, a section of the journal Frontiers in Chemistry

Received: *20 February 2019*
Accepted: *11 April 2019*
Published: *14 May 2019*

Citation:
Marín-Luna M, Nieto Faza O and Silva López C (2019) Gold-Catalyzed Homogeneous (Cyclo)Isomerization Reactions. Front. Chem. 7:296. doi: 10.3389/fchem.2019.00296

1. INTRODUCTION

Historically, most civilizations have considered gold as synonym of power, purity, beauty and wealth. In contrast, for a long time, gold was chemically ignored and misconceived as an inert element. It was only at the end of the twentieth century and the beginning of the twenty first when a "gold rush" in synthesis started with the publication of the original works of Fukuda (Fukuda and Utimoto, 1991), Teles (Teles et al., 1998), and Tanaka (Mizushima et al., 2002) on the homogeneous gold-catalyzed addition of water and alcohol to alkynes. The seminal contributions that sparked the interest in gold catalysis in the ending years of the twentieth century were due to Hashmi et al. who showed the catalytic reactivity of $AuCl^3$ on cycloisomerization reactions of alkyne-based compounds leading to furans and arenes (Hashmi et al., 2000; Stephen et al., 2000). Since then the interest on this metal has increased notably as revealed by the vast number of publications on gold catalysis[1]. Located in group 11 of the periodic table, gold behaves as a soft carbophilic Lewis acid with the ability to stabilize an adjacent carbocation through back-donation. Relativistic effects in this atom promote the contraction of its *6s* orbital, which becomes the main reason for this relatively uncommon behavior across the periodic table (Gorin and Toste, 2007; Faza and López, 2015). Nevertheless, gold complexes are usually poorly-reactive in their precatalytic state and they need prior transformation *in-situ*, most commonly through the abstraction of one ligand, generally a chloride group. Among others, silver salts are the most used agents for this purpose (Ranieri et al., 2015). Furthermore, both the electronic nature of ligands (Wang et al., 2012; Ebule et al., 2016; Gung et al., 2016; Ferrer and Echavarren, 2018a) and of the counterion (Homs et al., 2014; Ciancaleoni et al., 2015; Jia and Bandini, 2015; Rocchigiani et al., 2015; Gatto et al., 2016; Yuan et al., 2018; Schießl et al., 2018a,b) have a significant influence on the reactivity of the gold-catalyzed processes.

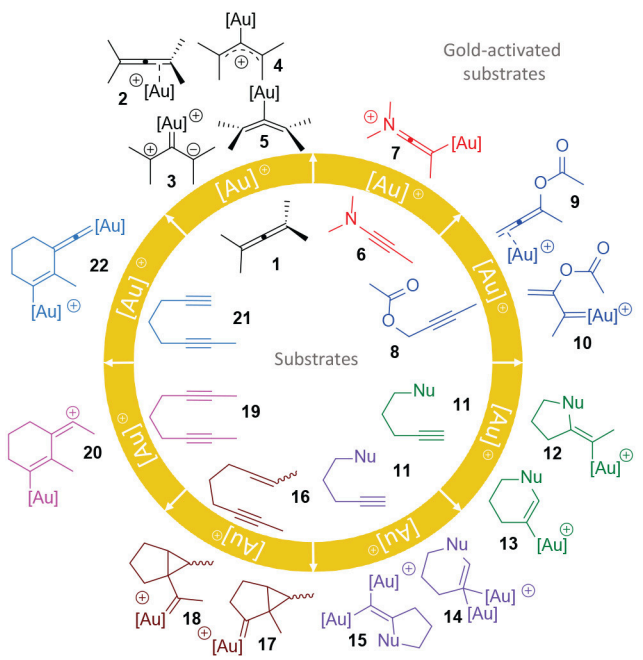

FIGURE 1 | Gold activation reaction patterns toward different unsaturated substrates.

Thus, gold(I)- and gold(III)-complexes are mostly intended for the activation of unsaturated groups, such as allene and alkyne derivatives (Jones, 2015; Blons et al., 2018). **Figure 1** shows the possible activation modes exerted by a generic cationic gold complex $[Au]^+$ toward common starting materials which will be the subject of revision in this report. Four possibilities have been described for the coordination of gold to an allene moiety **1**: η^2-coordinated complexes (**2**), zwitterionic carbenes (**3**), σ-allylic cations (**4**) or η^1-coordinated bent allenes (**5**) (Soriano and Fernández, 2014). Cumulenic derivatives could also be formed under gold activation. The π-coordination of gold to the alkyne group of an ynamide substrate **6** promotes the formation of an electrophilic keteniminium ion **7** susceptible to a nucleophilic attack. Propargylic carbonate/ester substrates **8** are prone to rearrange under gold-catalysis, usually trough a 1,3- or 1,2-migration of the carbonate/ester group over the π-system toward either the allene intermediate **9** or the gold-carbene **10**, respectively (Ghosh et al., 2014; Swift and Gronert, 2016). Alkynes containing and internal nucleophilic functional group **11** can cyclize either in an *exo-dig* or *endo-dig* fashion leading to **12** and **13**. Otherwise, it is possible that two gold complexes coordinate simultaneously to the terminal alkyne **11** forming a σ,π-digold alkyne and then furnishing intermediates **14** and **15** (Cheong et al., 2008; Larsen et al., 2015). Cyclopropane gold carbene-like intermediates **17** and **18** are, respectively, achieved through an *endo-dig* and an *exo-dig* carbocyclization of the enyne **16** (Obradors and Echavarren, 2014). Two internal alkynes placed in an diyne **19** can react onto each other under gold-π-activation forming a conjugated vinyl cation intermediate **20**. Recently, the possibility of dual gold-activation has started to garner attention. It is a reactivity pattern for diyne systems, in which one gold center simultaneously enhances the nucleophilic character of the terminal alkyne trough a σ-bond while a second gold center turns the other alkyne motif more electrophilic trough a classical π-coordination (Cheong et al., 2008; Odabachian et al., 2009; Stephen et al., 2012; Ye et al., 2012; Hashmi, 2014). This reactivity is represented in the transformation of dyine **21** toward intermediate **22**. The diversity in the activation patterns shown by gold opens a large window of possibilities for the use of this metal as a powerful tool in the design and synthesis of relevant compounds in different fields. In fact, an increasing number of structurally complex molecules, such as natural products, biologically active compounds or polycyclic systems are reachable from synthetically accessible alkyne, alkene and allene reagents under metal-mediated isomerization process (Aubert et al., 2011; Yamamoto, 2012; Zhang et al., 2012; Stathakis et al., 2016; Hu et al., 2017; Herndon, 2018). In this sense, gold shines over other metals mostly due to its tolerance to diverse functional groups, low toxicity and the usually mild thermal conditions that are required to run these kind of transformations, in some occasions even showing tolerance to aqueous media or green solvents (Gatto et al., 2018).

This review focuses on homogeneous gold-mediated intramolecular (cyclo)isomerizations without the direct intervention of external agents in the intermediate mechanistic steps, except water in some unavoidable cases. It is organized according to both the kind of substrates to be activated by the gold complex: Allenes, 1,*n*-dienynes and 1,*n*-diynes and to the first mechanistic step in the global transformation such as carbocyclization, nucleophilic attack or carbonate/ester group rearrangement processes. Due to the overwhelming number of studies and the recently published reviews about gold-mediated isomerization reactions (Belmont and Parker, 2009; Fensterbank and Malacria, 2014; Yang and Hashmi, 2014; Dorel and Echavarren, 2015; Asiri and Hashmi, 2016; Day and Chan, 2016; Maes et al., 2016; Quintavalla and Bandini, 2016; Siva Kumari et al., 2016; Wei and Shi, 2016; García-Morales and Echavarren, 2018; Lee and Kumar, 2018; McGee et al., 2018; Toullec and Michelet, 2018), we will include here the most relevant contributions of the last years.

2. GOLD-CATALYZED ISOMERIZATION PROCESSES INVOLVING ALLENES

Allenes are cumulenic compounds in which one carbon atom stablishes a π-bond with two adjacent carbon centers, adopting an ideal bond angle of 180° (Patel and Bharatam, 2011; Soriano and Fernández, 2014). Both the structural architecture of this triatomic system and the electronic nature of the substituents on it direct the metal coordination modes and therefore the reactivity of the activated allene (**Figure 1**). In addition, the initial mode in which gold coordinates to the cumulenic motif, and the further transformations, determines the spatial disposition

[2]The Scopus database returns 30,000 entries when looking for *gold catalyst, gold cataysis or gold-mediated* keywords (search performed in January 2019)

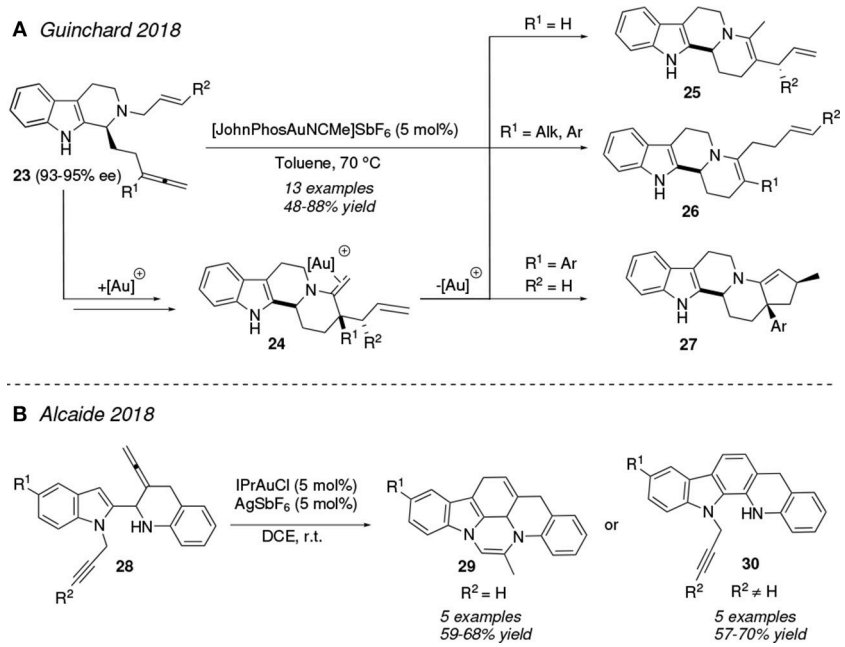

FIGURE 2 | Gold-mediated cycloisomerization of allene derivatives.

of the substituents observed in the isomeric products (Yang and Hashmi, 2014) and even turns the mechanistic pathway away from that of the uncatalyzed reaction (Mandal and Datta, 2018). Interestingly, gold complexes are able to catalyze the racemization of 1,3-disubstituted allenes, a process which has been theoretically studied for the particular case of IPrAuOTf acting as the catalyst (Li et al., 2016).

In 2018, Guinchard et al. reported an elegant thermal ring closure of enantionenriched *N*-allyltryptamines **23** catalyzed by the Echavarren catalyst, [JohnPhosAuNCMe]SbF_6 (**Figure 2A**). The initial gold(I)-activation of the allene motif promotes the tandem 6-*exo-dig*/aza-Cope rearrangement process affording intermediates **24**. The nature of the R^1 and R^2 substituents placed at both the original allene and alkene groups direct the subsequent evolution of **24** toward the different indolo[2,3-*a*]quinazolines **25**, **26** and **27**. Thus, for R^1 = H **24** undergoes an isomerization process of the exocyclic C—C double bond yielding **25** whereas when R^1 = alkyl, aryl the mechanism evolves trough a [3,3]-Cope rearrangement to afford compounds **26**. Pentacyclic substrates **27** were isolated for the special case of R^1 = aryl and R^2 = H (Gobé et al., 2018). In the same line, the (non-)substitution at the terminal position of the alkyne group contained in the initial indole-tethered amino allenynes **28** is the responsible for the divergent synthesis of the fused polyciclic indoles **29** and **30** (**Figure 2B**). $[IPrAu]^+$ would activate the allene group toward a 6-*endo*-carboauration at the C3 atom of the indole ring as initial step whereas the subsequent hydroamination process over the *N*-pendant terminal alkyne ends in the hexacycle **29**. This process does not occur in the case of alkynes bearing bulky R^2 groups. Pentacycles **30** are therefore accessed in these latter transformations (Alcaide et al., 2018).

Other gold-mediated carbocyclization reactions have been described for allenes. Daphnane/tigliane diterpene natural products contain a common scaffold based on a 5-7-6 carbotricyclic ring system. In this sense, Li et al. published a gold(I)-mediated sequential transformation of allenynes **31** into the polycyclic ethers **33** (**Figure 3A**). The authors noted that the overall direct gold-catalyzed process was unfruitful, requiring the optimization of a two-step sequence under different reaction conditions and gold(I)-complexes. Thus, $[PPh_3Au]^+$ promotes the initial *5-exo-dig* hydroalkoxylation onto the alkyne group toward intermediates **32** (Riedel et al., 2017) which subsequently undergo a furan-allene (4+3) cycloaddition under thermal treatment (60°C), and with the participation of $[tBuXPhosAu]^+$, to afford the isomeric mixture of the desired product **33** plus **33'**. This last step is highly influenced by the nature of the R^1 substituent at the allene site. Terminal allenes (R^1 = H) are poor substrates for this (4+3) cycloaddition, producing a complex mixture of products whereas tricyclic systems **33b** and **33c** are obtained in good yields and with a moderate isomeric ratio for the target product **33** vs. the undesired ether (Li et al., 2017b).

In 2017, the combination of gold(I) and copper(II) complexes was reported as an efficient catalyst to promote the site- and regiocontrolled carbocyclization of a racemic mixture of allenes **34**. In order to explain the mechanistic sequence behind these transformations Schomaker et al. proposed a double metal activation in which $Cu(OTf)_2$ would form a Cu-enolate chelate whereas $[R_3PAu]^+$ (R = Ph or Cy) would activate the allene motif (**35**) to then furnish the cylopentene species **36** in >1:1 dr (*anti:syn* of the two starred carbon centers). Remarkably, the stereochemistry at the junction of the two 5-member rings at **36** remains *syn* during the process. The different dr observed in

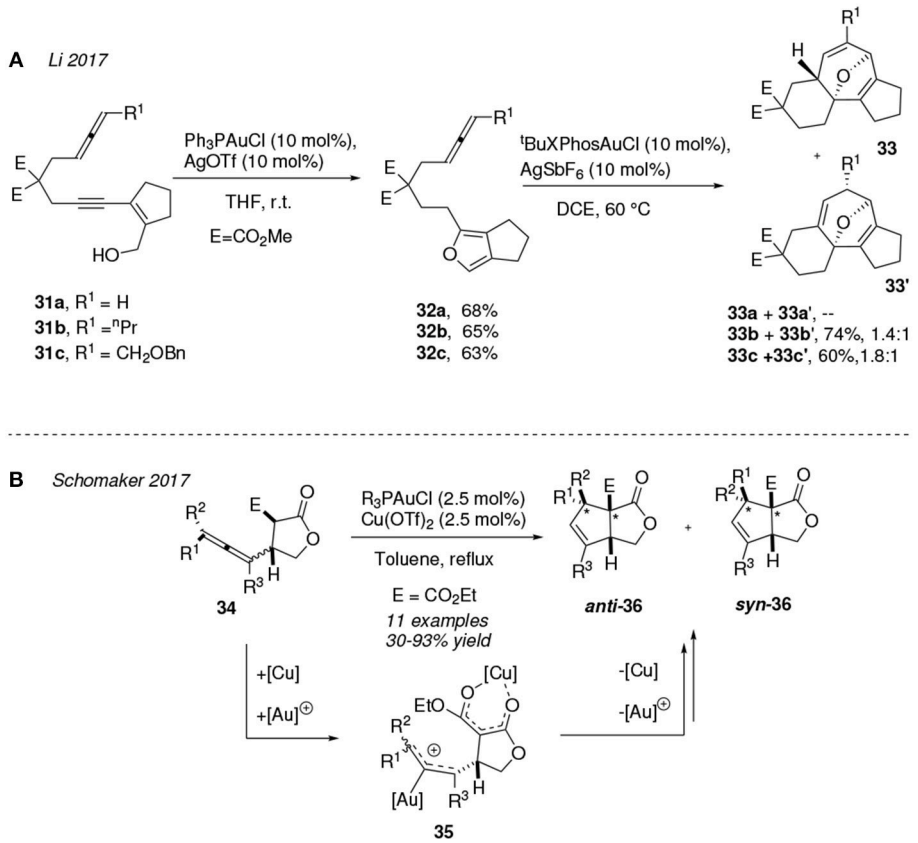

FIGURE 3 | Gold-mediated cycloisomerization of allene derivatives.

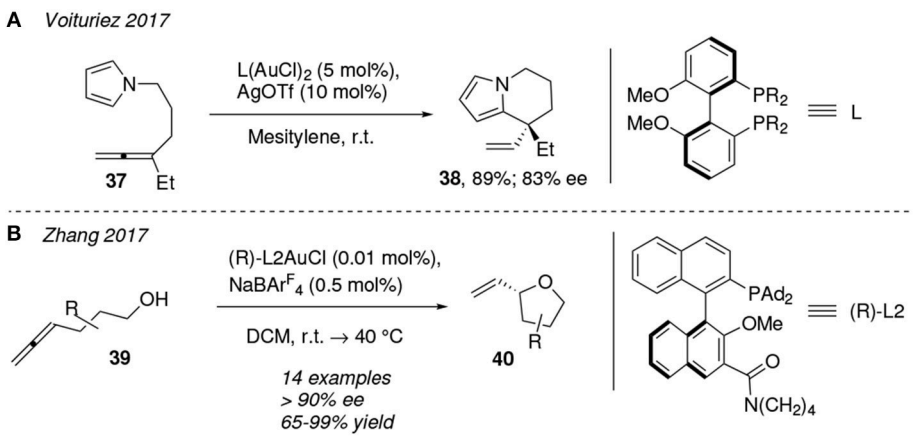

FIGURE 4 | Cycloisomerization of allene derivatives by chiral gold-catalysts.

products **36** respect to the 1:1 dr in the initial mixture of allenes **34** is reasoned assuming that the rate of the gold-activated allene epimerization is faster than that of the carbocyclization process at the intermediate **35** (**Figure 3B**) (Reeves et al., 2017).

In the last few years many chemists have focused their efforts in developing enantioselective reactions, which is currently one of the most active arenas in the field of gold catalysis (Wang et al., 2014). An illustrative example is that published by Voituriez et al. in the course of the total synthesis of the natural product (-)-rhazinilam. They reported the use of a digold(I) complex attached to the chiral biphenyl-phosphine ligand L to mediate in the enantionselective 6-*exo-trig* cycloisomerization of the allene-functionalized pyrrole **37**, which leads to the tetrahydroindolizine derivative **38** in 89% yield and 83% ee. This reaction is conducted in a solution of mesitylene at room temperature (**Figure 4A**) (Magné et al., 2017).

In the same line, asymmetric gold-catalysis via the combined use of a non-spectator chiral ligand and a metal center has been described for the cyclization of the 4-allen-1-ol substrates **39** affording chiral 2-substituted tetrahydrofurans **40** (>90% ee, **Figure 4B**). The pendant amide group at the chiral binaphtyl-based ligand (R)-L2 seems to play a crucial role in the rate acceleration of the reaction due to its abilities to act as general base. Authors propose that the preferred gold-allene coordination is that in which that amide group is placed close to the alcohol group, whereby forming a hydrogen bond C=O· · · H-O which increases the nucleophilicity of the oxygen atom and thus the rate of the reaction (Wang et al., 2017a).

Furthermore, the highly stereoselective cycloisomerization of optically active 4,5-alkadienoic acids leading to gamma-butyrolactones has been reported to occur under catalysis of chiral gold-complexes (Zhou et al., 2018a). Also, non-chiral gold catalysts have been reported to promote related cycloisomerizations of cumulenols (Alcaide et al., 2016) or allenols (Lempke et al., 2016). For this later example, the effects governing the mechanism of the gold-catalyzed attack mode of hydroxylamines onto allenes yielding either dihydrooxazine or *N*-hydroxypyrroline derivatives (that is O- vs. NH-attack and 5- vs. 6-member ring formation) were computationally studied and described in detail by Silva and coworkers in 2017 (Kiriakidi et al., 2017).

3. GOLD-CATALYZED ISOMERIZATION PROCESSES INVOLVING AN INITIAL ALKYNE ACTIVATION

Most of the studies on gold-mediated isomerization reactions are devoted to the transformation of alkynes bearing a second insaturation (an alkene or alkyne group), that is 1,*n*-enyne and 1,*n*-diyne substrates (Jiménez-Núñez and Echavarren, 2008; Asiri and Hashmi, 2016; Day and Chan, 2016; Lee and Kumar, 2018). Nonetheless, cycloisomerization processes have also been described in molecules containing solely a reactive alkyne or alkene group. This is the case of the gold(I)-directed ring-contraction process of cyclooctyne to 5-member bicyclic alkenes (Das et al., 2016) or the intramolecular hydroamination of 6-alkenyl-2-pyridones to yield 1,6-carboannulated 2-pyridones (Timmerman et al., 2017). In those circumstances where both types of unsaturations are present, the well-known preference of gold for alkyne over alkene groups is rationalized in terms of the HOMO-LUMO energy gap of the coordinated π-systems rather than through intrinsic considerations of the metal itself (Gorin and Toste, 2007). Henceforth, (cyclo)isomerization processes initiated by the gold activation of an alkyne group will be described.

3.1. Gold-Catalyzed Cycloisomerization of Ynamides

Ynamides are special amines substituted by an alkyne group and an electro-withdrawing group which modulate its stability and reactivity (Pan et al., 2016). Yeh et al. reported the gold(I)-catalyzed double cyclization of the 3-enynamides **41** in dichloromethane at room temperature (**Figure 5A**). The authors propose an initial cyclization involving the gold-activated alkyne motif and the pendant endocyclic C=C bond that provides vinyl cation **42**. This cationic intermediate **42** could cyclize forming either a 6-member ring, by attack of the pendant phenyl ring

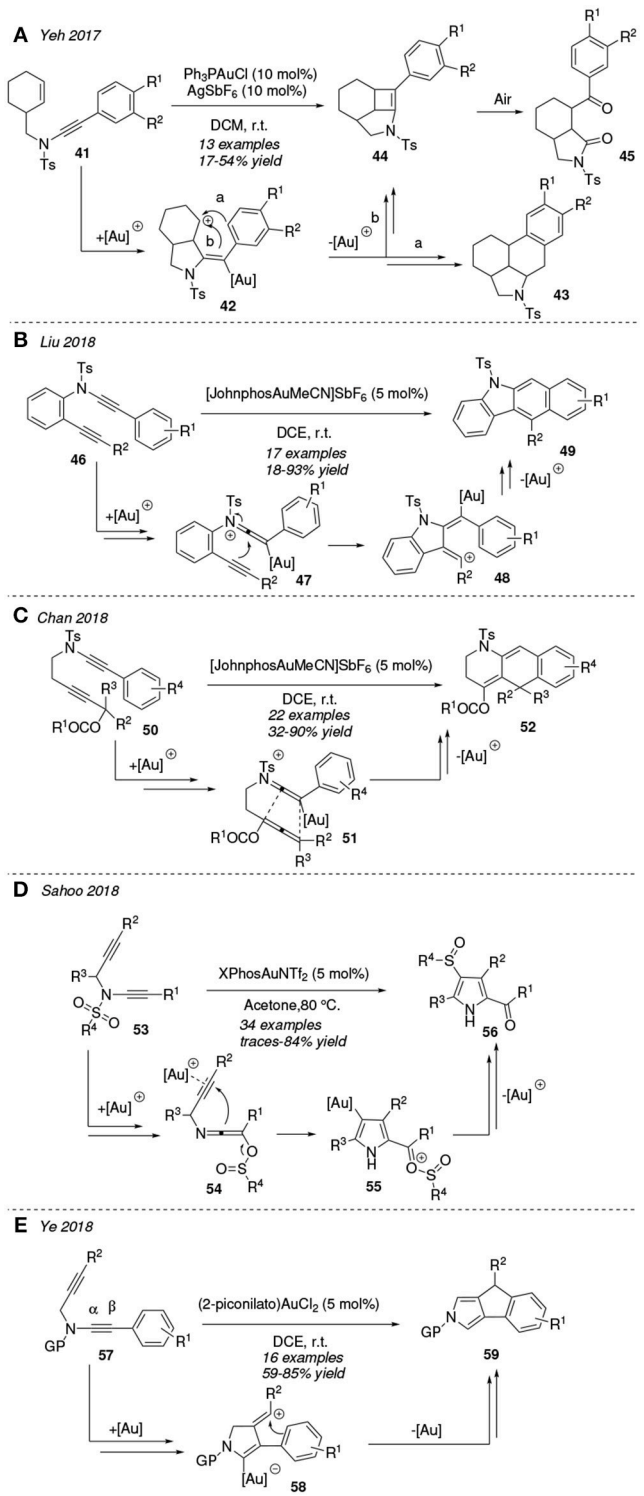

FIGURE 5 | Gold-mediated cycloisomerization processes of ynamides.

onto the deficient carbon center (path *a* toward **43**, traces) or a 4-member ring, involving the exocyclic alkene (path *b* leading to **44**). The strained cyclobutene compounds **44** are quickly oxidized when exposed to air, affording the respective 1,4-diketones compounds **45**, which are isolated as major products (Zhong et al., 2017).

In 2018, Liu et al. designed a new route toward benzo[*b*]carbazoles **49** involving the $[JohnPhosAuNCMe]^+$-catalyzed cycloisomerization of the ynamide-ynes **46** via a formal dehydro-Diels-Alder reaction at room temperature (**Figure 5B**). Initial gold-activated keteniminium ions **47** undergo a cyclization affording the vinyl cations **48** which evolve toward the final tetracycles **49** by a benzoannulation reaction (Xu et al., 2018). The same catalyst, $[JohnPhosAuNCMe]SbF^6$, mediates the transformation of ynamides **50** into tetrahydro[*g*]quinolines **52** (**Figure 5C**). An initial [3,3]-sigmatropic rearrangement of the acetate group and activation of the ynamide group would yield the keteniminium ion **51** which would experiment a formal [4+2]-cycloaddition yielding **52**. This protocol is efficient even in the presence of air and moisture, indicating the tolerance of the gold catalysts to diverse reaction conditions (Chen et al., 2018).

A very interesting case is that of *N*-substituted ynamides decorated with functional groups with migratory abilities. **Figure 5D** shows the unconventional thermal transformation of *N*-sulfonyl ynamides **53** to 4-sulfinylated pyrrol derivatives **56** in presence of $XPhosAuNTf_2$ catalyst. The authors proposed a mechanism initiated by a [1,3]-sulfonyl migration from the N atom to the distal carbon atom of the alkyne fragment resulting in intermediate **54**. The subsequent gold-activation of the alkyne moiety promotes an umpolung at the unsaturations and facilitates a 5-*endo*-dig cyclization toward **55**, which is transformed into the indole **56** via a deaurative [1,5]-sulfinylation process. This kind of sulfonyl/sulfinyl shift proceeds in a regioselective fashion. These results were also supported by a computational study (Sahoo et al., 2018).

Furthermore, gold(III)-complexes are able to promote the activation of ynamides toward cycloisomerization reactions. In 2018, Ye et al. reported the practical synthesis of indeno[1,2-*c*]pyrroles **59** in good yields under mild conditions from *N*-propargyl ynamides **57** and with gold(III) catalysis. In contrast to the usual metal-catalyzed cyclization of π-tethered ynamides over the central α-carbon atom, authors reported a regioselective attack on the β-carbon of the ynamide **57** leading to the vinyl cation **58**, mostly associated to a lower ring strain of the formed pentacycle with respect to the four-member ring alternative (**Figure 5E**) (Shen et al., 2018).

3.2. Gold-Catalyzed Cycloisomerization of 1,*n*-dienynes and 1,*n*-diynes Containing a Propargyl Carbonate/Ester

In the last 3 years a great number of studies devoted to gold-mediated cyclizations of compounds containing a propargylic carbonate/ester motif have been reported. It is worth to note that the usual initial carboxy rearrangement determines the fate and further transformations that encompass this chemistry. For this reason substrate design is key to successfully obtain the desired target molecule through these reactions. Recently, Zhang et al. introduced the application of frustrated Lewis pairs as a synthetic strategy, that is, basic tertiary amine as ligands to design gold cationic complexes which improve the regio- and stereoselective ratios of propargylic ester isomerizations (Wang et al., 2017b). In this sense, related 1,*n*-enyne derivatives are well-exploited reactants and powerful synthethic tools to build carbonyl-based compounds. **Figure 6A** describes the diasterospecific synthesis of cyclopentanones **62** owning two contiguous stereogenic carbons published by Tius et al. The authors use a gold(I) complex to catalyze a tandem [1,3]-OAc shift/cyclization/acetate hydrolysis process. This cycloisomerization reaction can be conducted at room temperature with substrates **60** bearing different functional groups such as esters, $-CF_3$ or alkyl chains. The high diastereoselectivity observed in the transformation is related to the rapid alkenyl isomerization of the pentadienyl intermediate **61** (Congmon and Tius, 2018).

A couple of years earlier, the preparation of benzazocines **66** was accomplished from terminal 1,9-enynyl esters **63** through a gold-catalyzed cascade reaction. Xie et al proposed the initialization of the mechanism with a 1,2-acyloxy shift that further evolves with a *O*-cyclization to yield 1,3-dipolar intermediates **64**. These **64** species engage in a [3+2] cycloaddition reaction involving the terminal alkene to afford the polycyclic scaffolds **65**, which convert into the final substituted benzocines **66** by a hydrolisis process. Two different diastereoisomers were isolated and fully characterized, the *trans* isomers **66** being the major products of the reaction (**Figure 6B**) (Feng et al., 2016). The same group has reported on the successful attempts to obtain complex tetracyclic frameworks by appliying a similar gold-catalyzed protocol on related linear enynyl esters (Sun et al., 2017).

Liu et al. published the gold(I)-mediated diastereoselective formation of 8-oxabicyclo[3.2.1]octanes **70** from glycal bearing porpargylic esters **67** (**Figure 6C**). The authors proposed that the $[PPh_3Au]^+$ catalyst has a dual role during the course of the reaction. First, the gold(I)-complex activates the alkyne group to facilitate a 1,3-acyloxy migration leading to the allene intermediates **68**. Further along into the mechanistic pathway, the metal acts as Lewis acid promoting the intramolecular Ferrier reaction with the departure of the alcoxy group, which is integrated as a new ligand in the gold complex $[Au]OR^2$ furnishing the oxocarbenium species **69**. Lastly the bicyclic structure of **70** is formed by cyclization and formation of $AcOR^2$ as a by-product (Liao et al., 2017).

In conjunction with the latter works, functionalized anthracenes **73** can also be generated under thermal conditions (50°C) with bulky gold(I)-catalysts promoting the cyclization of 2-(2-ethynylbenzyl)furan featuring propargyl carbonate or ester groups **71**. Intermediates **72** are proposed to be formed after a 3,3-rearrangement of the propargyl carboxylate OR^2 moiety, and then evolve to products **73** via a [4+2]-cycloaddition between the furanyl system and the distal C=C double bond of the allene. A similar protocol was applied in the cycloisoimerization of the related 1,5-furan-ynes **74** to obtain

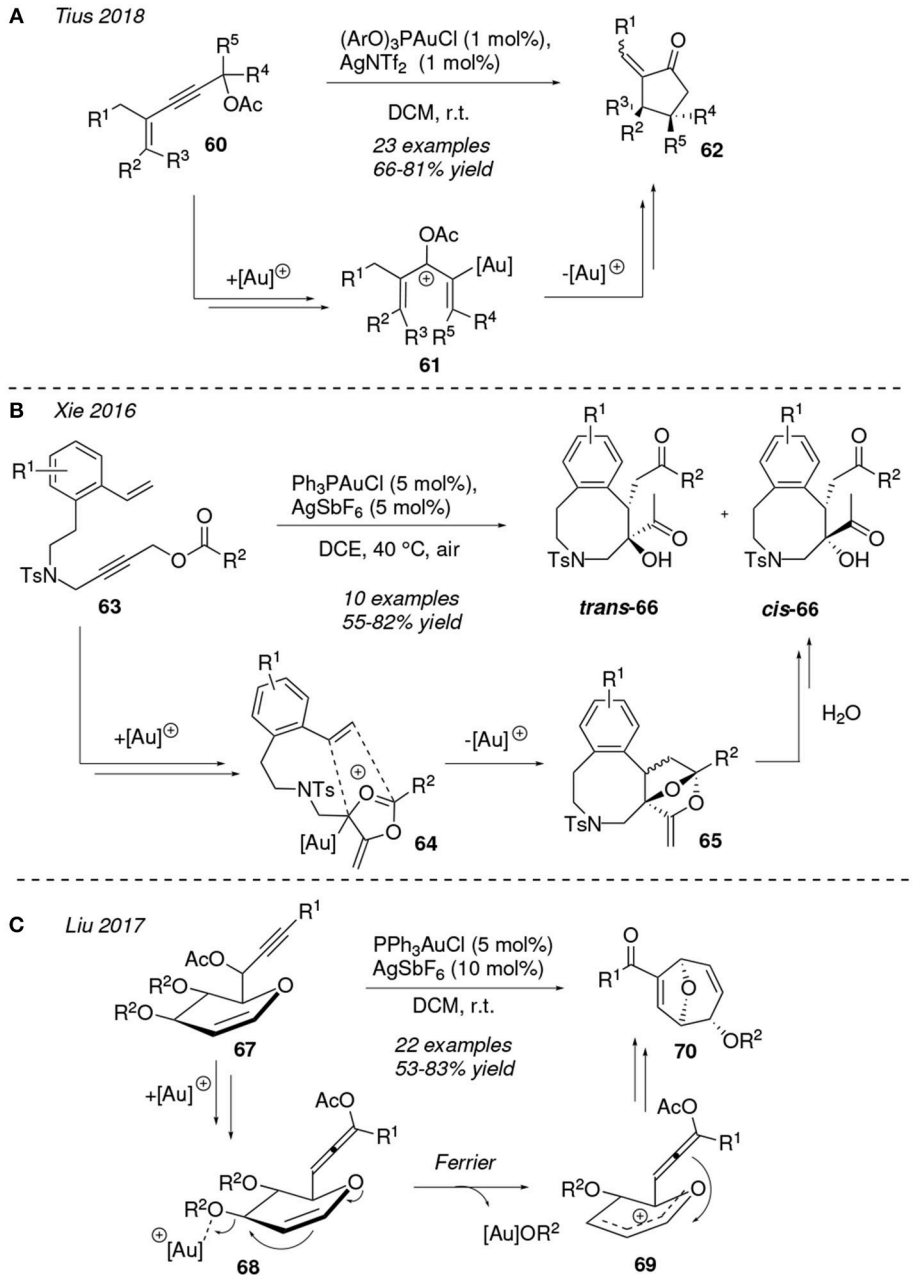

FIGURE 6 | Gold-mediated cycloisomerization of 1,*n*-dieniynes started by an acyloxy shift process.

antracen-1(2*H*)ones **75**; in this case a late 1,2-R^1 shift is required after the [4+2]-cycloaddition step to afford the final ketone (**Figure 7A**) (Sun et al., 2016).

An unusual chemoselective gold-activation of alkenes over allenes using sterically bulky ligands as di^{t}BuXphos has been described by Shi et al. Substituted bicyclic[4.4.0]dihydronaphthalenes **78** were accessed from the dienynes **76** through an initial 1,3-OPiv rearrangement and subsequent alkene-activation at intermediate **77**, which then experiments an allene-ene cyclization and hydrolysis. Interestingly, the pivaloyl group (Piv) migrates selectively during the formation of hydrobenzopyranes (**78**, X = O) as indicated in **Figure 7B** (Thummanapelli et al., 2016).

As in the case of 1,*n*-enynes, reactions initiated by migration of a carbonate or ester group have been subject of study in related 1,*n*-diyne derivatives (Day and Chan, 2016; Li et al., 2017a). Chan et al. reported in two different studies the gold(I)-mediated cycloisomerization of 1-en-4,*n*-enynes **79** (Chen et al., 2016a) and 1-en-3,9-enynes **81** (**Figure 8A**) (Rao et al., 2016). Both reactions were conducted under the same solvent and temperature conditions (DCE, 80°C) but with different gold catalysts. Thus, for the conversion

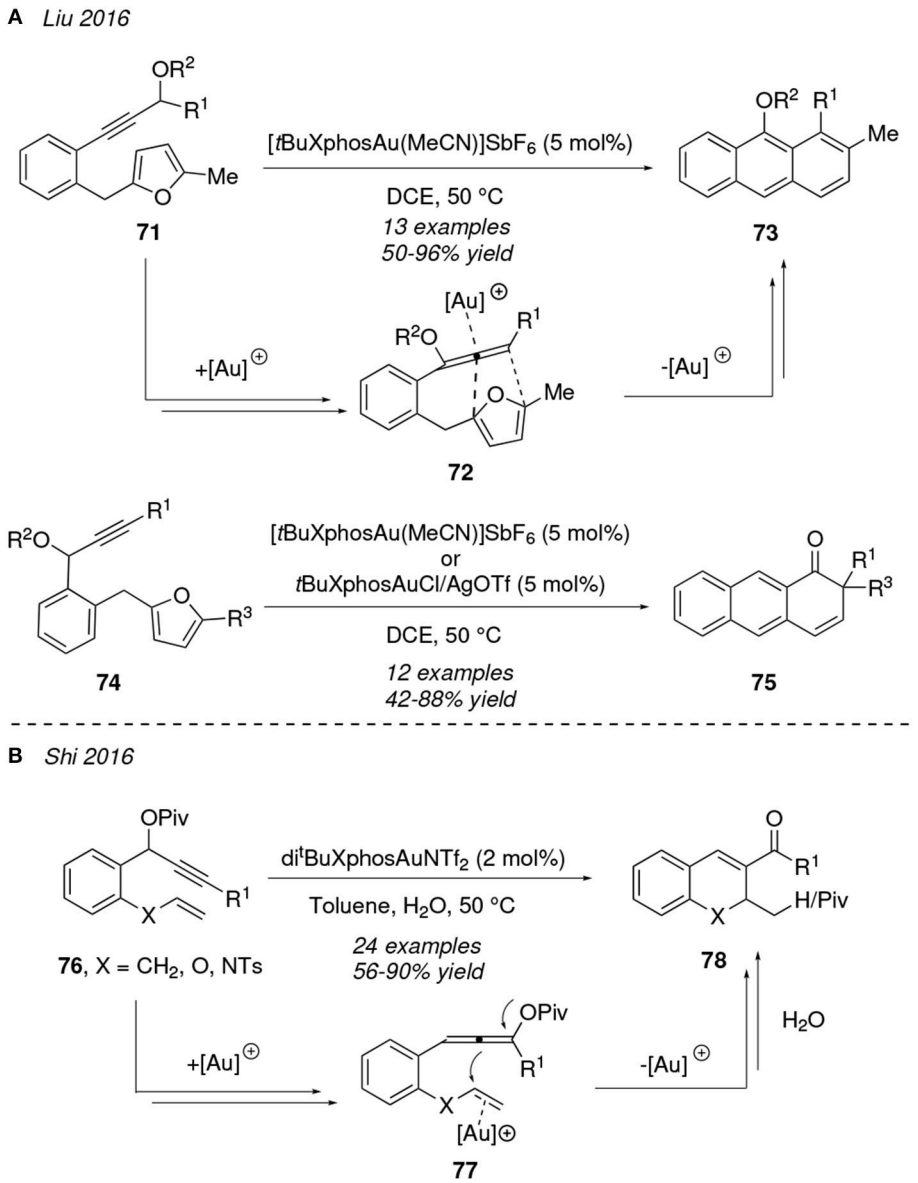

FIGURE 7 | Gold-mediated cycloisomerization of 1,*n*-dienynes started by an acyloxy shift process.

79→**80** [JohnPhosAuNCMe]$^+$ was the active cationic gold species which provided the best results, whereas in the case of the cycloisomerization of the diyne **81** [LAuCHPh]$^+$ was employed. In the latter, therefore a cationic catalyst featuring a *N*-heterocyclic carbene ligand is used. In both cases the mechanistic route would be initiated by the gold-activation of the propargyl moiety promoting a 1,3-acyloxy transfer followed by several cyclizations. In fact, the relative position of the olefine moiety determines whether the evolution of the mechanisms at the first cyclization occurs through either a 1,4-eneallene cycloisometization toward **80** or a metallo-Nazarov cyclization toward the tetracycles **82**. In 2018, the synthesis of naphtho[2,3-*c*]furan-1(3-*H*)-ones **84** was reported via cycloisomerization of propargylic ynoates **83**, under thermal conditions with BrettPhosAuCl as catalyst and in presence of $NaBAr_4^F$ as an activator of the gold complex (**Figure 8B**) (Li et al., 2018a). The reaction mechanism would involve a [3,3]-rearrangement of the propargyl ester leading to a carboxyallene intermediate followed by an intramolecular Diels-Alder cyclization. The authors were able to synthesize up to 24 examples of **84** combining diverse alkyl and aryl substituents and they also describe a new method for the *in-situ* generation of carboxyallene intermediates.

An interesting formation of primitive dendrimer systems containing bicyclic structures from substrates incorporating two sets of dialkynes were described by Oh et al. The hydrated $NaAuCl_4$ mediates in the thermal cycloisomerization of **85** trough a dual 1,3- and 1,2-acyloxy transposition at the terminal and inner alkyne moieties, respectively, followed by

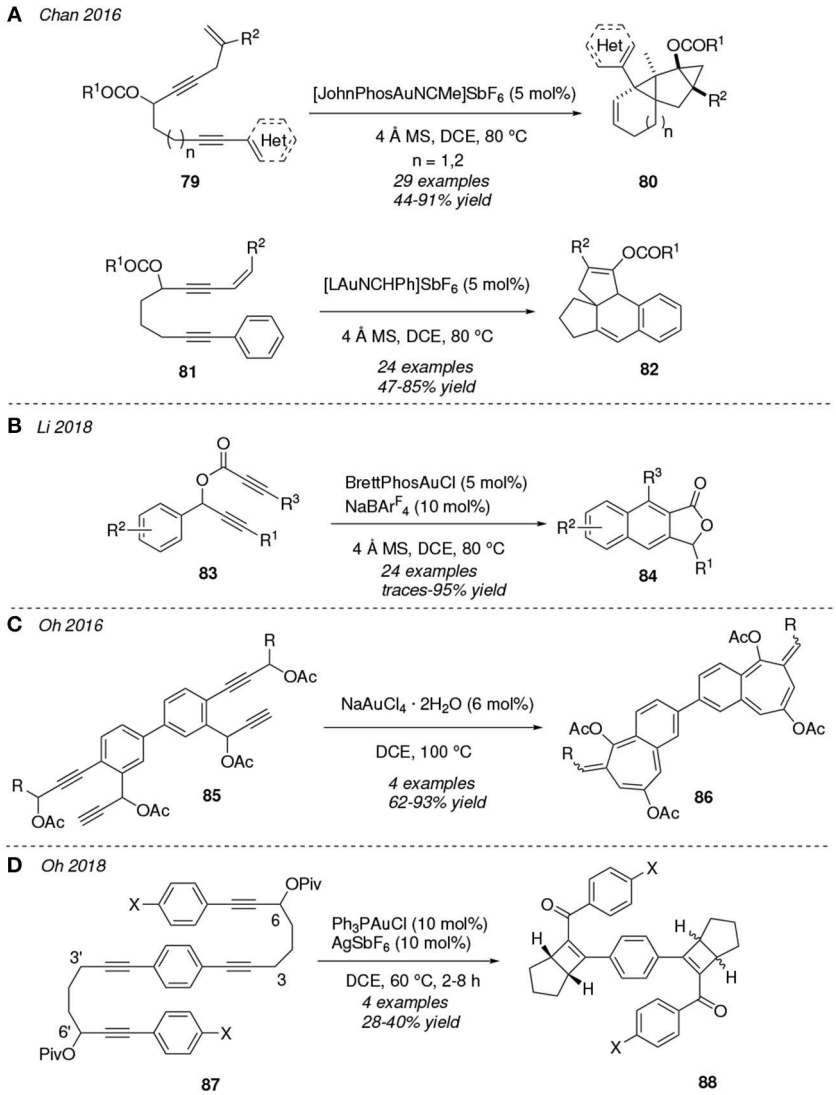

FIGURE 8 | Gold-mediated cycloisomerization of 1,*n*-diynes started by an acyloxy shift process.

an annulation process leading to the benzo-fused 7-member cycles **86** (**Figure 8C**) (Lee et al., 2016). In a related work, the $[Ph_3PAu]^+$-activation of propargyl ester motifs promotes the 1,3-acyl shift/[2+2]/hydrolysis cascade reaction of the diynes **87** furnishing a diastereomeric mixture of the polycyclic systems **88** (**Figure 8D**). The authors were able to resolve the diasteromeric mixture and even extend this protocol to other diynes in which the pivaloate substituents are located at positions 3 and 3' (Lee et al., 2018).

3.3. Gold-Catalyzed Cycloisomerization Processes of 1,*n*-enynes and 1,*n*-diynes Initiated by a Nucleophilic Attack Onto the Alkyne Group

Gold is able to activate an alkyne group toward a nucleophilic addition and, for instance, make it susceptible to act as the receptor motif in a hydride shift reaction (Xie et al., 2014; Nahide et al., 2018). In this sense, Wong et al. reported the gold-alkyne activation of 1,5-enynes **81** toward a rare 1,6-hydride shift leading to the gold-activated oxonium intermediate **90**, which then experiments a Prins-type cascade forming two new C—C bonds and furnishing the final tricyclic system **91** (**Figure 9A**) (Lu et al., 2018). This mechanistic proposal is supported by deuterium-labeling cross-over experiments. According to the authors, there is no precedent of cycloisomerizations initiated by a gold-catalyzed 1,6-hydride transfer reaction. This protocol provides rapid access to fused polycyclic compounds presented in many bioactive natural products as Nominine or Walsuranin B.

An activated alkyne group could act as electrophile in an intramolecular nucleophilic attack if a functional group present within the system has such nature. An experimental gold(I)-mediated double 6-*endo* cascade cyclization strategy of enynes

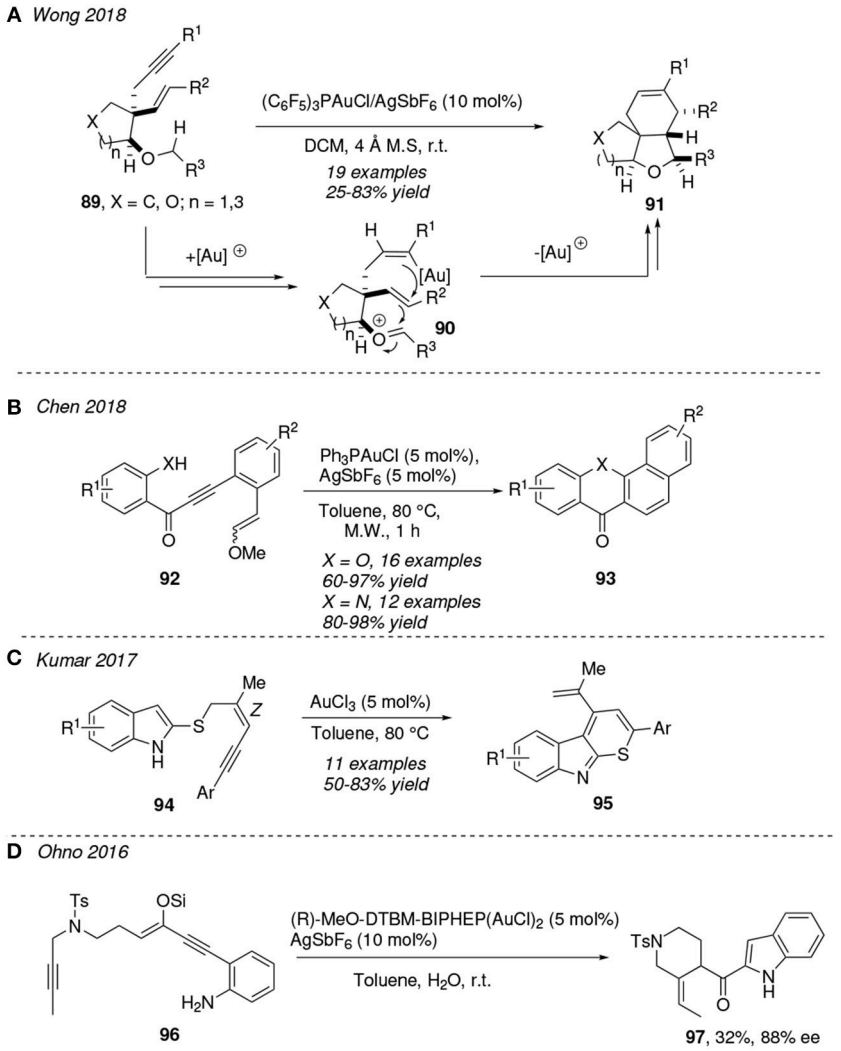

FIGURE 9 | Gold-mediated cycloisomerization reactions of 1,*n*-enynes containing an internal atom-centered nucleophile.

92 to form benzoxanthenone and benzoacridone derivatives **93** has been described by Cheng et al. (**Figure 9B**). The tandem process starts with an X-attack (X = O, N) to the alkyne moiety and further carbocyclization involving the pendant alkene motif, ending with the formation of both C—N and C—C bonds and releasing a methanol molecule. This reaction is conducted in toluene at 80°C under microwave irradiation; this provides a better yield when compared with conventional thermal treatment (Xiong et al., 2018). Before this study, the same group had reported a similar protocol to obtain benzo[*a*]carbazoles via gold(I)-mediated cycloisomerization of structurally related *ortho*-alkynylanilines in toluene at 100°C (Peng et al., 2017). Likewise, gold(III)-complexes have been reported to be excellent catalysts in similar transformations. Kumar et al. developed an elegant gold(III)-mediated strategy for the synthesis of substituted thiopyrano[2,3-*b*]indoles **95**. This implies that enyne tethered indole sulfides **94** undergo a tandem σ-bond migration/*6-endo-trig* cyclization/oxidative aromatization process. The authors highlight the significance of the *Z* orientation of the C=C bond to assist the rearrangement step (**Figure 9C**) (Jha et al., 2017).

Besides, the use of bimetallic complexes has become more popular in gold chemistry during the last years (El Sayed Moussa et al., 2016; Trommenschlager et al., 2017; Arif et al., 2018). The synthesis of the (+)-conolidine alkaloid has been reported via a gold(I)-catalyzed cascade cyclization of the conjugated enyne **96**. The bulky bimetalic gold complex (R)-MeO-DTBM-BIPHEP$(AuCl)_2$ bearing a chiral ligand is used as effective precatalyst to form the ketone intermediate **97** (32% yield and 88% ee) (**Figure 9D**) (Naoe et al., 2016). Recently, Zi et al. achieved the first desymmetrization of prochiral bisphenols via gold(I)-catalyzed enantioselective hydroetherification of alkynes. This protocol was applied successfully in (di)alkyne compounds bearing P-stereogenic

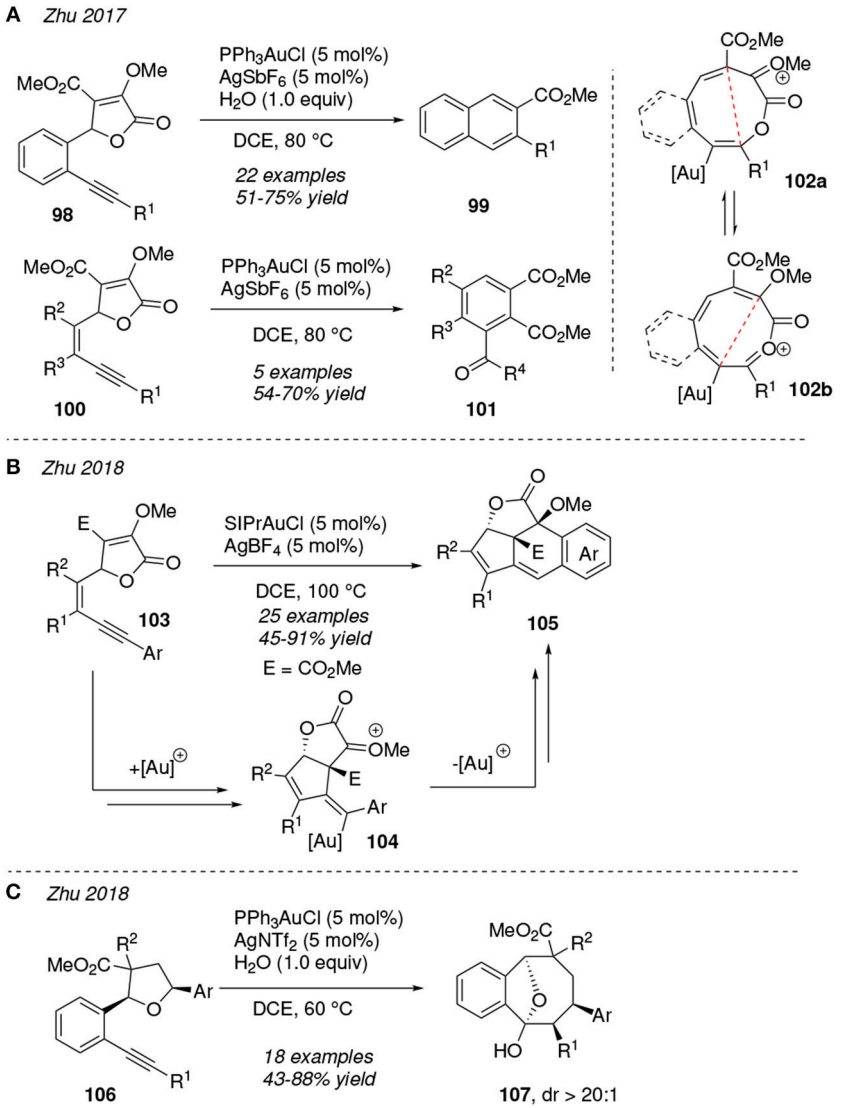

FIGURE 10 | Gold-mediated cycloisomerization of enyne-lactones.

centers using the bimetallic chiral precatalyst (S)-DTBM-Segphos$(AuCl)_2$ (Zheng et al., 2018).

Several reports pivoting about cycloisomerization reactions of enyne-lactones by gold(I)-catalysis have been published by Zhu et al. (**Figure 10**). Under $[Ph_3PAu]^+$ catalysis, the lactone-enynes **98** and **100** are proposed to experiment a ring-expansion reaction of the lactone ring affording the previously unknown 2-oxoninium intermediate **102a** which exists in equilibrium with **102b**. The presence of the benzo-fused ring at intermediates **102** displaces the equilibrium reaction toward the most stable 2-oxoninium **102a**, whereas, in its absence, intermediate **102b** is the preferred product. Both intermediates **102a** and **102b** then undergo an interesting 6π electrocyclization reaction and subsequent aromatization process toward compounds **99** and **101**, respectively. The addition of one equivalent of water is required for the formation of **99** whereas the diester **101** is isolated even in anhydrous media (**Figure 10A**) (Luo et al., 2017). On the other hand, the nature of the ligand at the gold(I)-catalyst seems to have a high influence in the evolution of the mechanism allowing the transformation of related enyne-lactones **103**. Thus, benzo-fused polycyclic compounds **105** are achieved using a carbene derivate gold complex as precatalyst (SIPrAuCl) in presence of the activating partner $AgBF_4$ (**Figure 10B**). The authors reasoned that an initial vinyl ether addition onto the activated-alkyne toward the **104** motif might be favored rather than an oxygen attack, as in the previous transformations, mostly due to the strong σ-donor and weak π-acceptor nature of the SIPr ligated gold center (Luo et al., 2018). If the lactone motif is replaced by a tetrahydrofuran group as in compound **106**, then the bicyclo **107** is obtained via a gold(I)-catalyzed *5-exo-dig*/[1,3] O-to-C tandem process in a diastereoselective fashion (**Figure 10C**) (Zhang et al., 2018a). With this set of papers Zhu

et al. demonstrated the versatility of diverse gold(I) complexes in the ring-expansion process of lactones and related structural motifs via a nucleophilic attack onto an activated alkyne group.

1,*n*-Diynes are prone to be transformed into valuable heterocyclic systems through the attack of an internal nucleophile, in particular -NH, -CO, or -OH groups, when present, either onto one or both of the gold π-activated C—C triple bonds. Lamellarins are a group of pyrrole alkaloids based in a pyrano[3,4-*b*]pyrrol-7(1*H*)-one scaffold which present anticancer activity. Thibonett et al. designed a gold(I)-catalyzed cycloisomerization of the 1,4-diynes **108** furnishing the substituted pyrano-pyrrol-ones **109** via two consecutive intramolecular *5-endo-dig* and *6-endo-dig* additions to both activated alkyne motifs (**Figure 11A**). The former cyclization proceeds involving the amine group in the formation of the pyrrol ring, whereas in the latter it is one of the ester groups who is involved in the formation of the pyranone ring (Delaye et al., 2017).

In 2017, Xu et al. reported an elegant gold(I)-catalyzed cyclization/carbonylation cascade reaction of diynes containing an amide group which operates under mild reaction conditions. Thus, 1,6-diynes **110** undergo a *6-exo-dig* cyclization with the carbonyl oxygen of the amide group leading to the 1,3-oxazine gold intermediate **111**, which is then intercepted by the remaining alkyne affording the intermediate **112**. After protodeauration and hydration β,γ-unsaturated ketones **113** are obtained in good yields (**Figure 11B**) (Bao et al., 2017). Otherwise, 1,6-diynes bearing *ortho*-benzyl alcohols **114** evolve to dihydroisobenzofuran derivatives **116** trough a gold(I)-catalyzed protocol initiated by two consecutive unsual *5-exo-dig* hydroxyalkilation processes and a further Prins-like cyclization. Authors reasoned the formation of the *5-exo-dig* cyclized product taking into account the more favorable six-membered ring chelated gold complex **115** when compared to the alternative bigger chelate, which would result in a more usual *6-endo-O*-cyclization (**Figure 11C**) (Hashmi et al., 2007). This kind of transformation has not only been described as regioselective but also as stereoselective at the spiro-quaternary center placing the oxygen atom in the axial disposition (Cao et al., 2016).

Chan et al. designed an efficient method to prepare azacycle-fused pyrroles **121-123** by gold(I)-catalyzed dehydrative cycloisomerization of β-amino-1,*n*-diynols **117**. The mechanistic sequence would be initiated with the formation of the pyrrole ring (**118**) promoted by the nucleophilic attack of the pendant amine toward the closer gold-activated alkyne and departure of a water molecule. A subsequent gold activation of the remaining alkyne motif would promote a cyclization leading to the intermediates **119** and **120**. The type of cyclization depends on both the length of the alkyl chain and the nature of the X linker (X = -NTs, O or CH_2), as is shown in **Figure 11D**. Furthermore, the intermediate **119** is the precursor of the fused pyrroles **121** and **122** whereas pyrroles **123** result from the expansion and further protodeauration of **120** (Kothandaraman et al., 2016). The nature of the substituents of the amide groups at the diynes **124** direct the gold(I)-catalyzed formation of the lactams **125** and **126**. Thus, for a bulky R^4 group and an electron-rich migrating R^3 group path *a* is more favorable and involves a tandem NR^3-nucleophilic cyclization/1,3-R^3 migration/1,5-enyne cycloisomerization process to yield **125**. In contrast, if R^3 is a poor shifting group, the dienynes **124** evolve trough a cascade hydroamination/Michael addition reaction (path *b*) to afford the spirocycle **126** (**Figure 11E**) (Li et al., 2018b).

3.4. Gold-Catalyzed Carbocyclization Processes of 1,*n*-enynes and 1,*n*-diynes

Those processes in which 1,*n*-enyne substrates are transformed into isomeric products trough an initial carbocyclization step are very well documented. In 2018, Percy et al. have shown for the first time the intramolecular carbocyclization of difluorinated enol acetals bearing a pendant unsaturated group **127** leading to the cyclohexanone scaffolds **128** in a moderate diastereoisomeric ratio (**Figure 12A**). The reaction is conducted in a mixture of dichloromethane and methanol solvents at 40 °C in presence of IPrAuCl as precatalyst and $AgSbF_6$ acting as activator agent of the previous one. The carbonyl group is further reduced to obtain difluorinated diols. Besides, a mixture of difluorinated pyran scaffolds **130** and **131** are isolated, the gem-diol derivate **131** being the major product when using propargyl ethers **129** as starting reactants and 2-MeTHF as solvent (McCarter et al., 2018).

In a very recent publication, Echavarren et al. reported the gold(I)-catalyzed cascade cyclization reaction of oxime-tethered 1,6-enynes **132** furnishing the substituted oxazines (n = 1) and dihydroisoxazoles (n = 0) **133** in a diastereospecific fashion and very good yields (**Figure 12B**). The mechanism ruling this transformation has been proposed to proceed stepwise through an intramolecular addition of the O atom of the oxime onto the transient gold-carbene intermediate, as revealed by the DFT computations performed. The *Z* orientation at the C=N bond of the oxime group is determining to obtain **133**, otherwise, with the *E*-oxime variant, dihydropyrrole *N*-oxides are isolated. The latter substrates resulted from the initial *N*-attack of the oxime over the gold-carbene intermediate (Muratore et al., 2018).

The use of gold-homogeneus catalysis to achieve complex poly-annulated-cyclic systems is also gaining attention as, for instance, in the formation of the biologically active compound (+)-aureol (Wildermuth et al., 2016). In this sense, stable functionalized hydroacenes **135** are easily accessible up to nine rings trough a gold(I)-catalyzed cyclization of aryl-tethered 1,7-enynes **134**, under mild reaction conditions (**Figure 12C**). A great number of different substituents R^1 and R^2 decorating the aryl motifs or even fused aromatic rings are compatible with the conditions, revealing the high synthethic value of this protocol (Dorel et al., 2016).

In 2016, Sanz et al. demonstrated that β,β-diaryl-*o*-(alkynyl)-styrenes **136** are transformed at 80 °C into dihydroindeno[2,1-*a*]indenes **137** under gold(I)-catalysis whereas benzofulvenes **138** are obtained at 0 °C . The formation of the tetracycles **137** implies a formal [4+1] cycloaddition trough a tandem 5-*endo*-cyclization-diene/iso-Nazarov cyclization process (**Figure 12D**) (Sanjuán et al., 2016). A computational study for related gold(I)-mediated transformations in which the initial styrenes bear alkyl groups at the β positions has been reported by Zhou et al.

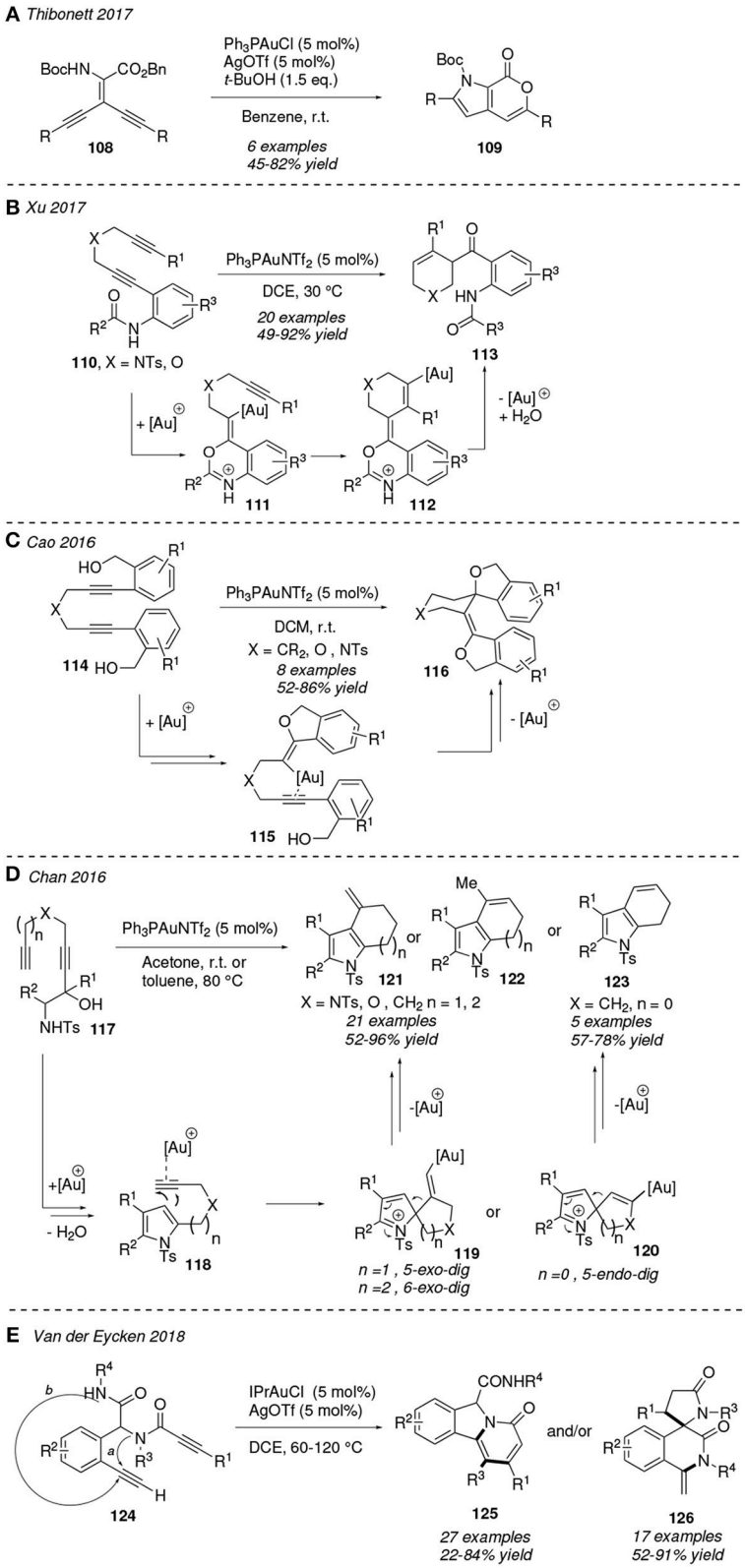

FIGURE 11 | Gold-mediated cycloisomerization of 1,*n*-diynes containing an internal atom-centered nucleophile.

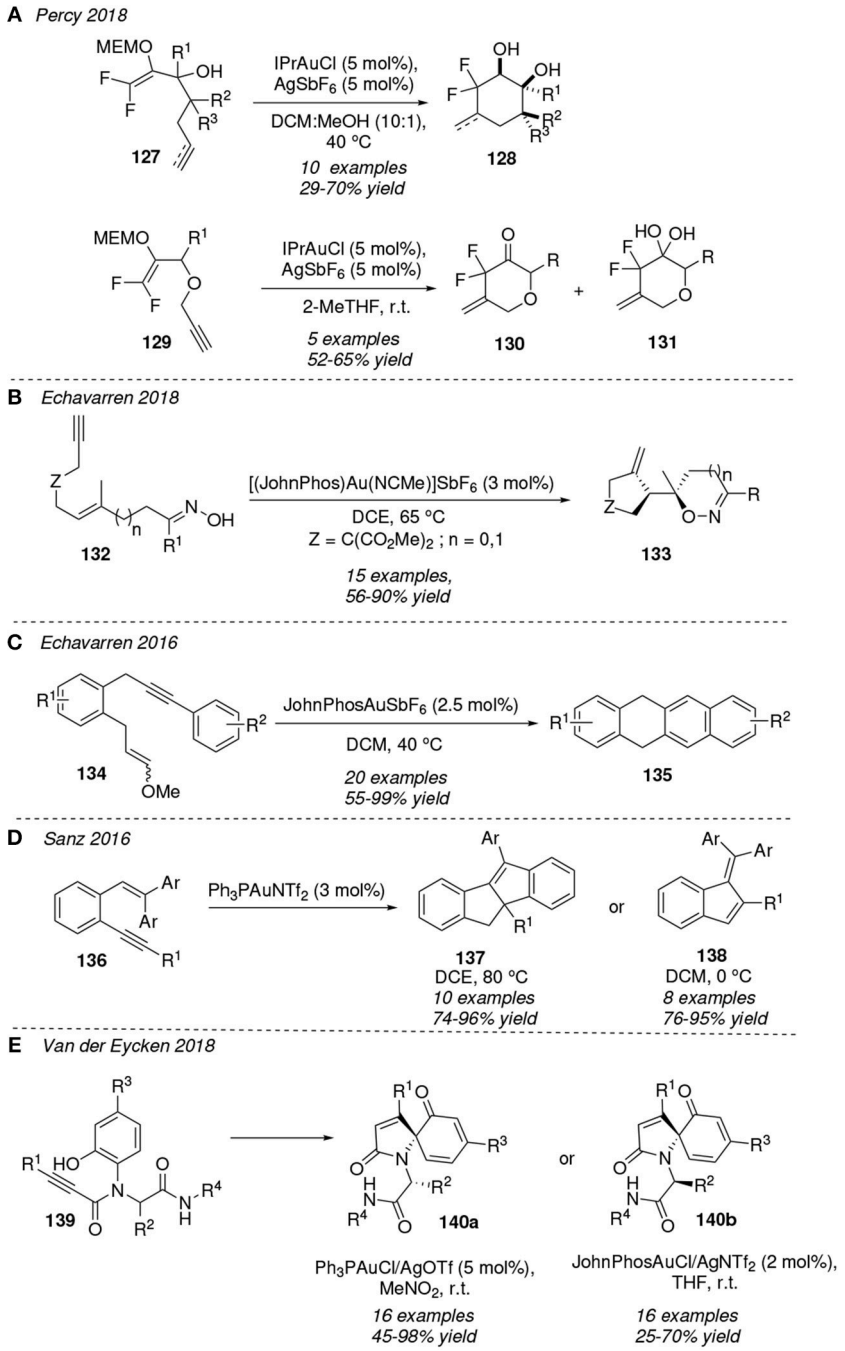

FIGURE 12 | Gold-mediated cycloisomerization of 1,*n*-enynes.

(2018b) The authors concluded that the reaction would evolve trough a [1,2]-H shift on the isopropyl moiety rather than a cyclopropane expansion, as suggested in the experimental work (Sanjuán et al., 2015).

The Van der Eycken research group has reported the elegant one-pot synthesis of spirocyclic pyrrol-2-one-dienones **140** via a gold(I)-catalyzed intramolecular Friedel-Craft reaction of the Ugi adducts **139** (**Figure 12E**). Two diastereomeric dienones were isolated depending on both the gold-catalyst and the reaction conditions. Taking the **140** yields into account and supported by a conformational theoretical analysis, the authors concluded that the isomer **140a** resulting from the catalytic treatment with Ph_3PAuCl is energetically more favorable than that derived from the bulkier JhonPhosAuCl precatalyst (**140b**) (Nechaev et al.,

2018). A related work had been previously published by the same group (He et al., 2017).

Continuing with carbocyclization processes, it was reported that several gold(I) salts (L = t-Bu_3P, IPr; X = [OTf]-, $[NTf_2]^-$, $[SbF_6]^-$) activate the 1,5-enynes **141** toward gold-allenes **142** via a [3,3]-rearrangement. The subsequent tandem Nazarov cyclization/[1,2]-H shift process allows the formation of the fused cyclopentadienes **143**, which were exposed to a further reduction to obtain primary alcohols **144** (**Figure 13A**). The position of the two double bonds at the final cyclopentadiene ring strongly depends on the size and type of the fused cycle, mostly carbocycles and *N*-heterocycles (Rinaldi et al., 2018). Bandini et al. described a related [3,3]-sigmatropic rearrangement for the site-selective gold(I)-mediated dearomatization of napthylpropynol derivatives toward dihydrofurylnaphthalen-2(1*H*)-ones (An et al., 2017).

In 2018, Nakamura et al. published the gold(I)-catalyzed intramolecular S_EAr reaction of isoxazoles **145** substituted by a propargyl amine or ether at C4 position. This cycloisomerization furnishes the fused isoxazolo substrates **146** in good yields at 60°C (**Figure 13B**). Moreover, the authors demonstrated that the addition of an external hydride acceptor as *N*-phenylbenzaldimine increased the yield in the synthesis of isoxazolopyridines (**146**, X = NH). Remarkably, the use of bulky gold(I)-complexes, such as $[JhonPhosAu]^+$, is essential for the satisfactory formation of products (Morita et al., 2018).

Gold-catalyzed cyclizations in 1,6-enynes on indole scaffolds have also been reported in the last years (Pérez-Galán et al., 2016). **Figure 13C** shows a recent example in which *N*-substituted indoles **147** containing an alkene-tethered diyne cycloisomerize to eight-membered ring indoziline derivatives **148** under gold(I)-catalysis. Shi et al. described the use of bulky-phosphine gold complexes to promote, under thermal treatment (80°C), two intramolecular nucleophilic attacks at the C2 and C3 centers of the indole moiety of both activated internal alkyne groups. Interestingly, compounds **148** exhibit yellow-green fluorescence, so they may have potential applications in the field of OLEDs (Liu et al., 2018). Related gold(I)-mediated carbocyclizations of enynes involving an eight-membered ring formation have been described recently in the synthesis of dibenzo[*b,e*][1,4]diazocines (Ito et al., 2018). Likewise, gold(III) complexes have been reported to be able to promote carbocyclization processes. Thus, bis(indoyl)methyl alkynols **149** are transformed into substituted carbazoles **150** under catalysis of hydratated $NaAuCl_4$ (**Figure 13D**). The mechanism for this transformation was found computationally to proceed via an unsual 1,2-migration of an indolylmethyl moiety as key step (Suárez et al., 2017). 1,2- And 1,3-quinazolinone fused pyrroles **152** and **154** were achieved involving a $AuCl_3$-mediated cycloisomerization of alkynyl pyrroles **151** and **153** (**Figure 13E**). 1,2-Quinazolinones **152** are formed via an initial 1,3-R^3 rearrangement followed by a 6-*exo-trig* cyclization involving the pendant pyrrol ring at **151**, while **153** is transformed into **154** directly through a 6-*exo-dig* cyclization onto the terminal akyne unit (Wei et al., 2018). Nevertheless, related structurally pyrroles bearing a non-terminal akyne experiments a 7-*endo-dig* cyclization rather than a 6-*exo-dig* (Kong et al., 2018).

Reactants containing a cyclopropane unit have gained considerable attention lately, and a number of remarkable transformations using this kind of substrates have been achieved through gold-chemistry. The *cis*-to-*trans* isomerization of cyclopropane rings has been experimental and computationally studied under gold(I) and gold(III) catalysis, concluding that chiral bisoxazoline-Au(III) complexes are the best catalysts for promoting this isomerization (Reiersølmoen et al., 2018).

Shi and co-workers reported a set of works on gold(I)-catalyzed cycloisomerization of enynes containing methylenecyclopropanes. The $IPrAuSbF_6$ catalyst is able to activate the alkyne motif of enynes toward an intramolecular cyclization and further ring expansion of the methylenecyclopropane scaffold. For instance, aniline-linked 1,6-enynes bearing a cyclopropane ring **155** can be converted into 1,2-dihydroquinolines **156** and **157** under thermal conditions in a solution of dichloroethane. Under gold-catalysis, products **156**, containing a cyclobutene ring were the major product compared to compounds **157**, in which the cyclopropane is not expanded (**Figure 14A**). This product ratio is inverted when using $AgSbF_6$ as catalyst (Jiang et al., 2018). This methodology was extended to methylenecyclopropane-contained ynamides **158**. Thus, substrates **158** evolve at room temperature to the polycyclic system **159** using Ph_3PAuCl as catalyst whereas spirocyclics **160** were obtained by using a more sterically bulky catalyst, such as JohnphosAuCl. In both cases the gold-catalyst promotes the expansion of the alkylidencyclopropane to a four-member ring but only in the latter the catalyst facilities the subsequent intramolecular Friedel-Crafts process in the formation of **160** (**Figure 14B**) (Zhang et al., 2018b). A similar situation is reported for the intramolecular hydroarylation of the enynes **161** toward oxacycles **162** and **163** . Thus, whereas both catalysts, $IPrAuSbF_6$ and $(p\text{-}CF_3C_6H_4)_3PAuSbF_6$, promote the carbocyclization step, only the former promotes the methylenecyclopropane expansion to a cyclobutene ring (**Figure 14C**). The authors reasoned this different reactivity attending to the inability of the gold complex containing electron-deficient phosphine ligands to activate the alkene moiety toward the ring expansion process (Fang et al., 2016). Temperature can also be a determining factor in these reactions, as shown in the isomerization of 1,5-enynes containing a cyclopropane ring, **164**. These systems cycloisomerize to related bicyclic or spirobicyclic compounds depending on the catalyst and the thermal conditions. For instance, **164** furnishes **165** in presence of $IPrAuNTf_2$ at -30°C. However, substrate **164** is converted into the biscyclopropanes **166** at 0°C under catalysis of the bulky gold complex $[JohnPhosAu(MeCN)]SbF_6$ whereas bicycles **167** can be obtained at 60°C in a good diastereoisomeric ratio (**Figure 14D**). The authors proposed a catalytic cycle in which compounds **165** and **166** are precursors of **167** (Chen et al., 2016b). In the same line, Voituriez et al. described the enantioselective synthesis of cyclobutanone derivatives **169** via gold(I)-catalyzed cycloisomerization of enyne-methylenecyclopropanes **168**. The most broadly tested catalyst was a binuclear gold complex bearing a bulky

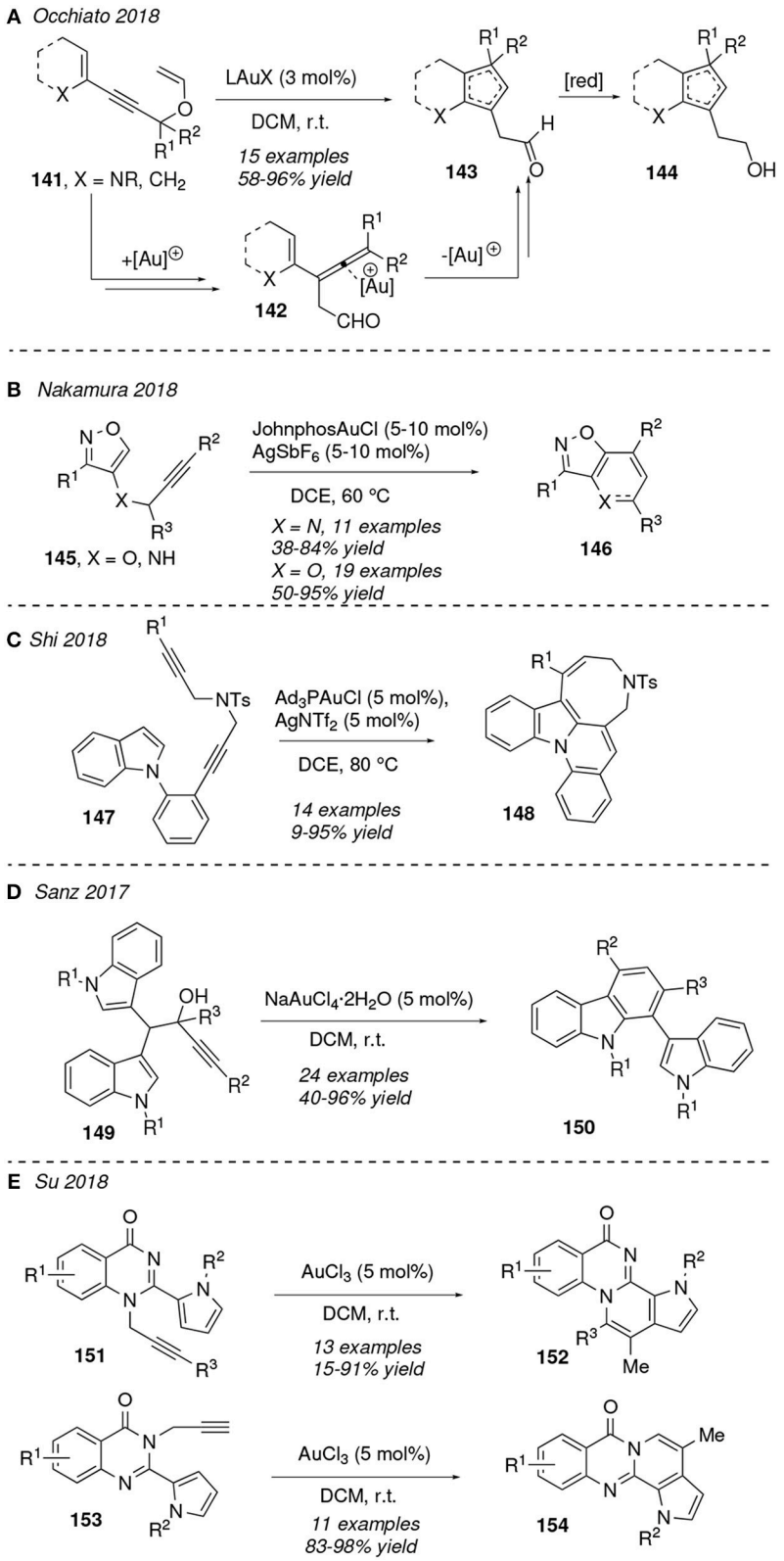

FIGURE 13 | Gold-mediated cycloisomerization of 1,*n*-enynes.

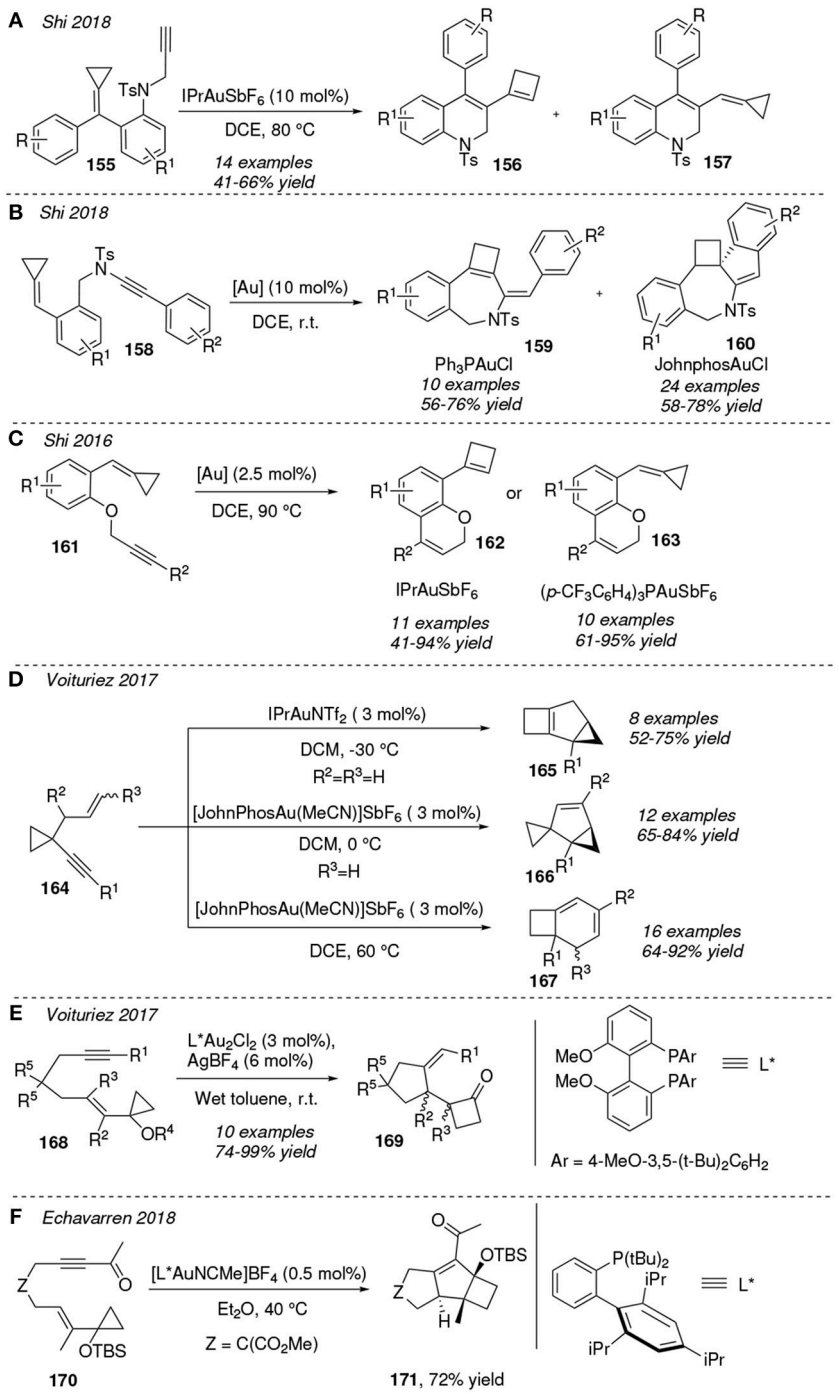

FIGURE 14 | Gold-mediated cycloisomerization of 1,n-dienynes containing a cyclopropane ring.

chiral-phosphine ligand, as represented in **Figure 14E**. The major isolated products are those with substituents R^2 and R^3 presenting *cis* configuration (Wu et al., 2017). A similar approach was used as the key step in the total synthesis of the sesquiterpene Repraesentin F. Echavarren et al. reported a highly diastereoselective gold(I)-mediated cyclization of the 1,6-enyne **170** via a tandem cycloisomerization/Prins-type reaction furnishing the tricyclic systems **171** containing the unsual skeleton of this natural product. Through this protocol the diasteroisomer with the desired *anti* ring fusion configuration

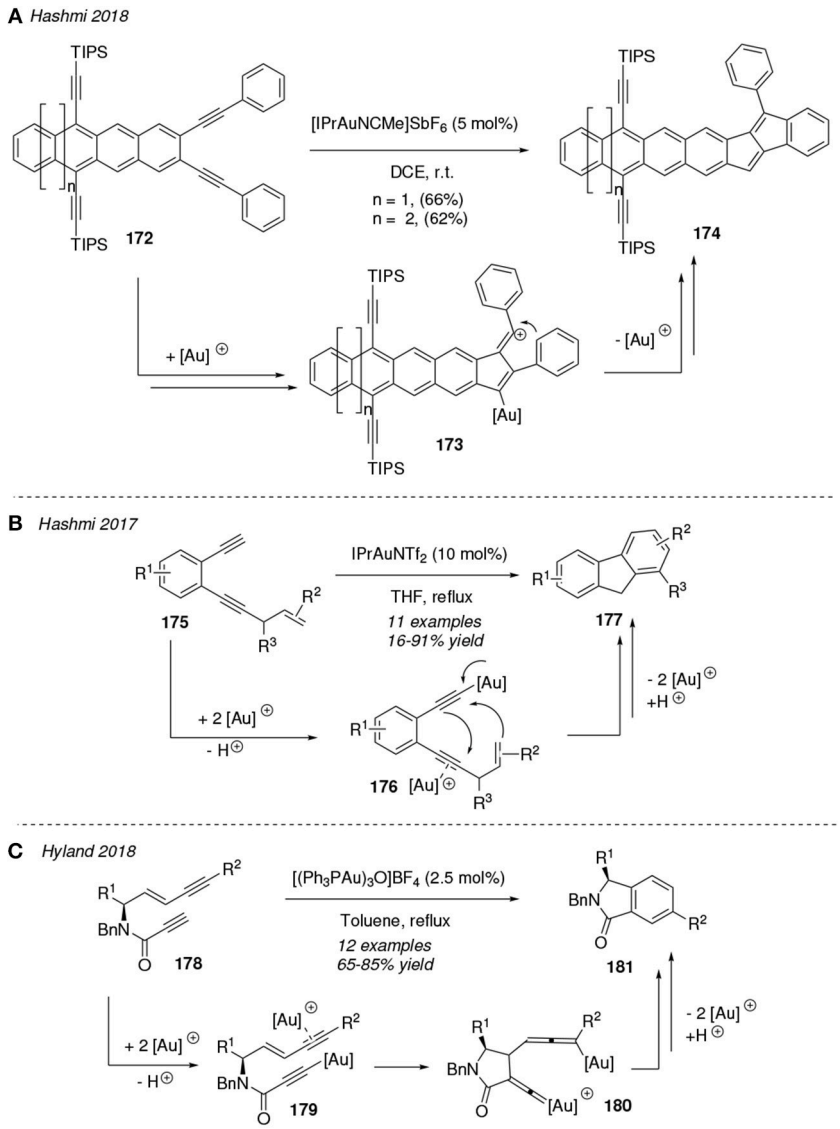

FIGURE 15 | Gold-mediated cycloisomerization reactions of 1,*n*-diynes.

is obtained as major product in a 7.2:1 ratio with respect to that with the *syn* fusion (**Figure 14F**) (Ferrer and Echavarren, 2018b).

The reactivity pattern of 1,*n*-diynes has also been smartly exploited toward the construction of complex highly π-conjugated polycyclic systems (Asiri and Hashmi, 2016). In this sense, the works from Hashmi stand out with several remarkable publications on this topic in the last years (Tšupova et al., 2017; Wurm et al., 2017, 2018). A representative example is shown in **Figure 15A**. They described the gold-mediated cycloisomerization of 1,5-diynes building on an aromatic ring **172** toward aromatic polycyclic-annulated systems **174**. The reaction mechanism involves a vinyl cation intermediate **173** and operates under mild reaction conditions. Interestingly optical properties have been described in this kind of annulated-pentalene compounds making them potential candidates for future optoelectronic devices (Sekine et al., 2018). Another example by Hashmi et al. was reported in 2017 and was highlighted as the first intramolecular trapping of dually gold-activated intermediates **176** with an olefinic C(sp^2)-H bond (**Figure 15B**). 1,5-Diynes bearing an allyl-substituted alkene attached to an aromatic skeleton (**175**) could also be converted into fluorene derivatives **177** via a dehydrogenative dual gold-catalyzed activation at reflux of tetrahydrofuran (Bucher et al., 2017). In this sense, dual-gold catalysis has been implemented in the cycloaromatization of unconjugated *(E)*-enedynes **178** toward isoindolines **181** by using the trigold oxo complex $[(Ph_3PAu)_3O]BF_4$ as catalyst (**Figure 15C**). Both specific experiments with deuterated reactants and a detailed theoretical study indicate that the most feasible mechanistic pathway is that involving the very reactive allenyl-gold/gold-vinylidene

intermediate **180**, which is generated from a dual-gold activated substrate **179** via a 5-*exo*-trig cyclization. The subsequent carbocyclization and rearomatization afforded the enantioriched isoindolines **181** in good yields (Zamani et al., 2019).

4. CONCLUSIONS

In this review, the interest on gold and its relevance in intramolecular isomerization reactions is confirmed by taking into account the vast number of studied reported in the last 3 years and covered here. Most of the isomerization processes included in this review are initiated by three main different kind of transformations at allene and alkyne sites: nucleophilick attack onto the activated alkyne, 1,3 or 1,2- rearrangement of a carbonate/ester group over the π-system or a carbocyclization process. As we have shown, structurally complex molecules can be synthesize from easily reachable reactants under gold-catalysis and mild reaction conditions. Fewer in number but still important, some studies have developed gold(III)-catalysts although gold(I)-complexes seem to be more versatile, effective and preferred in this kind of reactions. Nowadays, enantioselective synthesis is a paramount goal, particularly when chemists are involved in biologically relevant molecules. Accordingly, the number of studies involving gold-complexes containing chiral ligands is growing notably. Although we can consider gold as a "young" metal, chemically speaking, it is clear that this metal center has many advantages to take into account when designing and performing innovative, complexity oriented and efficient chemical transformations.

AUTHOR CONTRIBUTIONS

CS, ON, and MM-L contributed conception of the review article, scope and structure. MM-L drafted the article. CS and ON revised its scientific and formal content.

FUNDING

This work has been funded by the Ministerio de Economía, Industria y Competitividad (CTQ2016-75023-C2-2P) and the Xunta de Galicia (ED431C 2017/27).

ACKNOWLEDGMENTS

MM-L thanks Xunta de Galicia for a post-doctoral research contract (ED481B 2016/166-0).

REFERENCES

Alcaide, B., Almendros, P., Cembellín, S., Fernández, I., and Martínez del Campo, T. (2016). Metal-catalyzed cyclization reactions of 2,3,4-Trien-1-ols: a joint experimental-computational study. *Chem. A Eur. J.* 22, 11667–11676. doi: 10.1002/chem.201601838

Alcaide, B., Almendros, P., Fernández, I., Herrera, F., and Luna, A. (2018). Gold-catalyzed divergent ring-closing modes of indole-tethered amino allenynes. *Chem. Eur. J.* 24, 1448–1454. doi: 10.1002/chem.201705294

An, J., Parodi, A., Monari, M., Reis, M. C., Lopez, C. S., and Bandini, M. (2017). Gold-catalyzed dearomatization of 2-naphthols with alkynes. *Chem. Eur. J.* 23, 17473–17477. doi: 10.1002/chem.201704942

Arif, T., Cazorla, C., Bogliotti, N., Saleh, N., Blanchard, F., Gandon, V., et al. (2018). Bimetallic gold(i) complexes of photoswitchable phosphines: synthesis and uses in cooperative catalysis. *Catal. Sci. Technol.* 8, 710–715. doi: 10.1039/c7cy01614j

Asiri, A. M., and Hashmi, A. S. K. (2016). Gold-catalysed reactions of diynes. *Chem. Soc. Rev.* 45, 4471–4503. doi: 10.1039/c6cs00023a

Aubert, C., Fensterbank, L., Garcia, P., Malacria, M., and Simonneau, A. (2011). Transition metal catalyzed cycloisomerizations of 1, n-allenynes and-allenenes. *Chem. Rev.* 111, 1954–1993. doi: 10.1021/cr100376w

Bao, M., Lu, W., Cai, Y., Qiu, L., and Xu, X. (2017). Gold(I)-catalyzed cyclization/carbonylation cascade reaction of 1,6-diynes: an access to β,γ-unsaturated ketones. *J. Org. Chem.* 82, 13386–13395. doi: 10.1021/acs.joc.7b02461

Belmont, P., and Parker, E. (2009). Silver and gold catalysis for cycloisomerization reactions. *Eur. J. Org. Chem.* 2009, 6075–6089. doi: 10.1002/ejoc.200900790

Blons, C., Amgoune, A., and Bourissou, D. (2018). Gold(III) π complexes. *Dalt. Trans.* 47, 10388–10393. doi: 10.1039/c8dt01457d

Bucher, J., Wurm, T., Taschinski, S., Sachs, E., Ascough, D., Rudolph, M., et al. (2017). Dual gold catalysis: synthesis of fluorene derivatives from diynes. *Adv. Synth. Catal.* 359, 225–233. doi: 10.1002/adsc.201600987

Cao, Z., Li, S., Li, J., Meng, X., Zhang, H., Sun, X., et al. (2016). Gold-catalyzed π-directed regioselective cyclization of bis(: O -alkynyl benzyl alcohols): rapid access to dihydroisobenzofuran derivatives. *New J. Chem.* 40, 8211–8215. doi: 10.1039/c6nj02066f

Chen, C., Zou, Y., Chen, X., Zhang, X., Rao, W., and Chan, P. W. H. (2016a). Gold-catalyzed tandem 1,3-migration/double cyclopropanation of 1-Ene-4,n-diyne esters to tetracyclodecene and tetracycloundecene derivatives. *Org. Lett.* 18, 4730–4733. doi: 10.1021/acs.orglett.6b02404

Chen, G. Q., Fang, W., Wei, Y., Tang, X. Y., and Shi, M. (2016b). Divergent reaction pathways in gold-catalyzed cycloisomerization of 1,5-enynes containing a cyclopropane ring: dramatic: ortho substituent and temperature effects. *Chem. Sci.* 7, 4318–4328. doi: 10.1039/c6sc00058d

Chen, X., Merrett, J. T., and Hong Chan, P. W. (2018). Gold-catalyzed formal [4 + 2] cycloaddition of 5-(Ethynylamino)pent-2-yn-1-yl Esters to 1,2,3,5-tetrahydrobenzo [g] quinolines. *Org. Lett.* 20, 1542–1545. doi: 10.1021/acs.orglett.8b00267

Cheong, P. H. Y., Morganelli, P., Luzung, M. R., Houk, K. N., and Toste, F. D. (2008). Gold-catalyzed cycloisomerization of 1,5-allenynes via dual activation of an ene reaction. *J. Am. Chem. Soc.* 130, 4517–4526. doi: 10.1021/ja711058f

Ciancaleoni, G., Belpassi, L., Zuccaccia, D., Tarantelli, F., and Belanzoni, P. (2015). Counterion effect in the reaction mechanism of nhc gold(i)-catalyzed alkoxylation of alkynes: computational insight into experiment. *ACS Catal.* 5, 803–814. doi: 10.1021/cs501681f

Congmon, J., and Tius, M. A. (2018). Contiguous quaternary centers from a Au I -catalyzed nazarov cyclization. *Eur. J. Org. Chem.* 2018, 2926–2930. doi: 10.1002/ejoc.201800604

Das, A., Hua, Y., Yousufuddin, M., Cundari, T. R., Jeon, J., and Dias, H. V. (2016). Gold-mediated isomerization of cyclooctyne to ring fused olefinic bicycles. *Eur. J. Inorg. Chem.* 2016, 995–1001. doi: 10.1002/ejic.201600021

Day, D. P., and Chan, P. W. H. (2016). Gold-catalyzed cycloisomerizations of 1,n-diyne carbonates and esters. *Adv. Synth. Catal.* 358, 1368–1384. doi: 10.1002/adsc.201600005

Delaye, P. O., Petrignet, J., Thiery, E., and Thibonnet, J. (2017). Gold-silver catalyzed straightforward one pot synthesis of pyrano[3,4-: B] pyrrol-7(1 H)-ones. *Org. Biomol. Chem.* 15, 7290–7295. doi: 10.1039/c7ob01849e

Dorel, R., and Echavarren, A. M. (2015). Gold(I)-catalyzed activation of alkynes for the construction of molecular complexity. *Chem. Rev.* 115, 9028–9072. doi: 10.1021/cr500691k

Dorel, R., McGonigal, P. R., and Echavarren, A. M. (2016). Hydroacenes made easy by gold(I) catalysis. *Angew. Chem. - Int. Ed.* 55, 11120–11123. doi: 10.1002/anie.201604952

Ebule, R. E., Malhotra, D., Hammond, G. B., and Xu, B. (2016). Ligand effects in the gold catalyzed hydration of alkynes. *Adv. Synth. Catal.* 358, 1478–1481. doi: 10.1002/adsc.201501079

El Sayed Moussa, M., Chen, H., Wang, Z., Srebro-Hooper, M., Vanthuyne, N., Chevance, S., et al. (2016). Bimetallic Gold(I) complexes with ethynyl-helicene and bis-phosphole ligands: understanding the role of aurophilic interactions in their chiroptical properties. *Chem. Eur. J.* 22, 6075–6086. doi: 10.1002/chem.201600126

Fang, W., Tang, X. Y., and Shi, M. (2016). Gold(i)-catalyzed intramolecular hydroarylation and the subsequent ring enlargement of methylenecyclopropanes to cyclobutenes. *RSC Adv.* 6, 40474–40479. doi: 10.1039/c6ra02549h

Faza, O. N., and López, C. S. (2015). *Computational Approaches to Homogeneous Gold Catalysis*. London: Springer International Publishing. doi: 10.1007/128_2014_591

Feng, S., Wang, Z., Zhang, W., Xie, X., and She, X. (2016). An efficient synthesis of benzazocines by gold(I)-catalyzed tandem 1,2-acyloxy shift/[3+2] cycloaddition of terminal 1,9-enynyl esters. *Chem. An Asian J.* 11, 2167–2172. doi: 10.1002/asia.201600593

Fensterbank, L., and Malacria, M. (2014). Molecular complexity from polyunsaturated substrates: the gold catalysis approach. *Acc. Chem. Res.* 47, 953–965. doi: 10.1021/ar4002334

Ferrer, S., and Echavarren, A. M. (2018a). Role of σ,π-Digold(I) alkyne complexes in reactions of enynes. *Organometallics* 37, 781–786. doi: 10.1021/acs.organomet.7b00668

Ferrer, S., and Echavarren, A. M. (2018b). Total synthesis of repraesentin F and configuration reassignment by a gold(I)-catalyzed cyclization cascade. *Org. Lett.* 20, 5784–5788. doi: 10.1021/acs.orglett.8b02478

Fukuda, Y., and Utimoto, K. (1991). Effective transformation of unactivated alkynes into ketones or acetals with a gold(iii) catalyst. *J. Org. Chem.* 56, 3729–3731. doi: 10.1021/jo00011a058

García-Morales, C., and Echavarren, A. (2018). From straightforward gold(I)-catalyzed enyne cyclizations to more demanding intermolecular reactions of alkynes with alkenes. *Synlett* 29, 2225–2237. doi: 10.1055/s-0037-1610203

Gatto, M., Baratta, W., Belanzoni, P., Zotto, A. D., Tarantelli, F., and Zuccaccia, D. (2018). Hydration and alkoxylation of alkynes catalyzed by NHC-Au-OTf. *Green. Chem.* 20, 2125–2134 doi: 10.1039/c8gc00508g

Gatto, M., Belanzoni, P., Belpassi, L., Biasiolo, L., Del Zotto, A., Tarantelli, F., et al. (2016). Solvent-, silver-, and acid-free NHC-Au-X catalyzed hydration of alkynes. The pivotal role of the counterion. *ACS Catal.* 6, 7363–7376. doi: 10.1021/acscatal.6b01626

Ghosh, A., Basak, A., Chakrabarty, K., Ghosh, B., and Das, G. K. (2014). Ligand-assisted acyl migration in au-catalyzed isomerization of propargylic ester to diketone: a DFT study. *J. Org. Chem.* 79, 5652–5663. doi: 10.1021/jo500822v

Gobé, V., Dousset, M., Retailleau, P., Gandon, V., and Guinchard, X. (2018). Dissecting the gold(I)-catalyzed carboaminations of N-Allyl tetrahydro-β-carbolines to allenes. *J. Org. Chem.* 83, 898–912. doi: 10.1021/acs.joc.7b02900

Gorin, D. J., and Toste, F. D. (2007). Relativistic effects in homogeneous gold catalysis. *Nature* 446, 395–403. doi: 10.1038/nature05592

Gung, B. W., Holmes, M. R., Jones, C. A., Ma, R., and Barnes, C. L. (2016). Structure-enantioselectivity correlation in nhc-au(i) catalysis for 1,6-enynecyclizations. *Tetrahedron Lett.* 57, 3912–3915. doi: 10.1016/j.tetlet.2016.07.046

Hashmi, A. S., Frost, T. M., and Bats, J. W. (2000). Highly selective gold-catalyzed arene synthesis [24]. *J. Am. Chem. Soc.* 122, 11553–11554. doi: 10.1021/ja005570d

Hashmi, A. S. K. (2014). Dual gold catalysis. *Acc. Chem. Res.* 47, 864–876. doi: 10.1021/ar500015k

Hashmi, A. S. K., Schäfer, S., Wölfle, M., Gil, C. D., Fischer, P., Laguna, A., et al. (2007). Gold-catalyzed benzylic C-H activation at room temperature. *Angew. Chem. Int. Ed.* 46, 6184–6187. doi: 10.1002/anie.200701521

He, Y., Li, Z., Tian, G., Song, L., Van Meervelt, L., and Van der Eycken, E. V. (2017). Gold-catalyzed diastereoselective domino dearomatization/ipso-cyclization/aza-Michael sequence: a facile access to diverse fused azaspiro tetracyclic scaffolds. *Chem. Commun.* 53, 6413–6416. doi: 10.1039/C7CC03152A

Herndon, J. W. (2018). The chemistry of the carbon-transition metal double and triple bond: Annual survey covering the year 2017. *Coord. Chem. Rev.* 377, 86–190. doi: 10.1016/j.ccr.2018.08.007

Homs, A., Obradors, C., Leboeuf, D., and Echavarren, A. M. (2014). Dissecting anion effects in gold(I)-catalyzed intermolecular cycloadditions. *Adv. Synth. Catal.* 356, 221–228. doi: 10.1002/adsc.201300704

Hu, Y., Bai, M., Yang, Y., and Zhou, Q. (2017). Metal-catalyzed enyne cycloisomerization in natural product total synthesis. *Org. Chem. Front.* 4, 2256–2275. doi: 10.1039/c7qo00702g

Ito, M., Inoue, D., Takaki, A., Kanyiva, K. S., and Shibata, T. (2018). 8-exo-dig-Selective Cycloisomerization for the Synthesis of Dibenzo[b,e][1,4]diazocines Using Cationic AuI Catalysts. *Eur. J. Org. Chem.* 2018, 4740–4747. doi: 10.1002/ejoc.201801037

Jha, M., Dhiman, S., Cameron, T. S., Kumar, D., and Kumar, A. (2017). Au-catalyzed synthesis of thiopyrano[2,3-b]indoles featuring tandem rearrangement and hydroarylation. *Org. Lett.* 19, 2038–2041. doi: 10.1021/acs.orglett.7b00617

Jia, M., and Bandini, M. (2015). Counterion effects in homogeneous gold catalysis. *ACS Catal.* 5, 1638–1652. doi: 10.1021/cs501902v

Jiang, B., Wei, Y., and Shi, M. (2018). Gold- and silver-catalyzed intramolecular annulation and rearrangement of aniline-linked 1,6-enynes containing methylenecyclopropanes. *Org. Chem. Front.* 5, 2091–2097. doi: 10.1039/C8QO00358K

Jiménez-Núñez, E. and Echavarren, A. M. (2008). Gold-catalyzed cycloisomerizations of enynes: a mechanistic perspective. *Chem. Rev.* 108, 3326–3350. doi: 10.1021/cr0684319

Jones, A. C. (2015). *Gold π-Complexes as Model Intermediates in Gold Catalysis.* Cham: Springer International Publishing.

Kiriakidi, S., Nieto Faza, O., Kolocouris, A., and López, C. S. (2017). Governing effects in the mechanism of the gold-catalyzed cycloisomerization of allenic hydroxylamine derivatives. *Org. Biomol. Chem.* 15, 5920–5926. doi: 10.1039/c7ob01275f

Kong, X. F., Zhan, F., He, G. X., Pan, C. X., Gu, C. X., Lu, K., et al. (2018). Gold-catalyzed selective 6-exo-dig and 7-endo-dig cyclizations of alkyn-tethered indoles to prepare rutaecarpine derivatives. *J. Org. Chem.* 83, 2006–2017. doi: 10.1021/acs.joc.7b02956

Kothandaraman, P., Zhao, Y., Lee, B. R., Le Ng, C. J., Lee, J. Y., Ayers, B. J., et al. (2016). Gold-catalyzed aminoalkenylation of β-Amino-1,n-diynols to cycloalkyl-, piperidinyl- and pyranyl-fused pyrroles. *Adv. Synth. Catal.* 358, 1385–1391. doi: 10.1002/adsc.201600011

Larsen, M. H., Houk, K. N., and Hashmi, A. S. K. (2015). Dual gold catalysis: stepwise catalyst transfer via dinuclear clusters. *J. Am. Chem. Soc.* 137, 10668–10676. doi: 10.1021/jacs.5b05773

Lee, K. H., Jillella, R., Kim, J., and Oh, C. H. (2018). Synthesis of primitive dendrimer systems bearing bicyclo[3,2,0]Hept-6-en-6-yl groups via unique Au-catalyzed [2+2] cyclization. *Bull. Korean Chem. Soc.* 39, 651–656. doi: 10.1002/bkcs.11445

Lee, Y.-C., and Kumar, K. (2018). Gold(I) catalyzed enyne cycloisomerization - a roadmap to privileged heterocyclic scaffolds. *Isr. J. Chem.* 58, 531–556. doi: 10.1002/ijch.201700067

Lee, Y. J., Heo, H. G., and Oh, C. H. (2016). Syntheses of 2,2'-bibenzo[7]annulenes by double au-catalyzed sequential activation of propargylic carboxylates. *Tetrahedron* 72, 6113–6117. doi: 10.1016/j.tet.2016.07.060

Lempke, L., Sak, H., Kubicki, M., and Krause, N. (2016). Gold-catalyzed cycloisomerization of trifluoromethylated allenols: sustainability and mechanistic studies. *Org. Chem. Front.* 3, 1514–1519. doi: 10.1039/c6qo00423g

Li, H., Harris, R. J., Nakafuku, K., and Widenhoefer, R. A. (2016). Kinetics and mechanism of allene racemization catalyzed by a gold N-heterocyclic carbene complex. *Organometallics* 35, 2242–2248. doi: 10.1021/acs.organomet.6b00307

Li, T., Wang, H., Qian, P., Yang, Y., Li, B., and Zhang, L. (2018a). Au(I)-Catalyzed expeditious access to naphtho[2,3-*c*]furan-1(3-*H*)-ones from readily available propargylic ynoates. *Chem. Commun.* 54, 10447–10450. doi: 10.1039/C8CC06056H

Li, Y., Kirillov, A. M., Fang, R., and Yang, L. (2017a). Effect of substituent on the mechanism and chemoselectivity of the gold(I)-catalyzed propargyl ester tandem cyclization. *Organometallics* 36, 1164–1172. doi: 10.1021/acs.organomet.7b00042

Li, Y., Wei, M., and Dai, M. (2017b). Gold catalysis-facilitated rapid synthesis of the daphnane/tigliane tricyclic core. *Tetrahedron* 73, 4172–4177. doi: 10.1016/j.tet.2016.11.005

Li, Z., Song, L., Meervelt, L. V., Tian, G., and Van der Eycken, E. V. (2018b). Cationic gold(I)-catalyzed cascade bicyclizations for divergent synthesis of (Spiro)polyheterocycles. *ACS Catal.* 8, 6388–6393. doi: 10.1021/acscatal.8b01789

Liao, H., Leng, W. L., Le Mai Hoang, K., Yao, H., He, J., Voo, A. Y. H., et al. (2017). Asymmetric syntheses of 8-oxabicyclo[3,2,1]octane and 11-oxatricyclo[5.3.1.0]undecane from glycals. *Chem. Sci.* 8, 6656–6661. doi: 10.1039/c7sc02625k

Liu, R., Wang, Q., Wei, Y., and Shi, M. (2018). Synthesis of indolizine derivatives containing eight-membered rings: via a gold-catalyzed two-fold hydroarylation of diynes. *Chem. Commun.* 54, 1225–1228. doi: 10.1039/c7cc09250d

Lu, X.-L., Lyu, M.-Y., Peng, X.-S., and Wong, H. N. C. (2018). Gold(I)-catalyzed tandem cycloisomerization of 1,5-enyne ethers by hydride transfer. *Angew. Chem. Int. Ed.* 57, 11365–11368. doi: 10.1002/anie.201806842

Luo, K., Cao, T., Jiang, H., Chen, L., and Zhu, S. (2017). Gold-catalyzed ring expansion of enyne-lactone: generation and transformation of 2-oxoninonium. *Org. Lett.* 19, 5856–5859. doi: 10.1021/acs.orglett.7b02834

Luo, K., Zhang, L., Jiang, H., Chen, L., and Zhu, S. (2018). Selectivity-switchable construction of benzo-fused polycyclic compounds through a gold-catalyzed reaction of enyne-lactone. *Chem. Commun.* 54, 1893–1896. doi: 10.1039/c7cc09786g

Maes, B., Cossy, J., and Polanc, S. (2016). *Au-Catalyzed Synthesis and Functionalization of Heterocycles*, Vol. 46. Basel: Springer Nature.

Magné, V., Lorton, C., Marinetti, A., Guinchard, X., and Voituriez, A. (2017). Short enantioselective total synthesis of (-)-rhazinilam using a gold(I)-catalyzed cyclization. *Org. Lett.* 19, 4794–4797. doi: 10.1021/acs.orglett.7b02210

Mandal, N., and Datta, A. (2018). Gold(I)-catalyzed intramolecular diels-alder reaction: evolution of trappable intermediates via asynchronous transition states. *J. Org. Chem.* 83, 11167–11177. doi: 10.1021/acs.joc.8b01752

McCarter, A. W., Sommer, M., Percy, J. M., Jamieson, C., Kennedy, A. R., and Hirst, D. J. (2018). Atom efficient synthesis of selectively difluorinated carbocycles through a gold(I) catalyzed cyclization. *J. Org. Chem.* 83, 8888–8905. doi: 10.1021/acs.joc.8b01121

McGee, P., Brousseau, J., and Barriault, L. (2018). Development of new gold (I)-catalyzed carbocyclizations and their applications in the synthesis of natural products. *Isr. J. Chem.* 58, 511–520. doi: 10.1002/ijch.201700054

Mizushima, E., Sato, K., Hayashi, T., and Tanaka, M. (2002). Highly efficient aui-catalyzed hydration of alkynes. *Angew. Chem. Int. Ed.* 41, 4563–4565. doi: 10.1002/1521-3773(20021202)41:23<4563::AID-ANIE4563>3.0.CO;2-U

Morita, T., Fukuhara, S., Fuse, S., and Nakamura, H. (2018). Gold(I)-catalyzed intramolecular SEAr reaction: efficient synthesis of isoxazole-containing fused heterocycles. *Org. Lett.* 20, 433–436. doi: 10.1021/acs.orglett.7b03760

Muratore, M. E., Konovalov, A. I., Armengol-Relats, H., and Echavarren, A. M. (2018). Diastereospecific gold(I)-catalyzed cyclization cascade for the controlled preparation of N- and N,O-heterocycles. *Chem. Eur. J.* , 15613–15621. doi: 10.1002/chem.201802770

Nahide, P. D., Jiménez-Halla, J. O. C., Wrobel, K., Solorio-Alvarado, C. R., Ortiz Alvarado, R., and Yahuaca-Juárez, B. (2018). Gold(I)-catalysed high-yielding synthesis of indenes by direct Csp3-H bond activation. *Org. Biomol. Chem.* 16, 7330–7335. doi: 10.1039/C8OB02056F

Naoe, S., Yoshida, Y., Oishi, S., Fujii, N., and Ohno, H. (2016). Total synthesis of (+)-conolidine by the gold(I)-catalyzed cascade cyclization of a conjugated enyne. *J. Org. Chem.* 81, 5690–5698. doi: 10.1021/acs.joc.6b00720

Nechaev, A. A., Van Hecke, K., Zaman, M., Kashtanov, S., Ungur, L., Pereshivko, O. P., et al. (2018). Gold-catalyzed post-ugi ipso-cyclization with switchable diastereoselectivity. *J. Org. Chem.* 83, 8170–8182. doi: 10.1021/acs.joc.8b00953

Obradors, C., and Echavarren, A. M. (2014). Gold-catalyzed rearrangements and beyond. *Acc. Chem. Res.* 47, 902–912. doi: 10.1021/ar400174p

Odabachian, Y., Le Goff, X. F., and Gagosz, F. (2009). An unusual access to medium sized cycloalkynes by a new gold(i)-catalysed cycloisomerisation of diynes. *Chem. Eur. J.* 15, 8966–8970. doi: 10.1002/chem.200901312

Pan, F., Shu, C., and Ye, L. W. (2016). Recent progress towards gold-catalyzed synthesis of N-containing tricyclic compounds based on ynamides. *Org. Biomol. Chem.* 14, 9456–9465. doi: 10.1039/c6ob01774f

Patel, D. S., and Bharatam, P. V. (2011). To bend or not to bend! the dilemma of allenes. *J. Org. Chem.* 76, 2558–2567. doi: 10.1021/jo102432a

Peng, X., Zhu, L., Hou, Y., Pang, Y., Li, Y., Fu, J., et al. (2017). Access to Benzo[a]carbazoles and Indeno[1,2-c]quinolines by a Gold(I)-Catalyzed Tunable Domino Cyclization of Difunctional 1,2-Diphenylethynes. *Org. Lett.* 19, 3402–3405. doi: 10.1021/acs.orglett.7b01358

Pérez-Galán, P., Waldmann, H., and Kumar, K. (2016). Building polycyclic indole scaffolds via gold(I)-catalyzed intra- and inter-molecular cyclization reactions of 1,6-enynes. *Tetrahedron* 72, 3647–3652. doi: 10.1016/j.tet.2016.03.020

Quintavalla, A., and Bandini, M. (2016). Gold-catalyzed allylation reactions. *ChemCatChem* 8, 1437–1453. doi: 10.1002/cctc.201600071

Ranieri, B., Escofet, I., and Echavarren, A. M. (2015). Anatomy of gold catalysts: facts and myths. *Org. Biomol. Chem.* 13, 7103–7118. doi: 10.1039/c5ob00736d

Rao, W., Boyle, J. W., and Chan, P. W. H. (2016). Gold-catalyzed sequential cyclization of 1-En-3,9-diyne esters to partially hydrogenated 3H-Dicyclopenta[a,b]naphthalenes. *Chem. Eur. J.* 22, 6532–6536. doi: 10.1002/chem.201600915

Reeves, R. D., Phelps, A. M., Raimbach, W. A., and Schomaker, J. M. (2017). Diastereoselective Au-catalyzed allene cycloisomerizations to highly substituted cyclopentenes. *Org. Lett.* 19, 3394–3397. doi: 10.1021/acs.orglett.7b01350

Reiersølmoen, A. C., Østrem, E., and Fiksdahl, A. (2018). Gold(III)-catalysed cis -to- trans cyclopropyl isomerization. *Eur. J. Org. Chem.* 2018, 3317–3325. doi: 10.1002/ejoc.201800419

Riedel, S., Maichle-Mössmer, C., and Maier, M. E. (2017). Intramolecular diels-alder reactions of tethered enoate substituted furans induced by dialkylaluminum chloride. *J. Org. Chem.* 82, 12798–12805. doi: 10.1021/acs.joc.7b02117

Rinaldi, A., Petrović, M., Magnolfi, S., Scarpi, D., and Occhiato, E. G. (2018). Pentannulation reaction by tandem Gold(I)-catalyzed propargyl claisen rearrangement/nazarov cyclization of enynyl vinyl ethers. *Org. Lett.* 20, 4713–4717. doi: 10.1021/acs.orglett.8b02141

Rocchigiani, L., Jia, M., Bandini, M., and Macchioni, A. (2015). Assessing the role of counterion in gold-catalyzed dearomatization of indoles with allenamides by nmr studies. *ACS Catalysis* 5, 3911–3915. doi: 10.1021/acscatal.5b00502

Sahoo, A. K., Prabagar, B., Mallick, R. K., Prasad, R., and Gandon, V. (2018). Umpolung reactivity of ynamides: an unconventional [1,3]-sulfonyl and [1,5]-sulfinyl migration cascade. *Angew. Chem. Int. Ed.* doi: 10.1002/anie.201813143

Sanjuán, A. M., Rashid, M. A., García-García, P., Martínez-Cuezva, A., Fernández-Rodríguez, M. A., Rodríguez, F., et al. (2015). Gold(I)-catalyzed cycloisomerizations and alkoxycyclizations of ortho-(alkynyl)styrenes. *Chem. Eur. J.* 21, 3042–3052. doi: 10.1002/chem.201405789

Sanjuán, A. M., Virumbrales, C., García-García, P., Fernández-Rodríguez, M. A., and Sanz, R. (2016). Formal [4 + 1] cycloadditions of β,β-diaryl-substituted ortho-(Alkynyl)styrenes through Gold(I)-catalyzed cycloisomerization reactions. *Org. Lett.* 18, 1072–1075. doi: 10.1021/acs.orglett.6b00191

Schießl, J., Schulmeister, J., Doppiu, A., Wörner, E., Rudolph, M., Karch, R., et al. (2018a). An industrial perspective on counter anions in gold catalysis: on alternative counter anions. *Adv. Synth. Catal.* 360, 3949–3959. doi: 10.1002/adsc.201800629

Schießl, J., Schulmeister, J., Doppiu, A., Wörner, E., Rudolph, M., Karch, R., et al. (2018b). An industrial perspective on counter anions in gold catalysis: underestimated with respect to "Ligand Effects". *Adv. Synth. Catal.* 360, 2493–2502. doi: 10.1002/adsc.201800233

Sekine, K., Stuck, F., Schulmeister, J., Wurm, T., Zetschok, D., Rominger, F., et al. (2018). N-heterocycle-fused pentalenes by a gold-catalyzed annulation of diethynyl-quinoxalines and -phenazines. *Chem. Eur. J.* 24, 12515–12518. doi: 10.1002/chem.201803096

Shen, W.-B., Zhou, B., Zhang, Z.-X., Yuan, H., Fang, W., and Ye, L.-W. (2018). Gold-catalyzed cascade cyclization of N -propargyl ynamides: rapid access to functionalized indeno[1,2- c]pyrroles. *Org. Chem. Front.* 5, 2468–2472. doi: 10.1039/C8QO00552D

Siva Kumari, A. L., Siva Reddy, A., and Swamy, K. C. (2016). Exploring the gold mine: [Au]-catalysed transformations of enynals, enynones and enynols. *Org. Biomol. Chem.* 14, 6651–6671. doi: 10.1039/c6ob00698a

Soriano, E., and Fernández, I. (2014). Allenes and computational chemistry: from bonding situations to reaction mechanisms. *Chem. Soc. Rev.* 43, 3041–3105. doi: 10.1039/c3cs60457h

Stathakis, C. I., Gkizis, P. L., and Zografos, A. L. (2016). Metal-catalyzed cycloisomerization as a powerful tool in the synthesis of complex sesquiterpenoids. *Nat. Prod. Rep.* 33, 1093–1117. doi: 10.1039/c6np00026f

Stephen, A., Hashmi, K., Braun, I., Rudolph, M., and Rominger, F. (2012). The role of gold acetylides as a selectivity trigger and the importance of gem-diaurated species in the gold-catalyzed hydroarylating-aromatization of arene-diynes. *Organometallics* 31, 644–661. doi: 10.1021/om200946m

Stephen, A., Hashmi, K., Schwarz, L., Choi, J. H., and Frost, T. M. (2000). A new gold-catalyzed C-C bond formation. *Angew. Chem. - Int. Ed.* 39, 2285–2288. doi: 10.1002/1521-3773(20000703)39

Suárez, A., Suárez-Pantiga, S., Nieto-Faza, O., and Sanz, R. (2017). Gold-catalyzed synthesis of 1-(indol-3-yl)carbazoles: selective 1 2-alkyl vs 1 2-vinyl migration. *Org. Lett.* 19, 5074–5077. doi: 10.1021/acs.orglett.7b02303

Sun, H., Xu, S., Xing, Z., Liu, L., Feng, S., Fang, B., et al. (2017). Rapid construction of complex tetracyclic frameworks via a gold(i)-catalyzed tandem 1,2-acyloxy migration/[3 + 2] cycloaddition/Friedel-Crafts type cyclization reaction of linear enynyl esters. *Org. Chem. Front.* 4, 2109–2113. doi: 10.1039/c7qo00511c

Sun, N., Xie, X., Chen, H., and Liu, Y. (2016). Gold-catalyzed cyclization of furan-ynes bearing a propargyl carbonate group: intramolecular diels-alder reaction with *in situ* generated allenes. *Chem. Eur. J.* 22, 14175–14180. doi: 10.1002/chem.201603055

Swift, C. A., and Gronert, S. (2016). Gold(I)-induced rearrangements of propargyl derivatives: a gas-phase study. *Organometallics* 35, 3844–3851. doi: 10.1021/acs.organomet.6b00719

Teles, J. H., Brode, S., and Chabanas, M. (1998). Cationic gold(i) complexes: highly efficient catalysts for the addition of alcohols to alkynes. *Angew. Chem. Int. Ed.* 37, 1415–1418

Thummanapelli, S. K., Hosseyni, S., Su, Y., Akhmedov, N. G., and Shi, X. (2016). Ligand-controlled gold-catalyzed cycloisomerization of 1,*n*-enyne esters toward synthesis of dihydronaphthalene. *Chem. Commun.* 52, 7687–7690. doi: 10.1039/c6cc03032g

Timmerman, J. C., Laulhé, S., and Widenhoefer, R. A. (2017). Gold(I)-catalyzed intramolecular hydroamination of unactivated terminal and internal alkenes with 2-pyridones. *Org. Lett.* 19, 1466–1469. doi: 10.1021/acs.orglett.7b00450

Toullec, P. Y., and Michelet, V. (2018). Gold-catalyzed polycyclization toward natural products synthesis. *Isr. J. Chem.* 58, 578–585. doi: 10.1002/ijch.201800002

Trommenschlager, A., Chotard, F., Bertrand, B., Amor, S., Dondaine, L., Picquet, M., et al. (2017). Gold(i)-BODIPY-imidazole bimetallic complexes as new potential anti-inflammatory and anticancer trackable agents. *Dalt. Trans.* 46, 8051–8056. doi: 10.1039/c7dt01377a

Tšupova, S., Hansmann, M. M., Rudolph, M., Rominger, F., and Hashmi, A. S. K. (2017). Gold-catalyzed formal cyclisation/dimerization of thiophene-tethered diynes. *Chem. Eur. J.* 23, 5716–5721. doi: 10.1002/chem.201700061

Wang, W., Hammond, G. B., and Xu, B. (2012). Ligand effects and ligand design in homogeneous gold(I) catalysis. *J. Am. Chem. Soc.* 134, 5697–5705. doi: 10.1021/ja3011397

Wang, Y.-M., Lackner, A. D., and Toste, F. D. (2014). Development of catalysts and ligands for enantioselective gold catalysis. *Acc. Chem. Res.* 47, 889–901. doi: 10.1021/ar400188g

Wang, Z., Nicolini, C., Hervieu, C., Wong, Y. F., Zanoni, G., and Zhang, L. (2017a). Remote cooperative group strategy enables ligands for accelerative asymmetric gold catalysis. *J. Am. Chem. Soc.* 139, 16064–16067. doi: 10.1021/jacs.7b09136

Wang, Z., Ying, A., Fan, Z., Hervieu, C., and Zhang, L. (2017b). Tertiary amino group in cationic gold catalyst: tethered frustrated lewis pairs that enable ligand-controlled regiodivergent and stereoselective isomerizations of propargylic esters. *ACS Catal.* 7, 3676–3680. doi: 10.1021/acscatal.7b00626

Wei, L. S., He, G. X., Kong, X. F., Pan, C. X., Mo, D. L., and Su, G. F. (2018). Gold(III)-catalyzed selective cyclization of alkynyl quinazolinone-tethered pyrroles: synthesis of fused quinazolinone scaffolds. *J. Org. Chem.* 83, 6719–6727. doi: 10.1021/acs.joc.8b00168

Wei, Y., and Shi, M. (2016). Divergent synthesis of carbo- and heterocycles via gold-catalyzed reactions. *ACS Catal.* 6, 2515–2524. doi: 10.1021/acscatal.6b00048

Wildermuth, R., Speck, K., and Magauer, T. (2016). Gold(i)-catalyzed enyne cyclizations: studies toward the total synthesis of (+)-aureol. *Synthesis* 48, 1814–1824. doi: 10.1055/s-0035-1561589

Wu, Z., Lebœuf, D., Retailleau, P., Gandon, V., Marinetti, A., and Voituriez, A. (2017). Enantioselective gold(i)-catalyzed rearrangement of cyclopropyl-substituted 1,6-enynes into 2-oxocyclobutyl-cyclopentanes. *Chem. Commun.* 53, 7026–7029. doi: 10.1039/c7cc03234j

Wurm, T., Bucher, J., Rudolph, M., Rominger, F., and Hashmi, A. S. K. (2017). On the gold-catalyzed generation of phenyl cations from 1,5-diynes. *Adv. Synth. Catal.* 359, 1637–1642. doi: 10.1002/adsc.201700231

Wurm, T., Rüdiger, E. C., Schulmeister, J., Koser, S., Rudolph, M., Rominger, F., et al. (2018). A golden access to acenopentalenes. *Chem. Eur. J.* 24, 2735–2740. doi: 10.1002/chem.201705456

Xie, J., Pan, C., Abdukader, A., and Zhu, C. (2014). Gold-catalyzed C(sp3)-H bond functionalization. *Chem. Soc. Rev.* 43, 5245–5256. doi: 10.1039/c4cs00004h

Xiong, Z., Zhang, X., Li, Y., Peng, X., Fu, J., Guo, J., et al. (2018). Syntheses of 12 H -benzo[a]xanthen-12-ones and benzo[a]acridin-12(7 H)-ones through Au(i)-catalyzed Michael addition/6- endo -trig cyclization/aromatization cascade annulation. *Org. Biomol. Chem.* 16, 7361–7374. doi: 10.1039/C8OB01684D

Xu, W., Wang, G., Xie, X., and Liu, Y. (2018). Gold(I)-catalyzed formal intramolecular dehydro-diels-alder reaction of ynamide-ynes: synthesis of functionalized benzo[b]carbazoles. *Org. Lett.* 20, 3273–3277. doi: 10.1021/acs.orglett.8b01145

Yamamoto, Y. (2012). Transition-metal-catalyzed cycloisomerizations of α,ω-dienes. *Chem. Rev.* 112, 4736–4769. doi: 10.1021/cr300050n

Yang, W., and Hashmi, A. S. K. (2014). Mechanistic insights into the gold chemistry of allenes. *Chem. Soc. Rev.* 43, 2941–2955. doi: 10.1039/c3cs60441a

Ye, L., Wang, Y., Aue, D. H., and Zhang, L. (2012). Experimental and computational evidence for gold vinylidenes: generation from terminal alkynes via a bifurcation pathway and facile C-H insertions. *J. Am. Chem. Soc.* 134, 31–34. doi: 10.1021/ja2091992

Yuan, B., He, R., Guo, X., Shen, W., Zhang, F., Xu, Y., et al. (2018). DFT study on the Au(i)-catalyzed cyclization of indole-allenoate: counterion and solvent effects. *New J. Chem.* 42, 15618–15628. doi: 10.1039/C8NJ02375A

Zamani, F., Babaahmadi, R., Yates, B., Gardiner, M. G., Ariafard, A., Pyne, S. G., et al. (2019). Dual gold-catalyzed cycloaromatization of unconjugated (E)-enediynes. *Angew. Chem. Int. Ed.* 58, 2114–2119. doi: 10.1002/anie.201810794

Zhang, D. H., Zhang, Z., and Shi, M. (2012). Transition metal-catalyzed carbocyclization of nitrogen and oxygen-tethered 1,n-enynes and diynes: synthesis of five or six-membered heterocyclic compounds. *Chem. Commun.* 48, 10271–10279. doi: 10.1039/c2cc34739c

Zhang, J., Liao, Z., Chen, L., Jiang, H., and Zhu, S. (2018a). Catalytic [1,3] O-to-C rearrangement: rapid access to bridged bicyclic systems. *Chem. Eur. J.* 24, 6927–6931. doi: 10.1002/chem.201801062

Zhang, J.-h., Wei, Y., and Shi, M. (2018b). Gold-catalyzed ring enlargement and cycloisomerization of alkynylamide tethered alkylidenecyclopropanes. *Org. Chem. Front.* 5, 2980–2985. doi: 10.1039/C8QO00907D

Zheng, Y., Guo, L., and Zi, W. (2018). Enantioselective and regioselective hydroetherification of alkynes by gold-catalyzed desymmetrization of prochiral phenols with P-stereogenic centers. *Org. Lett.* 20, 7039–7043. doi: 10.1021/acs.orglett.8b02982

Zhong, C. Z., Tung, P. T., Chao, T. H., and Yeh, M. C. P. (2017). Gold-catalyzed stereoselective synthesis of bicyclic lactams and ketones from N-tosylynamidomethyl-tethered cyclohexenes. *J. Org. Chem.* 82, 481–501. doi: 10.1021/acs.joc.6b02479

Zhou, J., Fu, C., and Ma, S. (2018a). Gold-catalyzed stereoselective cycloisomerization of allenoic acids for two types of common natural γ-butyrolactones. *Nat. Commun.* 9, 1–10. doi: 10.1038/s41467-018-03894-6

Zhou, L., Zhang, Y., Fang, R., and Yang, L. (2018b). Computational exploration of counterion effects in gold(I)-catalyzed cycloisomerization of ortho -(Alkynyl)styrenes. *ACS Omega* 3, 9339–9347. doi: 10.1021/acsomega.8b01131

Conflict of Interest Statement: The authors declare that the research was conducted in the absence of any commercial or financial relationships that could be construed as a potential conflict of interest.

frontiers in Chemistry

ORIGINAL RESEARCH
published: 17 May 2019
doi: 10.3389/fchem.2019.00325

MoS_2 Nanosheets Assembled on Three-Way Nitrogen-Doped Carbon Tubes for Photocatalytic Water Splitting

Yujia Zhang†, Yan Liu†, Wen Gao, Ping Chen, Hongyu Cui, Yanfei Fan, Xifeng Shi, Yingqiang Zhao, Guanwei Cui and Bo Tang**

Key Laboratory of Molecular and Nano Probes, Ministry of Education, Shandong Provincial Key Laboratory of Clean Production of Fine Chemicals, College of Chemistry, Chemical Engineering and Materials Science, Collaborative Innovation Centre of Functionalized Probes for Chemical Imaging in Universities of Shandong, Shandong Normal University, Jinan, China

OPEN ACCESS

Edited by:
Wee-Jun Ong, Xiamen University, Malaysia, Malaysia

Reviewed by:
Kangle Lv, South-Central University for Nationalities, China
Hui Pan, University of Macau, China
Junhua Hu, Zhengzhou University, China

***Correspondence:**
Guanwei Cui
cuiguanwei77@163.com
Bo Tang
tangb@sdnu.edu.cn

†These authors have contributed equally to this work

Specialty section:
This article was submitted to Catalysis and Photocatalysis, a section of the journal Frontiers in Chemistry

Received: *24 January 2019*
Accepted: *23 April 2019*
Published: *17 May 2019*

Citation:
Zhang Y, Liu Y, Gao W, Chen P, Cui H, Fan Y, Shi X, Zhao Y, Cui G and Tang B (2019) MoS_2 Nanosheets Assembled on Three-Way Nitrogen-Doped Carbon Tubes for Photocatalytic Water Splitting. Front. Chem. 7:325. doi: 10.3389/fchem.2019.00325

In this work, a micron-sized three-way nitrogen-doped carbon tube covered with MoS_2 nanosheets (TNCT@MoS_2) was synthesized and applied in photocatalytic water splitting without any sacrificial agents for the first time. The micron-sized three-way nitrogen-doped carbon tube (TNCT) was facilely synthesized by the calcination of commercial sponge. The MoS_2 nanosheets were assembled on the carbon tubes by a hydrothermal method. Compared with MoS_2, the TNCT@MoS_2 heterostructures showed higher H_2 evolution rate, which was ascribed to the improved charge separation efficiency and the increased active sites afforded by the TNCT.

Keywords: photocatalysis, MoS_2, three-way nitrogen-doped carbon tubes, hydrogen evolution, water splitting

INTRODUCTION

Photocatalytic water splitting is one of the promising strategies to address the global energy and environmental problems (Hinnemann et al., 2005; Dong et al., 2013; Jiang et al., 2013; Chang et al., 2014; Pan et al., 2016; Wang et al., 2016; Anna et al., 2018; Chen et al., 2018; Zeng et al., 2018). TiO_2 is the most investigated material in the semiconductor photocatalysis research field. However, due to the wide bandgap, it is only responsive to UV light, which greatly limits its photocatalytic efficiency (Cui et al., 2013; Shi et al., 2018). In recent years, many visible-light-driven semiconductors have been designed and applied in solar energy conversion research fields (Wang et al., 2014; Pan, 2016; Shao et al., 2017, 2018; Cheng et al., 2018, 2019; Marchal et al., 2018; Wolff et al., 2018; Yang et al., 2019). Molybdenum disulfide (MoS_2) is one of the most attractive materials. As a graphene-like hexagonal material with close-packed layered structure, MoS_2 has a sandwich architecture, in which the strong covalent bonds among S-Mo-S atoms lies in the layer while the weak van der Waals force exists between the layers (Cheiwchanchamnangij and Lambrecht, 2012). With the variable atomic coordination and the electronic structure, MoS_2 exhibits extremely fast carriers mobility (over 200 $cm^2 \cdot V^{-1} \cdot s^{-1}$). Furthermore, the band gap is adjustable from 1.19 to 1.80 eV through the variation of layer thickness, nanometer size and ion doping. Hence, MoS_2 is an excellent light absorbing material and has high utilization of sunlight. Additionally, the nano-scale molybdenum disulfide has a complicated edge structure with high unsaturation and high reactivity (Wang et al., 2018). In a word, MoS_2 has optimal band gap, high reactive spots and fast mobility of charge carriers, which is beneficial for the photocatalysis. However, the photocatalytic efficiency of pure MoS_2 is still limited by the fast recombination of photogenerated carriers. The construction

of heterostructure of nano-sized MoS_2 coupled with other semiconductor or carbon materials has attracted great interest (Xiang et al., 2012; Jia et al., 2013; Guo et al., 2015; Lang et al., 2015; Pan et al., 2016). It was proposed that the hybrids could provide appropriate band structure for water splitting and improve the separation efficiency of photogenerated carriers.

Herein, MoS_2 nanosheets assembled on a micron-sized three-way nitrogen-doped carbon tube (TNCT@MoS_2) was synthesized and applied in the photocatalytic water splitting for the first time. As illustrated in **Scheme 1**, the micron-sized three-way nitrogen-doped carbon tube (TNCT) was first prepared by a calcination method. Then, the MoS_2 nanosheets were loaded on the TNCT by a hydrothermal method. The as-prepared TNCT@MoS_2 composite exhibits much higher photocatalytic activities than pure MoS_2, which is ascribed to the improved charge separation and transfer efficiency afforded by the TNCT.

EXPERIMENTAL SECTION

Materials

Ammonium molybdate tetrahydrate, thiourea, ethanol, and terephthalic acid (TA) were supplied by China National Pharmaceutical Group Chemical Testing Co., Ltd. Melamine sponge is purchased from Zhengzhou Fengtai nanomaterial Co., Ltd. The water used in the experiment is secondary deionized water.

Preparation of TNCT

The commercial melamine sponge was calcined at 450°C for 3 h in vacuum, and the sponge changed from white to black. At this time, the required three-way nitrogen-doped carbon tube (TNCT) was initially formed.

Fabrication of TNCT@MoS_2

First, 1.24 g ammonium molybdate tetrahydrate, 2.26 g thiourea and 35 ml deionized water was mixed and stirred at room temperature for 20 min. Then, the mixture and the as-prepared black TNCT were transferred to a 100 mL polytetrafluoroethylene reactor. The reactor was heated in an oven at 220°C for 24 h. After the reaction, the supernatant is poured off, and the sponge block is clamped out. After being mashed, the sponge block was centrifuged and washed with distilled water and ethanol for several times. Then, it was dried in a vacuum drying box at 60°C for 12 h, and a black powder was obtained. Finally, the black powder was calcined at 800°C in N_2 atmosphere for 4 h.

Instruments

Scanning Electron Microscope (SEM) equipped with a field-emission gun operated at 5.0 kV was used to characterize the morphology of the as-obtained product. High-Resolution Transmission Electron Microscopy (HRTEM) was taken on JEM-2100F instrument at an accelerating voltage of 200 kV. X–ray diffraction (XRD) analyses carried out on a Bruker D8 Advance Diffractmeter with Cu Kα radiation (1.5418 Å). X-ray photoelectron spectroscopy (XPS) was carried on Thermo Scientific Escalab 250Xi with Al Kα as the excitation source. Photoelectrochemical performance measurements were performed in a standard three-electrode PEC cell, with three-way nitrogen-doped carbon tube@MoS_2, saturated calomel electrode, and Pt wire as the working electrode, reference electrode, and counter electrode, respectively. The fluorescence spectrum was carried out with an Edinburgh FLS920 spectrofluorimeter (Edinburgh Instruments Ltd, England) equipped with a xenon lamp. Raman spectra were measured by LabRAM HR800 confocal microscope Raman spectrometer from Horiba Jobin-Yvon, France. The UV/Vis diffuse reflection spectra (DRS) were taken on a Shimadzu UV-2550 spectrophotometer with an integrated sphere attachment and $BaSO_4$ used as the reference sample.

Photocatalytic Activity for Water Splitting

In a typical process, 20 mg of the as-prepared photocatalysts and 10 mL aqueous solution in a 20 mL Quartz bottle sealed with silicone rubber septum. Prior to photocatalysis experiment, the sample solutions were thoroughly deaerated by evacuation and purged with nitrogen for 10 min. Then it was irradiated

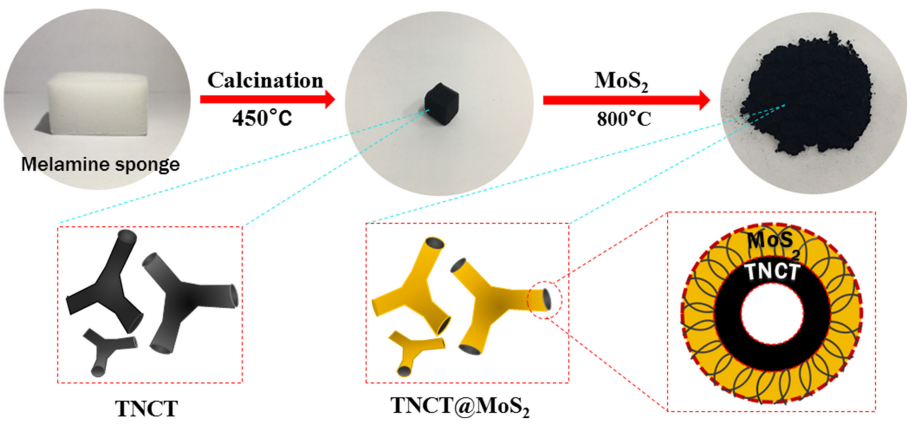

SCHEME 1 | Illustration of the synthesis process of TNCT@MoS_2.

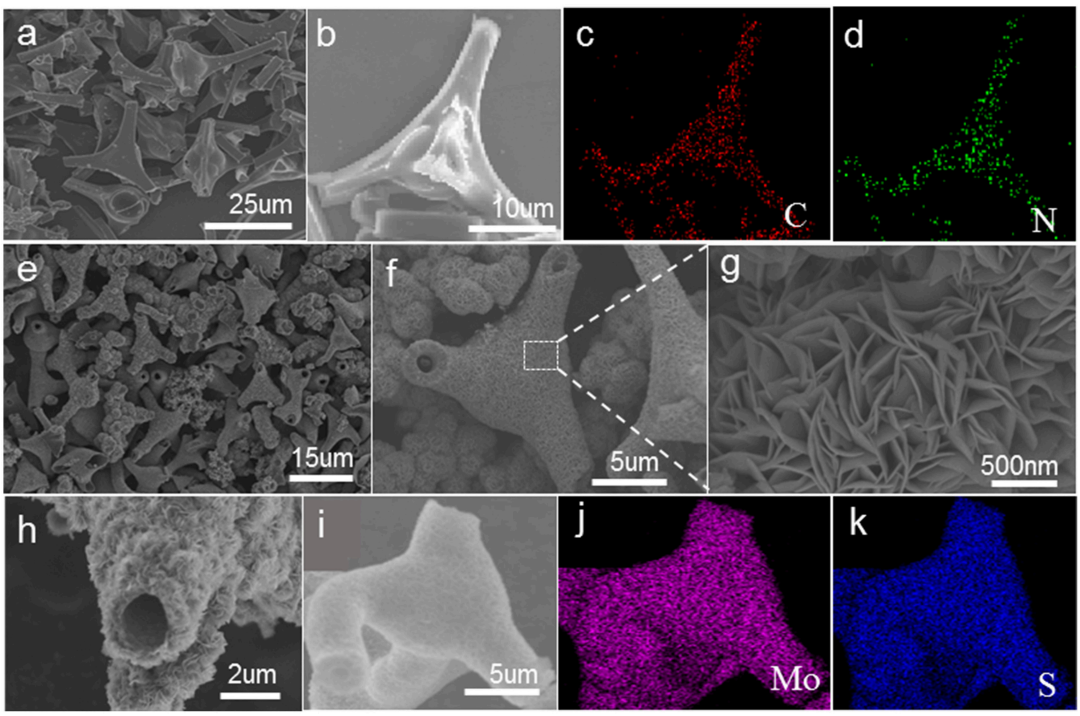

FIGURE 1 | SEM images of TNCT **(a,b)** and TNCT@MoS_2 **(e–i)**. The down two panels shows the element mapping images of C,N of TNCT **(c,d)** and Mo, S of TNCT@MoS_2 **(j,k)**.

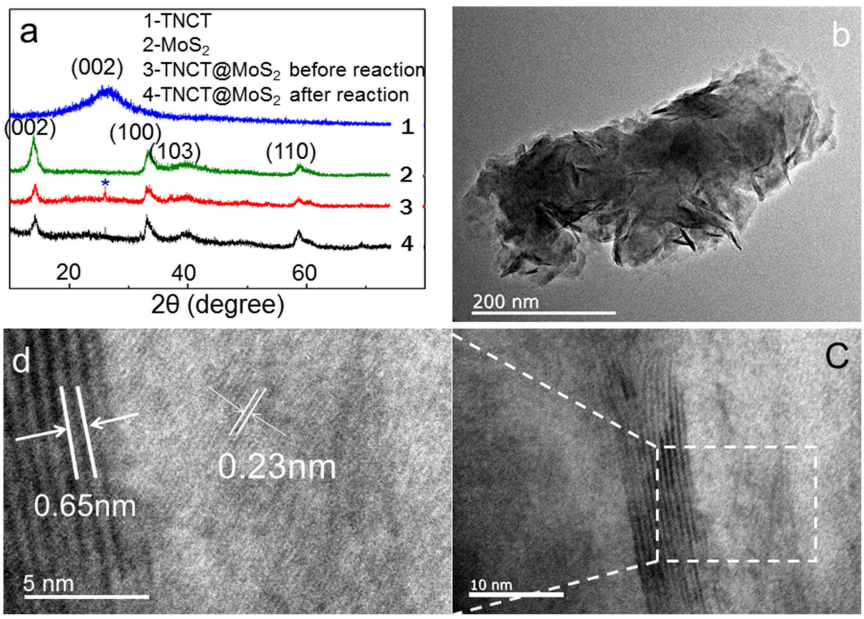

FIGURE 2 | XRD **(a)**, HRTEM **(b–d)** patterns of TNCT@MoS_2. * indicates the (002) crystal plane of TNCT.

by a 1,000 W Xenon lamp (the light intensity irradiating the photocatalysts was 0.17 W) at room temperature under constant stirring. The produced gas was analyzed by gas chromatography (FULI 9750, TCD, Nitrogen as the carrier gas, and 5 Å molecular sieve column).

Because there was no O_2 detected in this photocatalytic water splitting system, to confirm the photocatalytic water splitting process, the intermediate OH directly photogenerated from water was determined as following (Yang et al., 2009). A fluorescence probe named terephthalic acid (TA) was

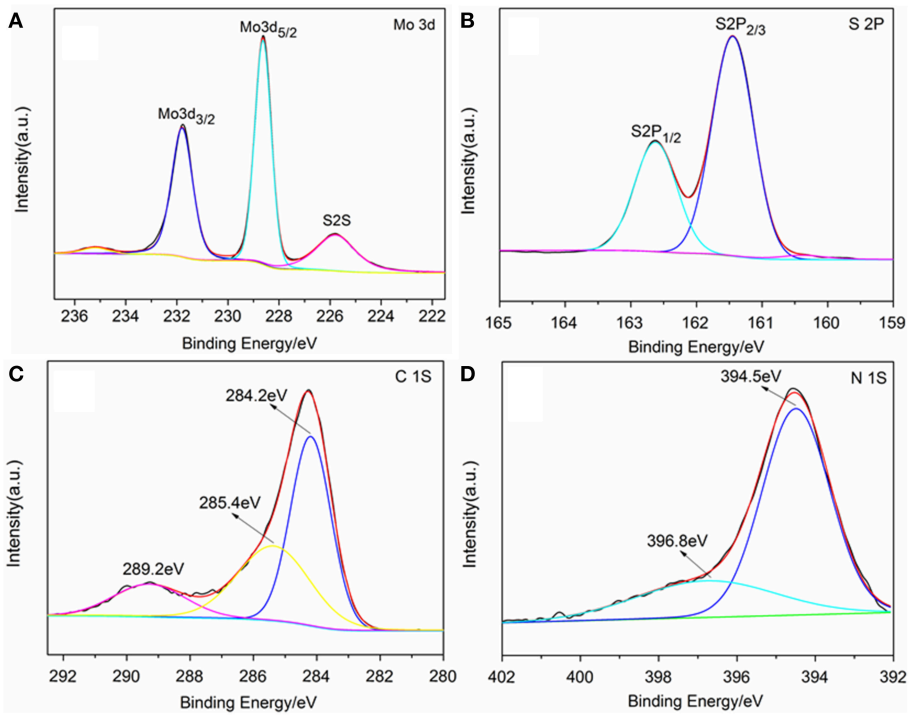

FIGURE 3 | XPS spectrum of TNCT@MoS_2. Mo 3d spectrum **(A)**, S 2p spectrum **(B)**, C 1s spectrum **(C)**, and N 1S spectrum **(D)**.

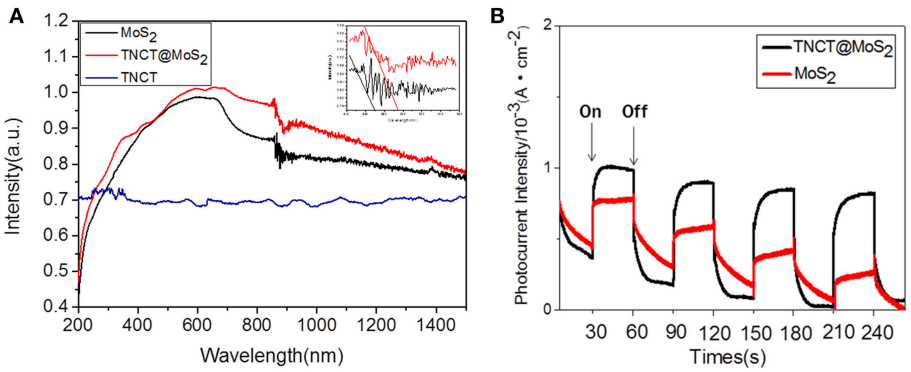

FIGURE 4 | UV-Vis-IR absorbance spectrum **(A)** and photocurrent of the samples **(B)**.

added into the above-mentioned photocatalytic H_2 evolution measurement system to capture OH photogenerated from water, in a result of producing TAOH. Typically, 0.01M TA, 20 mg TNCT@MoS_2, and 10 mL water were mixed in a 20 mL Pyrex bottle at ambient temperature and atmospheric pressure, sealed with silicone rubber septum. The sample solutions were thoroughly deaerated by evacuation and argon bubbling for 2 h prior to photocatalysis experiment. Then it was irradiated by a 1,000-W Xe lamp under ambient conditions and magnetic stirring for certain time. The produced solutions containing TAOH were analyzed by fluorescence spectra.

RESULTS AND DISCUSSION

As shown in **Figures 1a,b**, most of these nitrogen-doped carbon tubes have three-way branches, each of which is about 20 microns in length and 3 micron in diameter. The EDS-mapping pictures show that the doped nitrogen elements are uniformly dispersed in the carbon tubes (**Figures 1c,d**). The SEM image of TNCT@MoS_2 heterostructures is shown in **Figures 1e–h**. It can be seen that the MoS_2 nanosheets layer with thickness of 500 nm are uniformly coated on the TNCTs. The MoS_2 nanosheets are interconnected with each other, forming the 2D nanosheets networks. Additionally, the EDS mapping pictures show that

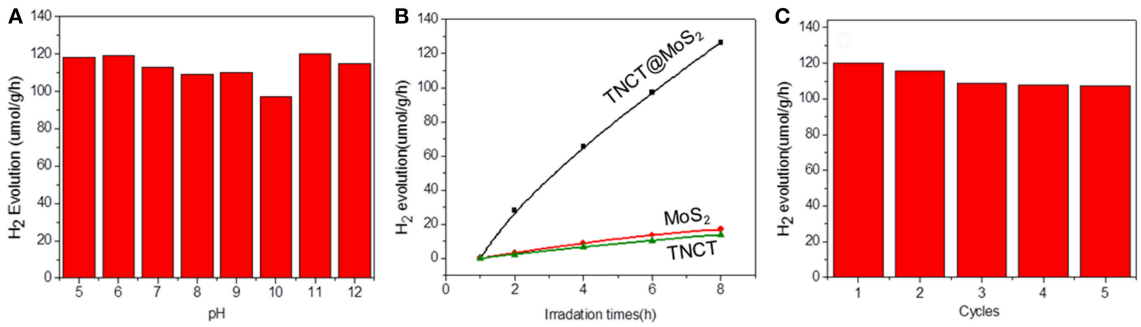

FIGURE 5 | Photocatalytic hydrogen production activity at different pH values **(A)**, hydrogen production data for different samples **(B)**, and recycling performance for TNCT@MoS_2 **(C)**.

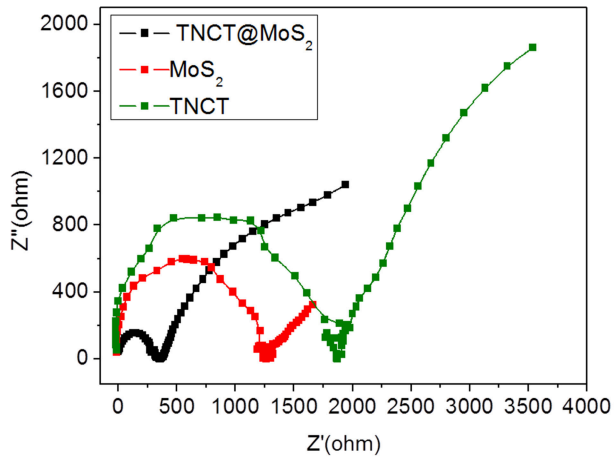

FIGURE 6 | EIS Nynquist plots of the prepared samples.

MoS_2 nanosheets are uniformly dispersed on the surface of TNCT (**Figures 1j,k**).

XRD peaks of TNCT@MoS_2 localized at 2θ values of 13.8, 33.5, 39.8, and 58.8° are ascribed to MoS_2 with typical hexagonal phase(JCPDS:00-037-1492, **Figure 2a**). The (002) crystal plane diffraction peak is stronger than the diffraction peaks on other crystal planes, indicating that MoS_2 has a good layered packing structure (Zong et al., 2008). An obvious reflection located at 2θ = 26.5°is ascribed to the TNCT (002) crystal plane (**Figure 2a**; Tang et al., 2015). The heterogeneous lattice interfaces of MoS_2 and TNCT were clearly observed on the HRTEM images (**Figures 2b,d**). The lattice fringe spacing of 0.65 nm is ascribed to hexagonal phase MoS_2 (Choi et al., 2017). The lattice fringes of TNCT are not significant maybe due to the doping of nitrogen atoms, a dimly visible lattice spacing of 0.22 nm was ascribed to the (100) facet of graphite (Baker and Baker, 2010). The strong wide peaks located at 1,379 cm^{-1} (D-band) in the Raman spectra showed that the presence and partial graphitization of carbon (**Supplementary Figure 1**; Matthews et al., 1999) in agreement with the results observed from the HRTEM images.

The chemical state of surface species of the samples was further determined by X-ray photoelectron spectroscopy (XPS). The survey XPS spectra showed that Mo, S, N, C, and O elements existed in the surface layer of the as-papered nanostructures (**Supplementary Figure 2**). Two peaks located at 228.62 and 231.79 eV are attributed to Mo 3d5/2 and Mo 3d3/2, respectively (**Figure 3B**; Wang et al., 2017). The peak located at 161.8 eV corresponds to the S 2p3/2 and another one located at 162.7 eV was assigned to S 2p1/2 (**Figure 3C**; Hu et al., 2014). Three peaks were observed in the C 1s binding region peaks centered at 284.2, 285.4 and 289.2 eV, which were ascribed to graphite-C, -C*-C=O and -C* =O groups, respectively (**Figure 3D**; Christie et al., 1983; Beamson and Briggs, 1993; Witek et al., 1996). Two peaks were observed in the N1s binding region peaks (**Figure 3A**). The peak centered at 394.5 eV indicated that the doped nitrogen in TNCT was connected with the carbon frame by -N* =N*-C bond (Kudo et al., 1986). It is worth noting that another peak for N1s centered at 396.8 eV was ascribed to Mo(-N* =N-)$_2$-C (George and Kwarcinski, 1995), which indicated that the MoS_2 could closely bond with TNCT by the surface -N=N- group.

The UV-Vis-IR absorbance spectrum shows that TNCT @MoS_2 exhibits higher and broader spectral absorption including IR light than that of TNCT and MoS_2 (**Figure 4A**). As shown in **Figure 4B**, TNCT@MoS_2 obviously shows higher photocurrent density than that of MoS_2. It indicates that TNCT@ MoS_2 maybe has better photocatalytic activity.

The photocatalytic activity of the as-prepared catalyst was investigated for the photocatalytic water splitting process without addition of any sacrificial agents, which was performed by a 1,000 W xenon lamp source. It was found that the catalyst showed almost the same photocatalytic activity in the wide pH range of 5-11 and pure water (**Figure 5A**). The optimal hydrogen production rate of TNCT@MoS_2 was 120 μmol/g·h, which is about 9 times faster than that of pure MoS_2 (**Figure 5B**).

For a typical photocatalytic water splitting process, both H_2 and O_2 are usually produced from water. However, in this work, whereas this system readily produces hydrogen under illumination, the simultaneous liberation of oxygen is not observed. This phenomenon has been observed in much water splitting systems (Duonghong and Grätzel, 1984; Liu et al., 2012; Zhang et al., 2014). It is because the produced O_2 or intermediate oxygen species such as OH are readily absorbed by the metal elements such as Mo and W to form steady peroxide complexes,

in a result of inhibiting the release of O_2 (Cui et al., 2015). Herein, although there was no O2 determined in this photocatalytic water splitting system, intermediate OH directly photogenerated from water was detected by the fluorescence probe TA (Yang et al., 2009). The fluorescence spectra of TAOH, which is produced through the oxidation of TA by OH, exhibited a peak at 426 nm, indicating the presence of OH (**Supplementary Figure 3**). Although the surface of molybdenum sulfide suffer from the produced intermediate active oxygen, the XRD (**Figure 2a**) and Raman spectroscopy (**Supplementary Figure 4**) showed that the crystal structure of the material did not change fundamentally and maintain the same photoactivity for five photocatalytic reaction runs (**Figure 5C**).

The excellent photocatalytic performance of TNCT@MoS_2 is ascribed to the effective separation and transfer of photogenerated carriers. Herein, it was verified by the photoluminescence spectroscopy and photoelectrochemical performance measurements. The photoluminescence (PL) of semiconductors was caused by recombination of photoinduced electrons and holes. If the recombination was suppressed, the PL emission of semiconductors would be quenched.As shown in **Supplementary Figure 5**, after being combined with TNCT, the PL intensity of MoS_2 emission peak obviously quenched. It indicated that the photoinduced charge separation efficiency of TNCT@MoS_2 would improve. The photogenerated carriers' transfer capacity of the as prepared materials was confirmed by electrochemical impedance tests. As shown in **Figure 6**, TNCT, MoS_2, and TNCT@MoS_2 all showed classical semicircular Nyquist diagram. The arc radius of TNCT@MoS_2 was obviously smaller than that of TNCT and MoS_2, which indicated that the photogenerated charges in TNCT@MoS_2 would suffer less resistance. It is ascribed to the fast charge transfer from MoS_2 nanosheets to carbon tube under full-light irradiation. The formed Mo(-N* =N-)$_2$-C bonding connection between MoS_2 and TNCT maybe acts as carrier transfer bridge (**Figure 3D**), which will improve the photogenerated carriers separation and transfer efficiency of TNCT@MoS_2. The detailed mechanism and remained questions would be studied in our future work.

CONCLUSIONS

In summary, a micron-sized three-way nitrogen-doped carbon tube covered with MoS_2 nanosheets was synthesized and applied in the photocatalytic water splitting without any sacrificial agents for the first time. The micron-sized three-way nitrogen-doped carbon tube is facilely synthesized by the calcination of sponge at 450°C in vacuum. And then the MoS_2 nanosheets are deposited on the three-way nitrogen-doped carbon tubes by a simple hydrothermal method. Compared with MoS_2, the TNCT@MoS_2 heterostructures showed higher H_2 evolution rate, which may be ascribed to the improved charge separation and transfer efficiency caused by the three-way nitrogen-doped carbon tube. This work may provide a new design idea for the design of low-cost and efficient photocatalysts.

AUTHOR CONTRIBUTIONS

GC and BT conceived and designed the experiments. YuZ, YL, PC, HC, and YF performed the experiments. WG, XS, and YiZ analyzed the data. GC and YuZ co-wrote the paper.

FUNDING

This work was supported by the National Natural Science Foundation of China (21535004, 91753111, 21575082, 21775092, 21507074) and the Key Research and Development Program of Shandong Province (2018YFJH0502), Development plan of science and technology for Shandong Province of China (2013GGX10706), Shandong Province Natural Science Foundation (ZR2015BM023, ZR2018JL008), and the Project of Shandong Province Higher Educational Science and Technology Program (J13LD06).

SUPPLEMENTARY MATERIAL

The Supplementary Material for this article can be found online at: https://www.frontiersin.org/articles/10.3389/fchem.2019.00325/full#supplementary-material

REFERENCES

Anna, M.-M., Lluís, S., Miquel, T., Pol, S., Jordi, L., and Anna, R. (2018). Fast and Simple Microwave synthesis of TiO_2/Au nanoparticles for gas-phase photocatalytic hydrogen generation. *Front Chem*. 6:110. doi: 10.3389/fchem.2018.00110

Baker, S. N., and Baker, G. A. (2010). Luminescent carbon nanodots: emergent nanolights. *Angew. Chem. Int. Ed*. 49, 6726–6744. doi: 10.1002/chin.201103270

Beamson, G., and Briggs, D. (1993). High resolution XPS of organic polymers: the scienta ESCA300 database. *J. Chem. Educ*. 70:A25 doi: 10.1021/ed070pA25.5

Chang, K., Mei, Z. W., Wang, T., Kang, Q., Ouyang, S. X., and Xe, J. H. (2014). MoS_2/graphene cocatalyst for efficient photocatalytic H_2 evolution under visible light irradiation. *ACS Nano*. 8, 7078–7087. doi: 10.1021/nn5019945

Cheiwchanchamnangij, T., and Lambrecht, W. R. L. (2012). Quasiparticle band structure calculation of monolayer, bilayer, and bulk MoS_2. *Phys. Rev. B*. 85:205302. doi: 10.1103/PhysRevB.85.205302

Chen, X., Zhang, W. J., Tang, J. T., Pan, C. Y., and Yu, G. P. (2018). Porous organic polymers: an emerged platform for photocatalytic water splitting. *Front Chem*. 6:592. doi: 10.3389/fchem.2018.00592

Cheng, J. S., Zhao, H., Kangle, L., Wu, X. F., Li, Q., Li, Y. H., et al. (2018). Drastic promoting the visible photoreactivity of layered carbon nitride by polymerization of dicyandiamide at high pressure. *Appl. Cataly. B Environ*. 232, 330–339. doi: 10.1016/j.apcatb.2018.03.066

Cheng, J. S., Zhao, H., Li, Q., Li, X. F., Fang, S., Wu, X. F., et al. (2019). Fabrication of high photoreactive carbon nitride nanosheets by polymerization of amidinourea for hydrogen production. *Appl. Cataly. B Environ*. 245, 197–206. doi: 10.1016/j.apcatb.2018.12.044

Choi, J., Reddy, D. A., Han, N. S., Jeong, S., Hong, S., Kumar, D. P., et al. (2017). Modulation of charge carrier pathways in CdS nanospheres by integrating MoS_2 and Ni_2P for improved migration and separation toward enhanced photocatalytic hydrogen evolution. *Catal. Sci. Technol*. 7, 641–649. doi: 10.1039/c6cy02145j

Christie, A. B., Lee, J., Sutherland, I., and Walls, J. M. (1983). An XPS study of ion-induced compositional changes with group II and group IV compounds. *Appl. Surf. Sci*. 15, 224–237. doi: 10.1016/0378-5963(83)90018-1

Cui, G.-W., Wang, W.-L., Ma, M.-Y., Zhang, M., Xia, X.-Y., Han, F.-Y., et al. (2013). Rational design of carbon and TiO_2 assembly materials: covered or

strewn, which is better for photocatalysis? *Chem. Commun*. 49, 6415–6417. doi: 10.1039/c3cc42500b

Cui, G. W., Wang, W., Ma, M. Y., Xie, J. F., Shi, X. F., Deng, N., et al. (2015). IR-driven photocatalytic water splitting with WO_2-NaxWO_3 hybrid conductor material. *Nano Lett*. 15, 7199–7203. doi: 10.1021/acs.nanolett.5b01581

Dong, S., Sun, J., Li, Y., Yu, C., Li, Y., and Sun, J. (2013). $ZnSnO_3$ hollow nanospheres/reduced graphene oxide nanocomposites as high-performance photocatalysts for degradation of metronidazole. *Appl. Catal. B* 144, 386–393. doi: 10.1016/j.apcatb.2013.07.043

Duonghong, D., and Grätzel, M. (1984). Colloidal TiO_2 particles as oxygen carriers in photochemical water cleavage systems. *J. Chem. Soc. Chem. Commun*. 1597–1599. doi: 10.1039/C39840001597

George, T. A., and Kwarcinski, M. E. (1995). PreparAtion and properties of diazenido, hydrazido(2-), and hydrido-hydrazido(2-) complexes of tungsten. x-rayphotoelectron spectroscopy of dinitrogen and hydrazido(2-) complexes of molybdenum and tungsten. *J. Coord. Chem*. 35, 349–357. doi: 10.1080/00958979508024047

Guo, X., Cao, G.-L., Ding, F., Li, X. Y., Zhen, S. Y., Xue, Y.-F., et al. (2015). A bulky and flexible electrocatalyst for efficient hydrogen evolution based on the growth of MoS_2 nanoparticles on carbon nanofiber foam. *J. Mater. Chem. A*. 3, 5041–5046. doi: 10.1039/c5ta00087d

Hinnemann, B., Moses, P. G., Bonde, J., Jørgensen, K. P., Nielsen, J. H., Horch, S., et al. (2005). Biomimetic hydrogen evolution: MoS_2 nanoparticles as catalyst for hydrogen evolution. *J. Am. Chem. Soc*. 127, 5308–5309. doi: 10.1021/ja0504690

Hu, S., Chen, W., Zhou, J., Yin, Y., Uchaker, E., Zhang, Q. F., et al. (2014). Preparation of carbon coated MoS_2 flower-like nanostructure with self-assembled nanosheets as high-performance lithium-ion battery anodes. *J. Mater. Chem. A*. 2, 7862–7872. doi: 10.1039/c4ta01247j

Jia, T. T., Kolpin, A., Ma, C. S., Chan, R. C.-T., Kwok, W. M., and Tsang, S. C. E. (2013). A graphene dispersed CdS–MoS_2 nanocrystal ensemble for cooperative photocatalytic hydrogen production from water. *Chem. Commun*. 50, 1185–1188. doi: 10.1039/c3cc47301e

Jiang, Y.-R., Lee, W., Chen, K.-T., Wang, M.-C., Chang, K.-H., and Chen, C.-C. (2013). Hydrothermal synthesis of b-ZnMoO4 crystals and their photocatalytic degradation of Victoria Blue R and phenol. *J. Taiwan Inst. Chem. Eng*. 45, 207–218. doi: 10.1016/j.jtice.2013.05.007

Kudo, Y., Yoshida, N., Fujimoto, M., Tanaka, K., and Toyoshima, I. (1986). Acid-dissociation behavior of para-hydroxyl group in the N,N,O-terdentate ligand, 4-(4-methyl-2-pyridylazo)resorcinol, coordinated to a transition metal ion. *Bull. Chem. Soc. Jpn*. 59, 1481–1486. doi: 10.1246/bcsj.59.1481

Lang, D., Shen, T. T., and Xiang, Q. J. (2015). Roles of MoS_2 and graphene as cocatalysts in the enhanced visible-Light photocatalytic H_2 production activity of multiarmed CdS nanorods. *Chemcatchem* 7, 943–951. doi: 10.1002/cctc.201403062

Liu, J. H., Zhang, Y. W., Lu, L. H., Wu, G., and Wei, C. (2012). Self-regenerated solar-driven photocatalytic water-splitting by urea derived graphitic carbon nitride with platinum nanoparticles. *Chem. Commun*. 48, 8826–8828. doi: 10.1039/C2CC33644H

Marchal, C., Cottineau, T., Méndez-Medrano, M. G., Colbeau-Justin, C., Caps, V., and Keller, V. (2018), Au/TiO_2-gC_3N_4 nanocomposites for enhanced photocatalytic H_2 production from water under visible light irradiation with very low quantities of sacrificial agents. *Adv. Energy Mater*. 8:1702142. doi: 10.1002/aenm.201702142

Matthews, M. J., Pimenta, M. A., Dresselhaus, G., et al.(1999). Origin of dispersive effects of the raman d band in carbon materials. *Physical Review B* 59:R6585. doi: 10.1103/PhysRevB.59.R6585

Pan, H. (2016). Principles on design and fabrication of nanomaterials as photocatalysts for water-splitting. *Renew. Sustain. Energy Rev*. 57, 584–601. doi: 10.1016/j.rser.2015.12.117

Pan, Y., Lin, Y., Liu, Y. Q., and Liu, C. G. (2016). A novel CoP/MoS_2-CNTs hybrid catalyst with Ptlike activity for hydrogen evolution. *Catal. Sci. Technol*. 6, 1611–1615. doi: 10.1039/c5cy02299a

Shao, M. M., Shao, Y. F., Chai, J. W., Qu, Y. J., Yang, M. Y., Wang, Z. L., et al. (2017). Synergistic effect of 2D Ti_2C and g-C_3N_4 for efficient photocatalytic hydrogen production. *J. Mater. Chem. A*. 5, 16748–16756. doi: 10.1039/c7ta04122e

Shao, M. M., Shao, Y. F., Ding, S. J., Wang, J. W., Xu, J. C., Qu, Y. J., et al. (2018). Vanadium disulfide decorated graphitic carbon nitride for super-efficient solar-driven hydrogen evolution. *Appl. Cataly. B Environ*. 237, 295–301. doi: 10.1016/j.apcatb.2018.05.084

Shi, T., Duan, Y., Lv, K., Hu, Z., Li, Q., Li, M., et al. (2018). Photocatalytic oxidation of acetone over high thermally stable TiO_2 nanosheets with exposed (001) facets. *Front Chem*. 6:175. doi: 10.3389/fchem.2018.00175

Tang, J., Salunkhe, R. R., Liu, J., Torad, N. L., Imura, M., Furukawa, S., et al. (2015). Thermal conversion of core–Shell metal–organic frameworks: a new method for selectively functionalized nanoporous hybrid carbon. *J. Am. Chem. Soc*. 137, 1572–1580. doi: 10.1021/ja511539a

Wang, J. Z., Dong, S. Y., Guo, T., Jin, J., and Sun, J. H. (2017). pH-dictated synthesis of novel flower-like MoS_2 with augmented natural sunlight photocatalytic activity. *Mater. Lett*. 191, 22–25. doi: 10.1016/j.matlet.2016.12.090

Wang, L. J., Fan, J., Cao, Z., Zheng, Y., Yao, Z., Shao, G., et al. (2014). Fabrication of predominantly Mn^{4+}-doped TiO_2 nanoparticles under equilibrium conditions and their application as visible-light photocatalyts. *Chem Asian. J*. 9, 1904–1912. doi: 10.1002/asia.201402114

Wang, L. J., Zhang, X., Gao, H. Q., Hu, J. H., Mao, J., Liang, C. H., et al. (2016). 3D CuO network supported TiO_2 nanosheets with applications for energy storage and water splitting. *Sci. Adv. Mater*. 8, 1256–1262. doi: 10.1166/sam.2016.2714

Wang, Q. S., Wen, Y., Cai, K. M., Cheng, R. Q., Yin, L., Zhang, Y., et al. (2018). Nonvolatile infrared memory in MoS_2/PbS van der Waals heterostructures. *Sci. Adv*. 4:eaap7916. doi: 10.1126/sciadv.aap7916

Witek, G., Noeske, M., Mestl, G., Shaikhutdinov, S., and Behm, R. J. (1996). Interaction of platinum colloids with single crystalline oxide and graphite substrates: a combined AFM, STM and XPS study. Catal. *Lett*. 37, 35–39. doi: 10.1007/BF00813516

Wolff, C. M., Frischmann, P. D., Schulze, M., Bohn, B. J., Wein, B., Livadas, P., et al. (2018). All-in-one visible-light-driven water splitting by combining nanoparticulate and molecular co-catalysts on CdS nanorods. *Nat. Energy*. 3, 862–869. doi: 10.1038/s41560-018-0229-6

Xiang, Q. J., Yu, J. G., and Jaroniec, M. (2012). Synergetic effect of MoS_2 and graphene as cocatalysts for enhanced photocatalytic H_2 production activity of TiO_2 nanoparticles. *J. Am. Chem. Soc*. 134,6575–6578. doi: 10.1021/ja302846n

Yang, C., Li, Q., Xia, Y., Lv, K., and Li, M. (2019). Enhanced visible-light photocatalytic CO_2 reduction performance of $ZnIn_2S_4$ microspheres by using CeO_2 as cocatalyst. *Appl. Surf. Sci*. 464, 388–395. doi: 10.1016/j.apsusc.2018.09.099

Yang, H. G., Liu, G., Qiao, S. Z., Sun, C. H., Jin, Y. G., Smith, S. C., et al. (2009). Solvothermal synthesis and photoreactivity of anatase TiO_2 nanosheets with dominant {001} facets. *J. Am. Chem. Soc*. 131, 4078–4083. doi: 10.1021/ja808790p

Zeng, D., Xu, W., Ong, W.-J., Xu, J., Ren, H., Chen, Y., et al. (2018). Toward noble-metal-free visible-light-driven photocatalytic hydrogen evolution: monodisperse sub−15 nm Ni_2P nanoparticles anchored on porous g-C_3N_4 nanosheets to engineer 0D-2D heterojunction interfaces. *Appl. Catal. B*. 221, 47–55. doi: 10.1016/j.apcatb.2017.08.041

Zhang, M., Respinis, M. D., and Frei, H. (2014). Time-resolved observations of water oxidation intermediates on a cobalt oxide nanoparticle catalyst. *Nat. Chem*. 6, 362–367. doi: 10.1038/nchem.1874

Zong, X., Yan, H. J., Wu, G. P., Ma, G. J., Wen, F. Y., Wang, L., et al. (2008). Enhancement of photocatalytic H_2 evolution on CdS by loading MoS_2 as cocatalyst under visible light irradiation. *J. Am. Chem. Soc*. 130, 7176–7177. doi: 10.1021/ja8007825

Conflict of Interest Statement: The authors declare that the research was conducted in the absence of any commercial or financial relationships that could be construed as a potential conflict of interest.

frontiers in Chemistry

ORIGINAL RESEARCH
published: 17 June 2019
doi: 10.3389/fchem.2019.00444

Catalytically Active Sites on Ni_5P_4 for Efficient Hydrogen Evolution Reaction From Atomic Scale Calculation

Jun Hu[1,2], Xiaofei Cao[1], Xin Zhao[2], Wei Chen[3], Guo-ping Lu[2,4], Yong Dan[1] and Zhong Chen[2]**

[1] School of Chemical Engineering, Northwest University, Xi'an, China, [2] School of Materials Science and Engineering, Nanyang Technological University, Singapore, Singapore, [3] School of Pharmaceutical and Chemical Engineering, Taizhou University, Taizhou, China, [4] School of Chemical Engineering, Nanjing University of Science and Technology, Nanjing, China

Ni_5P_4 has received considerable attention recently as a potentially viable substitute for Pt as the cathode material for catalytic water splitting. The current investigation focuses on theoretical understandings of the characteristics of active sites toward water splitting using first-principle calculations. The results indicate that the activity of bridge NiNi sites is highly related on the bond number with neighbors. If the total bond number of NiNi is higher than 14, the sites will exhibit excellent HER performance. For the top P sites, the activity is greatly affected by the position of coplanar atoms besides the bond number. Data of bond length with neighbors can be used to predict the activity of P sites as reviewed by machine learning. Partial density of state (PDOS) analysis of different P sites illustrates that the activity of P sites should form the appropriate bond to localize some 3p orbits of the P atoms. Bond number and position of neighbors are two key parameters for the prediction of the HER activity. Based on the current work, most of the low-energy surfaces of Ni_5P_4 are active, indicating a good potential of this materials for hydrogen evolution reactions.

Keywords: nickel phosphides, water splitting, hydrogen evolution reaction, density functional theory, machine learning

OPEN ACCESS

Edited by:
Xiaoguang Duan, University of Adelaide, Australia

Reviewed by:
Michael Nolan, University College Cork, Ireland
Marta C. Figueiredo, Eindhoven University of Technology, Netherlands

***Correspondence:**
Xin Zhao
xinzhao@ntu.edu.sg
Zhong Chen
aszchen@ntu.edu.sg

Specialty section:
This article was submitted to Catalysis and Photocatalysis, a section of the journal Frontiers in Chemistry

Received: *10 April 2019*
Accepted: *29 May 2019*
Published: *17 June 2019*

Citation:
Hu J, Cao X, Zhao X, Chen W, Lu G, Dan Y and Chen Z (2019) Catalytically Active Sites on Ni_5P_4 for Efficient Hydrogen Evolution Reaction From Atomic Scale Calculation. Front. Chem. 7:444. doi: 10.3389/fchem.2019.00444

INTRODUCTION

Growing concerns on the energy crisis and environmental problems urgently demand for the development of clean and affordable renewable energy sources as feasible alternatives to the diminishing fossil fuels. Water electrolysis is the most promising option to generate high purity hydrogen as a clean energy source, but unfortunately, the required cathode materials for electrochemical water splitting, such as Pt, is too expensive for large-scale application (Li et al., 2016). This has prompted continued research effort toward searching for earth-abundant elements as the cathode materials for large-scale applications. The potential candidates include transition metals (McKone et al., 2013), and their dichalcogenides (Chen et al., 2011; Voiry et al., 2013; Xie et al., 2013; Yang et al., 2013), carbides (Chen et al., 2013a,b), borides (Vrubel and Hu, 2012), nitrides (Cao et al., 2013), phosphides (Feng et al., 2016), and metal-free carbon nitrides (Merlet et al., 2012; Meng et al., 2017), etc.

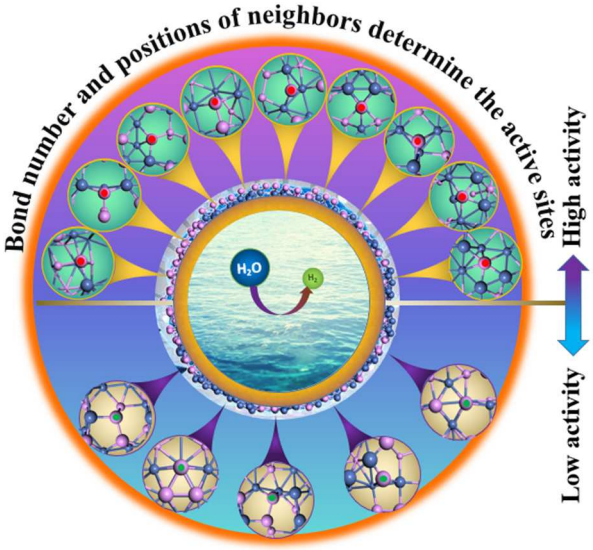

GRAPHICAL ABSTRACT | Bond number and relative position with neighbors are two important factors on the activity of Ni_5P_4 for HER.

Among these materials, nickel phosphides (Ni_xP_y) have shown great promise due to their high activity and stability (Gerasimov and Simirskii, 2008; Laursen et al., 2018). Ni_xP_y has been reported in more than 10 stoichiometric compositions (Feng et al., 2014; Huang et al., 2014; García-Muelas et al., 2018). Among them, Ni_5P_4 has drawn lots of attentions recently on its synthesis, structure, and reactivity (Shu et al., 2005; Zhao et al., 2015). For example, Pan et al. investigated the electrocatalytic property for hydrogen evolution reaction (HER) of $Ni_{12}P_5$, Ni_2P, and Ni_5P_4, and found that the catalytic property followed the order of $Ni_5P_4 > Ni_2P > Ni_{12}P_5$ (Pan et al., 2015). Laursen et al. found that the Tafel slope and overpotential at -100 mA cm^{-2} are 33 mV dec^{-1} and -62 mV in 1 M H_2SO_4, which are very close to Pt in strong acidic solution (Laursen et al., 2015). Although Ni_5P_4 has high activity for HER, an atomic-scale understanding of their reactivity has been elusive, because of the diversity of possible active sites on its different crystal surfaces. While experimental approaches will face a great challenge, theoretical studies can provide insight of the active sites and therefore become an important tool for understanding the catalytic activity of Ni_5P_4.

Some researchers believed that the superior performance of Ni_5P_4 can be attributed to a high positive charge on Ni atoms and the ensemble effect of P, where the number of Ni3-hollow sites that bind H very strongly is decreased due to the abundance of P, which therefore leads to more thermoneutral adsorption (Liu and Rodriguez, 2005; Liu et al., 2005). However, recent experimental research indicates that NiP_2 material is also able to exhibit excellent HER activity although there are no Ni3-hollow sites on the surfaces due to the enriched P atoms, as shown in **Figure S1** (Jiang et al., 2014; Pu et al., 2017). Recently, Wexler et al. found through simulation that P site was the most active site, but the hollow Ni sites on Ni_2P and Ni_5P_4 (0001) surfaces were not active (Wexler et al., 2017). This result agrees with Jin et al. and our recent work, where we found P sites were suitable for HER for Ni_3P (Jin et al., 2016; Hu et al., 2018a). However, it was also found not all P sites are active. Therefore, it is necessary to obtain a fundamental understanding of the activity for P sites from the atomic scale, which are important for the development of a broad range of catalytic materials. Till now, no such model exists to reveal an in-depth understanding of the catalytically active sites. Therefore, finding the key parameters affecting the HER activity becomes an essential task for the rational design and optimization of efficient catalysts.

Herein, we report a comprehensive theoretical study on the atomic active sites of Ni_5P_4 for HER. It was found that there are three types of active sites, namely the bridge NiNi sites, bridge NiP sites, and top P sites. The activity of these active sites is closely associated with the bond number and position with respect to the neighbors. A direct link between the macroscopic activity and the atomic-scale properties was therefore established by regression and machine learning method based on the generated understandings. The outcome provides not only an improved understanding of Ni_5P_4, but also a guideline for the design and synthesis of this material as an electrocatalyst for HER.

COMPUTATIONAL METHODS

All calculations were implemented in the CASTEP module of the Materials Studio package (Accelrys Inc., San Diego, CA, USA). During the calculations, self-consistent periodic DFT was adopted by generalized gradient approximation with Perdew-Burke-Ernzerhof exchange-correlation functional. The plane-wave ultrasoft pseudopotential method, describing the ionic cores of Ni-$3d^84s^2$ and P-$3s^33p^2$, were represented the electron-ion interaction in reciprocal space. The Broyden-Fletcher-Goldfarb-Shanno (BFGS) scheme was selected as the minimization algorithm. The energy cutoff is 380 eV and the SCF tolerance is 5.0×10^{-7} eV atom^{-1}. The k-points samplings is set as $1 \times 1 \times 1$ for different surfaces. The optimization is completed when the energy, maximum force, maximum stress and maximum displacement are smaller than 5.0×10^{-6} eV atom^{-1}, 0.01 eV Å^{-1}, 0.02 GPa, and 5.0×10^{-4} Å, respectively. These parameters were verified by experimental data, as listed in **Table S1** and **Figure S2**, and our previous calculations (Hu et al., 2018a).

The surfaces, containing at least six layers, were obtained from the bulk Ni_5P_4 (space group *hP*36, 186, as shown in **Figure S3**) with a vacuum region of 15 Å. Considering the symmetry of bulk Ni_5P_4, seven low-index surfaces, viz., the (001), (100), (110), $(1\bar{1}0)$, (101), (111), and $(1\bar{1}1)$, with different terminations were chosen during calculation. Different terminations are indicated using capital letters A, B, C, D, and E (more information can be found in **Figures S4, S5**). It was found that only P-rich and stoichiometric surfaces are stable in all low-index surfaces (**Figure S6**). Based on the surface energies, seven low energy surfaces (details in **Figure S7**) are selected for the investigation

of the catalytic activity. The energies of species related to the calculation can be found in **Table S2**.

The Gibbs free energy of adsorption hydrogen atom is calculated by Equation (1) (Hu et al., 2018b):

$$\Delta G_H = E[Ni_5P_4 + H] - E[Ni_5P_4] - 1/2E[H_2] + \Delta E_{ZPE} - T\Delta S_H \quad (1)$$

where $E[Ni_5P_4+H]$ is the total energy of the system, including the adsorbed molecules and the Ni_5P_4 facet; $E[Ni_5P_4]$ is the energy of Ni_5P_4 facet; $E(H_2)$ represents the total energy of a gas phase H_2 molecule; ΔE_{ZPE} denotes the zero-point energy of the system simplified as 0.05 eV. The term $-T\Delta S_H$ is the contribution from entropy at temperature K, taken as 0.20 eV at 298 K (Tang and Jiang, 2016).

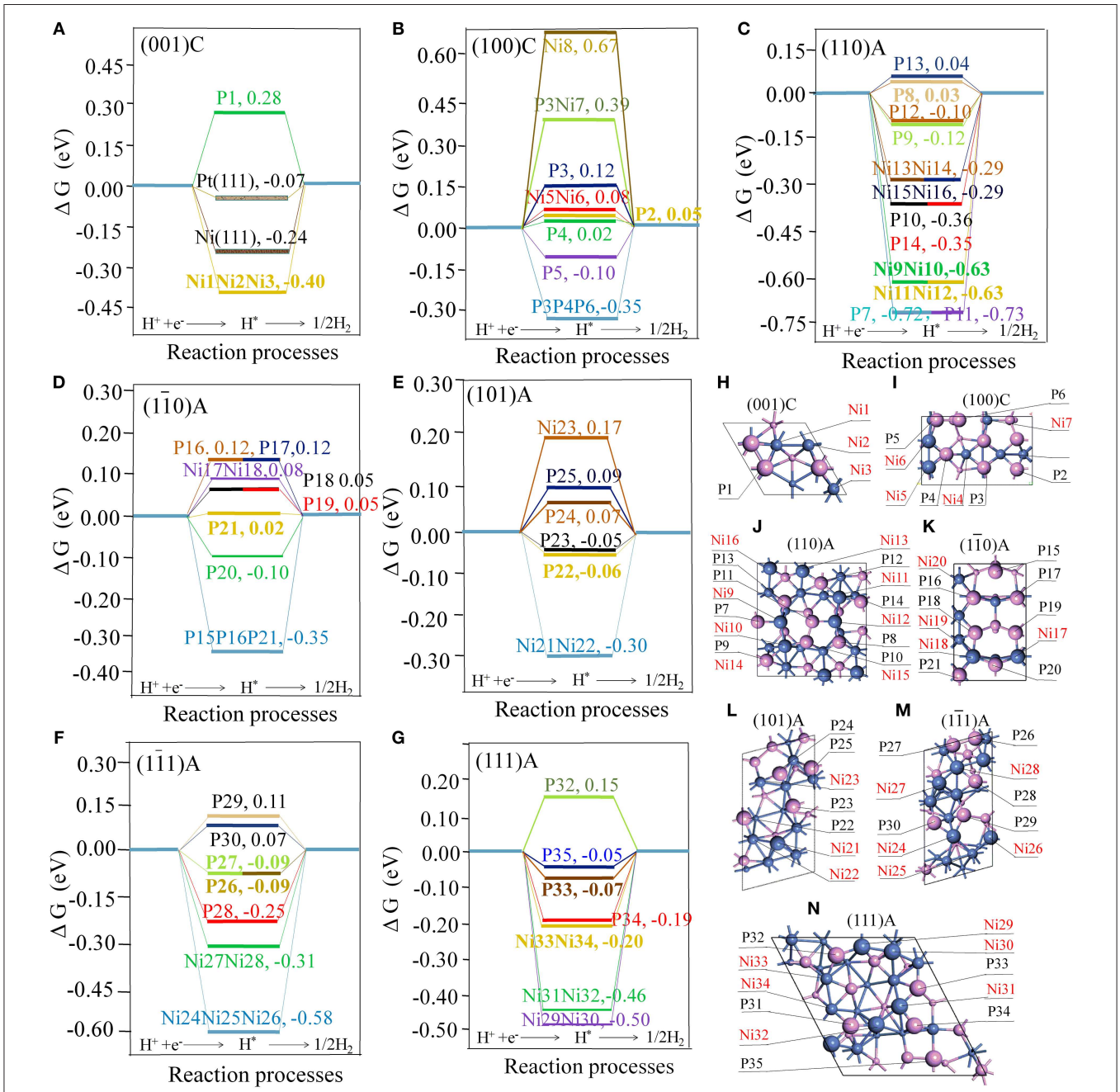

FIGURE 1 | Free energy profile of H_2 generation on different active site of surfaces with the units in eV **(A)** the (001)C surface, with Pt(111) and Ni(111) surfaces included for comparison; **(B)** the (100)C surface; **(C)** the (110)A surface; **(D)** the (1$\bar{1}$0) A surface; **(E)** the (101)A surface; **(F)** the (1$\bar{1}$1) A surface; **(G)** the (111)A surface. The geometry structures of different surfaces **(H)** the (001)C surface **(I)** the (100)C surface; **(J)** the (110)A surface; **(K)** the (1$\bar{1}$0) A surface; **(L)** the (101)A surface; **(M)** the (1$\bar{1}$1)A surface; **(N)** the (111)A surface; Violet spheres stand for P atoms and blue spheres stand for Ni atoms. Large, medium, and small spheres stand for the atoms located in the first, second, and third layer.

RESULTS AND DISCUSSION

Active Sites for HER

ΔG_H is considered as a good descriptor of materials for catalyzing hydrogen generation following either the Volmer-Tafel or the Heyrovsky mechanism (Hinnemann et al., 2005). In principle, smaller of $|\Delta G_H|$ means better HER activity (Zheng et al., 2014). **Figure 1** displays details of the adsorption energies involved in the water splitting process on the different sites.

As illustrated in **Figure 1H**, we found that ΔG_H for Ni(111) and Pt(111) surfaces are −0.23 and −0.07 eV, respectively. This is largely consistent with previous experimental and calculated results (Nørskov et al., 2005; Tan et al., 2013). As seen from **Figure 1**, some hollow NiNiNi sites, hollow PPP sites, bridge NiNi sites, and top P sites are able to stably adsorb the hydrogen atom (H^*). If we consider a site is active when the $|\Delta G_H|$ is smaller than 0.15 eV, the hollow sites are not catalytically active while some bridge NiNi sites and top P sites may be active. In order to reveal the characteristic of the active sites, detailed structures for bridge NiNi sites and top P sites are illustrated in **Figures 2**, **3**.

As indicated in **Figures 2A–K**, only a few bridge NiNi sites are active, such as the bridge Ni5Ni6 and Ni17Ni18 while others are not. It is notable the linear correlation coefficient is 0.869 between total bond number of Ni and ΔG_H, and the linear fit between bond number of Ni (x) and ΔG_H (y) obeys $y = -1.98 + 0.13x$. Therefore, the bond number plays an important role to the activity and it may exhibit excellent HER performance when the total bond number of Ni equals to 15 or 16 (**Figure 2L**).

Furthermore, it is interesting to notice that the ΔG_H for most top P sites are closer to zero (P2, P3, P4, P5, P8, P9, P12, P13, P16, P17, P18, P19, P20, P21, P22, P23, P24, P25, P26, P27, P29, P30, P33, and P35). It means these sites are able to trap protons and bond the atomic hydrogen while still able to desorb H_2 easily. This finding agrees well with the results reported by Jin et al., where it was reported that top P may be the active sites for Ni_3P (Jin et al., 2016). Additionally, other top P sites are not suitable for HER such as P1, P7, P10, P11, P14, P28, P32, and P34. In order to clearly recognize the key parameters affecting the activity, more detailed geometry structures of P sites are plotted in **Figure 3**.

As indicated in **Figure 3**, P sites can be divided into three types based on the number of PP bond during the surface cleavage. The first type is the one that has two PP bonds, these P sites are active if one of the PP bond is a double bond (P35, P5, and P20) while the other is not (P7, P11, and P1). The second type is the P sites with 1 PP bond. All such P sites have three bond number with Ni. These P sites are active if only one neighboring atom (regardless of Ni or P atom) is coplanar with this P site (P2, P18, P19, P29, P30, P33, P22, P23, P26, and P27). While the P

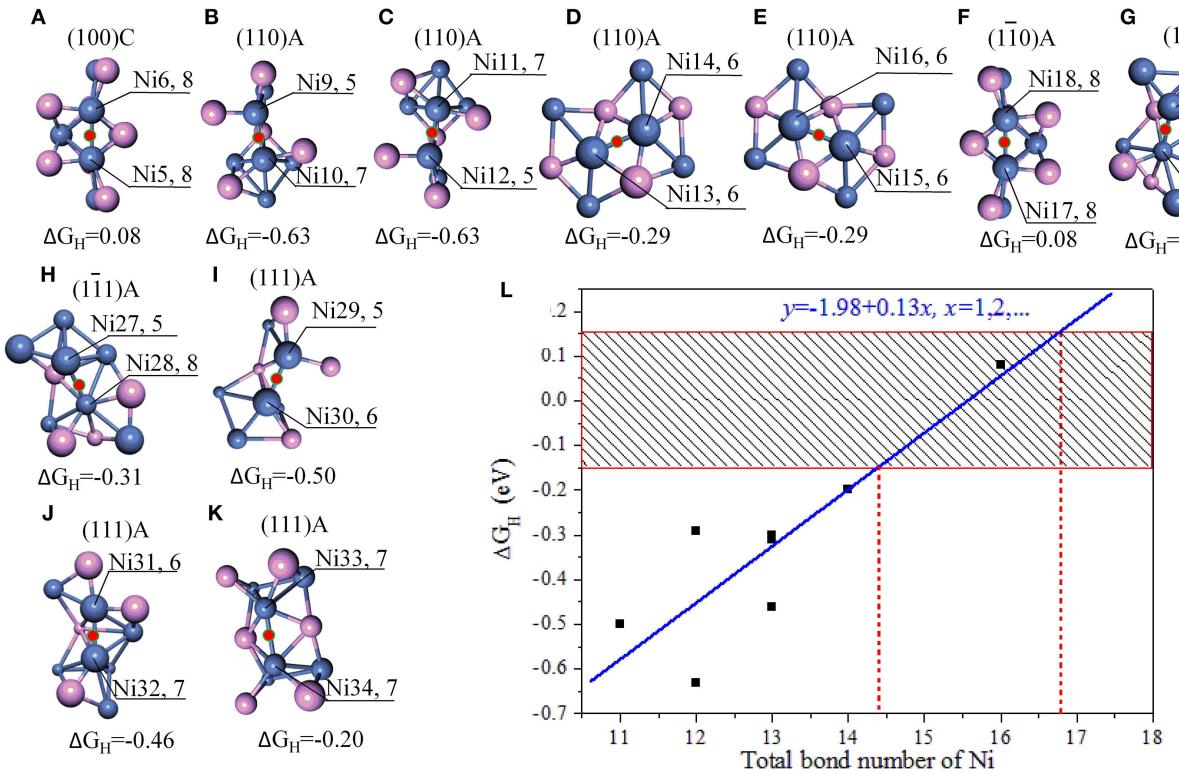

FIGURE 2 | (A–K) Stable adsorption sites with bridge NiNi; **(L)** the relationship between the bond number of Ni and ΔG_H. The bonds are marked when the bond tolerance changes from 0.600 to 1.185, and violet spheres stand for P atoms and blue spheres stand for Ni atoms. In order for easy comparison, the ΔG_H are also manifested in the units of eV.

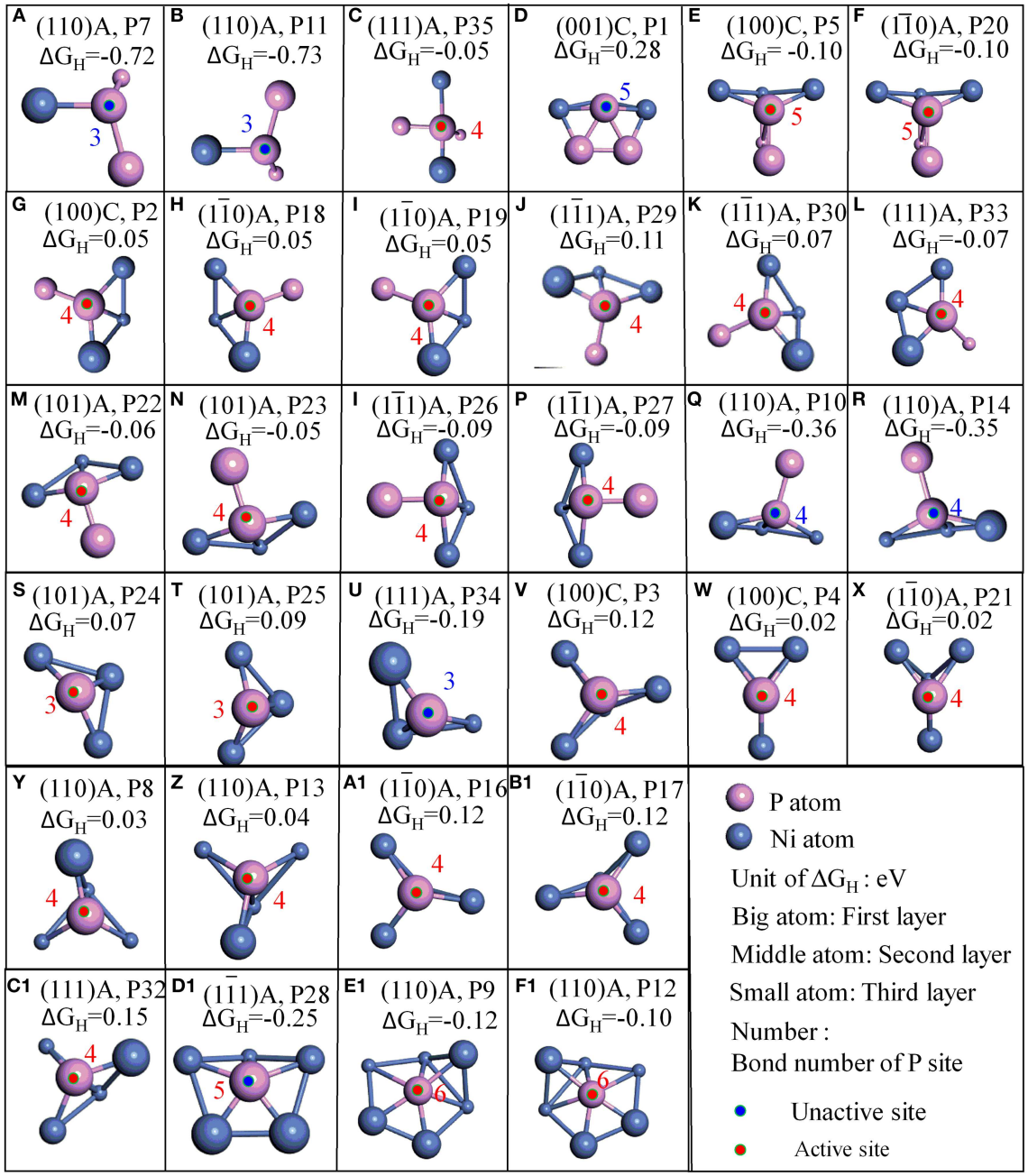

FIGURE 3 | Stable adsorption sites with surface P atoms **(A–F)** surface P sites with 2 PP bonds; **(G–R)** surface P sites with 1 PP bonds; **(S–F1)** surface P sites with 0 PP bonds; The bond number (red number) of P are marked when the bond tolerance changes from 0.600 to 1.185.

sites are not active if the two neighboring atoms are coplanar with the P site. For example, P10 and P14 are coplanar with one neighboring Ni and one neighboring P. The third is the P site without PP bond. This type of P sites have 3, 4, 5, and 6 bond number with Ni. For the P sites with three bond number, the P sites are active if no neighboring atom is coplanar with this P site (P24, P25), while it is not active if one neighboring atom is coplanar with this P site (P34). Furthermore, P sites with four or six bond number are active while P sites with five bond number are not active. The information thus displays a "structure sensitivity" of this material. The determination of the bond number on the activity has also been found in other catalysts (Zhao et al., 2016; Wang et al., 2018). In this work, not only the bond number but also the relative position with neighbors play an important role to determine the activity of P atom for HER (**Graphical Abstract**).

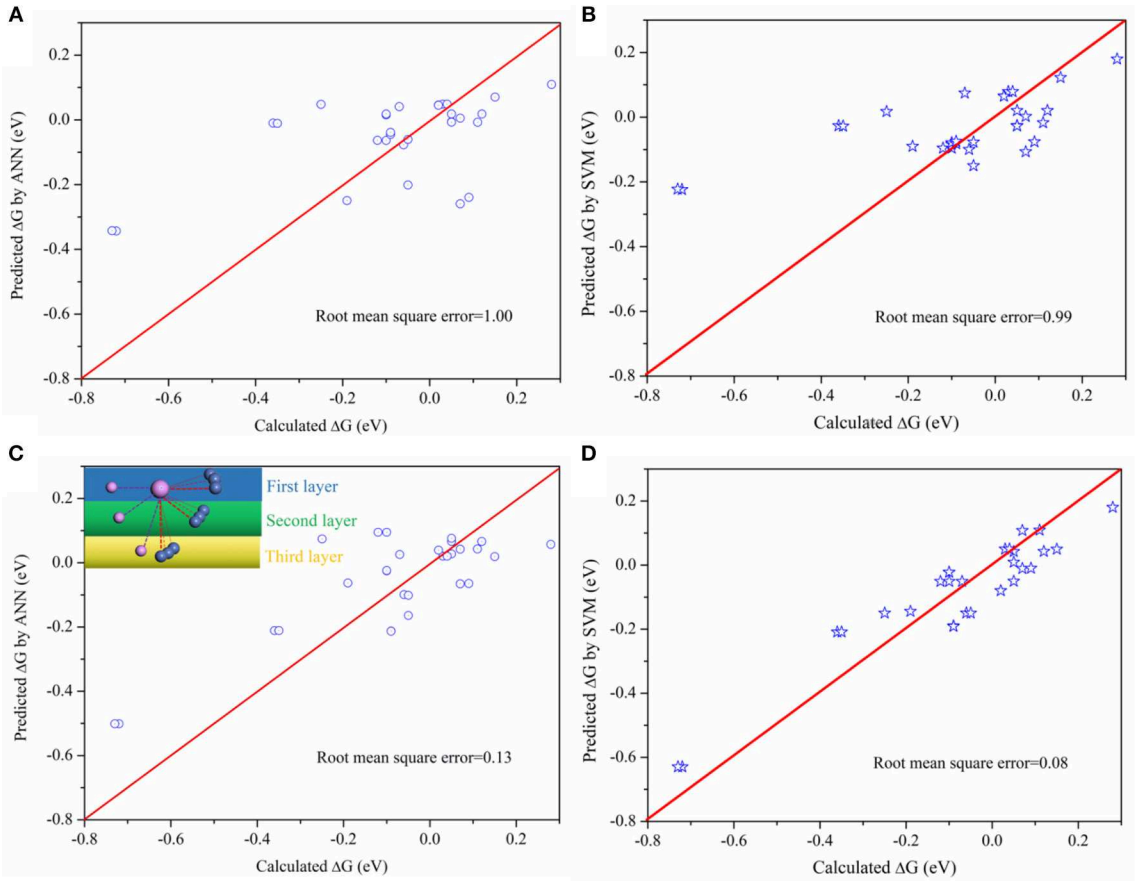

FIGURE 4 | Comparing the predicted ΔG with calculated ΔG on P sites **(A)** the predicted ΔG by ANN method based on the BL data, arranged from largest to smallest; **(B)** the predicted ΔG by SVM method based on the BL data; **(C)** The predicted ΔG by ANN method based on the BLP data; **(D)** the predicted ΔG by SVM method based on the BLP data.

Although this connection between activity and bond property is obvious, it is difficult to fit by mathematical models due to the complexity. Machine learning method, which is capable of analyzing complex data, is used to analyze the results obtained. Two machine learning methods, the Artificial Neural Network (ANN) and Support Vector Machine (SVM), were used to predict the activity. During the ANN training, the number of input layer, middle layer, and output layer were chosen based on the characteristics of the data. This data were randomly split into training (50%) and testing (50%) groups to prevent overtraining. For the SVM model, the regularization parameter is set as 10 in order to balance the classification accuracy and overfitting for the training data. The Kernel type is Radial Basis Function (RBF) with RBF gamma equals to 0.1. Furthermore, the model will stop the optimization when the error between the adjacent steps is <0.1%. The results are shown in **Figure 4**. There are two database during the training, one for the bond length (BL) (**Table S3**), where the bond length of active sites are arranged from long to short, and the other the bond length–position (BLP) (**Table S4**), arranged from the first, second, and third layer based on position of active P site as indicated in the inset image of **Figure 4C**.

As indicated in **Figure 4**, there is a larger root mean square error based on BL data while the error will be greatly reduced based on BLP data. The different between BLP and BL data is only whether the data contains the information of relative positions or not. The result verifies our early finding (**Figure 3**) that the positions of neighboring atoms indeed play an important role on the catalytic activity. Furthermore, The SVM model is more appropriate for the catalytic activity prediction than the ANN model. Therefore, this work demonstrates that it is possible to establish a relationship between activity (macroscopic activity) of P sites and their bond length (an atomic-scale property) by using appropriate machine learning method. This method is potentially useful for high-throughput calculations because it can drastically reduce the amount of calculations.

Electronic Characteristics of Active Sites

As indicated above, most of P sites are active sites in Ni_5P_4. To reveal the origin of HER activity, partial density of states (PDOS) of different P sites are illustrated in **Figure 5**.

Comparing the PDOS of different sites (**Figure 5A** and **Figure S8**), we found the separated 3*p* orbits, one localized

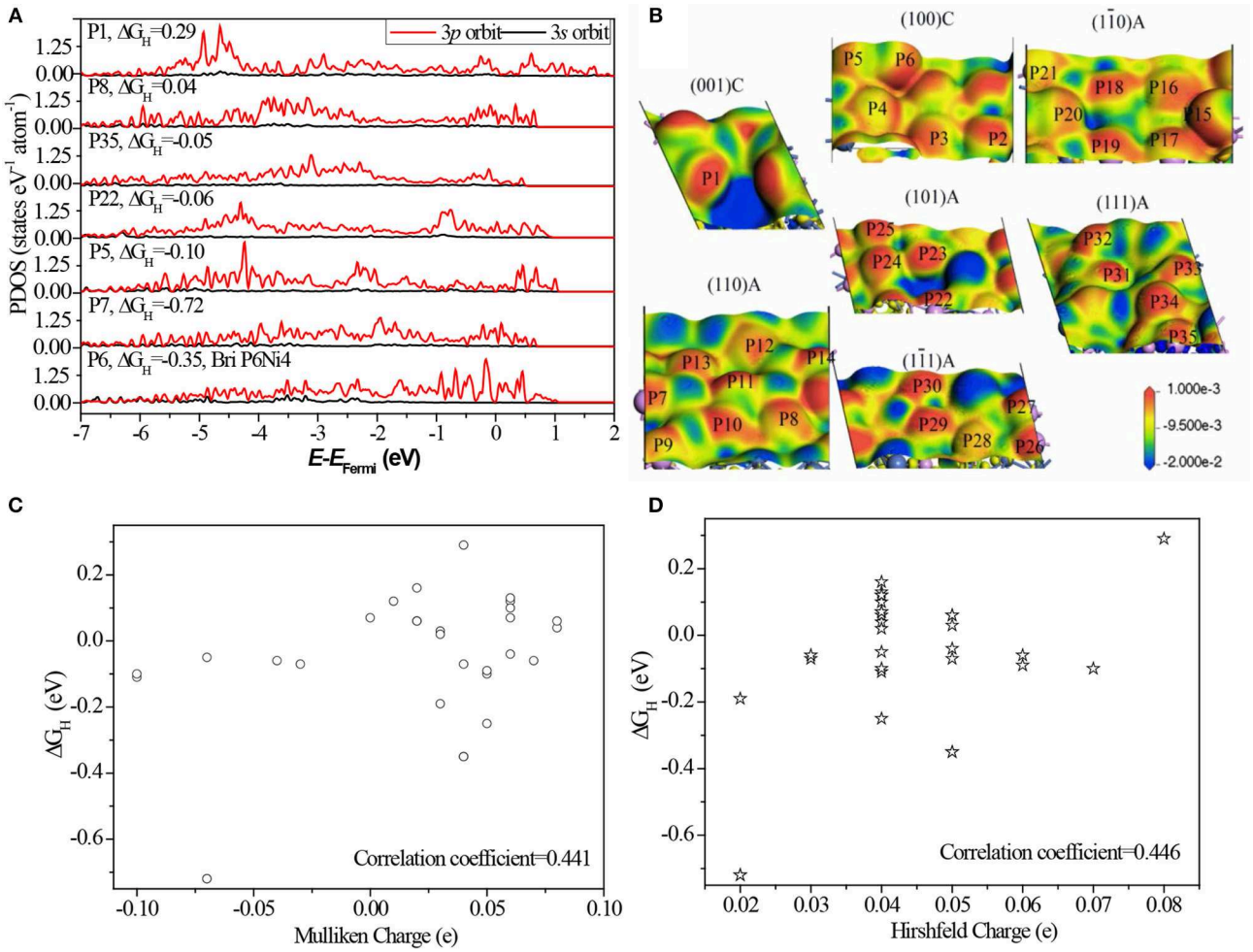

FIGURE 5 | (A) The corresponding PDOS of P atoms. The corresponding PDOS of all P sites can be found in **Figure S8**; **(B)** the electron density difference map of different surfaces with potential isovalue equals to 2.0 eV are inserted in, where a loss of electrons is indicated in blue and electron enrichment is indicated in red; **(C)** the relationship between Mulliken charge and ΔG_H; **(D)** the relationship between Hirshfeld charge and ΔG_H; Details data of charge can be found in **Table S5**.

in the region of −5.0 to −3.0 eV and another localized in the region of −1.0 to 1.0 eV, have a high activity. While greatly localized 3*p* orbits near the Fermi level (P6) and deeper energy level (P1) are not active. This finding suggests that the activity of P sites comes from the appropriate bond to localize some 3*p* orbits of the P atom: weakly bonded or strongly bonded P atom weakens its activity. The weakly bonded P sites, such as P6 and P7, tend to form strong stable bonds with H*, where the atoms have few electron-state fluctuations and the charge-transfer is more common. Strongly bonded P sites, such as P1, tend to form weak but stable bonds with H* and make it impossible to form H bond on the sites (Falicov and Somorjai, 1985).

Based on the electron density difference map (**Figure 5B**), the catalytic activity has a strong relation with the electron distribution. The same distribution has almost same activity, for example, between P6 and P15, and P2 and P18. As known, the neighboring bonds largely affect the electron distribution, therefore, the activity of P sites are greatly related to the bond number and relative position of neighbors. Furthermore, the relationship between charge states with ΔG_H was also analyzed. Some literatures indicated that the catalytic activity has a strong relation with charge of the surface atom (Balteanu et al., 2004). Statistical analysis (**Figures 5C,D**) shows that the linear correlation coefficient is only 0.441 between Mulliken charge and ΔG_H, and 0.446 between Hirshfeld charge and ΔG_H. This indicates that there is no strong relationship between charge states and HER activity of Ni_5P_4. The main reason is the charge states do not contain the relative position with neighbors while charge distribution includes this information.

CONCLUSIONS

In this paper, a comprehensive theoretical analysis is presented on the catalytic characteristics of different active sites of Ni_5P_4

for electrochemical water splitting. The results indicate the bond number and relative position with neighbors play an important role on the activity of Ni_5P_4 for HER. There are two active sites, namely the bridge NiNi sites and top P sites. The bridge NiNi sites with a total bond number of Ni equals to 15 or 16 exhibit good HER performance. For the top P sites, the activity is greatly affected by bond number of P as well as the coplanar atoms. Data on the bond length with neighbors can be used to predict the activity of P sites as reviewed by machine learning. PDOS of different P sites illustrates that the activity of P sites should form the appropriate bond to localize some 3p orbits of P atom. Weakly bonded or strongly bonded P atom will weaken its activity. Therefore, bond number and positions of neighbors are two key parameters for HER activity of Ni_5P_4 material. The current work establishes a clear connection between the macroscopic activity and geometrical structures of Ni_5P_4 material. The outcome not only provides important insights into the surface activity for water splitting, but also opens up an exciting opportunity to quickly design and optimize the materials with high catalytic activity. Except the (001)C that is non-active, most of the investigated surfaces of Ni_5P_4, e.g., the (100)C, (110)A, $(1\bar{1}0)$A, (101)A, are active for HER, indicating that this material is a good candidate for practical hydrogen production.

DATA AVAILABILITY

The raw data supporting the conclusions of this manuscript will be made available by the authors, without undue reservation, to any qualified researcher.

AUTHOR CONTRIBUTIONS

JH and ZC conceived and designed the calculations. XC, WC, and YD performed the calculations. XZ and GL analyzed the data. JH and ZC revised the paper.

ACKNOWLEDGMENTS

Financial support from the Ministry of Education of Singapore (RG15/16), the National Natural Science Foundation of China (No. 21676216, 21576224), China Postdoctoral Science Foundation (No. 2014M550507; 2015T81046), and National Natural Science Foundation of Shaanxi (2019JM-294) are gratefully acknowledged.

SUPPLEMENTARY MATERIAL

The Supplementary Material for this article can be found online at: https://www.frontiersin.org/articles/10.3389/fchem.2019.00444/full#supplementary-material

REFERENCES

Balteanu, I., Balaj, O. P., Beyer, M. K., and Bondybey, V. E. (2004). Reactions of platinum clusters $^{195}Pt_n\pm$, n = 1–24, with N_2O studied with isotopically enriched platinum. *Phys. Chem. Chem. Phys.* 6, 2910–2913. doi: 10.1039/B405211K

Cao, B. F., Veith, G. M., Neuefeind, J. C., Adzic, R. R., and Khalifah, P. G. (2013). Mixed close-packed cobalt molybdenum nitrides as non-noble metal electrocatalysts for the hydrogen evolution reaction. *J. Am. Chem. Soc.* 135, 19186–19192. doi: 10.1021/ja4081056

Chen, W. F., Iyer, S., Sasaki, K., Wang, C. H., Zhu, Y. M., Muckerman, J. T., et al. (2013b). Biomass-derived electrocatalytic composites for hydrogen evolution. *Energy Environ. Sci.* 6, 1818–1826. doi: 10.1039/c3ee40596f

Chen, W. F., Wang, C. H., Sasaki, K., Marinkovic, N., Xu, W., Muckerman, J. T., et al. (2013a). Highly active and durable nanostructured molybdenum carbide electrocatalysts for hydrogen production. *Energy Environ. Sci.* 6, 943–951. doi: 10.1039/c2ee23891h

Chen, Z., Cummins, D., Reinecke, B. N., Clark, E., Sunkara, M. K., and Jaramillo, T. F. (2011). Core–shell MoO_3-MoS_2 nanowires for hydrogen evolution: a functional design for electrocatalytic materials. *Nano Lett.* 11, 4168–4175. doi: 10.1021/nl2020476

Falicov, L. M., and Somorjai, G. A. (1985). Correlation between catalytic activity and bonding and coordination number of atoms and molecules on the transition metal surfaces: theory and experimental evidence. *Proc. Natl. Acad. Sci. U.S.A.* 82, 2207–2211. doi: 10.1073/pnas.82.8.2207

Feng, L., Vrubel, H., Bensimon, M., and Hu, X. (2014). Easily-prepared dinickel phosphide (Ni2P) nanoparticles as an efficient and robust electrocatalyst for hydrogen evolution. *Phys. Chem. Chem. Phys.* 16, 5917–5921. doi: 10.1039/c4cp00482e

Feng, Y., Yu, X. Y., and Paik, U. (2016). Nickel cobalt phosphides quasi-hollow nanocubes as an efficient electrocatalyst for hydrogen evolution in alkaline solution. *Chem. Commun.* 52, 1633–1636. doi: 10.1039/C5CC08991C

García-Muelas, R., Li, Q., and López, N. (2018). Initial stages in the formation of nickel phosphides. *J. Phys. Chem. B* 122, 672–678. doi: 10.1021/acs.jpcb.7b06020

Gerasimov, M. V., and Simirskii, Y. N. (2008). Relationship between the electrochemical behavior of phosphides and amorphous iron alloys that contain chromium and phosphorus. *Metallurgist* 52, 477–481. doi: 10.1007/s11015-008-9064-5

Hinnemann, B., Moses, P. G., Bonde, J., Jørgensen, K. P., Nielsen, J. H., Horch, S., et al. (2005). Biomimetic hydrogen evolution: MoS_2 nanoparticles as catalyst for hydrogen evolution. *J. Am. Chem. Soc.* 127, 5308–5309. doi: 10.1021/ja0504690

Hu, J., Chen, W., Zhao, X., Su, H., and Chen, Z. (2018a). Anisotropic electronic characteristics, adsorption, and stability of low-index BiVO4 surfaces for photoelectrochemical applications. *ACS Appl. Mater. Interfaces* 10, 5475–5484. doi: 10.1021/acsami.7b15243

Hu, J., Zheng, S., Zhao, X., Yao, X., and Chen, Z. (2018b). A theoretical study on the surface and interfacial properties of Ni_3P for the hydrogen evolution reaction. *J. Mater. Chem. A* 6, 7827–7834. doi: 10.1039/C8TA00437D

Huang, Z., Chen, Z., Chen, Z., Lv, C., Meng, H., and Zhang, C. (2014). $Ni_{12}P_5$ nanoparticles as an efficient catalyst for hydrogen generation via electrolysis and photoelectrolysis. *ACS Nano.* 8, 8121–8129. doi: 10.1021/nn5022204

Jiang, P., Liu, Q., and Sun, X. (2014). NiP_2 nanosheet arrays supported on carbon cloth: an efficient 3D hydrogen evolution cathode in both acidic and alkaline solutions. *Nanoscale* 6, 13440–13445. doi: 10.1039/C4NR04866K

Jin, L., Xia, H., Huang, Z., Lv, C., Wang, J., Humphrey, M. G., et al. (2016). Phase separation synthesis of trinickel monophosphide porous hollow nanospheres for efficient hydrogen evolution. *J. Mater. Chem. A* 4, 10925–10932. doi: 10.1039/C6TA03028A

Laursen, A. B., Patraju, K. R., Whitaker, M. J., Retuerto, M., Sarkar, T., Yao, N., et al. (2015). Nanocrystalline Ni_5P_4: a hydrogen evolution electrocatalyst of exceptional efficiency in both alkaline and acidic media. *Energy Environ. Sci.* 8, 1027–1034. doi: 10.1039/C4EE02940B

Laursen, A. B., Wexler, R. B., Whitaker, M. J., Izett, E. J., Calvinho, K. U. D., Hwang, S., et al. (2018). Climbing the volcano of electrocatalytic activity

while avoiding catalyst corrosion: Ni3P, a hydrogen evolution electrocatalyst stable in both acid and alkali. *ACS Catal.* 8, 4408–4419. doi: 10.1021/acscatal.7b04466

Li, X., Hao, X., Abudula, A., and Guan G. (2016). Nanostructured catalysts for electrochemical water splitting: current state and prospects. *J. Mater. Chem. A* 4, 11973-12000. doi: 10.1039/C6TA02334G

Liu, P., and Rodriguez, J. A. (2005). Catalysts for hydrogen evolution from the [NiFe] hydrogenase to the $Ni_2P(001)$ surface: the importance of ensemble effect. *J. Am. Chem. Soc.* 127, 14871–14878. doi: 10.1021/ja0540019

Liu, P., Rodriguez, J. A., Asakura, T., Gomes, J., and Nakamura, K. (2005). Desulfurization reactions on $Ni_2P(001)$ and α-$Mo_2C(001)$ surfaces: complex role of P and C sites. *J. Phys. Chem. B* 109, 4575–4583. doi: 10.1021/jp044301x

McKone, J. R., Sadtler, B. F., Werlang, C. A., Lewis, N. S., and Gray, H. B. (2013). Ni–Mo nanopowders for efficient electrochemical hydrogen evolution. *ACS Catal.* 3, 166–169. doi: 10.1021/cs300691m

Meng, S., Li, B., Li, S., and Yang, S. (2017). Carbon nitride frameworks padded with graphene as efficient metal-free catalyst for HER in acidic and alkali electrolytes. *Mater. Res. Express.* 4:055602. doi: 10.1088/2053-1591/aa6df6

Merlet, C., Rotenberg, B., Madden, P. A., Taberna, P. L., Simon, P., Gogotsi, Y., et al. (2012). On the molecular origin of supercapacitance in nanoporous carbon electrodes. *Nat. Mater.* 11, 306–310. doi: 10.1038/nmat3260

Nørskov, J. K., Bligaard, T., Logadottir, A., Kitchin, J. R., Chen, J. G., Pandelov, S., et al. (2005). Trends in the exchange current for hydrogen evolution. *J. Electrochem. Soc.* 152, J23–J26. doi: 10.1149/1.1856988

Pan, Y., Liu, Y., Zhao, J., Yang, K., Liang, J., Liu, D., et al. (2015). Monodispersed nickel phosphide nanocrystals with different phases: synthesis, characterization and electrocatalytic properties for hydrogen evolution. *J. Mater. Chem. A* 3, 1656–1665. doi: 10.1039/C4TA04867A

Pu, Z., Xue, Y., Li, W., Amiinu, I. S., and Mu, S. (2017). Efficient water splitting catalyzed by flexible NiP_2 nanosheet array electrodes under both neutral and alkaline solutions. *New J. Chem.* 41, 2154–2159. doi: 10.1039/C6NJ03194C

Shu, Y., Lee, Y. K., and Oyama, S. T. (2005). Structure-sensitivity of hydrodesulfurization of 4,6-dimethyldibenzothiophene over silica-supported nickel phosphide catalysts. *J. Catal.* 236, 112–121. doi: 10.1016/j.jcat.2005.08.015

Tan, T. L., Wang, L. L., Johnson, D. D., and Bai, K. (2013). Hydrogen deposition on Pt(111) during electrochemical hydrogen evolution from a first-principles multiadsorption-site study. *J. Phys. Chem. C* 117, 22696–22704. doi: 10.1021/jp405760z

Tang, Q., and Jiang, D. (2016). Mechanism of hydrogen evolution reaction on 1T-MoS_2 from first principles. *ACS Catal.* 6, 4953–4961. doi: 10.1021/acscatal.6b01211

Voiry, D., Yamaguchi, H., Li, J., Silva, R., Alves, D. C., Fujita, T., et al. (2013). Enhanced catalytic activity in strained chemically exfoliated WS_2 nanosheets for hydrogen evolution. *Nat. Mater.* 12, 850–855. doi: 10.1038/nmat3700

Vrubel, H., and Hu, X. (2012). Molybdenum boride and carbide catalyze hydrogen evolution in both acidic and basic solutions. *Angew. Chem. Int. Ed.* 51, 12703–12706. doi: 10.1002/anie.201207111

Wang, X., Chen, Z., Zhao, X., Yao, T., Chen, W., You, R., et al. (2018). Regulation of coordination number over single Co sites: triggering the efficient electroreduction of CO_2. *Angew. Chem. Int. Ed.* 57, 1944–1948. doi: 10.1002/anie.201712451

Wexler, R. B., Martirez, J. M. P., and Rappe, A. M. (2017). Active role of phosphorus in the hydrogen evolving activity of nickel phosphide (0001) surfaces. *ACS Catal.* 7, 7718–7725. doi: 10.1021/acscatal.7b02761

Xie, J., Zhang, H., Li, S., Wang, R., Sun, X., Zhou, M., et al. (2013). Defect-rich MoS_2 ultrathin nanosheets with additional active edge sites for enhanced electrocatalytic hydrogen evolution. *Adv. Mater.* 25, 5807–5813. doi: 10.1002/adma.201302685

Yang, J., Voiry, D., Ahn, S. J., Kang, D., Kim, A. Y., Chhowalla, M., et al. (2013). Two-dimensional hybrid nanosheets of tungsten disulfide and reduced graphene oxide as catalysts for enhanced hydrogen evolution. *Angew. Chem. Int. Ed.* 52, 13751–13754. doi: 10.1002/anie.201307475

Zhao, H., Oyama, S. T., Freund, H. J., Włodarczyk, R., and Sierka, M. (2015). Nature of active sites in Ni_2P hydrotreating catalysts as probed by iron substitution. *Appl. Catal. B* 164, 204–216. doi: 10.1016/j.apcatb.2014.09.010

Zhao, Z., Chen, Z., Zhang, X., and Lu, G. (2016). Generalized surface coordination number as an activity descroptor for CO_2 reduction on Cu surface. *J. Phys. Chem. C* 120, 28125–28130. doi: 10.1021/acs.jpcc.6b10155

Zheng, Y., Jiao, Y., Zhu, Y., Li, L. H., Han, Y., Chen, Y., et al. (2014). Hydrogen evolution by a metal-free electrocatalyst. *Nat. Commun.* 5:3783. doi: 10.1038/ncomms4783

Conflict of Interest Statement: The authors declare that the research was conducted in the absence of any commercial or financial relationships that could be construed as a potential conflict of interest.

frontiers in Chemistry

ORIGINAL RESEARCH
published: 26 November 2019
doi: 10.3389/fchem.2019.00799

Catalytic Activity and Kinetic Modeling of Various Modules HZMS-5 and Treated MCM-41 Catalysts, for the Liquid-Phase Ketalization of Glycerol With Acetone

*Murad Alsawalha**

Department of Chemical and Process Engineering Technology, Jubail Industrial College, Al Jubail, Saudi Arabia

Studies of the Ketalization reaction using trivalent alcohol glycerol in combination with acetone and their kinetics modeling are still limited. The focus of this current study is an investigation into HZSM-5 with various silica to alumina molar ratios (M = 35, 90, and 160) for the reaction between glycerol and acetone. In addition, the influence of reaction temperatures (25, 50, and 60°C) on the rate of the reaction have also been considered. Additionally, this investigation established the rate law for all HZMS-5 models (M = 35, 90, and 160) which showed "*n*" order equals half while the activation energy was found to be 164.34 kJ mol^{-1} with a constant reaction rate of $k_0 = 5.2678*10^{28}$ ($Concentration^{1/2}$. min^{-1}). Furthermore, MCM-41 pure mesoporous materials were separately treated using various methods. The first involved treatment using Dichlorodimethylsilane MCM 41(TD) and later treatment of a pure sample with sulfuric acid MCM-41. The sulfated MCM-41 sample (MCM41-SU) showed that reaction order equals $n = -1$ and a rate constant of (k) = 3.9×10^2 ($Concentration^{-2}$. min^{-1}). A close correlation and agreement was found between the experimental modeling and the theory. Additionally, this current kinetic study showed that water production has no effect on the conversion activity within 10 min from the start of reaction. Besides, further kinetics investigations were performed to ascertain the estimated time for water production based on the conditions applied during the reaction system. It resulted in an average time of 3 min for equilibrium to be reached in the reaction system. It was found that the estimated reaction equilibrium time (t_{eq}) is within the range from zero to 10 min in agreement with the proposed kinetic model in this work. Finally, it was also observed that a low equilibrium conversion (X_{Aeq}) had been obtained in the present work about 0.42 (42%). At a reaction temperature of 60°C (333.15 K) and at one atmosphere, the acetone was shown to exert a vapor pressure of about 113.737 mm Hg. Hence, the overall order of the reaction was determined by the method of initial rates. Similarly, in order to ascertain the dispersion of aluminum, together with its distribution on the surface of a catalyst for a zeolite that has varying molar ratios of silica to alumina as is the case for example with ZSM-5 (35), a mathematical approach is proposed in this study for its calculation.

Keywords: kinetic study, ketalization reaction, reaction rate, HZSM-5 zeolites, MCM-41, glycerol

OPEN ACCESS

Edited by:
Hadi Nur, University of Technology Malaysia, Malaysia

Reviewed by:
Pedro Maireles-Torres, University of Málaga, Spain
Zifeng Yan, China University of Petroleum (Huadong), China

***Correspondence:**
Murad Alsawalha
murad_s@jic.edu.sa

Specialty section:
This article was submitted to Catalysis and Photocatalysis, a section of the journal Frontiers in Chemistry

Received: *05 August 2019*
Accepted: *06 November 2019*
Published: *26 November 2019*

Citation:
Alsawalha M (2019) Catalytic Activity and Kinetic Modeling of Various Modules HZMS-5 and Treated MCM-41 Catalysts, for the Liquid-Phase Ketalization of Glycerol With Acetone. Front. Chem. 7:799. doi: 10.3389/fchem.2019.00799

INTRODUCTION

Zeolite materials have an important role in terms of their applications in the various industries (Alsawalha, 2019; Pan et al., 2019). There are a variety of definitions in use which do not differ significantly, but the most commonly accepted is by Breck (1974). Zeolites are crystalline, hydrated aluminosilicates, synthesized or naturally occurring which contain alkali or alkaline earth cations, namely, sodium, potassium, magnesium, calcium, strontium, and barium.

Structurally, zeolites are Aluminosilicate frameworks based on an infinite, three-dimensional network of AlO_4 and SiO_4 tetrahedrals interconnected by sharing oxygen atoms (Corma et al., 1997; Loganathan et al., 2013). The synthesis of MCM-41 occurs via organic amphiphiles (e.g., quaternary ammonium salts), which are used as structure-directing reagents (Loganathan et al., 2013). Beck et al. (1992) describe the production of MCM-41 using the LCT mechanism (liquid crystal template). These MCM-41 materials are forms of liquid-crystalline phases of water/ surfactant systems and the periodic pore systems of the M41S group (Beck et al., 1992). The MCM-41 with periodic cavities can be synthesized with pore diameters ranging from 1.5 nm to over 10 nm (Beck et al., 1992). Heterogeneously catalyzed dehydration reactions have long been known. However, the mechanism of these types of reactions are not fully understood. Pines and Pillai (1960) suggest that both acidic and basic centers are required for catalyzed dehydration reactions. With regard to zeolites, the dehydration of alcohols on an HZSM-5 has been studied in particular (Derouane et al., 1978; Jingfa et al., 1988; Schulz and Bandermann, 1994). The literature describes the application of H-zeolites for the condensation reaction (Clarkson et al., 2001; **Figure 1**). In the heterogeneously catalyzed condensation reaction between glycerol and acetone, the catalytic condensation of glycerol with acetone leads to the formation of 2, 2-dimethyl-4-methanol-1,3-dioxolane, which is commonly referred to as solketal (Clarkson et al., 2001).

Solketal is a ring-shaped diether that has an additional hydroxyl group. The first developments of this synthesis began in the 1920s, when Fischer et al. (Fischer and Pfähler, 1920) devoted themselves to the study of a variety of glycerides. Further studies employing hydrochloric and sulfuric acid were performed (Fischer and Pfähler, 1920), but the preferred catalyst in the field of research is p-toluenesulfonic acid (Newman and Renoll, 1945). There is a dramatic and ever increasing interest in glycerol production from biodiesel, since it is manufactured as a by-product of fatty acid methyl ester production. The need for crude glycerol does not increase in proportion to the increase in the volume of biodiesel in production, resulting in its loss of value. Moreover, the literature (Rossa et al., 2017) presents a possibility of further processing glycerol which may then be added to various fuels as oxygenate. Thus, the trihydric alcohol could be converted either to acetone or to a compound, which also has a carbonyl group. Ketalization product, Solketal could be then added as an additive in gasoline, diesel, or biodiesel to increase ignitability and reduce particle emissions.

The challenge that water, a coproduct, appears in the reaction is based on the fact that glycerol and acetone form a heterotopic mixture and there is a need for the removal of the water from the equilibrium reaction (Fischer and Pfähler, 1920).

When feasible, it is possible to use a desiccant in the removal of water such as sodium sulfate, potassium carbonate or phosphorus pentoxide. However, employing desiccant has the disadvantage that on a production scale, waste products are obtained in large quantities, especially water (Fischer and Pfähler, 1920). The reaction temperature can range anywhere from room temperature up to the boiling point of acetone (56°C). Under the influence of acid catalysts, ketones react with polyhydric alcohols to form ketals (Nanda et al., 2016; Zong et al., 2018; **Figure 2**). In the first step of the reaction (Nanda et al., 2016; Zong et al., 2018), the acetone carbonyl group is activated by a coordination of the Lewis acid metal sites. Then, an alcoholic (hydroxyl) group of glycerol attacks a carbon atom within the carbonyl group. This attack coincides with the bond formation of an atom of carbonyl oxygen with a secondary one of carbon glycerol. Lastly, the dehydration process results in the product Solketal.

In the first step of the reaction, the acetone carbonyl group of the acetone is protonated and the secondary carbenium ion obtained is later attacked (nucleophilic) by a hydroxyl group of the glycerol before the final elimination of a proton. The newly formed hydroxyl group of the acetone or the mediate hydroxyl group of glycerol is affected because of protonation and the fact that water splits off to form another secondary carbenium ion. An intermolecular nucleophilic attack by a hydroxyl group leads to the desired product solketal (García et al., 2008; Nanda et al., 2016). The solketal reaction is selected for this work so as to examine the catalytic activity as well for performing a kinetics study over H-ZSM-5 and treated MCM-41 samples. There are few studies or references available in the literature regarding the study of kinetics using solketal reaction in particular for the MCM-41 samples. For this reason, the entire focus of this work is to establish a kinetics study for the ketalization reactions of both HZSM-5 (with various modules 35, 90, 160) and MCM-41. These solid-state acids are investigated with respect to a possible relationship between the modulus and the catalytic activity. Moreover, a sample of the pure, original source of MCM 41 was treated with Dichlorodimethylsilane and another with Sulfuric acid. After treatment, the first is named MCM 41 (TD) while, the second sulfated sample is named MCM 41 (SU) and both are included in this current work.

Samples were examined for both catalytic activity and for establishing reaction kinetics modeling. As is known to date, kinetics modeling in particular for HZSM-5 and MCM-41, have not yet been investigated by the Ketalization reaction. Accordingly, the current investigation seeks to contribute in the exploration of knowledge of mathematical and kinetics materials chemistry and its development and potential use in future industrial applications.

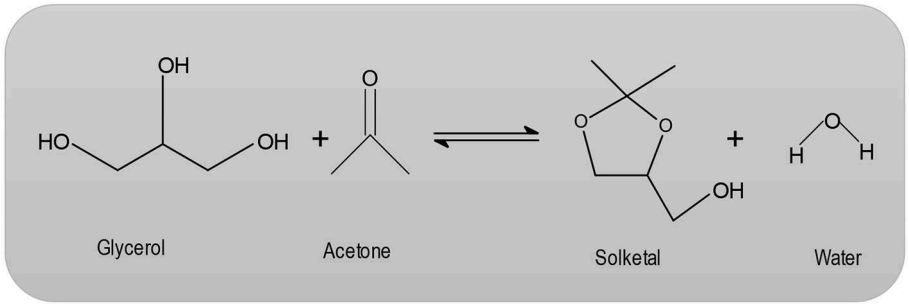

FIGURE 1 | Condensation reaction between glycerol and acetone.

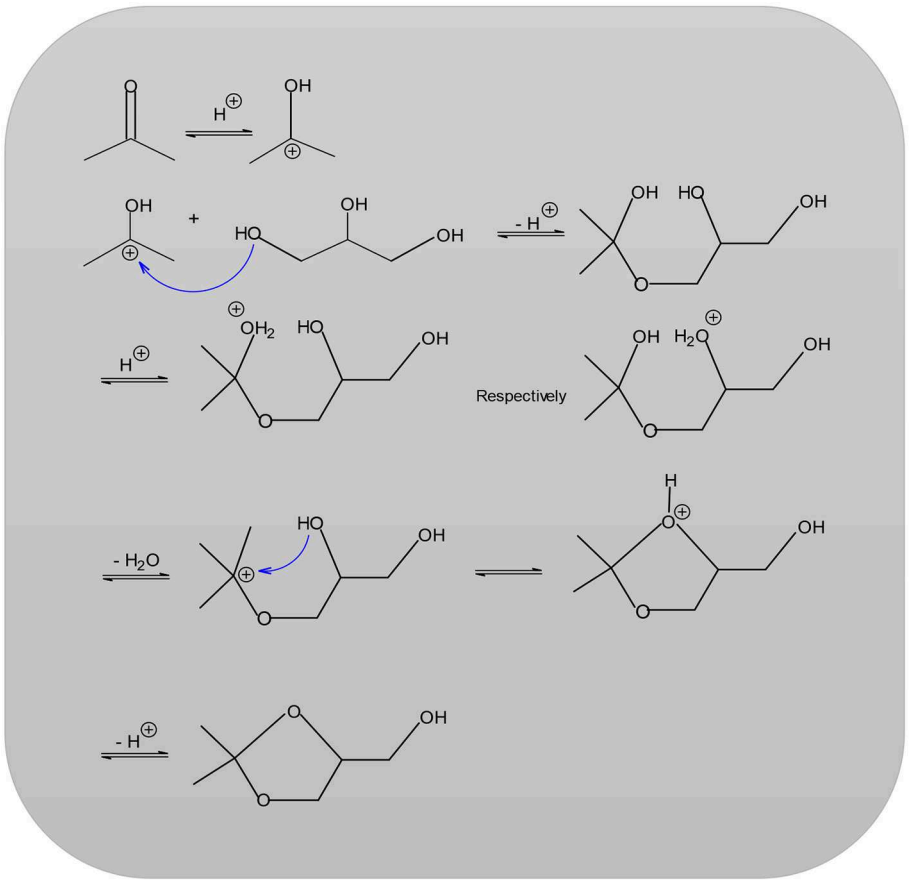

FIGURE 2 | Mechanism for the formation of solketal reaction.

MATERIALS AND METHODS

MCM-41 Silylated With Dichlorodimethylsilane (MCM 41-TD)

Purely siliceous MCM-41 (pure MCM-41), glycerol and acetone (99.5%) were purchased from Merck-Aldrich. Further modification of the (MCM-41 pure) was conducted in two stages. Twenty grams of (MCM-41 pure) was first silylated with 20 (mL) Dichlorodimethylsilane (99.5%) to produce a hydrophobic surface and stirred continuously at room temperature in a fume hood for a period of 1 h. Finally, the mixture was filtered and was left exposed in the open air for a period of 24 h again in a fume hood. At a later time, the preparation was heated in a furnace at 120°C for a period of 2 h. For each Ketalization reaction, an amount of 2 grams of catalyst material was used.

Sulphated MCM-41 (MCM 41-SU)

A 15 gram sample of commercial MCM 41 samples purchased from Süd-Chemie AG, München was calcined for 2 h at 150°C, after which 20 milliliters of dichloromethane was added. This

solution was then mixed magnetically whilst gradually adding drops of sulfuric acid measuring 10 milliliters were gradually added over a period of 2 h. The preparation continued to be magnetically stirred until the H_2SO_4 had been removed. Next, the sample was washed in 25 milliliters of acetonitrile and left to dry at room temperature to obtain Sulphated (MCM 41-SU). For the Ketalization reaction, an amount of 2 grams of catalyst was utilized.

Catalyst Activation

A list of companies and zeolite types that were sourced for the study are presented in **Table 1**.

It is noteworthy to mention that ZSM-5 zeolites number in the parenthesis [$(SiO_2)x(Al_2O_3)y$] corresponds either to Si/Al ratio or the ratio of the oxides, so called module, SiO_2/Al_2O_3 (this value is twice as high as the Si/Al ratio).

Zeolites have the capacity to absorb increasingly larger amounts of water from the air when stored for extended periods of time. Such a situation causes blockages in both their pores, as well as the active centers. Therefore, in order to enhance their activity, zeolites must be thermally treated before use (Corma et al., 1998; Konno et al., 2014; Jelena et al., 2015; Joris and Bert, 2018). In this process of treatment, any remaining ammonium compounds that were used as templates in the synthesis are removed.

With the decomposition of these zeolite molecules, ammonia and protons are formed (Corma et al., 1998; Jelena et al., 2015).

Before any zeolite could be used, it was important to have activated them first by using a tube furnace, for example. Thus, glass spoons were employed to introduce the catalyst samples into the glass tube. Then, in an atmosphere (I bar) of nitrogen, the oven was heated at 18°C per min to the respective final temperature of 350°C. Gauging correct temperatures and time duration is necessary for successful activation. These however, also depend on the catalyst system used. For example, the Zeolite HZSM-5 needed to be heated at 400°C for 1 h. Whilst, the MCM-41, whether in pure or modified form, required a temperature of only 130°C, but for an extended period of 8 h. Note that the reaction temperatures for all MCM-41 samples were at room temperature.

However, for determining the temperature influence on the kinetics behavior using HZSM-5 (M = 90) to assess how zeolite successfully converts a reactant to a Solketal product, two additional reaction temperatures of 50 and 60°C were applied.

Condensation Reaction of Glycerin and Acetone

The homogeneous or heterogeneously catalyzed reaction between glycerol and acetone was carried out in a batch process. The reaction vessel used was a 50 mL, three-necked flask equipped with a thermometer, a reflux condenser, and a drying tube together with 8 grams of glycerol, 20 mL ($20 \times 0.784 = 15.68$ g) of acetone and 0.3 mL of 1,4-dioxane. The implemented conditions for the kinetics investigations were determined at 600 rpm, a molar ratio of glycerol: Acetone, is $\left(\frac{8}{92.1} : \frac{15.68}{58.1} = 0.087 : 0.27 = 1 : 3\right)$, and 4 w% (0.32 g) of catalyst relative to the mass of glycerol, for 100 min.

TABLE 1 | Different commercial samples.

Zeolite type	Manufacture
ZSM-5 (Si/Al = 35) and ZSM-5 (Si/Al = 160)	The PQ corporation Valley Forge, Philadelphia
ZSM-5 (Si/Al = 90)	Süd-Chemie AG, München
p-Toluenesulfonic acid	Merck

The 1,4-dioxane served as an internal standard for gas chromatographic analysis. In addition, an internal standard was also used because it was not possible to detect glycerol. As an example, acetonitrile can be used as a solvent on the analysis samples because it has the quantitative ability to dissolve both glycerol and acetone.

However, the disadvantage is that retention times of the reactant acetone do not differ from those of acetonitrile. This then prompted the use of an internal standard. However, there are usually no resulting negative effects of the use of acetone nor any influence on the process or results of the study. Additionally, the use of any alcohol was excluded as a solvent because it reacts adversely to the acetone.

GC Conditions of Analysis

The various analyses were performed with the help of gas chromatography (GC) analysis type Perkin Elmer Auto system with flame ionization detector (FID). The temperature of the GC detector was 200°C under a gas stream of 35 mL/min H_2. The applied carrier gas of H_2 reached a pressure of 60 kPa. The GC column type is Carbowax (30 m × 0.25 mm × 0.25 μM polyethylene glycol). Temperature program of the gas chromatography began at 75°C isotherm for 1 min. It was raised gradually by 40°C per min up to 150°C. Thereafter, the same temperature was maintained for a further 2 min. The retention time of the detected compounds, acetone, 1,4-Dioxane, and the solketal product were found to be 1.2, 1.4, and 1.9, respectively. No other additional compounds have been detected.

An internal standard was employed to determine the condensation reaction. The peak area is multiplied with the correction factor of the internal standard. This represents 100% of the reactant peak areas largely because acetone, not glycerol, was identified. The correction factor that results can be calculated in the following way;

$$Cr = \frac{P_{Ac}}{P_{In} \, . M_{ex_{ac}}}$$

Cr, Correction factor
P_{Ac}, Peak area of the acetone in the chromatogram
P_{In} , Peak area of the internal standard in the chromatogram
$M_{ex_{ac}}$, Molar excess of acetone in the reaction mixture.

The correction factor for the conversion calculation of the condensation reaction between glycerol and acetone was calculated using the internal standard 1,4-dioxane. This was determined by means of the peak areas detected by an FID. However, the molar excess of acetone had to be considered.

The following is an example calculation for determining the correction factor. The detected peak are of acetone gave a value of 108, 680,851 and the 1,4 dioxane (internal standard) of 260,805 resulting in the following factor.

Example:

$$Cr = \frac{P_{Ac}}{P_{In}\,.M_{ex_{ac}}}$$
$$Cr = \frac{108680851}{260805 * 3}$$
$$Cr = 138.90$$

then,

$$Cr.P_{In} = A_{100\%}$$

where; $A_{100\%}$ is the 100% of the peak areas resulted from the chromatogram.

As a result, the conversion can be calculated from the following equation;

$$X = 1 - \frac{P_{Ac}}{A_{100\%}} = \frac{A_s}{A_{100\%}}$$

where A_S is the peak area of the Solketal.

Surface Area and Pore Volume Characterizations

In the study, Tristar 3000 Surface Area and Porosimetry Analyzer (Micromeritics) equipment was employed to analyze different HZM5 and pure MCM 41 zeolites. Calculations of specific areas, volumes, and pore sizes were performed. Firstly, the BET (Brunauer, Emmet, and Teller) method determined the specific area. Secondly, the BJH method was used to ascertain the specific volume together with pore diameters. Third, the samples were weighed, then dry heated for 14 h at 350°C in a 6×10^{-3} vacuum. Following cooling at room temperature, the samples were then weighed a second time and later exposed to a temperature of −196°C. The sorption (adsorption/desorption) isotherms of N_2 at different partial pressures of N_2 were then ascertained. Microporous structures, consistent with zeolite materials, were noted.

RESULTS

Table 2 presents the results for different zeolite samples. Results revealed that zeolite H-ZSM5 possesses a higher specific area. This is likely due to a greater occurrence of micropores and external area specifically pore volumes together with mesopore volume of 0.07–0.13 [$cm^3\ g^{-1}$]. In general, these findings are as expected for microparticles HZSM-5 (Nda-Umar et al., 2018).

Moreover, the content of Na_2O (%) in all commercial ZSM-5 samples is <0.2. All ZSM-5 commercial samples have been calcined in an oven at 450°C for 5 h with a ramp of 15°C/min. The samples were later stored in an oven at 120°C in order to avoid contact with water. Conversely, **Table 3** presents the textural properties of various MCM 41 samples.

In this study, findings concerning the characterization of the surface area of the pure commercial siliceous MCM-41 (pure MCM-41) were in the range of 820 (m^2g^{-1}), with pore volumes of 0.76 (cm^3g^{-1}) and pore diameter measuring 2.5 nm. On the other hand, higher surface area was recorded for sulfated sample (MCM 41-SU) in the range of 1,382 (m^2g^{-1}), with total pore volume of 1.1 (cm^3g^{-1}) and pore diameter with the value of 2.81 nm. It is possible that treatment with sulfuric acid precipitates changes in the MCM 41-SU. The treatment process itself may have resulted in an unexpected higher pore volume of MCM 41-SU, possibly due to the partial deterioration of walls of the mesopores.

Additionally, this higher surface area of the MCM-SU is likely to be a result of the acidic species of the sulfuric acid that were grafted onto the surface of Si-MCM-41 in the treated sample.

Likewise, the literature details how purely siliceous MCM-41 was treated with Phosphorus acid for a shortened period (Kawi et al., 2002). The results showed that the surface phosphorus species had grafted onto the surface of MCM-41 and that an increase in the number of selectively formed Brønsted acid sites on the surface had also occurred without the formation of Lewis acid sites (Kawi et al., 2002).

In the future and as a follow on from our study, more investigation is required in order to examine in greater detail the effects of various acidic treatments over the surface areas for the samples studied.

Reaction of Glycerol and Acetone Using p-toluenesulfonic Acid as a Homogeneous Catalyst

In order to check if Solketal takes form in the absence of a catalyst, an additional "unanalyzed" reaction was performed. It was noted that no product could be detected using Gas chromatography during the 24-h period. Thus, the time it takes for product formation is only attributable

TABLE 2 | Textural properties of various HZSM-5 with different of SiO_2/Al_2O_3 ratios.

HZSM-5 with different SiO_2/Al_2O_3 ratios	Micropore volume (cm^3g^{-1})	Mesopore volume (cm^3g^{-1})	Total pore volume (cm^3g^{-1})	BET surface area SBET (m^2g^{-1})
ZSM-5 (35)	0.05	0.02	0.07	388.4
ZSM-5 (90)	0.06	0.04	0.1	425.6
ZSM-5 (160)	0.08	0.05	0.13	460.3

TABLE 3 | Textural properties of various MCM-41 samples.

MCM-41 samples	BET surface area SBET (m^2g^{-1})	Total pore volume (cm^3g^{-1})	Average pore diameter (nm)
MCM 41 (pure)	820	0.69	2.50
MCM 41 (TD)	988	0.76	2.54
MCM 41 (SU)	1,382	1.10	2.81

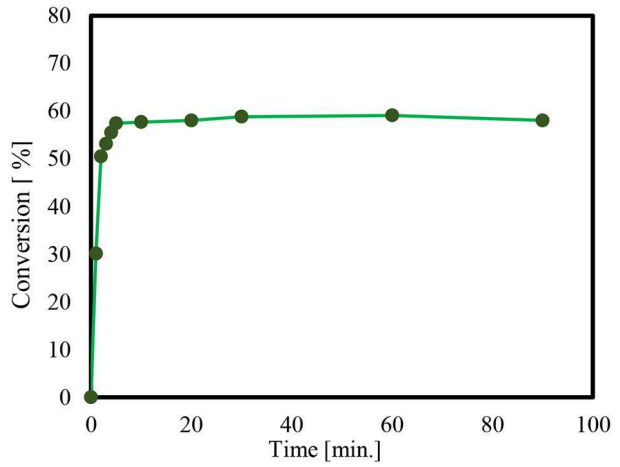

FIGURE 3 | Reaction of glycerol and acetone using p-toluenesulfonic acid (PTSA), as a homogeneous catalyst, at 60°C.

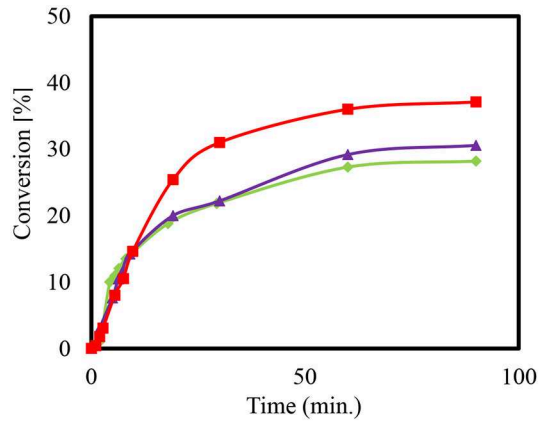

FIGURE 4 | Conversion (%) to Solketal using HZSM-5 with different ratio (SiO_2/Al_2O_3); 35 (♦), 90 (▲), and 160 (■), at reaction temperature 50°C.

to the activity of the catalyst employed. Moreover, the reaction of glycerol and acetone by p-toluenesulfonic acid (PTSA), as a homogeneous catalyst is presented in **Figure 3**.

The conversion of the condensation reaction between glycerol and acetone on different p-toluene sulfonic acids (PTSA) (Breck, 1974; Alsawalha, 2019; Pan et al., 2019) as a homogeneous catalyst showed about a 38% catalytic activity 10 min after the start of the reaction. The maximum conversion of 58% was reached within 30 min. The conversion results obtained in this present work is in agreement with the work in literature (Nda-Umar et al., 2018), where a molar ratio of 1:4, conversion is 70.9%, and at a molar of 1:2, the conversion is 54.9% using similar catalyst. That is to say, the conversion of glycerol at 1:3 molar ratio of glycerol to acetone in the present study is within the range 58%.

The obtained result is also an agreement with the documented conversion of glycerol to acetone over p-toluene sulfonic acid (PTSA) which reached 60% after 15 min, increasing to 80% after 45 min and with a reaction temperature 70°C (Da Silva et al., 2009). For an objective comparison of this current result with that found in the literature, note that the different conversions of glycerol were found to reach to reach 87 and 79%, over acid catalysts like H-β zeolite and $Zr(SO_4)_2$, respectively, and at a reaction temperature of 40°C (Nanda et al., 2014a). Notably, water as by-product forms and appears to impede the acetalization reaction (Smirnov et al., 2018). It acts as a barrier to the successful conversion of glycerol, a kind of thermodynamic and kinetic obstacle. It is likely that the presence of water, even in very small amounts resulted in only a modest conversion of 58%. It also increased the need for longer reaction time so as to manage and lessen the effect of water forming in the pores (Smirnov et al., 2018).

On the other hand, for acetalization of 2.74 mol glycerol with 8.22 mol acetaldehyde, one study employed 0.27 mol p-toluenesulfonic acid as a catalyst (García et al., 2008). The reaction time was for 16 h as the reflux was heated. This resulted in a 90% yield of the product 2,2-dimethyl-1,3-dioxolan-4-yl methanol (García et al., 2008).

Heterogeneous Catalyzed Condensation

Zeolites

The conversion of the condensation reaction between glycerol and acetone on different zeolites was investigated. The acidity of zeolites is dependent on the ratio of silica to alumina. The smaller the value of the module, the more that Brønsted acid sites are present. Moreover, the medium-pore zeolite of ZSM-5 was added to the condensation reaction in the H form with the modulus values 35, 90, and 160. **Figure 4** shows the presented conversions over time.

When using the heterogeneous catalyst HZSM-5 (M = 90) it can be observed that more time is needed to reach the maximum conversion of about 38% compared to HZSM-5 with modulus (SiO_2/Al_2O_3) value (M = 35). The final set of conversions that were realized are estimated to be as equivalent since they are within the range of the measuring accuracy of the sampling and that of the gas chromatographic analysis. This equivalency may be explained by changes in the acid center density without affecting the conversion of the reaction (Rossa et al., 2017). Moreover, lower conversions for the condensation reactions using HZSM-5 compared to the homogeneously catalyzed experiment may be attributed to the reaction anhydrous system (Da Silva and Mota, 2011). The preexisting water molecules that formed can block the catalytically active centers of the zeolites, which would result in a lower efficiency. The literature reports a higher conversion with zeolite beta in the range of 90 and 95% (Da Silva and Mota, 2011). Moreover, the selectivity of the Solketal product obtained for all tested samples yielded around 98%, which is in agreement with results in the literature (Rossa et al., 2017).

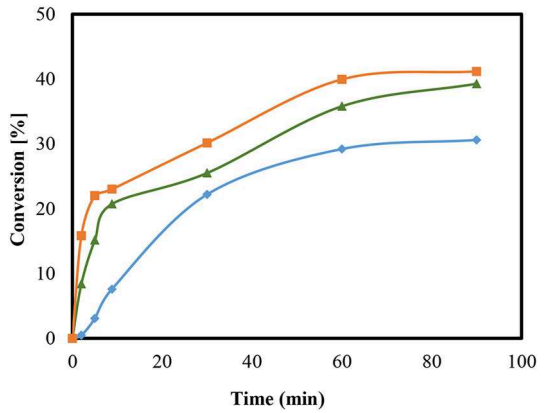

FIGURE 5 | Conversion of the condensation reaction using HZSM-5 with a modulus of M = 90 at temperature of 25°C (♦), 50°C (▲), and 60°C (■).

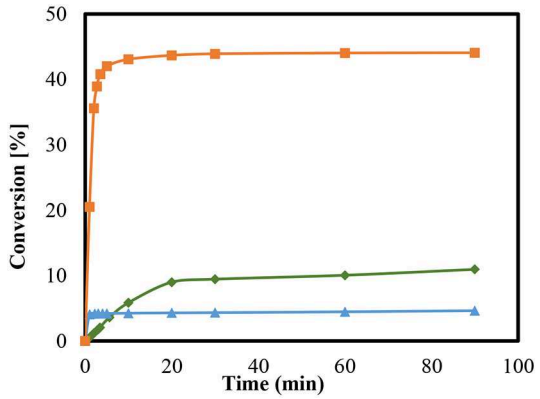

FIGURE 6 | Conversions of condensation reaction between glycerol and acetone at room temperature using modified and unmodified MCM-41; MCM-41pure (▲), MCM 41- TD (♦), and MCM 41- SU (■).

Temperature Influence

To investigate a possible influence of the temperature on the reaction, an examination was carried out on HZSM-5 (M = 90) at 25, 50, and 60°C as presented in **Figure 5**. The amount of catalyst used was 5 wt.%.

Variations in temperature were found to possibly influence the conversion. After 90 min, the conversion at 25°C was 20.7% and at a temperature of 50°C, the conversion raised to 39% at 60°C, a slight increase in conversion was observed about 41%. The study results obtained here are also in agreement with the figures presented in the literature (Rossa et al., 2017). The alteration in the reaction temperature using H-BEA zeolite and the same reaction of glycerol with acetone stimulated a positive impact on conversions (Rossa et al., 2017). In addition, other results from Kowalska-Kus et al. (2016) showed that the conversion over HZSM-5 increases as the particle size of the catalysts decrease (Kowalska-Kus et al., 2016). Moreover, no further investigations were possible at higher temperatures because of the low boiling point of acetone. Additionally, the use of open equipment and the extension of the sampling time would likely lead to a reduction in the content amount of acetone and so cause distortions in any further comparative analysis.

Furthermore, an earlier study of the application of zeolites was conducted by Da Silva et al. (2009). In this, conversion of glycerol to fuel-additives was investigated with the use of zeolite Beta and p-toluene sulfonic acid and with the addition of acetone and formaldehyde. Moreover, mesoporous Lewis acid catalysts could be active in acetalization of glycerol with acetone to produce solketal (Da Silva et al., 2009). A five-membered-ring solketal was proposed in the acetalization of acetone with glycerol and for catalyzation with solid Brønsted acids (Li et al., 2012). By proper coordination and activation of the carbonyl group of the acetone, the study (Li et al., 2012) contended that Lewis acid metal sites could function in similar ways as those oxidation reactions shown in Meerwein–Ponndrof–Verley reduction studies (Li et al., 2012). In the same instance that the primary alcoholic group of glycerol attacks the carbon atom of the carbonyl, a bond is formed between the carbonyl β-carbon and oxygen atoms. The resulting dehydration precipitates the formation of a five-membered-ring solketal (Li et al., 2012). Moreover, literature (Rossa et al., 2017) reported that during the reaction, it is almost certain that water was formed. As a result, the structure of the H-BEA zeolite destabilized (Li et al., 2012).

Similarly, the zeolite-catalyzed condensation reactions with MCM-41 was used in various modifications for ketalization reaction. Every sample of the mesoporous material was examined at room temperature as is presented in **Figure 6**. The conversions are presented as a function of time for MCM41 (pure), MCM41-TD, and MCM 41-SU. As shown in **Figure 6**, the conversions are dependent on the degree of modification of the MCM-41. The silanol groups of the surface revealed higher catalytic activity than the untreated sample (pure MCM-41). These groups have a slightly acidic property and revealed up to 10% conversion. In contrast, the use of MCM41-SU in this reaction provided very low conversion and revealed up to around 5% after 90 min.

Conversely, the catalytic species of the mesoporous materials generated by introducing sulfonic acid groups with the aid of sulfuric acid yielded a remarkably higher condensation reaction. This particular conversion yielded almost 44%, after 90 min, which accords with the reaction equilibrium and subsequently indicating a high activity of the catalyst. The conversion of treated sample appears to be greater by comparison than that of pure MCM 41, which is much slower. The ketalization of glycerol over on sulfated sample (MCM 41- SU) may be catalyzed by these sulfate groups and any homogenous catalysis should add to the process of global catalysis. This appears to be the cause of the highest conversion of this catalyst in the case of sulphuric acid over MCM-41.

The literature (Li et al., 2012) also reported that both water and impurities combined to affect the activity of the sample. This may explain why higher catalytic activity was not observed with increased reaction time.

Researchers recently modified the sample of MCM-41 with vanadium for the Ketalization of glycerol (Abreu et al., 2019). The results (Abreu et al., 2019) showed that the conversion relies on the amount of acid sites engendered in the silica structure. Other literature (Yasmin and Müller, 2010) reported a varying range of modifications for MCM-41, with trifunctional alkylsilanes. These particular modifications (Yasmin and Müller, 2010) resulted in a better reduction of the physical properties of the sample (MCM-41) than those modified with monofunctional silanes (Yasmin and Müller, 2010).

Additionally, a high selectivity toward solketal was achieved using supported SiW and MCM-41 catalysts (30% SiW11/MCM-41, 30% SiW12/MCM-41) together with benzaldehyde (Narkhede and Patel, 2014). The results showed that the highest solketal selectivity of 82, with 85% glycerol conversion and at a 30°C room temperature could be achieved on the 30%-SiW11/MCM-41. It also showed that in 1 h, a 100 mg catalyst weight and a 1/1.2 molar ratio of glycerol to benzaldehyde are achievable. Additionally, an increase in the selectivity toward solketal was observed by adjusting the acidity levels of the parent SiW. Acidity strength together with larger pores and surface areas accounts for the high activity noted in these catalysts (Narkhede and Patel, 2014).

It is worth noting that in this current investigation, there was a decrease in the surface area values for all samples after the reaction that also included a loss in the microspore area. Higher catalytic activity was observed with a higher surface area on Zeolite ZSM-5 (160). However, the adsorption of the products on the catalysts surface led to a decrease in the BET surface areas in the range of 30–40 [m^2/g]. It was also found that increasing the reaction time did not result in a proportionally higher glycerol conversion. This occurrence can be explained by the fact that in the acetalisation of acetone with glycerol, full conversion can be only obtained when either H_2O is removed from the system or when acetone is used in large quantities.

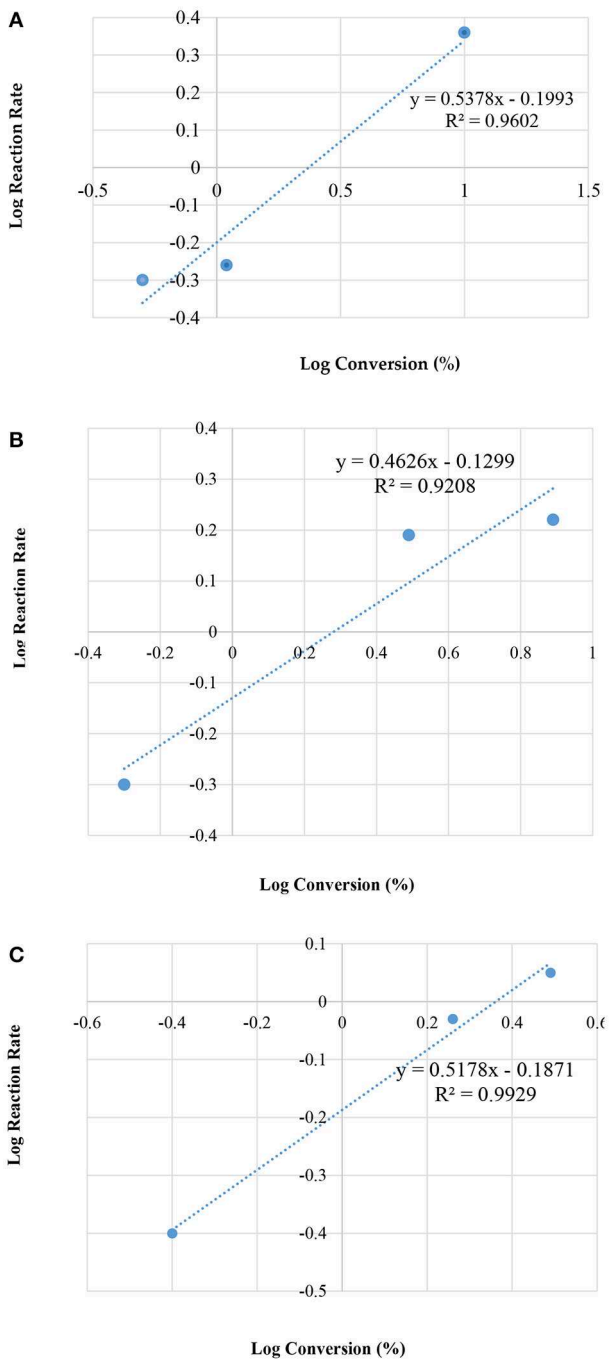

FIGURE 7 | Plot of log reaction rate vs. log concentrations, for different modulus of HZSM-5; **(A)** 35; **(B)** 90; and **(C)** 160, by the condensation reaction between glycerol and acetone.

Kinetic Modeling of Zeolites Adsorption and Desorption Paths by the Condensation Reaction Between Glycerol and Acetone

Figure 7 illustrates the kinetic energy for zeolite HZSM-5 with different modulus; 35, 90, and 160, respectively.

Table 4 presents the rate constant (k) and the overall rate (*n*), for the three different HZMS-5 zeolite and with different silica to alumina modules ratios at 25°C. The kinetic parameters were ascertained using only the method of initial rate. The standard procedure dictates that three points are sufficient to draw a straight line graphs. Over a period of 10 min the three points were obtained.

TABLE 4 | Rate constant (k) and overall rate (*n*), for three types of HZMS-5 zeolite and with different silica to alumina modules (ratios) and at the reaction temperature of 25°C.

HZSM-5 with different Si/Al modules	Kinetic rate constant (k) (Conc.$^{1/2}$ min^{-1})	Reaction rate order (*n*)
M = 35	0.6320	n = 1/2
M = 90	0.7415	n = 1/2
M = 160	0.6500	n = 1/2

In addition, the rate data showed that the overall rate equation follows the half order ($n = 1/2$). The following equation represents rate reaction for the initial rate from zero to 10 min together with and the rate equation:

$$\frac{d[conversion]}{d[time]} = k_1[Conversion]^{n=1/2}$$
$$\frac{d[conversion]}{d[time]} = 0.6745\ (min^{-1})\ [Conversion]^{1/2}$$

After 10 min, the rate of desorption follows the average overall rate equation as in the following;

$$\frac{d[conversion]}{d[Time]} = k_2[Conversion]^{n=-1}.$$

Effect of Temperature on the Kinetics Reaction Rate

For the reaction system with HZSM-5 samples were at different temperatures of 25, 50, and 60°C.

Table 5, shows kinetic constant (k) and, rate order (n) with HZSM-5 (M = 90), at different reaction temperatures.

It is interesting to note that the reaction at 25°C with a M = 90 sample gave the same rate law as presented in the current paper (**Table 5**).

The reaction systems at 50 and at 60°C yielded different orders (n) indicating that at these relatively high temperatures the reactions follow different reaction pathways for each respective temperature and in turn create more complexities in the reaction system mechanism. Reaction at 50°C, produced order n = −2.5 and the k = 4.436 × 10^3 (min^{-1}) whereas the reaction at 60°C yielded n = −1.3 and k = 1.3256*10^2 (min^{-1}).

The unanticipated values recorded are likely due to the behavior of acetone during the gaseous phase of the reaction. Acetone evaporates at 50 and at 60°C. As a result, the catalyst active sites become saturated and glycerol is impeded and adsorption onto the catalyst surface ceases.

The reason is that glycerol molecules are not taken up onto sites into which acetone molecules were previously adsorbed. Glycerol adsorption can only occur on vacant sites. Glycerol molecules become attached at a rate, which is inversely proportional to the concentration of the vacant sites existing on the catalyst surface. During the gaseous phase, there is one mole of glycerol and three of acetone present.

Figure 8 illustrates the relation between the conversion and the initial reaction rate.

TABLE 5 | Kinetic constant (k) and rate order (n) over HZSM-5 (M = 90), at different reaction temperatures.

Temperature (°C)	Kinetic rate constant (k) (Conc.$^{1/2}$ min^{-1})	Reaction rate order (n)
25	0.74478	$n = 1/2$
50	4.436 × 10^3	$n = -2.5$
60	1.3256 × 10^2	$n = -1.3$

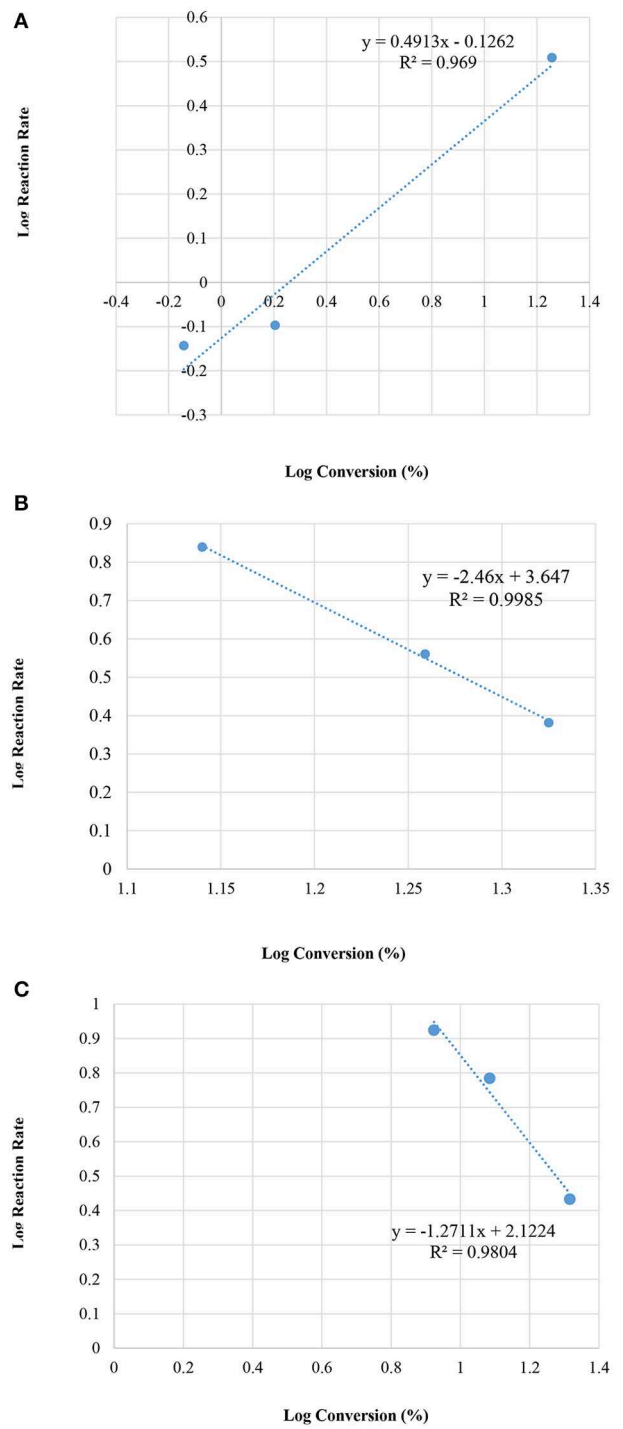

FIGURE 8 | Plot of log initial reaction rate (before 10 min of the reaction) vs. log concentrations, at various reaction temperatures; **(A)** room temperature 25°C, **(B)** 50°C, and **(C)** 60°C.

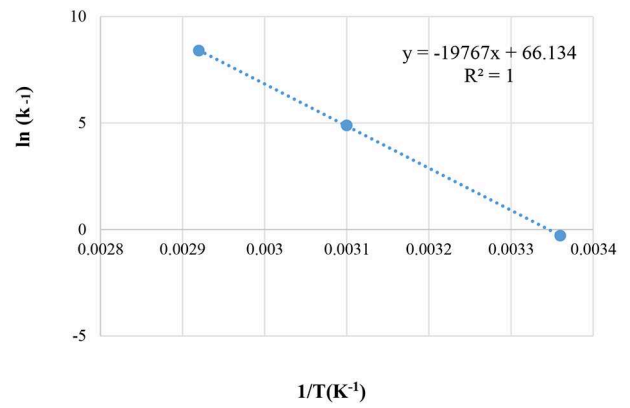

FIGURE 9 | Arrhenius Energy (E_A) for HZSM-5 at different reaction temperatures; of 25°C, 50°C, and 60°C.

Estimation of Arrhenius Energy (E_A) for HZSM-5, at Various Reaction Temperatures (25, 50, and 60°C)

The Arrhenius energy E_A is calculated from the equations:

$$k = k_0 e^{-\frac{E_A}{RT}}$$
$$Ink = Ink_0 - \frac{E_A}{R}\frac{1}{T}$$

k = specific rate constant for a forward or reverse reaction (Conc.^{½} min^{-1}). k_0, pre-exponential factor; R, universal gas constant, in this case: 8.314 J mol^{-1} K^{-1}; T, temperature in Kelvin (K); and E_A, activation energy (kJ mol^{-1}). A plot of $\frac{1}{T}$ vs. lnk gives the Arrhenius plot of the HZSM-5.

The reaction temperatures are presented in **Figure 9**.

The activation energy using the liquid-phase ketalization of glycerol with acetone was also described in the literature (Esteban et al., 2015; Esposito et al., 2019). This current study found that an estimated $E_{A,}$ from the figure above is equal to 164.34 kJmol^{-1} and $k_0 = 5.2678*10^{28}$ (Con$^{1/2}$. min^{-1}). In the literature (Rossa et al., 2017) the activation energy (E_A) for solketal reaction with H-BEA zeolite was calculated at reaction temperature ranging between 60 and 80°C and revealed Ea = 44.77 kJ mol^{-1} (Rossa et al., 2017). Conversely, in this current work, the reaction was performed at the lower reaction and temperatures ranging between 25 and 60°C. The result was a higher activation energy level of (164.34 kJ mol^{-1}).

KINETIC STUDY FOR PURE AND TREATED MCM-41 SAMPLES

The reaction for the pure MCM- 41 seems to be very slow. The reaction itself is independent of the conversion, where n is zero ($n = 0.1$) and rate constant k = 0.5766 (Conc.½ min^{-1}). Hence, more in-depth investigations are required to establish the reaction rate law. The reduced capacity to convert the acetone–glycerol adduct into solketal by Lewis acid sites over pure MCM 41 may in some measure explain the results obtained. This low rate is due to its hydrophobic property and to the absence of acidic centers (Rossa et al., 2017). The literature (Li et al., 2012) also reported that both water and impurities combined to affect the activity of the sample.

Moreover, the boiling point of Acetone is 56°C at one atmosphere, which corresponds to about 113.737 mm Hg vapor pressure. This saturates the active centers of the catalysts and reduces the efficiency of the catalysts within 10 min of reaction time.

On the other hand, the MCM-41 Silanol reaction seemed to be saturated after 1 min following the reaction. Therefore, the rate law could not be determined. Furthermore, the sulfated MCM-41 presented the order of the reaction to be n = −1 and the rate constant, k = 3.9 * 10^2 (Conc.^{½} min^{-1}). **Figure 10** presents an analysis of the kinetics data with the MCM-41 series from zero to 10 min.

KINETIC MODELING OF THE REACTION SYSTEM

Reaction Rate Equation for the Ketalization Reaction, Without Effect of Water

The Solketal reaction presented in **Figure 1** shows the overall reaction equation. With the kinetic study proposed, it is assumed that water has a significant effect on the reaction mechanism.

$$Glycerol\ (\textbf{reactant A}) + Acetone\ (\textbf{reactant B}) \equiv Solketal\ (\textbf{product C})$$
$$\frac{d[C]}{dt} = k[A][B] - k_{-1}[C]$$

If: $K_{eq} = K_{\text{equilibrium}}$ then:

$$K_{eq} = \frac{[C]}{[A][B]}$$
$$[C] = (K_{eq})[A][B] = \frac{k_1}{k_{-1}}[A][B]$$

since;

$$\frac{k_1}{k_{-1}} = K_{eq}$$

then,

$$\frac{d[C]}{dt} = k_1[A][B] - K_{eq}[A][B]$$
$$\frac{d[C]}{dt} = k_1[A][B] - \frac{k_1}{k_{-1}}[A][B]$$
$$\frac{d[C]}{dt} = k_1[A][B]\ (1 - \frac{1}{k_{-1}})$$

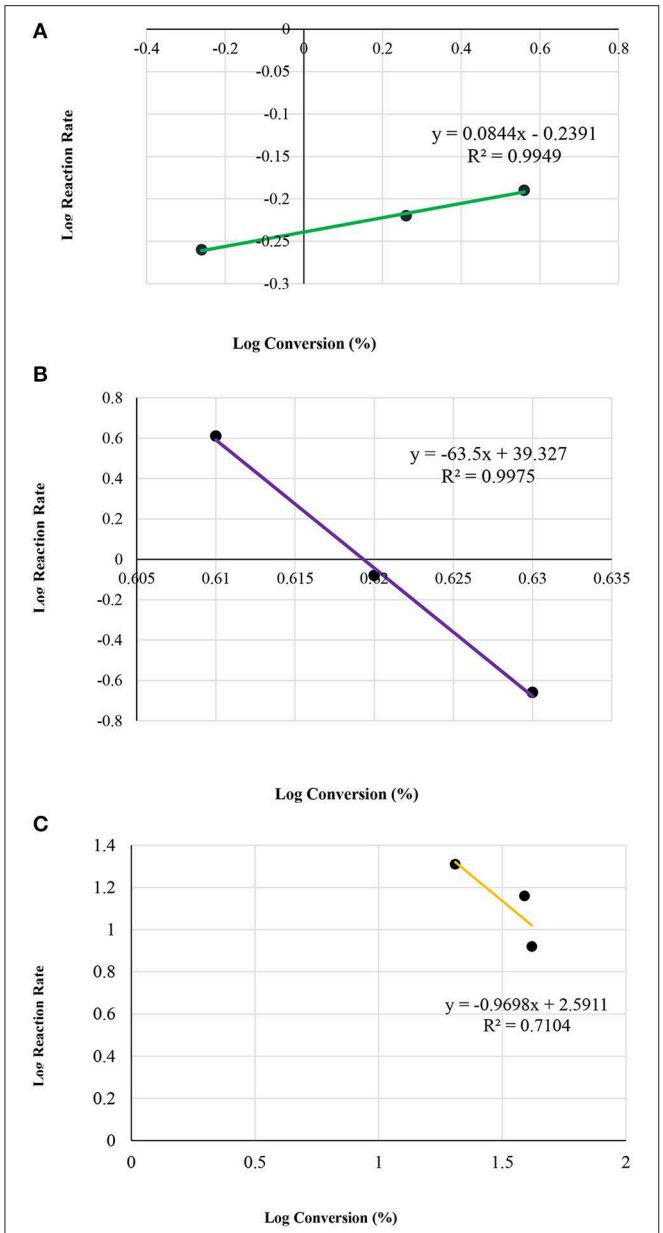

FIGURE 10 | Plot of log initial reaction rate (before 10 min of reaction) vs. log concentrations, of the MCM-41 series; **(A)** MCM-41(pure); **(B)** MCM 41-TD, and **(C)** MCM 41-SU.

In general, if the molar ratio of acetone (reactant B) is higher than the molar ratio of Glycerol (reactant A):

$$\text{If } [B] > [A]$$
$$k = k_1 [B] \text{ and,}$$
$$\frac{d[C]}{dt} = k[A](1 - \frac{1}{k_{-1}})$$

If: $k_{-1} > k$ then;

$$\left(1 - \frac{1}{k_{-1}}\right) = 1$$
$$\frac{d[C]}{dt} = k[A]$$

The rate order for the current study as shown in **Table 4** was found to be $n = 1/2$. The final equation then, can be generated as follows;

$$\frac{d[C]}{dt} = k[A]^{\frac{1}{2}}$$

In general, the proposed kinetic model, as shown above, is in agreement with the literature (Rossa et al., 2017) where the only exception is that in the literature (Rossa et al., 2017), reaction temperature has occurred between 60 and 80°C and in the current investigation, reaction temperatures ranged between 25 and 60°C. In addition, order in the literature (Rossa et al., 2017) was found to be $n = 1$ and in the current study the rate order was estimated as $n = 1/2$ indicating that the reaction is very complex. This may be due to the fact to the catalyst surface is taking an active part in the reaction mechanism. Thereby, the relation between the surface area of the catalyst and absorption-desorption the mechanism should be more investigated in further detail.

Reaction Rate Equation With Effect of Water

$$\textit{Glycerol } (\textbf{\textit{reactant A}}) + \textit{Acetone } (\textbf{\textit{reactant B}}) \equiv$$
$$\textit{Solketal } (\textbf{\textit{product C}}) + \textit{Water } (\textbf{\textit{product D}})$$
$$\frac{d[C]}{dt} = k[A][B] - k_{-1}[C][D]$$

At equilibrium;

$$\frac{d[C]}{dt} = 0$$
$$k[A][B] = k_{-1}[C][D]$$
$$\frac{k_1}{k_{-1}} = \frac{[D][D]}{[A][B]} = k_{eq}$$
$$[C][D] = k_{eq}[A][B]$$

Substitute in the first equation, we receive;

$$\frac{d[C]}{dt} = k_1[A][B] - k_{eq}[A][B]$$
$$[A][B] = k_1 - k_{eq}$$
$$\frac{d[C]}{dt} = [A][B](k_1 - \frac{k_1}{k_{-1}})$$
$$\frac{d[C]}{dt} = k_1[A][B](1 - \frac{1}{k_1})$$

In general, if the molar ratio of acetone (reactant B) is higher than the molar ratio of Glycerol (reactant A):

$$\frac{d[C]}{dt} = k[A](1 - \frac{1}{k_{-1}})$$

The above final kinetics equation shows that water has no effect on the reaction from the point of view of kinetics. The current paper shows that the initial kinetics are calculated for a time reaction that occurs within the first 10 min. However, after these 10 min elapse, the reaction kinetics follow a different reaction equation with order $n = -1$. Water produced in the initial reaction during the first 10 min may well have a very significant role in the conversion activity.

In consequence, as the production of water is significant in the reaction system. The results obtained in this study are in agreement with the calculated kinetic parameters shown in **Table 6** of the literature (Rossa et al., 2017), where for $k_{-1} > k_1$, for the Ketalization reaction of Glycerol with Acetone using H-BEA catalyst at reaction temperatures between 40 and 80°C (Rossa et al., 2017).

Evaluation of Constant Equilibrium (K_{eq}) With the Effect of Water Production

$$\textit{Glycerol}\ (\textbf{\textit{reactant A}}) + \textit{Acetone}\ (\textbf{\textit{reactant B}}) \equiv \textit{Solketal}\ (\textbf{\textit{product C}}) + \textit{Water}\ (\textbf{\textit{product D}})$$

$$\frac{k_1}{k_{-1}} = k_{eq} = \frac{C_c * C_D}{C_A * C_B}$$

For equal molar ratio of Glycerol and acetone: $C_{A0} = C_{B0}$ the following initial equations apply:

$$C_A = C_{A0} - C_{A0}\,X_{A0}$$
$$C_B = C_{B0} - C_{A0}\,X_{A0}$$
$$C_C = C_{C0} + C_{A0}\,X_{A0}$$
$$C_D = C_{D0} + C_{A0}\,X_{A0}$$

where,
C_{A0}, Initial Concentration of Glycerol (mol/L)
C_{B0}, Initial Concentration of Acetone (mol/L)
C_{C0}, Initial Concentration of solketal product (mol/L)
C_{D0}, Initial Concentration of water produced (mol/L)
C_A, Concentration of Glycerol (mol/L), at time t (min.)
C_B, Concentration of Acetone (mol/L), at time t (min.)
C_C, Concentration of solketal product (mol/L), at time t (min.)
C_D, Concentration of water produced (mol/L), at time t (min.)
X_{Aeq}, Equilibrium Conversion Glycerol.

Assuming that molar ratio of glycerol to molar ratio of acetone is 1:1, then:

$$K_{eq} = \frac{[C_{C0} + C_{A0}\,X_{Aeq}][C_{D0} + C_{A0}\,X_{A0}]}{[C_{A0} - C_{A0}\,X_{Aeq}][C_{A0} - C_{A0}\,X_{Aeq}]}$$

If $C_{C0} = C_{D0} = 0$
Then,

$$K_{eq} = \frac{[C_{A0}\,X_{Aeq}][C_{A0}\,X_{A0}]}{[C_{A0} - C_{A0}\,X_{Aeq}][C_{A0} - C_{A0}\,X_{Aeq}]}$$
$$K_{eq} = \frac{{X_{Aeq}}^2}{[1 - X_{Aeq}]^2}$$
$$K_{eq}(1 - X_{Aeq})^2 = X_{Aeq}^2$$
$$K_{eq}\left(1 - 2X_{Aeq} + X_{Aeq}^2\right) = X_{Aeq}^2$$
$$K_{eq} - 2K_{eq}X_{Aeq} + K_{eq}{X_{Aeq}}^2 = X_{Aeq}^2$$
$$K_{eq} - 2K_{eq}X_{Aeq} + (K_{eq})X_{Aeq}^2 = X_{Aeq}^2$$
$$K_{eq} - 2K_{eq}X_{Aeq} + (K_{eq} - 1)X_{\mathrm{Aeq}}^2 = 0$$
$$A = K_{eq} - 1$$
$$B = -2K_{eq}$$
$$C = K_{eq}$$
$$X_{Aeq} = \frac{B \pm \sqrt{B^2 - 4AC}}{2A}$$
$$X_{Aeq} = \frac{2k_{eq} \pm \sqrt{\left(-2K_{eq}\right)^2 - 4\left(K_{eq} - 1\right)\left(4K_{eq}\right)}}{2(K_{eq} - 1)}$$
$$X_{Aeq} = \frac{2k_{eq} \pm \sqrt{4K_{eq}^2 - 4K_{eq}^2 + 4K_{eq}}}{2(K_{eq} - 1)}$$
$$X_{Aeq} = \frac{2k_{eq} \pm 2\sqrt{K_{eq}}}{2(K_{eq} - 1)}$$

Then final proposed kinetic model generated is the following:

$$X_{\mathrm{Aeq}} = \frac{k_{eq} \pm \sqrt{K_{eq}}}{(K_{eq} - 1)}.$$

TABLE 6 | Kinetic parameter (k_1 and k_{-1}, L mol^{-1} min^{-1}) responses calculated using R2W for the ketalization reaction of glycerol with acetone and the H-BEA catalyst (Rossa et al., 2017).

Parameter	40°C	50°C	60°C	70°C	80°C
k_1	0.0082	0.0085	0.0082	0.0115	0.0213
k_{-1}	0.0158	0.0159	0.0159	0.0205	0.0372
K_{eq}	0.5159	0.5366	0.5179	0.5598	0.5720
$X_{A\ EXP}$	76.01	75.17	74.16	74.52	75.54
$X_{A\ CAL}$	70.70	71.16	70.80	71.90	72.00
$X_{A\ eq\ CAL}$	70.75	71.18	70.81	71.90	72.05
Residue Q	254.22	154.77	193.22	100.50	56.58

($X_{A\ EXP}$, X_{CAL}, and $X_{A\ eq\ CAL}$, %; Residue Q, mol L^{-1}).

Testing the Proposed Kinetic Model

The tabulated data in **Table 6** obtained from the literature was used to test the proposed kinetic model (Rossa et al., 2017). The data is presented in **Table 6** (Rossa et al., 2017) in its entirety for both reference and comparison (Rossa et al., 2017).

In order to achieve a valid comparison of the work done by Rossa et al. (2017), results in **Table 6** above must be used at the current reaction conditions.

Since, catalyst will only have influence in the rate of reaction without affecting the equilibrium, a graph of 1/T vs. Ln K_{eq}, using Gibbs free equation energy (Rossa et al., 2017), was drawn and is shown in **Figure 11**.

$$\Delta G = -RT\ln K_{eq}$$

where,
ΔG, Gibbs free energy
T, temperature in Kelvin (K)
R, Gas constant, 8.314 JK^{-1} mol^{-1}
K_{eq}, Dissociation rate.

In **Figure 11**, the Regression ($R^2 = 0.7294$) of the curve is not low, but it is very good for the scattered data in **Table 6** of literature (Rossa et al., 2017). This positive result is possibly due to the reaction having occurred at a temperature above the boiling point of acetone (56°C). In this way, the behavior of the system is homogenous possibly due to the fact that the reaction is occurring during the gaseous phase and not on the catalytic surface.

In **Figure 11**, the equation representing the graph above ($\ln(K_{eq}) = -248.2 * \left(\frac{1}{T}\right) + 0.1299$) can be used to generate K_{eq}, x_{Aeq}, and t_{eq} for reaction temperatures (25, 50, and 60°C) for the current study using the model equation in section Reaction Rate Equation for the Ketalization Reaction, Without Effect of Wateras in the following:

$$\frac{d[C]}{dt} = k[A]^{\frac{1}{2}}$$

Where $[A] = C_{AO}\text{-}C_{AOeq}$ and $\frac{d[C]}{dt} = \frac{-C_{AO}dX_{Aeq}}{dt}$

$$-C_{AO}\frac{dX_{Aeq}}{dt} = C_{AO}k\sqrt{(1-X_{Aeq})}$$

$$-\frac{dX_{Aeq}}{\sqrt{(1-X_{eq})}} = kt$$

$$t_{eq} = \frac{2\sqrt{1-X_{Aeq}}}{k}$$

where, t_{eq} is the time for the reaction equilibrium to be obtained.

Applying the above kinetic proposed model for the current temperatures (25, 50, and 60°C); from **Figure 9**, X_{Aeq} and the equilibrium time (t_{eq}) can be estimated and is shown in **Table 7**.

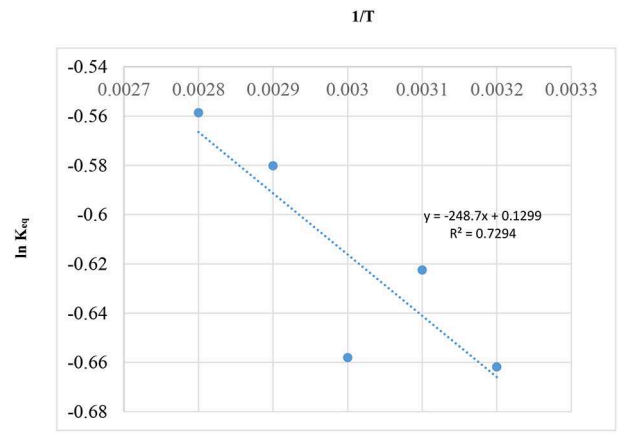

FIGURE 11 | Plot of $1/T$ vs. ln K_{eq}, using Gibbs free equation energy.

It has been found that the estimated reaction equilibrium time (t_{eq}) is within the range from zero to 10 min and, is in agreement with the proposed kinetic model in section Kinetic Modeling of the Reaction System. It was determined that the estimated reaction equilibrium time (t_{eq}) is within the range of zero to 10 min and this agrees with the proposed kinetic model in Section Reaction Rate Equation for the Ketalization Reaction, Without Effect of Wateras ($k_{-1} > k$) of the current study.

Table 8 shows a comparison of the k_1, equilibrium constant and equilibrium conversion values contained in the current study with those by Rossa et al. as shown in **Table 6** (Rossa et al., 2017).

Table 8 above shows that the equilibrium constant **(K_{eq})** at temperatures 50 and 60°C are within the same order of magnitude. In this work, a low equilibrium conversion **(X_{Aeq})** approximately 0.42 (42%) was obtained.

Meanwhile, Rossa et al. (2017) report a relatively high equilibrium conversion reaching up to 0.75 (75%). The sizeable difference between the two results can be accounted for when considering a number of factors; the reaction environment, the catalyst type including its physical and chemical properties and the turnover frequency (TOF). This is a quantitative measure of the activity of the catalyst.

However, for this current study, the turnover frequency (TOF) was not measured since a large quantity of the reactant acetone employed for solketal production would be in a gaseous state at temperatures of 50 and 60°C.

By definition the Turnover Frequency (TOF) is used to quantify the activity of the catalyst. It refers to the number of reacting molecules per active site per second at the condition of the experiment (Scott Fogler, 2006). When a metal catalyst is deposited on a support, the metal atoms are considered active sites (Nda-Umar et al., 2018).

Thus,

$$r'_M = f_{Product} * D * \left(\frac{1}{MW_{Metal}}\right)\left(\frac{\%\ Metal}{100}\right)$$

where:
r'_M, the rate of formation of product turnover frequency.
$f_{Product}$: Turnover Frequency 3.1 min^{-1} = 0.052 s^{-1} at one bar (1 atmosphere) (Nda-Umar et al., 2018).

Usually, the Turnover Frequency is calculated based on the glycerol conversion/* product yield per gram catalyst per total reaction time.

D, The dispersion of the catalyst as a fraction of metal atom deposited on the surface.

TABLE 7 | Testing the proposed kinetic model and its correlation with the literature (Rossa et al., 2017).

Temperature (°C)	Equilibrium constant (K_{eq})	Equilibrium conversion (XA_{eq})	Reaction equilibrium time teq (min)
25	0.4830	0.4115	2.28
50	0.5348	0.4205	2.26
60	0.5488	0.4236	2.25

TABLE 8 | Comparison of the k_1 values, equilibrium constant values, and equilibrium conversion values of the present study and values from Rossa et al. (2017).

Temperature (°C)	Rate constant (k_1)		Equilibrium constant (K_{eq})		Equilibrium conversion ($X_{A\ eq}$)	
	Present work (Conc.$^{1/2}$ min^{-1})	Rossa et al. (2017) (Conc.$^{-1}$ min^{-1})	Present work (Calculated)	Rossa et al. (2017)	Present work (Calculated)	Rossa et al. (2017)
25	0.74478	–	0.4830	–	0.4115	–
50	4.436×10^3	0.0085	0.5348	0.5366	0.4205	0.7517
60	1.3256×10^2	0.0082	0.5488	0.5279	0.4236	0.7452

MW_{Metal}, The Molecular Weight of Metal deposited on the surface $= Al_{\text{MWt}} = 27\frac{g}{mol}$

$\%Metal$, The catalysts dispersion percentage of atoms exposed and determined from the reactant chemisorption.

In the current study, the number in the parenthesis in $[(SiO_2)x(Al_2O_3)y]$ corresponds to the ratio of the oxides, the so called module; SiO_2/Al_2O_3 (usually this value is twice as high as the Si/Al ratio). Hence, it is important to mention that the value "percentage dispersion of alumina on silicon" is quite unusual because of Aluminum (Al), as single atom and due to the Loewenstein's rule, there are no Al-O-Al bonds. The Aluminum (Al) is randomly distributed in silica. For example, each atom of Aluminum creates a negative charge which is compensated by counter-ion, e.g., Na^+ or H^+. The number of Aluminum (Al) determines the number of acidic sites. Hence, when the weight of the catalyst is ascertained, the amount of Aluminum can be calculated.

The molecular weight Al_2O_3 is 102 [g/mol], and the molecular weight SiO_2 is 60.081 [g/mol]. From that, the dispersion or the distribution of Al on the catalyst surface of a sample like for example, ZSM-5 (35) can be calculated as the following:

$n = \mathbf{35} * 60.081\,\text{g}\,(SiO_2) + 1 * 102\,\text{g}\,(Al_2O_3) = 2204.835\,\text{g}$, i.e., 712 g zeolite contains 54 g Aluminum (because of the 2 atoms in the oxide). Therefore, 1 g (water free) zeolite contains:

$(54*1/2204.835) = 0.0245$ g Aluminum and, 1 g (water free) zeolite contains $(28*1/2204.835) = 0.013$ g Silicon. As a result, the dispersion or the distribution of Al on the catalyst surface $= \left(\frac{0.0245}{0.0245+0.013}\right)*100 = 65.3\%\ Al-\ metal.$

On the other hand, three mechanisms predominate in the catalytic reaction process; Adsorption, Catalytic Surface reaction and Desorption processes. For the present study, the Langmuir-Hinshelwood approach for determining the catalytic and heterogeneous mechanism is employed in order to illustrate the catalytic reaction process involved in solketal production from glycerol and acetone that is to say;

$$Glycerol\,[A] + Acetone\,[B] = Solketal\,[C] + Water[D]$$

The following adsorption mechanism is envisaged;

$$\begin{Bmatrix} A + S \leftrightarrow A.S \\ B + S \leftrightarrow B.S \end{Bmatrix} \quad \text{Fast}$$

$$\{A.S + B.S \leftrightarrow C.S + D.S\} \quad \text{Slow and rate limiting step}$$

$$\begin{Bmatrix} C.S \leftrightarrow C + S \\ D.S \leftrightarrow D + S \end{Bmatrix} \quad \text{Fast}$$

where S represents the surface of catalyst.

From any Chemical Engineering standard textbook (Scott Fogler, 2006) and using the method of initial rate and when products C and D are present:

$$-r'_A = k_A P_A P_B$$

where;

P_A, Partial pressure of Glycerol

P_B, Partial pressure of Acetone

Under the experimental conditions of the present study $P_B \gg P_A$

So $k_A P_B = k$ and the initial rate of reaction becomes:

$$-r'_A = kP_A$$
$$P_A = P_{Total} * x_A$$

where;

P_{Total} = System total Pressure

x_A = mole fraction of glycerol in the reaction system.

The initial rate equation in terms of fractional conversion is given by

$$-r'_A = kP_{\text{Total}} * x_A$$

and; $k_{\text{Avg}} = kP_{\text{Total}}$ gives:

$$\mathbf{-r'_A = k_{Avg} * x_A}.$$

It is surmised that the mechanism governing steps like Adsorption process, Catalytic Surface reaction process and Desorption process are fast functioning relative to those remaining others outlined in the list. Mass transfer activity does not affect the overall reaction rate since the concentration of the surrounding area of the active sites are indistinguishable from those of the bulk fluid. In one study (Stawicka et al., 2016), both glycerol and the ratio of acetone molar substantially affected the kinetics and thermodynamics of the reaction in a procedure to condense glycerol with acetone (Stawicka et al., 2016). Molar of acetone to glycerol ratios reached 1,48:1, and 2.46:1 and in turn produced solketal yields of 68 and 74, respectively (Nanda et al., 2014a).

Current literature (Nanda et al., 2014b; Esteban et al., 2015) shows models for the pseudo-homogeneous (Esteban et al., 2015)

and heterogeneous models (Nanda et al., 2014b; Esteban et al., 2015). However, no homogeneous model exists showing the ketalization reaction of glycerol with acetone. In spite of this, a pseudo-homogeneous model was proposed yielding values of $k_{-1} > k_1$ using sulfonated resin as a catalyst. Water that is formed in the product must be extracted before equilibrium can be established. For this reason, there should be no additional water in the reaction system before a catalyst is employed. The pseudo-homogeneous model works best if any analysis is conducted at temperatures exceeding the boiling point (Esteban et al., 2015). Since 56°C is the boiling point of Acetone, this model will yield accurate results from reactions conducted in temperatures in temperatures that are in excess of it. This is apparent even when taking into consideration the reaction temperatures when they are close to, even exceeding the boiling point of acetone.

Excessive glycerol conversions, when treated with acetone, were the subject of another study by Ferreira et al. (2010). An increase in the glycerol to acetone molar ratio from 1:3 to 1: 12 coincided with an improvement in the glycerol conversion. However, the selectivity of solketal stayed the same (Ferreira et al., 2010).

Moreover, a reaction equation involving water equilibrium (K_w) is proposed in the literature (Li et al., 2012; Nanda et al., 2016). However, for this study a water equilibrium is not especially important. For reasons discussed previously in section Kinetic Modeling of the Reaction System, as significant quantities of water are produced, adverse reactions immediately occur in the main product. In addition, reverse, as opposed to forward reaction is faster and therefore water equilibrium does not have any special role. By this reasoning and those suggested in references (Ferreira et al., 2010; Reddy et al., 2011; Royon et al., 2011; Ortiz et al., 2012; Menezes et al., 2013; Nanda et al., 2014b; Aghbashlo et al., 2018, 2019; Ammaji et al., 2018; Fatimah et al., 2019), water equilibrium is not reached nor is it considered necessary for this current proposed kinetic model. Since water is formed during the experimental reaction process, experimentally the effect of water has not been studied in the current work.

Moreover, at a reaction temperature of 60°C (333.15 K) and at one atmosphere, the acetone was shown to exert a vapor pressure of about 113.737 mm Hg. Hence, the overall order of the reaction was determined by the method of initial rates.

CONCLUSIONS

In summary, the catalytic effect of HZSM-5 with a variety of silica to alumina ratios were investigated. The conversions ranged between 30% to around 38%. More significantly, the current research was able to establish the rate law for HZMS-5 zeolite with different silica to alumina ratios (M = 35, 90, and 160), the 'n' order equal to half and with an average rate constant $k = 0.6745$ (Conc.$^{1/2}$ min^{-1}). Additionally, the results of the Arrhenius plots for HZSM-5 at different reaction temperatures (25, 50, and 60°C) showed activation energy of $E_A = 164.34$ 164.34 kJmol^{-1} and $k_0 = 5.2678*10^{28}$ (min^{-1}). Furthermore, the results conclude that the reaction with pure MCM- 41 occurs very slowly, and that the reaction also occurs independent of the conversion, where 'n' is zero ($n = 0.1$) and rate constant $k = 0.5766$ (Conc.$^{1/2}$ min^{-1}).

Henceforth, more in depth investigation is needed in order to establish the reaction rate law. The rate of the reaction equation for the system ketalization reaction was established with the effect of production of water but again without a significant water effect on the reaction system. To end, the equilibrium time for the reaction system was observed as constant with an average duration of around 3 min ($\approx$ 2.26 min).

Furthermore, a mathematical approach has been proposed in this current work to calculate the dispersion or the distribution of Al on the catalyst surface like for example ZSM-5 that has different modules [i.e., different molar ratios of (SiO_2/Al_2O_3)].

DATA AVAILABILITY STATEMENT

All datasets generated for this study are included in the article/supplementary material.

AUTHOR CONTRIBUTIONS

MA analyzed and interpreted the data and wrote the paper.

ACKNOWLEDGMENTS

The author gratefully acknowledges Prof. Frank Roessner of Carl Von Ossietzky University, Germany and Professor Elaref Ratemi of Jubail Industrial College, Saudi Arabia for their support. In addition, many thanks are due to Prof. Kingsley Ofosu-Asiedu for the valuable discussions on kinetics. The author also appreciates and acknowledges Mr. Mohammed Francis Smith for editing of the manuscript. My thanks and appreciation extend to Jubail Industrial College for its support while conducting the research and in the writing of this manuscript.

REFERENCES

Abreu, T. H., Meyer, C. I., Padró, C., and Martins, L. (2019). Acidic V-MCM-41 catalysts for the liquid-phase ketalization of glycerol with acetone. *Microporous Mesoporous Mater*. 273, 219–225. doi: 10.1016/j.micromeso.2018.07.006

Aghbashlo, M., Hosseinpour, S., Tabatabaei, M., Rastegari, H., and Ghaziaskar, H. S. (2019). Multi-objective exergoeconomic and exergoenvironmental optimization of continuous synthesis of solketal through glycerol ketalization with acetone in the presence of ethanol as co-solvent. *Renew. Energy,* 130, 735–748. doi: 10.1016/j.renene.2018.06.103

Aghbashlo, M., Tabatabaei, M., Hosseinpour, S., Rastegari, H., and Ghaziaskar, H. S. (2018). Multi-objective exergy-based optimization of continuous glycerol ketalization to synthesize solketal as a biodiesel additive in subcritical acetone. *Energy Convers. Manage*. 160, 251–261. doi: 10.1016/j.enconman.2018.01.044

Alsawalha, M. (2019). Overview of current and future perspectives of Saudi Arabian natural clinoptilolite zeolite: a case review. *J. Chem*. 2019:3153471. doi: 10.1155/2019/3153471

Ammaji, S., Rao, G. S., and Chary, K. V. R. (2018). Acetalization of glycerol with acetone over various metal-modified SBA-15 catalysts. *Appl. Petrochem. Res.* 8, 107–118. doi: 10.1007/s13203-018-0197-6

Beck, J. S., Vartuli, J. C., Roth, W. J., Leonowicz, M. E., Kresge, C. T., Schmitt, K. D., et al. (1992). A new family of mesoporous molecular sieves prepared with liquid crytal templates. *J. Am. Chem. Soc.* 114, 10834–10843. doi: 10.1021/ja00053a020

Breck, D. W. (1974). *Zeolite Molecular Sieves: Structure, Chemistry, and Use*. New York, NY: John Wiley and Sons, 4.

Clarkson, J. S., Walker, A. J., and Wood, M. A. (2001). Continuous reactor technology for ketal formation: an improved synthesis of solketal. *Org. Process Res. Dev.* 5, 630–635. doi: 10.1021/op000135p

Corma, A., Fornes, V., Pergher, S. B., Maesen, T. L. M., and Buglass, J. G. (1998). Delaminated zeolite precursors as selective acidic catalysts. *Nature* 396, 353–356. doi: 10.1038/24592

Corma, A., Kan, Q., Navarro, M. T., Pariente, J. P., and Rey, F. (1997). Synthesis of MCM-41 with different pore diameters without addition of auxiliary organics. *Chem. Mater.* 9, 2123–2126. doi: 10.1021/cm970203v

Da Silva, C. X. A., Gonçalves, V. L. C., and Mota, C. J. A. (2009). Water-tolerant zeolite catalyst for the acetalisation of glycerol. *Green Chem.* 11, 38–41. doi: 10.1039/B813564A

Da Silva, C. X. A., and Mota, C. J. A. (2011). The influence of impurities on the acid-catalyzed reaction of glycerol with acetone. *Biomass Bioenergy* 35, 3547–3551. doi: 10.1016/j.biombioe.2011.05.004

Derouane, E. G., Nagy, J. B., Dejaifve, P., van Hooff, J. H. C., Spekman, B. P., Vedrine, J. C., et al. (1978). Elucidation of the mechanism of conversion of methanol and ethanol to hydrocarbons on a new type of synthetic zeolite. *J. Catal.* 53, 40–55. doi: 10.1016/0021-9517(78)90006-4

Esposito, R., Raucci, U., Cucciolito, M. E., Di Guida, R., Scamardella, C., Rega, N., et al. (2019). Iron(III) complexes for highly efficient and sustainable ketalization of glycerol: a combined experimental and theoretical study. *ACS Omega* 4, 688–698. doi: 10.1021/acsomega.8b02546

Esteban, J., Ladero, M., and Garcia-Ochoa, F. (2015). Kinetic modelling of the solvent less synthesis of solketal with a sulphonic ion exchange resin. *Chem. Eng. J.* 269, 194–202. doi: 10.1016/j.cej.2015.01.107

Fatimah, I., Sahroni, I., Fadillah, G., Musawwa, M. M., Mahlia, T. M. I., and Muraza, O. (2019). Glycerol to solketal for fuel additive: recent progress in heterogeneous catalysts. *Energies* 12:2872. doi: 10.3390/en12152872

Ferreira, P., Fonseca, I. M., Ramos, A. M., Vital, J., and Castanheiro, J. E. (2010). Valorisation of glycerol by condensation with acetone over silica-included heteropolyacids. *Appl. Catal. B, Environ* 98, 94–99. doi: 10.1016/j.apcatb.2010.05.018

Fischer, E., and Pfähler, E. (1920). Glycerol acetone and its applicability for the preparation of pure a-glycerides; a phosphoric acid compound of glycol. *Ber. Dt. Chem. Ges.* 53, 1606–1621. doi: 10.1002/cber.19200530903

García, E., Laca, M., Pérez, E., Garrido, A., and Peinado, J. (2008). New class of acetal derived from glycerin as a biodiesel fuel component. *Energy Fuels* 22, 4274–4280. doi: 10.1021/ef800477m

Jelena, A. M., Elisabeth, S. R., and Elisabeth, M. M. (2015). Modification of natural clinoptilolite and ZSM-5 with different oxides and studying of the obtained products in lignin pyrolysis. *J. Ser. Chem. Soc.* 80, 717–729. doi: 10.2298/JSC310714109M

Jingfa, D., Guirong, Z., Shuzhong, D., Haishui, P., and Huaiming, W. (1988). Acidic properties of ZSM-5 zeolite and conversion of ethanol to diethyl ether. *Appl. Catal.* 41, 13–22. doi: 10.1016/S0166-9834(00)80378-4

Joris, G., and Bert, M. W. (2018). Spatiotemporal coke formation over zeolite ZSM-5 during the methanol-to-olefins process as studied with operando UV-vis spectroscopy: a comparison between H-ZSM-5 and Mg-ZSM-5. *Catalys. Sci. Techno.* 8, 1632–1644. doi: 10.1039/C7CY02459B

Kawi, S., Shen, S. C., and Chew, P. L. (2002). Generation of Brønsted acid sites on Si-MCM-41 by grafting of phosphorus species. *J. Mater. Chem.* 12, 1582–1586. doi: 10.1039/b107795n

Konno, H., Ohnaka, R., Nishimura, J. I., Tago, T., Nakasaka, Y., and Masuda, T. (2014). Kinetics of the catalytic cracking of naphtha over ZSM-5 zeolite: effect of reduced crystal size on the reaction of naphthenes. *Catalys. Sci. Techno.* 4, 4265–4273. doi: 10.1039/C4CY00733F

Kowalska-Kus, J., Held, A., and Nowinska, K. (2016). Enhancement of the catalytic activity of H-ZSM-5 zeolites for glycerol acetalization by mechanical grinding. *React. Kinet. Mech. Catal.* 117, 341–352. doi: 10.1007/s11144-015-0922-4

Li, L., Korányi, T. I., Sels, B. F., and Pescarmona, P. P. (2012). Highly efficient conversion of glycerol to solketal over heterogeneous Lewis acid catalysts. *Green Chem.* 14, 1611–1619. doi: 10.1039/c2gc16619d

Loganathan, S., Tikmani, M., and Ghoshal, A. K. (2013). Novel pore-expanded MCM-41 for CO2 capture: synthesis and characterization. *Langmuir* 29, 3491–3499. doi: 10.1021/la400109j

Menezes, F. D. L., Guimaraes, M. D. O., and da Silva, M. J. (2013). Highly selective $SnCl_2$-catalyzed solketal synthesis at room temperature. *Ind. Eng. Chem. Res.* 52, 16709–16713. doi: 10.1021/ie402240j

Nanda, M. R., Yuan, Z., Qin, W., Ghaziaskar, H. S, Poirier, M,-A., and Xu, C. A. (2014a). A new continuous-flow process for catalytic conversion of glycerol to oxygenated fuel additive: catalyst screening. *Appl. Energy* 123, 75–81. doi: 10.1016/j.apenergy.2014.02.055

Nanda, M. R., Yuan, Z., Qin, W., Ghaziaskar, H. S., Poirier, M.-A., and Xu, C. C. (2014b). Thermodynamic and kinetic studies of a catalytic process to convert glycerol into solketal as an oxygenated fuel additive. *Fuel* 117, 470–477. doi: 10.1016/j.fuel.2013.09.066

Nanda, M. R., Zhang, Y., Yuan, Z., Qin, W., Ghaziaskar, H. S., and Xu, C. (Charles). (2016). Catalytic conversion of glycerol for sustainable production of solketal as a fuel additive: a review. *Renew. Sustain. Ener. Rev.* 56, 1022–1031. doi: 10.1016/j.rser.2015.12.008

Narkhede, N., and Patel, A. (2014). Room temperature acetalization of glycerol to cyclicacetals over anchored silicotungstates under solvent free conditions. *R. Soc. Chem. Adv.* 4, 19294–19301. doi: 10.1039/c4ra01851f

Nda-Umar, U. I., Ramli, I., Taufiq-Yap, Y., and Muhamad, E. (2018). An overview of recent research in the conversion of glycerol into biofuels, fuel additives and other bio-based chemicals. *Catalysts* 9:15. doi: 10.3390/catal9010015

Newman, M. S., and Renoll, M. (1945). Improved preparation of isopropylidene glycerol. *J. Am. Chem. Soc.* 67, 1621–1621 doi: 10.1021/ja01225a511

Ortiz, F. G., Ollero, P., Serrera, A., and Galera, S. (2012). Anenergy and exergy analysis of the supercritical water reforming of glycerol for power production. *Int. J. Hydrogen Energy* 37, 209–226. doi: 10.1016/j.ijhydene.2011.09.058

Pan, T., Wu, Z., and Yip, A. C. K. (2019). Advances in the green synthesis of microporous and hierarchical zeolites: a short review. *Catalysts* 9:274. doi: 10.3390/catal9030274

Pines, H., and Pillai, C. N. (1960). Dehydration of alcohols over alumina modified by ammonia. *J. Am. Chem. Soc.* 82, 2401–2402. doi: 10.1021/ja01494a080

Reddy, P. S., Sudarsanam, P., Mallesham, B., Raju, G., and Reddy, B. M. (2011). Acetalisation of glycerol with acetone over zirconia and promoted zirconia catalysts under mild reaction conditions. *J. Ind. Eng. Chem.* 17, 377–381. doi: 10.1016/j.jiec.2011.05.008

Rossa, V., Pessanha, Y. S. P., Díaz, G. C., Câmara, L. D. T., Pergher, S. B. C., and Aranda, D. A. G. (2017). Reaction kinetic study of solketal production from glycerol ketalization with acetone. *Ind. Eng. Chem. Res.* 56, 479–488. doi: 10.1021/acs.iecr.6b03581

Royon, D., Locatelli, S., and Gonzo, E. E. (2011). Ketalization of glycerol to solketal in supercritical acetone. *J. Supercrit. Fluids* 58, 88–92. doi: 10.1016/j.supflu.2011.04.012

Schulz, J., and Bandermann, F. (1994). Conversion of ethanol over zeolite H-ZSM-5. *Chem. Eng. Technol.* 17, 179–186. doi: 10.1002/ceat.270170306

Scott Fogler, H. (2006). *Elements of Chemical Reaction Engineering, 4th Edn.* Upper Saddle River, NJ: Prentice Hall PTR.

Smirnov, A. A., Selishcheva, S. A., and Yakovlev, V. A. (2018). Acetalization catalysts for synthesis of valuable oxygenated fuel additives from glycerol. *Catalysts* 8:595. doi: 10.3390/catal8120595

Stawicka, K., Díaz-Álvarez, A. E., Calvino-Casilda, V., Trejda, M., Bañares, M. A., and Ziolek, M. (2016). The role of brønsted and lewis acid sites in acetalization of glycerol over modified mesoporous cellular foams. *J. Phys. Chem. C* 120, 16699–16711 doi: 10.1021/acs.jpcc.6b04229

Yasmin, T., and Müller, K. (2010). Synthesis and surface modification of mesoporous mcm-41 silica materials. *J. Chromatogr. A* 1217, 3362–3374. doi: 10.1016/j.chroma.2010.03.005

Zong, Y., Yang, L., Tang, S., Li, L., Wang, W., Yuan, B., et al. (2018). Highly efficient, acetalization and ketalization catalyzed by cobaloxime under solvent-free condition. *Catalysts* 8:48. doi: 10.3390/catal8020048

Conflict of Interest: The author declares that the research was conducted in the absence of any commercial or financial relationships that could be construed as a potential conflict of interest.

frontiers in Chemistry

ORIGINAL RESEARCH
published: 12 December 2019
doi: 10.3389/fchem.2019.00847

UV-Induced Photodegradation of Naproxen Using a Nano γ-FeOOH Composite: Degradation Kinetics and Photocatalytic Mechanism

Zhanyi Li[1], Guoguang Liu[1], Qing Su[2], Chunyan Lv[3]*, Xiaoyu Jin[1] and Xiaoqing Wen[1]*

[1] School of Environmental Science and Engineering, Guangdong University of Technology, Guangzhou, China, [2] School of Computer Science and Technology, Guangdong University of Technology, Guangzhou, China, [3] Department of Materials Chemistry, Huzhou University, Huzhou, China

Naproxen (NPX) is one of the most common pharmaceutical and personal care products found in surface water, which is recalcitrant to degradation by biological treatment or complete removal via traditional sewage treatment processes. In this study, nanoscale γ-FeOOH was synthesized and characterized by X-ray diffraction, scanning electron microscopy, surface analysis, and analysis of the forbidden bandwidth. Under UV irradiation, γ-FeOOH had the capacity to rapidly photodegrade NPX. The photodegradation rate of NPX was dependent on the concentration of γ-FeOOH in solution, initial NPX concentration, and pH. By increasing the concentration of γ-FeOOH, the NPX photodegradation rate was increased and then remained stable. Furthermore, the highest photodegradation rate for NPX was observed under acidic conditions. Through the analysis of the active substances (such as h^+, e^-, OH, $^1O_2$, and $O_2^{\cdot-}$) by electron spin resonance, the photocatalytic mechanism of NPX degradation on γ-FeOOH was determined to be semiconductor photocatalysis.

Keywords: γ-FeOOH, NPX, photodegradation, photocatalysis, active substances

OPEN ACCESS

Edited by:
Shaobin Wang,
Curtin University, Australia

Reviewed by:
Giovanni Palmisano,
Khalifa University,
United Arab Emirates
Zhou Baoxue,
Shanghai Jiao Tong University, China

***Correspondence:**
Qing Su
suqing@gdut.edu.cn
Chunyan Lv
lcy@zjhu.edu.cn

Specialty section:
This article was submitted to Catalysis and Photocatalysis, a section of the journal Frontiers in Chemistry

Received: *24 April 2019*
Accepted: *21 November 2019*
Published: *12 December 2019*

Citation:
Li Z, Liu G, Su Q, Lv C, Jin X and Wen X (2019) UV-Induced Photodegradation of Naproxen Using a Nano γ-FeOOH Composite: Degradation Kinetics and Photocatalytic Mechanism. Front. Chem. 7:847. doi: 10.3389/fchem.2019.00847

INTRODUCTION

With continuous improvements in anthropogenic living standards, the contamination of natural waterways has become an unavoidable and often neglected environmental issue. At present, however, water monitoring standards do not include pharmaceutical and personal care products (PPCPs), which are recalcitrant to biodegradation or complete removal via traditional sewage treatment processing technologies (Christina et al., 2014). Concurrently, PPCPs are constantly released into the environment from the medical and livestock industries; hence, they have garnered the attention of researchers and the public due to their "pseudo persistence." Common PPCPs include non-steroidal anti-inflammatory and analgesic drugs such as Ibuprofen, Naproxen, Aspirin, and Diclofenac. Naproxen (NPX) is a commonly used anti-inflammatory and analgesic with negligible side effects; thus, it is one of the four most commonly consumed prescriptions on a global scale (Jones et al., 2002). Although the NPX concentration in water is low, it has accumulated to ng/L concentration levels (Dai et al., 2014). Medical studies have revealed that the long-term ingestion of trace NPX levels can induce heart disease, stroke, and toxic pulmonary effects (Isidori et al., 2005; Karl et al., 2006; Domínguez et al., 2011; Hasan et al., 2012). Current NPX treatment methods encompass adsorption (Xu et al., 2009; Hasan et al., 2012) photocatalytic degradation

(Méndez-Arriaga et al., 2008), and radiation (Zheng et al., 2011), which commonly employ FeOOH (the primary component of rust, a corrosion product on metal surfaces) (Molgaard, 1974). It has been reported that FeOOH exists not only in marine shellfish (Lee et al., 2000), but also within soils, sediments, and water, and the physical and chemical properties of FeOOH are stable. This compound possesses a relatively large surface area, which likely plays a critical role in the removal of contaminants from the natural environment (Fortin and Langley, 2005; Zhou et al., 2007); hence, it is receiving increased attention in the areas of environmental restoration and governance.

Nano-γ-FeOOH exhibits surface resident and interfacial effects as well as unique properties at the nanoscale and quantum levels (Nurmi et al., 2005). It can effectively adsorb organic matter in water and demonstrates a good flocculation effect. Under certain conditions of light and oxygen exposure, it may also catalyze the degradation of adsorbed organic matter without producing secondary pollution. At present, γ-FeOOH is mainly used for industrial desulfurization; thus, there have been few studies on the adsorption and photocatalysis of PPCP contaminants. Further, investigations of NPX-related adsorption and photocatalytic processes and mechanisms have rarely been reported.

For this investigation, nano-γ-FeOOH is synthesized, and on the basis of previous studies that examined its adsorption performance for NPX (Zhanyi et al., 2018), the primary focus here is centered on the effects of nano-γ-FeOOH on the photocatalytic degradation of NPX. The effects of the photocatalyst dosage, initial NPX concentration, pH, and other factors are investigated. This work culminates in the proposal of an environmentally compatible photocatalytic strategy for the effective treatment of NPX-infused wastewater.

EXPERIMENT

Materials and Reagents

NPX (A-methyl-6-methoxy-2-naphthaleneacetic acid, 98% purity) was obtained from West Asia Reagent Company. Acetonitrile (CR), methanol (CR), and ethanol (CR) were obtained from USA ACS Enke Chemical. $FeSO_4{\cdot}7H_2O$ (AR), $NH_3{\cdot}H_2O$ (AR), EDTA (AR), NaOH (AR), H_2SO_4 (AR), KI (AR), IPA (Isopropanol, AR), NaN_3 (AR), and p-BQ (p-Benzoquinone, AR) were obtained from Shanghai Aladdin Bio-Chem Technology Co., Ltd. Ultrapure water employed in the experiments was obtained via an integrated Smart2 Pure ultrapure water system, obtained from TKA Wasseraufbereitungs system GmbH, Germany.

Synthesis of Nanostructured γ-FeOOH

Freshly prepared under magnetic stirring, 10 ml of pure $NH_3{\cdot}H_2O$ was added to a 110 ml 0.3 $mol{\cdot}L^{-1}$ $FeSO_4$ solution, which had a pH of 8.6. Subsequently, 10 ml of 0.015 $mol{\cdot}L^{-1}$ EDTA and ultrapure water were added to a 150-ml volume. Then, 1 $L{\cdot}min^{-1}$ O_2 was introduced into the solution for about 30 min until the precipitation color changed from blue-green to orange under a controlled system temperature of 20°C, after which the pH was maintained at 4.3. Once the orange precipitate was filtered and rinsed, it was placed in a vacuum drying oven for 24 h at 30°C. Thereafter, the sample was finely ground and screened (200 mesh) (He et al., 2005).

Characterization of Nanostructured γ-FeOOH

X-ray diffraction (XRD) was carried out with a Cu K(α) source (λ = 0.15406 nm) at 40 kV and 30 mA over the range of $2\theta = 20–80°$.

Scanning electron microscopy (SEM) was used for investigating the morphology and dispersion of the samples. Prior to measurements, the sample was affixed to an aluminum sheet and sprayed with gold.

BET surface area (BET) analysis was used to determine the pore structure, specific surface area, and porosity of the samples. The porosity and pore distribution were determined by a nitrogen adsorption–desorption isotherm and the Barrett–Joyner–Halenda (BJH) method.

Photocatalytic NPX Degradation Experiments

Photoreaction Apparatus and Procedure

The photocatalytic NPX degradation experiments using γ-FeOOH were carried out using a multifunctional photochemical reaction instrument with magnetic stirring bars and a cooling circulation system (**Figure 1**). The illumination source in the experiment was a 300-W mercury lamp (**Table 1**), which was 10 cm away from the quartz tubes, and the temperature was held steady at 25°C during all tests. Prior to the photocatalytic degradation tests, the γ-FeOOH/NPX system was allowed to reach adsorption–desorption equilibrium in the dark for 240 min (He et al., 2005; Zhanyi et al., 2018). Subsequently, each experiment was conducted in triplicate with 20-ml samples under UV irradiation, and the rotary reactor was rotated at 5 rpm for 1 min, accompanied by constant magnetic stirring at 100 rpm for 1 min. A 10-ml sample was extracted via syringe every 2 min for each test and immediately passed through a 0.45-μm filter. The filtrate was then analyzed by high-performance liquid chromatography.

Photodegradation of NPX by γ-FeOOH

To determine the effect of γ-FeOOH dosage, 0.05, 0.1, 0.2, 0.4, and 0.6 $g{\cdot}L^{-1}$ of γ-FeOOH was added to the NPX solution at a concentration of 10 $mg{\cdot}L^{-1}$.

To determine the effect of initial NPX concentration, NPX solutions with several concentrations of 5, 10, 20, 30, and 40 $mg{\cdot}L^{-1}$ were prepared, to which 0.2 $g{\cdot}L^{-1}$ of γ-FeOOH was added.

To determine the effect of pH, the pH was adjusted to 5, 7, and 9 by adding 0.1 $mol{\cdot}L^{-1}$ H_2SO_4 or 0.1 $mol{\cdot}L^{-1}$ NaOH to the NPX solution with a concentration of 10 $mg{\cdot}L^{-1}$, to which exactly 0.2 $g{\cdot}L^{-1}$ of γ-FeOOH was added.

The above experiments proceeded as described above.

Langmuir–Hinshelwood Kinetics

Heterogeneous photocatalysis includes two basic reaction steps, which are physical adsorption and a chemical reaction. For our

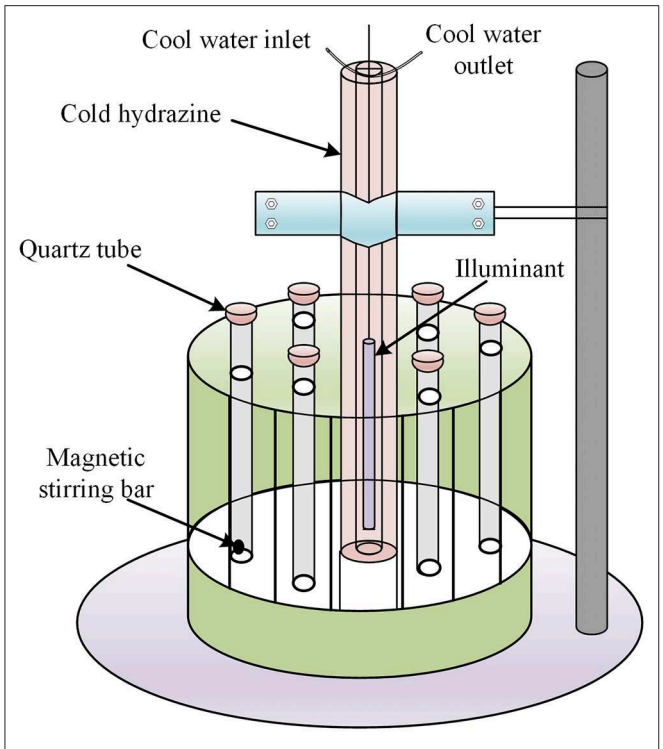

FIGURE 1 | Multifunctional photochemical reaction instrument.

TABLE 1 | Mercury lamp energy distribution.

Wavelength λ (nm)	Relative energy (%)	Wavelength λ (nm)	Relative energy (%)
1,367	15.3	289	6.0
1,129	12.6	280	9.3
1,014	40.6	275	2.7
577–579	76.5	270	4.0
546	93.0	265	15.3
436	77.5	257	6.0
405–408	42.2	254	16.6
365–366	100.0	248	8.6
334	9.3	240	7.3
313	49.9	238	8.6
302–303	23.9	236	6.0
297	16.6	232	8.0

experiments, Langmuir–Hinshelwood kinetics (L–H equation) were employed to fit the relationship between the photocatalytic reaction rate (r) and solution concentration (C):

$$r = \frac{dC}{dt} = k_{\mathrm{L-H}} \frac{KC}{1 + KC} \tag{1}$$

where r is the initial photodegradation rate of NPX measured in $\mathrm{mg{\cdot}L^{-1}{\cdot}min^{-1}}$, $k_{\mathrm{L-H}}$ is the photocatalytic degradation rate constant measured in $\mathrm{mg{\cdot}L^{-1}{\cdot}min^{-1}}$, K is the adsorption constant of NPX on the surface of γ-FeOOH measured in $\mathrm{L{\cdot}mg^{-1}}$, and C is the instantaneous concentration of NPX measured in $\mathrm{mg{\cdot}L^{-1}}$.

There was a linear relationship between the reciprocal of r ($1/r$) and the reciprocal of C ($1/C$). Linear fitting was applied with the data from the experiment; hence, the photocatalytic degradation rate constant $k_{\mathrm{L-H}}$ and the adsorption constant K were obtained and found to be independent of the NPX concentration.

$$\frac{1}{r} = \frac{1}{k_{L-H}} + \frac{1}{k_{L-H}K} \cdot \frac{1}{C} \tag{2}$$

Active Species Analysis

In order to investigate the role of free radicals in the photocatalytic degradation of NPX, radical quenching experiments were carried out. Four solutions were prepared, comprising 10 $\mathrm{mg{\cdot}L^{-1}}$ NPX and 0.2 $\mathrm{g{\cdot}L^{-1}}$ γ-FeOOH, to which 50 $\mathrm{mmol{\cdot}L^{-1}}$ potassium iodide (KI), 0.10 $\mathrm{mmol{\cdot}L^{-1}}$ isopropanol (IPA), 0.01 $\mathrm{mmol{\cdot}L^{-1}}$ sodium azide (NaN_3), and 0.01 $\mathrm{mmol{\cdot}L^{-1}}$ benzoquinone (BQ) were added. In particular, KI was employed to quench the h^+ and ·OH radicals (Zhang et al., 2011).

RESULTS AND DISCUSSION

Characterization of γ-FeOOH

The physical properties of metal oxides, such as their crystal structures and surface characteristics, may influence their photocatalytic activity. Eight peaks were observed in the XRD pattern of FeOOH that were attributed to the (120), (011), (031), (111), (060), (220), (151), and (080) planes, indicating the presence of the γ structure (**Figure 2A**). When compared with the standard diffraction peaks of γ-FeOOH, the prepared powder was in the form of a pure crystal phase.

Surface morphological studies of γ-FeOOH by SEM revealed that the prepared powder was in the form of a mixed crystal phase, which contained, for the most part, nanoparticles (∼50 nm) and short nanorods (∼200 nm in length) (**Figure 2B**), due to differences in pH during the preparation of γ-FeOOH (Farcasiu et al., 1991). The smooth and dispersible properties of the mixed crystal phase revealed that the morphology was relatively regular.

The adsorption capacity of metal oxides for organic pollutants is affected by the BET size. On the basis of the N_2 adsorption–desorption isotherm and pore size distribution, the specific surface area of γ-FeOOH was determined to be 125.7 $\mathrm{m^2{\cdot}g^{-1}}$ (**Figure 2C**). As shown in **Figure 2C**, we found that there was a significant hysteresis loop in the adsorption–desorption curve, which means that the sample possessed a mesoporous structure. According to the BJH desorption curve method (Kruk et al., 1997), which was employed to calculate the pore size distribution, the pore size range of the sample was ∼50 nm. In photocatalytic experiments, γ-FeOOH was recovered and washed with pure water three times before drying. The XRD pattern showed no obvious change (**Figure 2D**) after this test. The degradation of NPX was reduced by only 1% when performing photodegradation with the recovered γ-FeOOH. These results show that the γ-FeOOH photocatalyst is highly stable.

As shown in **Figure 3A**, γ-FeOOH displayed a typical absorption edge at ∼650 nm, and a bandgap width of 1.94 eV

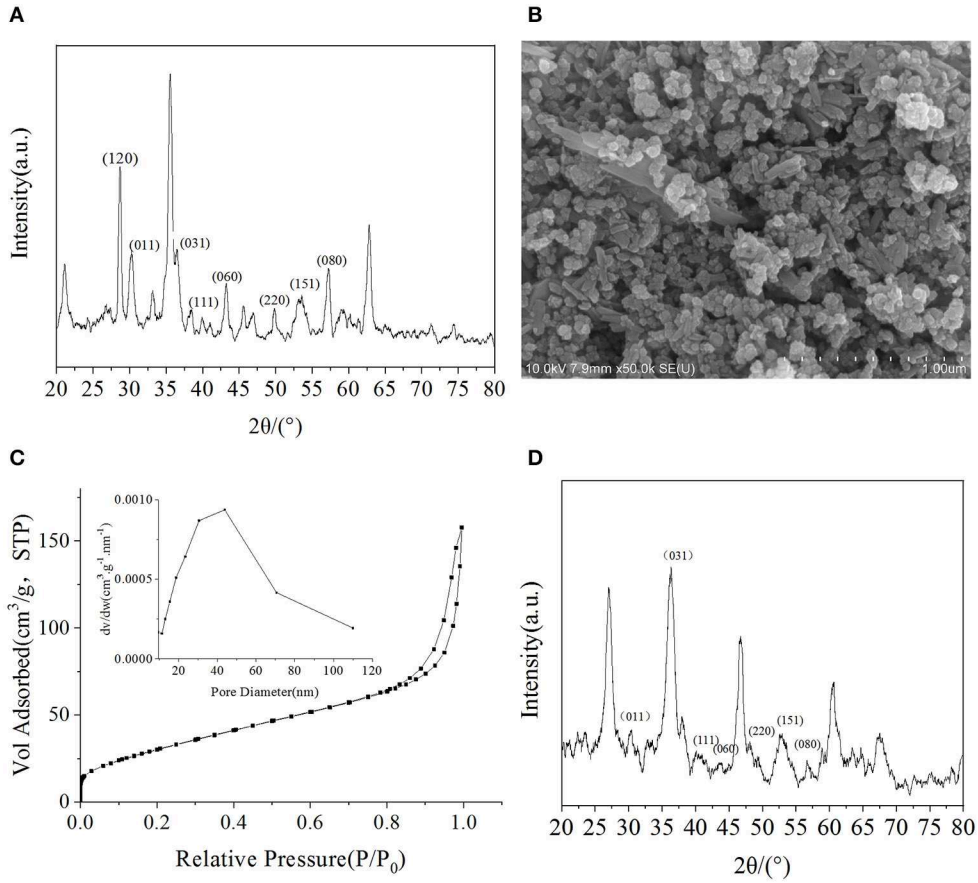

FIGURE 2 | (A) XRD pattern of γ-FeOOH, **(B)** SEM image of γ-FeOOH, **(C)** N_2 adsorption-desorption isotherm and pore size distribution of γ-FeOOH, **(D)** XRD pattern of recycled γ-FeOOH.

was calculated (**Figure 3B**). In order to further study the bandgap position of the semiconductor γ-FeOOH, X-ray photoelectron spectroscopy (XPS) was used to probe the valence band (XPS-VB). This revealed that the valence band of γ-FeOOH was located at 1.80 eV, as shown in **Figure 3C**. Therefore, it can be deduced that the rewind position of γ-FeOOH was −0.14 eV and the band gap structure is shown in **Figure 3D**.

Effect of γ-FeOOH Dosage on the Photocatalytic Degradation of NPX

A suspension was formed in the multiphase photocatalytic reaction system, as the catalyst is insoluble in water. With increased catalyst dosages, the effective surface area of the solution was increased; hence, its reaction efficacy was enhanced proportionally. Excessive catalyst loading caused reflection and scattering, which reduced the transmittance of the solution and thus the catalytic efficiency. It was observed that the γ-FeOOH dosage played a very important role in the photodegradation of NPX. To investigate the effect of γ-FeOOH dosage on the photodegradation of NPX, γ-FeOOH solutions were prepared at concentrations of 0.05, 0.1, 0.2, 0.4, and 0.6 $g{\cdot}L^{-1}$, which were then introduced into separate NPX solutions. As shown in **Figure 4A**, the data collected from the photodegradation of NPX following the addition of different concentrations of γ-FeOOH were fitted to a first-order kinetic equation. It was observed that the NPX photodegradation rate increased with increased γ-FeOOH loading in water.

When the dosage of γ-FeOOH was varied from 0.05 to 0.6 $g{\cdot}L^{-1}$, the NPX photodegradation rate increased from 0.0344 to 0.0509 min^{-1}. The position and photogenic charge of photocatalytic reactions in the system were enhanced with increased γ-FeOOH loading; however, the shielding, reflection, and scattering of light were increased with higher γ-FeOOH loads. With appropriate loads of γ-FeOOH, the transmittance of light in the solution decreased and the reaction rate slowly increased.

During the process of photodegradation, the relationship between the reaction rate constant k and the concentration of γ-FeOOH was fitted to the following empirical formula (Galindo et al., 2001):

$$k = a[\gamma - FeOOH]^n \quad (3)$$

$$ln\, k = ln\, a + n\, ln[\gamma - FeOOH] \quad (4)$$

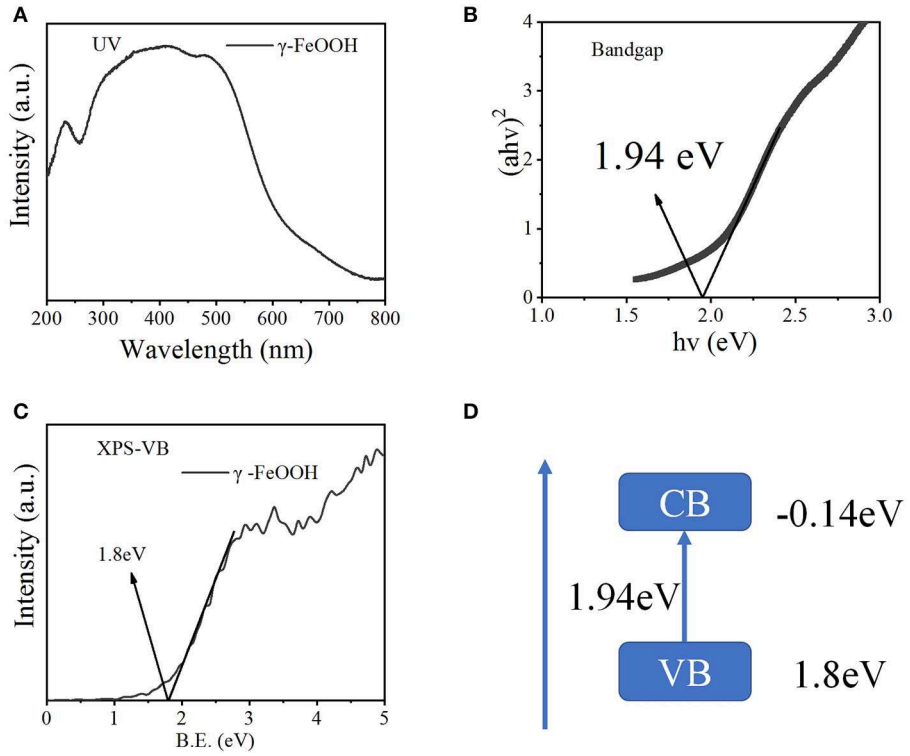

FIGURE 3 | (A) UV-Vis diffuse spectra of γ-FeOOH, **(B)** bandgap width of γ-FeOOH, **(C)** XPS-VB spectra of γ-FeOOH, and **(D)** band structure alignments of γ-FeOOH.

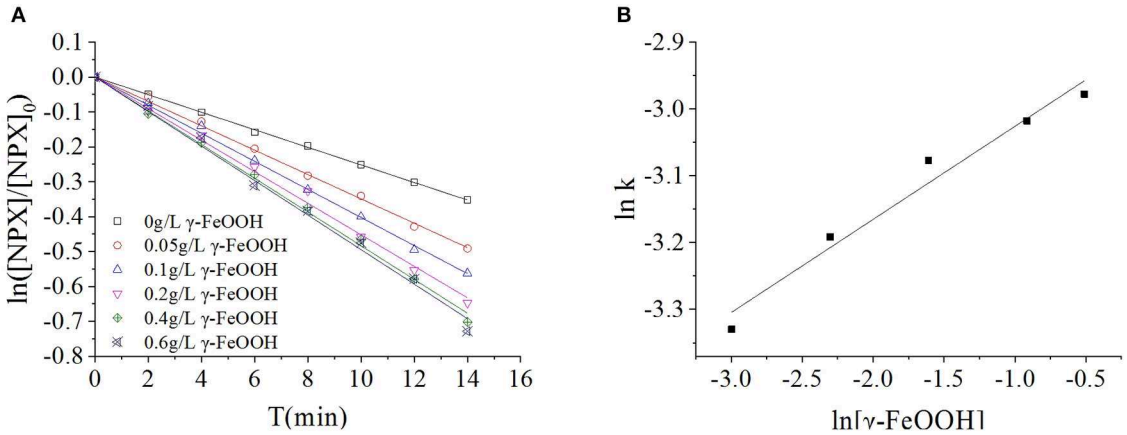

FIGURE 4 | (A) Influence of γ-FeOOH dosage on NPX photodegradation, and **(B)** influence of γ-FeOOH dosage on the NPX photodegradation rate constant.

where n is the correlation index and [γ-FeOOH] is the concentration of γ-FeOOH ($g{\cdot}L^{-1}$).

The kinetic constants of NPX photodegradation and the dosage of γ-FeOOH (0.05 to 0.6 $g{\cdot}L^{-1}$) in this experiment were analyzed by linear regression, with the relationship between k and [γ-FeOOH] shown in **Figure 4B**:

$$ln\,k = ln\,0.05577 + 0.1394\,ln[\gamma{-}FeOOH] \quad (R^2 = 0.9832)$$

To: $k = 0.05577[\gamma - FeOOH]^{0.1394}$

Effect of Initial NPX Concentration on the γ-FeOOH/NPX System

It has been suggested that the charge transfer process between the contaminants adsorbed to the catalyst surface and the light-generated active species (h^+, ·OH, and O_2·) facilitates the photocatalytic oxidation of pollutants in solution. Therefore, the

coverage of pollutants on the catalyst surface has an important influence on photocatalytic activity.

In this section, the photodegradation of NPX by 0.2 g·L^{-1} γ-FeOOH was investigated at initial NPX concentrations of 5, 10, 20, 30, and 40 mg·L^{-1}, with the results shown in **Figure 5A**. These experiments revealed that the photodegradation of NPX followed first-order kinetics at different initial concentrations upon the addition of γ-FeOOH. The activities of semiconductor photocatalysts arise primarily from photogenic e^- and h^+, where, in the competitive process of photocatalysis, they may be recombined very rapidly (generally at the nanosecond level) (Hoffmann et al., 1995). From the kinetics perspective, only the adsorbents on the surface of the catalyst may be oxidized by e^-. However, our results revealed that the NPX photodegradation rate decreased with higher initial concentrations in solution.

Under a certain light intensity, higher initial NPX concentrations resulted in a lower population of photons available per NPX molecule; hence, a lower photodegradation rate was obtained. An identical result was reported in previous NPX research (Ma et al., 2013). Secondly, higher initial NPX concentrations, with additional particles adsorbed to the γ-FeOOH surface, acted to lower the number of photocatalytically active sites that were available at the surface. Hence, the population of photogenerated e^-/h^+ pairs per unit of time was correspondingly reduced. Simultaneously, prior to the photodegradation of NPX molecules, they were required to undergo charge exchange with the active species generated at the γ-FeOOH surface and diffuse into the solution. Finally, when the initial NPX concentration was increased, it was difficult to completely decompose the reaction-generated intermediate products in a timely manner. This increased the opposition against adsorption to the surface of the γ-FeOOH, where these intermediates could once again reform the NPX matrix. Therefore, the photodegradation rate was finally decreased.

We considered the derivative of the obtained first-order kinetic equation with respect to t and set $t = 0$ to obtain the photodegradation rate r_0 under different initial concentrations of C_0, as shown in **Figure 5B**. When the initial concentration of NPX was increased from 5 to 40 mg·L^{-1}, the initial photodegradation rate r_0 also increased gradually, from 0.1415 to 0.7997 mg·L^{-1}·min^{-1}. This indicated that the photocatalytic degradation of NPX occurred on the surface of γ-FeOOH, and the photodegradation rate was an increasing function of the level of surface adsorption. When the Metastable-Equilibrium Adsorption Theory (Pan and Liss, 1998) is regarded under certain thermodynamic conditions, the adsorption amount is related to the surface binding strength and the adsorption configuration, while being balanced with the concentration of the solute. In this section, when the initial NPX concentration was raised, the coverage rate of the NPX molecules on the surface of γ-FeOOH increased accordingly. Consequently, the electron transfer efficiency of the NPX molecules that was adsorbed to the surface and the photogenerated charge were increased, which led to an increase of the initial photodegradation rate r_0.

A large quantity of experimental data has indicated that the photocatalytic degradation of organic pollutants on the surface of semiconductors conforms to the Langmuir–Hinshelwood kinetic equation (Hoffmann et al., 1995; Houas et al., 2001; Andreozzi et al., 2003; Du et al., 2008; Li et al., 2008). The applicable premise of the L–H kinetic equation is that the organic pollutant molecules are adsorbed to a solid surface (Turchi and Ollis, 1990; Alfano et al., 1997). Although researchers have not clarified the photocatalytic mechanisms of FeOOH, surface complexes (Faust and Hoffmann, 1986) and semiconductor-initiated photocatalytic mechanisms (Bandana et al., 1999) have had their respective supporters. More recent studies have supported semiconductor photocatalytic mechanisms and highlighted the role of organic pollutant molecules adsorbed to the FeOOH surface (Bandana et al., 1999, 2001a,b). In examining the FeOOH-facilitated photocatalysis of orange II, Du et al. (2008) analyzed the initial reaction rate, amount of FeOOH surface adsorption, and the position of the FeOOH activity. Thus, Du considered that the FeOOH photocatalytic reaction takes place at the solid surface; therefore, the available L–H kinetic equation could be employed to describe FeOOH photocatalysis. Based on this, $1/C_0$ and $1/r_0$ were calculated according to Equation (2), and a plot was created for $1/C_0$-$1/r_0$ (as shown in **Figure 5C**). A linear relationship was found between them within the experimental concentration range ($R^2 = 0.9996$), $k_{L-H} = 2.1867$ mg·L^{-1}·min^{-1}, $K = 0.01377$ L·mg^{-1}. This signified that the photocatalytic degradation of NPX on the surface of γ-FeOOH satisfies the L–H kinetic equation, and that the adsorption of NPX on γ-FeOOH is of importance to its photocatalytic degradation (Li et al., 2008).

Within the range of experimental concentrations, the photodegradation kinetic constant of NPX gradually decreased (from 0.0285 to 0.0200 min^{-1}), whereas the correlation coefficient R^2 decreased from 0.9949 to 0.9791. The relationship between the reaction rate constant k and the initial substrate concentration during the photocatalytic process could be generally described by the following empirical formula:

$$k = a[NPX]^n \tag{5}$$

$$ln\, k = ln\, a + n\, ln[NPX] \tag{6}$$

where n is the correlation index and [NPX] is the initial concentration of NPX (mg·L^{-1}).

Linear regression was used to analyze the relationship between the NPX photodegradation kinetic constant and its initial concentration (5–40 mg·L^{-1}) within the experimental range. It can be seen in **Figure 5D** that the relationship between the reaction rate constant k and NPX concentration was as follows:

$$ln\, k = ln\, 0.03790 - 0.1673\, ln[NPX] \quad (R^2 = 0.9848)$$

$$k = 0.03790[NPX]^{-0.1673}$$

Effect of pH on the γ-FeOOH/NPX System

It is understood that pH is a critical factor that influences the photocatalytic degradation kinetics during semiconductor multiphase photocatalysis. First, pH can change the charge properties of the catalyst surface and affect how organic molecules adsorb on the catalyst surface (Barnard et al., 2005). Secondly, photogenerated charge carriers can combine with H^+/OH^- in solution to form active species, such as OH^-, which

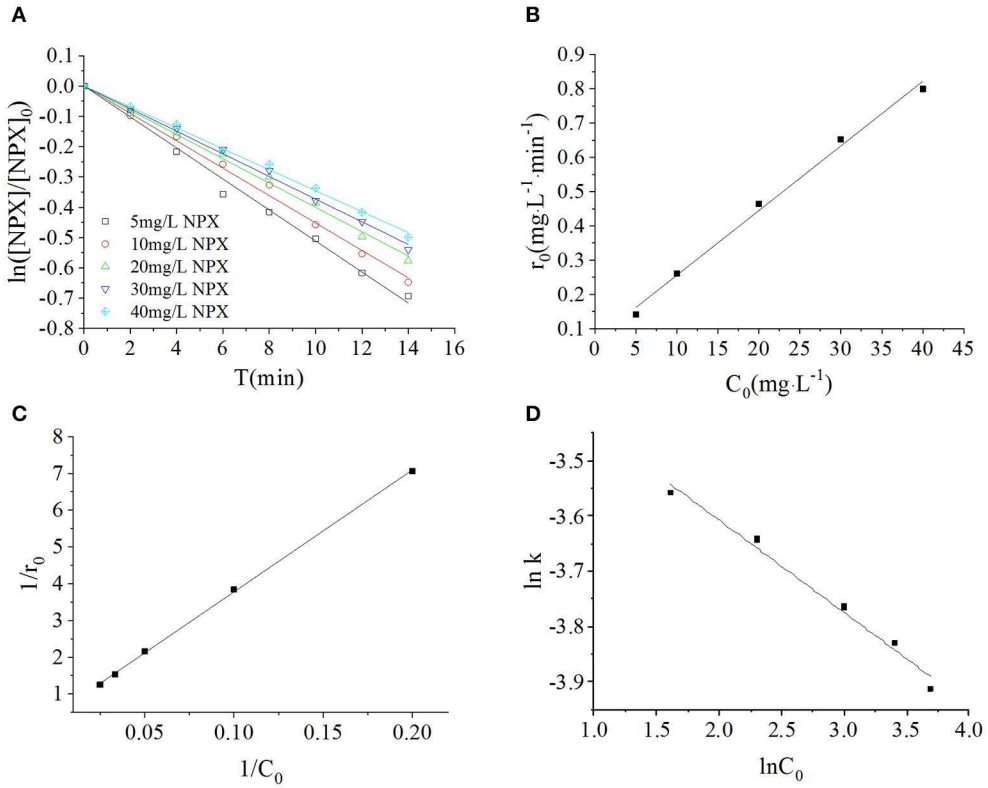

FIGURE 5 | (A) Influence of initial NPX concentrations on the photodegradation of γ-FeOOH/NPX; **(B)** the initial reaction rate r_0 as a function of initial NPX concentration C_0; **(C)** Langmuir-Hinshelwood model of photocatalytic NPX degradation by γ-FeOOH; **(D)** influence of initial NPX concentrations on the photodegradation rate constant of γ-FeOOH/NPX.

can capture photogenerated holes H^+ to form ·OH. Finally, pH may alter the electron cloud density distribution of organic molecules, thus affecting photocatalytic degradation.

As the effects of pH on photocatalytic degradation kinetics are relatively complex, definitive studies of γ-FeOOH are relatively rare. In this section, to investigate the effects of initial pH on the photodegradation of γ-FeOOH/NPX reaction systems, the initial NPX concentration was established as 10 $mg{\cdot}L^{-1}$, whereas that of γ-FeOOH was 0.2 $g{\cdot}L^{-1}$, and the initial pH of the photodegradation solution was set at 5, 7, and 9. As shown in **Figure 6A**, at a pH of 5, the γ-FeOOH /NPX system demonstrated the fastest photocatalytic rate with a pH of 9 in the second place, while the slowest rate was observed at a pH of 7, much the same as the photocatalytic rates observed in water (**Figure 6B**).

As $pH_{ZPC} = 8.47$ for γ-FeOOH, the hydroxylation of the γ-FeOOH surface in an alkaline solution could allow OH^- to react with h^+ to produce ·OH as follows:

$$Fe^{III} - OH^- + h^+ \rightarrow Fe^{III} + \cdot OH \quad (7)$$

Concurrently, the ether bonds of the NPX molecules are less stable under acidic conditions (Chen et al., 2013). Hence, γ-FeOOH was favorable for the photocatalytic degradation of NPX at pH < 7.

Based on the above analysis, when the pH was low, the stability of the ether bonds within the NPX molecules was decreased, which enabled the γ-FeOOH-based photocatalytic degradation of NPX. When the pH was high, OH^- combined with h^+ to form ·OH, which facilitated the photocatalytic degradation of NPX. Due to the combined effect of these two factors, the reaction rate was lowest when the pH was 7 within the range of our experiments.

Analysis of the Photocatalytic Degradation Mechanism of γ-FeOOH

Quenching experiments were carried out (**Figure 7A**) by measuring the generation of active species during the photodegradation of NPX in pure water. It can be seen that there was not only direct photodegradation caused by $^3NPX^*$, but also self-sensitized photodegradation involving hydroxyl radicals (·OH), singlet oxygen ($^1O_2$), and superoxide anions ($O_2^{\cdot-}$) which were produced in the photodegradation process of NPX (**Figure 7B**) (Zhanyi et al., 2018).

To further investigate the active radicals that participate in the photodegradation of NPX, electron paramagnetic resonance (EPR) measurements were carried out. As shown in **Figure 8A**, there was no signal in the dark, while the signal 1:1:1:1 appeared after 5 min of illumination. It could thus be concluded that

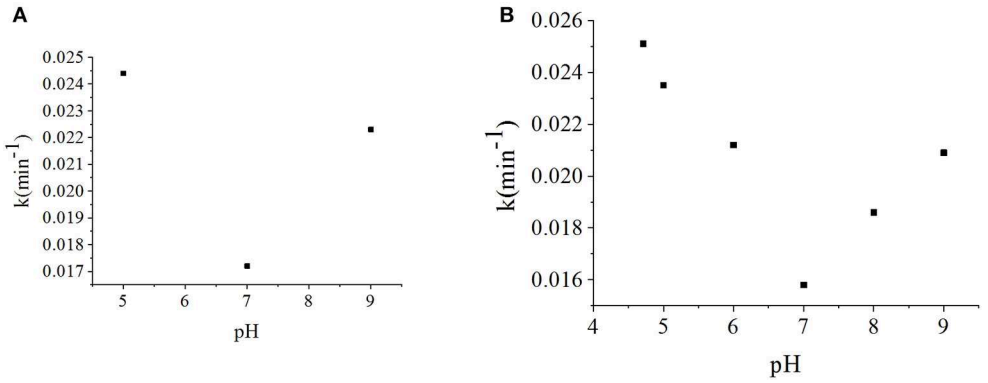

FIGURE 6 | (A) Influence of the pH value on photodegradation rate constant of γ-FeOOH/NPX, and **(B)** influence of the pH value on photodegradation of NPX.

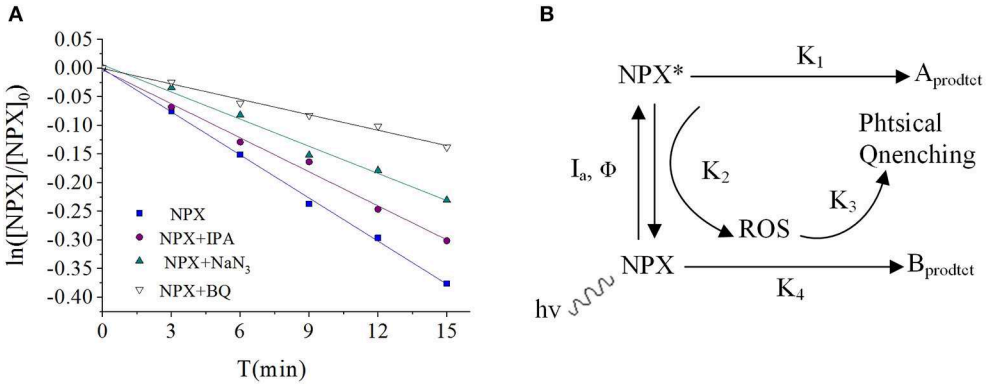

FIGURE 7 | (A) Influence of scavengers on the NPX photodegradation rate constant, and **(B)** photodegradation of NPX in the water.

$O_2^{\cdot-}$ was present and its concentration would be increased by illumination. As shown in **Figure 8B**, it was observed that the signal 1:2:2:1 appeared. This suggests that ·OH appeared and increased in concentration with illumination. It was also confirmed that $^1O_2$ was present by TEMP from **Figure 8C**, while the signal 1:1:1 was detected in the light. So, the active radicals in the γ-FeOOH/NPX system were evidenced by electron spin resonance (ESR).

Photocatalytic degradation typically generates a variety of active substances, such as h^+, e^-, ·OH, $^1O_2$, and $O_2^{\cdot-}$ (Hao et al., 2016), with the production processes shown in Equations (8)–(14):

$$\gamma - \text{FeOOH} + \text{hv} \rightarrow h^+ + e^- \quad (8)$$

$$h^+ + H_2O \rightarrow \cdot OH + H^+ \quad (9)$$

$$e^- + O_2 \rightarrow O_2^{\cdot-} \quad (10)$$

$$O_2^{\cdot-} + H^+ + \rightarrow HO_2^{\cdot} \quad (11)$$

$$2HO_2^{\cdot} \rightarrow H_2O_2 + {}^1O_2 \quad (12)$$

$$H_2O_2 + e^- \rightarrow \cdot OH + OH^- \quad (13)$$

$$\text{Active substances} + \text{NPX} \rightarrow \text{Products} \quad (14)$$

According to the quenching experiment described in the section "Active Species Analysis," when KI, IPA, NaN_3, and BQ were added to the solution, the photocatalytic NPX degradation rate was reduced by different degrees, as shown in **Figure 8D**. It may be seen from **Figure 8D** that free radicals such as h^+, e^-, ·OH, $^1O_2$, and $O_2^{\cdot-}$ were involved in the γ-FeOOH-mediated photocatalytic degradation of NPX.

On one hand, γ-FeOOH is a semiconductor material with an energy band structure, where the energy barrier (Eg) between the valence band (VB) and the conduction band (CB) is only 2.2 eV. When the γ-FeOOH surface was irradiated with photons of energy equal to or greater than the forbidden band, the e^- in the VB were excited and jumped to the CB, with h^+ being generated in the VB to form e^-/h^+ pairs. Because of the discontinuous region between the energy bands, the resulting e^-/h^+ pairs had greater longevity; hence, they migrated to the particle surface in large quantities. The oxidizing properties of the nanoparticle surfaces were potent enough to oxidize the NPX molecules that were adsorbed to the γ-FeOOH surfaces. Additionally, the cavities reacted with H_2O molecules, which were also attached to the surface of γ-FeOOH, which then generated ·OH. Due to the strong oxidization ability of ·OH, the NPX molecules on the surface of γ-FeOOH could also be oxidized

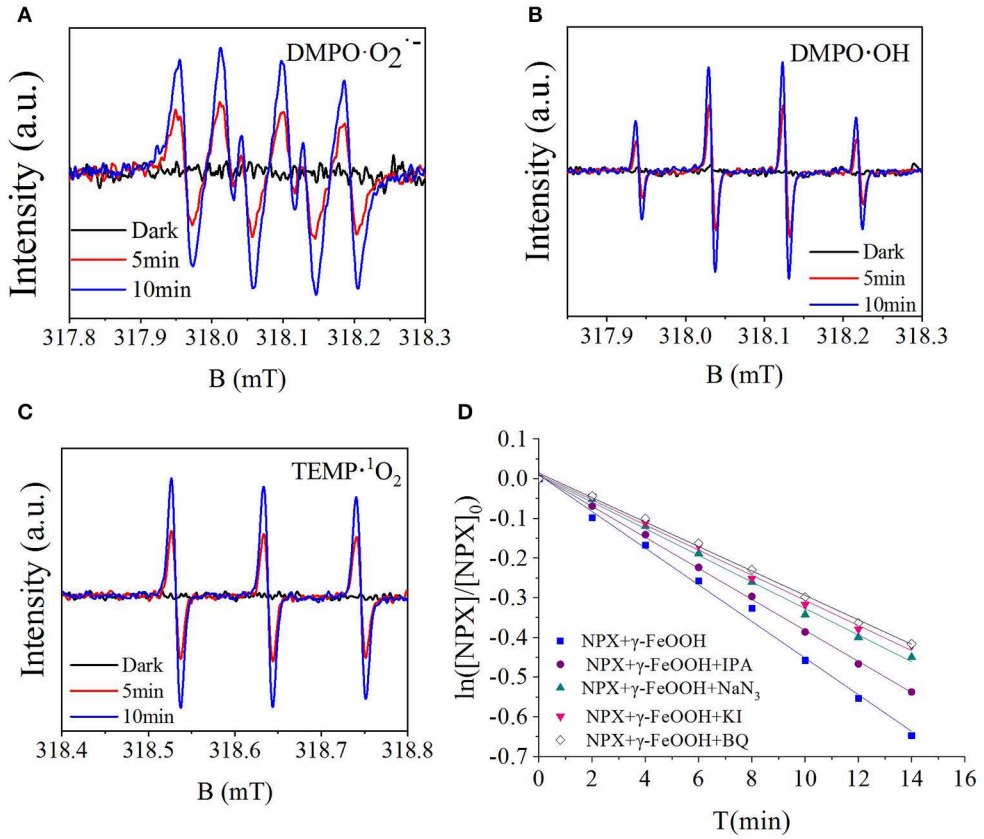

FIGURE 8 | (A) ESR spectra of the DMPO-$O_2^{\cdot-}$, **(B)** DMPO-·OH, **(C)** TEMP-$^1O_2$, and **(D)** influence of scavengers on the γ-FeOOH/NPX photodegradation rate constant.

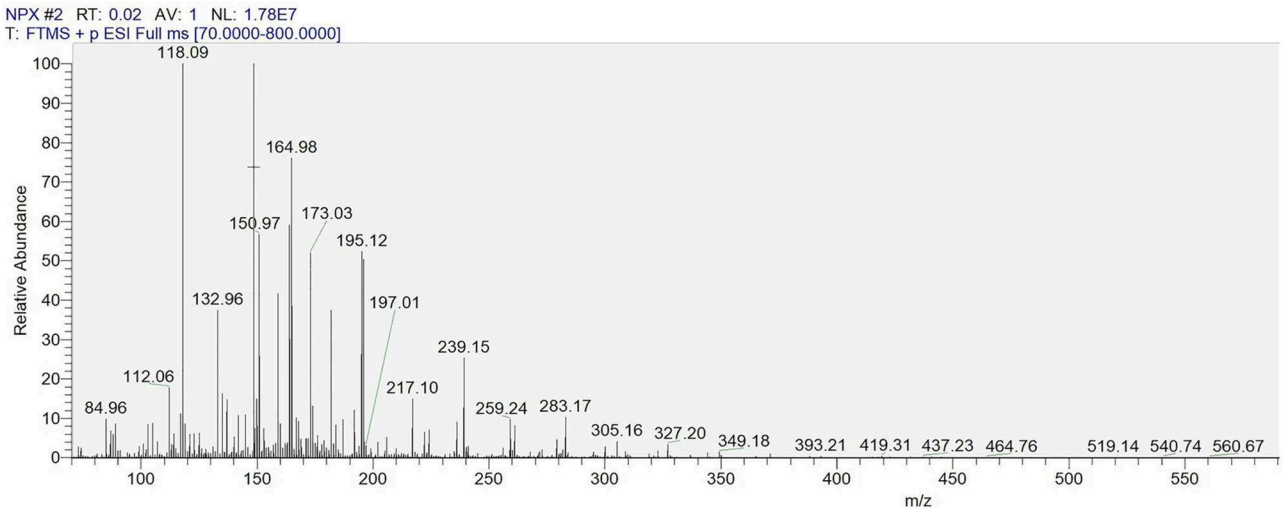

FIGURE 9 | HRLC-MS-MS spectrum of the intermediates on the γ-FeOOH/NPX system.

and degraded. Simultaneously, conducting electrons were combined with O_2 at the surface of the γ-FeOOH to generate $O_2^{\cdot-}$, which could also facilitate the oxidative degradation of NPX.

On the other hand, under sunlight exposure, Fe (III) could accelerate the oxidation of carboxylic acid. As NPX contains a carboxyl group, it could form strong complexes with Fe (III), which rapidly photochemically reacted under light

irradiation (Zuo and Hoigne, 1992; Faust and Zepp, 1993), thereby accelerating the oxidative degradation of NPX. Several studies have suggested that the photochemical reaction of these complexes follows the H_2O_2 production process in water.

$$\mathrm{Fe}\left(\mathrm{OX}_n^{(3-2n)+}\right) + \mathrm{hv} \rightarrow \mathrm{Fe}\left(\mathrm{OX}_{n-1}^{(4-2n)+}\right) + \mathrm{OX}^{\cdot -} \quad (15)$$

$$\mathrm{OX}^{\cdot -} + \mathrm{O_2} \rightarrow \mathrm{O_2^{\cdot -}} + 2\mathrm{CO_2} \quad (16)$$

$$\mathrm{O_2^{\cdot -}} + \mathrm{H^+} \rightarrow \mathrm{HO_2^{\cdot}} \quad (17)$$

$$\mathrm{HO_2^{\cdot}/O_2^{\cdot -}} + \mathrm{Fe\,(III)} + \mathrm{H^+} \rightarrow \mathrm{Fe\,(II)} + \mathrm{O_2} \quad (18)$$

$$\mathrm{HO_2^{\cdot}/O_2^{\cdot -}} + \mathrm{Fe\,(II)} + \mathrm{H^+} \rightarrow \mathrm{Fe\,(III)} + \mathrm{H_2O_2} \quad (19)$$

For this photodegradation experiment, the effect of hydrokinetics must also be considered, as light exposure under stirring was first applied. With agitation, the mass transfer rate of NPX from the solution to the γ-FeOOH surface was increased, so additional NPX was oxidized prior to e^-/h^+ recombination and thus the photodegradation of NPX was increased. Moreover, DO present in the solution could capture the photogenerated electrons generated during the photocatalytic process, which reduced the probability of the recombination of photogenerated electrons and holes, and thus increased the probability of holes oxidizing the NPX. When exposed to UV light, the e^- at the surface of the γ-FeOOH could reduce O_2 to $O_2^{\cdot -}$, as shown in Equation (20). Subsequently, $O_2^{\cdot -}$ reacted with photogenerated holes h^+ to form ·OH or peroxide in the presence of organic capture agents, as in Equations (21)–(23). Each of these species contributed to the photodegradation of NPX.

$$\mathrm{e^- + O_2} \rightarrow \mathrm{O_2^{\cdot -}} \quad (20)$$

$$\mathrm{2O_2^{\cdot -} + 2H^+} \rightarrow \mathrm{O_2 + H_2O_2} \quad (21)$$

$$\mathrm{H_2O_2 + e^-} \rightarrow \mathrm{HO\cdot + OH^-} \quad (22)$$

$$\mathrm{O_2^{\cdot -} + NPX} \rightarrow \mathrm{NPX - OO^{\cdot}} \quad (23)$$

Identification of Intermediates

The degradation by-products of NPX on the γ-FeOOH /NPX system were identified by Thermo Scientific Ultimate 3000 RSLC and Q Exactive Orbitrap (HRLC-MS-MS). As shown in **Figure 9**, seven intermediates were detected. From attacked by h^+, e^-, ·OH, $^1O_2$, and $O_2^{\cdot -}$, compounds were generated because of the losses of the CO_2, H_2O, and/or CH_3 group. According to the deduced structure of the compounds and the early study, we speculated the reasonable reaction approach as shown in **Figure 10**.

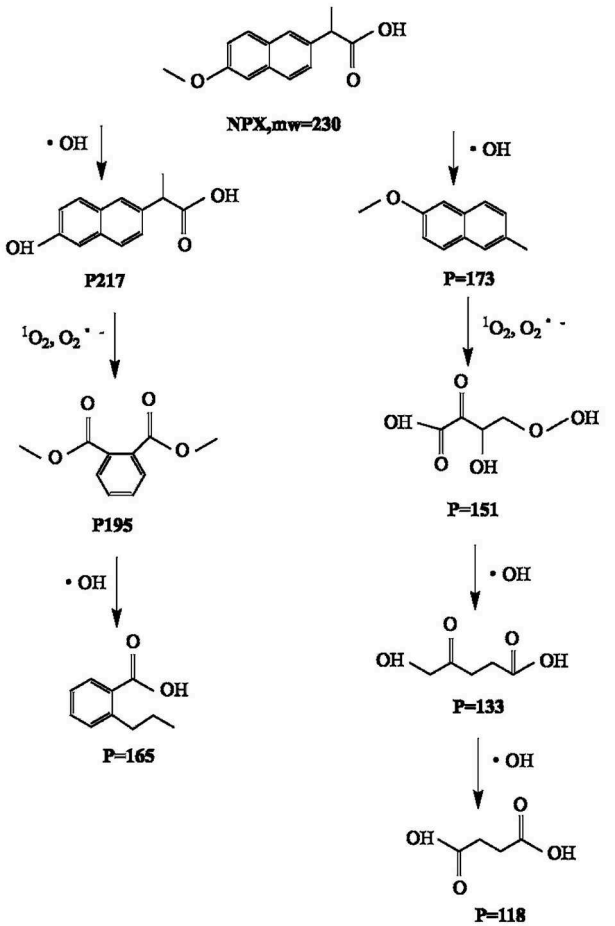

FIGURE 10 | Speculated degradation approach of NPX on the γ-FeOOH/NPX system.

CONCLUSIONS

This study concludes that the photodegradation rate of NPX was positively correlated with the concentration of γ-FeOOH in solution, which was related to the absorption of light energy. With increased initial concentrations of NPX, the photodegradation rate decreased while the γ-FeOOH concentration was constant. This was because the population of photons available per NPX molecule was reduced due to the invariable intensity of light, and the numbers of e^-/h+ pairs generated on the surface of the γ-FeOOH were reduced per unit. At the same time, the intermediate products generated by the reaction could not be completely decomposed in time, so they engaged in a reverse reaction to reconstitute the NPX matrix. At the tested pH values (5.0, 7.0, and 9.0), the photocatalytic rate was noticeably accelerated at higher and lower pH, while the worst pH for photocatalysis was 7.0. Based on quenching experiments and analysis of the photocatalytic mechanism, we conclude that the photocatalysis of NPX degradation by γ-FeOOH is derived from semiconductor photocatalysis. At last, the intermediates of NPX on the γ-FeOOH /NPX System were identified by HRLC-MS-MS.

DATA AVAILABILITY STATEMENT

All datasets generated for this study are included in the manuscript.

AUTHOR CONTRIBUTIONS

ZL and GL formulated the problem and designed the experiments. ZL, XJ, and XW performed the experiments. ZL and

QS took part in data collection and analysis and wrote the paper. QS and CL revised the manuscript.

FUNDING

This work was supported by National Natural Science Foundation of China (No. 21677040), Guangdong Provincial Science and Technology Planning Project of China (No. 2017A050506052), Zhejiang Provincial Natural Science Foundation of China (No. LY17F050001), and China Scholarship Council (No. [2018]5028).

ACKNOWLEDGMENTS

The authors would like to thank the reviewers and editors for their assistance toward the improvement of this paper.

REFERENCES

Alfano, O. M., Cabrera, M. I., and Cassano, A. E. (1997). Photocatalytic reactions involving hydroxyl radical attack. *J. Catal.* 172, 370–379. doi: 10.1006/jcat.1997.1858

Andreozzi, R., Caprio, V., and Marotta, R. (2003). Iron (III)(hydr) oxide-mediated photooxidation of 2-aminophenol in aqueous solution: a kinetic study. *Water Res.* 37, 3682–3688. doi: 10.1016/S0043-1354(03)00271-9

Bandana, J., Mielczarski, J., and Kiwi, J. (1999). Molecular mechanism of surface recognition. azo degradation on Fe, Ti, and Al oxides through metal sulfonate complexes. *Langmuir*15, 767–7679. doi: 10.1021/la9900270

Bandana, J., Mielczarski, J. A., Lopez, A., and Kiwi, J. (2001a). Sensitized degradation of chlorophenols on iron oxides induced by visible light : Comparison with titanium oxide. *Appl. Catal. B Environ.* 34, 321–333. doi: 10.1016/S0926-3373(01)00225-9

Bandana, J., Tennakone, K., and Kiwi, J. (2001b). Surface mechanism of molecular recognition between aminophenols and iron oxide surfaces. *Langmuir* 17, 3964–3969. doi: 10.1021/la001411w

Barnard, A. S., Zapol, P., and Curtiss, L. (2005). Anatase and ruble surface with adsobates representative of acidic and basic conditions. *Surf. Sci.* 582, 173–188. doi: 10.1016/j.susc.2005.03.014

Chen, Y. L., Liu, G. G., Yao, K., and Lü, W. (2013). Treatment of naproxen-containing water in low concentration by ultraviolet irradiation. *Chin. J. Environ. Eng.* 2, 473–476. Available online at: http://www.cjee.ac.cn/article/id/20130212

Christina, I. K., Dimitra, A. L., and Triantafyllos, A. A. (2014). Investigation of PPCPs in wastewater treatment plants in Greece: Occurrence, removal and environmental risk assessment. *Sci. Total Environ.* 466–467, 421–438. doi: 10.1016/j.scitotenv.2013.07.044

Dai, G., Huang, J., Chen, W., Wang, B., Yu, G., and Deng, S. (2014). Major pharmaceuticals and personal care products (PPCPs) in wastewater treatment plant and receiving water in Beijing, China, and associated ecological risks. *B Environ. Contam. Tox.* 92, 655–661. doi: 10.1007/s00128-014-1247-0

Domínguez, J. R., González, T., Palo, P., and Cuerda-Correa, E. M. (2011). Removal of common pharmaceuticals present in surface waters by Amberlite XAD-7 acrylic-ester-resin: influence of pH and presence of other drugs. *Desalination* 269, 231–238.doi: 10.1016/j.desal.2010.10.065

Du, W., Xu, Y., and Wang, Y. (2008). Photoinduced degradation of orange II on different iron (hydr) oxides in aqueous suspension: rate enhancement on addition of hydrogen peroxide, silver nitrate, and sodium fluoride. *Langmuir* 24, 175–181. doi: 10.1021/la7021165

Farcasiu, M., Smith, C., Pradhan, V. R., and Wender, I. (1991). Iron compounds and iron catalysts: activity in reactions relevant to direct coal liquefaction. *Fuel Process. Technol.* 29, 199–208. doi: 10.1016/0378-3820(91)90036-C

Faust, B. C., and Hoffmann, M. R. (1986). Photoinduced reductive dissolution of a-Fe_2O_3 by bisulfate. *Environ. Sci. Technol.* 20, 943–948.

Faust, B. C., and Zepp, R. G. (1993). Photochemistry of aqueous iron (III)-polycarboxylate complexes: roles in the chemistry of atmospheric and surface waters. *Environ. Sci. Technol.* 27, 2517–2522. doi: 10.1021/es00048a032

Fortin, D., and Langley, S. (2005). Formation and occurrence of biogenic iron- rich minerals. *Earth Sci. Rev.* 72. 1–19. doi: 10.1016/j.earscirev.2005.03.002

Galindo, C., Jacques, P., and Kalt, A. (2001). Photooxidation of the phenylazonaphthol AO20 on $Ti0_2$: kinetic and mechanist investigations. *Chemosphere* 45, 997–1005. doi: 10.1016/S0045-6535(01)00118-7

Hao, R., Wang, G., and Tang, H. (2016). Template-free preparation of macro/mesoporous g-C_3N_4/TiO_2 heterojunction photocatalysts with enhanced visible light photocatalytic activity. *Appl. Catal. B Environ.* 187, 47–58. doi: 10.1016/j.apcatb.2016.01.026

Hasan, Z., Jeon, J., and Jhung, S. H. (2012). Adsorptive removal of naproxen and clofibric acid from water using metal-organic frameworks. *J. Hazard. Mater.* 209–210, 151–157. doi: 10.1016/j.jhazmat.2012.01.005

He, Y. P., Miao, Y. M., Li, C. R., Wang, Q., Cao, L., Xie, S. S., et al. (2005). Size and structure effect on optical transitions of iron oxide nanocrystals. *Phys. Rev. B.* 71:125411. doi: 10.1103/physrevb.71.125411

Hoffmann, M. R., Martin, S. T., Choi, W., and Bahnemann, D. W. (1995). Environmental applications of semiconductor photocatalysis. *Chem. Rev.* 95, 69–96. doi: 10.1021/cr00033a004

Houas, A., Lachheb, H., Ksibi, M., Elaloui, E., Guillard, C., and Herrmann, J. M. (2001). Photocatalytic degradation pathway of methylene blue in water. *Appl. Catal. B Environ.* 31, 145–157. doi: 10.1016/S0926-3373(00)00276-9

Isidori, M., Lavorgna, M., Nardelli, A., Parrella, A., Previtera, L., and Rubino, M. (2005). Ecotoxicity of naproxen and its phototrans formation products. *Sci. Total Environ.* 348, 93–101. doi: 10.1016/j.scitotenv.2004.12.068

Jones, O. A. H., Voulvorlis, N., and Lester, J. N. (2002). Aquatic environmental assessment of the top 25 English prescription pharmaceuticals. *Water Res.* 36, 5013–5022. doi: 10.1016/S0043-1354(02)00227-0

Karl, F., Anna, A. W., and Daniel, D. (2006). Ecotoxicology of human pharmaceuticals. *Aquat. Toxicol.* 76, 122–159. doi: 10.1016/j.aquatox.2005.09.009

Kruk, M., Jaroniec, M., and Sayari, A. (1997). Application of large pore MCM-41 molecular sieves to improve pore size analysis using nitrogen adsorption measurements. *Langmuir* 13, 6267–6273. doi: 10.1021/la970776m

Lee, A. P., Brooker, L. R., Macey, D. J., van Bronswijk, W., and Webb, J. (2000). Apatite mineralization in teeth of the chiton acanthopleura echinata. *Calc. Tissue Int.* 67, 408–415. doi: 10.1007/s002230001156

Li, Y., Sun, S., Ma, M., Ouyang, Y., and Yan, W. (2008). Kinetic study and model of the photocatalytic degradation of rhodamine B (RhB) by a TiO_2-coated activated carbon catalyst: effects of initial RhB content, light intensity and TiO_2 content in the catalyst. *Chem. Eng. J.* 142, 147–155. doi: 10.1016/j.cej.2008.01.009

Ma, D. J., Liu, G. G., Lü, W. Y., Yao, K., Zhou, L. H., and Xie, C. P. (2013). Photodegradation of Naproxen in aqueous systems by UV irradiation: mechanism and toxicity of photolysis products. *Environ. Sci.* 34, 1782–1789. Available online at: http://www.hjkx.ac.cn/hjkx/ch/reader/view_abstract.aspx?flag=1&file_no=20130517&journal_id=hjkx

Méndez-Arriaga, F., Gimenez, J., and Esplugas, S. (2008). Photolysis and TiO_2 photocatalytic treatment of naproxen: degradation, mineralization, intermediates and toxicity. *J. Adv. Oxid. Technol.* 3, 435–444. doi: 10.1515/jaots-2008-0302

Molgaard, J. (1974). "Corrosion of cast iron in chlorinated sea water," in *5th International Congress on Metallic Corrosion* (Tokyo), 792–795.

Nurmi, J. T., Tratnyek, P. G., Sarathy, V., Baer, D. R., Amonette, J. E., Pecher, K., et al. (2005). Characterization and properties of metallic iron nanoparticles: Spectroscopy,electrochemistry, and kinetics. *Environ. Sci. Technol.* 39, 1221–1230. doi: 10.1021/es049190u

Pan, G., and Liss, P. S. (1998). Metastable-equilibrium adsorption theory: II. Experimental. *J. Coll. Interface Sci.* 201, 71–76. doi: 10.1006/jcis.1998.5397

Turchi, C. S., and Ollis, D. F. (1990). Photocatalytic degradation of organic water contaminants: Mechanisms involving hydroxyl radical attack. *J. Catal.* 122, 178–192. doi: 10.1016/0021-9517(90)90269-P

Xu, J., Wu, L., and Chang, A. C. (2009). Degradation and adsorption of selected pharmaceuticals and personal care products (PPCPs) in agricultural soils. *Chemosphere* 77, 1299–1305. doi: 10.1016/j.chemosphere.2009.09.063

Zhang, N., Liu, G., Liu, H., Wang, Y., He, Z., and Wang, G. (2011). Diclofenac photodegradation under simulated sunlight: Effect of different forms of nitrogen and Kinetics. *J. Hazard. Mater.* 192, 411–418. doi: 10.1016/j.jhazmat.2011.05.038

Zhanyi, L., Guoguang, L., Qing, S., Jin, X., Wen, X., Zhang, G., et al. (2018). Kinetics and thermodynamics of NPX adsorption by γ-FeOOH in aqueous media. *Arab. J. Chem.* 11, 910–917. doi: 10.1016/j.arabjc.2018.02.005

Zheng, B. G., Niu, J. L., Zheng, Z., Zhang, J., Luo, X., Zhao, Y., et al. (2011). Catalytic degradation of Naproxen in aqueous solutions by gamma-ray irradiation. *Environ. Chem.* 12, 2022–2025. doi: 10.1007/s11783-010-0264-4

Zhou, S. G., Zhou, L. X., and Chen, F. X. (2007). Characterization and heavy metal adsorption properties of Schwertmannite synthesized by bacterial oxidation of ferrous sulfate solutions. *Spectr. Spectr. Anal.* 27, 367–370. doi: 10.1016/j.sab.2007.02.003

Zuo, Y., and Hoigne, J. (1992). Formation of hydrogen peroxide and depletion of oxalic acid in atmospheric water by photolysis of iron (III)-oxalato complexes. *Environ. Sci. Technol.* 26, 1014–1022. doi: 10.1021/es00029a022

Conflict of Interest: The authors declare that the research was conducted in the absence of any commercial or financial relationships that could be construed as a potential conflict of interest.

frontiers in Chemistry

ORIGINAL RESEARCH
published: 09 January 2020
doi: 10.3389/fchem.2019.00805

One-Step Synthesis of N, P-Codoped Carbon Nanosheets Encapsulated CoP Particles for Highly Efficient Oxygen Evolution Reaction

Yuchuan Liu, Xu Guan, Baobing Huang, Qiaohua Wei and Zailai Xie**

Fujian Provincial Key Laboratory of Electrochemical Energy Storage Materials, College of Chemistry, Fuzhou University, Fuzhou, China

Oxygen electrocatalysis, especially oxygen evolution reaction (OER), is a central process during the actual application of rechargeable metal-air battery. It is still challenging to develop ideal electrocatalysts to substitute the commercial noble metal-based materials. In this work, we have constructed a new material, CoP nanoparticles, which are encapsulated by a biomolecule-derived N, P-codoped carbon nanosheets via a simple and facile one-step strategy. The as-prepared material releases a high electrocatalytic activity and stability for OER, with an overpotential of 310 mV to achieve 10 mA/cm^2 in 1 M KOH. Importantly, we found that the phosphoric acid can not only introduce phosphorus dopant into 2D N-doped carbon nanosheets and play a role of pore-forming agent, but also participate in the formation of active center (cobalt phosphide). Moreover, the coverage of N, P-doped carbon can prevent the CoP nanoparticles from corrosion under the harsh reaction medium to achieve high and stable activity. We believe that our strategy can offer a novel pathway to synthesize new transition metal-based catalysts for electrocatalysis or other heterogeneous catalysis.

Keywords: one-step strategy, OER, CoP, carbon nanosheets, biomolecule

OPEN ACCESS

Edited by:
Chundong Wang,
Huazhong University of Science and Technology, China

Reviewed by:
Yuxiao Ding,
Max Planck Institute for Chemical Energy Conversion, Germany
Yejun Li,
Central South University, China

****Correspondence:***
Qiaohua Wei
qhwei76@fzu.edu.cn
Zailai Xie
zlxie@fzu.edu.cn

Specialty section:
This article was submitted to Catalysis and Photocatalysis, a section of the journal Frontiers in Chemistry

Received: *09 October 2019*
Accepted: *08 November 2019*
Published: *09 January 2020*

Citation:
Liu Y, Guan X, Huang B, Wei Q and Xie Z (2020) One-Step Synthesis of N, P-Codoped Carbon Nanosheets Encapsulated CoP Particles for Highly Efficient Oxygen Evolution Reaction. Front. Chem. 7:805. doi: 10.3389/fchem.2019.00805

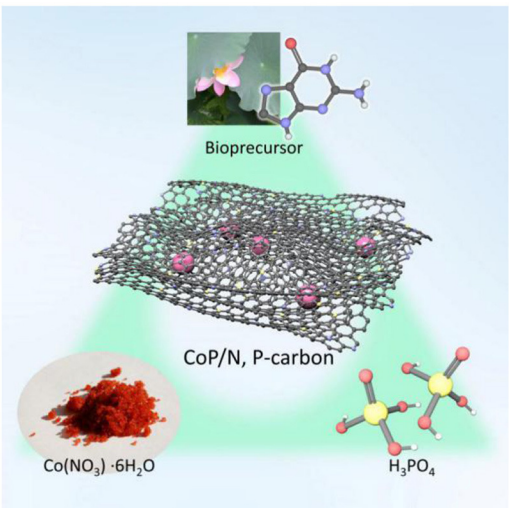

GRAPHICAL ABSTRACT | Bioprecursor-derived CoP/N, P-carbon material via one-step strategy.

INTRODUCTION

The extensive application of renewable fuel cells and rechargeable transition metal-based air battery is an efficient and eco-friendly way to substitute traditional fossil fuels like petroleum and coal for energy demands (Guo et al., 2018; Huang et al., 2018; Miao et al., 2018). Among them, oxygen evolution reaction (OER) and oxygen reduction reaction (ORR) have drawn marvelous attention because of their high energy barrier of activating reactant and poor reaction kinetics, especially the OER process (Tan et al., 2017; Zhang et al., 2018; Hu et al., 2019b; Liu et al., 2019b). Generally, in order to facilitate the OER process, the noble metal-based catalysts, like RuO_2 and IrO_2, have been considered as high active electrocatalysts for OER (Li et al., 2018b; Teng et al., 2018). However, even though they exhibit high activities for electrocatalytic OER, the poor stability and high cost are two main reasons to impede their practical applications (Hu et al., 2018; Lei et al., 2018; Qiu et al., 2018). To deal with the poor stability of RuO_2, recently, Shan et al. reported a nanocrystalline Ru@IrO_x, where the high active site Ru is protected by IrO_x, showing a high activity and stability for OER in acidic conditions (Shan et al., 2019). Unfortunately, the high cost of ruthenium and iridium is still an inevitable issue that is waiting for a better solution.

Recently, a great number of new materials that are effective for the OER process have been reported. Among them, transition metal phosphides, such as CoP_x, have drawn a great deal of attention due to their high electrocatalytic activity and especially the low cost compared to the general RuO_2 or IrO_2 (Li et al., 2017; Fu et al., 2018; Liu et al., 2018). Thus, a great deal of effort has been made to design and synthesize CoP_x-based materials with different nanostructures in order to further improve the actual performance (Xiao et al., 2017; Yan et al., 2017; Han et al., 2019; Li et al., 2019). Based on the previous reported works, the synthesis of CoP_x material generally consists of two processes: the formation of semi-finished product and the subsequent phosphorization at high temperature using Na_2HPO_2 as phosphor sources. For instance, Li et al. reported CoP/CoP_2 nanoparticles encapsulated in N, P-doped CNTs via the decomposition of CoAl-LDH at high temperature and Na_2HPO_2 as phosphor source (Li et al., 2018a). The phosphorization via decomposition obviously complicates the preparing process and the release of PH_3 gas is also poisonous. An ideal structure not only requires well-developed porous structure to promote mass transfer but also increases the electron conductivity (Chen et al., 2019; Jiang et al., 2019; Zhang et al., 2019). To access these, typical templates (hard or soft templates) are often required. Lin et al. used P123 as soft template to synthesize defective carbon–CoP hybrid material (Lin et al., 2018). Yuan et al. used $CaCO_3$ as hard template to synthesize 3D carbon with *in situ* growing CoP nanoparticles (Yuan et al., 2016). From these previous works, it is obvious that although the template methods make the design of structure easier, the tedious processes impede the large-scale application.

In this work, we have successfully prepared a new 2D CoP-based carbon material via a simple and template-free one-step strategy. The CoP nanoparticles are encapsulated by 2D N, P-codoped carbon nanosheets that were derived from biomolecule guanine. The 2D nanosheet-like structure was clearly observed by an electron microscope. The N, P-doped carbon nanosheets not only provide a well-developed porous structure to promote mass transfer but also cover the CoP nanoparticles to preserve them from harsh conditions in alkaline electrolyte. The as-prepared material CoP-CGP2 exhibits an overpotential of 310 mV to achieve 10 mA cm^{-2} for OER in 1 M KOH. We believe that this work not only supplies a competitive electrocatalyst for OER but also opens a new pathway to design other kinds of catalysts.

EXPERIMENTAL SECTION

Synthesis of CoP-CGP

The N, P-doped carbon-covered CoP material was synthesized via a one-step strategy. Specifically, 2 g of guanine, 720 μL of H_3PO_4, and 30 mL of deionized water were added together into a 100-ml beaker and stirred for 30 min. Then, $Co(NO_3)_2{\cdot}6H_2O$ was added. When forming homogeneous solution, the beaker was transferred into an oil bath and heated at 80°C to evaporate water. Finally, the precursor was transferred to a tube furnace and calcined at 1,000°C for 2 h under continuous N_2 flow. The products were noted as "CoP-CGP1, CoP-CGP2, and CoP-CGP3" depending on the usage amount of $Co(NO_3)_2{\cdot}6H_2O$ for 0.10, 0.20, and 0.30 g, respectively.

Synthesis of Co-CG

The synthesis process of Co-CG is similar to that of CoP-CGP only without the addition of H_3PO_4.

Synthesis of CGP

Specifically, 2 g of guanine was first mixed with 720 μl of H_3PO_4 and 30 ml of deionized water and then evaporated at 80°C. Finally, the guanine-based precursor was carbonized at 1000°C for 2 h under continuous N_2 flow again.

Synthesis of CG

The synthesis of CG is similar to that of CGP, just without the usage of H_3PO_4.

Physical Characterization

Powder X-ray diffraction (XRD) was performed by RIGAKU Ultima IV, and diffraction patterns were attained by Cu Kα (λ = 1.5406 Å) radiation at a scanning of 10 min^{-1} from 5° to 80°. X-ray photoelectron spectroscopy (XPS) was conducted using ESCALAB 250. The Raman spectra were measured by Renishaw inVia with a 532-nm laser excitation. Surface area and porosity of materials were measured by Micromeritics ASAP 2020 plus and ASAP 2060. A field emission scan electron microscope (FESEM), Hitachi S-4800, was used, operating at 5.0 kV. A transmission electron microscope (TEM), FEI Talos F200s, was acquired, operating at 200 kV. The element analysis was done using an Elementar Vario EL.

Electrochemical Tests

The electrochemical tests were conducted over a three-electrode cell where glassy carbon (GC, 4 mm), graphite rod, and Ag/AgCl

electrode are the working electrode, counter electrode, and reference electrode, respectively. For sample preparation, 3 mg of sample, 280 μl of ethanol, 140 μl of deionized water, and 32 μl of Nafion (5%) were added together and subjected by ultrasonic treatment for 30 min to form homogeneous sample ink. Before the test, 12.8 μl of ink was dropped on the surface of GC, which had been polished before, and dried at 60°C. All electrochemical data were recorded by IviumStat multichannel electrochemical workstation (Ivium, Netherland). The OER performance was evaluated via linear sweep voltammetry (LSV) in 1 M KOH with iR compensated at a scan rate of 10 mV/s (the solution resistance was manually measured via EIS before LSV test). All of the potentials are converted to the reversible hydrogen electrode scale E (RHE) (V) = E (Ag/AgCl) + 0.1989 + 0.0591 pH. During the cycle voltammetry (CV) test, the potential range is 1.2–1.65 V (vs. RHE) and the scan rate is 50 mV/s. The electrochemical impedance spectroscopy (EIS) was recorded from 100,000 to 0.01 Hz at 10 mV amplitude potential.

RESULT AND DISCUSSION

The CoP-CGP material was synthesized by means of a simple one-step strategy, as shown in **Scheme 1**. Typically, guanine, H_3PO_4, and $Co(NO_3)_2{\cdot}6H_2O$ were dispersed homogeneously in 30 ml of deionized water. After evaporating the solvent, the mixture was directly carbonized at 1,000°C for 2 h under N_2 flow. Guanine cannot merely *in situ* form the two-dimensional structure at high temperature but also introduce nitrogen atom into the carbon matrix (Huang et al., 2017, 2018). Moreover, the existence of phosphoric acid, which will decompose at high temperature, on one hand, participates in the formation of cobalt phosphide and, on the other hand, is *in situ* doped into the carbon matrix. In general, based on this simple and novel one-step preparation strategy, the CoP nanoparticles covered by 2D N, P-codoped carbon nanosheets can be successfully synthesized. The as-prepared materials were denoted as CoP-CGP1, CoP-CGP2, and Co-CGP3 according to the usage amount of $Co(NO_3)_2{\cdot}6H_2O$ for 0.10, 0.20, and 0.30 g, respectively. The blank samples without H_3PO_4 and the pure guanine-derived N, P-doped carbon were denoted as Co-CG and CGP, respectively.

The morphology of the as-prepared materials was first observed via FESEM. As shown in **Figure S1**, the pure guanine-derived N-doped carbon, CG, displays a typical 2D nanosheet-like structure with wrinkles. When being carbonized in the existence of phosphoric acid, the *in situ* formed N, P-codoped carbon, CGP, still maintains the 2D structure as shown in **Figure 1a**, which suggests that the phosphoric acid will not impede the self-assembly of guanine to form 2D nanosheets. Moreover, the carbon nanosheets are transparent under the electron beam when observing the CGP by the TEM shown in **Figure S2**, which implies the thinness of those self-assemble 2D carbon nanosheets. The corresponding EDS elemental mappings (**Figure S2**) show the well dispersion of N and P on the surface of CGP.

When introducing Co during the synthesis process, the CoP nanoparticles will be *in situ* formed during the carbonization process. As shown in **Figures 1b–d**, the SEM images exhibit the N, P-doped carbon nanosheets covering the CoP nanoparticles. Here, we synthesized three samples with different usage amount of $Co(NO_3)_2{\cdot}6H_2O$. As shown from the SEM images, the size of CoP nanoparticles increases with the increasing amount of $Co(NO_3)_2{\cdot}6H_2O$. CoP-CGP2 was chosen to be further observed under the TEM. As shown in **Figure 2a**, the thin nanosheet is transparent under the electron beam and decorated by CoP nanoparticles with a size of ∼20 nm. In **Figure 2b**, it is noticeable that the CoP nanoparticle is covered by several carbon layers. The HAADF-STEM (**Figure 2c**) and EDS elemental mapping (**Figures 2d–g**) also show the dispersion of N and P. As the discussion aforementioned, the cobalt phosphide is generally considered as a competitive candidate because of its high activity to electrocatalysis. The coverage of heterogeneous doped carbon is expected to not only improve the electron conductivity but also play a role of protecting the CoP nanoparticle away from the harsh reaction condition.

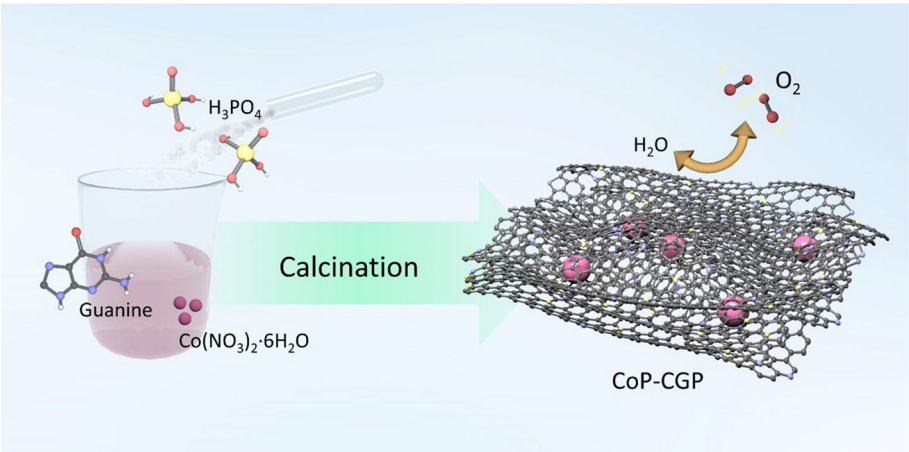

SCHEME 1 | Illustration of the preparation process of the CoP-CGP material.

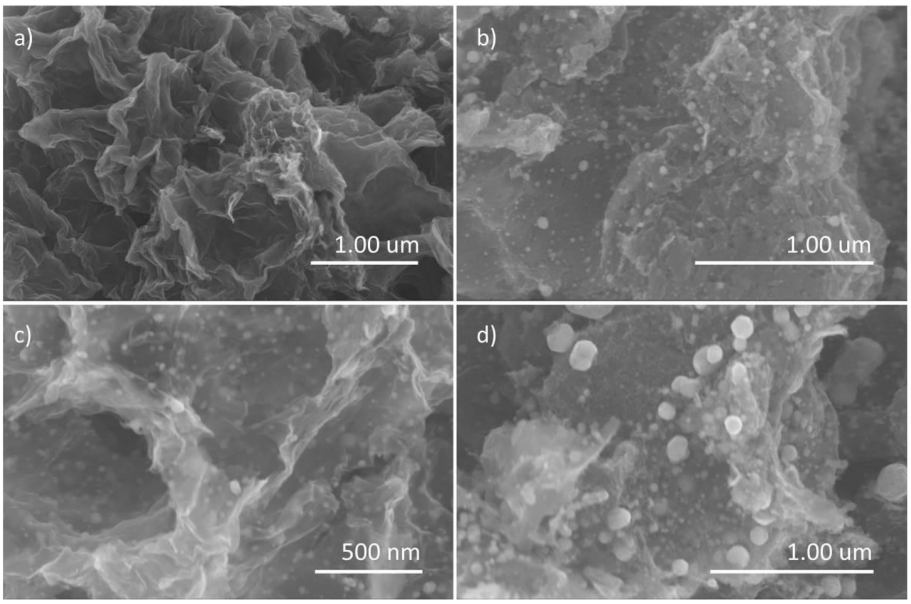

FIGURE 1 | SEM images of **(a)** CGP, **(b)** CoP-CGP1, **(c)** CoP-CGP2, and **(d)** CoP-CGP3.

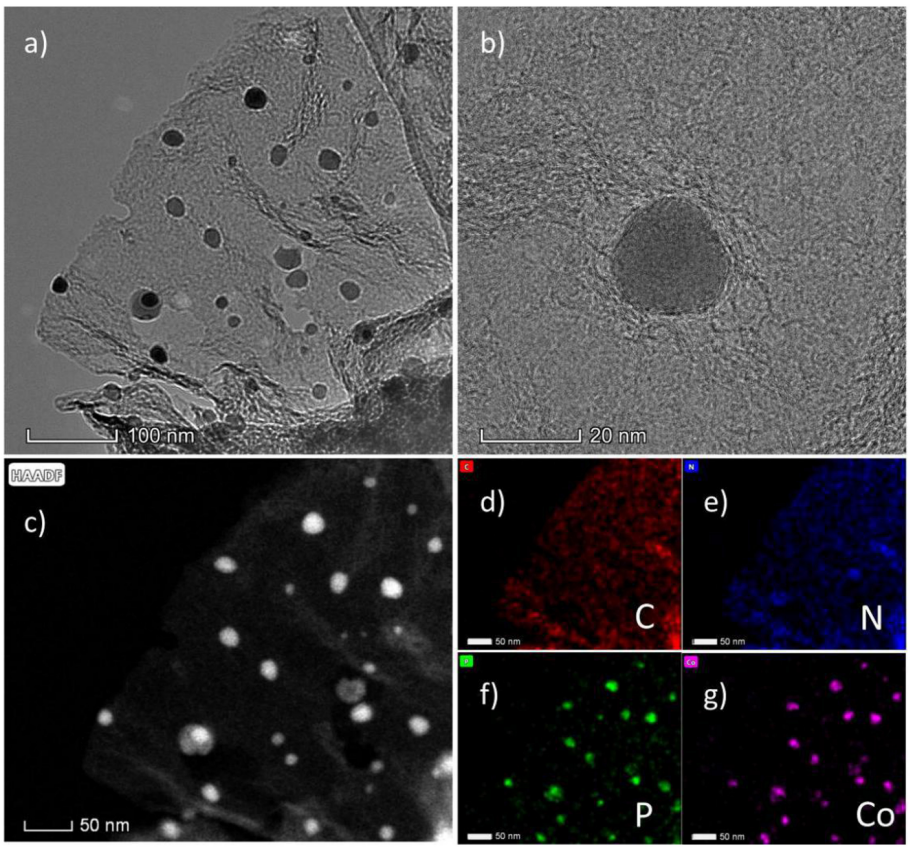

FIGURE 2 | (a,b) TEM images of CoP-CGP2; **(c)** HAADF-STEM image and **(d–g)** EDS elemental mapping.

The one-step formation of CoP was further confirmed by X-ray diffraction pattern (XRD). As shown in **Figure 3A**, the CGP exhibits two broad diffraction peaks located at 26° and 42°, which correspond to the (002) and (100) planes of carbon material, respectively (Yuan et al., 2015; Hu et al., 2019a). When calcining the Co-based precursor, a broad peak is still shown at 26°. Besides, there exist several diffraction peaks that can be assigned to CoP (PDF No. 29-0497), suggesting the successful formation of CoP nanoparticles. For comparison, the blank sample synthesized without the usage of phosphoric acid was denoted as Co-CG. As shown in **Figure 3A**, the Co-CG displays diffraction peaks located at 44.2, 51.5, and 75.8°, which correspond to Co (PDF No. 15-0806). These results confirm again that the phosphoric acid not only plays the role in the formation of cobalt phosphide but also has little influence on the 2D nanosheet-like structure.

Raman spectra were then conducted and recorded. As shown in **Figure 3B**, three samples all show D band and G band located at 1,358 and 1,598 cm^{-1}, respectively. The broad 2D band at around 2,600 cm^{-1} implies the sheet stack structure. Generally, the intensity ratio of D band to G band (I_D/I_G) is generally used to evaluate the graphitization and defect degree of carbon material (Qu et al., 2016; Liu et al., 2019a). We calculated and found that the Co-CG possesses the highest value of $I_D/I_G$of 0.97, suggesting a relatively higher graphitization degree. It may be attributed to the existence of Co, which plays a role of catalyst to facilitate the graphitization of guanine. Oppositely, the CGP shows the lowest I_D/I_Gvalue of 0.92, suggesting a relatively higher defect degree. The value of CoP-CGP2 is 0.95, suggesting that the CoP-CGP2 keeps an ideal balance between graphitization and defect.

A N_2 adsorption–desorption experiment at 77 K was conducted to explore the porous structure of samples. As shown in **Figure 3C**, three samples show similar isotherms. The presence of a sharp nitrogen uptake at low pressure is the monolayer filling of micropores. The following uptake between 0.10 and 0.40 is attributed to the initial few multi-layer adsorption on the external surface of mesopore or macropore. Finally, there is a hysteresis loop shown between 0.40 and 1.00. Hence, the three samples all show a micro-mesopore structure, which is also confirmed by the calculated pore size distribution (PSD) via nonlocal density function theory (NLDFT) method, shown in **Figure 3D**. From these results, the three samples all display micro-mesopore structures, which are beneficial to mass transfer. However, these samples possess different surface areas. Specifically, CGP shows the highest Brunauer–Emmett–Teller (BET) specific surface area of 871.9 m^2/g, while Co-CG shows the lowest value of 234.5 m^2/g (see **Figure S3**). It is noticeable that the phosphoric acid plays the role of pore-forming agent during the carbonization process. Benefiting from the H_3PO_4, the CoP-CGP2 shows a relatively high specific surface area of 609.9 m^2/g. The addition of Co actually had an influence on the surface area. As shown in **Table 1**, the specific surface area decreases with increasing the usage amount of $Co(NO_3)_2$ and achieve 503.1 m^2/g for CoP-CGP3. In **Table 1**, it clearly displays that the phosphoric acid can increase the microporous and mesoporous volumes, compared with those of Co-CG. These results confirm that the phosphoric acid not merely improves the specific surface area, but extends the micro-mesoporous volume, which will promote the mass transfer during catalysis.

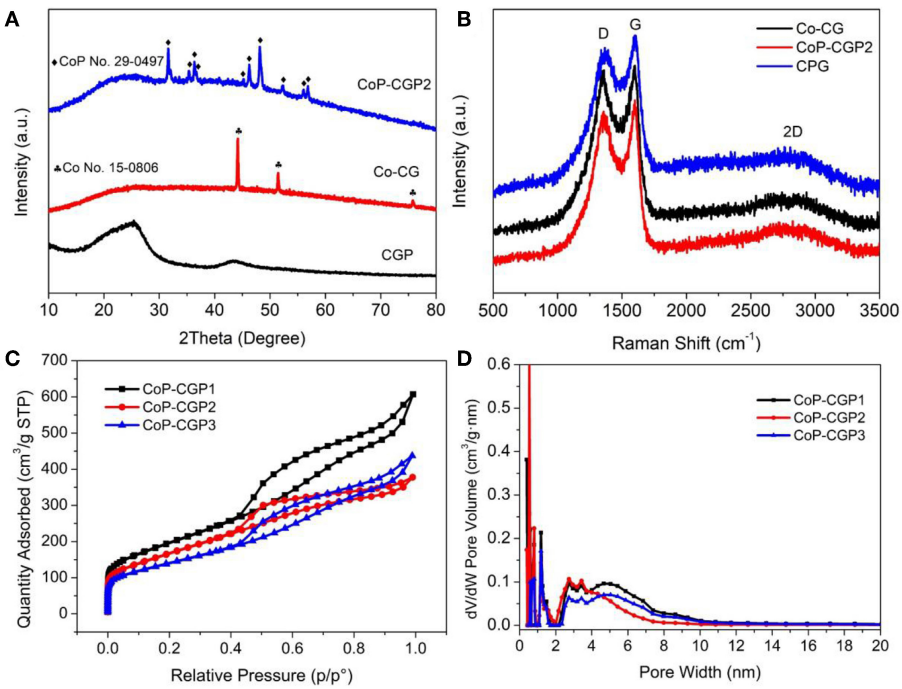

FIGURE 3 | (A) X-ray diffraction (XRD) patterns; **(B)** Raman spectra; **(C)** N_2 adsorption/desorption isotherms; and **(D)** pore size dispersion plots.

TABLE 1 | Textural properties and elemental compositions of various catalysts.

Samples	Porosity				Elemental compositions, wt%[a]		
	S_{BET} [m^2/g]	V_{total} [cm^3/g]	V_{meso}[cm^3/g]	V_{micro}[cm^3/g]	C	H	N
CoP-CGP1	705.6	0.703	0.103	0.580	77.74	0.94	4.26
CoP-CGP2	609.9	0.451	0.099	0.346	79.96	0.72	2.85
CoP-CGP3	503.1	0.482	0.070	0.404	84.92	0.85	3.29
Co-CG	234.5	0.399	0.026	0.309	74.60	0.56	2.18
CGP	871.9	0.830	0.658	0.134	77.03	1.39	3.22

[a] *Determined by element analysis (EA).*

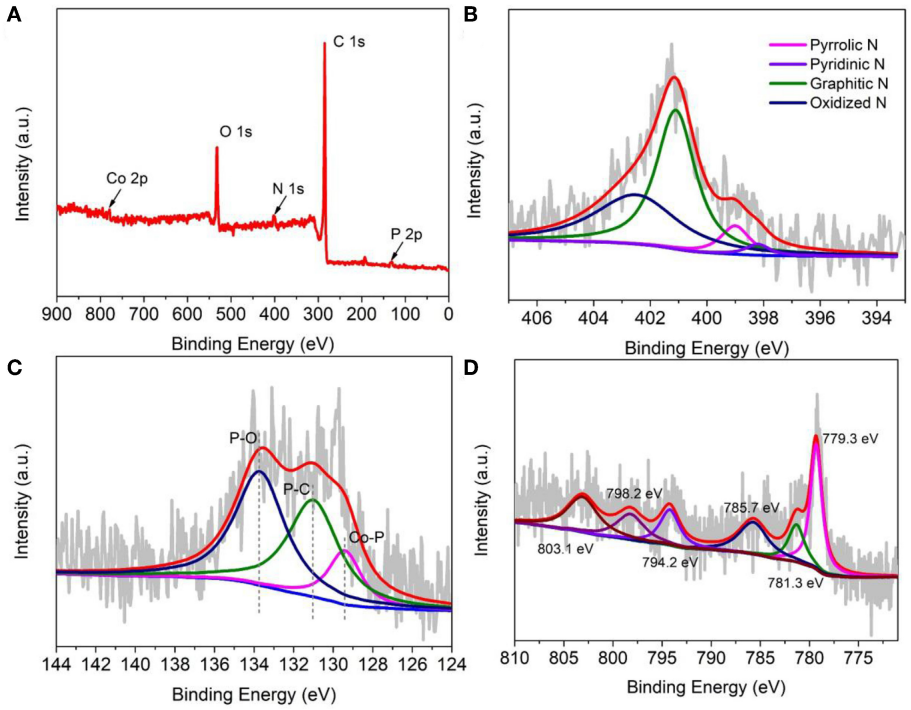

FIGURE 4 | X-ray photoelectron spectroscopy (XPS) of CoP-CGP2: **(A)** survey; **(B)** N 1s; **(C)** P 2p; and **(D)** Co 2p spectra.

To further analyze the surface electron state of the as-prepared cobalt phosphide material, X-ray photoelectron spectroscopy (XPS) was conducted and recorded. Here, we representatively discuss CoP-CGP2, which shows much better electrocatalytic performance. From the survey spectrum as shown in **Figure 4A**, the as-prepared CoP-CGP2 material consists of five elements, i.e., C, N, O, P, and Co, which confirms again the successful doping of N and P. The N and P contents are 3.69 and 2.39 at%, respectively, based on the XPS data. For the high-resolution N 1s spectrum shown in **Figure 4B**, the fitted peaks at 398.2, 399.0, 401.1, and 402.5 eV assigned to pyridinic N, pyrrolic N, graphitic N, and oxidized N prove the doping of N atoms (Huang et al., 2019). The high ratio of graphitic N may be attributed to the introduction of Co, which catalyzes the graphitization of guanine. The high graphitic N will promote the electron conductivity of as-prepared material during the electrocatalysis process. For P 2p spectrum, the peaks at 131.0 and 133.7 eV of the P 2p spectrum (**Figure 4C**) can be assigned to P-C and P-O, respectively, suggesting the doping of P into the carbon matrix, while the peak at 129.4 eV corresponds to Co-P (Huang et al., 2018; Hou et al., 2019). Furthermore, as shown in the high-resolution Co 2p spectra (**Figure 4D**), the peaks at 781.3 eV (Co 2p 3/2) and 798.2 eV (Co 2p 1/2) can be assigned to Co^{2+}. The peaks centered at 779.3 eV (Co 2p 3/2) and 794.2 eV (Co 2p 1/2) reflect Co^{3+}. The other two peaks located at 785.7 and 803.1 eV are the satellite peaks, which correspond to the shake-up excitation of Co^{3+} (Li et al., 2018a). In short, the 779.3 eV of Co 2p and 129.4 eV of P 2p are ascribed to the binding energy of Co-P binding of CoP, which confirms again the formation of cobalt phosphide (Yang et al., 2019a).

ELECTROCHEMICAL TESTS

From the physical characterizations we discussed, we have successfully prepared CoP nanoparticles covered by 2D N, P-codoped carbon nanosheets, which is by means of a facile one-step strategy. Among the synthesis process, the addition of phosphoric acid not only participates in the formation

of CoP and N, P-doped carbon, but also plays the role of pore-forming agent leading to a micro-mesoporous structure. Considering the active CoP sites and desirable structure, it can be expected that this as-prepared material will release a satisfying electrocatalytic performance.

Based on these considerations, we evaluated the OER activity of as-prepared materials. All the electrochemical tests were conducted in a typical three-electrode configuration cell in 1 M KOH solution. First, the activity was evaluated by means of LSV. As shown in **Figure 5A**, CGP displays the lowest OER activity with a high overpotential of 540 mV to release the current density of 10 mA/cm^2. When adding Co during synthesis process, the obtained Co-CG exhibits an improved activity with a corresponding overpotential of 420 mV. For CoP-CGP2, this as-prepared CoP-based material shows the highest activity with a low overpotential of only 310 mV to drive the current density of 10 mA/cm^2. It is obvious that the addition of phosphoric acid participates in the formation of CoP during the carbonization process, which is the OER active site; thus, the final obtained CoP-based material exhibits an ideal electrocatalytic activity. For comparison, the overpotential of commercial RuO_2 to release 10 mA/cm^2 is 330 mV, a bit larger than that of CoP-CGP2.

Furthermore, Tafel slope is another important parameter to analyze the reaction kinetics on the surface of catalyst. As shown in **Figure 5C**, the RuO_2 shows the lowest value of only 48 mV/dec, suggesting the best OER reaction kinetics. The as-prepared CoP-CGP2 exhibits a relatively higher Tafel slope than that of RuO_2, but lower than those of Co-CG and CGP, indicating a relatively ideal kinetics on the Co-CGP2. The effective amount of $Co(NO_3)_2$ was also explored. As the LSV curves shown

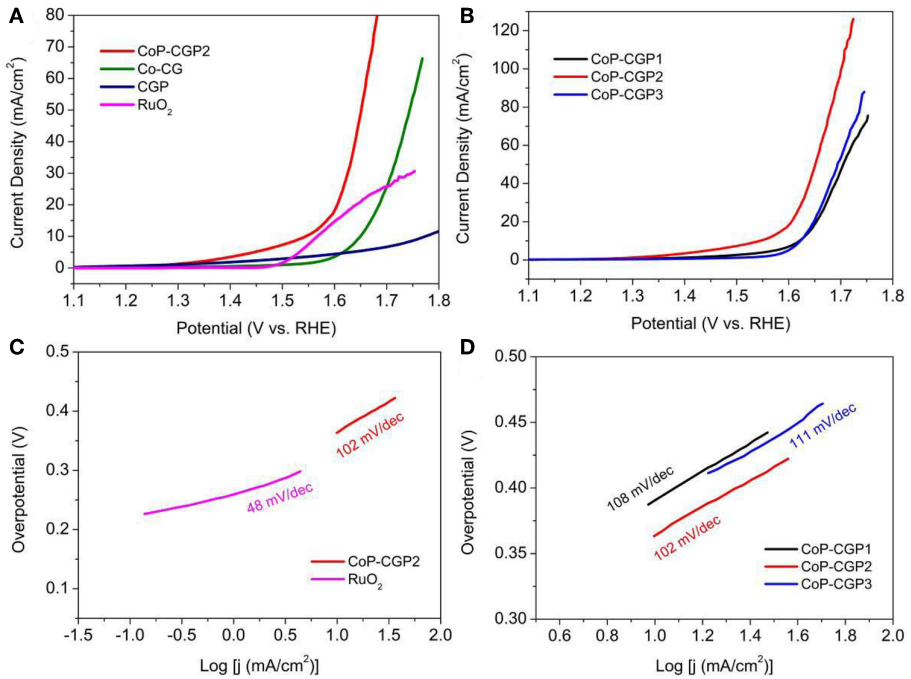

FIGURE 5 | (A,B) Linear sweep voltammetry (LSV) curves in 1 M KOH; **(C,D)** Tafel plots.

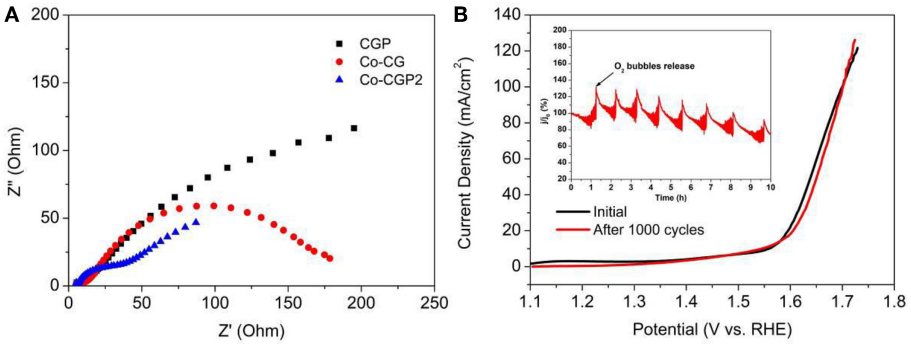

FIGURE 6 | (A) Nyquist plots and **(B)** LSV curves before and after 1000 cycles (inset: current retention–time curve).

TABLE 2 | The OER activity comparison of recent Co-based catalysts.

Sample	Electrolyte	Overpotential (mV)	References
Co-CGP1	1 M KOH	390	This work
Co-CGP2	1 M KOH	310	This work
Co-CGP3	1 M KOH	400	This work
RuO_2	1 M KOH	330	This work
CoP/CoP_2@NPCNT	1 M KOH	330	Li et al., 2018a
Ni/Co-P	1 M KOH	360	Zheng et al., 2019
CoP@NG	1 M KOH	354	Lu et al., 2019
CoP_2@3D-NPC	1 M KOH	350	Yang et al., 2019b

in **Figure 5B**, when increasing the amount of $Co(NO_3)_2$, the activity of as-prepared CoP material was first increased and then decreased, wherein CoP-CGP2 achieves the best performance. Furthermore, CoP-CGP2 also exhibits the lowest value of Tafel slope (**Figure 5D**). Combined with the physical characterization, less $Co(NO_3)_2$ leads to higher specific surface area but less active CoP sites. Oppositely, more Co precursor will inevitably lead to agglomeration, which reduces the exposure of active sites. Thus, the moderate amount of the Co precursor is very important to achieve a good balance between specific surface area and CoP active site. In brief, the superior activity of CoP-CGP2 is likely attributed to the micro-mesoporosity property with relatively high specific surface area and ideal exposure of active CoP sites.

To further explore the high OER performance of this as-prepared CoP-based catalyst, the interfacial charge-transfer resistance (R_{ct}) was measured by EIS. As shown in **Figure 6A**, the Nyquist plots exhibit a semicircle in the high-frequency range, which is related to the resistance of the surface between catalyst and electrolyte. It clearly shows that the CoP-CGP2 possesses the smallest semicircle, suggesting a faster electron transfer process on the interface of the as-prepared CoP-CGP2.

In addition, as a potential electrocatalyst with high activity for OER, the stability is also an important property to ensure that the catalyst can release a high activity for a long time (Ding et al., 2018). As shown in the inset curve of **Figure 6B**, chronoamperometry was conducted at an overpotential of 310 mV for CoP-CGP2. The regular peaks are the cumulated O_2 bubble releasing. It can be observed that activity slightly dropped after 5 h. Furthermore, the stability of CoP-CGP2 was evaluated again by the CV method. As shown in **Figure 6B**, the LSV curves of before and after 1000 cycles present a very small change. All of these results prove that the as-prepared CoP-CGP2 shows not only high activity but also good stability. We also take our as-prepared materials into comparison with previous reported OER electrocatalysts, which is shown in **Table 2**. Our as-prepared materials can release a relatively high OER activity in 1 M KOH, which make them potential candidates for OER electrocatalysts. Furthermore, the HER activity was also evaluated in 1 M KOH shown in **Figure S4**.

CONCLUSION

In summary, we have successfully synthesized a novel CoP-based OER electrocatalyst by means of a facile one-step calcination strategy, where the CoP nanoparticles are encapsulated by 2D N, P-codoped carbon nanosheets. The added phosphoric acid during the synthesis process not only plays the role of phosphor source in the formation of CoP and pore-forming agent but also is doped into the N-doped carbon matrix. Benefiting from the ideal structure, the biomolecule-based 2D N, P-doped carbon nanosheets can supply well-developed porosity to promote the mass transfer and meanwhile preserve the covering CoP nanoparticles during a long-time electrocatalytic performance. As expected, the as-prepared electrocatalyst shows a superior OER activity with good stability in alkaline condition. Considering the simple synthesis strategy and high OER electrocatalytic performance, we believe that this work can not only supply a potentially competitive electrocatalyst but also be extended to design and synthesize other kinds of catalysts.

DATA AVAILABILITY STATEMENT

All datasets generated for this study are included in the article/**Supplementary Material**.

AUTHOR CONTRIBUTIONS

YL conducted the experiments and wrote the manuscript. XG and BH helped with operating the experiments and data analysis. QW and ZX supervised the research. BH and QW analyzed the electrochemical test and discussion. All authors approved the submission of the final manuscript.

ACKNOWLEDGMENTS

The award Program for Fujian Minjiang Scholar Professorship is acknowledged. We thank financial support from the National Natural Science of China (NSFC grant number: 21571035).

SUPPLEMENTARY MATERIAL

The Supplementary Material for this article can be found online at: https://www.frontiersin.org/articles/10.3389/fchem.2019.00805/full#supplementary-material

REFERENCES

Chen, Y., Wang, M., Xiang, S., Liu, J., Feng, S., Wang, C., et al. (2019). Hierarchical hollow nanocages derived from polymer/cobalt complexes for electrochemical overall water splitting. *ACS Sustain. Chem. Eng.* 7, 10912–10919. doi: 10.1021/acssuschemeng.9b01789

Ding, Y., Klyushin, A., Huang, X., Jones, T., Teschner, D., Girgsdies, F., et al. (2018). Cobalt-bridged ionic liquid polymer on a carbon nanotube for enhanced oxygen evolution reaction activity. *Angew. Chem. Int. Ed.* 57, 3514–3518. doi: 10.1002/anie.201711688

Fu, Q., Wu, T., Fu, G., Gao, T., Han, J., Yao, T., et al. (2018). Skutterudite-type ternary Co1–xNixP3 nanoneedle array electrocatalysts for enhanced hydrogen and oxygen evolution. *ACS Energy Lett.* 3, 1744–1752. doi: 10.1021/acsenergylett.8b00908

Guo, Y., Yuan, P., Zhang, J., Hu, Y., Amiinu, I. S., Wang, X., et al. (2018). Carbon nanosheets containing discrete Co-Nx-By-C active sites for efficient oxygen

electrocatalysis and rechargeable Zn-air batteries. *ACS Nano* 12, 1894–1901. doi: 10.1021/acsnano.7b08721

Han, X., Yu, C., Huang, H., Guo, W., Zhao, C., Huang, H., et al. (2019). Phase controllable synthesis of Ni2+ post-modified CoP nanowire for enhanced oxygen evolution. *Nano Energy* 62, 136–143. doi: 10.1016/j.nanoen.2019.04.088

Hou, C.-C., Chen, Q.-Q., Li, K., Wang, C.-J., Peng, C.-Y., Shi, R., et al. (2019). Tailoring three-dimensional porous cobalt phosphides templated from bimetallic metal–organic frameworks as precious metal-free catalysts towards the dehydrogenation of ammonia-borane. *J. Mater. Chem. A* 7, 8277–8283. doi: 10.1039/C9TA00607A

Hu, E., Feng, Y., Nai, J., Zhao, D., Hu, Y., and Lou, X. W. (2018). Construction of hierarchical Ni–Co–P hollow nanobricks with oriented nanosheets for efficient overall water splitting. *Energy Environ. Sci.* 11, 872–880. doi: 10.1039/C8EE00076J

Hu, X., Chen, Y., Huang, B., Liu, Y., Huang, H., and Xie, Z. (2019a). Pd-supported N/S-codoped graphene-like carbons boost quinoline hydrogenation activity. *ACS Sustain. Chem. Eng.* 7, 11369–11376. doi: 10.1021/acssuschemeng.9b01015

Hu, X., Zhang, S., Sun, J., Yu, L., Qian, X., Hu, R., et al. (2019b). 2D Fe-containing cobalt phosphide/cobalt oxide lateral heterostructure with enhanced activity for oxygen evolution reaction. *Nano Energy* 56, 109–117. doi: 10.1016/j.nanoen.2018.11.047

Huang, B., Hu, X., Liu, Y., Qi, W., and Xie, Z. (2019). Biomolecule-derived N/S co-doped CNT-graphene hybrids exhibiting excellent electrochemical activities. *J. Power Sources* 413, 408–417. doi: 10.1016/j.jpowsour.2018.12.047

Huang, B., Liu, Y., Huang, X., and Xie, Z. (2018). Multiple heteroatom-doped few-layer carbons for the electrochemical oxygen reduction reaction. *J. Mater. Chem. A* 6, 22277–22286. doi: 10.1039/C8TA06743K

Huang, B., Liu, Y., and Xie, Z. (2017). Biomass derived 2D carbons via a hydrothermal carbonization method as efficient bifunctional ORR/HER electrocatalysts. *J. Mater. Chem. A* 5, 23481–23488. doi: 10.1039/C7TA08052B

Jiang, M., Li, J., Li, J., Zhao, Y., Pan, L., Cao, Q., et al. (2019). Two-dimensional bimetallic phosphide ultrathin nanosheets as non-noble electrocatalysts for a highly efficient oxygen evolution reaction. *Nanoscale* 11, 9654–9660. doi: 10.1039/C8NR10521A

Lei, C., Chen, H., Cao, J., Yang, J., Qiu, M., Xia, Y., et al. (2018). Fe N4 sites embedded into carbon nanofiber integrated with electrochemically exfoliated graphene for oxygen evolution in acidic medium. *Adv. Energy Mater.* 8:1801912. doi: 10.1002/aenm.201801912

Li, H., Xu, S. M., Yan, H., Yang, L., and Xu, S. (2018a). Cobalt Phosphide composite encapsulated within N,P-doped carbon nanotubes for synergistic oxygen evolution. *Small* 14:1800367. doi: 10.1002/smll.201800367

Li, L., Song, L., Xue, H., Jiang, C., Gao, B., Gong, H., et al. (2019). CoP nanoparticles encapsulated by graphitic layers and anchored to N-doped carbon nanoplates for enhanced bifunctional electrocatalytic properties for overall water splitting. *Carbon* 150, 446–454. doi: 10.1016/j.carbon.2019.05.034

Li, X., Lei, H., Liu, J., Zhao, X., Ding, S., Zhang, Z., et al. (2018b). Carbon nanotubes with cobalt corroles for hydrogen and oxygen evolution in pH 0-14 solutions. *Angew. Chem. Int. Ed.* 57, 15070–15075. doi: 10.1002/anie.201807996

Li, Y., Zhang, H., Jiang, M., Zhang, Q., He, P., and Sun, X. (2017). 3D self-supported Fe-doped Ni2P nanosheet arrays as bifunctional catalysts for overall water splitting. *Adv. Funct. Mater.* 27:1702513. doi: 10.1002/adfm.201702513

Lin, Y., Yang, L., Zhang, Y., Jiang, H., Xiao, Z., Wu, C., et al. (2018). Defective carbon-CoP nanoparticles hybrids with interfacial charges polarization for efficient bifunctional oxygen electrocatalysis. *Adv. Energy Mater.* 8:1703623. doi: 10.1002/aenm.201703623

Liu, K., Zhang, C., Sun, Y., Zhang, G., Shen, X., Zou, F., et al. (2018). High-performance transition metal phosphide alloy catalyst for oxygen evolution reaction. *ACS Nano* 12, 158–167. doi: 10.1021/acsnano.7b04646

Liu, Y., Huang, B., Hu, X., and Xie, Z. (2019a). Surfactant-assisted hydrothermal synthesis of nitrogen doped Mo2C@C composites as highly efficient electrocatalysts for hydrogen evolution reaction. *Int. J. Hydrogen Energy* 44, 3702–3710. doi: 10.1016/j.ijhydene.2018.12.096

Liu, Y., Huang, B., Zhang, X., Huang, X., and Xie, Z. (2019b). *In-situ* fabrication of nitrogen-doped carbon nanosheets containing highly dispersed single iron atoms for oxygen reduction reaction. *J. Power Sources* 412, 125–133. doi: 10.1016/j.jpowsour.2018.11.024

Lu, Y., Hou, W., Yang, D., and Chen, Y. (2019). CoP nanosheets in-situ grown on N-doped graphene as an efficient and stable bifunctional electrocatalyst for hydrogen and oxygen evolution reactions. *Electrochim. CTA* 307, 543–552. doi: 10.1016/j.electacta.2019.03.208

Miao, Z., Wang, X., Tsai, M.-C., Jin, Q., Liang, J., Ma, F., et al. (2018). Atomically dispersed Fe-N x /C electrocatalyst boosts oxygen catalysis via a new metal-organic polymer supramolecule strategy. *Adv. Energy Mater.* 8:1801226. doi: 10.1002/aenm.201801226

Qiu, B., Cai, L., Wang, Y., Lin, Z., Zuo, Y., Wang, M., et al. (2018). Fabrication of nickel-cobalt bimetal phosphide nanocages for enhanced oxygen evolution catalysis. *Adv. Funct. Mater.* 28:1706008. doi: 10.1002/adfm.201706008

Qu, K., Zheng, Y., Dai, S., and Qiao, S. Z. (2016). Graphene oxide-polydopamine derived N, S-codoped carbon nanosheets as superior bifunctional electrocatalysts for oxygen reduction and evolution. *Nano Energy* 19, 373–381. doi: 10.1016/j.nanoen.2015.11.027

Shan, J., Guo, C., Zhu, Y., Chen, S., Song, L., Jaroniec, M., et al. (2019). Charge-redistribution-enhanced nanocrystalline Ru@IrOx electrocatalysts for oxygen evolution in acidic media. *Chem* 5, 445–459. doi: 10.1016/j.chempr.2018.11.010

Tan, B., Wu, Z.-F., and Xie, Z.-L. (2017). Fine decoration of carbon nanotubes with metal organic frameworks for enhanced performance in supercapacitance and oxygen reduction reaction. *Sci. Bull.* 62, 1132–1141. doi: 10.1016/j.scib.2017.08.011

Teng, Y., Wang, X.-D., Liao, J.-F., Li, W.-G., Chen, H.-Y., Dong, Y.-J., et al. (2018). Atomically thin defect-rich Fe-Mn-O hybrid nanosheets as high efficient electrocatalyst for water oxidation. *Adv. Funct. Mater.* 28:1802463. doi: 10.1002/adfm.201802463

Xiao, X., He, C.-T., Zhao, S., Li, J., Lin, W., Yuan, Z., et al. (2017). A general approach to cobalt-based homobimetallic phosphide ultrathin nanosheets for highly efficient oxygen evolution in alkaline media. *Energy Environ. Sci.* 10, 893–899. doi: 10.1039/C6EE03145E

Yan, L., Cao, L., Dai, P., Gu, X., Liu, D., Li, L., et al. (2017). Metal-organic frameworks derived nanotube of nickel-cobalt bimetal phosphides as highly efficient electrocatalysts for overall water splitting. *Adv. Funct. Mater.* 27:1703455. doi: 10.1002/adfm.201703455

Yang, S., Chen, L., Wei, W., Lv, X., and Xie, J. (2019a). CoP nanoparticles encapsulated in three-dimensional N-doped porous carbon for efficient hydrogen evolution reaction in a broad pH range. *Appl. Surf. Sci.* 476, 749–756. doi: 10.1016/j.apsusc.2019.01.131

Yang, S., Xie, M., Chen, L., Wei, W., Lv, X., Xu, Y., et al. (2019b). Cobalt phosphide nanoparticles embedded in 3D N-doped porous carbon for efficient hydrogen and oxygen evolution reactions. *Int. J. Hydrogen Energy* 44, 4543–4552. doi: 10.1016/j.ijhydene.2019.01.036

Yuan, H., Hou, Y., Wen, Z., Guo, X., Chen, J., and He, Z. (2015). Porous carbon nanosheets codoped with nitrogen and sulfur for oxygen reduction reaction in microbial fuel cells. *ACS Appl. Mater. Interfaces* 7, 18672–18678. doi: 10.1021/acsami.5b05144

Yuan, W., Wang, X., Zhong, X., and Li, C. M. (2016). CoP nanoparticles *in situ* grown in three-dimensional hierarchical nanoporous carbons as superior electrocatalysts for hydrogen evolution. *ACS Appl. Mater. Interfaces* 8, 20720–20729. doi: 10.1021/acsami.6b05304

Zhang, G., Wang, B., Bi, J., Fang, D., and Yang, S. (2019). Constructing ultrathin CoP nanomeshes by Er-doping for highly efficient bifunctional electrocatalysts for overall water splitting. *J. Mater. Chem. A* 7, 5769–5778. doi: 10.1039/C9TA00530G

Zhang, Y., Wu, C., Jiang, H., Lin, Y., Liu, H., He, Q., et al. (2018). Atomic iridium incorporated in cobalt hydroxide for efficient oxygen evolution catalysis in neutral electrolyte. *Adv. Mater.* 30:1707522. doi: 10.1002/adma.201707522

Zheng, H., Huang, X., Gao, H., Lu, G., Li, A., Dong, W., et al. (2019). Cobalt-tuned nickel phosphide nanoparticles for highly efficient electrocatalysis. *Appl. Surf. Sci.* 479, 1254–1261. doi: 10.1016/j.apsusc.2019.01.258

Conflict of Interest: The authors declare that the research was conducted in the absence of any commercial or financial relationships that could be construed as a potential conflict of interest.

frontiers in Chemistry

ORIGINAL RESEARCH
published: 17 January 2020
doi: 10.3389/fchem.2019.00940

Visible-Light-Induced C–C Coupling Reaction to Synthesize Bipyridine From 3-Cyano-1,4-Dihydropyridines

Shijun Chen[1], Qidi Zhong[1], Hao Zhu[2]*, Chunyan Liu[1], Pengyu Zhuang[1] and Wuji Sun[2]*

[1] School of Pharmacy, North China University of Science and Technology, Tangshan, China, [2] School of Public Health, North China University of Science and Technology, Tangshan, China

A concise and efficient photocatalytic C–C coupling of 1-benzyl-3-cyano-1, 4-dihydropyridine for synthesis of 1,1′-dibenzyl-3, 3′-dicyano-1,1′,4,4′-tetrahydro-4, 4′-bipyridine is described. The reporter system provides a novel technique that facilitates synthesis of C–C coupling derivatives without addition of transition metals and oxidants or other additives. A plausible synthetic pathway is proposed, and the coupling product was characterized via nuclear magnetic resonance spectroscopy (^{1}H and ^{13}C NMR), high-resolution electrospray ionization mass spectrometry (ESI-HRMS) and X-ray analyses.

Keywords: photocatalytic, C–C coupling, pyridines, radical reactions, 1,4-dihydropyridine

OPEN ACCESS

Edited by:
Francis Verpoort, Wuhan University of Technology, China

Reviewed by:
Balaraman Ekambaram, National Chemical Laboratory (CSIR), India
Metwally Madkour, Kuwait University, Kuwait

***Correspondence:**
Qidi Zhong
qidizhong@hotmail.com
Hao Zhu
haoyue570126@163.com

Specialty section:
This article was submitted to Catalysis and Photocatalysis, a section of the journal Frontiers in Chemistry

Received: *17 September 2019*
Accepted: *24 December 2019*
Published: *17 January 2020*

Citation:
Chen S, Zhong Q, Zhu H, Liu C, Zhuang P and Sun W (2020) Visible-Light-Induced C–C Coupling Reaction to Synthesize Bipyridine From 3-Cyano-1,4-Dihydropyridines. Front. Chem. 7:940. doi: 10.3389/fchem.2019.00940

INTRODUCTION

Coupling of pyridines and diazines results in the generation of heterobiaryls, a privileged pharmacophore found in commercial drugs as well as numerous therapeutic candidates, such as the examples in **Figure 1** (Capdeville et al., 2002; Martina et al., 2005; Roecker et al., 2014). These heterocycles often play a key role in drug-receptor binding and confer other important properties, such as net polarity, aqueous solubility, and resistance to oxidative metabolism (Hilton et al., 2018; Zhang et al., 2019). The most common aryl-aryl coupling is achieved through metal-catalyzed cross-coupling reactions (Tahsini et al., 2019). C–C coupling reactions have become fundamental routes in natural product synthesis, materials science, biological-, medicinal-, and supramolecular chemistry, in addition to catalysis, coordination chemistry and polymer synthesis (Cocuzza et al., 1999; Akihiro et al., 2007; Heravi and Hashemi, 2012).

While C–C bond generation methods are effective reliable, these reactions require pre-activation steps, such as halogenation or metallization of reactants, thereby increasing the number of reaction steps and chemical reagents, and reducing the efficiency of synthesis.

Photocatalysis has developed significantly over the past decade, making possible synthetic transformations that were previously impossible (Ravelli et al., 2016; Romero and Nicewicz, 2016; She et al., 2018). The photochemical reaction does not require additional additives or reagents, thus embodying the concept of green chemistry (Norbert, 2008; Fan et al., 2017). To date, photochemical reactions have been applied to various fields of organic chemistry as eco-friendly and efficient synthesis method, including metal catalysis (Condie et al., 2010), green organic synthesis (Yu et al., 2018), total synthesis (Reddy and Rawal, 2000) and asymmetric synthesis (Richard et al., 2015) of compounds. Photosensitive 1,4-dihydropyridine is often used as a photoreactive substrate for various reactions under light-induced conditions, such as photoinduced rearrangement (Zhong et al., 2017), aromatization (Memarian and Mirjafari, 2005), and [2+2] photocycloaddition reactions (Eisner et al., 1970; Hilgeroth et al., 2000; Hilgeroth and Baumeister, 2001).

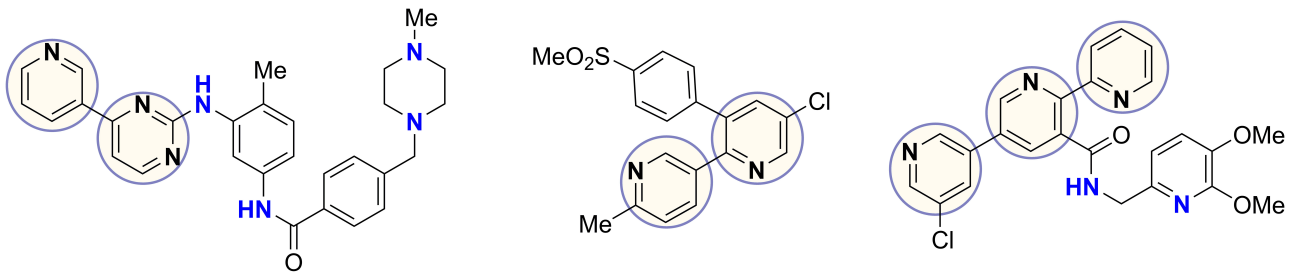

FIGURE 1 | Important heterobiaryl containing drugs.

Unexpectedly, the photoreaction product of 1,4-dihydropyridine we obtained was distinct from that reported previously. In the absence of electrochemical reduction (Carelli et al., 1998), photocatalysis can directly promote activation of sp3 bonds to form a coupled product form a coupled product (**Scheme 1**).

Based on earlier literature and our research on visible-light, we have developed a novel method for the construction of C–C bonds via visible light catalysis using 3-cyano-1,4-dihydropyridine as the light substrate and ethanol as solvent (**Scheme 1**). The visible-light-activated C-H bond is used for selective formation of new C–C bonds. This method has a number of advantages: (1) the reaction is carried out with no requirement for catalyst and transition metal, (2) the solvent is environmentally friendly, non-toxic and easy to use, and (3) reaction specificity and conversion rates are high, with few by-products.

MATERIALS AND METHODS

General Information

Unless otherwise specified, all commercial reagents and solvents were used without further purification. Melting points were uncorrected and determined in open capillary tubes with WRX-4 micro melting point apparatus (China). Mass spectra (ESI-HRMS) were recorded on an Agilent Accurate-Mass Q-TOF LC/MS 6520 instrument. ^{1}H NMR and ^{13}C NMR spectra were recorded at 400 and 500 MHz using deuterated $CDCl_3$ or DMSO-d_6 solvent. Chemical shifts were expressed as parts per million (δ) relative to tetramethylsilane (TMS). Data are presented as follows order: chemical shift (δ) in ppm whereby; multiplicities are indicated as s (singlet), d (doublet), t (triplet), q (quartet), dd (doublet of doublets), td (triplet of doublets), tt (triplet of triplets), ddd (doublet of doublet of doublets), m (multiplet), qui (quint), sext (sextet), h(hept); coupling constants (*J*) in Hertz (Hz). Single-crystal X-ray diffraction was performed on a Bruker APEX-II instrument. Silica gel (200–300 mesh) for column chromatography and silica GF254 for TLC were obtained from Qingdao Marine Chemical Company (China).

Preparation of Starting Materials

Substrates 1 (1a−1t) were synthesized according to documented literature (Paul et al., 2013), with slight modifications. In brief, benzyl bromide (40 mmol) was added to 3-cyanopyridine (4.16 g, 40 mmol) using acetonitrile (40 mL) as the solvent. The mixture was reacted for 7 h, and diethyl ether was added after cooling to precipitate the product. After filtering, the mixture was rinsed with ether three times (3 × 10 mL) and the bromide salt obtained as a powder. Under nitrogen atmosphere, bromide salt (10.9 mmol) was dissolved in H_2O (60 mL) and mixed with $NaHCO_3$ (3.06 g, 36.4 mmol). Sodium dithionite (7.59 g, 43.6 mmol) was added slowly in stages and the reaction mixture stirred at room temperature for 1–3 h in the dark, during which time the solution was observed as a yellow precipitate. The solid was filtered, and washed with pure water (3 × 10 mL) to generate product **1a−1t** as a yellow powder (**Supplementary Material**).

General Procedure for Synthesis of Compounds 2a−2t

1a−1t (5 mmol) was dissolved in 25 mL absolute ethanol and placed in a three-necked quartz round bottomed flask. Argon-protection LED with a wavelength of 410 nm was used as the light source. After 3 days, the solvent was removed under reduced pressure and the crude reaction mixture was directly charged on silica gel and purified via column chromatography (petroleum ether/ethyl acetate rations of 4:1–5:1) to generate the corresponding 2a−2t product.

Characterization of Products 2a

Synthesized according to the general procedure; Mp = 145–146°C (from CH_3OH); ^{1}H NMR (400 MHz, DMSO-d_6): δ 7.40–7.26 (m, 12H), 6.08 (dd, J = 8, 1.2 Hz, 2H), 4.58 (dd, J = 8, 3.6 Hz, 2H), 4.42 (s, 4H), 3.19 (d, J = 3.6 Hz, 2H) ppm; ^{13}C NMR (100 MHz, DMSO-d_6) δ 145.6, 137.9, 130.9, 129.0, 128.0, 127.8, 121.3, 101.7, 77.3, 56.4 ppm; HRMS (ESI): $C_{26}H_{22}N_4$ $[M+H]^+$: 391.1878; found: 391.1897.

Characterization of Products 2b

Synthesized according to the general procedure; Mp = 182–183°C (from CH_3OH); ^{1}H NMR (500 MHz, $CDCl_3$): δ 7.28

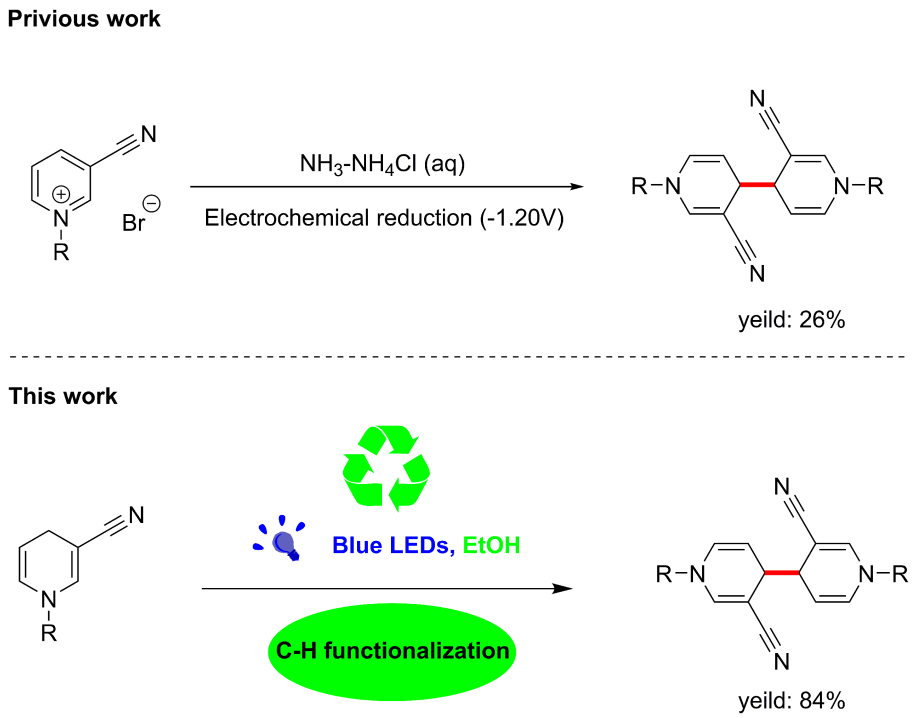

SCHEME 1 | C–C coupling reaction of visible-light-catalyzed 1,4-dihydropyri-dine derivative.

(d, J = 8, 2H), 7.30–7.26 (m, 2H), 7.22–7.17 (m, 4H), 6.74(d, J = 1.5, 2H), 5.9 (dd, J = 8.5, 1.5 Hz, 2H), 4.77 (dd, J = 8 3.5 Hz, 2H), 4.36(s, 4H), 3.44 (d, J = 3.5 Hz, 2H) ppm; ^{13}C NMR (125 MHz, $CDCl_3$) δ 144.2, 135.3, 133.3, 129.9, 129.8, 129.3, 127.8, 123.2, 120.6, 103.0, 79.5, 57.4, 39.6 ppm; HRMS (ESI): $C_{26}H_{20}Br_2N_4$ $[M+H]^+$: 547.0088; found: 547.0107.

Characterization of Products 2c

Synthesized according to the general procedure; Mp = 174–175°C (from CH_3OH); ^{1}H NMR (400 MHz, DMSO-d_6): δ 7.46–7.43 (m, 2H), 7.33–7.27 (m, 8H), 6.13 (d, J = 8.4 Hz, 2H), 4.66 (dd, J = 8, 3.6 Hz, 2H), 4.51 (s, 4H), 3.22 (d, J = 3.6 Hz, 2H) ppm; ^{13}C NMR (100 MHz, DMSO-d_6) δ 145.8, 135.3, 132.5, 130.9, 129.9, 129.7, 129.5, 127.9, 121.1, 102.0, 77.7, 54.2, 39.6 ppm; HRMS (ESI): $C_{26}H_{20}Cl_2N_4$ $[M+H]^+$: 459.1098; found: 459.1088.

Characterization of Products 2d

Synthesized according to the general procedure; Mp = 135–136°C (from CH_3OH); ^{1}H NMR (400 MHz, DMSO-d_6): δ 7.39–7.34 (m, 2H), 7.29 (d, J = 1.5 Hz, 2H), 7.11–7.04 (m, 6H), 6.06 (dd, J = 8, 1.2 Hz, 2H), 4.51 (dd, J = 8, 3.6 Hz, 2H), 4.41 (s, 4H), 3.17 (d, J = 3.2 Hz, 2H) ppm; ^{13}C NMR (100 MHz, DMSO-d_6) δ 163.9, 161.4, 145.6, 145.5, 140.9, 131.1, 131.0, 130.8, 130.6, 123.7, 121.2, 114.8, 114.6, 114.4, 102.0, 101.8, 77.7, 55.8, 39.5 ppm; HRMS (ESI): $C_{26}H_{20}F_2N_4$ $[M+H]^+$: 427.1689; found: 427.1676.

Characterization of Products 2e

Synthesized according to the general procedure; Mp = 155–157°C (from CH_3OH); ^{1}H NMR (400 MHz, DMSO-d_6): δ 7.20–7.12 (m, 10H), 6.12 (dd, J = 8.4, 1.2 Hz, 2H), 4.64 (dd, J = 8, 3.6 Hz, 2H), 4.42 (s, 4H), 3.25 (d, J = 3.2 Hz, 2H), 2.21 (s, 6H) ppm; ^{13}C NMR (100 MHz, DMSO-d_6) δ 145.7, 136.2, 135.9, 131.1, 130.7, 127.9, 127.8, 126.5, 121.3, 101.7, 77.4, 54.6, 39.7, 19.2 ppm; HRMS (ESI): $C_{28}H_{26}N_4$ $[M+H]^+$: 419.2191; found: 419.2188.

Characterization of Products 2f

Synthesized according to the general procedure; Mp = 122–124°C (from CH_3OH); ^{1}H NMR (500 MHz, $CDCl_3$): δ 7.24–7.21 (t, J = 8 Hz 2H), 6.80 (dd, J = 8, 1.5 Hz, 2H), 6.72 (t, J = 7.5 Hz, 6H), 5.91 (dd, J = 8 1 Hz, 2H), 4.72 (dd, J = 8 3.5 Hz, 2H), 4.24 (s, 4H) 3.76 (s, 6H), 3.39 (s, 2H) ppm; ^{13}C NMR (125 MHz, $CDCl_3$) δ 160.1, 144.2, 137.9, 130.2, 130.0, 120.8, 119.4, 113.4, 112.8, 102.7, 79.1, 57.4, 55.3, 39.6 ppm; HRMS (ESI): $C_{26}H_{20}Br_2N_4$ $[M+H]^+$: 547.0088; found: 547.0083.

Characterization of Products 2g

Synthesized according to the general procedure; Mp = 134–136°C (from CH_3OH); ^{1}H NMR (500 MHz, $CDCl_3$): δ 7.43–7.08 (m, 8H), 6.72 (d, J = 1.5 Hz, 2H), 6.58 (dd, J = 8 1.5 Hz, 2H), 4.75 (dd, J = 8 3.5 Hz, 2H), 4.28 (d, J = 2 Hz, 4H), 3.41 (d, J = 3.5 2H) ppm; ^{13}C NMR (125 MHz, $CDCl_3$) δ 144.7, 144.0, 138.7, 131.3, 130.5, 130.2, 130.1, 129.7, 126.0, 125.8, 123.0, 120.5, 103.0, 102.9, 79.6, 57.1, 57.0, 40.7, 39.5 ppm; HRMS (ESI): $C_{26}H_{20}Br_2N_4$ $[M+H]^+$: 547.0088; found: 547.0083.

Characterization of Products 2h

Synthesized according to the general procedure; Mp = 128–130°C (from CH_3OH); ^{1}H NMR (500 MHz, $CDCl_3$): δ 7.26–7.22(m, 4H), 7.15 (s, 2H), 7.05 (d, J = 4 Hz, 2H), 6.72(s, 2H), 5.95 (d, J = 8 Hz, 2H), 4.76 (dd, J = 8 3 Hz, 2H), 4.28 (d, J = 2.5 Hz, 4H), 3.42 (d, J = 3.5 Hz, 2H) ppm; ^{13}C NMR (125 MHz, $CDCl_3$) δ 144.0, 138.5, 134.8, 130.1, 128.3, 127.1, 125.3, 102.4, 103.0, 79.7, 77.2, 57.0, 39.5 ppm; HRMS (ESI): $C_{26}H_{20}Cl_2N_4$ $[M+H]^+$: 459.1098; found: 459.1097.

Characterization of Products 2i

Synthesized according to the general procedure; Mp = 129–130°C (from CH_3OH); ^{1}H NMR (500 MHz, $CDCl_3$): δ 7.34–7.30 (m, 2H), 7.18–7.05 (m, 6H), 6.72 (d, J = 1 Hz, 2H), 5.82 (dd, J = 8 1.5 Hz, 2H), 4.65 (dd, J = 8 3.5 Hz, 2H), 4.29 (s, 4H), 3.34 (d, J = 3.5 2H) ppm; ^{13}C NMR (125 MHz, $CDCl_3$) δ 161.7, 159.7, 144.0, 130.2, 129.6, 124.5, 123.4, 123.3, 120.6, 115.9, 115.7, 102.7, 79.3, 77.2, 51.5, 39.5 ppm; HRMS (ESI): $C_{26}H_{20}F_2N_4$ $[M+H]^+$: 427.1689; found: 427.1683.

Characterization of Products 2j

Synthesized according to the general procedure; Mp = 121–123°C (from CH_3OH); ^{1}H NMR (400 MHz, DMSO-d_6): δ 7.25–7.13 (m, 10H), 6.01 (dd, J = 8.4, 1.2 Hz, 2H), 4.53 (dd, J = 8, 3.2 Hz, 2H), 4.32 (s, 4H), 3.25 (d, J = 3.6 Hz, 2H), 2.27 (S, 6H) ppm; ^{13}C NMR (100 MHz, DMSO-d_6) δ 145.5, 137.2, 134.8, 130.8, 129.5, 127.8, 121.3, 101.7, 77.2, 56.2, 39.6, 21.1 ppm; HRMS (ESI): $C_{28}H_{26}N_4$ $[M+H]^+$: 419.2191; found: 419.2205.

Characterization of Products 2k

Synthesized according to the general procedure; Mp = 155–156°C (from CH_3OH); ^{1}H NMR (500 MHz, $CDCl_3$): δ 7.45 (d, J = 8.5 Hz, 4H), 7.04 (d, J = 8.5 Hz, 4H), 6.69 (d, J = 1.5 Hz, 2H), 5.83 (dd, J = 8.5 1.5 Hz, 2H), 4.71 (dd, J = 8 4 Hz, 2H), 4.23 (s, 4H), 3.39 (d, J = 4 Hz, 2H) ppm; ^{13}C NMR (125 MHz, $CDCl_3$) δ 144.1, 135.1, 132.1, 129.8, 128.9, 122.2, 120.5, 103.2, 79.6, 77.2, 57.0, 39.7 ppm; HRMS (ESI): $C_{26}H_{20}Br_2N_4$ $[M+H]^+$: 547.0088; found: 547.0081.

Characterization of Products 2l

Synthesized according to the general procedure; Mp = 160–161°C (from CH_3OH); ^{1}H NMR (400 MHz, DMSO-d_6): δ 7.29–7.11 (m, 10H), 6.06 (dd, J = 8.4, 0.8 Hz, 2H), 4.58 (dd, J = 8.4, 3.6 Hz, 2H), 4.41 (s, 4H), 3.16 (d, J = 3.6 Hz, 2H) ppm; ^{13}C NMR (100 MHz, DMSO-d_6) δ 163.2, 160.8, 145.5, 134.2, 134.1, 130.8, 129.9, 129.8, 121.3, 115.8, 115.6, 101.9, 77.4, 55.6, 39.5 ppm; HRMS (ESI): $C_{26}H_{20}F_2N_4$ $[M+H]^+$: 427.1689; found: 427.1687.

Characterization of Products 2m

Synthesized according to the general procedure; Mp = 163–165°C (from CH_3OH); ^{1}H NMR (500 MHz, $CDCl_3$): δ 7.38(d, J = 8 Hz, 2H), 7.23 (d, J = 2 Hz, 2H), 7.01 (dd, J = 9.5 3 Hz, 2H), 6.73 (d, J = 1.5 Hz, 2H), 5.94 (dd, J = 8, 1 Hz, 2H), 4.79 (dd, J = 8.5, 4 Hz, 2H), 4.26 (d, J = 3 4H), 3.43 (d, J = 3.5 Hz, 2H) ppm; ^{13}C NMR (125 MHz, $CDCl_3$) δ 144.0, 136.6, 133.0, 132.3, 130.9, 129.9, 128.8, 126.4, 120.3, 103.3, 79.9, 56.5, 39.6 ppm; HRMS (ESI): $C_{26}H_{18}Cl_4N_4$ $[M+H]^+$: 527.0319; found: 527.0312.

Characterization of Products 2n

Synthesized according to the general procedure; Mp = 157–158°C (from CH_3OH); ^{1}H NMR (500 MHz, $CDCl_3$): δ 7.05–7.00 (m, 2H), 6.98–6.89 (m, 4H), 6.74 (d, J = 1.5 Hz, 2H), 5.89 (dd, J = 8, 1.5 Hz, 2H), 4.75 (q, J = 4 Hz, 2H), 4.31 (s, 4H), 3.41 (d, J = 4 Hz, 2H) ppm; ^{13}C NMR (125 MHz, $CDCl_3$) δ 159.6, 157.7, 157.4, 157.3, 155.4, 143.9, 129.8, 125.4, 125.3, 125.2, 125.2, 120.2, 117.0, 116.8, 116.4, 116.3, 116.2, 116.1, 115.7, 115.5, 103.1, 79.9, 51.3, 39.3 ppm; HRMS (ESI): $C_{26}H_{18}F_4N_4$ $[M+H]^+$: 463.1501; found: 463.1493.

Characterization of Products 2o

Synthesized according to the general procedure; Mp = 133–135°C (from CH_3OH); ^{1}H NMR (500 MHz, $CDCl_3$): δ 7.19–7.14(td, J = 8.5, 6.5 Hz, 2H), 6.89–6.82 (m, 4H), 6.72 (s, 2H), 5.83 (dd, J = 8, 1 Hz, 2H), 4.66 (dd, J = 6.4 2.8 Hz, 2H), 4.26 (s, 4H), 3.34 (d, J = 3.5 Hz, 2H) ppm; ^{13}C NMR (125 MHz, $CDCl_3$) δ 164.0, 163.9, 162.0, 161.9, 161.8, 159.9, 159.8, 143.8, 130.6, 130.5, 129.4, 120.5, 119.4, 119.3, 111.8, 111.7, 111.6, 104.6, 104.4, 104.2, 103.0, 79.6, 51.1, 39.59 ppm; HRMS (ESI): $C_{26}H_{18}F_4N_4$ $[M+H]^+$: 463.1501; found: 463.1487.

Characterization of Products 2p

Synthesized according to the general procedure; Mp = 149–151°C (from CH_3OH); ^{1}H NMR (500 MHz, $CDCl_3$): δ 7.12 (dt, J = 10 8.5 Hz, 2H), 7.01–6.97 (m, 2H), 6.93–6.90 (m, 2H), 6.72 (d, J = 1.5 Hz, 2H), 5.90 (dd, J = 8.5 1.2 Hz, 2H), 4.78 (dd, J = 8.5, 4 Hz, 2H), 4.27 (d, J = 3 4H), 3.43 (d, J = 3.5 Hz, 2H) ppm; ^{13}C NMR (125 MHz, $CDCl_3$) δ 151.5, 151.4, 151.0, 150.9, 149.6, 149.5, 149.0, 148.9, 144.0, 133.4, 133.3, 129.9, 123.2, 120.3, 117.9, 117.8, 116.1, 116.0, 103.4, 79.9, 56.5, 39.7 ppm; HRMS (ESI):$C_{26}H_{18}F_4N_4$ $[M+H]^+$: 463.1501; found: 463.1500.

Characterization of Products 2q

Synthesized according to the general procedure; Mp = 185–186°C (from CH_3OH); ^{1}H NMR (500 MHz, $CDCl_3$): δ 7.52 (dd, J = 9, 5.5 Hz, 2H), 6.99 (dd, J = 9 3 Hz, 2H), 6.89–6.85 (m, 2H), 5.9 (d, J = 1, Hz, 2H), 5.97 (d, J = 6 Hz, 2H), 4.88 (dd, J = 8.5, 3.5 Hz, 2H), 4.39–4.31 (m, 4H), 4.36 (d, J = 3.5 Hz, 2H) ppm; ^{13}C NMR (125 MHz, $CDCl_3$) δ 163.1, 161.1, 144.1, 137.9, 134.5, 130.2, 120.1, 116.6, 116.5, 116.1, 115.9, 103.3, 80.1, 77.2, 57.4, 39.4 ppm; HRMS (ESI): $C_{26}H_{18}Br_2F_2N_4$ $[M+H]^+$: 582.9899; found: 582.9886.

Characterization of Products 2r

Synthesized according to the general procedure; Mp = 132–133°C (from CH_3OH); ^{1}H NMR (500 MHz, $CDCl_3$): δ 6.64 (d, J = 1.5 Hz, 2H), 5.86 (dd, J = 8.5 1.5 Hz, 2H), 4.70 (dd, J = 8 3.5 Hz, 2H), 3.34 (d, J = 3.5 Hz, 2H), 2.97 (s, 6H) ppm; ^{13}C NMR (125 MHz, $CDCl_3$) δ 144.7, 130.5, 121.0, 102.9, 78.4, 40.9, 39.6 ppm; HRMS (ESI): $C_{14}H_{14}N_4$ $[M+H]^+$: 239.1252; found: 239.1249.

Characterization of Products 2s

Synthesized according to the general procedure; Mp = 128–129°C (from CH_3OH); ^{1}H NMR (500 MHz, $CDCl_3$): δ 6.66 (d, J = 1.5 Hz, 2H), 5.89 (dd, J = 8 1.5 Hz, 2H), 4.70 (dd, J = 8.5 4 Hz, 2H), 3.36 (d, J = 3.5 Hz, 2H), 3.12–3.03 (m, 4H), 1.59–1.53 (m, 4H), 0.91 (t, J = 7.5 Hz, 6H) ppm; ^{13}C NMR (125 MHz, $CDCl_3$) δ

144.2, 129.8, 121.2, 102.5, 78.0, 55.9, 39.9, 23.1, 10.8 ppm; HRMS (ESI): $C_{18}H_{22}N_4$ $[M+H]^+$: 295.1878; found: 295.1876.

Characterization of Products 2t

Synthesized according to the general procedure; Mp = 99–101°C (from CH_3OH); ^1H NMR (500 MHz, $CDCl_3$): δ 6.75 (d, J = 1.5 Hz, 2H), 5.97 (d, J = 8 Hz, 2H), 4.73–4.70 (m, 2H), 3.36–3.35 (m, 2H), 3.06–2.95 (m, 4H), 1.00–0.93(m, 2H), 0.61–0.58 (m, 4H), 0.21 (q, J = 5 Hz, 4H) ppm; ^{13}C NMR (125 MHz, $CDCl_3$) δ 143.9, 130.0, 121.3, 102.4, 78.2, 77.3, 77.1, 76.9, 58.4, 39.9, 10.8, 3.4 ppm; HRMS (ESI):$C_{18}H_{22}N_4$ $[M+H]^+$: 319.1878; found: 319.1869.

Characterization of Products 3a

Synthesized according to the general procedure; ^1H NMR (400 MHz, DMSO-d_6): δ 7.47 (dd, J = 7.6 1.6 Hz, 1H), 7.39–7.28 (m, 3H), 7.08 (s, 1H), 6.14 (d, J = 5.2 Hz 1H), 4.65–4.61 (m, 2H), 4.43 (d, J = 16 Hz 1H), 2.32–2.23 (m, 1H), 2.05–1.99 (m, 1H) 1.85–1.79 (m, 1H), 1.59–1.50 (m, 1H) ppm; ^{13}C NMR (100 MHz, DMSO-d_6) δ 146.9, 135.8, 132.8, 130.0, 129.8, 129.6, 127.9, 123.0, 75.5, 74.4, 53.1, 28.0, 17.2 ppm; HRMS (ESI): $C_{13}H_{14}N_2O$ $[M+H]^+$: 214.1187; found: 214.1191.

RESULTS AND DISCUSSION

The majority of substituents of the photochemical reaction substrate, 1,4-dihydropyridine, at the −3-position are ester groups, with few reports of attachment of other groups at this position (Jin et al., 1998; Hilgeroth and Heinemann, 1999; Hilgeroth et al., 1999).

We initially used commercially available -cyano substituted pyridine as the model substrate under irradiation with blue LED light (**Table 1**).

The yield of 2a in acetone (Ace), tetrahydrofuran (THF), methanol, or 95% ethanol (EtOH) was moderate and reaction time was 57–67 h (entries 1–4). Interestingly, the amount of water in solvent was associated with reaction time. To further explore this result, a significant amount of water was added to alcohol. While the reaction time decrease with increasing moisture, yield of the corresponding product 2a was also decreases (entries 5, 6). Next, we examined the effect of an anhydrous solvent on the reaction. As expected, yield of 2a was successfully increased to 84% by limiting the amount of added water (entry 7). Notably, moisture in the air and impurities were contributory factors to decreased yield (entry 8). Data obtained from control experiments confirmed the necessity of light (entry 9). Irradiation with 365 nm and 450 nm sources not only prolonged the reaction time but also reduced yield of 2a (entries 10, 11). Simultaneously, a higher-power high-pressure mercury lamp was used for irradiation. In this case, reaction time was greatly reduced but no product 2a was generated (entry 12).

Irradiation of 1a (5 mmol) in anhydrous EtOH at ambient temperature under Ar atmosphere for 72 h were determined as the optional conditions. Next, we investigated the scope

TABLE 1 | Optimization of the reaction parameters[a].

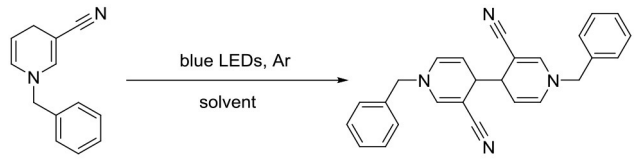

Entry	Solvent	Atmosphere	Light source[d]	Time (h)[b]	Yield (%)[c]
1	Ace	Ar	LED (410 nm)	59	54
2	THF	Ar	LED (410 nm)	57	46
3	MeOH	Ar	LED (410 nm)	67	68
4	95% EtOH	Ar	LED (410 nm)	62	65
5	EtOH/H_2O (1:1)	Ar	LED (410 nm)	42	33
6	EtOH/H_2O (1:2)	Ar	LED (410 nm)	39	25
7	EtOH	Ar	LED (410 nm)	72	84
8	EtOH	Air	LED (410 nm)	68	79
9	EtOH	Ar	–	72	Trace
10	EtOH	Ar	LED (365 nm)	82	64
11	EtOH	Ar	LED (450 nm)	78	60
12	EtOH	Ar	Hg-500 W	6	—

[a] *Irradiation of 1a (5 mmol) in various solvents (25 mL) with blue LED lamps at room temperature.*
[b] *Reaction time was determined based on complete consumption of 1a.*
[c] *Isolated yield.*
[d] *10 W blue LED, high-pressure mercury lamp (500 W).*

and generality of the photocatalytic coupling reaction 1,4-dihydropyridines by introducing different substituents under the established optimal conditions results are summarized in **Table 2**.

First, in the absence of a substituent on the benzyl group, yield of the product 2a reached 85%. When the benzyl group contained -F, -Cl, -Br, or -CH_3 in the ortho-position, yield with electron-withdrawing groups was superior to that with electron-donating groups (**Table 2**, 2b−2e). In cases where the substituent was in the meta- or para-position, good yield of the target product was obtained (**Table 2**, 2f−2l). With different positions of the same substituent product yield with the substituent in the para-position was higher than that the ortho- and meta-positions owing to a steric hindrance effect (**Table 2**, 2d, 2i, and 2l).

Notably, the benzyl group with multiple substituents generated a moderate yield (**Table 2**, 2m−2q). In addition, the benzyl group at the 1-position could be effectively replaced with an alkyl or cycloalkyl group (**Table 2**, 2r−2t).

The molecular structures of 2a and 3a are depicted in **Figure 2** (CCDC 1876160[1] and 1497344[2]). In the case of 4,4′-linked dimers, a maximum of three diastereoisomers could exist with, possible RR, SS or RS configurations. The reaction generated

[1]Crystallographic data for the compound 2a has been deposited with the CCDC 1876160.
[2]Crystallographic data for the compound 3a has been deposited with the CCDC 1497344.

TABLE 2 | Scope and generality of coupling reactions of 1,4-dihydropyridine derivatives under photocatalytic conditions[a].

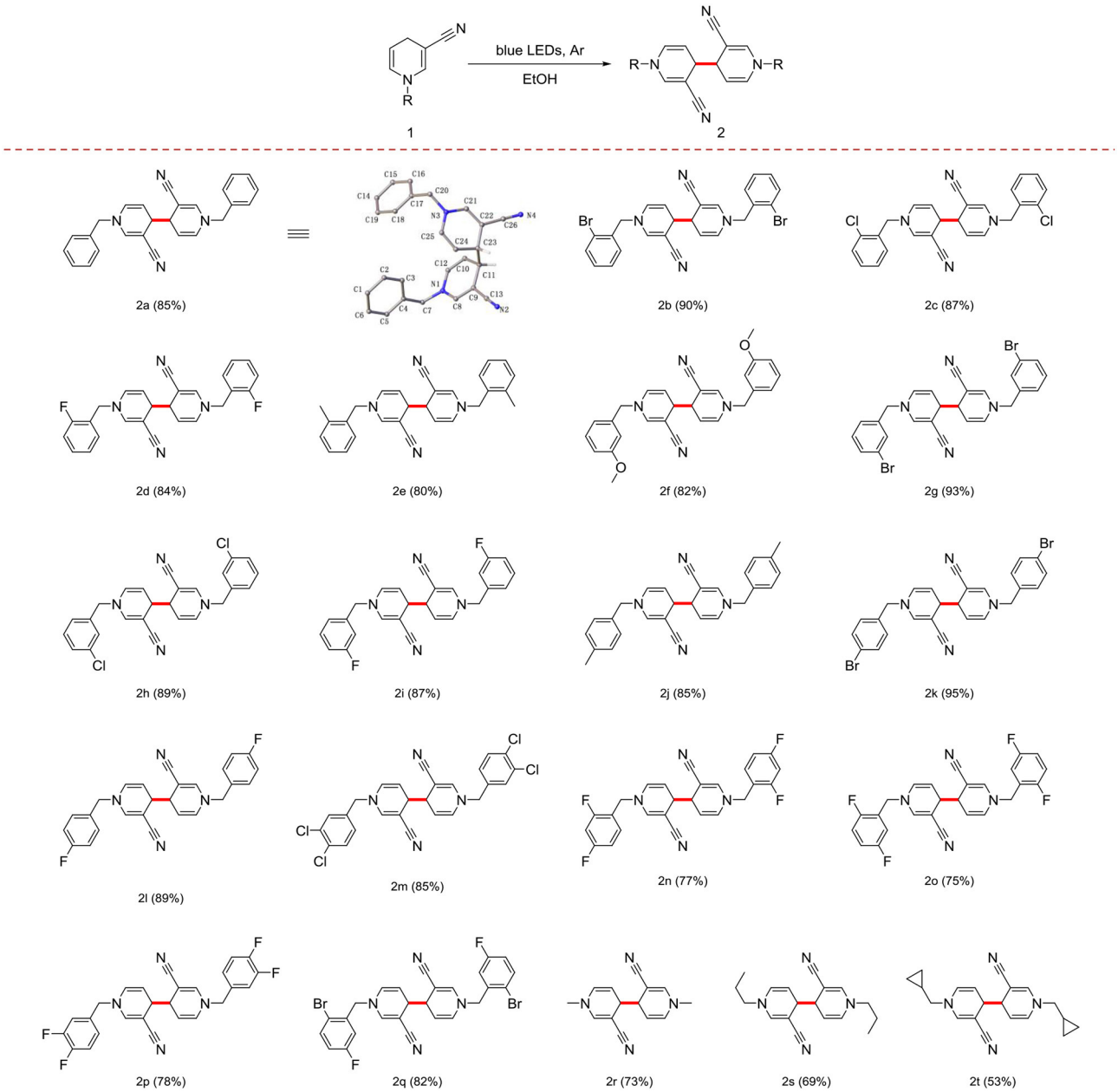

[a]*Irradiation of 1a (5 mmol) in anhydrous EtOH (25 mL) with blue LED lamps at room temperature. Products were purified via column chromatography using silica gel (200–300 mesh) and percentage yields of the isolated products are presented.*

a levoisomer, which was confirmed via single crystal X-ray crystallography (**Figure 2**). In 2a, the two molecules were not on different sides as envisaged. Bipyridine compounds mainly consisted of two pyridine rings [A (N1-C8-C12), B (N3-C21-C25)] and two benzene rings[C (C1-C6), D (C14-C19)]. No molecular hydrogen bonds were observed. Unexpectedly, in contrast to previous olefin and water reactions requiring high temperature or high pressure under acidic conditions, photocatalysis promoted reaction of water molecules with the double bond to form the by-product 3a (**Scheme 2**). Moreover, π-π stacking was not evident in the X-ray structures of 2a and 3a.

Gram-scale synthesis of dipyridyl was additionally conducted. In general, photoreaction is difficult at high concentrations. However, dipyridyl 2a was obtained with a good yield, even at a scale of 25.5 mmol (80%) (**Scheme 3A**), supporting the practical application of this method in the industrial field.

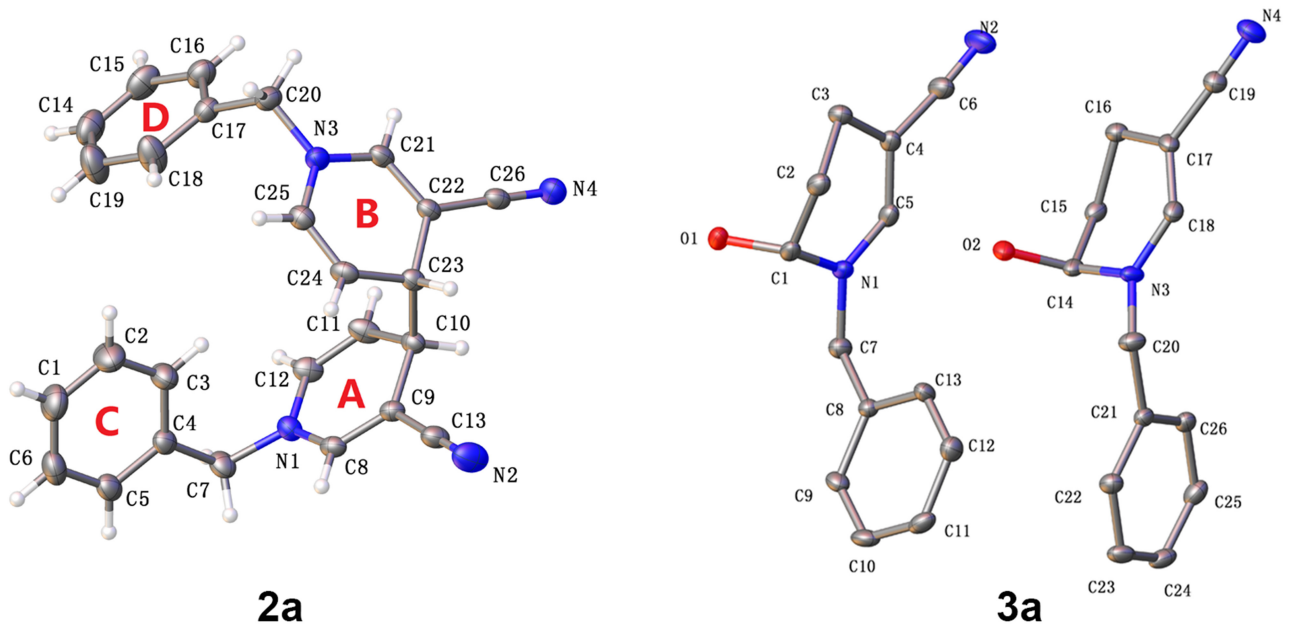

FIGURE 2 | Olex2 diagram (30%) of compound 2a and 3a.

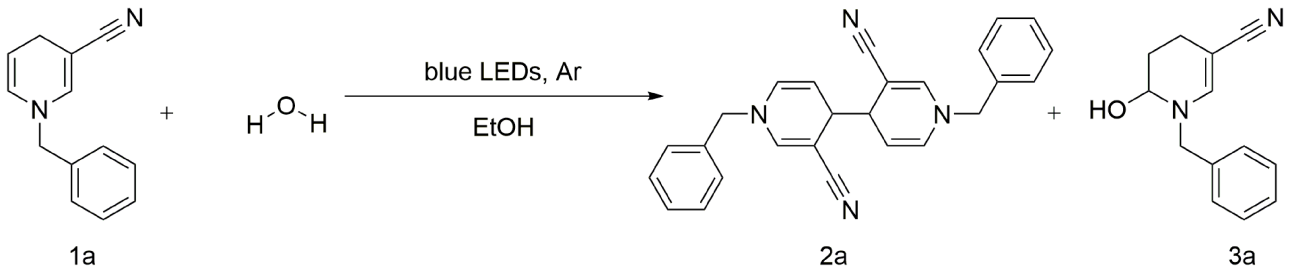

SCHEME 2 | Reaction of 1,4-dihydropyridine derivatives in the presence of water molecules.

Water was added in the case of a standard reaction. The photocatalytic reaction revealed that the reaction was completely inhibited in the absence of light, indicating that continuous irradiation of visible light is essential for this photo-catalytic conversion (**Scheme 3B**). Next, we used the solid-phase illumination method for analysis. However, 2a was not produced in the system, indicating the importance of the solvent (**Scheme 3C**). To gain insights into the underlying mechanism, control experiments were performed. Since several photocatalytic coupling reactions proceed via the free radical pathway, we performed our model reaction in the presence of the radical scavenger 2,2,6,6-tetramethyl-1-piperidinyloxy (TEMPO), under optimized reaction conditions. In the presence of TEMPO as the scavenger, no product 2a was detected (**Scheme 3D**).

Based on our findings and previous reports (Deb et al., 2017; Rahaman et al., 2018), an outline of the potential mechanism is illustrated in **Figure 3**.

Under blue-LED light irradiation, if the reaction system contains water molecules, paths A and B are simultaneously activated, the methylene in the para position is activated to single electron methyl radical, while the proton attacks the π-electron cloud on the double bond, and generates a positively charged intermediate on the double bond carbon through the transition state, afterward the hydroxyl radical attacks the positive ion to form the product 3a (path A). By contrast, in the absence of moisture, the methylene group is homogenized by light. The single-electron methylene group is highly reactive with a strong tendency to pair electrons and dimerizes with another single electron methylene collision to forms a new C–C bond (path B).

CONCLUSION

In summary, we have developed a C–C coupling method for pyridine compounds via photocatalysis, which represents

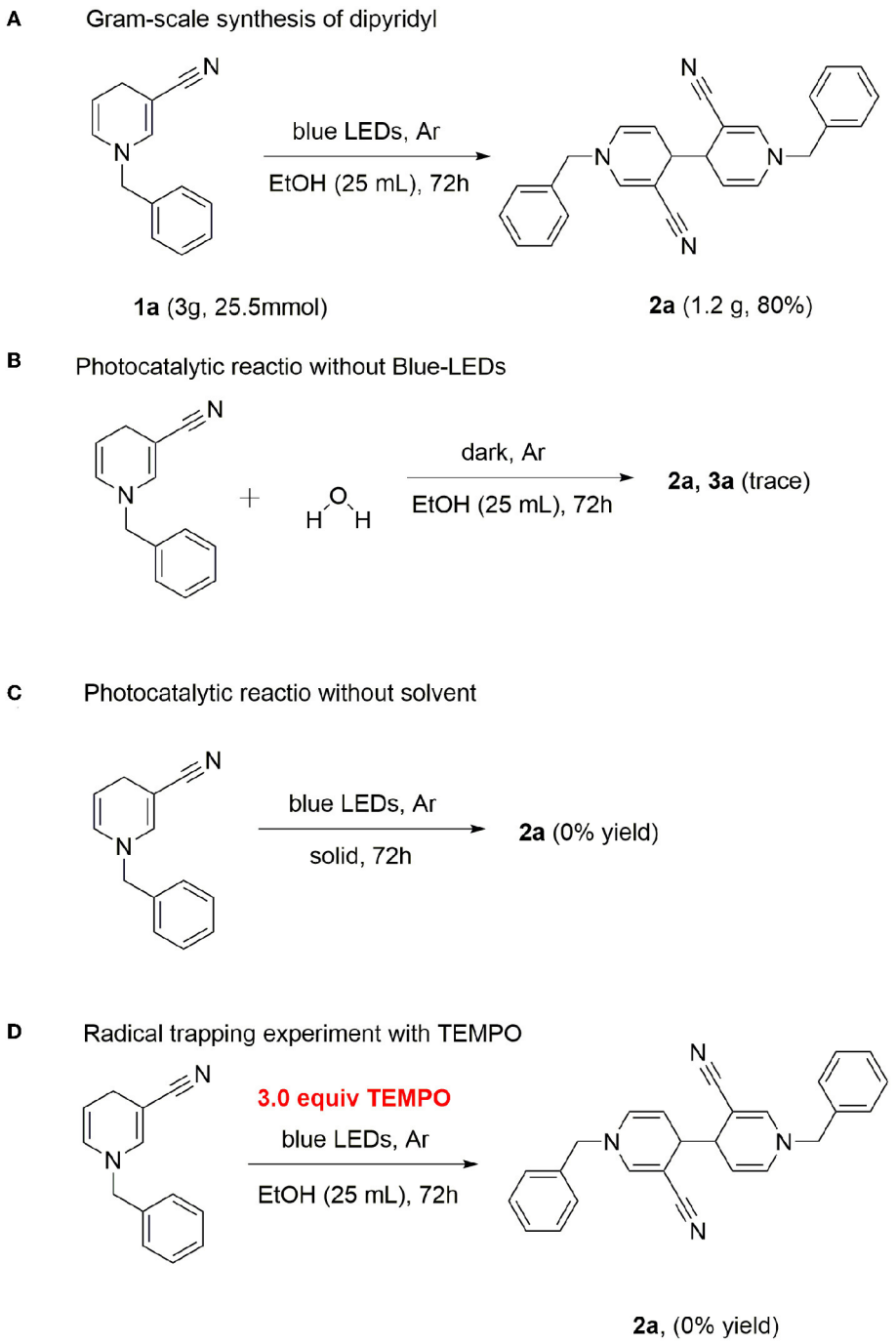

SCHEME 3 | Gram-scale synthesis and control experiments.

a novel, efficient and green approach for selective C–C coupling under mild reaction conditions. Notably, no catalyst or precious metal is required for completion of the reaction and anhydrous ethanol is used as the solvent. The reaction step is relatively simple, which makes construction of the C–C bond more sustainable. Further investigations into the applicability of this methodology for other organic reactions are currently underway. The photo-mediated C–C coupling reaction described in this study should aid in the design of more interesting, useful, and sustainable reactions in the future.

DATA AVAILABILITY STATEMENT

All datasets generated for this study are included in the article/**Supplementary Material**.

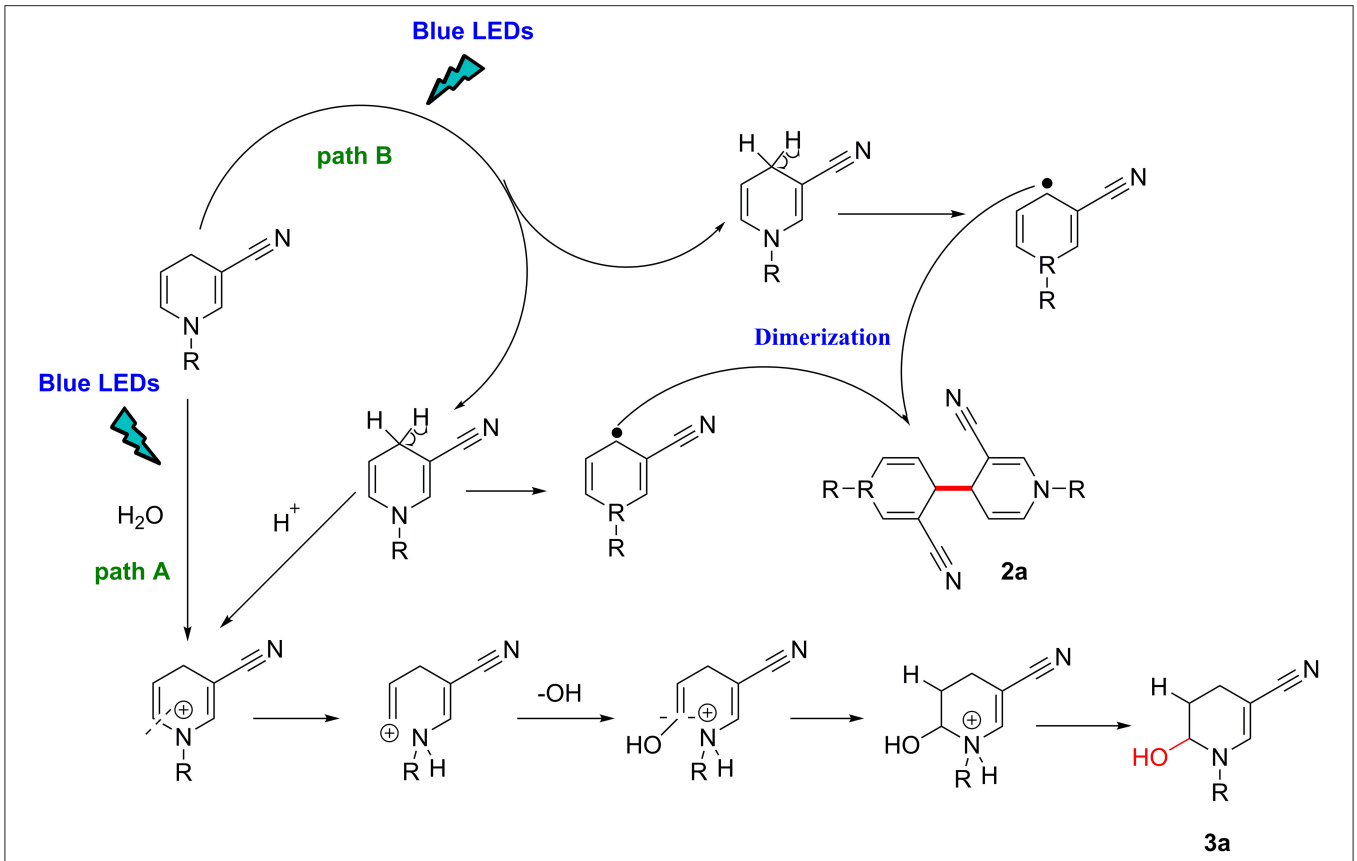

FIGURE 3 | Proposed mechanism.

AUTHOR CONTRIBUTIONS

SC synthesized all of the compounds with the help of HZ, CL, PZ, and WS. QZ supervised this work and wrote the paper with the help of SC.

FUNDING

This work was supported by the Youth Foundation of Hebei Educational Committee (Project No. QN2019165), the Technology and Science Research Foundation of North China University of Science and Technology, the Graduate Student Innovation Fund of North China University of Science (Project No. 2019S37).

SUPPLEMENTARY MATERIAL

The Supplementary Material for this article can be found online at: https://www.frontiersin.org/articles/10.3389/fchem.2019.00940/full#supplementary-material

REFERENCES

Akihiro, Y., Hirofumi, S., Yasuhiro, K., Kazuei, O., Hideyuki, H., and Tsutomu, Y. (2007). Chain-growth polymerization for the synthesis of polyfluorene via suzuki-miyaura coupling reaction from an externally added initiator unit. *J. Am. Chem. Soc.* 129, 7236–7237. doi: 10.1021/ja070313v

Capdeville, R., Buchdunger, E., Zimmermann, J., and Matter, A. (2002). Glivec (STI571, imatinib), a rationally developed, targeted anticancer drug. *Nat. Rev. Drug Discov.* 1:493. doi: 10.1038/nrd839

Carelli, V., Liberatore, F., Casini, A., Tortorella, S., Scipione, L., and Rienzo, B. D. (1998). On the regio- and stereoselectivity of pyridinyl radical dimerization. *New J. Chem.* 22, 999–1004. doi: 10.1039/a800631h

Cocuzza, A. J., Chidester, D. R., Culp, S., Fitzgerald, L., and Gilligan, P. (1999). Use of the suzuki reaction for the synthesis of aryl-substituted heterocycles as corticotropin-releasing hormone (CRH) antagonists. *Bioorg. Med. Chem. Lett.* 9, 1063–1066. doi: 10.1016/S0960-894X(99)00133-X

Condie, A. G., González-Gómez, J. C., and Stephenson, C. R. J. (2010). Visible-light photoredox catalysis: aza-henry reactions via C-H functionalization. *J. Am. Chem. Soc.* 132, 1464–1465. doi: 10.1021/ja909145y

Deb, M. L., Pegu, C. D., Borpatra, P. J., Saikia, P. J., and Baruah, P. K. (2017). Catalyst-free multi-component cascade C-H-functionalization in water using molecular oxygen: an approach to 1,3-oxazines. *Green Chem.* 19, 4036–4042. doi: 10.1039/C7GC01494E

Eisner, U., Williams, J. R., Matthews, B. W., and Ziffer, H. (1970). The photochemistry of 3,5-disubstituted 1,4-dihydropyridines. *Tetrahedron* 26, 899–909. doi: 10.1016/S0040-4020(01)97888-3

Fan, J. M., Wang, T., Li, C. C., Wang, R., Lei, X. Y., Zhang, Z. T., et al. (2017). Synthesis of benzoaryl-5-yl (2-hydroxyphenyl) methanones via photoinduced rearrangement of (E)-3-arylvinyl-4 H-chromen-4-ones. *Org. Lett.* 19, 5984–5987. doi: 10.1021/acs.orglett.7b03007

Heravi, M. M., and Hashemi, E. (2012). Recent applications of the suzuki reaction in total synthesis. *Tetrahedron* 45, 9145–9178. doi: 10.1016/j.tet.2012.08.058

Hilgeroth, A., and Baumeister, U. (2001). Formation of novel photodimers from 4-Aryl-1, 4-dihydropyridines. *Chem. Eur. J.* 7, 4599–4603. doi: 10.1002/1521-3765(20011105)7:21<4599::AID-CHEM4599>3.0.CO;2-U

Hilgeroth, A., Baumeister, U., and Heinemann, F. W. (2000). Solution-dimerization of 4-Aryl-1,4-dihydropyridines. *Eur. J. Org. Chem*. 2000, 245–249. doi: 10.1002/(SICI)1099-0690(200001)2000:2<245::AID-EJOC245>3.0.CO;2-2

Hilgeroth, A., and Heinemann, F. W. (1999). Novel solid-state synthesis of dimeric 4-aryl-1, 4-dihydropyridines. *J. Heterocycl. Chem.* 13, 231–243.

Hilgeroth, A., Hempel, G., Baumeister, U., and Reichert, D. (1999). Solid-state photodimerization of 4-aryl-1, 4-dihydropyridines studied by 13C CPMAS NMR spectroscopy. *Solid State Nucl. Mag.* 13, 231–243. doi: 10.1016/S0926-2040(98)00090-3

Hilton, M. C., Zhang, X., Boyle, B. T., Alegre-Requena, J. V., Paton, R. S., and McNally, A. (2018). Heterobiaryl synthesis by contractive C–C coupling via P (V) intermediates. *Science* 362, 799–804. doi: 10.1126/science.aas8961

Jin, M., Yang, L., Wu, L., Liu, Y., and Liu, Z. (1998). Novel photoinduced aromatization of hantzsch 1,4-dihydropyridines. *Chem. Commun.* 22, 2451–2452. doi: 10.1039/a807093h

Martina, S. D., Vesta, K. S., and Ripley, T. L. (2005). Etoricoxib: a highly selective COX-2 inhibitor. *Ann. Pharmacother*. 39, 854–862. doi: 10.1345/aph.1E543

Memarian, H. R., and Mirjafari, A. (2005). Solid state photochemistry of 1,4-dihydropyridines. *Bioorg. Med. Chem. Lett.* 15, 3423–3425. doi: 10.1016/j.bmcl.2005.05.026

Norbert, H. (2008). Photochemical reactions as key steps in organic synthesis. *Chem. Rev.* 108, 1052–1103. doi: 10.1021/cr0680336

Paul, C. E., Serena, G., Opperman, D. J., Iván, L., Vicente, G. F., Vicente, G., et al. (2013). Mimicking nature: synthetic nicotinamide cofactors for C-C bioreduction using enoate reductases. *Org. Lett.* 15, 180–183. doi: 10.1021/ol303240a

Rahaman, R., Das, S., and Barman, P. (2018). Visible-light-induced regioselective sulfenylation of imidazopyridines with thiols under transition metal-free conditions. *Green Chem.* 20, 141–147. doi: 10.1039/C7GC02906C

Ravelli, D., Protti, S., and Fagnoni, M. (2016). Carbon-carbon bond forming reactions via photogenerated intermediates. *Chem. Rev.* 116, 9850–9913. doi: 10.1021/acs.chemrev.5b00662

Reddy, T. J., and Rawal, V. H. (2000). Expeditious syntheses of (±)-5-oxosilphiperfol-6-ene and (±)-silphiperfol-6-ene. *Org. Lett.* 2, 2711–2712. doi: 10.1021/ol006292q

Richard, B., Dominik, L., Maturi, M. M., and Thorsten, B. (2015). Enantioselective catalysis of photochemical reactions. *Angew. Chem. Int. Ed.* 54, 3872–3890. doi: 10.1002/anie.201411409

Roecker, A. J., Mercer, S. P., Schreier, J. D., Cox, C. D., Fraley, M. E., Steen, J. T., et al. (2014). Discovery of 5′′-chloro-N-[(5,6-dimethoxypyridin-2-yl)methyl]-2, 2′: 5′, 3′′-terpyridine-3′-carboxamide(MK-1064): a selective orexin 2 receptor antagonist (2-SORA) for the treatment of insomnia. *Chem. Med. Chem*. 9, 311–322. doi: 10.1002/cmdc.201300447

Romero, N. A., and Nicewicz, D. A. (2016). Organic photoredox catalysis. *Chem. Rev.* 116, 10075–10166. doi: 10.1021/acs.chemrev.6b00057

She, H., Li, L., Zhou, H., Wang, L., Huang, J. W., and Wang, Q. Z. (2018). Photocatalytic activation of saturated C–H bond over the CdS mixed-phase under visible light irradiation. *Front. Chem*. 6:466. doi: 10.3389/fchem.2018.00466

Tahsini, L., Minnick, J. L., Domyati, D., and Ammons, R. (2019). C–X (X=N, O) cross-coupling reactions catalyzed by copper-pincer bis (N-heterocyclic carbene) complexes. *Front. Chem*. 7:12. doi: 10.3389/fchem.2019.00012

Yu, Y., Yu, F., and Zhong, F. (2018). Benign catalysis with iron: facile assembly of cyclobutanes and cyclohexenes via intermolecular radical cation cycloadditions. *Green Chem.* 20, 1743–1747. doi: 10.1039/C8GC00299A

Zhang, E. X., Wang, D. X., and Wang, M. X. (2019). Hydroxy-substituted azacalix [4] pyridines: synthesis, structure and construction of functional architectures. *Front. Chem*. 7:553. doi: 10.3389/fchem.2019.00553

Zhong, Q. D., Fan, Q. W., and Yan, H. (2017). Synthesis of 2,3-dihydropyrroles by photo rearrangement of hantzsch 1,4-di-hydropyridines with high diastereoselectivity. *Tetrahedron Lett.* 58, 1292–1295. doi: 10.1016/j.tetlet.2017.02.041

Conflict of Interest: The authors declare that the research was conducted in the absence of any commercial or financial relationships that could be construed as a potential conflict of interest.

frontiers in Chemistry

ORIGINAL RESEARCH
published: 20 March 2020
doi: 10.3389/fchem.2020.00151

Selective Catalytic Oxidation of Benzyl Alcohol to Benzaldehyde by Nitrates

Shurui Xu[1], Jie Wu[1], Peng Huang[1], Chunwen Lao[1], Hanchao Lai[1], Yuxiong Wang[1], Zhenyu Wang[1], Guoyu Zhong[1], Xiaobo Fu[1,2] and Feng Peng[3]**

[1] Engineering Research Center of None-food Biomass Efficient Pyrolysis and Utilization Technology of Guangdong Higher Education Institutes, Dongguan University of Technology, Dongguan, China, [2] Key Laboratory of Distributed Energy Systems of Guangdong Province, School of Chemical Engineering and Energy Technology, Dongguan University of Technology, Dongguan, China, [3] Guangzhou Higher Education Mega Center, School of Chemistry and Chemical Engineering, Guangzhou University, Guangzhou, China

In this paper, ferric nitrate was used to oxidize benzyl alcohol in a mild condition and demonstrated its better performance compared to HNO_3. In the reaction, the conversion rate and product selectivity could be both as high as 95% in N_2 atmosphere, while the benzaldehyde yield also reached 85% in air. Similar to $Fe(NO_3)_3{\cdot}9H_2O$, the other metallic nitrates such as $Al(NO_3)_3{\cdot}9H_2O$ and $Cu(NO_3)_2{\cdot}3H_2O$ could also oxidize the benzyl alcohol with high activity. The applicability of $Fe(NO_3)_3{\cdot}9H_2O$ for other benzylic alcohol was also investigated, and the reaction condition was optimized at the same time. The results showed the $Fe(NO_3)_3{\cdot}9H_2O$ would be more conducive in oxidizing benzyl alcohol under the anaerobic condition. The experiments in N_2 or O_2 atmospheres were conducted separately to study the catalytic mechanism of $Fe(NO_3)_3$. The results showed the co-existence of Fe^{3+} and NO_3^- will generate high activity, while either was with negligible oxidation property. The cyclic transformation of Fe^{3+} and Fe^{2+} provided the catalytic action to the benzyl alcohol oxidation. The role of NO_3^- was also an oxidant, by providing HNO_2 in anaerobic condition, while NO_3^- would be regenerated from NO in aerobic condition. O_2 did not oxidize the benzyl alcohol conversion directly, while it could still be beneficial to the procedure by eliminating the unwelcome NO and simultaneously reinforcing the circulation of Fe^{2+} and Fe^{3+}, which therefore forms a green cyclic oxidation. Hence, the benzyl alcohol oxidation was suggested in an air atmosphere for efficiency and the need of green synthesis.

Keywords: selective oxidation, benzyl alcohol oxidation, green oxidation, ferric nitrate, catalytic mechanism

OPEN ACCESS

Edited by:
Hadi Nur, University of Technology Malaysia, Malaysia

Reviewed by:
Giovanni Palmisano, Khalifa University, United Arab Emirates
Dong Guohui, Shaanxi University of Science and Technology, China

***Correspondence:**
Guoyu Zhong
zhonggy@dgut.edu.cn
Feng Peng
fpeng@gzhu.edu.cn

Specialty section:
This article was submitted to Catalysis and Photocatalysis, a section of the journal Frontiers in Chemistry

Received: *07 January 2020*
Accepted: *17 February 2020*
Published: *20 March 2020*

Citation:
Xu S, Wu J, Huang P, Lao C, Lai H, Wang Y, Wang Z, Zhong G, Fu X and Peng F (2020) Selective Catalytic Oxidation of Benzyl Alcohol to Benzaldehyde by Nitrates. Front. Chem. 8:151. doi: 10.3389/fchem.2020.00151

INTRODUCTION

Benzaldehyde (BzH) is one of the most important chemicals among the aromatic aldehyde family. It is used as the raw material for a large number of products, including perfume, beverage, pharmaceutical intermediates, and so on (Jachuck et al., 2006; Ragupathi et al., 2015; Ndolomingo and Meijboom, 2017; Zhu et al., 2017). Traditionally, BzH was synthesized by hydrolysis of benzal chloride or vapor/liquid-phase oxidation of toluene. In the former method, the chlorinated

by-products and corresponding toxic acidic would be generated, which brought troubles to the industrial application (Mal et al., 2018; Lu et al., 2019), while the vapor/liquid oxidation of toluene was also limited because of the harsh reaction conditions and low selectivity (Miao et al., 2016). Recently, BzH production with benzyl alcohol oxidation was widely adopted in industry, based on its advantages of easy-control condition and high yield (Lv et al., 2018; Thao et al., 2018). In this method, potassium permanganate ($KMnO_4$) (Mahmood et al., 1999) and dichromate ($K_2Cr_2O_7$) (Thottathil et al., 1986) with a strong oxidizing property are chosen as oxidants. While those oxidants were not perfect industrial reagents, leading to a series of environmental issues and high cost.

Nitric acid (HNO_3), as a rather inexpensive and high-performance oxidant, is commonly used in industry (Joshi et al., 2005; Aellig et al., 2012). For example, the niacin (vitamin B3) is synthesized from substituted pyridines oxidized by HNO_3 (Yu et al., 2011). HNO_3 is also regarded as the initiator in benzyl alcohol oxidation in the presence of O_2 (Miao et al., 2011; Luo et al., 2012, 2014). In this approach, HNO_3 initiates the oxidation of alcohols by decomposing NO_2, which further formed HNO_2 with H_2O. HNO_2 subsequently attacks substrate and generates the products by a series of reactions with releasing NO_x. Finally, the HNO_3 is regenerated by the NO_x oxidation by O_2. However, the disadvantages of HNO_3 should not be ignored totally, due to the risks of pollution and corrosion. Green oxidants such as hydrogen peroxide (H_2O_2) (Cánepa et al., 2017) and O_2 (Yu et al., 2011; Cao et al., 2013, 2015; Zhu et al., 2017; Chen et al., 2018a,b; Yuan et al., 2018) have been attracting extensive attention for many years. It is noted that O_2 or H_2O_2 itself has almost no activity and its oxidative performance needs to be activated by other materials.

Besides oxidants, the catalytic systems, including homogeneous and heterogeneous, have been developed. In the past decade, the heterogeneous precious metals catalysts, like Au (Zhan et al., 2012; Albadi et al., 2014), Pt (Liu et al., 2017), Ru (Ganesamoorthy et al., 2013), and Pd (Villa et al., 2010), were employed for selective oxidation of benzyl alcohols to BzH, based on their excellent performances. However, the high cost and limited resource of noble metals hindered their practical application. Moreover, the catalytic activity of heterogeneous catalysts would be lower than their homogeneous counterparts after several recycles (Parmeggiani and Camilla, 2012). Hence, the metal-based homogeneous catalysts, including Ru (Shimizu et al., 2005), V (Hanson et al., 2008), Cu (Hansen et al., 2013; Jia et al., 2014), and Fe (Jiang et al., 2016; Li et al., 2016; Miao et al., 2016; Hu et al., 2018), continued to gain great interests.

Among those homogenous catalysts, non-toxic, abundant, and bio-friendly, iron-based metals have widely aroused attentions (Martin and Suárez, 2002; Wang et al., 2005; Zhang et al., 2013; Hu et al., 2016, 2018). Zhang and co-workers reported a series of Fe catalysts, such as $FeBr_3$, Fe_2O_3, and $Fe_2(SO_4)_3$, with performance catalyzing benzylamine to imine in air atmosphere (Zhang et al., 2013). Wang et al. (2005) found an effective $FeCl_3$/TEMPO/$NaNO_2$ catalyst for benzyl alcohol oxidation, whose yield of benzaldehyde was as high as 99.0%. In this catalytic system, $NaNO_2$ activated the catalytic reaction by releasing NO_2, which oxidized Fe^{2+}-TEMPOH to Fe^{3+}-TEMPO. Consequently, Fe^{3+}-TEMPO oxidized the benzyl alcohol to be benzaldehyde (Wang et al., 2005). Zhang and co-workers introduced Fe into imidazolium and successfully prepared a nice iron-based catalyst [Imim-TEMPO][$FeCl_4$]/$NaNO_2$ (Miao et al., 2011), showing a good activity for the selective oxidation of aromatic alcohols under 5% $NaNO_2$. The catalytic mechanism of [Imim-TEMPO][$FeCl_4$]/$NaNO_2$ was similar to that of $FeCl_3$/TEMPO/$NaNO_2$, and the aromatic alcohol was oxidized in the process of redox between Fe^{3+} and NO_2. Martin and co-workers (Martin and Suárez, 2002) discovered an efficient system by combining $Fe(NO_3)_3$ and $FeBr_3$ for selective oxidation of benzylic alcohol to corresponding aldehyde. Though the Fe-based catalysts had good activity, problems are obvious. For example, the introduction of Br or co-catalyst (TEMPO) has increased the cost as well as environmental concerns, resulting in weaker competitive when industrial applications.

The reported Fe-based catalytic systems usually contain NO_2^-. In fact, NO_2^- releases active NO_2 and initiate the alcohol oxidation by several redox reactions. Inspired by this, we are intrigued whether the combination of metal iron (M^{n+}) and NO_3^-/NO_2^- can construct an efficient catalytic system for the alcohol oxidation. Studies from Jachuck et al. (2006) and Dressen et al. (2009) verified that $Fe(NO_3)_3$ could successfully oxidize benzyl alcohol to benzaldehyde under microwave irradiation. They deemed Fe^{3+} in the oxidation of benzyl alcohol as catalyst, because overall Fe^{3+} remained in its original oxidative state. However, this study was limited in microwave irradiation and lacked the universality for actual application. Besides, the oxidation performances of other system composed of metal iron (Cu, Al, Mg, Co, Ni) and NO_3^-/NO_2^- were unclear, and the role of M^{n+} had not been reported.

Hence, we studied the performance of $Fe(NO_3)_3{\cdot}9H_2O$ by continuous heating in O_2 and N_2 (He) atmosphere. Interestingly, the results were different from the phenomenon in microwave irradiation. The catalytic performance of $Fe(NO_3)_3{\cdot}9H_2O$ in N_2 was significantly improved compared to that in O_2. Further, the oxidation performance of other nitrates was studied. To expand the applicability of the combination of M^{n+} and NO_3^-, we conducted systematic research using $Fe(NO_3)_3 9H_2O$ as an example. The reaction conditions such as temperature and solvent were optimized. The optimized conditions were applied to the oxidation of a variety of alcohols. Finally, the catalytic mechanism was put forward.

EXPERIMENTAL

Materials

Benzyl alcohol, nitrates with crystalline waters, and other reagents were analytical grade. Gas chromatography (GC) analysis was performed on SHIMAZDU GC-2014 equipped with a HP-5 column (30 m × 0.32 mm × 0.25 um) and a flame ionization detector.

The Oxidation of Benzyl Alcohol

Typically, 3 mmol of benzyl alcohol, 3 mmol of naphthalene as an internal standard, and 15 mL of 1,4-dioxane as solvent were

added to a 25 mL three-necked flask. Then the three-necked flask provided with a reflux condenser was evacuated using an aspirator and followed by the attachment of a nitrogen balloon. Subsequently, the solution was heated to the desired temperature. When the temperature of solution reached the set point, 2 mmol of ferric nitrate ($Fe(NO_3)_3 \cdot 9H_2O$) was added into it. Samples were taken at appropriate intervals through a silicon septum using a hypodermic needle and were filtered with a membrane filter (PVDF) with 13 mm × 0.22 μm pore prior to GC analysis.

The Product Analysis

The analysis of benzyl alcohol and oxidation products was carried out on Aglient 7980 series with a HP-5 column and a flame ionization detector. The condition of GC for the HP-5 capillary column (30 m, DF = 0.25 mm, 0.25 mm i.d.), and temperature program was carried out (initial temperature = 100°C, 3 min; final temperature = 250°C, heating rate = 10°C min^{-1}, temperature of injector = 280°C, temperature of detector = 280°C). The quantitative results of products were based on the internal standard method, using naphthalene as an internal standard. The typical analytic procedure was as following: (1) 0.4 ml sample was taken from reaction solutions and was then filtered with a membrane filter (PVDF) with 13 mm × 0.22 μm; (2) then, the sample would be diluted 10-fold before GC analysis; (3) when the GC temperature reached the set points, the diluted solution was injected into this equipment to analyze products according to the different retention times and response peak area. The typical results of GC measurements and internal standard working curve were shown in **Figure S1**. The results reported as conversion and selectivity are expressed in mol%, based on the total benzyl alcohol intake. The calculation of the conversion and selectivity was as follows:

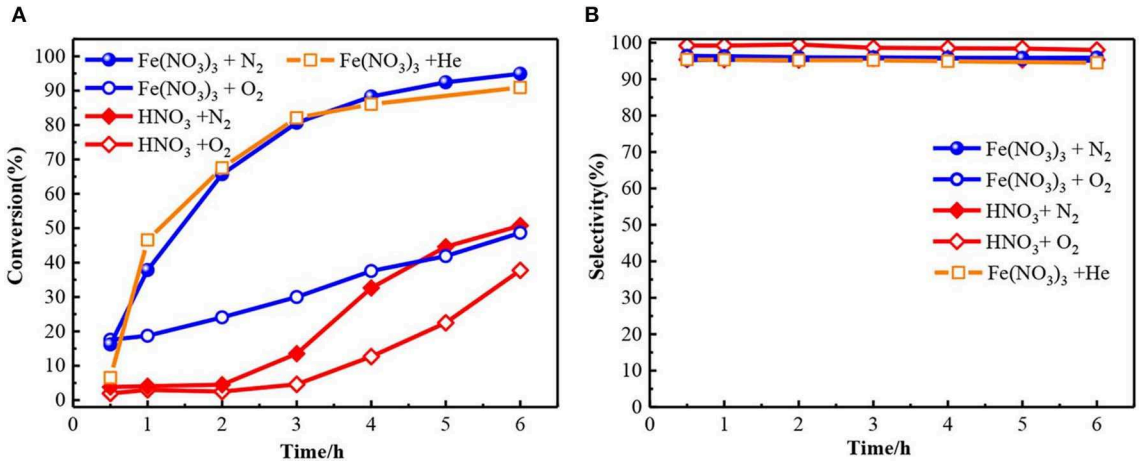

FIGURE 1 | The conversion **(A)** and selectivity **(B)** for benzyl alcohol oxidation to benzaldehyde with $Fe(NO_3)_3 \cdot 9H_2O$ and HNO_3. $Fe(NO_3)_3$ denotes $Fe(NO_3)_3 \cdot 9H_2O$ unless otherwise noted.

TABLE 1 | Catalytic results for benzyl alcohol oxidation with different catalysts.

Entry	Material	Oxidant	Temperature [°C]	Time [h]	Con. [%]	Sel. [%]	References
1	$Fe(NO_3)_3^a$	–	80.0	6	96.84	94.5	This work
2	CNT+HNO_3	O_2	90.0	5	96.2	88.3	Luo et al., 2012
3	Au-γAl_2O_3	TBHP	125.0	5	73.4	84.4	Ndolomingo and Meijboom, 2017
4	Fe/MCM41	H_2O_2	70.0	7	55	90.0	Cánepa et al., 2017
5	NG-900	O_2	70.0	3	12.8	100.0	Long et al., 2012
6	Fe-N-C	O_2^b	80.0	8	78.0	90.0	Xie et al., 2017
7	Au/Al_2O_3	O_2	130.0	5	69.0	65.0	Choudhary et al., 2005
8	CeO_2	H_2O_2	50.0	6	68.0	92.0	Tamizhdurai et al., 2017
9	Co_3O_4	O_2	100.0	7	38.6	67.6	Nie et al., 2013
10	$Co_3O_4/RGO\text{-}_N$	O_2	100.0	7	93.9	>99.0	Nie et al., 2013
11	MnO_x	O_2	80.0	3	72.7	–	Jing et al., 2007
12	NiO_2	O_2	90.0	6	80.0	100.0	Ji et al., 2005
13	$CrBO_3$	O_2	90.0	5	41	51	Öztürk et al., 2008
14	Co-ZIF-67	O_2	100.0	8	50.0	97.6	Yang et al., 2016

[a] *The benzyl alcohol oxidations were conducted in the inert atmosphere.*
[b] *The pressure of O_2 in this reference was 1 MPa.*

$$\text{Conversion of benzyl alcohol} = \frac{\text{Moles of benzyl alcohol reacted}}{\text{Initial moles of benzyl alcohol}} \times 100\% \quad (1)$$

$$\text{Selectivity of benzaldehyde} = \frac{\text{Moles of benzaldehyde formed}}{\text{Moles of benzyl alcohol reacted}} \times 100\% \quad (2)$$

$$\text{Yield of benzaldehyde} = \text{Conversion} \times \text{Selectivity} \quad (3)$$

RESULTS AND DISCUSSION

The Oxidation of Benzyl Alcohol by Ferric Nitrate

Figures 1A,B showed the oxidation results of benzyl alcohol to benzaldehyde in the presence of ferric nitrate and nitric acid. In N_2 condition, the conversion of benzyl alcohol catalyzed by ferric nitrate was 94.9% after 6 h. To ensure reproducibility, the experimental error-based three parallel experiments was shown in **Figure S2** and the carbon balance during experiments was also evaluated (**Table S1**). The results showed that performance of $Fe(NO_3)_3$ had a good testing repeatability and was highly efficient. Interestingly, the benzyl alcohol conversion catalyzed by $Fe(NO_3)_3$ could be as high as 96.84% with 94.5% selectivity when replacing N_2 with He. Compared with HNO_3, ferric nitrate exhibited an excellent activity in the benzyl alcohol oxidation. The conversion of benzyl alcohol catalyzed by ferric nitrate was 46.2%—higher than that by nitric acid. Similarly, under aerobic conditions (O_2), the conversion of benzyl alcohol catalyzed by ferric nitrate was about 13% higher than that by nitric acid with similar selectivity. The results indicated the oxidation performance of ferric nitrate was markedly

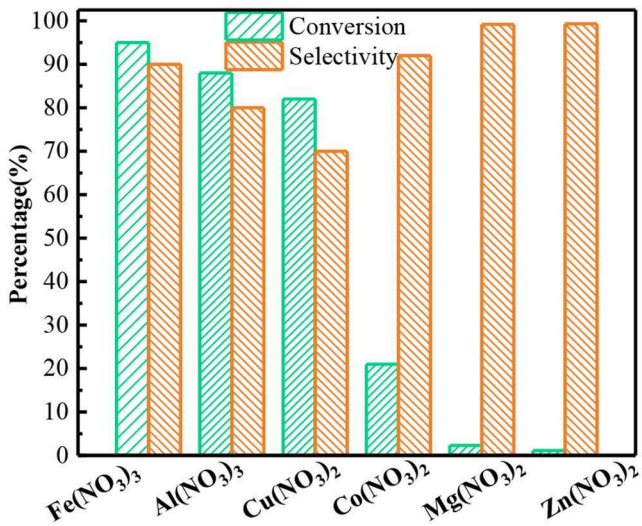

FIGURE 2 | The oxidation of benzyl alcohol to benzaldehyde by different nitrates. Reaction conditions: benzyl alcohol (3 mmol), 1,4-dioxane (15 mL), $Fe(NO_3)_3$ and $Al(NO_3)_3$ (2 mmol), or other nitrates (3 mmol), 80°C, 6 h ball N_2.

TABLE 2 | The oxidation of different alcohols by Fe $(NO_3)_3$.

Samples	Conversion	Selectivity	Yield
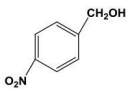	72.3	90.1	65.1
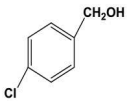	82.6	91.0	75.1
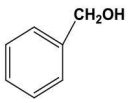	94.9	94.8	89.7
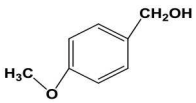	96.8	95.0	91.9
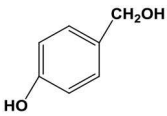	98.2	95.1	93.4

Reaction conditions: Alcohol (3 mmol); 1,4-dioxane (15 mL); $Fe(NO_3)_3$ (2 mmol); 80°C, 6 h ball N_2.

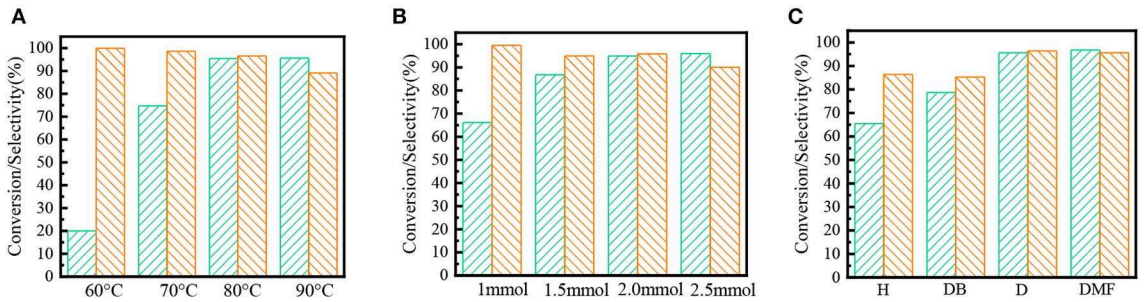

FIGURE 3 | The effect of different factors on the oxidation activity of $Fe(NO_3)_3$. Green square: conversion; Orange square: selectivity; **(A)** temperature; **(B)** dosage of $Fe(NO_3)_3$; **(C)** solvent polarity: n-hexane (H), dimethylbenzene (DB); 1,4-dioxane (D); N,N-dimethylformamide (DMF).

better than that of nitric acid, no matter under anaerobic or aerobic conditions.

Compared with other typical catalysts, the catalytic activity of $Fe(NO_3)_3$ was also outstanding. The conversion of benzyl alcohol catalyzed by $Fe(NO_3)_3$ with any oxidant (96.84%) was close to that by CNT-HNO_3 (Luo et al., 2012) (96.2%), as shown in **Table 1** (Entry 2). Besides, the performance of $Fe(NO_3)_3$ surpassed the typical metal-based catalyst, such as Au/γ-Al_2O_3 (73.4%) (Ndolomingo and Meijboom, 2017), Fe/MCM41 (55%) (Cánepa et al., 2017), or Fe-N-C (78.0%) (Xie et al., 2017). Moreover, $Fe(NO_3)_3$ also exhibited comparable activity with transition-metal oxides, such as Co_3O_4/RGO-$_N$ (93.9%) (Nie et al., 2013), MnO_x (72.7%) (Jing et al., 2007). The excellent catalytic activity of $Fe(NO_3)_3$ may be attributed to the combined action of Fe^{3+} and NO_3^-. On the one hand, NO_3^- could produce NO_2, and then NO_2 with H_2O was converted to HNO_2, which had been proved as a pivotal role in benzyl alcohol oxidation (Aellig et al., 2012; Luo et al., 2012). On the other hand, the valence change of Fe could catalyze benzyl alcohol oxidation according to the literatures (Miao et al., 2016; Hu et al., 2018). Coincidentally, the transformation between Fe^{3+} and Fe^{2+} was demonstrated by the $K_3[Fe(CN)_6]$ solution. As shown in **Figure S3**, the Prussian blue precipitate appeared in the experimental process due to the existence of Fe^{2+}. Therefore, $Fe(NO_3)_3$ exhibited the excellent oxidation activity via Fe^{3+} initiating a series of electron and proton transfer. It was noted that the anaerobic condition was beneficial to improve the oxidation performance of ferric nitric. The reason is discussed in detail in mechanism Part 3.4.

The Performance of Other Metallic Nitrates

Subsequently, the catalytic performance of other nitrates was also studied. The benzyl alcohol oxidation catalyzed by other nitrates including was investigated, as shown in **Figure 2**. The result proves other nitrates are also capable for converting the benzyl alcohol to benzaldehyde. In $Al(NO_3)_3$ system, the conversion of benzyl alcohol and the selectivity to benzaldehyde was 88.1% and 80% after 6 h, lower than those in $Fe(NO_3)_3$ system. Similarly, $Cu(NO_3)_2$ could also oxidize the benzyl alcohol with the conversion of 82.3%. While the selectivity to benzadehyde was only 70%, and the other 30% was benzoic acid from the excessive oxidation. The catalytic performance of $Co(NO_3)_2$ significantly decreased. While $Mg(NO_3)_2$ and $Zn(NO_3)_2$ had almost no catalytic activity. The order of activity of different nitrates is $Fe(NO_3)_3 > Al(NO_3)_3 > Cu(NO_3)_2 > Co(NO_3)_2 > Mg(NO_3)_2 \approx Zn(NO_3)_2$. Yuvaraj et al. (2003) tested the decomposition temperature of these nitrates by TG/DAT. And they found $Fe(NO_3)_3$ and $Al(NO_3)_3$ had the lowest the decomposition temperature (130°C), followed by $Cu(NO_3)_2$ (227°C) and $Co(NO_3)_2$ (247°C), and $Zn(NO_3)_2$ (367°C) was the highest. Their decomposition products were metal oxide, NO_2 and O_2. NO_2 and H_2O together would convert into HNO_2 which could attack the benzyl alcohol, finally producing benzaldehyde. Hence, the nitrates with lower decomposition temperature could easily produce NO_2 and oxidize more benzyl alcohol. As expected, the rank of conversion of benzyl alcohol in different nitrate system was related to the decomposition temperature of these nitrates.

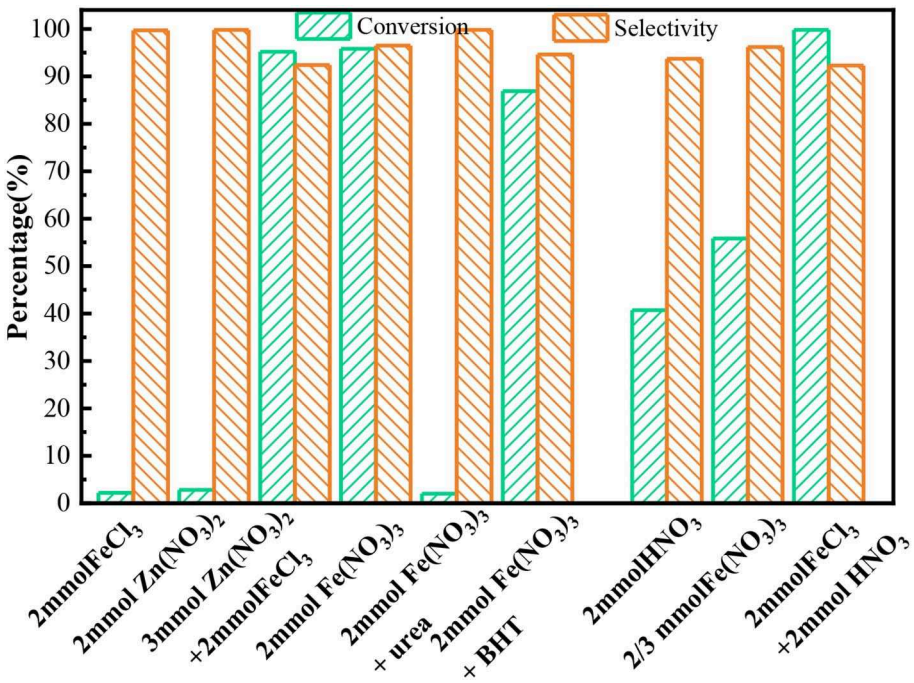

FIGURE 4 | The conversion and selectivity for the oxidation of benzyl alcohol in different system. Benzyl alcohol (3 mmol), 1,4-dioxane (15 mL), 80°C, 6 h, ball N_2.

Effect of Reaction Conditions on Oxidation Performance of $Fe(NO_3)_3$

$Fe(NO_3)_3$ is an excellent catalyst among several nitrates; the effect of reaction condition and solvent on the performance of $Fe(NO_3)_3$ was investigated. As the results shown in **Figure 3A**, the higher temperature would markedly enhance the yields of benzaldehyde. Since high temperature would increase the risk of the over oxidation from benzaldehyde to benzoic acid, the optimum temperature was 80°C. Similarly, 2 mmol $Fe(NO_3)_3$ could selectively oxidize the benzyl alcohol to benzaldehyde with 91.5% yields shown in **Figure 3B**. Besides, the solvent had an important effect on the activity of $Fe(NO_3)_3$. The results in **Figure 3C** show the strong polar solvent could bring a mutual solution containing the aqueous (HNO_2) and organic phase (benzyl alcohol), which would be more favorable to form of benzyl nitrite, resulting in high conversion and selectivity.

The Applicability of $Fe(NO_3)_3$ Catalyst

Subsequently, to demonstrate the general applicability of $Fe(NO_3)_3$, selective oxidation of substituted benzyl alcohols

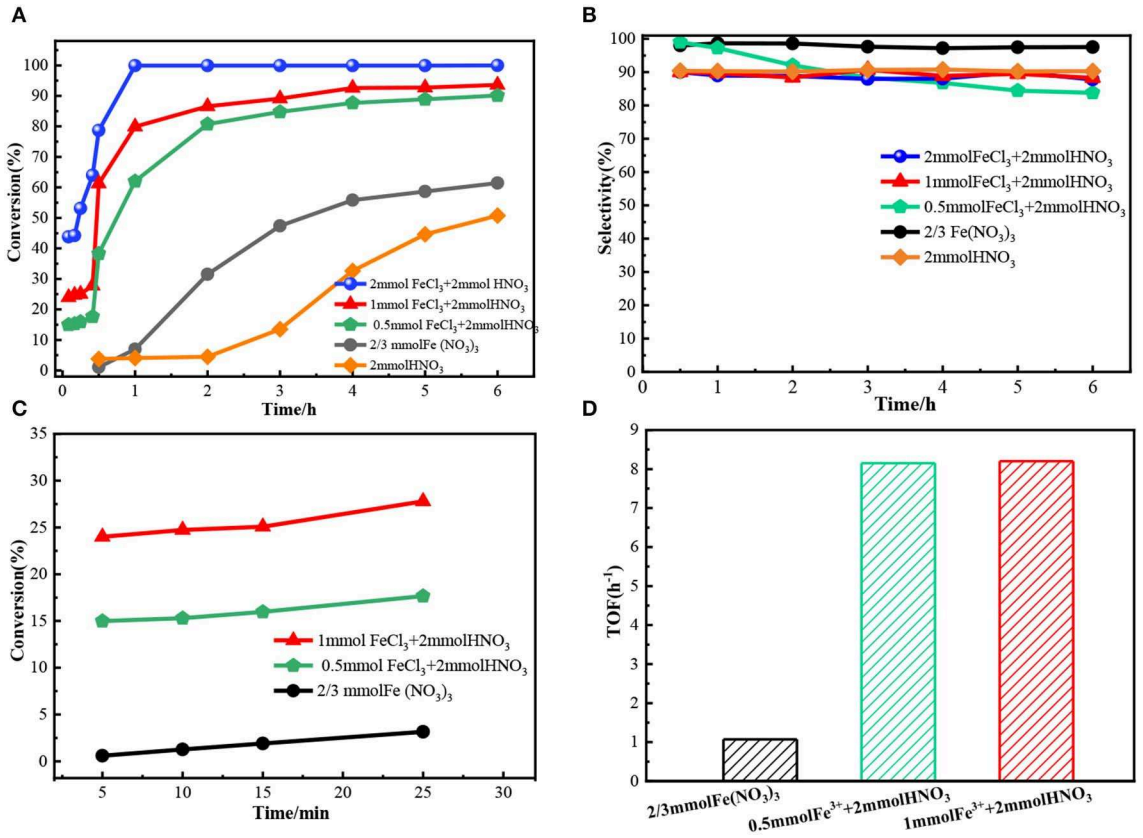

FIGURE 5 | The oxidation results of benzyl alcohol in different catalyst systems. The TOF was defined as $\frac{benzyl\ alcohol\ converted(g)}{Fe\ content(g)\ \times reaction\ time}$ and were calculated at 15 min, for which the conversion was lower than 25.0%. **(A)** The benzyl alcohol conversion in 6 h. **(B)** The selectivity of benzaldehyde. **(C)** The benzyl alcohol conversion in 30 min. **(D)** TOF.

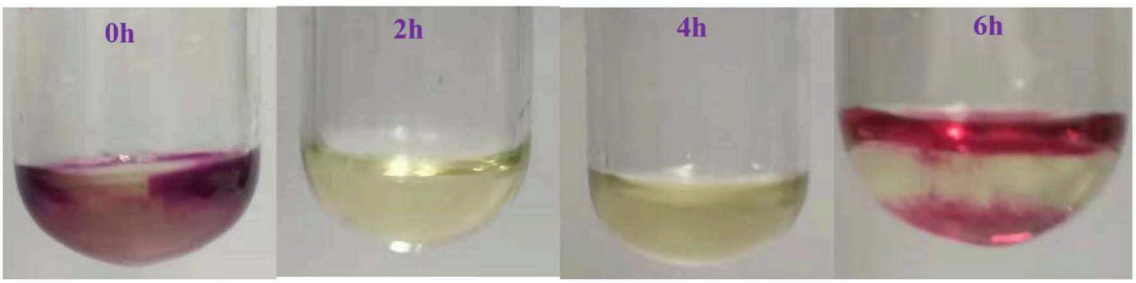

FIGURE 6 | The phenomena in the experimental process at different moments after adding 1 mol/L $KMnO_4$ to the reaction solution.

with different functional groups was investigated. The results presented in **Table 2** showed all these primary benzylic alcohols could be converted to corresponding aldehydes. The oxidation results were somewhat related to the substituent groups on the phenyl ring. The alcohols with electron withdrawing groups (–NO_2, –Cl) gained lower yields of products than those with electron donating groups (–MeO, –OH). The effect rule of substituent groups in $Fe(NO_3)_3$ system is consistent with that in HNO_3 system (Joshi et al., 2005). The formation of benzyl nitrite, a vital intermediate product, can be regarded as the electrophilic substitution reaction of benzyl alcohol. Thus, the electron-donating substituents would enhance the yield of product by increasing the electron density on the benzyl ring and vice versa. The results proved that the electron density on the aromatic ring played a critical role in the oxidation of benzylic alcohol.

Reaction Mechanism

Combined with the experimental results and literature reports, the following catalytic mechanism hypothesis was preliminarily put. Both Fe^{3+} and NO_3^- may have an important effect on the oxidation process. Fe^{3+} provides catalytic function by the electron transferring, while the NO_x produced from the experimental process may have certain oxidation performance. To verify above possible speculations and analyze the catalytic mechanism, a series of experiments were designed, and the results were shown as follows.

To illustrate the role of Fe^{3+} and NO_3^-, $Zn(NO_3)_2$ or $FeCl_3$ was individually added to the reaction mixtures. The result showed benzyl alcohol conversion in both systems was very low (**Figure 4**), indicating that only Fe^{3+} or NO_3^- had poor oxidation activity. While in $Zn(NO_3)_2$ + $FeCl_3$ system, the conversion of benzyl alcohol was as high as 95.8% with 93.6% selectivity, which was similar to that in $Fe(NO_3)_3$ system with the same amount of Fe^{3+} and NO_3^-. The results proved the Fe^{3+} and NO_3^- together could oxidize the benzyl alcohol. To illuminate how Fe^{3+} and NO_3^- together catalyze the benzyl alcohol, introducing urea as a known HNO_2 scavenger into $Fe(NO_3)_3$ system. The results in **Figure 4** showed the catalytic activity of $Fe(NO_3)_3$ was almost prevented. This phenomenon proved that the oxidation process of $Fe(NO_3)_3$ was mainly achieved by HNO_2 attacking benzyl alcohol. The intermediate benzyl nitrite detected by GC-MS in our experiments further verified the reaction between benzyl alcohol and HNO_2. Besides, when butylated hydroxytoluene (BHT) as a radical trapping agent was added into the $Fe(NO_3)_3$ system, the conversion still kept a high level of 86.3%, proving that the benzyl alcohol oxidation catalyzed by $Fe(NO_3)_3$ is not a radical-involved reaction. Interestingly, the conversion would increase obviously, and the selectivity also kept at a high value (95%) when Fe^{3+} instead of H^+ with the same mole of NO_3^- as shown in **Figure 4**. Furthermore, the addition of Fe^{3+} into HNO_3 system also significantly enhanced the conversion of benzyl alcohol compared with the HNO_3 system. From these results, we speculated Fe^{3+} had a special catalytic function in the process of benzyl alcohol oxidation.

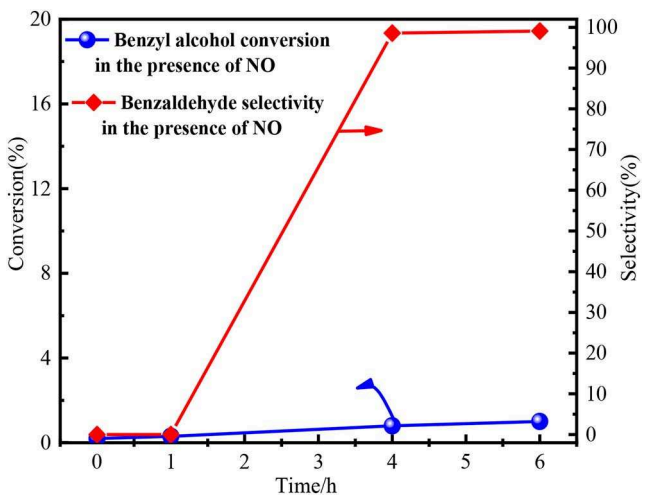

FIGURE 7 | The performance of NO in benzyl alcohol oxidation process. Reaction condition: 3 mmol benzyl alcohol, 15.0 ml 1,4-dioxane, 80°C.

A series of experiments were conducted to further illuminate the catalysis of Fe^{3+}. As the results shown in **Figure 5A**, the reaction rate increased as the amount of Fe^{3+} increased in $FeCl_3$-HNO_3 system. Meanwhile, the results shown in **Figure 5B** proved that the variation of selectivity was little. To quantify the effect of Fe^{3+}, the turnover frequency (TOF) was calculated based on Fe content at the conversion lower than 25.0%, as shown in **Figure 5C**. The results proved the Fe^{3+} had a remarkable effect on the oxidation reaction. The TOF of Fe^{3+} in the $FeCl_3$-HNO_3 system further enlarged compared to that in the $Fe(NO_3)_3$ system. As shown in **Figure 5D**, the TOF of Fe^{3+} in the $FeCl_3$-HNO_3 system was almost unchanged (8.1 h^{-1}), even if the amount of Fe^{3+} increased from 0.5 to 1 mmol.

Furthermore, the change of Fe in benzyl alcohol oxidation was analyzed by experiments. The transformation between Fe^{3+} and Fe^{2+} was detected *in situ* by 1 mol/L $KMnO_4$ solution in the oxidation process. For comparison, the reaction solvent (1,4-dioxane) was added to the $KMnO_4$ solution, the solution was black-purple as shown in **Figure 6**. The color of $KMnO_4$ solution changed from black-purple to yellow when $KMnO_4$ solution was added into reaction solution at 2 h. This phenomenon showed the $KMnO_4$ was reduced by Fe^{2+}, and the Fe^{2+} existed in the reaction process. However, the $KMnO_4$ solution changed from yellow to brown when it was added into the reaction solution at the reaction time of 6 h. The phenomenon illustrated that there were less Fe^{2+} in the reaction solution. Because the oxidation reaction of benzyl alcohol almost completed, most of Fe^{3+} did not convert anymore and Fe^{2+} would further oxidized to Fe^{3+} by the O_2 from the decomposition of $Fe(NO_3)_3$. So, the cyclic conversion of Fe^{3+} and Fe^{2+} really occurred in benzyl alcohol oxidation. According to the reported results, the valence transformation of metal iron such as Mn^{III}/Mn^{II} (Yang et al., 2014; Fei et al., 2017; Gurrala et al., 2018), Co^{III}/Co^{II} (Zhou et al., 2015; Cordoba et al., 2017; Li et al., 2017), Cr^{III}/Cr^{II} (Thao et al., 2018) could catalyze the oxidation of alcohols. Especially, the transformation of Fe^{3+}/Fe^{2+} possessed high catalytic activity by initiating a series of electron transfer (Hu et al., 2016, 2018; Miao et al., 2016). Combined with above results, Fe^{3+} could be regard

as a catalyst and the electron transfer between of Fe^{3+} and Fe^{2+} would catalyze the oxidation process.

Finally, the function of NO_x was investigated by a series of auxiliary experiments. As we know, nitric oxide (NO) would be immediately oxidized to nitrogen dioxide (NO_2) by O_2 (Wang et al., 2005; Shen et al., 2015, 2019; Miao et al., 2016; Hu et al., 2018; Dong et al., 2019; Zhao et al., 2019). O_2 was flowed into the reaction system in the experimental process to detect the NO. Brown fumes immediately occurred (**Figure S4**), proving the presence of NO in the inert atmosphere. Subsequently, NO was prepared by the reaction between Cu and 35 wt % nitric acid ($3Cu + 8HNO_3 \rightarrow 3Cu(NO_3)_2 + 2NO + 4H_2O$). The oxidation of benzyl alcohol by NO was conducted and the detailed experimental process was shown in **Figure S5**. The conversion of benzyl alcohol by NO was only 1% at 6 h with 99% selectivity, as shown in **Figure 7**. The results indicated NO itself could not oxidize benzyl alcohol. Hence, the NO_2 from the decomposition of $Fe(NO_3)_3$ played the key role in oxidation process by forming HNO_2.

According to the above investigation, the mechanism of the benzyl alcohol oxidation in N_2 condition was put forward and shown in **Scheme 1**. At the suitable reaction temperature, the $Fe(NO_3)_3$ decomposes into Fe_2O_3, NO_2, and O_2 (Yuvaraj et al., 2003) by Equation 1. Subsequently, the HNO_2 and HNO_3 can be formed by the reaction between NO_2 and H_2O, see Equation 2. Then, the oxidation reaction successfully gets into the propagation stage and HNO_2 attacks the benzyl alcohol ($PhCH_2OH$) and gives benzyl nitrite ($PhCH_2ONO$). Benzyl nitrite decomposes into benzaldehyde (PhCHO) and HNO at experimental temperature by Equation 4. In the termination stage, as shown in Equation 6, $Fe(NO_3)_2$ can be formed by the reaction between the HNO_2 and Fe_2O_3 with consuming O_2. At the same time, $Fe(NO_3)_2$ is oxidized to $Fe(NO_3)_3$ by O_2. Consequently, from Reaction 1 to Reaction 7, NO_3^- can be

SCHEME 1 | The probable routes for oxidation of benzyl alcohol by $Fe(NO_3)_3$.

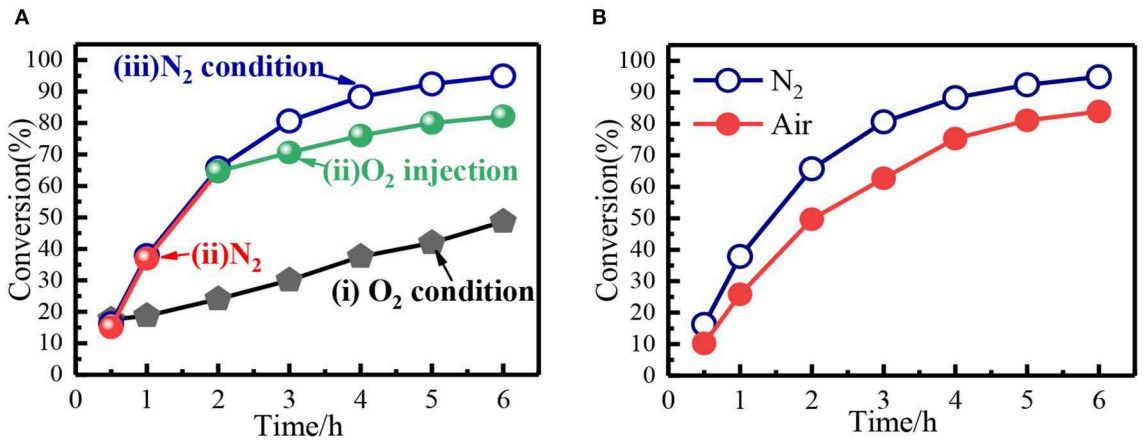

FIGURE 8 | (A) The benzyl alcohol conversion under different conditions: (i) O_2; (ii) N_2 (1-2 h) and O_2 (2–6 h); (iii) N_2. **(B)** Comparison of the benzyl alcohol conversion in N_2 and air.

considered as the real oxidant, and the Fe ion acts a catalyst through the transformation between Fe^{2+} and Fe^{3+}.

From the reaction mechanism, when the system was filled with O_2, the decomposition of $Fe(NO_3)_3$ would be hindered, leading to low conversion compared with anaerobic condition (N_2 or He). Interestingly, the O_2 was double-edged gas since it could oxidize the Fe^{2+} to Fe^{3+} and eliminate NO Equation 7. In the presence of adequate oxygen, the Fe^{2+} was completely oxidized into Fe^{3+}, and oxidative state of Fe remained the same before and after the reaction. The conversion of benzyl alcohol in $Fe(NO_3)_3$-O_2 system was relatively low (**Figure 8A**), but it was still higher than that in HNO_3 system. Moreover, in $Fe(NO_3)_3$ system, the conversion of benzyl alcohol could reach 82% when O_2 replaced N_2 after the reaction continuing 2 h (**Figure 8A**). As expected, the conversion of benzyl alcohol in air (N_2 + O_2) condition was close to that in N_2 condition (**Figure 8B**). In the aerobic conditions, NO_3^- would be regenerated and the Fe^{2+} was completely oxidized to Fe^{3+}, indicating O_2 was the actual oxidation. Though the O_2 would be not good for the high conversion, it could build a green cyclic oxidation process via removing NO and regenerating $Fe(NO_3)_3$. Hence, the benzyl alcohol conversion would be relatively high in air atmosphere, which also meet the need of green synthesis due to removing the NO.

CONCLUSION

As a bio-friendly and economical material, ferric nitrate showed an outstanding oxidation performance for benzyl alcohol oxidation. The conversion of benzyl alcohol in ferric nitrate system reached 95%, which was 46% higher than that in nitric acid system under N_2 atmosphere. Other metallic nitrates that could release NO_2 at reaction temperature also had high properties for benzyl alcohol oxidation. Moreover, ferric nitrate is of excellent applicability for other primary benzylic alcohols oxidation under optimized condition. The mechanism study indicated ferric nitrate was as initiator in the reaction. In the procedure, it would decompose into Fe_2O_3 and NO_2 which immediately became HNO_2, attacking benzyl alcohol, and forming the benzaldehyde afterward. While in anaerobic atmosphere, NO_3^- was the oxidant by providing HNO_2 and the transformation cycle between Fe^{3+} and Fe^{2+} generates a catalytic effectiveness. Hence, the balance of high conversion and green synthesis requirement would be obtained for the benzyl alcohol oxidation in the air atmosphere.

DATA AVAILABILITY STATEMENT

The datasets generated for this study are available on request to the corresponding author.

AUTHOR CONTRIBUTIONS

SX, GZ, and FP designed experiments. JW, PH, CL, HL, YW, and ZW carried out experiments. SX, GZ, XF, and FP analyzed experimental results, analyzed data, and wrote the manuscript.

FUNDING

This work was supported by Engineering Research Center of None-food Biomass Efficient Pyrolysis and Utilization Technology of Guangdong Higher Education Institutes (2016GCZX009), National Natural Science Foundation of China (No. 21905044), Natural Science Foundation of Guangdong Province (No. 2018A030310004), and Research Start-up Funds of Dongguan University of Technology (GC300501-077).

SUPPLEMENTARY MATERIAL

The Supplementary Material for this article can be found online at: https://www.frontiersin.org/articles/10.3389/fchem.2020.00151/full#supplementary-material

REFERENCES

Aellig, C., Ulrich, N., and Hermans, I. (2012). Acid-catalyzed decomposition of the benzyl nitrite intermediate in HNO_3-mediated aerobic oxidation of benzyl alcohol. *ChemCatChem* 4, 525–529. doi: 10.1002/cctc.201100439

Albadi, J., Alihoseinzadeh, A., and Razeghi, A. (2014). Novel metal oxide nanocomposite of Au/CuO–ZnO for recyclable catalytic aerobic oxidation of alcohols in water. *Catal. Commun*. 49, 1–5. doi: 10.1016/j.catcom.2014.01.030

Cánepa, A. L., Elías, V. R., Vaschetti, V. M., Sabre, E. V., Eimer, G. A., Casuscelli, S. G., et al. (2017). Selective oxidation of benzyl alcohol through eco-friendly processes using mesoporous V-MCM-41, Fe-MCM-41 and Co-MCM-41 materials. *Appl. Catal. A Gen.* 545, 72–78. doi: 10.1016/j.apcata.2017.07.039

Cao, Y., Li, Y., Yu, H., Peng, F., and Wang, H. (2015). Aerobic oxidation of α-pinene catalyzed by carbon nanotubes. *Catal. Sci. Technol*. 5, 3935–3944. doi: 10.1039/C5CY00136F

Cao, Y., Luo, X., Yu, H., Peng, F., Wang, H., Ning, G., et al. (2013). sp 2-and sp 3-hybridized carbon materials as catalysts for aerobic oxidation of cyclohexane. *Catal. Sci. Technol*. 3, 2654–2660. doi: 10.1039/c3cy00256j

Chen, C. T., Nguyen, C. V., Wang, Z. Y., Bando, Y., Yamauchi, Y., Bazziz, M. T. S., et al. (2018a). Hydrogen peroxide assisted selective oxidation of 5-hydroxymethylfurfural in water under mild conditions. *ChemCatChem* 10, 361–365. doi: 10.1002/cctc.201701302

Chen, H., Shen, J., Chen, K., Qin, Y., Lu, X., Ouyang, P., et al. (2018b). Atomic layer deposition of Pt nanoparticles on low surface area zirconium oxide for the efficient base-free oxidation of 5-hydroxymethylfurfural to 2,5-furandicarboxylic acid. *Appl. Catal. A Gen.* 555, 98–107. doi: 10.1016/j.apcata.2018.01.023

Choudhary, V. R., Dhar, A., Jana, P., Jha, R., and Uphade, B. S. (2005). A green process for chlorine-free benzaldehyde from the solvent-free oxidation of benzyl alcohol with molecular oxygen over a supported nano-size gold catalyst. *Green Chem*. 7, 768–770. doi: 10.1039/b509003b

Cordoba, M., Miranda, C., Lederhos, C., Coloma-Pascual, F., Ardila, A., Fuentes, G., et al. (2017). Catalytic performance of Co3O4 on different activated carbon supports in the benzyl alcohol oxidation. *Catalysts* 7:384. doi: 10.3390/catal7120384

Dong, G., Zhao, L., Wu, X., Zhu, M., and Wang, F. (2019). Photocatalysis removing of NO based on modified carbon nitride: the effect of celestite mineral particles. *Appl. Catal. B Environ*. 245, 459–468. doi: 10.1016/j.apcatb.2019.01.013

Dressen, M. H. C. L., Stumpel, J. E., van de Kruijs, B. H. P., Meuldijk, J., Vekemans, J. A. J. M., and Hulshof, L. A. (2009). The mechanism of the oxidation of benzyl alcohol by iron(III)nitrate: conventional versus microwave heating. *Green Chem*. 11, 60–64. doi: 10.1039/B813030B

Fei, J., Sun, L., Zhou, C., Ling, H., Yan, F., Zhong, X., et al. (2017). Tuning the synthesis of manganese oxides nanoparticles for efficient oxidation

of benzyl alcohol. *Nanoscale Res. Lett*. 12:23. doi: 10.1186/s11671-016-1777-y

Ganesamoorthy, S., Tamizh, M. M., Shanmugasundaram, K., and Karvembu, R. (2013). Immobilization of Ru (III) complex on silica: a heterogenized catalyst for selective oxidation of alcohols in water at room temperature. *Tetrahedron Lett.* 54, 7035–7039. doi: 10.1016/j.tetlet.2013.10.070

Gurrala, L., Nagpure, A. S., Gurav, H. R., and Chilukuri, S. (2018). Spinel-type mixed oxides for stable and selective partial oxidation of benzyl alcohol. *Chemistryselect* 3, 3751–3761. doi: 10.1002/slct.201800321

Hansen, T. S., Sádaba, I., García-Suárez, E. J., and Riisager, A. (2013). Cu catalyzed oxidation of 5-hydroxymethylfurfural to 2,5-diformylfuran and 2,5-furandicarboxylic acid under benign reaction conditions. *Appl. Catal. A Gen.* 456, 44–50. doi: 10.1016/j.apcata.2013.01.042

Hanson, S. K., Baker, R. T., Gordon, J. C., Scott, B. L., Sutton, A. D., and Thorn, D. L. (2008). Aerobic oxidation of pinacol by vanadium (V) dipicolinate complexes: evidence for reduction to vanadium (III). *J. Am. Chem. Soc*. 131, 428–429. doi: 10.1021/ja807522n

Hu, Y., Chen, L., and Li, B. (2016). Iron nitrate/TEMPO-catalyzed aerobic oxidative synthesis of quinazolinones from alcohols and 2-aminobenzamides with air as the oxidant. *RSC Adv*. 6, 65196–65204. doi: 10.1039/C6RA12164K

Hu, Y., Chen, L., and Li, B. (2018). Fe(NO 3) 3 /2,3-dichloro-5,6-dicyano-1,4-benzoquinone (DDQ): an efficient catalyst system for selective oxidation of alcohols under aerobic conditions. *Catal. Commun*. 103, 42–46. doi: 10.1016/j.catcom.2017.09.019

Jachuck, R. J. J., Selvaraj, D. K., and Varma, R. S. (2006). Process intensification: oxidation of benzyl alcohol using a continuous isothermal reactor under microwave irradiation. *Green Chem*. 8, 29–33. doi: 10.1039/B512732G

Ji, H., Wang, T., Zhang, M., She, Y., and Wang, L. (2005). Simple fabrication of nano-sized NiO2 powder and its application to oxidation reactions. *Appl. Catal. A Gen*. 282, 25–30. doi: 10.1016/j.apcata.2004.11.043

Jia, X., Ma, J., Wang, M., Du, Z., Lu, F., Wang, F., et al. (2014). Promoted role of Cu(NO3)2 on aerobic oxidation of 5-hydroxymethylfurfural to 2,5-diformylfuran over VOSO4. *Appl. Catal. A Gen*. 482, 231–236. doi: 10.1016/j.apcata.2014.05.031

Jiang, X., Zhang, J., and Ma, S. (2016). Iron catalysis for room-temperature aerobic oxidation of alcohols to carboxylic acids. *J. Am. Chem. Soc*. 138, 8344–8347. doi: 10.1021/jacs.6b03948

Jing, H., Keqiang, S., Daiping, H., and Boqing, X. (2007). Amorphous manganese oxide for catalytic aerobic oxidation of benzyl alcohol. *Chin. J. Catal*. 28, 1025–1027. doi: 10.1016/S1872-2067(08)60001-7

Joshi, S. R., Kataria, K. L.,Sawant, S. B., and Joshi, J. B. (2005). Kinetics of oxidation of benzyl alcohol with dilute nitric acid. *Indust. Eng. Chem. Res*. 44, 325–333. doi: 10.1021/ie0303911

Li, M., Wu, S., Yang, X., Hu, J., Peng, L., Bai, L., et al. (2017). Highly efficient single atom cobalt catalyst for selective oxidation of alcohols. *Appl. Catal. A Gen*. 543, 61–66. doi: 10.1016/j.apcata.2017.06.018

Li, M., Xu, F., Li, H., and Wang, Y. (2016). Nitrogen-doped porous carbon materials: promising catalysts or catalyst supports for heterogeneous hydrogenation and oxidation. *Catal. Sci. Technol*. 6, 3670–3693. doi: 10.1039/C6CY00544F

Liu, J., Zou, S., Lu, L., Zhao, H., Xiao, L., and Fan, J. (2017). Room temperature selective oxidation of benzyl alcohol under base-free aqueous conditions on Pt/TiO2. *Catal. Commun*. 99, 6–9. doi: 10.1016/j.catcom.2017.05.015

Long, J., Xie, X., Xu, J., Gu, Q., Chen, L., and Wang, X. (2012). Nitrogen-doped graphene nanosheets as metal-free catalysts for aerobic selective oxidation of benzylic alcohols. *ACS Catal*. 2, 622–631. doi: 10.1021/cs3000396

Lu, C., Hu, J. M., Meng, Y. N., Zhou, A. D., Zhang, F., and Zhang, Z. B. (2019). The synergistic effect of benzyl benzoate on the selective oxidation of toluene to benzaldehyde. *Chem. Eng. Res. Des*. 141, 181–186. doi: 10.1016/j.cherd.2018.10.019

Luo, J., Peng, F., Yu, H., and Wang, H. (2012). Selective liquid phase oxidation of benzyl alcohol catalyzed by carbon nanotubes. *Chem. Eng. J*. 204–206, 98–106. doi: 10.1016/j.cej.2012.07.098

Luo, J., Yu, H., Wang, H., Wang, H., and Peng, F. (2014). Aerobic oxidation of benzyl alcohol to benzaldehyde catalyzed by carbon nanotubes without any promoter. *Chem. Eng. J*. 240, 434–442. doi: 10.1016/j.cej.2013.11.093

Lv, L. B., Yang, S. Z., Ke, W. Y., Wang, H. H., Zhang, B., Zhang, P., et al. (2018). Mono-atomic Fe centers in nitrogen/carbon monolayers for liquid-phase selective oxidation reaction. *ChemCatChem* 10, 3539–3545. doi: 10.1002/cctc.201800707

Mahmood, A., Robinson, G. E., and Powell, L. (1999). An improved oxidation of an alcohol using aqueous permanganate and phase-transfer catalyst. *Organ. Proc. Res. Dev*. 3, 363–364. doi: 10.1021/op990021h

Mal, D. D., Khilari, S., and Pradhan, D. (2018). Efficient and selective oxidation of toluene to benzaldehyde on manganese tungstate nanobars: a noble metal-free approach. *Green Chem*. 20, 2279–2289. doi: 10.1039/C8GC00123E

Martin, S. E., and Suárez, D. F. (2002). Catalytic aerobic oxidation of alcohols by Fe(NO3)3–FeBr3. *Tetrahedron Lett*. 43, 4475–4479. doi: 10.1016/S0040-4039(02)00829-8

Miao, C., Zhao, H., Zhao, Q., Xia, C., and Sun, W. (2016). NHPI and ferric nitrate: a mild and selective system for aerobic oxidation of benzylic methylenes. *Catal. Sci. Technol*. 6, 1378–1383. doi: 10.1039/C5CY01245G

Miao, C. X., Wang, J.-Q., Yu, B., Cheng, W.-G., Sun, J., Chanfreau, S., et al. (2011). Synthesis of bimagnetic ionic liquid and application for selective aerobic oxidation of aromatic alcohols under mild conditions. *Chem. Commun*. 47, 2697–2699. doi: 10.1039/c0cc04644b

Ndolomingo, M. J., and Meijboom, R. (2017). Selective liquid phase oxidation of benzyl alcohol to benzaldehyde by tert-butyl hydroperoxide over gamma-Al2O3 supported copper and gold nanoparticles. *Appl. Surf. Sci*. 398, 19–32. doi: 10.1016/j.apsusc.2016.12.020

Nie, R., Shi, J., Du, W., Ning, W., Hou, Z., and Xiao, F. S. (2013). A sandwich N-doped graphene/Co_3 O_4 hybrid: an efficient catalyst for selective oxidation of olefins and alcohols. *J. Mater. Chem. A* 1, 9037–9045. doi: 10.1039/c3ta11672g

Öztürk, Ö. F., Zümreoglu-Karan, B., and Karabulut, S. (2008). Solvent-free oxidation of benzyl alcohol over chromium orthoborate. *Catal. Commun.* 9, 1644–1648. doi: 10.1016/j.catcom.2008.01.016

Parmeggiani, C., and Camilla, F. (2012). Transition metal based catalysts in the aerobic oxidation of alcohols. *Green Chem*. 14, 547–564. doi: 10.1039/c2gc16344f

Ragupathi, C., Judith Vijaya, J., Narayanan, S., Jesudoss, S. K., and John Kennedy, L. (2015). Highly selective oxidation of benzyl alcohol to benzaldehyde with hydrogen peroxide by cobalt aluminate catalysis: a comparison of conventional and microwave methods. *Ceram Int*. 41, 2069–2080. doi: 10.1016/j.ceramint.2014.10.002

Shen, X., Dong, G., Wang, L., Ye, L., and Sun, J. (2019). Enhancing photocatalytic activity of NO removal through an *in situ* control of oxygen vacancies in growth of TiO_2. *Adv. Mater. Interf*. 6:1901032. doi: 10.1002/admi.201901032

Shen, Z., Chen, M., Fang, T., Li, M., Mo, W., Hu, B., et al. (2015). Transformation of ethers into aldehydes or ketones: a catalytic aerobic deprotection/oxidation pathway. *Tetrahedron Lett.* 56, 2768–2772. doi: 10.1016/j.tetlet.2015.04.033

Shimizu, H., Onitsuka, S., Egami, H., and Katsuki, T. (2005). Ruthenium(salen)-catalyzed aerobic oxidative desymmetrization of meso-diols and its kinetics. *J. Am. Chem. Soc.* 127, 5396–5413. doi: 10.1021/ja047608i

Tamizhdurai, P., Sakthinathan, S., Chen, S. M., Shanthi, K., Sivasanker, S., and Sangeetha, P. (2017). Environmentally friendly synthesis of CeO2 nanoparticles for the catalytic oxidation of benzyl alcohol to benzaldehyde and selective detection of nitrite. *Sci. Rep*. 7:46372. doi: 10.1038/srep46372

Thao, N. T., Nhu, N. T., and Lin, K. S. (2018). Liquid phase oxidation of benzyl alcohol to benzaldehyde over sepiolite loaded chromium oxide catalysts. *J. Taiwan Inst. Chem. Eng*. 83, 10–22. doi: 10.1016/j.jtice.2017.11.034

Thottathil, J. K., Moniot, J. L., Mueller, R. H., Wong, M. K., and Kissick, T. P. (1986). Conversion of L-pyroglutamic acid to 4-alkyl-substituted L-prolines. The synthesis of trans-4-cyclohexyl-L-proline. *J. Organ. Chem*. 51, 3140–3143. doi: 10.1021/jo00366a011

Villa, A., Wang, D., Dimitratos, N., Su, D., Trevisan, V., and Prati, L. (2010). Pd on carbon nanotubes for liquid phase alcohol oxidation. *Catal Today* 150, 8–15. doi: 10.1016/j.cattod.2009.06.009

Wang, N., Liu, R., Chen, J., and Liang, X. (2005). $NaNO_2$-activated, iron-TEMPO catalyst system for aerobic alcohol oxidation under mild conditions. *Chem. Commun*. 42, 5322–5324. doi: 10.1039/b509167e

Xie, J., Yin, K., Serov, A., Artyushkova, K., Pham, H. N., Sang, X., et al. (2017). Selective aerobic oxidation of alcohols over atomically-dispersed non-precious metal catalysts. *ChemSusChem* 10, 359–362. doi: 10.1002/cssc.201601364

Yang, M., Ling, Q., Yang, H., Li, C., and Zhang, A. (2014). Enhanced catalytic activity of K-birnessite MnO2 confined in carbon nanotubes

for selective oxidation of benzyl alcohol. *Catal. Commun*. 46, 238–241. doi: 10.1016/j.catcom.2013.12.031

Yang, X., Wu, S., Hu, J., Fu, X., Peng, L., Kan, Q., et al. (2016). Highly efficient N-doped magnetic cobalt-graphene composite for selective oxidation of benzyl alcohol. *Catal. Commun*. 87, 90–93. doi: 10.1016/j.catcom.2016.09.015

Yu, H., Peng, F., Tan, J., Hu, X., Wang, H., Yang, J., et al. (2011). Selective catalysis of the aerobic oxidation of cyclohexane in the liquid phase by carbon nanotubes. *Angew. Chem. Int. Ed*. 50, 3978–3982. doi: 10.1002/anie.201007932

Yuan, Z., Liu, B., Zhou, P., Zhang, Z., and Chi, Q. (2018). Aerobic oxidation of biomass-derived 5-hydroxymethylfurfural to 2, 5-diformylfuran with cesium-doped manganese dioxide. *Catal. Sci. Technol*. 8, 4430–4439. doi: 10.1039/C8CY01246F

Yuvaraj, S., Fan-Yuan, L., Tsong-Huei, C., and Chuin-Tih, Y. (2003). Thermal decomposition of metal nitrates in air and hydrogen environments. *J. Phys. Chem. B* 107, 1044–1047. doi: 10.1021/jp026961c

Zhan, G., Huang, J., Du, M., Sun, D., Abdul-Rauf, I., Lin, W., et al. (2012). Liquid phase oxidation of benzyl alcohol to benzaldehyde with novel uncalcined bioreduction au catalysts: high activity and durability. *Chem. Eng. J*. 187, 232–238. doi: 10.1016/j.cej.2012.01.051

Zhang, E., Tian, H., Xu, S., Yu, X., and Xu, Q. (2013). Iron-catalyzed direct synthesis of imines from amines or alcohols and amines via aerobic oxidative reactions under air. *Organ. Lett*. 15, 2704–2707. doi: 10.1021/ol4010118

Zhao, L., Dong, G., Zhang, L., Lu, Y., and Huang, Y. (2019). Photocatalytic nitrogen oxide removal activity improved step-by-step through serial multistep Cu modifications. *ACS Appl. Mater. Interfaces* 11, 10042–10051. doi: 10.1021/acsami.9b00111

Zhou, W., Liu, J., Pan, J., Sun, F. A., He, M., and Chen, Q. (2015). Effect of Mg2+ on the catalytic activities of CoMgAl hydrotalcites in the selective oxidation of benzyl alcohol to benzaldehyde. *Catal. Commun*. 69, 1–4. doi: 10.1016/j.catcom.2015.05.012

Zhu, S., Cen, Y., Yang, M., Guo, J., Chen, C., Wang, J., et al. (2017). Probing the intrinsic active sites of modified graphene oxide for aerobic benzylic alcohol oxidation. *Appl. Catal. B Environ*. 211, 89–97. doi: 10.1016/j.apcatb.2017.04.035

Conflict of Interest: The authors declare that the research was conducted in the absence of any commercial or financial relationships that could be construed as a potential conflict of interest.

frontiers in Chemistry

ORIGINAL RESEARCH
published: 29 April 2020
doi: 10.3389/fchem.2020.00317

Methane Decomposition Over ZrO_2-Supported Fe and Fe–Ni Catalysts—Effects of Doping La_2O_3 and WO_3

*Anis H. Fakeeha[1,2], Samsudeen Olajide Kasim[1], Ahmed Aidid Ibrahim[1], Abdulrhman S. Al-Awadi[1], Eman Alzahrani[3], Ahmed Elhag Abasaeed[1], Ahmed E. Awadallah[4] and Ahmed Sadeq Al-Fatesh[1]**

[1] Chemical Engineering Department, College of Engineering, King Saud University, Riyadh, Saudi Arabia, [2] King Abdullah City for Atomic and Renewable Energy (K.A.CARE), Energy Research and Innovation Center, Riyadh, Saudi Arabia, [3] Department of Chemistry, Faculty of Science, Taif University, Taif, Saudi Arabia, [4] Process Development Division, Egyptian Petroleum Research Institute, Cairo, Egypt

OPEN ACCESS

Edited by:
Kevin Morgan,
Queen's University Belfast,
United Kingdom

Reviewed by:
Ahmed I. Osman,
Queen's University Belfast,
United Kingdom
Shanhui Zhu,
Institute of Coal Chemistry (CAS),
China

***Correspondence:**
Ahmed Sadeq Al-Fatesh
aalfatesh@ksu.edu.sa

Specialty section:
This article was submitted to Catalysis and Photocatalysis, a section of the journal Frontiers in Chemistry

Received: 15 January 2020
Accepted: 30 March 2020
Published: 29 April 2020

Citation:
Fakeeha AH, Kasim SO, Ibrahim AA, Al-Awadi AS, Alzahrani E, Abasaeed AE, Awadallah AE and Al-Fatesh AS (2020) Methane Decomposition Over ZrO_2-Supported Fe and Fe–Ni Catalysts—Effects of Doping La_2O_3 and WO_3. Front. Chem. 8:317. doi: 10.3389/fchem.2020.00317

A leading method for hydrogen production that is free of carbon oxides is catalytic methane decomposition. In this research, Fe and Fe–Ni supported catalysts prepared by the wet impregnation method were used in methane decomposition. The effects of doping the parent support (ZrO_2) with La_2O_3 and WO_3 were studied. It was discovered that the support doped with La_2O_3 gave the best performance in terms of CH_4 conversion, H_2 yield, and stability at the test condition, 800°C and 4,000-ml h^{-1} g^{-1} cat. space velocity. The addition of Ni significantly improved the performance of all the monometallic catalysts. The catalysts were characterized by X-ray diffraction (XRD), Brunauer–Emmett–Teller (BET), temperature-programmed reduction/oxidation (TPR/TPO), thermogravimetric analyzer (TGA), and microscopy (SEM and Raman) techniques. Phases of the different forms of Fe were identified by XRD. BET showed a drastic decline in the specific surface area of the catalysts with respect to the supports. TPR profiles revealed a progressive change in the valency of Fe in its combined form to the zero valence-free metal. The La_2O_3-promoted support gave the best performance and maintained good stability during the time on stream.

Keywords: Fe, Fe–Ni, La_2O_3 + ZrO_2, WO_3 + ZrO_2, methane conversion, hydrogen, graphitization, Raman spectra

INTRODUCTION

Methane (CH_4) is the main component of natural and biogas. Its use as a feed is expected to increase in the current year due to greenhouse gas effects (Fakeeha et al., 2015; Calgaro and Perez-Lopez, 2019). Global warming has been a great concern for mankind. Emissions of greenhouse gases like CH_4 contribute aggressively to environmental issues. Methods of transforming CH_4 into handy products are worthy from the prospect of safety and the economic point of view of generating value-added fuels and chemicals (Ashok et al., 2008; Muhammad et al., 2018; Zhang et al., 2018). In this context, a direct approach is chosen for hydrogen (H_2) and elemental carbon production, as given in Equation (1). H_2, which has been considered to be among the greenest and lightest fuel, is pivotal in the broad requirement of energy, while the carbon that is produced as a by-product could function as a value-added product in power generation and as a catalyst. A filamentous form

of carbon and graphene, which is formed from the catalytic methane decomposition (CMD), is highly important in nanoscience because of its distinctive properties (i.e., electrical, chemical, and mechanical) (Pudukudy et al., 2016). Another form of carbon that is of interest and that can be obtained using this process is graphene (Jana et al., 2011; Ibrahim et al., 2015; Pudukudy et al., 2016). It has gained much attention in light of its excellent properties, such as its extraordinary chemical stability, large surface area, and good structural strength and conductivity (electrical and thermal) (Li et al., 2011; Wang and Lau, 2015; Ashik et al., 2017).

Furthermore, other methods by which H_2 could be generated from CH_4 exist. These include steam reforming, partial oxidation, and hydrogen sulfide methane reformation. Steam reforming is the cheapest source of H_2 at the moment, and it involves heating methane to around 700–1,100°C in the presence of steam and a catalyst (e.g., nickel). However, the downside of this process is that CO, CO_2, and other greenhouse gases are its major by-products. A ton of H_2 produced will consequently have 9–12 ton of CO_2 being produced alongside (Collodi, 2010).

Equation (1) implies a reaction that takes place at higher temperatures; consequently, the applications of catalysts are in binding to reduce the activation energy (Ashik et al., 2017). To enhance the CH_4 decomposition reaction, metal-based catalysts were often used by researchers. These include transition metals such as Fe and Ni with a partially filled d-orbital. These metals are characterized by a low price and better stability and activity (Ashik et al., 2015; Inaba et al., 2019). Supported Ni-based catalysts are preferable for the CMD process due to their high activity, cheap price, and wide availability.

$$CH_4 \rightarrow C + 2H_2 \; 74.9 \text{ kJ mol}^{-1} \quad (1)$$

Karaismailoglu et al. investigated catalytic methane decomposition using yttria-doped nickel-based catalysts (Karaismailoglu et al., 2019). They prepared their catalyst using a sol–gel technique and studied the activity in the temperature range between 390° and 845°C. Their results showed that increasing the temperature favored the formation of coke, and the CH_4 conversions of 14 and 50% at 500° and 800°C, respectively, were attained.

Another study that is of interest is methane decomposition without catalyst pre-reduction. This was aimed at reducing the operating cost of the whole process, and thus, reduction of the catalysts in the gas feed stream was performed. However, the hydrogen yields for such processes were reported to be low (Enakonda et al., 2016; Musamali and Isa, 2018).

Transition metals (e.g., Ni, Co, and Fe) supported on different oxides have been the widely used catalysts in CMD reactions (Cunha et al., 2009; Shen and Lua, 2015). The effects of different supports such as La_2O_3, ZrO_2, SiO_2, Al_2O_3, SiO_2/Al_2O_3, and TiO_2 on Ni-based catalysts have been studied (Muraza and Galadima, 2015; Khan et al., 2016). Furthermore, promising results were obtained in the investigation of Fe over La_2O_3 at the temperature range of 500–750°C (Ibrahim et al., 2018). As at the time of preparing this report, no study has been reported in the literature on catalytic methane decomposition using Fe supported on zirconia (ZrO_2) and WO_3. More so, the properties of a single metal catalyst have been reported to be enhanced *via* the introduction of a second metal, therefore leading to a bimetallic catalyst idea (Pudukudy et al., 2014). This study will also investigate the effect of adding Ni to the Fe supported catalysts.

The major problem of the CMD is the rapid deactivation of the catalyst caused by the deposition of amorphous carbon on the surface of the catalyst. This low-activity carbon covers the active metal particle (Calgaro and Perez-Lopez, 2017). It has been established that Ni catalysts are effective for methane decomposition reaction at temperatures of 500–600°C, which are below the equilibrium-required temperature. At higher temperatures, Ni catalysts deactivate rapidly, but Fe can withstand these necessary high temperatures. Also, Fe is relatively cheaper than Ni (Inaba et al., 2002).

During this investigation, monometallic Fe- and bimetallic Fe/Ni-based catalysts supported over zirconia and modified zirconia were used for the catalytic decomposition of CH_4. The effects of the catalyst composition, in terms of active metals and the support modification, were evaluated based on the characteristics of the catalyst's stability and activity. The best catalyst composition has been determined. The efficiency of the catalysts in the decomposition of CH_4, with respect to activity and stability, was studied.

MATERIALS AND METHODS

Catalyst Preparation

Monometallic supported Fe catalysts, as well as the bimetallic supported catalysts (Fe and Ni) used in this study, were synthesized using the technique called wet impregnation. The supports (ZrO_2, 9%La_2O_3-ZrO_2, and 10%WO_3-ZrO_2) were obtained from Daiichi Kigenso Kagaku Kogyo Co., Ltd. (Osaka, Japan), and the authors are really grateful for the support. Hydrated iron nitrate [$Fe(NO_3)_3 \cdot 9H_2O$, 99%] was used as the active metal for the monometallic supported catalysts, while iron and nickel nitrate salts were combined in appropriate proportions and used as the active metals in the bimetallic supported catalysts. The percentage loading of Fe was 40 wt% for the monometallic and 20 wt% for each one of Fe and Ni in the bimetallic supported catalysts. The stoichiometric amounts of all active metals were measured and added to distilled water (30 ml), followed by the supports. The support-active metal mixtures, present in separate crucibles, were stirred and dried at 80°C for 3 h over different hot plates. Subsequently, the samples were placed inside an oven for overnight drying at 120°C. Calcination of the samples was done at 800°C for 3 h in the oven.

Catalyst Activity

The CMD study was performed using Fe and bimetallic Fe–Ni supported catalysts in an upright, fixed-bed, stainless steel tubular micro-reactor (PID Eng&Tech microactivity reference), 9.1-mm ID and 30 cm long, at atmospheric pressure. Catalyst testing was performed using a catalyst mass of 0.3 g, which was carefully positioned over a bed of glass wool inside the reactor. The actual reactor temperature was read by an axially positioned

thermocouple (K-type), sheathed in stainless steel. The total time of analysis for each of the catalysts was 240 min. Before the start of the reaction, each of the catalysts was reduced under the flow of H_2 at 20 ml/min for 90 min at 800°C. Thereafter, the system was purged with N_2 for 15 min to remove any remnant of H_2. The temperature of the reactor was raised to that required for the reaction (i.e., 800°C) in the flow of N_2. The feed gas mixture was maintained at a total flow rate of 20 ml/min (13 and 7 ml/min for CH_4 and N_2, respectively) and an equivalent space velocity of 4,000 m h^{-1} g^{-1}-cat. The product gas composition was analyzed by gas chromatography (GC; Shimadzu, 2004), which was connected online. The GC is equipped with a thermal conductivity detector (TCD). The following expressions were used to determine the methane conversion and hydrogen yield:

$$CH_4 \text{ conversion} = \frac{CH_4 \text{ in} - CH_4 \text{ out}}{CH_4 \text{ in}} \times 100\%$$

$$H_2 \text{ Yield}: Y_{H_2} = \frac{\text{moles of } H_2 \text{ produced}}{2 \times \text{moles of } CH_4 \text{ in the feed}} \times 100\%$$

Catalyst Characterization

The phase formation and crystal structure of fresh catalyst samples were examined using an X-ray diffractometer (XRD). A Miniflex Rigaku diffractometer, having CuKα X-ray radiation, that operates at 40 kV and 40 mA was employed for the examination. The XRD pattern was taken at a diffraction angle (2θ) between 10 and 80° and a step size of 0.01°. X'pert HighScore Plus software was used to analyze the raw data file of the instrument. Different phases with their scores were matched with the Joint Committee of Powder Diffraction Standards (JCPDS) data bank.

The Micromeritics TriStar II 3020 surface area and porosity analyzer was used in the determination of the textural characteristics of the fresh samples. The analysis was done by N_2 physisorption performed at −196°C. Prior to the analysis, each sample was degassed at 200°C for 3 h in the flow of nitrogen gas. The specific surface area and pore volume of the catalyst samples were calculated by the Brunauer–Emmett–Teller (BET) and Barret–Joyner–Halenda (BJH) methods, respectively.

A Thermo Scientific X-ray photoelectron spectrometer (XPS) was used in recording the XPS data of the fresh catalyst samples. High-resolution scan was achieved using a monochromated Al Kα (1,486.6 eV) radiation source running at a power of 72 W with a pass energy of 50 eV–200 eV for survey scans.

Temperature-programmed reduction/oxidation (TPR/TPO) was performed on the fresh and spent catalysts, respectively, using Micromeritics AutoChem II 2920. For the TPR measurement, 70 mg of the catalyst samples were placed inside the sample tube and then carefully positioned in the machine's furnace. Thereafter, the sample was pretreated by flushing with argon at 150°C for an hour and then cooled to 23°C. Eventually, the furnace temperature was raised to 1,000°C at the ramp of 10°C/min in the presence of a H_2/Ar mixture flowing at 40 ml/min. A cold trap within the machine removes the water produced during the reduction process, while a thermal conductivity detector records the H_2 that was being consumed. For the TPO, measurements were carried out in the presence of oxygen to ascertain the kind of carbon that was deposited onto the surface of the used catalysts. Spent catalysts were subjected to the same pretreatment as in TPR, and the analysis was done at a range of 50–900°C in a mixture of 10% O_2/He flowing at 40 ml/min.

A scanning electron microscope was used to study the changes in the morphology of the calcined samples. A JEOL JSM-7100F (JEOL, Tokyo, Japan) field-emission scanning electron microscope was used for this study.

The determination of the amount of carbon deposits was carried out using a Shimadzu thermogravimetric analyzer (TGA). The temperature of the spent catalysts (10–15 mg) was raised from 23°C up to 1,000°C at the rate of 20°C/min, and the mass difference was recorded by the machine.

Raman spectra were obtained using an NMR-4500 laser Raman spectrometer (JASCO, Japan). The excitation beam was configured to a wavelength of 532 nm. The measurement was done using an objective lens with ×20 magnification. The beam power was set to 6 mW and the exposure time to 3 min to protect the sample from being damaged by laser irradiation. The spectra were measured in the range 500–3,000 cm^{-1} (Raman shift), while Spectra Manager Ver.2 software (JASCO, Japan) was used to process them.

RESULTS AND DISCUSSION

X-Ray Diffraction

The XRD diffractograms of the fresh Fe and Fe–Ni supported samples are presented in **Figure 1**. The XRD revealed the different phases existing on the catalysts. Monometallic catalysts exhibit almost the same peaks at the same 2θ angle.

On the one hand, hematite (Fe_2O_3) (JCPDS card no. 33-0664 at 2θ angles of 30, 40, 50, and 59°) and maghemite Fe_2O_3 (JCPDS card no. 00-039-1346 at 2θ angles of 35 and 62°) phases were obtained in both Fe and Fe–Ni supported catalysts. On the other hand, magnetite (Fe_3O_4, JCPDS card no. 00-019-0629 at 2θ angle of 56°) was obtained in the XRD diffractogram of the Fe–Ni supported catalysts. Besides, a NiO phase was noticed on the bimetallic catalysts at 2θ angle of 36°. The remaining diffraction peaks could be assigned to the tetragonal and monoclinic zirconia phases. It can also be seen that the relative intensities of all the diffraction peaks of Fe supported on the La_2O_3 + ZrO_2 catalyst were more pronounced compared with those of the other catalysts. This indicates that the introduction of La_2O_3 in the catalyst structure improved the dispersion of the metal particles.

Surface Characterization

The BET analysis showed the textural properties of the different supports and catalysts. **Tables 1A**,**B** contain the results of the analysis for the supports as well as that of the synthesized catalysts, respectively. Also, the N_2 adsorption–desorption isotherms are shown in **Figure 2**. An active metal addition to the support consequently led to a drastic decrease in the supports'

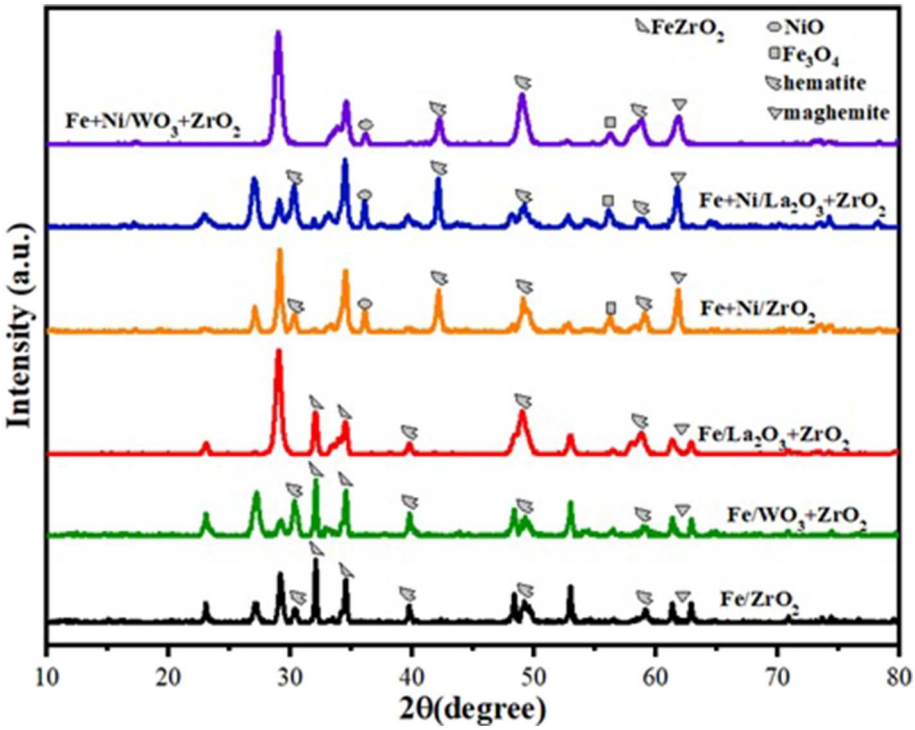

FIGURE 1 | XRD diffractograms for the Fe and Fe–Ni supported catalysts.

TABLE 1A | N_2 physisorption results for the supports.

Catalyst	Specific surface area (m^2/g)	Particle size D50 (μm)
ZrO_2	325	29.7
10%WO_3+ZrO_2	112	3.70
9%La_2O_3+ZrO_2	67.3	4.04

TABLE 1B | N_2 physisorption results for the synthesized catalysts.

Catalyst	BET surface area (m^2/g)	Av. Pore diameter (nm)	Pore volume (cm^3/g)
40%Fe/ZrO_2	11.23	36.88	0.09
40%Fe/La_2O_3+ZrO_2	16.34	30.14	0.11
40%Fe/WO_3+ZrO_2	21.75	20.33	0.10
20%Fe+20%Ni/ZrO_2	7.16	43.55	0.06
20%Fe+20%Ni/ La_2O_3+ZrO_2	21.12	27.37	0.13
20%Fe+20%Ni/ WO_3+ZrO_2	23.36	18.19	0.01

surface area, probably due to the blockage of the pores of the supports. These isotherms belong to the type IV category, according to the IUPAC classification. Also, all isotherms are characterized by capillary condensation at a higher relative pressure, which is typical of mesoporous materials. The pore size distribution of the supports is shown in **Figure 3**. From the figure, the pore diameters of the samples are within the range of 2–50 nm. It was observed that the addition of Ni led to an increase in the surface area of the catalysts, except for 20%Fe + 20%Ni/ZrO_2. This could be due to the doping effect and the aggregation of the metal particles due to the weak metal–support interaction. The explanation and figure on surface atom identification can be found in **Supplementary File**.

H_2 Temperature-Programmed Reduction

H_2 temperature-programmed reduction (H_2-TPR) was performed to investigate the reducibility and the extent of the metal–support interaction of the calcined single metal (40 wt%Fe)-based catalysts as well as the bimetallic (20 wt% Fe and 20 wt% Ni) counterpart. As shown in **Figure 4**, the H_2-TPR profiles for the single metal-supported catalysts (i.e., 40%Fe/ZrO_2, 40%Fe/La_2O_3 + ZrO_2, and 40%Fe/WO_3 + ZrO_2) showed three distinct reduction peaks at different temperature ranges. The peaks show the progressive reduction of Fe_2O_3 to zero valence Fe ($Fe_2O_3 \rightarrow Fe_3O_4 \rightarrow FeO \rightarrow Fe$). The reduction peak within 300–500°C could be attributed to the reduction of Fe_2O_3 to FeO·Fe_2O_3, while the peaks that appeared within the temperature range of 500–700°C could be assigned to the further reduction of Fe_2O_3 from Fe_3O_4 to FeO. Finally, the temperature range of 700–850°C showed the reduction peaks for FeO to metallic Fe particles. A similar reduction behavior was studied by Bayat et al. while investigating the decomposition of methane over Ni–Fe/Al_2O_3 catalysts intended for the production of CO_x-free hydrogen and carbon nanofiber (Bayat et al., 2016). On the

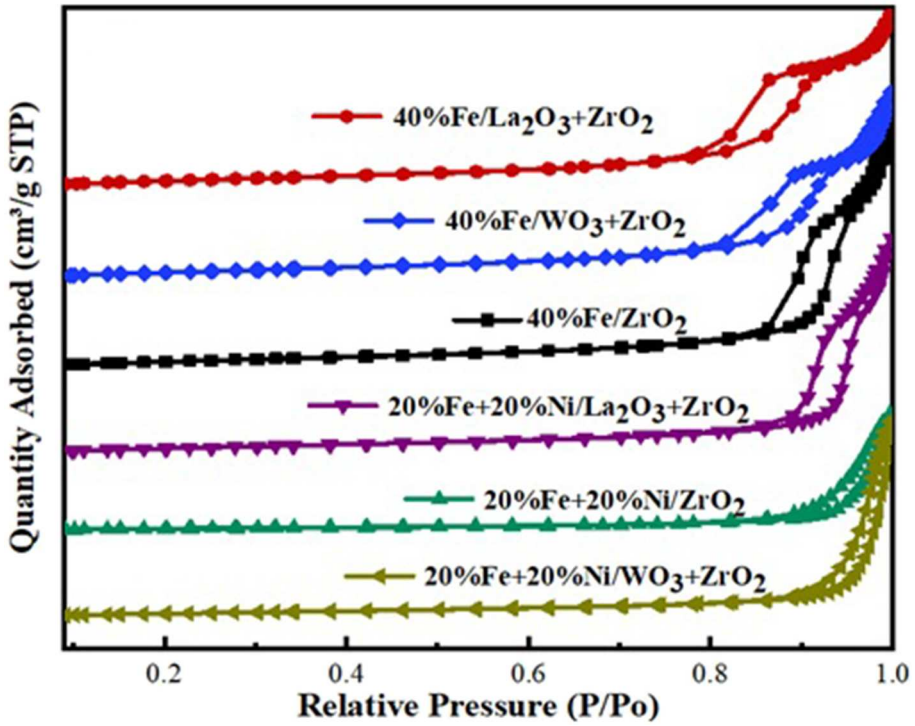

FIGURE 2 | Adsorption–desorption isotherms.

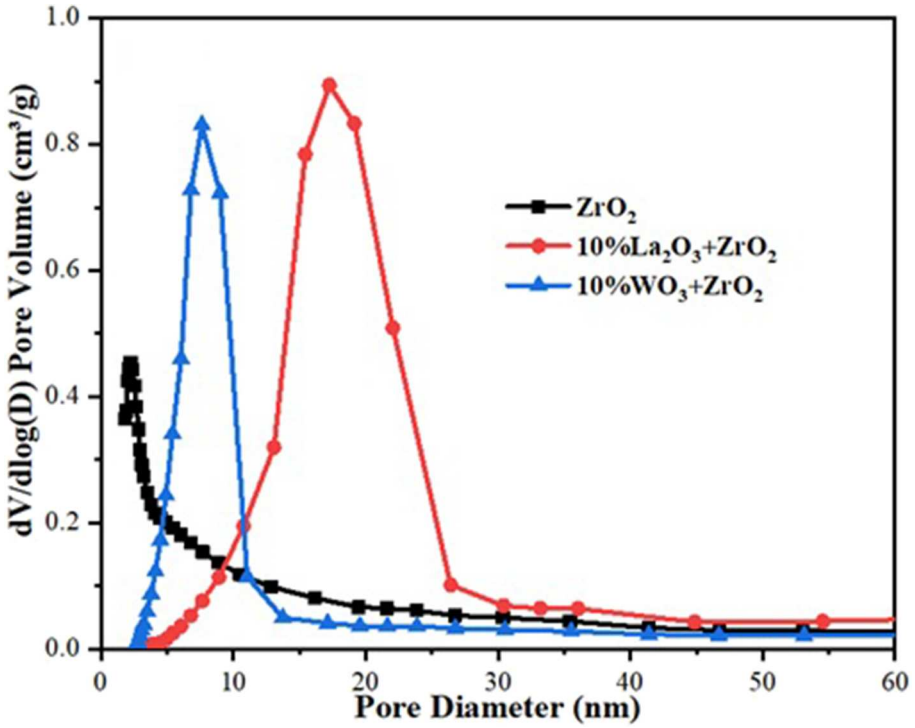

FIGURE 3 | Pore size distribution of Fe and Fe–Ni supported catalysts.

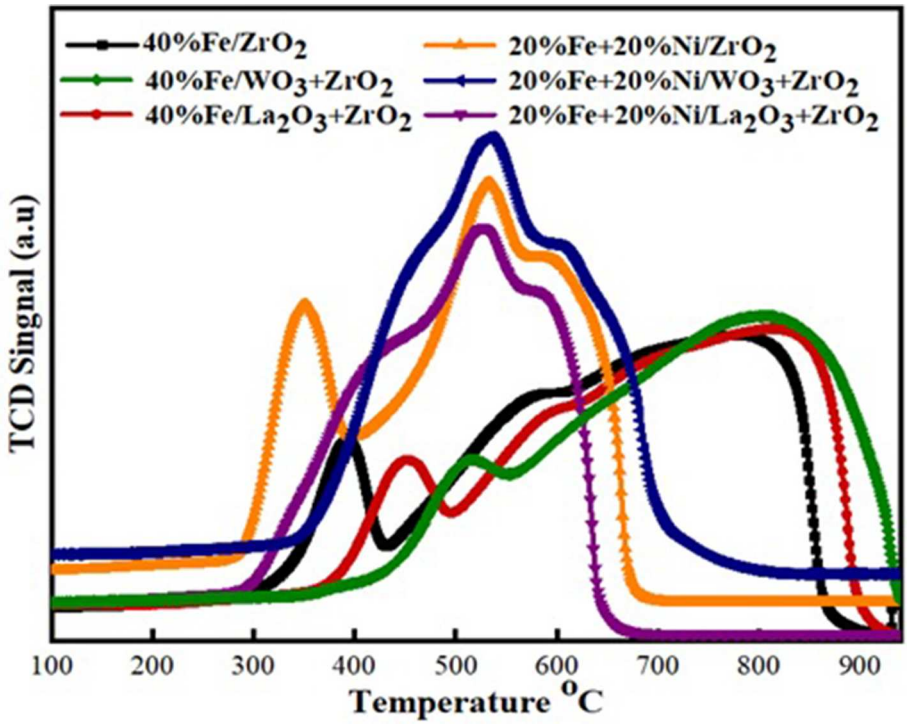

FIGURE 4 | Temperature-programmed reduction (TPR) profiles of the single metal and bimetallic supported catalysts.

one hand, the peaks for 40%Fe/WO_3 + ZrO_2 appeared at higher temperature ranges relative to the other single metal-supported catalysts. This could be attributed to the existence of a stronger interaction between Fe and the support. On the other hand, the reduction peaks for 40%Fe/La_2O_3 + ZrO_2 seemed to be at the intermediate relative to the other single metal-supported catalysts, i.e., the Fe metal is neither weakly nor strongly bound to the support to the extent that will make its activation difficult. H_2 consumption corresponding to the reduction peaks that were obtained during the H_2-TPR analysis is shown in **Table 2**. From this table, 40%Fe/La_2O_3 + ZrO_2 has the least H_2 uptake from among the single metal-supported catalysts, which implies that it could be activated with ease at moderate temperatures.

The same trend of reduction was observed for the bimetallic catalyst samples. The observed difference is that peaks of higher intensity/H_2 consumption were observed for the bimetallic samples owing to the presence of an additional metal oxide, i.e., NiO. Moreover, the reduction peak of NiO at a temperature of ∼350°C for the Fe–Ni/ZrO_2 catalyst disappeared after incorporating La_2O_3 and WO_3 in the catalyst compositions. This further demonstrates the role of these dopants in enhancing the metal dispersion. From **Table 2**, the average H_2 consumptions for the mono- and bimetallic samples are 5,045 and 7,693 μmol/g, respectively. Also, the reduction peaks for the bimetallic samples appeared at lower temperatures relative to the single metal-supported samples. This suggests that the addition of NiO does not only influence the reduction behavior of the catalysts but also improve their reducibility.

TABLE 2 | Quantitative analysis of H_2 consumption during H_2-TPR.

Samples	Temperature (°C)	Quantity consumed (μmol/g)	Total
40%Fe/ZrO_2	363	692.53	5117.28
	628	4192.77	
	743	231.98	
40%Fe/La_2O_3+ZrO_2	383	213.13	4531.15
	594	4184.96	
	754	126.86	
	981	6.20	
40%Fe/WO_3+ZrO_2	496	150.96	5487.09
	578	30.42	
	744	5305.71	
20%Fe+20%Ni/ZrO_2	351	1786.02	8037.23
	533	6251.21	
20%Fe+20%Ni/ La_2O_3+ZrO_2	528	7328.56	7328.56
20%Fe+20%Ni/ WO_3+ZrO_2	533	7713.91	7713.91

Scanning Electron Microscopy

The morphologies of the freshly calcined monometallic Fe- and bimetallic Fe/Ni-containing catalysts were investigated using the SEM technique. The images are displayed in **Figure 5**. The SEM images were recorded at the same magnification to study the

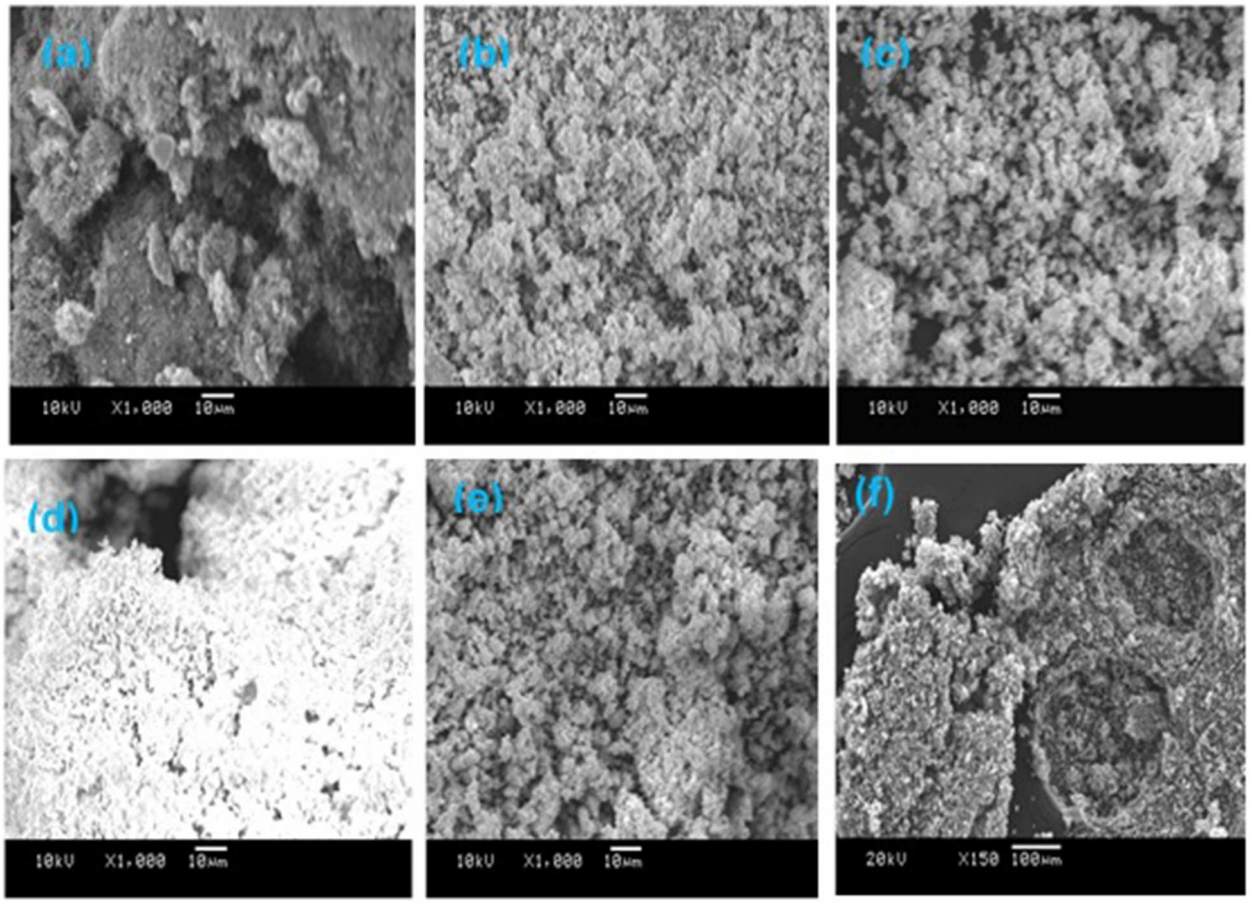

FIGURE 5 | SEM images of fresh calcined catalysts. **(a)** 40%Fe/ZrO2; **(b)** 40%Fe/La_2O_3 + ZrO_2; **(c)** 40%Fe/WO_3 + ZrO_2; **(d)** 20%Fe + 20%Ni/ZrO_2; **(e)** 20%Fe + 20%Ni/WO_3 + ZrO_2; and **(f)** spent 40%Fe/ZrO_2.

change in the surface morphology of the catalysts depending on the type of dopants. As illustrated in **Figure 4A**, the particles of the Fe/ZrO_2 catalyst were found to be large clusters with unclear crystal interfaces and irregular sizes. This manifests that the Fe oxide particles were randomly aggregated on the surface of the zirconia support. Upon the addition of La_2O_3 and WO_3 to the Fe/ZrO_2 catalyst, the particle sizes became smaller, more separated, and better distributed (**Figures 5B,C**). A similar surface morphology was also observed for the bimetallic Fe/Ni-containing catalysts, indicating that the addition of Ni also improved the dispersion of themetal particles (**Figures 5D,E**). The fresh samples have a homogeneous morphology compared to the spent sample (**Figure 5F**). The heterogeneous nature of the morphology of the spent sample is suggestive of the presence of an additional substance (e.g., carbon) that was formed during the reaction.

Catalyst Activity

The catalytic methane decomposition results over 240-min time on stream using 40 wt% Fe and 20 wt% Fe–Ni supported catalysts are shown in **Figures 6**, **7**. The feed was maintained at 4,000-ml h^{-1} g^{-1} cat. space velocity and the reaction was performed at an atmospheric pressure and temperature of 800°C. The results show the effect of doping the primary support (ZrO_2) for the single metal-supported catalysts as well as the effect of adding Ni. From the figure, 40%Fe/La_2O_3 + ZrO_2 gave the highest CH_4 conversion of about 79% compared with 40%Fe/ZrO_2 and 40%Fe/La_2O_3 + ZrO_2, both having 42 and 36%, respectively. 40%Fe/ZrO_2 and 40%Fe/WO_3 + ZrO_2 began with a considerable CH_4 conversion of about 60 and 46%, respectively, but suffered a fast deactivation throughout the study. Fe supported on WO_3 + ZrO_2, i.e., 40%Fe/WO_3 + ZrO_2, had the least conversion, while the catalyst having its support doped with La_2O_3 (i.e., 40%Fe/La_2O_3 + ZrO_2) did not only give a higher performance but also showed the best stability for the period of reaction. The poor performance of the Fe/ZrO_2 may not be unconnected to its low specific surface area. And for Fe/WO_3 + ZrO_2, it appeared that the addition of WO_3 increased the metal–support interaction to the detriment of the availability of the Fe for the reaction.

For the bimetallic catalysts, the addition of 20 wt% Ni improved the CH_4 conversion as well as the stability. The

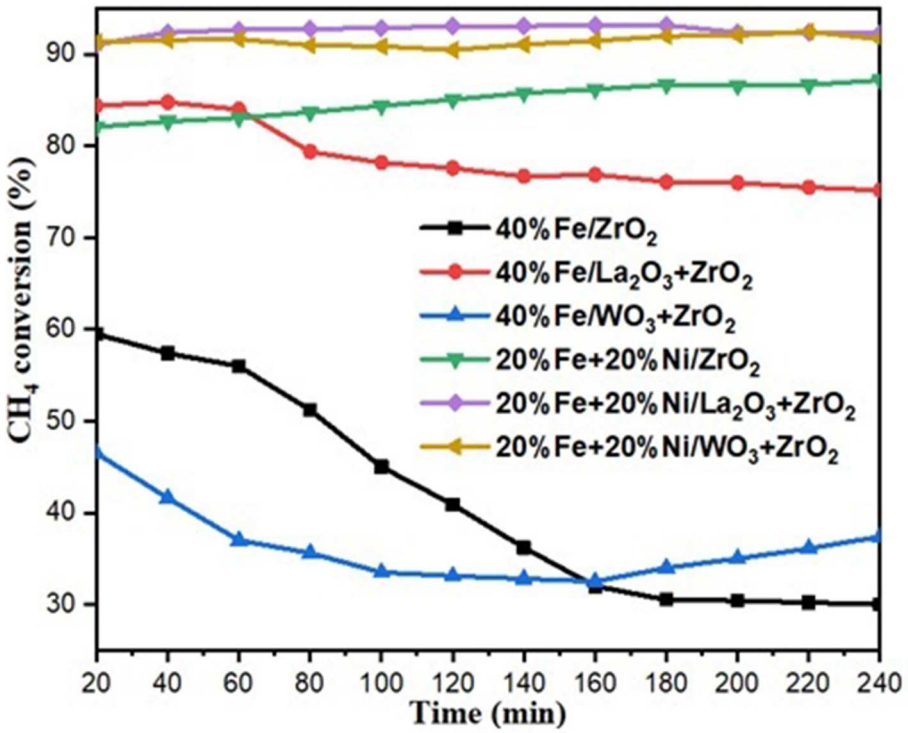

FIGURE 6 | CH_4 conversion for the catalysts under investigation.

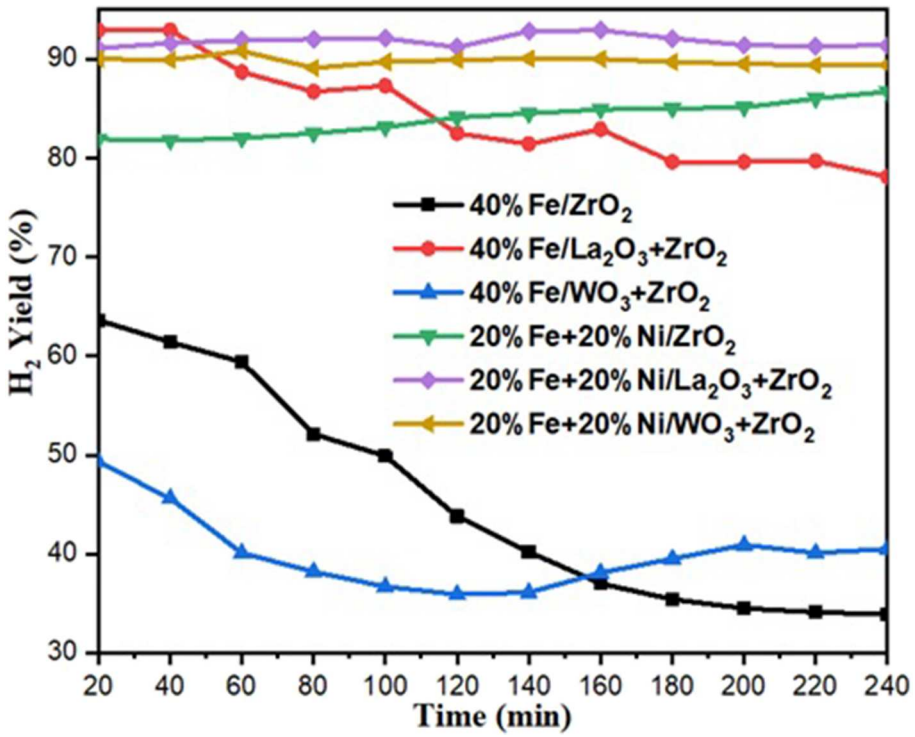

FIGURE 7 | H_2 yield for the catalysts under investigation.

conversion of CH_4 increased to about 85, 91, and 92% for Fe–Ni/ZrO_2, Fe–Ni/WO_3 + ZrO_2, and Fe–Ni/La_2O_3 + ZrO_2, respectively.

Anis et al. reported a similar behavior, where the addition of Ni enhanced the Fe/Al_2O_3 catalyst's performance in their study of the effect of activation temperature, in their paper "*Bimetallic Catalysts of Mesoporous Al_2O_3 Supported on Fe, Ni and Mn for Methane Decomposition: Effect of Activation Temperature*." It was discovered that adding Ni, in an equal amount of Fe, to Fe/Al_2O_3 led to a relatively higher CH_4 conversion of 61% during the reaction (Fakeeha et al., 2018).

Hydrogen yield for the monometallic catalysts revealed that 40%Fe/WO_3 + ZrO_2 gave the least H_2 yield (about 40%), followed by 40%Fe/ZrO_2 (45%), while the 40%Fe/La_2O_3 + ZrO_2 catalyst had the highest H_2 yield of about 84%. The best performance of the Fe catalyst supported on lanthanum-doped ZrO_2 is expected, as the BET results showed that, relatively, it has a considerable specific surface area and the largest pore volume[1]. Ahmed et al. has reported in their findings that higher surface area and pore volume usually enhance catalyst activity (Ahmed et al., 2015). Moreover, the improved metal dispersion after incorporating La_2O_3 into the Fe/ZrO_2 catalyst could also be responsible for its higher activity and stability. The addition of Ni to Fe/ZrO_2 and Fe/WO_3 + ZrO_2 as an active metal greatly raised the H_2 yield to about 84 and 90%, respectively. Also, the catalysts were observed to be stable throughout the investigation. A similar improvement was observed for the Fe–Ni/La_2O_3 + ZrO_2 catalyst, as the H_2 yield increased from 84%, for its monometallic, to 92%. These results are presented in **Figures 6**, **7**. From the results, it can be inferred that, among all the dopants used with ZrO_2, La_2O_3 improved the catalyst's activity.

Table 3 shows the comparison of the catalytic activities reported in the literature, on methane decomposition, with that of the present work. Some catalysts showed high initial conversion and lost their activities while the reaction was going on. Thus, it suffices to say that 20%Fe + 20%Ni/La_2O_3 + ZrO_2 demonstrated the best conversion and stability over the other catalysts being compared.

Thermal Analysis (TGA)

After 240 min of reaction, the spent catalysts were collected from the reactor and subjected to TGA to determine the amount of carbon deposited during the reaction. **Figure 8** shows the TGA curves that translate to the quantitative amount of carbon deposits for all the used catalysts. The total carbon deposited on the spent catalysts was expressed as a weight percentage. For the set of monometallic catalysts, Fe/La_2O_3 + ZrO_2 has the highest amount of carbon deposit of about 65%, while Fe/WO_3 + ZrO_2 has the least carbon deposit equivalent to 57% weight loss. This is in agreement with the results obtained from their CH_4 conversion.

For the bimetallic catalysts, a similar trend was noticed as the addition of Ni increased the activity of the catalysts, with the most active catalyst having the highest amount of carbon deposits.

[1]https://xpssimplified.com/elements/lanthanum.php

From these results, it can be inferred that the addition of Ni enhanced the conversion of CH_4 in all cases and consequently led to a higher carbon deposit since CH_4 is the only source of carbon.

Temperature-Programmed Oxidation

TPO is an essential characterization method useful in determining the kind of deposited carbon found on spent catalysts. The different kinds of carbon formed on a catalyst's surface during the CMD could be removed at different temperature ranges: <250°C (atomic carbon), 250–600°C (amorphous carbon), and >600°C (graphitic carbon) (Hao et al., 2009). In general, the carbon in the shape of a filament has been reported to be formed on the metal catalysts used in methane decomposition reaction (Takenaka et al., 2004; Chen et al., 2005; Nuernberg et al., 2008).

From the TPO results in **Figure 9**, the carbon deposits on Fe/WO_3 + ZrO_2 lie within the temperature range of amorphous and partly graphitic carbon. The deposits on Fe/ZrO_2 and Fe/La_2O_3 + ZrO_2 spanned across the amorphous and graphitic range.

Similarly, for the used bimetallic catalysts, the TPO curves appeared in the range of amorphous and graphitic carbon. All the bimetallic catalysts were observed to have higher activity and stability, as seen in the activity figure; owing to that, the addition of Ni promoted the formation of filamentous–graphitic carbon whose growth does not hinder access to the active metal sites. Zhang et al. reported in their study that the formation and growth of filamentous carbons during catalytic methane decomposition was beneficial in keeping the active Ni sites accessible for CH_4 molecules and, consequently, made it possible for the catalysts to maintain their activity and stability for a longer time (Zhanga et al., 2019).

Raman Spectroscopic Analysis

Raman spectroscopic analysis was performed to study the structure of carbon deposits over the spent catalysts. The obtained Raman spectra are shown in **Figure 10** below. For all the spent samples, two main spectra were observed at ∼1,470 and 1,532 cm^{-1}, corresponding to the D and G bands, respectively. The G band can be attributed to the ideal vibration of the graphite layers as a result of the in-plane carbon–carbon stretching. The D band (disorder mode) is attributed to the structural defect of graphite (Dresselhaus et al., 2010). Besides, a small shoulder (D′) that appeared at 1,596 cm^{-1} can be related to the disordered carbons at the edge (Darmstadt et al., 1997). The 2D band at 2,718 cm^{-1} can be regarded as an overtone of the D band at 1,470 cm^{-1}, but it does not depend on the density of defect. In general, the ratio of the intensity of the D band to the G band (i.e., I_D/I_G) gives a measure of the crystalline order of graphite in carbonaceous materials (Kameya and Hanamura, 2011). This implies that the degree of graphitization is higher for small values of I_D/I_G and *vice versa*. The I_D/I_G of all the spent catalysts shown in **Figure 8** indicate that the carbon deposits over the catalysts have almost equal disordered amorphous and graphitic structures.

TABLE 3 | Comparison of catalytic performance with published results.

Catalysts	Temperature (°C)	GHSV[a] (mL/(gh))	CH_4 conversion (%)	References
40%Fe/Al_2O_3	750	6,000	75	Qian et al., 2019
Ni-Fe/Al_2O_3	800	75,000	60	Tezel et al., 2019
2.5Ni-Y/SiO_2	800	60,000	9	Karaismailoglu et al., 2019
55Ni/MgO	600	48,000	65	Rastegarpanah et al., 2019
40%Fe/La_2O_3+ZrO_2	800	4,000	79	Present work
20%Fe+Ni/La_2O_3+ZrO_2	800	4,000	92	Present work

[a] *GHSV, Gas Hourly Space Velocity.*

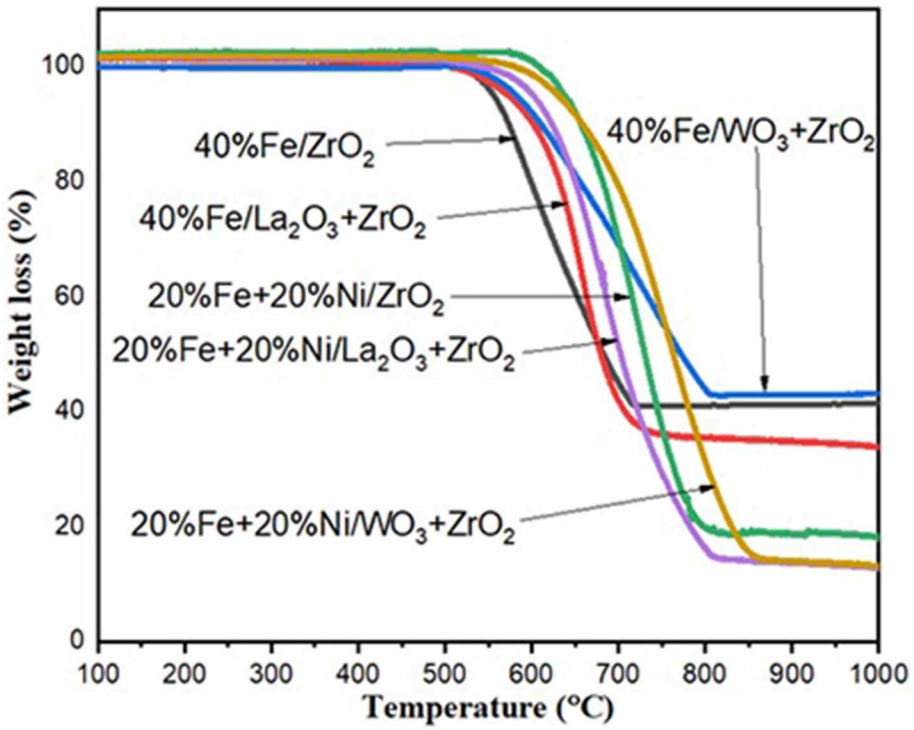

FIGURE 8 | Thermogravimetric analysis (TGA) results for Fe/ZrO_2, Fe/La_2O_3 + ZrO_2, and Fe/WO_3 + ZrO_2 and their corresponding bimetallic catalysts.

XRD of the Reduced Catalysts

XRD analysis was performed on the reduced catalysts to investigate the state of the catalysts after being reduced under the flow of H_2. The Fe in the fresh samples exists majorly in the form of Fe_2O_3 (hematite), and a substantial reduction in the peaks of Fe_2O_3 can be seen in the diffractograms of the reduced samples, indicating the reduction of the hematite. The peaks corresponding to the reduced FeO, Fe, and Ni have been identified in **Figure 11** concerning the analysis done by Ren et al. (2015). All other peaks are as identified in the fresh catalyst samples.

CONCLUSION

In this study, the wet impregnation method was used in the synthesis of Fe and Fe–Ni supported catalysts. The synthesized catalysts were used in catalytic methane decomposition. ZrO_2 was the primary support and was doped with metal oxides such as La_2O_3 and WO_3. This paper investigates the effect of doping the primary support (ZrO_2) as well as the effect of adding Ni. From the activity of the catalysts, Fe/La_2O_3 + ZrO_2 gave the highest methane conversion as well as hydrogen yield (79 and 84%, respectively) among the monometallic catalysts. This catalyst is seen to be the most stable. It was observed that the addition of Ni improved not only the performance of the catalysts but also their stability. In all cases, Ni enhanced the performance of the catalysts.

The fresh and used catalysts were subjected to many characterization techniques. The synthesized catalysts' surface area decreased significantly concerning the corresponding support. TPR showed the progressive reduction of iron(III)

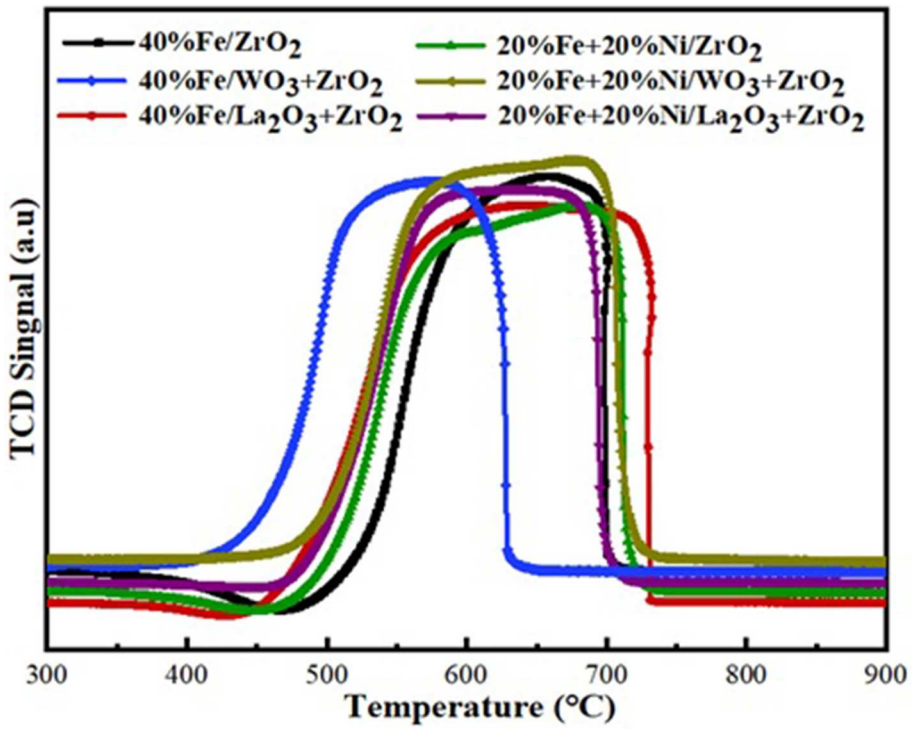

FIGURE 9 | Temperature-programmed oxidation (TPO) profiles for the spent catalysts.

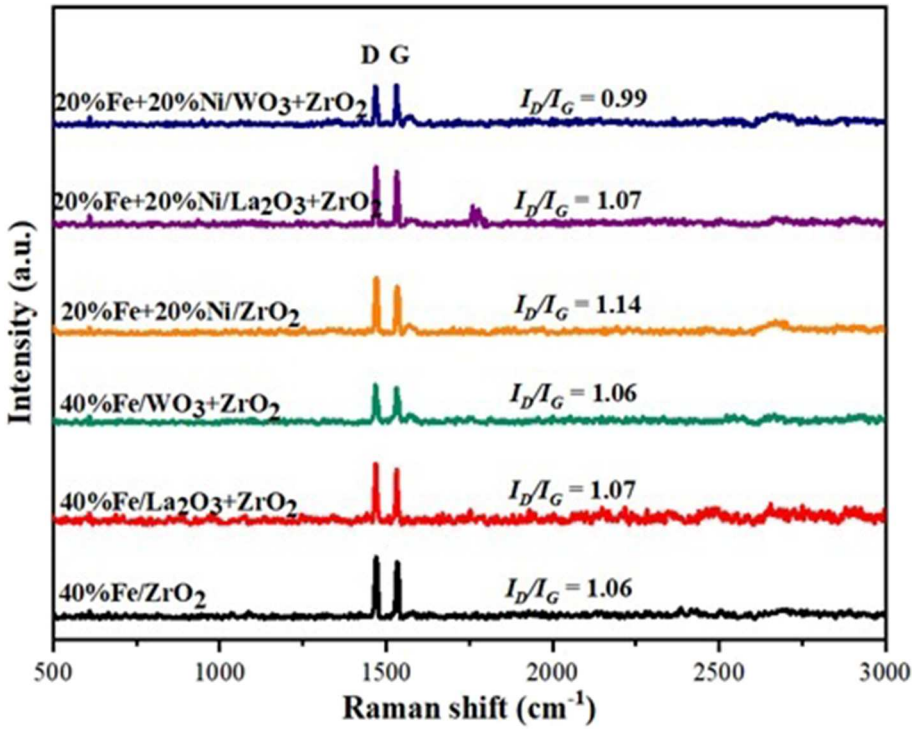

FIGURE 10 | Raman spectra for the used samples.

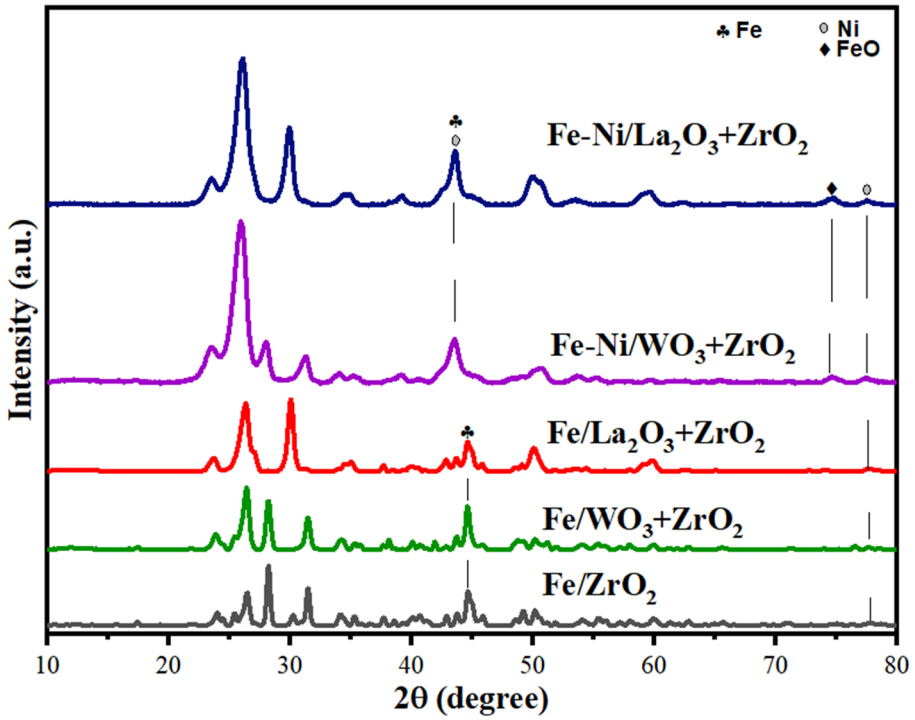

FIGURE 11 | XRD diffractograms of the reduced catalysts.

oxide to the zero valence free metal. The same trend was observed for both Fe and Fe–Ni supported catalysts. Also, a higher peak intensity was noticed for the bimetallic supported catalysts. The thermogravimetric analysis revealed a high amount of carbon deposit for both Fe and Fe–Ni supported on La_2O_3 + ZrO_2. The temperature-programmed oxidation showed that amorphous and graphitic carbons were the kinds of carbon deposited over the spent catalysts for the time on stream studied. The carbon deposits over the spent catalysts were characterized by a mixture of amorphous and graphitic carbon that are filamentous.

DATA AVAILABILITY STATEMENT

The raw data supporting the conclusions of this article will be made available by the authors, without undue reservation, to any qualified researcher.

AUTHOR CONTRIBUTIONS

AA-F, SK, and AI synthesized the catalysts, carried out all the experiments and characterization tests, and wrote the manuscript. AA-A and EA analysis XRD, SEM. AAb, AAw, and AF writing-review and editing.

FUNDING

The authors would like to express their sincere appreciation to the Deanship of Scientific Research at King Saud University for funding this research project (no. RGP-119).

SUPPLEMENTARY MATERIAL

The Supplementary Material for this article can be found online at: https://www.frontiersin.org/articles/10.3389/fchem.2020.00317/full#supplementary-material

REFERENCES

Ahmed, W., Noor El-Din, M. R., Aboul-Enein, A. A., and Awadallah, A. E. (2015). Effect of textural properties of alumina support on the catalytic performance of Ni/Al_2O_3 catalysts for hydrogen production via methane decomposition. *J. Nat. Gas. Sci. Eng.* 25, 359–366. doi: 10.1016/j.jngse.2015.05.015

Ashik, U. P. M., Wan Daud, W. M. A., and Abbas, H. F. (2015). Production of greenhouse gas free hydrogen by thermocatalytic decomposition of methane - a review. *Renew. Sustain. Energy Rev.* 44, 221–256. doi: 10.1016/j.rser.2014.12.025

Ashik, U. P. M., Wan Daud, W. M. A., and Hayashi, J. I. (2017). A review on methane transformation to hydrogen and nanocarbon: relevance of catalyst characteristics and experimental parameters on yield. *Renew. Sustain. Energy Rev.* 76, 743–767. doi: 10.1016/j.rser.2017.03.088

Ashok, J., Subrahmanyam, M., and Venugopal, A. (2008). Hydrotalcite structure derived Ni-Cu-Al catalysts for the production of H_2 by CH_4 decomposition. *Int. J. Hydrogen Energ.* 33 2704–2713. doi: 10.1016/j.ijhydene.2008.03.028

Bayat, N., Rezaei, M., and Meshkani, F. (2016). Methane decomposition over $Ni\text{-}Fe/Al_2O_3$ catalysts for production of COx-free hydrogen and carbon

nanofiber. *Int. J. Hydrogen Energ.* 41, 1574–1584. doi: 10.1016/j.ijhydene.2015.10.053

Calgaro, C. O., and Perez-Lopez, O. W. (2017). Decomposition of methane over Co_3-xAlxO_4 (x=0–2) coprecipitated catalysts: the role of Co phases in the activity and stability. *Int. J. Hydrogen Energ.* 42, 29756–29772. doi: 10.1016/j.ijhydene.2017.10.082

Calgaro, C. O., and Perez-Lopez, O. W. (2019). Graphene and carbon nanotubes by CH_4 decomposition over Co–Al catalysts. *Mater. Chem. Phys.* 226, 6–19. doi: 10.1016/j.matchemphys.2018.12.094

Chen, D., Christensen, K. O., Ochoa-Fernández, E., Yu, Z., Tøtdal, B., Latorre, N., et al. (2005). Synthesis of carbon nanofibers: effects of Ni crystal size during methane decomposition. *J. Catal.* 229, 82–96. doi: 10.1016/j.jcat.2004.10.017

Collodi, G. (2010). "Hydrogen production via steam reforming with CO_2 Capture," in *CISAP4 4th International Conference on Safety and Environment in the Process Industry* (Florence).

Cunha, A. F., Mahata, N., Órfão, J. J. M., and Figueiredo, J. L. (2009). Methane decomposition on La_2O_3-promoted raney-type Fe catalysts. *Energ. Fuels* 23, 4047–4050. doi: 10.1021/ef900385e

Darmstadt, H., Sümmchen, L., Ting, J.-M., Roland, U., Kaliaguine, S., and Roy, C. (1997). Effects of surface treatment on the bulk chemistry and structure of vapor grown carbon fibers. *Carbon* 35, 1581–1585. doi: 10.1016/S0008-6223(97)00116-4

Dresselhaus, M. S., Jorio, A., Hofmann, M., Dresselhaus, G., and Saito, R. (2010). Perspectives on carbon nanotubes and graphene Raman spectroscopy. *Nano Lett.* 10, 751–758. doi: 10.1021/nl904286r

Enakonda, L. R., Zhou, L., Saih, Y., Ould-Chikh, S., Lopatin, S., Gary, D., et al. (2016). Methane-induced activation mechanism of fused ferric oxide–alumina catalysts during methane decomposition. *Chem. Sus. Chem.* 9, 1–6. doi: 10.1002/cssc.201600500

Fakeeha, A. H., Al-Fatesh, A. S., Chowdhury, B., Ibrahim, A., Ullah Khan, W., Hassan, S., et al. (2018). Bi-metallic catalysts of mesoporous Al_2O_3 supported on Fe, Ni and Mn for methane decomposition: effect of activation temperature. *Chin. J. Chem. Eng.* 26, 1904–1911. doi: 10.1016/j.cjche.2018.02.032

Fakeeha, A. H., Khan, W. U., Al-Fatesh, A. S., Abasaeed, A. E., and Naeem, M. A. (2015). Production of hydrogen and carbon nanofibers from methane over Ni-Co-Al catalysts. *Int. J. Hydrogen Energ.* 40, 1774–1781. doi: 10.1016/j.ijhydene.2014.12.011

Hao, Z., Zhu, Q., Jiang, Z., Hou, B., and Li, H. (2009). Characterization of aerogel Ni/Al_2O_3 catalysts and investigation on their stability for CH_4-CO_2 reforming in a fluidized bed. *Fuel Process. Technol.* 90, 113–121. doi: 10.1016/j.fuproc.2008.08.004

Ibrahim, A. A., Al-Fatesh, A. A., Atia, H., Fakeeha, A. H., Kasim, S. O., and Abasaeed, A. E. (2018). Influence of promoted 5% Ni/MCM-41 catalysts on hydrogen yield in the CO_2 reforming of CH_4. *Int. J. Hydrogen Energ.* 42, 4120–4130. doi: 10.1002/er.4156

Ibrahim, A. A., Fakeeha, A. H., Al-Fatesh, A. S., Abasaeed, A. E., and Khan, W. U. (2015). Methane decomposition over iron catalyst for hydrogen production. *Int. J. Hydrogen Energ.* 40, 7593–7600. doi: 10.1016/j.ijhydene.2014.10.058

Inaba, M., Murata, K., Saito, M., Takahara, I., and Mimura, N. (2002). Hydrogen production by conversion of methane over nickel-supported USY-type zeolite catalysts. *React. Kinet. Catal. Lett.* 77, 109–115. doi: 10.1023/A:1020300105112

Inaba, M., Zhang, Z., Matsuoka, K., and Soneda, Y. (2019). Optimization of the reaction conditions for Fe-catalyzed decomposition of methane and characterization of the produced nanocarbon fibers. *Catal. Today* 332, 11–19. doi: 10.1016/j.cattod.2018.11.014

Jana, P., de la Peña O'Shea, V. A., Coronado, J. M., and Serrano, D. P. (2011). Co-production of graphene sheets and hydrogen by decomposition of methane using cobalt based catalysts. *Energ. Environ. Sci.* 4, 778–783. doi: 10.1039/c0ee00490a

Kameya, Y., and Hanamura, K. (2011). Kinetic and Raman spectroscopic study on catalytic characteristics of carbon blacks in methane decomposition. *Chem. Eng. J.* 173, 627–635. doi: 10.1016/j.cej.2011.08.017

Karaismailoglu, M., Figen, H. E., and Baykara, S. Z. (2019). Hydrogen production by catalytic methane decomposition over yttria doped nickel based catalysts. *Int. J. Hydrogen Energ.* 44, 9922–9929. doi: 10.1016/j.ijhydene.2018.12.214

Khan, W. U., Fakeeha, A. H., Al-Fatesh, A. S., Ibrahim, A. A., and Abasaeed, A. E. (2016). La_2O_3 supported bimetallic catalysts for theproduction of hydrogen and carbon nanomaterialsfrom methane. *Int. J. Hydrogen Energ.* 41, 976–983. doi: 10.1016/j.ijhydene.2015.10.112

Li, Y., Li, D., and Wang, G. (2011). Methane decomposition to COx-free hydrogen and nano-carbon material on group 8-10 base metal catalysts: a review. *Catal. Today* 162, 1–48. doi: 10.1016/j.cattod.2010.12.042

Muhammad, A. F. S., Awad, A., Saidur, R., Masiran, N., Salam, A., and Abdullah, B. (2018). Recent advances in cleaner hydrogen productions via thermo-catalytic decomposition of methane: admixture with hydrocarbon. *Int. J. Hydrogen Energ.* 43, 18713–18734. doi: 10.1016/j.ijhydene.2018.08.091

Muraza, O., and Galadima, A. (2015). A review on coke management during dry reforming of methane. *Int. J. Energy Res.* 39, 1196–1216. doi: 10.1002/er.3295

Musamali, R., and Isa, Y. M. (2018). A novel catalyst system for methane decomposition. *Int. J. Energy Res.* 42, 1–11. doi: 10.1002/er.4175

Nuernberg, G. B., Fajardo, H. V., Mezalira, D. Z., Casarin, T. J., Probst, L. F. D., and Carreño, N. L. V. (2008). Preparation and evaluation of Co/Al_2O_3 catalysts in the production of hydrogen from thermo-catalytic decomposition of methane: Influence of operating conditions on catalyst performance. *Fuel* 87, 1698–1704. doi: 10.1016/j.fuel.2007.08.005

Pudukudy, M., Yaakob, Z., Mohammad, M., Narayanan, B., and Sopian, K. (2014). Renewable hydrogen economy in Asia - opportunities and challenges: an overview. *Renew. Sust. Energy Rev.* 30, 743–757. doi: 10.1016/j.rser.2013.11.015

Pudukudy, M., Yaakob, Z., and Takriff, M. S. (2016). Methane decomposition into COx free hydrogen and multiwalled carbon nanotubes over ceria, zirconia and lanthana supported nickel catalysts prepared via a facile solid state citrate fusion method. *Energy Convers. Manag.* 126, 302–315. doi: 10.1016/j.enconman.2016.08.006

Qian, J. X, Enakonda, L. R., Wang, W. J., Gary, D., Del-Gallo, P., Basset, J.-M., et al. (2019). Optimization of a fluidized bed reactor for methanedecomposition over Fe/Al_2O_3catalysts: activity andregeneration studies. *Int. J. Hydrogen Energ.* 44, 31700–31711. doi: 10.1016/j.ijhydene.2019.10.058

Rastegarpanah, A., Rezaei, M., Meshkani, F., Zhang, K., Zhao, X., Pei, W., et al. (2019). Mesoporous Ni/MeO_x (Me = Al, Mg, Ti, and Si): highly efficient catalysts in the decomposition of methane for hydrogen production. *Appl. Surf. Sci.* 478, 581–593. doi: 10.1016/j.apsusc.2019.02.009

Ren, J., Qin, X., Yang, J.-Z., Qin, Z.-F., Guo, H.-L., Lin, J.-Y., et al. (2015). Methanation of carbon dioxide over Ni–M/ZrO2 (M = Fe, Co, Cu) catalysts: effect of addition of a second metal. *Fuel Process. Technol.* 137, 204–211. doi: 10.1016/j.fuproc.2015.04.022

Shen, Y., and Lua, A. C. (2015). Polyol synthesis of nickel-copper based catalysts for hydrogen production by methane decomposition. *Int. J. Hydrogen Energ.* 40, 311–321. doi: 10.1016/j.ijhydene.2014.10.071

Takenaka, S., Serizawa, M., and Otsuka, K. (2004). Formation of filamentous carbons over supported Fe catalysts through methane decomposition. *J. Catal.* 222, 520–531. doi: 10.1016/j.jcat.2003.11.017

Tezel, E., Figen, H. E., and Baykara, S. Z. (2019). Hydrogen production by methane decomposition using bimetallic Ni-Fe catalysts. *Int. J. Hydrogen Energ.* 44, 9930–9940. doi: 10.1016/j.ijhydene.2018.12.151

Wang, H. Y., and Lau, A. C. (2015). Methane decomposition using Ni-Cu alloy nano-particle catalysts and catalyst deactivation studies. *Chem. Eng. J.* 262, 1077–1089. doi: 10.1016/j.cej.2014.10.063

Zhang, J., Xie, W., Li, X., Hao, Q., Chen, H., and Ma, X. (2018). Methane decomposition over Ni/carbon catalysts prepared by selective gasification of coal char. *Energy Convers. Manag.* 177, 330–338. doi: 10.1016/j.enconman.2018.09.075

Zhanga, J., Xiea, W., Lia, X., Haoa, Q., Chena, H., and Ma, X. (2019). *In situ* generation of nickel/carbon catalysts bypartial gasification of coal char and application formethane decomposition. *Int. J. Hydrogen Energ.* 44, 2633–2644. doi: 10.1016/j.ijhydene.2018.12.005

Conflict of Interest: The authors declare that the research was conducted in the absence of any commercial or financial relationships that could be construed as a potential conflict of interest.

frontiers in Chemistry

ORIGINAL RESEARCH
published: 05 May 2020
doi: 10.3389/fchem.2020.00365

Photocatalytic Degradation of Aqueous Rhodamine 6G Using Supported TiO_2 Catalysts. A Model for the Removal of Organic Contaminants From Aqueous Samples

Eduardo Pino [1], Cristian Calderón [1]*, Francisco Herrera [1], Gerardo Cifuentes [2] and Gisselle Arteaga [3]*

[1] Facultad de Química y Biología, Universidad de Santiago de Chile, Santiago, Chile, [2] Departamento de Ingeniería Metalúrgica, Universidad de Santiago de Chile, Santiago, Chile, [3] Departamento de Ingeniería Química, Universidad de Santiago de Chile, Santiago, Chile

OPEN ACCESS

Edited by:
Kamila Kočí,
VŠB-Technical University of Ostrava, Czechia

Reviewed by:
Guohong Wang,
Hubei Normal University, China
Sebastián Murcia-López,
Institut de Recerca de l'Energia de Catalunya, Spain
Yi-en Du,
Jinzhong University, China

***Correspondence:**
Eduardo Pino
eduardo.pino@usach.cl
Cristian Calderón
cristian.calderon@usach.cl

Specialty section:
This article was submitted to Catalysis and Photocatalysis, a section of the journal Frontiers in Chemistry

Received: 13 November 2019
Accepted: 08 April 2020
Published: 05 May 2020

Citation:
Pino E, Calderón C, Herrera F, Cifuentes G and Arteaga G (2020) Photocatalytic Degradation of Aqueous Rhodamine 6G Using Supported TiO_2 Catalysts. A Model for the Removal of Organic Contaminants From Aqueous Samples. Front. Chem. 8:365. doi: 10.3389/fchem.2020.00365

As a model for the removal of complex organic contaminants from industrial water effluents, the heterogeneous photocatalytic degradation of Rhodamin 6G was studied using TiO_2-derived catalysts, incorporated in water as suspension as well as supported in raschig rings. UV and Visible light were tested for the photo-degradation process. TiO_2 catalysts were synthesized following acid synthesis methodology and compared against commercial TiO_2 catalyst samples (Degussa P25 and Anatase). The bandgap (E_g) of the TiO_2 catalysts was determined, were values of 2.97 and 2.98 eV were obtained for the material obtained using acid and basic conditions, respectively, and 3.02 eV for Degussa P25 and 3.18 eV for anatase commercial TiO_2 samples. Raschig rings-supported TiO_2 catalysts display a good photocatalytic performance when compared to equivalent amounts of TiO_2 in aqueous suspension, even though a large surface area of TiO_2 material is lost upon support. This is particularly evident by taking into account that the characteristics (XRD, RD, Eg) and observed photodegradative performance of the synthesized catalysts are in good agreement with the commercial TiO_2 samples, and that the RH6G photodegradation differences observed with the light sources considered are minimal in the presence of TiO_2 catalysts. The presence of additives induce changes in the kinetics and efficiency of the TiO_2-catalyzed photodegradation of Rh6G, particularly when white light is used in the process, pointing toward a complex phenomenon, however the stability of the supported photocatalytic systems is acceptable in the presence of the studied additives. In line with this, the magnitude of the chemical oxygen demand, indicates that, besides the different complex photophysical processes taking place, the endproducts of the considered photocatalytic systems appears to be similar.

Keywords: photocatalytic degradation, organic dyes, water treatment, contaminant, semiconductor sensitizer

INTRODUCTION

The removal of hazardous organic contaminants derived from human productive activities, present in the environment and particularly in water sources has become an important research topic aimed toward the development of sustainable water treatment strategies and processes.

The leather, paper, plastic and textile industries use dyes to color their products while using large volumes of water (Robinson et al., 2001; Yaseen and Scholz, 2019), with more than 10,000 types of commercial dyes and 70,000 tons of waste are produced annually. This discharge of wastewater to natural streams leads to major problems, such as an increase in toxicity and oxygen demand of the effluents, as well as a reduction of the amount of light that can pass through the water, producing a negative effect on the phenomena of photosynthesis of aquatic life. The color of wastewater is the first public perception of contamination, the presence of small amounts of dyes (1 ppm) is highly visible and undesirable, due to their high molar absorptivity coefficients.

For the vast array of wastewater treatment technologies currently in use, namely adsorption on activated carbon (Foo and Hameed, 2009), ultrafiltration, coagulation by chemical agents and resins of synthetic adsorbents, biological treatment, electrocatalytic decomposition (Fujishima and Honda, 1972; Daghrir et al., 2012), etc., factors such as the sheer complexity of the organic contaminants found in waste water effluents call for a simpler yet transversal solution, able to yield a proper removal of the contaminants by an aggressive oxidative decomposition. From this, advanced oxidation processes (AOPs) for chemical degradation have become simple and effective methods for the elimination of organic contaminants (Giménez et al., 2015).

Several research groups have sought to optimize the process for the degradation of organic pollutants in water (Rizzo et al., 2009; Chong et al., 2010), so that it meets the requirements of efficiency, easy to handle, and improved time of degradation, by allowing the pollutants complete mineralization, that is, the formation of carbon dioxide (CO_2), water (H_2O) and other inorganic compounds such as HCl, HNO_3, etc. and/or the generation of less toxic organic byproducts that are environmentally safe (Amenn et al., 2013). Based on this premise, photocatalytic degradation has become a widespread subject of study, focused on making use of the particular interactions that takes place between light and semiconductive materials (SCM), in a process termed as heterogeneous photocatalysis (Ahmed et al., 2011; Teoh et al., 2012), that allows the degradation of organic molecules via advanced oxidative pathways, due to the abundant generation of radicals on the surface of the SCM by electronic excitation elicited by the incident light.

Heterogeneous photocatalysis, has become an efficient alternative to achieve the degradation of many pollutants. This technique uses radiant energy, visible and / or ultraviolet light coming from artificial light sources or directly from the sun, which, upon interacting with a catalyst (semiconductor) (Smith and Nie, 2009), generates a charge separation by means of charge transfer processes, leading to the formation of reactive oxygen species (hydroxyl radicals, superoxide anion, hydrogen peroxide, etc.), necessary for the oxidation and subsequent mineralization of the organic contaminants (Módenes et al., 2012).

One of the most efficient SCM, in terms of both cost and photocatalytic properties, is Titanium dioxide (TiO_2) with a large number of works published elsewhere (Ajmal et al., 2014; Gaya, 2014), devoted to in-deep descriptions of the interesting photophysical properties of this material. Briefly, the ability of SCM such as TiO_2 to be activated by photon absorption is associated to the energy difference, or bandgap (Eg) that separates their valence band (VB) electrons from their counterparts in the conduction band (CB), where Eg is usually lower than 5 eV in common SCM (Smith and Nie, 2009). Upon light excitation, electrons move from VB to CB, leaving a hole (h^+) into the VB. Further, the transferred electrons can participate in the generation of reactive oxygen species (ROS), leading to occurrence of photocatalytic degradation. A general description of the photocatalytic degradation of dyes in the presence of TiO_2 is shown in Equations (1–6).

$$TiO_2 + h\nu\,(UV) \rightarrow TiO_2\left(e^-_{CB} + h^+_{VB}\right) \quad (1)$$

$$TiO_2\left(h^+_{VB}\right) + H_2O \rightarrow TiO_2 + H^+ + OH^\bullet \quad (2)$$

$$TiO_2\left(h^+_{VB}\right) + HO^- \rightarrow TiO_2 + OH^\bullet \quad (3)$$

$$TiO_2\left(e^-_{CB}\right) + O_2 \rightarrow TiO_2 + O_2^{\bullet -} \quad (4)$$

$$O_2^{\bullet -} + H^+ \rightarrow HO_2^\bullet \rightarrow H_2O_2 \rightarrow OH^\bullet \quad (5)$$

$$Dye + ROS \rightarrow Products \quad (6)$$

TiO_2 has three crystalline phases, anatase (tetragonal), rutile (octahedral) and brookite (orthorhombic) (Landmann et al., 2012), with anatase being the most active photocatalytically due to the combined effect of a lower recombination rate and a higher capacity of adsorption on the surface (Carreon et al., 2011). The TiO_2 in mixed phase have a greater photocatalytic activity compared to a pure crystalline phase (Hurum et al., 2003). TiO_2 use is limited by fact that the absorption of light corresponding to the Eg for the cristalline forms of TiO_2 falls in the ultraviolet range, which is one of the minority components of the solar spectrum. This disadvantage of the semiconductor is due to its high value of Eg, being 3.2 eV for anatase and 3.02 eV for rutile. To extend the range of absorption of the catalysts to the visible spectrum and decrease the recombination of the pair (h^+_{VB} / e^-_{CB}) one of the strategies used has been the use of photosensitizing dyes (Stracke and Heupel, 1999). Upon irradiation, the transfer of electrons from the excited state of the dye to the conduction band of the semiconductor can be produced, in a process defined as "sensitization" (equations 7-19) of the TiO_2 (Wu et al., 1998). This process only will be possible if the energy level of the excited state of the dye (Dye*) is higher than the energy level of the conduction band. The injected electrons can be transferred to the oxygen adsorbed on the TiO_2 surface to form superoxide anion radicals, which lead to the formation of ROS (Dyi-Hwa et al., 2012), these species being responsible for the oxidation of organic matter (Song et al., 2016). The sensitizing dye is also degraded in the process (equations 5 and 6), making this synergy between the sensitizing dye and TiO_2, ideal for the decomposition of organic contaminants able to sensitize TiO_2 using white light, minimizing

the use of high energy radiation (ca. UV light) by ignoring the Eg value of the photocatalyst.

$$Dye + hv \rightarrow Dye^{*} \quad (7)$$

$$Dye^{*} \rightarrow \text{bleaching or photophysical process} \quad (8)$$

$$TiO_2 + Dye^{*}\left(e^{-}\right) \rightarrow TiO_2\left(e^{-}_{cb}\right) + Dye^{\bullet +} \rightarrow Products \quad (9)$$

Besides of taking advantage of the dye-sensitizing of TiO_2, and in order to further extend the applications and usability of TiO_2 catalysts, the support of the photocatalytic material have become an interesting venture for catalysis research. Current developments for the use TiO_2 are focused on the support of the photocatalyst on a wide variety of materials (Ansón-Casaos et al., 2013; Ranjith et al., 2019) which may set the basis for the implementation of applied waste-water treatment solutions. Polymeric supports have been considered to enhance and control the photocatalytic properties of TiO_2. Recently, poly (ethyleneterephtalate)-supported TiO_2 composite films (Malesic-Eleftheriadou et al., 2019) have proven useful for the photocatalytic degradation of complex antibiotic mixtures irradiated with simulated solar light, leading to high photocatalytic efficiencies and good reusability even when low content (10%) of supported TiO_2 is used. Hyerarchical wrinkled mesoporous silica used as support for TiO_2 catalysts (Wan et al., 2018), have shown high TiO_2 support yield and enhanced photodegradation activity toward organic dyes, particularly the TiO_2 catalyzed photodegradation of Rhodamin B under UV light exposition, where the performance of the supported catalyst can be modulated by controlling the calcination temperature during the TiO_2 support step.

Studies evaluating the performance of metal oxide nanoparticles/TiO2 heterojunctions have reported an enhanced degradation of Rhodamine B. For example, ZnO/TiO_2 heterojunction photocatalysts (Wang et al., 2018), in a degradation process mediated by the formation of a direct Z-scheme heterojunction structure formed between ZnO and TiO_2, with hydroxyl and superoxide anion radical playin relevant roles in the phtocatalytic process. Similarly, enhanced photocatalytic performance under visible light irradiation have been observed for p-n heterojunctions formed in TiO_2 nanofibers decorated with Ag_2O nanoparticles (Liu et al., 2019), effect mainly attributed to the fast separation of the photogenerated electron-hole pairs and high light absorption efficiency of the fibers. On the other hand, nanophotocatalysts based on $TiO_2/SrTiO_3$ heterojunctions supported on activated carbon (Ali et al., 2019) have displayed exceptional activities, compared to commercial TiO_2 samples, on the photodegradation of pollutants such as 2,4-dichlorophenol and bisphenol A, where the presence of the activated carbon allows the enhancement of the photocatalystic activity by increasing the adsorption of O_2, as well as by accepting the electrons from the semiconductors heterojunction.

Degussa-P25 TiO_2 catalyst supported on mullite ceramic foam was tested in a photocatalytic ozonization process for the degradation of N-N-diethyl-m-toluamide (Rodríguez et al., 2019). The performance of the mullite supported catalysts was close to that observed when raschig rings where used as support, where the combination of the ozone and TiO_2 photocatalyzed degradation had a negative impact on the degradation rate, but higher efficiency on the mineralization process of the substrate.). TiO_2 supported in activated carbon has also been used for the photocatalytic decomposition of the micotoxin aflatoxin B1 (Sun et al., 2019), a carcinogen agent that can be found in vegetal and animal feedstock, with good performance of the photocatalyst when UV-Vis light is used for irradiation, with enhanced photodegradation of the supported material when compared with the bare photocatalysts. Similarly, hybrid TiO_2 catalysts supported on reduced graphene oxide (Ranjith et al., 2019) displayed good performance in the oxidative degradation of organic dyes (methylene blue and crystal violet) by irradiation with visible light, with the dye degradation taking place through electron-hole separation.

Beyond the development of TiO_2 supported in microgranular porous materials, larger structures of supporting material have been less explored. For example, periodic and flow reactors using TiO_2 catalysts in suspension as well as supported on glass fabric have been used for the UV-Vis photocatalyzed degradation of sertraline, an antidepressant drug, from aqueous samples (Rejek and Grzechulska-Damszel, 2018). The photodegradation yield where highly dependent on the configuration of photoreactor, where the highest degradation percentages where achieved using the periodic reactor containing the TiO_2-coated glass fabric. TiO_2 coated natural and synthetic non-woven fibers have also been tested on the photocatalyzed degradation of the textile dye reactive yellow 145 (Alahiane et al., 2014) where good degradation performance under irradiation with UV light, was achieved under several conditions, such as the presence of additives, namely ethanol, hydrogen peroxide, inorganic anions, as well as optimal degradation in acidic media (pH = 3).

The present work will focus on the study of TiO_2 catalysts supported on borosilicate glass rings (raschig rings), which will allow the development and optimization of a photocatalytic degradation process based on the use of both UV and white light, taking advantage of the ability of the different crystal structures of TiO_2, leading to a controllable photodegradation process of complex organic molecules by control of the free radical generation process on the supported TiO_2 catalysts, either by the energy of the incident light or the combination of different TiO_2 crystal structures, allocated on the vitreous support. The physically and chemically stable supported photocatalytic structures will yield reusable materials for the implementation of water decontamination strategies either for batch or continuous regime water treatment, providing stability to the TiO_2 particles, enhancement of the catalytic surface to the incident light as well as adsorption of the substrates for the degradation, combined with good mass transport through the material, by taking advantage of the intrinsic properties of the design of the raschig rings as packing material, for example, in engineering application of fractionation columns (Raja et al., 2005).

Due to the fact that colored dyes, commonly found as waste water organic contaminants usually share similarities in their structures, a model compound is required in order to test the proposed TiO_2 catalysts in a streamlined and proper fashion (Lasio et al., 2013; Bokhale et al., 2014), allowing

further analysis and interpretation of the obtained results. In this context, xanthenic dyes stands out as a suitable candidates. Rhodamine 6G (Rh6G) also known as Rhodamine 590, belongs to the xanthenes family, which are largely used to synthesize drugs and to prepare dyes of the fluorescein and eosin class. Rhodamine 6G is a cationic polar dye with a rigid heterocyclic structure, which exhibits a strong absorption in the visible and an intense fluorescence (Magde et al., 1999; Bujdak and Iyi, 2012; Zehentbauer et al., 2014). Rh6G is widely used in acrylic, nylon, silk, wool and dyeing, it is the dye most used for dye laser applications and as a fluorescent tracer to visualize flow patterns as for example in the field of hydraulics (Tarud et al., 2010). Rh6G is commonly used as a sensitizer (Wu et al., 1998). In recent years, a growing number of studies have attempted to incorporate Rh6G into inorganic and organic matrices (Vanamudan and Pamidimukkala, 2015) for application in fields such as solid-state laser action, optoelectronics and optical filters, among others (Barranco and Groening, 2006).

Our analysis comprises the use of TiO_2 catalysts synthesized by a sol-gel methodology, as well as commercial samples of TiO_2 (Anatase and Degussa P25) supported in raschig rings and the photocatalytic activity of the supported catalysts evaluated by monitoring the degradation of Rh6G under irradiation with UV (365 nm) and white light (400–700 nm) light sources. Further, the influence of additives that can be usually found accompanying organic dyes in waste water, such as sulfates and chlorides (Guillard et al., 2005), as well as photocatalysis promoters such as hydrogen peroxide (Li et al., 2001), will be evaluated in our photocatalytic systems.

EXPERIMENTAL

Materials

Nitric Acid, titanium dioxide (Anatase), titanium dioxide (Degussa P25), titanium isopropoxide, polyethylene graft maleic anhydride and Rhodamin 6G were purchased from Sigma-Aldrich. Sodium chloride, n-hexane, sodium hydroxide, hydrogen peroxide and sodium sulfate were purchased from Merck. All reagents were used as received.

Methods

Synthesis of TiO_2

The synthesis of TiO_2 was performed by the Sol-gel method (Ochoa et al., 2009). A mixture of 100 mL of ultrapure water and 27 mL of isopropanol was used to dissolve 16.6 ml of titanium isopropoxide (Mahshid et al., 2007), under constant stirring for 20 min. Later, depending of the acidity required, 3.1 mL HNO_3 0.032 M (acid synthesis) were added and the suspension kept under constant stirring at 80°C for 20 hrs. Finally, the resulting gel was treated in a muffle furnace for 4 h at 560°C and then left to cool at room temperature to recover the solid TiO_2.

TiO_2 Support on Raschig Rings

In a crystallizer containing 0.25 g of polyethylene graft maleic anhydride (PEGMA), completely dissolved in 25 mL of hexane, 50 Raschig rings were incorporated and the temperature raised up to 70°C to achieve total evaporation of the solvent. The dried rings were added to an aqueous TiO_2 suspension (10 g/L for the synthesized TiO_2 catalysts or 1 g/L for the commercial TiO_2 samples) and left to rest for 30 min. Later, the solvent was evaporated by heating the suspension at 150°C followed by elimination of residual organic matter by heating at 500°C for 2 h in a muffle furnace (Raja et al., 2005). The TiO_2 support efficiency was calculated by determining the amount of TiO_2 supported on the rings (the total amount of rings used on the support step) by weight differences, and the resulting mass of TiO_2 supported was expressed as a percentage in relation to the total mass of TiO_2 used in the support step.

Characterization of the TiO_2 Catalysts

X-ray diffraction analysis of the synthesized TiO_2 catalysts were performed in order to discriminate the crystal structures present in the resulting material, and the results were compared with commercial TiO2 samples. XRD data was obtained using a Shimadzu XRD-6000 (Cu, Kα, Ni Filter, 40 kV, 30 mA) difractometer, with a 2 min^{-1} scan speed. Scanning electronic microcopy (SEM) analysis of the samples was performed in a JEOL JSM-7800F scanning electron microscope equipped wtih a X-ACT Cambridge instruments detector for energy dispersive X-ray (EDX) analysis.

BET adsorption isotherms and specific surface area of the studied TiO_2 catalysts were determined by using a Micromeritics ASAP 2020 systing, with N_2 gas as adsorbate at 77K.

The bandgap energy (Eg) of the synthesized TiO_2 catalysts was determined by diffuse reflectance experiments (López and Gómez, 2012), using the Kubelka-Munk function (FKM) for the analysis of the diffuse reflectance (R) of TiO_2, according to Equations (1, 2).

$$R = \frac{R_{sample}}{R_{reference}} \tag{1}$$

$$FKM = F(R) = \frac{(1-R)^2}{2R} \tag{2}$$

The Tauc mathematical model was used for the accurate determination of the Eg values. Briefly, this model proposes that, for materials with a direct band gap [REF], the magnitude of Eg can be estimated by Equation 3.

$$\alpha h\nu = A(h\upsilon - E_g)^n \tag{3}$$

Where ν is the frequency of the incident light, A correspond to a proportionality constant and α is a linear absorption coefficient. For TiO_2 and other materials with direct band gap, n is equal to 2 (Smith and Nie, 2009; López and Gómez, 2012). Under specific conditions, the absorption coefficient α is proportional to the FKM, according to Equation 4.

$$F(R)\,h\nu = A(h\upsilon - E_g)^n \tag{4}$$

From plots of $F(R)\,h\nu^{1/2}$ vs. $h\upsilon$, the linear extrapolation at $F(R)\,h\nu^{1/2} = 0$ allows the determination of Eg.

Photodegradation Kinetics of Rhodamin 6G

Photostability of Rhodamin 6G

To evaluate the photostability of Rh6G in the absence of catalyst, from a 1.15 mM stock solution of Rh6G, 5 uM Rh6G solutions were freshly prepared and irradiated for 90 min in a Solsim-Luzchem photoreactor using either UV lamps (8 Hitachi FL8BL-B lamps, 365 nm, 8W rated power consumption) or white light lamps (8 Westinghouse 4000K white light T5BF-840 lamps, 8W rated power consumption). Aliquots of the samples were taken every 10 min and their absorbance was measured at 526 nm in an Agilent 8453 UV-Vis spectrophotometer. The same procedure was performed incorporating additives (H_2O_2, NaCl, Na_2SO_4) to the Rh6G solutions. All the solutions were prepared using ultrapure water and the determinations were performed by triplicate unless otherwise indicated.

For the Raschig rings-supported TiO_2 catalysts, the photodegradation procedure involve the addition of 10 catalyst-coated Raschig rings to the Rh6G solutions, and keeping the same irradiation protocol previously described for the samples in homogenenous media.

Degradation of Rh6G in aqueous suspensions of TiO_2 took place under constant irradiation for 30 min. For comparison sake, the amount of TiO_2 used in the studied suspensions was determined by comparison with the mass of supported catalysts in the experiments involving the Raschig rings.

All the degradation kinetic data was adjusted to a pseudo-first order kinetic model, according to the Langmuir-Hinshelwood kinetic model for reactions taking place in heterogeneous media (Loghambal et al., 2018). All of the kinetics were performed under constant air bubbling. The reported data correspond to the average of at least three independent determinations, unless otherwise stated.

Evaluation of the chemical oxygen demand for the photodegradation of Rhodamin 6G.

The determination of the chemical oxygen demand was performed over the remainder organic matter left after a short photocatalytic degradation course (ca. 10 min). To a tube containing $K_2Cr_2O_7$, sulfuric acid and silver as a catalyst, 1 mL of a centrifuged solution of Rh6G previously subjected to photodegradation were added. The sample tubes were subjected to digestion at 150°C for 2 hrs. Once the samples are cooled, the concentration of Cr^{+3} was determined by spectrophotometric analysis, measuring the absorbance of the samples at 620 nm (Lenore et al., 2009). Reported results correspond to samples ($n = 3$) measured by triplicate, where the results were deemed suitable when their standard error were under 10% of the average value determined.

RESULTS AND DISCUSSION

TiO_2 Catalysts Characterization

TiO_2 catalysts were synthesized by a Sol-Gel method, starting by the hydrolysis of the metallic alcoxide, followed by calcination of the resulting gel (**Scheme 1**). The hydrolytic step was performed in acid media, resulting in 90% yield for the reaction.

$$Ti(i-oPr)_4 + H_2O \dot{\rightarrow} Ti(OH)_4 + 4HO-Pr$$

$$Ti(OH)_4 \overset{\Delta}{\rightarrow} TiO_{2(prep)} + 2H_2O$$

SCHEME 1 | Chemical reactions involved in the synthesis of the studied TiO_2 catalysts.

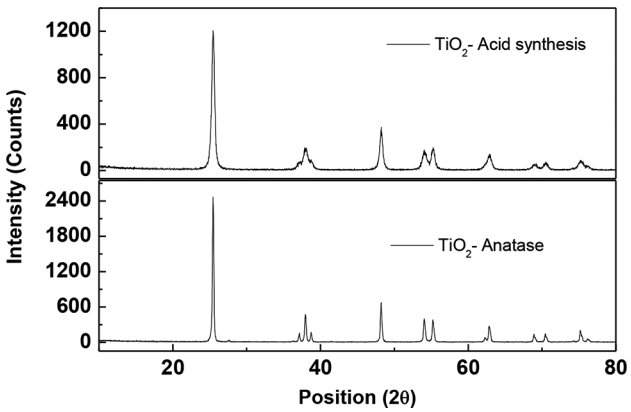

FIGURE 1 | X-ray powder diffraction pattern for the studied TiO_2 catalysts.

$$Ti(i-oPr)_4 + H_2OTi(OH)_4 + 4HO-Pr$$
$$Ti(OH)_4TiO_{2(prep)} + 2H_2O$$

X-ray diffraction analysis (**Figure 1**) of the synthesized TiO_2 catalysts herein named as acid synthesis TiO_2 (AS-TiO_2), show identical spatial features for the crystal structures of AS-TiO_2 and Anatase, with signals for AS-TiO_2 at 2θ values equals to: 25.4; 37.2; 37.9; 38.7; 48.2; 54.2; 55.3; 62.9; 69.0; 70.5; 74.1; 75.2, and 76.2. For Anatase is also observed the presence of minor signals (at values of 2θ equal to 27.6; 36.2 and 41.4), attributed to the presence of traces of the Rutil crystalline form of TiO_2, which are not observed in the XRD pattern of AS-TiO_2. The Rutil content in the commercial sample of Anatase is estimated as lower than 2%, according to calculations performed by using the relationship between the respective TiO_2 phase and the strongest reflection associated to each phase under consideration, according to: *phase* $\% = 100/(1+1.265I_R/I_A)$ (Spurr and Myers, 1957), where I_R and I_A are the respective intensities of the Anatase and Rutil signals at 2θ values of 25.1 and 27.6, respectively. For the Degussa P25 (DP25) samples, more intense signals at 2θ positions equivalent to those of Rutil are observed, associated with increased content of the Rutil crystalline phase in DP25, material comprised by the Anatase and Rutil phases of TiO_2 in an 85:15 ratio (See **Supplementary Figure 1** in the electronic supplementary information of this work, for the DP25 XRD pattern).

In order to establish further observations regarding the photocatalytic performance of the synthesized catalysts, their bandgap energy (Eg) was determined through diffuse refractance

measurements. **Figure 2** show diffuse refractance data plotted against the energy of the incident light, according to the Tauc modified Kubelka-Munk model (see methods for details). The values of Eg obtained for the synthesized catalyst (2.97 eV) are marginally lower than those determined for their commercial counterparts, with 3.03 eV and 3.17 eV for Degussa P25 and Anatase, respectively. The Eg results are in good agreement with the XRD data, particularly for the correspondence between AS-TiO_2 and Anatase structures. Considering that the energy of the bandgap for AS-TiO_2 is the lowest for the set of catalysts studied, and that the spectral response in the 250–400 nm range (**Figure 2**), between these catalysts is quite similar, it might be valid to expect for AS-TiO_2 to be particularly efficient when using white light in the photocatalytic process, by requiring

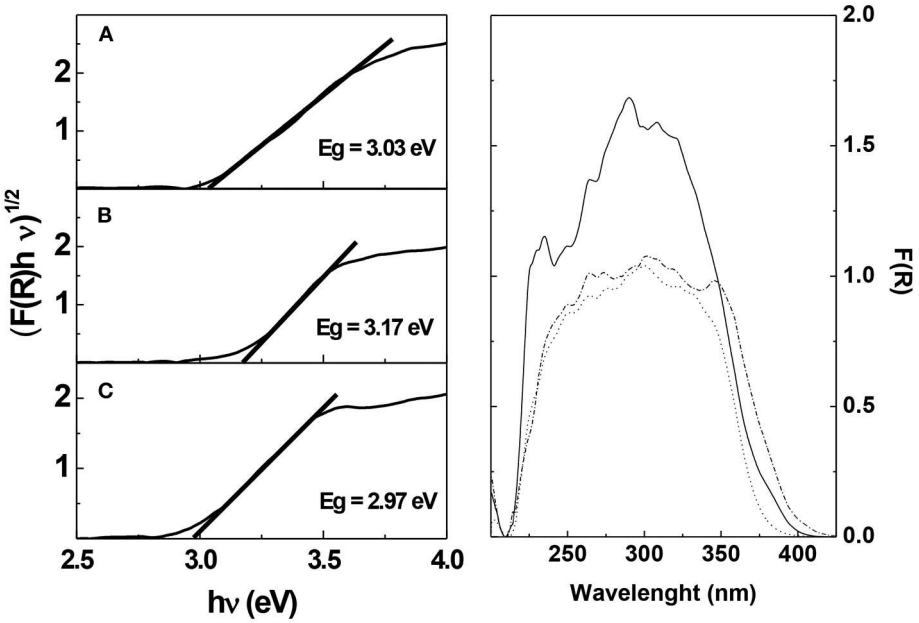

FIGURE 2 | (**Left**) Product between the diffuse refractance and the energy of the incident light represented against the energy of the incident light, according to the Tauc-modified Kubelka-Munk model. Linear regression for the determination of the bandgap energy is shown. Materials: (a) Degussa P25; (b) Anatase; (c) Acid synthesis TiO_2. (**Right**) Diffuse refractance spectra for the studied TiO_2 catalysts. (▬) Degussa P25; (•••) Anatase; (-•-•-) Acid synthesis TiO_2.

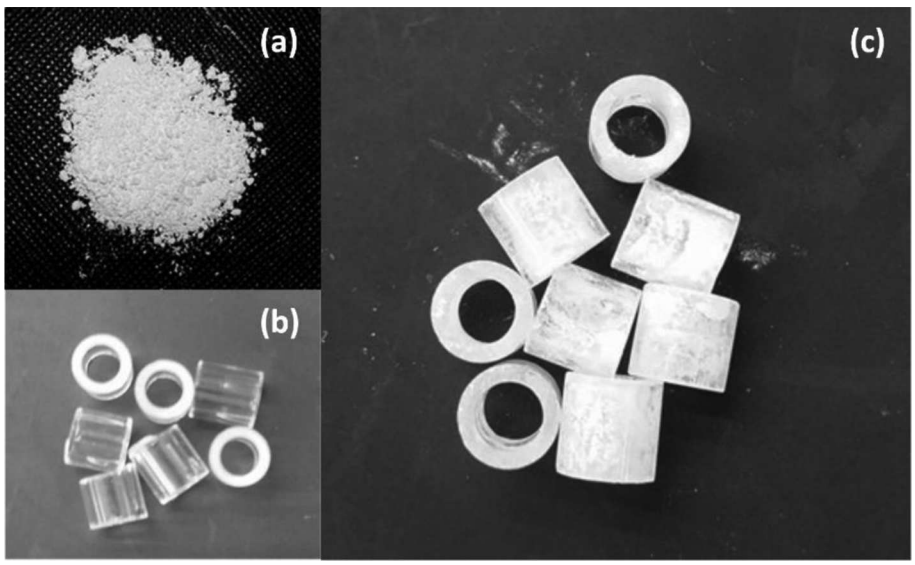

FIGURE 3 | (a) Synthesized TiO_2 catalyst. **(b)** Raschig rings without treatment. **(c)** Treated Raschig rings displaying supported TiO_2 catalyst.

less energy for the valency band electrons to transition to the conduction band of the catalyst (UV/Vis spectra of RH6G as well as UV and White light radiant emission spectra are available in **Supplementary Figure 2**).

The synthesized TiO_2 catalysts (**Figure 3a**), as well as commercial TiO_2 samples (Degussa P25 and Anatase), all of them in the form a finely divided powder, were supported on Raschig rings (RR), made up of borosilicate glass (**Figure 3b**) of 5.0 mm of height, with 4.0 and 5.0 mm of internal and external diameter, respectively. The supporting procedure was based the solvent evaporation of a TiO_2 suspension containing PEGMA-treated raschig rings, leading to the formation of an stable homogeneous layer of TiO_2 on both the external and internal surfaces of the rings, as shown in **Figure 3c**.

The TiO_2 support took place with varied efficiencies (**Table 1**). An important difference is observed on the support efficiency (SE) between AS-TiO_2 (8% SE) and the commercial TiO_2 samples. Degussa P-25 with a 20% SE and Anatase displaying the highest SE (26%). The observed differences in SE reported point toward raschig rings TiO_2-loading variations based on granularity differences of the supported material, where the packing of the commercial TiO_2 samples differs to that synthesized material, leading to the formation of layer(s) of different density between the samples studied.

In order to further support the claims regarding the differences in SE between the different TiO_2 samples, physcochemical characterization of the materials were performed. SEM images reveal relevant differences between the considered TiO_2 photocatalysts. AS-TiO_2 samples (**Figure 4A**) display defined crystalline microparticulated aggregates formed by nanometric clusters which are identifiable at larger magnifications (>30 k X; See **Supplementary Figure 3**). On the contrary both Anatase (**Figure 4B**) and Degussa P25 (**Figure 4C**) present a more disperse configuration, without the evidence of important cluster formation or identifiable discrete crystalline formations of micrometric dimensions. From N_2 adsorption/desorption isotherms evaluated under the BET model considerations, data shows (**Table 2**) that both AS-TiO_2 and Anatase share a similar adsorption performance with similar specific adsorption area, in the range from 60 to 65 m^2 per gram of adsorbent, whereas Degussa P25 shows a lower specific area, below 50 m^2 per gram of adsorbent. Regarding the porosity of the systems, AS-TiO_2 average pore size locates the material closer to the micro-mesoporous regime. Anatase on the other hand, operates on the mesoporous range, with an average pore size that is twice as large as that of AS-TiO_2 and nearly half of the average pore size determined for Degussa P25 (nearly 40 nm) indicating that the porosity regime of the latter leans toward the mesoporous/macroporous range.

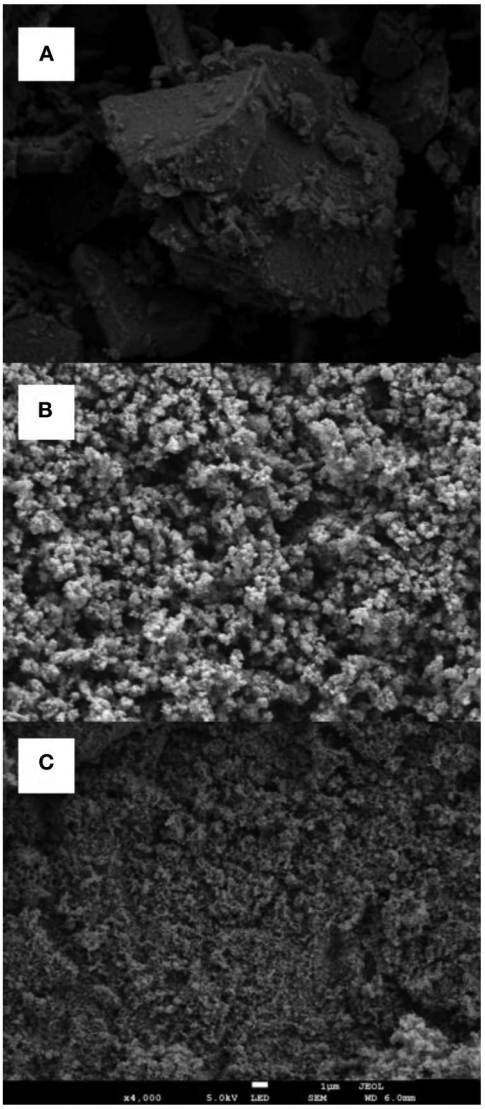

FIGURE 4 | Scanning electron microscopy characterization of the studied TiO_2 photocatalysts: **(A)** Acid synthesis TiO_2; **(B)** Anatase; **(C)** Degussa. Magnification: 4000X, Beam energy: 5,0 kV.

TABLE 1 | Support efficiency data for the thermal deposition of TiO_2 catalysts on borosilicate Raschig rings (Refer to methods section for further details).

TiO_2 catalyst	Support efficiency (%)
Degussa P25	20.1
Anatase	26.1
TiO_2 (acid synthesis)	8.3

TABLE 2 | Specific surface area (S_{BET}) of the studied TiO_2 photocatalysts, according to the Brunnauer, Emmet and Teller mode.

Sample	S_{BET} (m^2/g)	Pore diameter (nm)
AS-TiO_2	60.5	7.1
Anatase	65.9	18.9
Degussa P25	49.0	43.4

Textural identity is expressed as average pore diameter of the samples.

TABLE 3 | Kinetic data for the photodegradation of Rh6G in homogeneous media and in the presence of supported TiO_2 catalysts.

Light source/catalyst[a]	k_{obs} (min^{-1})	Degradation percentage
UV (365 nm)	$1.7\times10^{-2} \pm 2.9 \times 10^{-3}$	21.9 ± 3.2
UV (365 nm)/Degussa P25	$2.1 \times 10^{-2} \pm 6.7 \times 10^{-3}$	57.3 ± 6.8
UV (365 nm)/Anatase	$2.2 \times 10^{-2} \pm 1.4 \times 10^{-2}$	75.1 ± 3.0
UV (365 nm)/TiO_2 acid synthesis	$2.5 \times 10^{-2} \pm 9.0 \times 10^{-3}$	77.5 ± 7.8
White light	$2.0 \times 10^{-2} \pm 5.6 \times 10^{-3}$	22.9 ± 4.3
White light/Degussa P25	$4.0 \times 10^{-2} \pm 7.8 \times 10^{-3}$	27.1 ± 4.7
White light/Anatase	$2.6 \times 10^{-2} \pm 3.1 \times 10^{-3}$	36.8 ± 5.2
White light/TiO_2 acid synthesis	$3.1 \times 10^{-2} \pm 4.5 \times 10^{-3}$	66.8 ± 11.9

[a] *Experiments performed using 10 TiO_2-loaded Raschig rings.*

Photodegradation of Rhodamin 6G by Raschig Rings-Supported TiO_2

The photostability of Rh6G was studied in homogenous media by irradiating aqueous solutions of Rh6G using different light sources. The experimental configuration for the irradiation of the aqueous solutions of Rh6G, in the absence and the presence of supported catalysts, comprises a vertically-oriented sealed borosilicate glass tube located in a photoreactor with a series of lamps (UV or white light) lined up equally at each side of the tube (see **Supplementary Figure 4**), in order to achieve a total homogenous irradiation of the samples. Rh6G degradation kinetic data and degradation efficiency are shown in **Table 3**. The decrease of Rh6G concentration vs. time data behaved in accord to the pseudo-first order treatment (monoexponential decay), according to the Langmuir-Hinshelwood model for kinetics in solid-liquid interfaces and the kinetic profiles are shown in **Supplementary Figure 5** of this work.

When UV light (365 nm) is used to irradiate a solution of Rh6G a degradation percentage of 22% is determined, efficiency that is further increased in the presence of supported TiO_2 catalysts, with a near three-fold increase for Degussa P25 and a four-fold increase for Anatase and AS-TiO_2 with Rh6G degradation efficiencies above 70%. Similarly, the degradation rate is improved in the presence of the supported catalysts, with AS-TiO_2 displaying the highest degradation rate.

The degradation efficiency of Rh6G in solutions irradiated with white light (23%) is quite similar to that observed with UV light irradiated samples (22%). For the supported catalysts, particularly for Degussa P25 and Anatase, the degradation efficiency observed is lower (compared to UV light) when white light is used to irradiate the samples, with no significative differences between the degradation of Rh6G in homogeneous media compared to heterogeneous media using Degussa P25 as catalyst. Similarly, only a moderate enhancement of the degradation efficiency is observed when Anatase is used. Interestingly, the performance of the AS-TiO_2 supported catalyst is particularly good when irradiated with white light, inducing a three-fold increase on the degradation efficiency of Rh6G, increase that is only marginally lower than that observed with UV light.

Regarding the degradation rates observed for the white light irradiated samples, the analysis is not as straightforward as for UV light, with all of the catalysts moderately increasing the rate over the value observed in homogeneous media, with Degussa P25 doubling the degradation rate, followed by AS-TiO_2, and Anatase having almost no difference with the rate determined in homogenous media. In homogeneous media, namely in the absence of TiO_2, Rh6G absorbs light, undergoing a transition to its triplet state, in which this state Rh6G can release the energy and return to its ground state, get decomposed by photolysis or it can react with O_2 and generate singlet oxygen ($^1O_2$), which then can react with Rh6G leading to the formation of oxidation products. In the presence of the catalysts, the process becomes more complex, with the dye-mediated sensitization process and the intrinsic ability of TiO_2 working in tandem to generate ROS, which then readily contributes toward the degradation of Rh6G, further potentiating the photocatalytic process. From this, some observations can be made from the data in **Table 2**:

a) In the absence of TiO_2, degradation rates are similar irrespective of the light source used, indicating that the decomposition of Rh6G observed takes place by photolysis of the dye rather than ROS-induced oxidation.
b) When UV light is used the degradation of the dye takes place mainly by ROS generated due to the intrinsic photocatalytic activity of TiO_2 and by that induced by photosensitization, in all the TiO_2 variants studied.
c) The synthesized TiO_2 catalytic performance is slightly superior to its commercial counterpart (Anatase) when UV light is used, but greatly improves when visible light is used, this is due mainly by the decrease on the Eg of the synthesized catalyst (compared to Anatase), reduced photolysis of the dye, as well the enhancement of the photosensitization process.

In a comparison between the performance of the supported TiO_2 catalysts, and an equivalent mass of TiO_2 catalyst in suspension, it is revealed that an important fraction of the photodegradation efficiency is preserved in the supported material, going from ∼80 to 90% of photodegradation for all the TiO_2 suspensions (**Table 4**) to a 77% (UV light) and 66% (white light) as maximum values of photodegradation (**Table 3**) achieved by the supported materials (AS-TiO_2 and Anatase). The main cause of the observed differences might be associated to a loss of effective area of the supported TiO_2 catalysts due to adsorption on the rings surface vs. the total surface availability of the suspended particles of TiO_2. The percentage of retained photocatalytic activity in the supported TiO_2 catalyst is particularly good, particularly when taking into account the large surface area of TiO_2 catalysts lost upon support on the raschig rings, fact that is especially evident for the AS-TiO_2, material which displays the lower support efficiency and morphologically differs the most from the others TiO_2 variants (Anatase and Degusa P25), as presented in **Figure 4**.

In order to delve further in to the photocatalytic processes of the systems studied, the chemical oxygen demand (COD) for the photocatalyzed decomposition Rh6G was evaluated. The determination of the COD of the photocatalytic process can provide useful information in these type of complex oxidative

TABLE 4 | Kinetic data for the photodegradation of Rh6G on TiO_2 catalysts aqueous suspensions irradiated with UV light.

Catalyst[a]	k_{obs} (min^{-1})	Degradation percentage
Degussa P25	6.5×10^{-2}	80
Anatase	3.6×10^{-1}	89
TiO_2 acid synthesis	1.0×10^{-1}	91

[a] *Mass of suspended catalyst is determined as the equivalent mass of supported TiO_2 on 10 raschig rings.*

TABLE 5 | Chemical oxygen demand (COD) data for the photocatalytic degradation of Rhodamin 6G in the presence of supported TiO_2 catalysts irradiated with UV light.

Catalyst	COD (mg/L)	Degradation (%)
Degussa P25	20	25
Anatase	21	33
TiO_2 acid synthesis	21	33

TABLE 6 | Influence of additives on the kinetic data (21 °C) for the photodegradation of Rhodamin 6G in the presence of TiO_2 (acid synthesis) supported on Raschig rings.

Additive	k_{obs} (min^{-1})	Degradation percentage
UV light (365 nm)		
H_2O_2 (5 μM)	$1.9 \times 10^{-2} \pm 3.0 \times 10^{-3}$	60.1 ± 1.3
NaCl (5 μM)	$1.9 \times 10^{-2} \pm 4.0 \times 10^{-3}$	72.0 ± 2.6
Na_2SO_4 (5 μM)	$1.0 \times 10^{-2} \pm 1.9 \times 10^{-3}$	61.4 ± 8.8
NaCl (5 μM)/H_2O_2 (5 μM)	$2.5 \times 10^{-2} \pm 3.5 \times 10^{-3}$	63.3 ± 1.9
Na_2SO_4 (5 μM)/H_2O_2 (5 μM)	$2.4 \times 10^{-2} \pm 1.0 \times 10^{-3}$	68.6 ± 1.6
White light		
H_2O_2 (5 μM)	$1.7 \times 10^{-2} \pm 4.0 \times 10^{-3}$	51.6 ± 0.3
NaCl (5 μM)	$2.7 \times 10^{-2} \pm 4.2 \times 10^{-3}$	64.3 ± 6.9
Na_2SO_4 (5 μM)	$2.9 \times 10^{-2} \pm 4.0 \times 10^{-3}$	61.8 ± 5.6
NaCl (5 μM)/H_2O_2 (5 μM)	$1.8 \times 10^{-2} \pm 8.0 \times 10^{-3}$	55.4 ± 6.1
Na_2SO_4 (5 μM)/H_2O_2 (5 μM)	$2.5 \times 10^{-2} \pm 8.1 \times 10^{-3}$	59.3 ± 10.7

systems where parallel and sequential reactions might take place, systems in which common first order kinetics or initial rate kinetic methods might be somewhat limited to describe the overall process, particularly when spectrophotometric methods are used and the oxidative bleaching of the target molecule may not fully correspond with the whole oxidative pathway of said molecule (Mills et al., 2012). Similarly, COD has been successfully used in comparative studies involving semiconductor photocatalysts (El-Mekkawi et al., 2016). Data in **Table 5** shows COD values and Rh6D photodegradation percentages for the studied photocatalysts. The minor differences observed in the degradation percentages determined by COD in all of the supported TiO_2 variants, indicate that, besides the different complex photophysical processes taking place in various degrees, potentially involving different oxidation intermediaries, the endproducts of the considered photocatalytic systems appears to be similar.

Influence of Additives on the TiO_2-Catalyzed Photodegradation of Rhodamin 6G

The presence of additives and the study of their influence on the photocatalytic process is a matter of utmost importance, especially when considering the prospect of technological applications of the supported TiO_2 catalyst on waste water treatment, were salinity and the presence of oxidant agents may affect the performance of the catalysts. With this purpose, the addition of NaCl, Na_2SO_4, and H_2O_2 to the Rh6G solutions was considered, and their influence on the AS-TiO_2 photocatalytic activity was assessed (kinetic profiles in **Supplementary Figures 6, 7**). Data on **Table 6** shows that for H_2O_2 there is a decrease in the photodegradation efficiency (60%) compared to that in the absence of the additive (77%; **Table 3**) when UV light is used. Similarly, an almost equivalent decrease is observed when white light is used, with a 52 vs. 67% (**Table 3**) with and without H_2O_2 respectively. On the other hand, for NaCl, and for both of the light sources studied, a negligible decrease of the photodegradation efficiency is observed, with a 72% degradation with UV light and a 62 % for white light. As observed with NaCl, the addition of Na_2SO_4 induces no significative variation into the photodegradation efficiency observed with white light, contrary to a larger decrease when UV light is used, with a 62 and a 61% photodegradation with white light and UV light, respectively.

The kinetic data for the addition of H_2O_2 show a decrease on the rate constant (2.5×10^{-2} min^{-1} without H_2O_2; **Table 3**) for both light sources, whereas for SO_4^{-2} and Cl^- sodium salts there is no change in the rate constants when white light is used, but decreases when the samples are irradiated with UV light, with the largest decrease being observed for SO_4^{-2} (1.0×10^{-2} min^{-1}; **Table 6**).

Overall, the data presented regarding the influence of the SO_4^{-2}, Cl^- and hydrogen peroxide, shows a good tolerance of the photocatalytic system to these additives. The explanation for the observed influence of the anions in the system can be complex, for example both anions can interact with the vacant holes of the generated in the valence band, inhibiting the recombination of the hole/electron pair on the photocatalysts surface as well as to react with H_2O, generating hydroxyl radicals, leading to further degradation of Rh6G, however it has been also reported that these ions can also display an inhibitory behavior (Yan et al., 2012), by scavenging hydroxyl radicals generated on the surface of the catalyst, as well as by competing with Rh6G for the adsorption sites available, which seem to be the most likely explanation on the behavior of the data presented for the photodegradation of Rh6G in the studied system.

For the case of hydrogen peroxide, at nanomolar concentrations (Sahel et al., 2016; Kang et al., 2017), it can act as a scavenger of electrons from the conduction band of TiO_2, which promotes charge separation and the formation of hydroxyl radicals, which may lead to an enhanced degradation

of Rh6G. However, a decrease of photodegradation efficiency is observed in our system, indicating that at the considered H_2O_2 concentrations, electron and/or hydroxyl radical scavenging properties of hydrogen peroxide might be of relevance.

When equimolar ratios of H_2O_2 and salt are used, interesting results are observed. First, when UV light is used, the rate for the mixture $NaCl/H_2O_2$ is equal to that observed without additives, and higher than the values determined for the systems containing NaCl and H_2O_2 separately. On the contrary, for the samples irradiated with white light, the mixture shows a rate constant equal to that of the system containing only hydrogen peroxide, lower than the one determined in the absence of additives. The behavior observed for the samples containing the mixture Na_2SO_4/H_2O_2 is quite similar, for UV light, the rate of the photocatalytic process taking place in the presence of both SO_4^{-2} and H_2O_2 is higher than that of the additives separately, and equal to that observed in the absence of additives, the same being true for white light, but the rate of the mixture is now equal to that observed when Na_2SO_4 is the only additive present in the photocatalytic system.

CONCLUSIONS

Raschig rings-supported TiO_2 catalysts display a good photocatalytic performance when compared to equivalent amounts of TiO_2 in aqueous suspension, even though a large surface area of TiO_2 material is lost upon support. The comparative study between suspension vs. supported TiO_2 catalysts reveals that optimization of the available area in the raschig rings is imperative in order to improve the catalyzed photodegradation of Rh6G. This is particularly evident by taking into account that the characteristics (XRD, RD, Eg) and observed photodegradative performance of the synthesized catalysts are in good agreement with the commercial TiO_2 samples, and that the Rh6G photodegradation differences observed with the light sources considered are minimal in the presence of TiO_2 catalysts.

The presence of additives induce changes in the kinetics and efficiency of the TiO_2-catalyzed photodegradation of Rh6G, particularly when white light is used in the process, pointing toward a complex phenomenon, however the stability of the supported photocatalytic systems is acceptable in the presence of the studied additives. In line with this, the magnitude of the chemical oxygen demand, indicates that besides the different complex photophysical processes taking place, the intermediate products of the considered photocatalytic systems appears to be similar.

DATA AVAILABILITY STATEMENT

The raw data supporting the conclusions of this article will be made available by the authors, without undue reservation, to any qualified researcher.

AUTHOR CONTRIBUTIONS

EP designed the experiments, analyzed the results, and wrote and revised the manuscript. CC analyzed the results and wrote and revised the manuscript. FH and GA performed experimental activities. GC participated in the data analysis and discussions. All authors have approved the final revised manuscript.

FUNDING

This work was supported by DICYT-USACH 02184PL and Red CYTED318RT0551 grants.

ACKNOWLEDGMENTS

Universidad de Santiago de Chile, DICYT 02184PL, Vicerrectoria de investigación, desarrollo e innovación. Red CYTED318RT0551, University of Santiago of Chile. Thanks to the PAI: FQM 175 group directed by Dr. Julian Morales from the Department of Inorganic Chemistry and Chemical Engineering, School of Sciences, Campus Rabanales, University of Cordoba, Span.

SUPPLEMENTARY MATERIAL

The Supplementary Material for this article can be found online at: https://www.frontiersin.org/articles/10.3389/fchem.2020.00365/full#supplementary-material

REFERENCES

Ahmed, S., Rasul, M. G., Brownb, R., and Hashib, M. A. (2011). Influence of parameters on the heterogeneous photocatalytic degradation of pesticides and phenolic contaminants in wastewater: a short review. *J. Environ. Manage.* 92, 311–330. doi: 10.1016/j.jenvman.2010.08.028

Ajmal, A., Majeed, I., Malik, R. N., Idriss, H., and Nadeem, M. A. (2014). Principles and mechanisms of photocatalytic dye degradation on TiO_2 based photocatalysts: a comparative overview. *RSC Adv.* 4:37003. doi: 10.1039/C4RA06658H

Alahiane, S., Qourzal, S., El Ouardi, M., Abaamrane, A., and Assabbane, A. (2014). Factors influencing the photocatalytic degradation of reactive yellow 145 by TiO_2-coated non-woven fibers. *Am. J. Anal. Chem.* 5, 445–454. doi: 10.4236/ajac.2014.58053

Ali, S., Li, Z., Chen, S., Zada, A., Khan, I., Khan, I., et al. (2019). Synthesis of activated carbon-supported TiO_2-based nano-photocatalysts with well recycling for efficiently degrading high-concentration pollutants. *Catal. Today* 351. 557–564. doi: 10.1016/j.cattod.2019.03.044

Amenn, S., Akhtar, M. S., Seo, H-K., and Shin, H-S. (2013). Mineralization of rhodamine 6G dye over roseflower-like ZnO nanomaterials. *Mater. Lett.* 113, 20–24. doi: 10.1016/j.matlet.2013.09.004

Ansón-Casaos, A., Tacchini, I., Unzue, A., and Martínez, M. T. (2013). Combined modification of a TiO_2 photocatalyst with two different carbon forms. *Appl. Surf. Sci.* 270, 675–684. doi: 10.1016/j.apsusc.2013.01.120

Barranco, A., and Groening, P. (2006). Fluorescent plasma nanocomposite thin films containing nonaggregated rhodamine 6G laser dye molecules. *ACS J. Langumir Surf. Colloids* 22, 6719–6722. doi: 10.1021/la053304d

Bokhale, N. B., Bomble,S., Dalbhanjan, R. R., Mahale, D. D., Hinge,S. P., Banerjee,B. S., et al. (2014). Sonocatalytic and sonophotocatalytic degradation

of rhodamine 6G containing wastewaters. *Ultrason. Sonochem.* 21, 1797–1804. doi: 10.1016/j.ultsonch.2014.03.022

Bujdak, J., and Iyi, N. (2012). Highly fluorescent colloids based on rhodamine 6G, modified layered silicate and organic solvent. *J. Colloid Interf. Sci.* 388, 15–20. doi: 10.1016/j.jcis.2012.08.020

Carreon, M. L., Carreonet, H. G., Espino-Valencia, J., and Carreon, M. A. (2011). Photocatalytic degradation of organic dyes by mesoporous nanocrystalline anatase. *Mater. Chem. Phys.* 125, 474–478. doi: 10.1016/j.matchemphys.2010.10.030

Chong, M., Jin, B., Chow, W., and Saint,. C. (2010). Recent developments in photocatalytic water treatment technology a review. *Water Res.* 44, 2997–3027. doi: 10.1016/j.watres.2010.02.039

Daghrir, R., Droguie, P., Ka, I., El Khakanib, M. A. (2012). Photoelectrocatalytic degradation of chlortetracycline using Ti/TiO_2 nanostructured electrodes deposited by means of a pulsed laser deposition process. *J. Hazard. Mater.* 199-200, 15–24. doi: 10.1016/j.jhazmat.2011.10.022

Dyi-Hwa, T., Lain-Chuen, J., and Hsin-Hsu, H. (2012). Effect of oxygen and hydrogen peroxide on the photocatalytic degradation of monochlorobenzene in aqueous suspension. *Int. J. Photoenergy* 2012:328526. doi: 10.1155/2012/328526

El-Mekkawi, D. M., Galal, H. R., Abd EL Wahad, R. M., and Mohamed, W. A. A. (2016). Photocatalytic activity evaluation of TiO_2 nanoparticles based on COD analyses for water treatment applications: a standardization attempt. *Int. J. Environ. Sci. Technol.* 13, 1077–1088 doi: 10.1007/s13762-016-0944-0

Foo, K. Y., and Hameed, B. H. (2009). An overview of landfill leachate treatment via activated carbon adsorption process. *J. Hazard. Mater.* 171, 54–60. doi: 10.1016/j.jhazmat.2009.06.038

Fujishima, A., and Honda, K. (1972). Electrochemical photolysis of water at a semiconductor electrode. *Nature* 238, 37–38. doi: 10.1038/238037a0

Gaya, U. I. (2014). *Heterogeneous Photocatalysis Using Inorganic Semiconductor Solids*. Dordrecht: Springer. doi: 10.1007/978-94-007-7775-0

Giménez, J., Bayarri, B., González, O., Malato, S., Peral, J, and Esplugas, S. (2015). Advanced oxidation processes at laboratory scale: environmental and economic impacts. *ACS Sustain. Chem. Eng.* 3, 3188–3196. doi: 10.1021/acssuschemeng.5b00778

Guillard, C., Puzenat, E., Lachheb, H., Houas, A., and Herrmann, J. M. (2005). Why inorganic salts decrease the photocatalytic efficiency. *Int. J. Photoenergy* 7:641208. doi: 10.1155/S1110662X05000012

Hurum, D. C., Agrios, A. G., and Gray, K. A. (2003). Explaining the enhanced photocatalytic activity of degussa P25 mixed-phase TiO_2 using EPR. *J. Phys. Chem. B* 107, 4545–4549. doi: 10.1021/jp0273934

Kang, S., Zhang, L., Liu, C., Huang, L., Shi, H., and Cui, L. (2017). Hydrogen peroxide activated commercial P25 TiO_2 as efficient visible-light-driven photocatalyst on dye degradation. *Int. J. Electrochem. Sci.* 12, 5284–5293 doi: 10.20964/2017.06.54

Landmann, M., Rauls, E., and Schmidt, W. G. (2012). The electronic structure and optical response of rutile anatase and brookite TiO_2. *J. Phys.* 24, 195503–195508. doi: 10.1088/0953-8984/24/19/195503

Lasio, B., Malfatti, L., and Innocenzi, P. (2013). Photodegration of rhodamine 6G dimers in silica sol-gel films. *J. Photochem. Photobiol A Chem.* 271, 93–98. doi: 10.1016/j.jphotochem.2013.08.007

Lenore, S., Clescerl Arnold, E., and Greenberg Andrew, D., Eaton. (2009). *Standard Methods for Examination of Water & Wastewater, 20th Edn*. Washington, DC: American Public Health Association.

Li, X., Chen, C., and Zhao, J. (2001). Mechanism of photodecomposition of H_2O_2 on TiO_2 surfaces under visible light irradiation. *Langmuir* 17, 4118–4122. doi: 10.1021/la010035s

Liu, G., Wang, G., Hu, Z., Su, Y., and Li, Z. (2019). Ag_2O nanoparticles decorated TiO_2 nanofibers as a p-n heterojunction for enhanced photocatalytic decomposition of RhB under visible light irradiation. *Appl. Surf. Sci.* 465, 902–910. doi: 10.1016/j.apsusc.2018.09.216

Loghambal, S., Agvinos Catherine, A. J., and Velu Subash, S. (2018). Analysis of langmuir-hinshelwood kinetics model for photocatalytic degradation of aqueous direct blue 71 through analytical expression. *Int. J. Math. Appl.* 6, 903–913.

López, R., and Gómez, R. (2012). Band-gap energy estimation from diffuse reflectancemeasurements on sol–gel and commercial TiO_2: a comparative study. *J. Sol. Gel Sci. Technol.* 61, 1–7. doi: 10.1007/s10971-011-2582-9

Magde, D., Rojas, G. A., and Seybold, P. G. (1999). Solvent dependence of the fluorescence lifetimes of xanthene dyes. *Photochem. Photobiol.* 70, 737–744. doi: 10.1111/j.1751-1097.1999.tb08277.x

Mahshid, S., Askari, M., and Sasani Ghamsari, M. (2007). Synthesis of TiO_2 nanoparticles by hydrolysis and peptization of titanium isopropoxide solution. *J. Mater. Process. Technol.* 189, 296–300. doi: 10.1016/j.jmatprotec.2007.01.040

Malesic-Eleftheriadou, N., Evgenidou, E. N., Kyzas, G. Z., Bikiaris, D. N., and Lambropoulou, D. A. (2019). Removal of antibiotics in aqueous media by using new synthesized bio-based poly(ethyleneterephthalate)-TiO_2 photocatalysts. *Chemosphere* 234. 746–755. doi: 10.1016/j.chemosphere.2019.05.239

Mills, A., Hill, C., and Robertson, P. K. J. (2012). Overview of the current ISO tests for photocatalytic materials. *J. Photochem. Photobiol. A* 237, 7–23 doi: 10.1016/j.jphotochem.2012.02.024

Módenes, A. N., Espinoza-Quiñones, F. R., Manenti, D. R., Borba, F. H., Palácio, S. M., and Colombo, A. (2012). Performance evaluation of a photo-fenton process applied to pollutant removal from textile effluents in a batch system. *J. Environ. Manage.* 104, 1–8. doi: 10.1016/j.jenvman.2012.03.032

Ochoa, Y., Ortegón, Y., Vargas, M., and Rodríguez, J. (2009). Síntesis de TiO_2, fase anatasa, por el método Pechini. *Suplemento de la Revista Latinoamericana de Metalurgia y Materiales* 3, 931–937.

Raja, P., Bensimon, M., Kulik, A., Foschia, R., Laub, D., Albers, P., et al. (2005). Dynamics and characterization of an innovative raschig rings–TiO_2 composite photocatalyst. *J. Mol. Catal. A Chem.* 237, 215–223. doi: 10.1016/j.molcata.2005.04.060

Ranjith, R., Renganathan, V., Chen, S. M., Selvan, N. S., and Rajam, P. S. (2019). Green synthesis of reduced graphene oxide supported TiO_2/Co_3O_4 nanocomposite for photocatalytic degradation of methylene blue and crystal violet. *Ceram. Int.* 45, 12926–12933. doi: 10.1016/j.ceramint.2019.03.219

Rejek, M., and Grzechulska-Damszel, J. (2018). Degradation of sertraline in water by suspended and supported TiO_2. *Pol. J. Chem. Technol.* 20, 107–112. doi: 10.2478/pjct-2018-0030

Rizzo, L., Meric, S., Guida, M., Kassinos, D., and Belgiorno, V. (2009). Heterogenous photocatalytic degradation kinetics and detoxification of an urban wastewater treatment plant efluents contaminated with pharmaceuticals. *Water Res.* 43, 4070–4078. doi: 10.1016/j.watres.2009.06.046

Robinson, T., McMullan, G., Marchant, R., and Nigam, P. (2001). Remediation of dyes in textile effluent: a critical review on current treatment technologies with a proposed alternative. *Bioresour. Technol.* 77, 247–255. doi: 10.1016/S0960-8524(00)00080-8

Rodríguez, E. M., Rey, A., Mena, E., and Beltrán, F. J. (2019). Application of solar photocatalytic ozonation in water treatment using supported TiO_2. *Appl. Catal. B Environ.* 254, 237–245. doi: 10.1016/j.apcatb.2019.04.095

Sahel, K., Elsellami, L., Mirali, I., Dapozze, F., Bouhent, M., and Guillard, C. (2016). Hydrogen peroxide and photocatalysis. *Appl. Catal. B Environ.* 188, 106–112. doi: 10.1016/j.apcatb.2015.12.044

Smith, A. M., and Nie, S. (2009). Semiconductor nanocrystals: structure, properties, and band gap engineering. *Acc. Chem. Res.* 43, 190–200. doi: 10.1021/ar9001069

Song, H., Chen, C., Zhang, H., and Huang, J. (2016). Rapid decolorization of dyes in heterogeneous fenton-like oxidation catalyzed by Fe-incorporated Ti-HMS molecular sieve. *J. Environ. Chem. Eng.* 4, 460–467. doi: 10.1016/j.jece.2015.12.003

Spurr, R. A., and Myers, H. (1957). Quantitative analysis of anatase-rutile mixtures with an X-ray difractometer. *Anal. Chem.* 29, 760–762. doi: 10.1021/ac60125a006

Stracke, F., Heupel, M. A, and Thiel, E. (1999). Singlet molecular oxygen photosensitized by Rhodamine dyes: correlation with photophysical properties of the sensitizers. *J. Photochem. Photobiol. A Chem.* 126, 51–58. doi: 10.1016/S1010-6030(99)00123-9

Sun, S., Zhao, R., Xie, Y., and Liu, Y. (2019). Photocatalytic degradation of aflatoxin B_1 by activated carbon supported TiO_2 catalyst. *Food Control* 100, 183–188. doi: 10.1016/j.foodcont.2019.01.014

Tarud, F., Aybar, M., Pizarro, G., Cienfuegos, R., and Pastén, P. (2010). Integrating fluorescent dye flow-curve testing and acoustic doppler velocimetry profiling for *in situ* hydraulic evaluation and improvement of clarifier performance. *Water Environ. Res.* 82, 675–685. doi: 10.2175/106143009X425889

Teoh, W. Y., Scott, J. A., and Amal, R. (2012). Progress in heterogeneous photocatalysis: from classical radical chemistry to engineering nanomaterials and solar reactors. *J. Phys. Chem. Lett.* 3, 629–639. doi: 10.1021/jz3000646

Vanamudan, A., and Pamidimukkala, P. (2015). Chitosan, nanoclay and chitosan–nanoclay composite as adsorbents for rhodamine-6G and the resulting optical properties. *Int. J. Biol. Macromol.* 74, 127–135. doi: 10.1016/j.ijbiomac.2014.11.009

Wan, X., Ke, H., Yang, G., and Tang, J. (2018). Carboxyl-modified hierarchical wrinkled mesoporous silica supported TiO_2 nanocomposite particles with excellent photocatalytic performances. *Prog. Nat. Sci. Mater. Int.* 28, 683–688. doi: 10.1016/j.pnsc.2018.11.007

Wang, J., Wang, G., Wei, X., Liu, G., and Li, J. (2018). ZnO nanoparticles implanted in TiO_2 macrochannels as an effective direct Z-scheme heterojunction photocatalyst for degradation of RhB. *Appl. Surf. Sci.* 456, 666–675. doi: 10.1016/j.apsusc.2018.06.182

Wu, T., Liu, G., and Zhao, L. (1998). Photoassisted degradation of dye pollutants. V. self-photosensitized oxidative transformation of rhodamine B under visible light irradiation in aqueous TiO_2 dispersions. *J. Phys. Chem. B* 102, 5845–5851. doi: 10.1021/jp980922c

Yan, X., Bao, R., Yu, S., Li, Q., and Jin, Q. (2012). The roles of hydroxyl radicals, photo-generated holes and oxygen in the photocatalytic degradation of humic acid. *Russ. J. Phys. Chem.* 86, 1479–1485. doi: 10.1134/S0036024412070333

Yaseen, D. A., and Scholz, M. (2019). Textile dye wastewater characteristics and constituents of synthetic effluents: a critical review. *Int. J. Environ. Sci. Technol.* 16, 1193–1226. doi: 10.1007/s13762-018-2130-z

Zehentbauer, F. M., Moretto, C., Stephen, R., Thevar, T., Gilchrist, J. R., Pokrajac, D., et al. (2014). Fluorescence spectroscopy of rhodamine 6G: concentration and solvent effects. *Spectrochim. Acta A Mol. Biomol. Spectrosc.* 121, 147–151. doi: 10.1016/j.saa.2013.10.062

Conflict of Interest: The authors declare that the research was conducted in the absence of any commercial or financial relationships that could be construed as a potential conflict of interest.

frontiers in Chemistry

ORIGINAL RESEARCH
published: 05 May 2020
doi: 10.3389/fchem.2020.00334

FeCoNi Sulfides Derived From *In situ* Sulfurization of Precursor Oxides as Oxygen Evolution Reaction Catalyst

Wanqing Teng[1], Mengtian Huo[1], Zhaomei Sun[1], Wenrong Yang[1], Xiangjiang Zheng[1], Caifeng Ding[2]* and Shusheng Zhang[1]*

[1] Shandong Provincial Key Laboratory of Detection Technology for Tumor Markers, College of Chemistry and Chemical Engineering, Linyi University, Linyi, China, [2] Key Laboratory of Optic-Electric Sensing and Analytical Chemistry for Life Science, Ministry of Education, College of Chemistry and Molecular Engineering, Qingdao University of Science and Technology, Qingdao, China

It is highly promising to design and develop efficient and economical electrocatalysts for oxygen evolution reaction (OER) in alkaline solution. In this work, we prepare FeCoNi sulfide composites (including FeS, Co_3S_4, and Ni_3S_4) derived from *in situ* sulfurization of precursor oxides on carbon cloth (CC), which are used to become an OER catalyst. Such catalyst shows excellent OER performance, low overpotential, small Tafel slope, and high electrochemical stability, and it is a promising electrocatalyst for OER in alkaline media.

Keywords: oxygen evolution reaction, electrocatalyst, FeCoNi sulfides, nanowires array, *in situ* sulfurization

OPEN ACCESS

Edited by:
Xing Huang,
ETH Zürich, Switzerland

Reviewed by:
Yun Hau Ng,
City University of Hong Kong, Hong Kong
Fatwa Abdi,
Helmholtz-Gemeinschaft Deutscher Forschungszentren (HZ), Germany
Yuxiao Ding,
Max Planck Institute for Chemical Energy Conversion, Germany

****Correspondence:***
Xiangjiang Zheng
zxj4408@126.com
Caifeng Ding
dingcaifeng@qust.edu.cn

Specialty section:
This article was submitted to Catalysis and Photocatalysis, a section of the journal Frontiers in Chemistry

Received: *16 December 2019*
Accepted: *31 March 2020*
Published: *05 May 2020*

Citation:
Teng W, Huo M, Sun Z, Yang W, Zheng X, Ding C and Zhang S (2020) FeCoNi Sulfides Derived From In situ Sulfurization of Precursor Oxides as Oxygen Evolution Reaction Catalyst. Front. Chem. 8:334. doi: 10.3389/fchem.2020.00334

INTRODUCTION

The excessive consumption of fossil energy and the resulting serious environmental problems have triggered strong demand for renewable alternative energy (Chow et al., 2003; Zheng et al., 2014). Hydrogen energy is regarded as a clean and ideal energy carrier that could replace fossil energy (Dresselhaus and Thomas, 2001; Zheng et al., 2017, 2018b). Electrochemical water splitting provides us a promising strategy to largely produce hydrogen (Turner, 2004; Lu et al., 2017). However, hydrogen evolution is seriously restricted by anodic water oxidation due to the multi-electron transfer process and high activation energy barrier (Yin et al., 2010; Yang et al., 2017; Ke et al., 2018; Zheng et al., 2018a; Tang et al., 2019). Therefore, efficient catalysts to reduce activation energy should be developed to boost the water oxidation process. Noble metal oxides (RuO_2 and IrO_2) exhibit excellent catalytic characters in oxygen evolution reaction (OER), but their widespread applications are limited due to scarce resources and high costs (Lee et al., 2012; Reier et al., 2012). Hence, it is necessary to develop efficient and economical OER electrocatalysts.

In recent years, transition-metal oxides and hydroxyl oxide have attracted great interest for catalysts (Lu et al., 2016; Guo et al., 2017; Zhang et al., 2017; Jin et al., 2018; Zhao et al., 2018). Specifically, ferric oxyhydroxide (FeOOH) has shown efficient activity for the OER process (Chemelewski et al., 2014; Luo et al., 2017; Park et al., 2017). Regardless of its abundant reserves and low cost, its performance for OER has certain disparities in comparing with the noble metal catalysts. Many ways have been taken to improve catalysis performance, such as enhancing the conductivity of materials, increasing the specific surface area of materials, doping heteroatom modification, and so on (Feng et al., 2016a,b; Kuang et al., 2017; Li F. et al., 2018). Research shows that transition metal sulfides have better oxygen evolution catalysis performance than oxides because transit metal sulfides have diverse element composition, controllable electronic structure, and fast charge transfer speed (Liu et al., 2016; Chai et al., 2018; Li H. et al., 2018; Zhang et al., 2018).

In this manuscript, we design and develop FeCoNiS sulfides derived from *in situ* sulfurization of precursor oxides on carbon cloth (CC) through two-step hydrothermal methods. At first, FeCoNi-FeOOH nanoarray on CC is prepared through hydrothermal method. Secondly FeCoNiS sulfides derived from *in-situ* sulfurization is prepared through the second hydrothermal method. It shows excellent OER activity needing overpotentials of 220.5 and 269.9 mV to attain current densities of 10 and 100 mA cm^{-2} in 1.0 M KOH. It is a promising electrocatalyst for OER in alkaline media.

RESULTS AND DISCUSSIONS

X-ray diffraction (XRD) patterns of these catalysts are shown in **Figure 1A**. There are two broad diffraction peaks on the bottom curve, which are the amorphous peaks of CC. The middle curve is the XRD pattern of the precursor oxides without sulfide treatment. The peaks at 11.95, 16.87, 26.91, 35.26, 46.69, 56.21, and 64.78° can be indexed to the (110), (200), (310), (211), (411), (521), and (541) planes of FeOOH phase (PDF No. 97-003-1136). The XRD pattern of the product after sulfide treatment is on the top. The diffraction peak intensity is obviously lower than that of the middle curve. For better structural analysis of the product, the powder of the precursor oxides and sulfide products scrapped from CC are characterized by XRD again. XRD curves are shown in **Figures 1B,C**. The main component of precursor oxides is still FeOOH. Considered that Co and Ni are in the precursor, we name the precursor as FeCoNi-FeOOH. The XRD curve of sulfide product shows that there are new phases, including Fe_3O_4 (PDF No.97-005-0272), FeS (PDF No. 04-003-4477), Ni_3S_4 (PDF No. 97-003-6721), and Co_3S_4 (PDF No. 00-047-1738). Part of FeOOH is reduced to Fe_3O_4, so the product is named FeCoNiS-FeO_x.

Scanning electronic microscopy (SEM) pattern of the precursor (FeCoNi-FeOOH) is shown in **Figure 2A**. There are specific and uniform nanowires array on the surface of CC. SEM pattern of FeCoNiS-FeO_x is shown in **Figure 2B**. Obviously, the precursor (FeCoNi-FeOOH) nanowires are smooth, and the product (FeCoNiS-FeO_x) is relatively rough. This means that the product has structural change after sulfidation, which corresponded to the XRD patterns in **Figures 1B,C**. The catalyst nanowire feature is also shown in transmission electron microscopy (TEM) characterization (**Figure 2C**). Image taken from the product shows about 50-nm-thick nanowires. High-resolution TEM (HRTEM) reveals that the product is highly crystallized with well-resolved lattice fringes (**Figure 2D**). The interplanar spacing of 0.331 nm could be assigned to the (310) plane of FeOOH.

The corresponding energy-dispersive X-ray (EDX) elemental mapping images of FeCoNiS-FeO_x are shown in **Figure 3A**, which demonstrate unique distribution of Fe, Co, Ni, and S elements. EDX pattern is shown in **Figure 3B**, which exhibits types and relative amounts of different elements based on the position and intensity of element spectral lines.

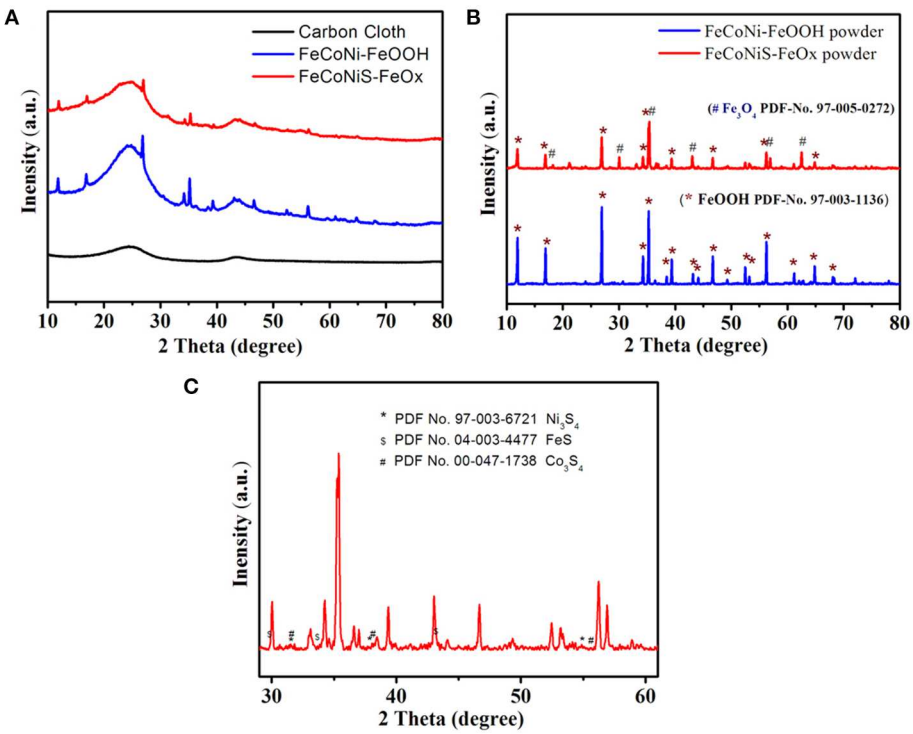

FIGURE 1 | (A) X-ray diffraction (XRD) patterns of different oxygen evolution reaction (OER) catalysts. **(B)** XRD patterns comparison of different catalysts powder. **(C)** XRD pattern of the product after sulfidation treatment.

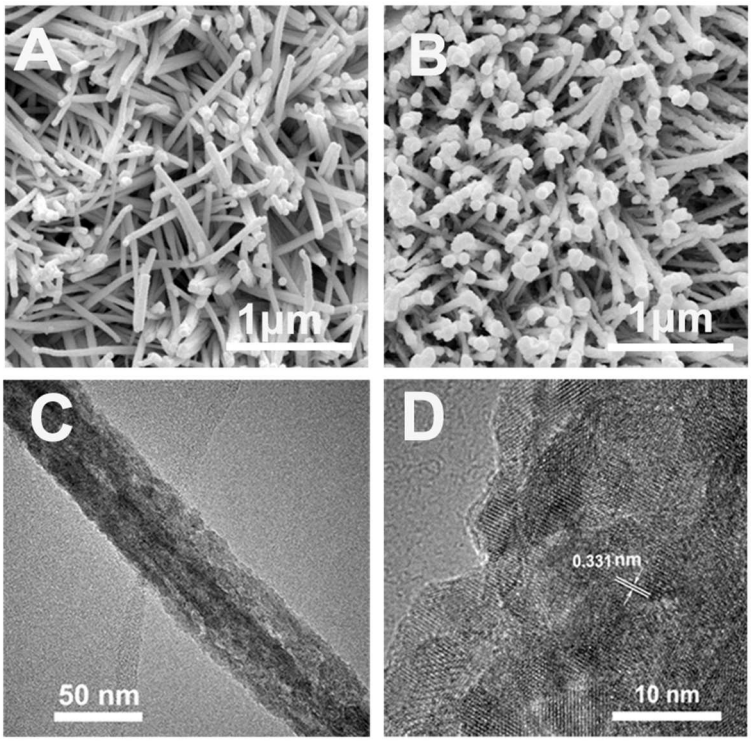

FIGURE 2 | (A) SEM pattern of precursor (FeCoNi-FeOOH). **(B)** SEM pattern of FeCoNiS-FeO_x. **(C)** TEM pattern of FeCoNiS-FeO_x. **(D)** HRTEM pattern of FeCoNiS-FeO_x.

X-ray photoelectron spectroscopy (XPS) of FeCoNiS-FeOOH is shown in **Figure 4**, which was performed to characterize the chemical states of different elements. **Figure 4A** is full-scale XPS spectrum, further revealing the presences of Fe, Co, Ni, S, and O elements in the catalyst. As shown in **Figure 4B**, high-spin Fe^{3+} of FeOOH contains unpaired electrons and therefore exhibit multiplet structures in Fe $2p_{3/2}$ area. The characteristic peaks of Fe $2p_{1/2}$ is at 725.8 eV. The satellite peaks (identified as "Sat.") are at 719.3 and 732.3 eV, which are relevant to Fe $2p_{3/2}$ and Fe $2p_{1/2}$ of FeOOH (Biesinger et al., 2011; Zeng et al., 2012; Zhou et al., 2018). There are two peaks at 714.4 and 723.9 eV, which are relevant to Fe_3O_4. In **Figure 4C**, there exhibit two spin-orbit doublets. The first doublet is at 778.6 and 793.5 eV, assigned to Co $2p_{3/2}$ and Co $2p_{1/2}$ of Co^{3+}, and the second doublet was at 781.9 and 797.8 eV, arising from Co $2p_{3/2}$ and Co $2p_{1/2}$ of Co^{2+}. In addition, two broad peaks located at 803.6 and 786.7 eV are attributed to the satellites, which indicated the presence of Co_3S_4 (Xiao et al., 2014; Liu et al., 2015; Gao et al., 2018; Wang X. et al., 2018).

In the Ni 2p spectrum (**Figure 4D**), there exist two main peaks at 855.7 and 873.5 eV assignable, respectively to Ni $2p_{3/2}$ and Ni $2p_{1/2}$ spin orbit doublets and two satellite peaks (862.4 and 880.1 eV). By deconvolution of the two main peaks, the Ni $2p_{3/2}$ orbit comprises two peaks with binding energy of 853.6 and 856.7 eV, which corresponded, respectively to the Ni^{2+} and Ni^{3+} oxidation states, and the Ni $2p_{1/2}$ orbit can also be fitted into two peaks belonging to Ni^{2+} (871.5 eV) and Ni^{3+} (875.2 eV) (Hu et al., 2015; Qin et al., 2016; Sivanantham et al., 2016). There show S $2p_{3/2}$ and S $2p_{1/2}$ peaks at 161.7 and 162.8 eV in **Figure 4E**, which can be related to S^{2-} (Wang H. et al., 2018). The component peak at 164.1 eV is characteristics of a metal–sulfur (M-S) bond (Ning et al., 2018). The peaks of 168.9 and 170.1 eV can be attributed to SO_4^{2-} due to air oxidation (Cheng et al., 2015). In the O 1s region (**Figure 4F**), the peaks of 530.0, 531.9, and 533.8 eV are observed on the surface of the catalyst, which are corresponding to O^{2-}, hydroxyl group, and adsorbed water molecules, respectively (Luo et al., 2017).

The catalysis performance of the catalyst in water oxidation reaction is evaluated by linear sweep voltammetry (LSV), shown in **Figure 5A**. For comparison, LSV curves of different catalysts with similar loading amounts, including CC, RuO_2, FeCoNi-FeOOH, FeCoNi-FeO_x, FeCoNiS-FeO_x, are also evaluated. Overpotentials in the same current density are often used to estimate the OER performance. FeCoNiS-FeOOH/CC exhibits outstanding OER performance with driving 100 mA cm^{-2} at a low overpotential of 269.9 mV, which is superior to RuO_2/CC and FeCoNi-FeOOH under the same conditions. FeCoNi-FeO_x is prepared through second hydrothermal method without sulfurizing reagent. The OER activity of FeCoNi-FeO_x is lower than FeCoNi-FeOOH. The existence of Fe_3O_4 will not enhance catalytic reactivity. The main active site of FeCoNiS-FeO_x is FeCoNi sulfides. Tafel plots of different OER catalysts were shown in **Figure 5B**, which are used to evaluate the catalytic kinetics. The Tafel slope of FeCoNiS-FeO_x is 45.1 mV dec^{-1}, lower than

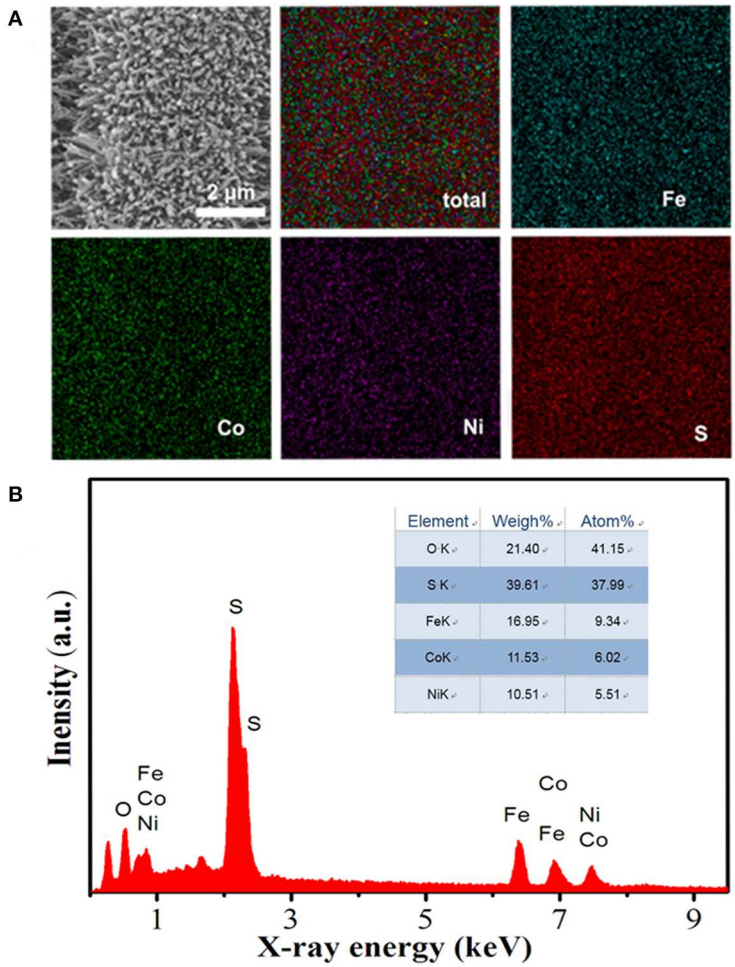

FIGURE 3 | (A) Energy-dispersive X-ray (EDX) mapping images of FeCoNiS-FeOx. **(B)** EDX element distribution pattern.

that of RuO_2/CC (52.3 mV dec^{-1}). It demonstrates that the FeCoNiS-FeO_x catalyst has more rapid reaction velocity in OER catalytic reaction.

Another important performance, stability of catalyst, is investigated by cyclic voltammetry and potentiostatic method. As shown in **Figure 5C**, there shows a comparison of two polarization curves, including original curve and another curve after 500 CV cycles. When the potential is 1.5 V, the current density is only 3% decrease after 500 cycles, which demonstrates that the FeCoNiS-FeO_x catalyst has a good cycle life. In **Figure 5D**, the electrochemical stability of FeCoNiS-FeOOH/CC is tested by potentiostatic electrolysis at a constant potential of 1.48 V for 30 h. There is only 5% decay of current density, which demonstrated the good long-term durability of the catalyst. Multistep chronopotentiometric curve of FeCoNiS-FeO_x is shown in **Figure 6**. There are 12 steps and the increment of current density is 20 mA cm^{-2} per 500 s. In every step, the corresponding potential remains constant. These results indicate that the catalyst has excellent conductivity and good mass transportation.

CONCLUSIONS

In this paper, a two-step hydrothermal routine is adopted to prepare FeCoNiS-FeO_x catalyst. At first, hydroxide nanowire array precursor is prepared. The precursor nanowire arrays serve as backbones for the catalyst not only constructs effective conductive channels but also provides rich active sites. Secondly, the final product is prepared via anion exchange and redox reactions with Na_2S as sulfurizing reagent. The catalyst shows excellent OER activity needing overpotentials of 220.5 and 269.9 mV to attain current densities of 10 and 100 mA cm^{-2} in 1.0 M KOH. Typically, the catalyst also shows long-term electrochemical stability for at least 30 h. The good catalysis performance is due to FeS, Co_3S_4, and Ni_3S_4. CC as substrate could enhance the conductivity of the material. Nanowire structure could increase the surface area of materials and expose more active sites. Most importantly, transition-metal sulfide could optimize material structure and give a full play to the synergy effect between different elements. FeCoNiS-FeO_x catalyst is a promising electrocatalyst for OER in alkaline media.

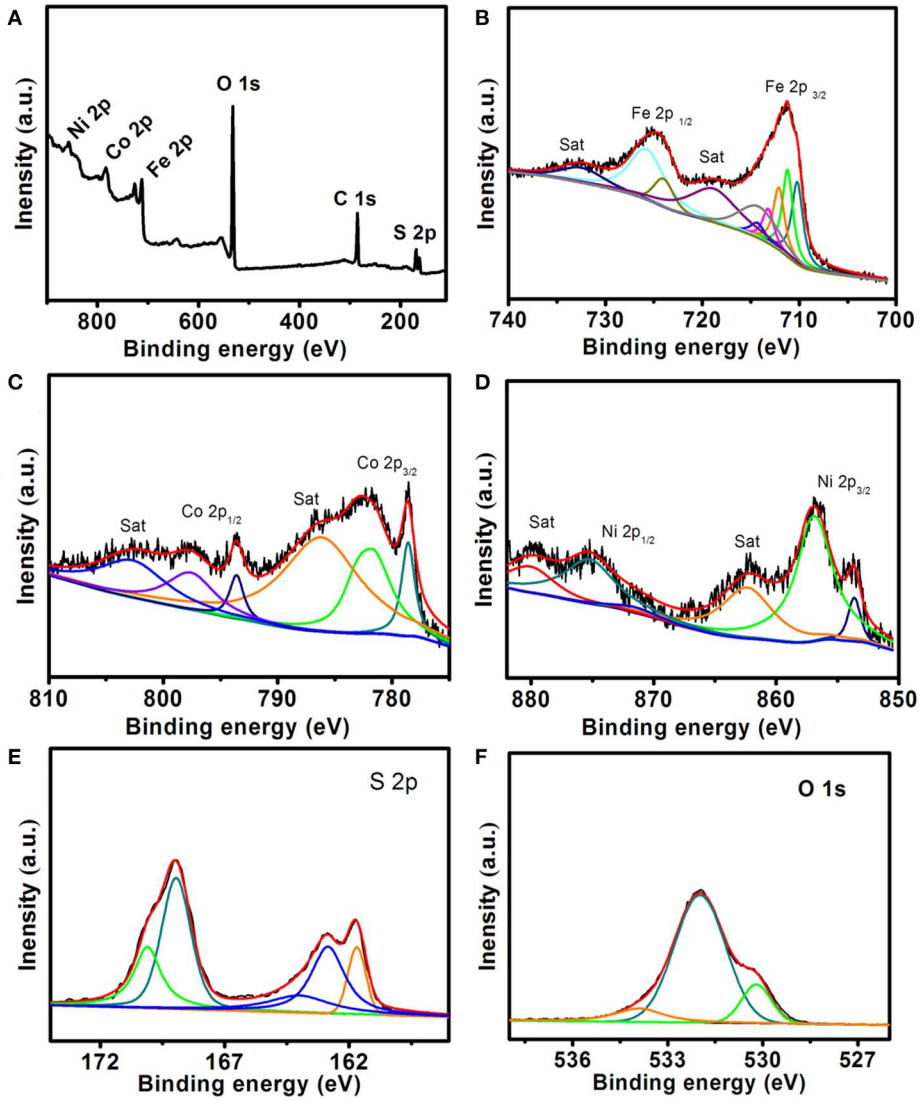

FIGURE 4 | X-ray photoelectron spectroscopy (XPS) spectra of FeCoNiS-FeO_x catalyst. **(A)** Survey spectrum. **(B)** Fe 2p. **(C)** Co 2p. **(D)** Ni 2p. **(E)** S 2p. **(F)** O 1s.

MATERIALS AND METHODS

Materials

Ferric nitrate [$Fe(NO_3)_3.9H_2O$, Mw = 404.00], nickel nitrate [$Ni(NO_3)_2.6H_2O$, Mw = 290.79], cobalt nitrate [$Co(NO_3)_2.6H_2O$, Mw = 291.03], ammonium fluoride NH_4F, Mw = 37.0), urea [$CO(NH_2)_2$, Mw = 60.06], potassium hydroxide (KOH, Mw = 56.1) are provided by Shanghai Aladdin Ltd. Sodium sulfide (Na_2S, Mw = 78.04) and ruthenium chloride ($RuCl_3.3H_2O \geq 43\%$) are bought from Sigma-Aldrich Co. Ltd. CC is supplied by Jingchong electronics technology company. The surface must be free from oil and dirt, then acetone, hydrochloric acid (3 mol/L), ethanol, and ultrapure water are used to clean the surface of CC. Ultrapure water (18.2 MΩ.cm) is used to prepare all aqueous solutions in this work. None of the reagents as received are further purified.

Preparation of Precursor

$Fe(NO_3)_3.9H_2O$ 0.323 g, $Ni(NO_3)_2.6H_2O$ 0.058 g, $Co(NO_3)_2.6H_2O$ 0.058 g, NH_4F 0.03 g, $CO(NH_2)_2$ 0.12 g are added to 20 ml ultrapure water to form mixture solution after 30 min stirring. The final solution and the pretreated CC are sealed in a 30-ml Teflon-lined stainless-steel high-pressure reactor and maintained at 120°C for 5 h. Then, the product is naturally cooled to room temperature. The product is taken from the reactor and washed for three times with ultrapure water and ethanol successively. Dried under 60°C for 2 h.

Preparation of FeCoNiS-FeO_x Nanowire

First, 0.035 g sodium sulfide is added to 20 ml ultrapure water with stirring. The formed solution and the

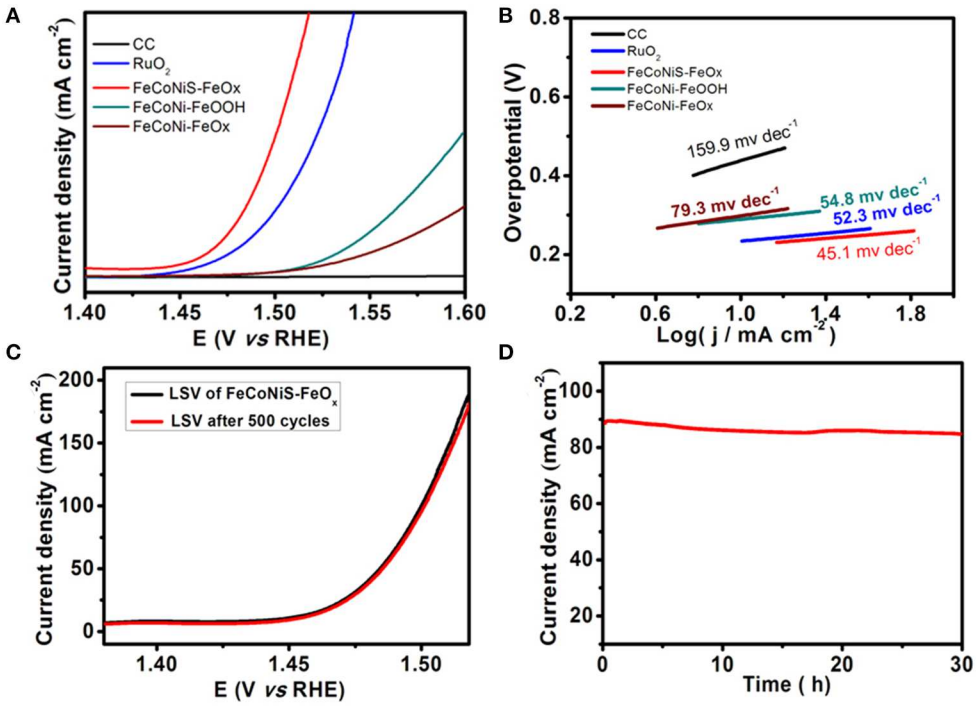

FIGURE 5 | (A) Linear sweep voltammetry (LSV) curves of different oxygen evolution reaction (OER) catalysts. **(B)** Tafel curves of different OER catalysts. **(C)** LSV curve of FeCoNiS-FeO_x catalyst and another curve after 500 CV cycles. **(D)** Time-dependent current density curve of FeCoNiS-FeO_x OER catalyst under constant potential.

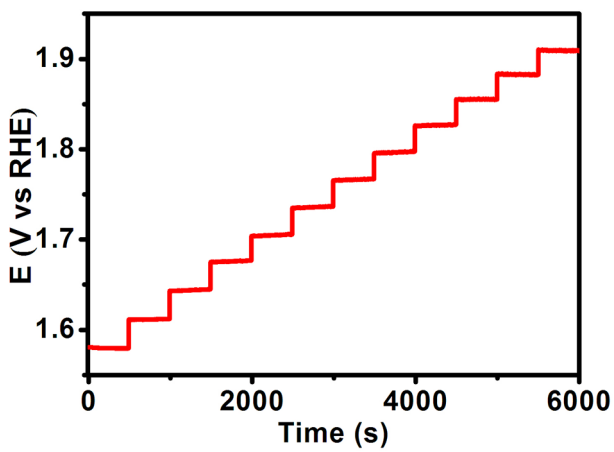

FIGURE 6 | Multistep chronopotentiometric of oxygen evolution reaction (OER) catalyst. The current density started at 60 mA cm^{-2} and finished at 280 mA cm^{-2}, with an increment of 20 mA cm^{-2} per 500 s without ohmic potential drop (IR) correction.

precursor are sealed in a 30-ml Teflon-lined stainless-steel high-pressure reactor and maintain at 120°C for 3 h. After naturally cooling to room temperature, the product is washed with ultrapure water and ethanol successively. At last, the product is dried for 2 h under 60°C.

Characterizations

A diffractometer (RigakuD/MAX 2550, Cu Kα radiation, λ = 1.5418 Å) is used to perform XRD characterization. The scan range is from 5 to 80° with a scanning rate of 5°/min. SEM characterizations are realized on a MERLIN compact SEM with the accelerating voltage of 20 kV. TEM characterizations are realized on TEM of Zeiss Libra 200FE with operation voltage of 200 kV. An ESCALABMK II X-ray photoelectron spectrometer is used to measure XPS spectrum with Mg as the exciting source.

Electrochemical Measurements

A CHI 660E electrochemical analyzer (CH Instruments, Inc., Shanghai) is used to perform all the electrochemical tests. In order to better characterize the electrode reaction, a three-electrode system is adopted. The catalysts/CC is used as working electrode. Mercuric oxide electrode (Hg-HgO) is as contrast electrode. Graphite rod is as auxiliary electrode. Potassium hydroxide solution (1.0 M) is used as the working electrolyte solution. All experiments are realized at 25°C. All potentials for LSV curves are calibrated on reversible hydrogen electrode (RHE) scale [E (RHE) = E + 0.059 × 14 + 0.098]. Unless stated otherwise, all LSV potentials are calibrated with ohmic potential drop (IR) due to solution resistance. Overpotentials (ΔE) are calculated based on the equation ΔE = E (RHE) - IR - 1.23.

DATA AVAILABILITY STATEMENT

All datasets generated for this study are included in the article.

AUTHOR CONTRIBUTIONS

WT has done the experimental work. MH, ZS, and WY helped in characterization. XZ has written the manuscript. CD and SZ have revised the manuscript.

FUNDING

This work was supported by the Natural Science Foundation of Shandong Province (ZR2014BL025).

REFERENCES

Biesinger, M. C., Payne, B. P., Grosvenor, A. P., Lau, L. W. M., Gerson, A. R., and Smart, R. S. C. (2011). Resolving surface chemical states in XPS analysis of first row transition metals, oxides and hydroxides: Cr, Mn, Fe, Co and Ni. *Appl. Surface Sci.* 257, 2717–2730. doi: 10.1016/j.apsusc.2010.10.051

Chai, Y.-M., Shang, X., Liu, Z.-Z., Dong, B., Han, G.-Q., Gao, W.-K., et al. (2018). Ripple-like NiFeCo sulfides on nickel foam derived from *in-situ* sulfurization of precursor oxides as efficient anodes for water oxidation. *Appl. Surface Sci.* 428, 370–376. doi: 10.1016/j.apsusc.2017.09.122

Chemelewski, W. D., Lee, H. C., Lin, J. F., Bard, A. J., and Mullins, C. B. (2014). Amorphous FeOOH oxygen evolution reaction catalyst for photoelectrochemical water splitting. *J. Am. Chem. Soc.* 136, 2843–2850. doi: 10.1021/ja411835a

Cheng, N., Liu, Q., Asiri, A. M., Xing, W., and Sun, X. (2015). A Fe-doped Ni_3S_2particle film as a high-efficiency robust oxygen evolution electrode with very high current density. *J. Mater. Chem. A* 3, 23207–23212. doi: 10.1039/c5ta06788j

Chow, J., Kopp, R. J., and Portney, P. R. (2003). Energy resources and global development. *Science* 302, 1528–1531. doi: 10.1126/science.1091939

Dresselhaus, M. S., and Thomas, I. L. (2001). Alternative energy technologies. *Nature* 414, 332–337. doi: 10.1038/35104599

Feng, J. X., Xu, H., Dong, Y. T., Ye, S. H., Tong, Y. X., and Li, G. R. (2016a). FeOOH/Co/FeOOH hybrid nanotube arrays as high-performance electrocatalysts for the oxygen evolution reaction. *Angew. Chem. Int. Ed Engl.* 55, 3694–3698. doi: 10.1002/anie.201511447

Feng, J. X., Ye, S. H., Xu, H., Tong, Y. X., and Li, G. R. (2016b). Design and synthesis of FeOOH/CeO_2 heterolayered nanotube electrocatalysts for the oxygen evolution reaction. *Adv. Mater.* 28, 4698–4703. doi: 10.1002/adma.201600054

Gao, Z., Chen, C., Chang, J., Chen, L., Wang, P., Wu, D., et al. (2018). Porous Co_3S_4@Ni_3S_4 heterostructure arrays electrode with vertical electrons and ions channels for efficient hybrid supercapacitor. *Chem. Eng. J.* 343, 572–582. doi: 10.1016/j.cej.2018.03.042

Guo, X., Kong, R.-M., Zhang, X., Du, H., and Qu, F. (2017). $Ni(OH)_2$ nanoparticles embedded in conductive microrod array: an efficient and durable electrocatalyst for alkaline oxygen evolution reaction. *ACS Catal.* 8, 651–655. doi: 10.1021/acscatal.7b03406

Hu, Q., Ma, W., Liang, G., Nan, H., Zheng, X., and Zhang, X. (2015). Anion-exchange reaction synthesized $CoNi_2S_4$ nanowires for superior electrochemical performances. *RSC Adv.* 5, 84974–84979. doi: 10.1039/c5ra18625k

Jin, Y., Huang, S., Yue, X., Du, H., and Shen, P. K. (2018). Mo- and Fe-Modified $Ni(OH)_2$/NiOOH nanosheets as highly active and stable electrocatalysts for oxygen evolution reaction. *ACS Catal.* 8, 2359–2363. doi: 10.1021/acscatal.7b04226

Ke, Z., Wang, H., He, D., Song, X., Tang, C., Liu, J., et al. (2018). Co_2P nanoparticles wrapped in amorphous porous carbon as an efficient and stable catalyst for water oxidation. *Front. Chem.* 6:580. doi: 10.3389/fchem.2018.00580

Kuang, M., Wang, Q., Ge, H., Han, P., Gu, Z., Al-Enizi, A. M., et al. (2017). $CuCoO^x$/FeOOH Core–shell nanowires as an efficient bifunctional oxygen evolution and reduction catalyst. *ACS Energy Lett.* 2, 2498–2505. doi: 10.1021/acsenergylett.7b00835

Lee, Y., Suntivich, J., May, K. J., Perry, E. E., and Shao-Horn, Y. (2012). Synthesis and activities of rutile IrO_2 and RuO_2 nanoparticles for oxygen evolution in acid and alkaline solutions. *J. Phys. Chem. Lett.* 3, 399–404. doi: 10.1021/jz2016507

Li, F., Du, J., Li, X., Shen, J., Wang, Y., Zhu, Y., et al. (2018). Integration of FeOOH and Zeolitic imidazolate framework-derived nanoporous carbon as an efficient electrocatalyst for water oxidation. *Adv. Energy Mater.* 8:1702598. doi: 10.1002/aenm.201702598

Li, H., Chen, S., Zhang, Y., Zhang, Q., Jia, X., Zhang, Q., et al. (2018). Systematic design of superaerophobic nanotube-array electrode comprised of transition-metal sulfides for overall water splitting. *Nat. Commun.* 9:2452. doi: 10.1038/s41467-018-04888-0

Liu, D., Lu, Q., Luo, Y., Sun, X., and Asiri, A. M. (2015). NiCo2S4 nanowires array as an efficient bifunctional electrocatalyst for full water splitting with superior activity. *Nanoscale* 7, 15122–15126. doi: 10.1039/c5nr04064g

Liu, T., Sun, X., Asiri, A. M., and He, Y. (2016). One-step electrodeposition of Ni–Co–S nanosheets film as a bifunctional electrocatalyst for efficient water splitting. *Int. J. Hydr. Energy* 41, 7264–7269. doi: 10.1016/j.ijhydene.2016.03.111

Lu, W., Liu, T., Xie, L., Tang, C., Liu, D., Hao, S., et al. (2017). *In situ* derived CoB nanoarray: a high-efficiency and durable 3D bifunctional electrocatalyst for overall alkaline water splitting. *Small* 13:1700805. doi: 10.1002/smll.201700805

Lu, Z., Qian, L., Xu, W., Tian, Y., Jiang, M., Li, Y., et al. (2016). Dehydrated layered double hydroxides: Alcohothermal synthesis and oxygen evolution activity. *Nano Res.* 9, 3152–3161. doi: 10.1007/s12274-016-1197-4

Luo, W., Jiang, C., Li, Y., Shevlin, S. A., Han, X., Qiu, K., et al. (2017). Highly crystallized α-FeOOH for a stable and efficient oxygen evolution reaction. *J. Mater. Chem. A* 5, 2021–2028. doi: 10.1039/c6ta08719a

Ning, Y., Ma, D., Shen, Y., Wang, F., and Zhang, X. (2018). Constructing hierarchical mushroom-like bifunctional NiCo/$NiCo_2S_4$@NiCo/Ni foam electrocatalysts for efficient overall water splitting in alkaline media. *Electrochim. Acta* 265, 19–31. doi: 10.1016/j.electacta.2018.01.150

Park, G., Kim, Y. I., Kim, Y. H., Park, M., Jang, K. Y., Song, H., et al. (2017). Preparation and phase transition of FeOOH nanorods: strain effects on catalytic water oxidation. *Nanoscale* 9, 4751–4758. doi: 10.1039/c6nr09790a

Qin, Z., Chen, Y., Huang, Z., Su, J., Diao, Z., and Guo, L. (2016). Composition-dependent catalytic activities of noble-metal-free NiS/Ni_3S_4 for hydrogen evolution reaction. *J. Phys. Chem. C* 120, 14581–14589. doi: 10.1021/acs.jpcc.6b05230

Reier, T., Oezaslan, M., and Strasser, P. (2012). Electrocatalytic Oxygen Evolution Reaction, (OER). on Ru, Ir, and Pt catalysts: a comparative study of nanoparticles and bulk materials. *ACS Catal.* 2, 1765–1772. doi: 10.1021/cs3003098

Sivanantham, A., Ganesan, P., and Shanmugam, S. (2016). Hierarchical $NiCo_2S_4$nanowire arrays supported on ni foam: an efficient and durable bifunctional electrocatalyst for oxygen and hydrogen evolution reactions. *Adv. Funct. Mater.* 26:201600566. doi: 10.1002/adfm.201600566

Tang, Y., Zheng, S., Xue, H., and Pang, H. (2019). Regulation of the Ni(2+). Content in a Hierarchical Urchin-Like MOF for high-performance electrocatalytic oxygen evolution. *Front. Chem.* 7:411. doi: 10.3389/fchem.2019.00411

Turner, J. A. (2004). Sustainable hydrogen production. *Science* 305, 972–974. doi: 10.1126/science.1103197

Wang, H., Yang, J., Yang, L., Zhang, G., Liu, C., Tang, H., et al. (2018). FeCoNi sulphide-derived nanodots as electrocatalysts for efficient oxygen evolution reaction. *Funct. Mater. Lett.* 11:1850058. doi: 10.1142/s1793604718500583

Wang, X., Liu, C., Li, Q., Li, H., Xu, J., Chu, X., et al. (2018). 3D Heterogeneous Co_3O_4@Co_3S_4 Nanoarrays grown on Ni Foam as a binder-free electrode for lithium-ion batteries. *ChemElectroChem* 5, 309–315. doi: 10.1002/celc.201701050

Xiao, J., Wan, L., Yang, S., Xiao, F., and Wang, S. (2014). Design hierarchical electrodes with highly conductive $NiCo_2S_4$ nanotube arrays grown on carbon fiber paper for high-performance pseudocapacitors. *Nano Lett.* 14, 831–838. doi: 10.1021/nl404199v

Yang, L., Xie, L., Ren, X., Wang, Z., Liu, Z., Du, G., et al. (2017). Hierarchical $CuCo_2S_4$ nanoarrays for high-efficient and durable water oxidation electrocatalysis. *Chem. Commun.* 54, 78–81. doi: 10.1039/c7cc07259g

Yin, Q., Tan, J. M., Besson, C., Geletii, Y. V., Musaev, D. G., Kuznetsov, A. E., et al. (2010). A fast soluble carbon-free molecular water oxidation catalyst based on abundant metals. *Science* 328, 342–345. doi: 10.1126/science.1185372

Zeng, L., Ren, W., Zheng, J., Wu, A., and Cui, P. (2012). Synthesis of water-soluble FeOOH nanospindles and their performance for magnetic resonance imaging. *Appl. Surface Sci.* 258, 2570–2575. doi: 10.1016/j.apsusc.2011.10.093

Zhang, L., Zhang, R., Ge, R., Ren, X., Hao, S., Xie, F., et al. (2017). Facilitating active species generation by amorphous NiFe-Bi layer formation on NiFe-LDH nanoarray for efficient electrocatalytic oxygen evolution at alkaline pH. *Chem. A Eur. J.* 23, 11499–11503. doi: 10.1002/chem.201702745

Zhang, S., Sun, Y., Liao, F., Shen, Y., Shi, H., and Shao, M. (2018). Co_9S_8-CuS-FeS trimetal sulfides for excellent oxygen evolution reaction electrocatalysis. *Electrochim. Acta* 283, 1695–1701. doi: 10.1016/j.electacta.2018.07.133

Zhao, Q., Yang, J., Liu, M., Wang, R., Zhang, G., Wang, H., et al. (2018). Tuning electronic Push/Pull of Ni-based hydroxides to enhance hydrogen and oxygen evolution reactions for water splitting. *ACS Catal.* 8, 5621–5629. doi: 10.1021/acscatal.8b01567

Zheng, X., Song, X., Wang, X., Zhang, Z., Sun, Z., and Guo, Y. (2018a). Nickel–copper bimetal organic framework nanosheets as a highly efficient catalyst for oxygen evolution reaction in alkaline media. *N. J. Chem.* 42, 8346–8350. doi: 10.1039/c8nj01035h

Zheng, X., Zhang, J., Sun, Z., Zhang, Z., and Xi, D. (2018b). Fabrication of Amorphous Cu-Co-P Nanofilms on $CuCo_2O_4$ anoarrays by *in situ* electrochemical reduction for efficient hydrogen evolution in alkaline solution. *Eur. J. Inorg. Chem.* 2018, 3565–3569. doi: 10.1002/ejic.201800492

Zheng, Y., Jiao, Y., Zhu, Y., Cai, Q., Vasileff, A., Li, L. H., et al. (2017). Molecule-level g-C_3N_4 coordinated transition metals as a new class of electrocatalysts for oxygen electrode reactions. *J. Am. Chem. Soc.* 139, 3336–3339. doi: 10.1021/jacs.6b13100

Zheng, Y., Jiao, Y., Zhu, Y., Li, L. H., Han, Y., Chen, Y., et al. (2014). Hydrogen evolution by a metal-free electrocatalyst. *Nat. Commun.* 5:3783. doi: 10.1038/ncomms4783

Zhou, Q., Chen, Y., Zhao, G., Lin, Y., Yu, Z., Xu, X., et al. (2018). Active-site-enriched iron-doped Nickel/Cobalt hydroxide nanosheets for enhanced oxygen evolution reaction. *ACS Catalysis* 8, 5382–5390. doi: 10.1021/acscatal.8b01332

Conflict of Interest: The authors declare that the research was conducted in the absence of any commercial or financial relationships that could be construed as a potential conflict of interest.

frontiers in Chemistry

MINI REVIEW
published: 17 November 2020
doi: 10.3389/fchem.2020.565489

Black TiO_2 Synthesis by Chemical Reduction Methods for Photocatalysis Applications

Luminita Andronic and Alexandru Enesca*

Department of Product Design, Mechatronics and Environment, Transilvania University of Brasov, Brasov, Romania

Applications of TiO_2 nanomaterials in photocatalysis, batteries, supercapacitors and solar cells, have seen widespread development in recent decades. Nowadays, black TiO_2 have won attention due to enhancing the solar light absorption by the formation of oxygen vacancies and Ti^{3+} defects, to promote the separation of photo-generated charge carriers leading to the improvement of the photocatalytic performance in H_2 production and pollutants degradation. The enhanced photocatalytic activity of black TiO_2 is also due to a lattice disorder on the surface and the presence of oxygen vacancies, Ti^{3+} ions, Ti-OH and Ti-H groups. Enhancing the optical absorption characteristics of TiO_2 and change of energy level and band-gap of materials have been successfully demonstrated to improve their photocatalytic activities, especially for black TiO_2 nanoparticles, which promote visible light absorption. The current review focuses on the investigation of the chemical reduction synthetic route for black TiO_2 nanomaterials, and their proposed association with green applications such as photodegradation of organic pollutants and photocatalytic water splitting. The synthesis methods of black TiO_2 involves the changes from Ti^{4+} to Ti^{3+} state, into different strategies: (1) The use of highly active hydrogen species such as H_2, H_2/Ar or H_2/N_2 gases, and metal hydrides ($NaBH_4$, CaH_2), (2) the reduction by active metals such as aluminum, magnesium and zinc, and (3) organic molecules such as imidazole and ascorbic acid.

Keywords: black TiO2, chemical reduction, defect chemistry, photocatalysis, visible light irradiation

OPEN ACCESS

Edited by:
Khalid Z. Elwakeel,
Jeddah University, Saudi Arabia

Reviewed by:
Mohd Hafiz Dzarfan Othman,
University of Technology Malaysia, Malaysia
Moamen S. Refat,
Taif University, Saudi Arabia

****Correspondence:***
Luminita Andronic
andronic-luminita@unitbv.ro

Specialty section:
This article was submitted to Catalysis and Photocatalysis, a section of the journal Frontiers in Chemistry

Received: *25 May 2020*
Accepted: *24 September 2020*
Published: *17 November 2020*

Citation:
Andronic L and Enesca A (2020) Black TiO_2 Synthesis by Chemical Reduction Methods for Photocatalysis Applications. Front. Chem. 8:565489. doi: 10.3389/fchem.2020.565489

THEORETICAL CONSIDERATION OF BLACK TIO_2

Chen et al. first reported black TiO_2 with a narrowed band-gap of 1.5 eV to expand the full spectrum sunlight absorption and promote an increase in the photocatalytic activity, by introducing surface disorders in the TiO_2 (Chen et al., 2011). Hu et al. observed in 2012 a remarkable enhancement in the visible-light absorption and the photocatalysis of TiO_2 after hydrogen treatment, attributed to surface disorder and the formation of oxygen vacancies (Hu, 2012; Wang and Chou, 2016; Zhu et al., 2016).

In the past decade, a considerable effort has been committed to preparing black TiO_2 by introducing Ti^{3+} defects and oxygen vacancies into the titanium oxide lattice (Di Valentin et al., 2009; Su et al., 2014; Li et al., 2015; Tian et al., 2015; Xin et al., 2015). Oxygen vacancy and Ti^{3+} defects are more detectable in black TiO_2 compared with white TiO_2. Oxygen vacancies have been detected by a few techniques (Zhang and Park, 2017): electron paramagnetic resonance (EPR), electron spin resonance (ESR), and Raman spectroscopy. Ti^{3+} defects are not proved in white

TiO_2, but they are detected in black TiO_2 based on X-ray photoelectron spectroscopy (XPS), by EPR (Jedsukontorn et al., 2017) or ESR spectroscopy (Tian et al., 2015). The yellow TiO_2 synthesis at a low temperature had more oxygen vacancies and Ti^{3+} defects compared with white TiO_2, which decreases the band-gap from 3.1 to 2.9 eV (Bi et al., 2020).

The formation defects in titanium oxide are given below (Jayashree and Ashokkumar, 2018):

Oxygen vacancy (Kröger-Vink notation $V_O^{\cdot\cdot}$) formation at a low oxygen pressure

$$O_O \leftrightarrow V_O^{\cdot\cdot} + 2e' + 1/2O_2 \quad (1)$$

Titanium interstitials Ti^{3+} (Kröger-Vink notation $Ti_i^{\cdot\cdot\cdot}$):

$$2O_O + Ti_{Ti} \leftrightarrow Ti_i^{\cdot\cdot\cdot} + 3e' + O_2 \quad (2)$$

Cui et al. (2014) described the generation of the Ti^{3+} and oxygen vacancies, by the equation of the defect (equation 3). They observed that the number of oxygen vacancies is half of the Ti^{3+} sites (equation 3). The absorption increases with the density of Ti^{3+} or O vacancies, as the density of Ti^{3+} increases with the Al reduction in temperature.

$$2Ti_{Ti}^x + O_O^x \rightarrow 2Ti_{Ti}' + 1/2O_2 + V_O^{\cdot\cdot} \quad (3)$$

The colorful TiO_2 with better absorption properties and improved photocatalytic activities compared with white TiO_2 have been designed through (i) metal doping in which metal replaces Ti^{4+} ions in the TiO_2 lattice (Chen et al., 2015), (ii) non-metal doping to replace O^{2-} ions in the TiO_2 lattice (Hamilton et al., 2014), (iii) to replace partial Ti^{4+} and O_2 ions in the TiO_2 lattice. To replace Ti^{4+} in TiO_2 with any cation is more accessible than to substitute O^{2-} with anions (such as nitrogen, carbon, sulfur) due to the difference in the charge state and ionic radii (Lee et al., 2014).

The structural modifications in black titanium oxide, involving Ti^{3+} centers and oxygen vacancies, conduct significant changes in crystallinity, and optoelectronic as well as the surface properties, and the most marked effect is the color changing. Increasing the optical absorption properties and diminishing electron-hole recombination of TiO_2 are expected to be meaningful for excellent photoactivity.

The optical band gaps of white anatase and rutile TiO_2 are reported as 3.2 and 3.0 eV, respectively (Haider et al., 2019), that means TiO_2 can adsorb only the UV part of the solar spectrum. A significant reduction in the TiO_2 band-gap around 1.23 eV and optical absorption near 1,000 nm in the near-infrared region (Ullattil et al., 2018), has been reported by hydrogenation of anatase nanocrystals under pressure resulting in the black TiO_2 materials (Chen et al., 2011; Liu et al., 2013).

The color change of titanium oxide from gray, blue, brown or black color, reflects in turn the optical properties and structural changes (Yan et al., 2017). By exposure to visible light, a heterojunction type I (Isac et al., 2019) is formed between white TiO_2 and colored TiO_2, the band energy levels of colored TiO_2 are included in that of the white TiO_2, and both heterojunction semiconductors could be excited to produce electrons and holes (**Figure 1**).

The colored TiO_2 shows a light absorption around 2eV, by introducing oxygen vacancies ($V_O^{\cdot\cdot}$) and Ti^{3+} formation into TiO_2 lattice (Naldoni et al., 2019) or introducing disordered layers in the surface of crystalline TiO_2 (Song et al., 2017) enhanced solar light adsorption and served to prove their photocatalytic performance. The oxygen vacancy can significantly affect the electric and optical properties of the materials, by forming a donor level below the conduction band, located at 1.8eV below conduction band of titania as shown in **Figure 1**. The Ti^{3+} defect is responsible for changes in the electronic conductivity and optical properties. The Ti^{3+} and $V_O^{\cdot\cdot}$ defects can be created by the reduction of TiO_2, either electrochemically, or through gas annealing and exposure in a vacuum (Lee et al., 2014).

Hu emphasize the importance of the crystalline phase of titanium oxide in the synthesis of black TiO_2; the rutile phase is theoretically easier to obtain than anatase crystalline phase because the formation energy of an oxygen vacancy in the rutile surface (110) is lower (5.5eV) than in the anatase surface (001) (7.54 eV) (Hu, 2012). The most common phase of the black TiO_2 is rutile or anatase; the rutile phase is formed at a temperature below 500°C. The oxygen deficiency and amorphous surface of TiO_{2-x} were also reported by Tan et al. (2014). The photocatalytic behavior of TiO_2 was found to depend on the crystalline phase; the white TiO_2 anatase phase has been shown to have higher photocatalytic efficiency than rutile TiO_2. Contrary to the previous statement, black rutile TiO_2 has been reported to have the best photocatalytic performance.

The synthesis methods of black TiO_2 are significantly affected by the structural, morphological and optical properties; involving the changes from Ti^{4+} to Ti^{3+} state, into different strategies, (i) the use of highly active hydrogen species such as H_2, H_2/Ar or H_2/N_2 gases, and metal hydrides ($NaBH_4$, CaH_2), (ii) the reduction by active metals such aluminum, magnesium and zinc, (iii) organic molecules such as imidazole and ascorbic acid, have been confirmed to be capable of reducing white TiO_2 to black titania.

SYNTHESIS APPROACH OF BLACK TIO_2 BY CHEMICAL REDUCTION

The synthesis methods explored through hydrogenation, plasma, chemical reduction, electrochemical reduction, laser ablation in liquid, and oxidation approaches were available in the literature over the last decade for black TiO_2 photocatalytic materials (Rajaraman et al., 2020).

The synthesis route influences the physicochemical properties and photocatalytic performance of black TiO_2. A significant number of studies highlight the formation of black TiO_2 by hydrogen thermal treatment when the samples had surface and bulk defects comparing with plasma treatment under Ar (95%)/H_2 (5%) atmosphere where the bulk defects were revealed (Wang and Chou, 2016). The color of the samples turned brown at 400°C, while the samples turned black at 500°C. The white TiO_2 Degussa powder was unchanged under hydrogenation,

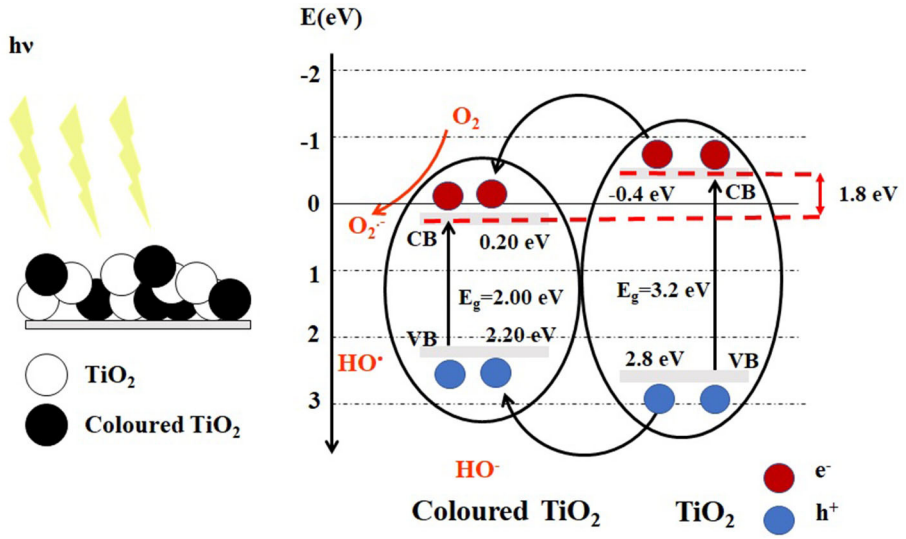

FIGURE 1 | The heterojunction between white TiO_2 and colored TiO_2.

emphasized the role of precursors and synthesis route (Leshuk et al., 2013).

The reduction strategy can be generally explained in Equation 4, where Red represents the reductant:

$$TiO_2 + Red \rightarrow TiO_{2-x} + RedO_x \tag{4}$$

The noble gas atmosphere has been considered as reductant due to defective TiO_{2-x} formation in argon, nitrogen atmosphere, and the disordered layer forms only if crystallization is performed in an oxygen-free environment (Tian et al., 2015).

$$TiO_2 \leftrightarrow TiO_{2-x} + x/2O_2 \tag{5}$$

The first synthesis of black titanium oxide consists of anatase nanoparticles through treating white TiO_2 nanoparticles (precursors, titanium tetra-isopropoxide, ethanol, hydrochloric acid, deionised water, and Pluronic F127 as an organic template) under a 20.0-bar H_2 atmosphere at about 200°C for 5 days (Chen et al., 2011).

$NaBH_4$ Reduction

By reducing hydrides, black titanium oxide can be obtained through three approaches: (i) physical mixing of white TiO_2 and hydride, followed by annealing in an inert atmosphere (Ar, N_2) at temperature of 300…400°C, (ii) hydrothermal synthesis (Ren et al., 2015) and (iii) sol-gel process (Fang et al., 2014).

The sodium borohydride ($NaBH_4$) is a commonly used reducing reagent (**Table 1**), due to its ability to reduce Ti^{4+} to Ti^{3+}, as in Equations (6) and (7), and to produce *in situ* active H_2 at room temperature, that reduces the white TiO_2 into black TiO_2 (Equation 8). During the $NaBH_4$ reduction process, boron oxide species are produced due to their insolubility in the ethanol, and it can be easily washed out by HCl solution to remove the surface impurities and expose the color centers on the surface of the catalyst, significantly increasing the visible light absorption. The degradation efficiency increases 9 times after washing with HCl solution (Fang et al., 2014).

$$NaBH_4 + 8OH^- \rightarrow NaBO_2 + 8e^- + 6H_2O \tag{6}$$

$$Ti^{4+} + e^- \rightarrow Ti^{3+} \tag{7}$$

$$BH_4^- + 2H_2O \rightarrow BO_2^- + 4H_2 \tag{8}$$

The rate of the generation of H_2 is higher in acidic conditions at experiments performed at 25°C with 20 g water per gram of sodium borohydride, and a wt. ratio accelerators/$NaBH_4$, around 1. The representative acidic materials that act as accelerators are tartaric acid, citric acid, succinic acid, oxalic acid (85…98% hydrogen liberated after 3 min), ammonium carbonate, maleic acid, aluminum sulfate, sodium diacid phosphate (90….80% of H_2 after 10 min), maleic anhydride, ammonium chloride, benzoic acid (80….65% of H_2 after 10 min). The catalytic effect of metals salt (cobalt, aluminum) was also demonstrated (Schlesinger et al., 1953).

The treatment of the TiO_2 nanotube in $NaBH_4$ for a short time (20–40 min) reduced the surface of TiO_2 into Ti^{3+}, and introduced an oxygen vacancy that creates localized states, producing a narrower band-gap of 2.46 eV, which extends its optical absorption to the visible region comparing with 3.09 eV for pristine TiO_2 nanotubes (**Table 1**) (Kang et al., 2013). The films show good stability and excellent reproducibility of the samples.

Tan et al. report a solid-state chemical reduction of TiO_2 at mild temperatures (300–350°C), for different times up to 1 h, an approach for large-scale production for visible light photocatalysis and solar-driven H_2 production (**Table 1**). The preparation of black TiO_2 followed the procedure: 4 g of TiO_2 Degussa P25 powder was mixed at room temperature with 1.5 g of $NaBH_4$ (98%) and heated in a tubular furnace under Ar

TABLE 1 | The chemical reduction synthesis methods, properties and photocatalytic applications of representative black TiO_2 materials.

Materials		Applications		References
Synthesis	**Characterization**	**Experimental**	**Photocatalysis efficiency**	
		$NaBH_4$ reduction		
TiO_2 sol-gel synthesis: Solution A: 5 mL tetrabutyl titanate and 25 mL EtOH. Solution B: 4 mL HNO_3 (0.6 M) and 5 mL EtOH *$NaBH_4$ reduction:* $NaBH_4$ add in the sol 0.025, 0.05, 0.1, 0.3 and 0.4 g	*Phase:* anatase, D= 9…35 nm *Band-gap energy:* 2.87 eV *BET surface area:* 18…27 m^2/g for black TiO_2 (priscine: 2 m^2/g)	Rhodamine B 10 mg/L Catalyst 1g/L *Light source:* 500 W tungsten halogen lamp, filter ($\lambda > 420$ nm), 300 W high-pressure Hg lamp, filter ($\lambda < 365$ nm)	*Degradation efficiency:* 100% after 5 h (sample 0.1-TiO_2). The degradation rate increase 9 time after washing with HCl.	Fang et al., 2014
TiO_2 synthesis: anodic oxidation of titanium foils, annealed *$NaBH_4$ reduction:* nanotube arrays were dipped in 0.1 M $NaBH_4$ for different times at room temperature	*Phase:* anatase, rutile and brookite *Morphology:* nanotube ∼7 mm, pore diameter ∼ 100 nm *Band gap energy:* 2.46 eV, (pristine 3.09 eV)	TiO_2 (working electrodes), Pt (counter-electrode), Ag/AgCl (reference electrode). *Light source:* 300 W Xe lamp, UV cut-off filter of 420 nm, light intensity 0.37 W cm^{-2}	*H_2 production rate:* 1.31% at 0.40 V_{RHE} after 40 min (pristine 0.32% at 0.48 V_{RHE})	Kang et al., 2013
TiO_2@TiO_{2-x} synthesis: 4.0 g of Degussa TiO_2 powder, 1.5 g of $NaBH_4$, heated to 300–400°C, Ar, 5–60 min, dark blue TiO_2 300°C/50 min	*Phase:* Anatase, rutile *Morphology:* core-shell *Band-gap energy:* 1.1…2.1 eV (priscine 3.1 eV) *BET surface area: 43…50* m^2/g for black TiO_2 (priscine: 45 m^2/g)	Methyl orange 20 ppm (V=50 mL, pH=1), Catalyst 1 g/L	*Degradation efficiency:* 90% after 10 min (Pristine 75%)	Tan et al., 2014
		Methanol (120 mL, 25%), Catalyst 50 mg/1 wt%Pt *Light source:* 300 W Xe lamp, UV cut-off filter of 400 nm	*H_2 production rate:* 6.5 $mmol{\cdot}h^{-1}{\cdot}g^{-1}$ (7.2 times better than pristine)	
TiO_2 synthesis: hydrothermal $TiCl_4$, ethylene glycol, heated at 150°C/6 h *Defective TiO_{2-x} synthesis:* dual-zone tube furnace, Ar, 500°C/1h, TiO_2:$NaBH_4$ mass ratio of 1 to 4	*Phase*: low crystallinity	Methanol (30 mL, 10%) Catalyst 0.03 g/0.03 wt% Rh *Light source:* 500 W mid-pressure Hg lamp and a 420 nm cut-off filter	*H_2 production rate:* 580 $mmol{\cdot}h^{-1}{\cdot}g^{-1}$	Xu et al., 2019
		Metal reduction		
Reduced TiO_{2-x} synthesis: Aluminum reduction into two zones tube furnace, $p < 0.5$ Pa, Al heated at 800°C, and TiO_2 heated at 300… 600°C, 6 h and 20 h Anneling: 500….900°C, 12h, Ar	*Phase:* anatase, rutile, highly crystalline *Morphology:* core-shell,∼25 nm in diameter *Band gap energy:* ∼3.2 eV similar to pristine *BET surface area: 42* m^2/g (priscine: 43 m^2/g)	Methyl orange 0.1 M (100 mL) Phenol 0.3 M Catalyst 1 g/L	*Degradation efficiecy:* 52% MO (4% pristine) after 6 h 78% Phenol (82% pristine) after 3.5	Wang et al., 2013
		Methanol 25% (120 mL) Catalyst (0.5 wt% Pt) 0.8 g/L *Light source:* UV irradiation: 300 W Hg lamp	*H_2 production rate:* H_2 6.4 mmol h^{-1} g^{-1} (8.5 times higher than that of pristine TiO_2 (0.75 mmol h^{-1} g^{-1})	
TiO_2 hallow sphere synthesis: 1 mmol tetrabutyl titanate, 0.5 g carbon spheres, stirred for 6 h, washed and dried at 90°C for 6 h. Annealing: 400–500°C, 4 h. *Black TiO_2*: Aluminum two-zones tube furnace, TiO_2 500°C zone, Al 800°C zone. Annealing: 6 h	*Phase:* high crystalline, D∼8 nm anatase, rutile (>500°C) *Morphology:* Hollow sphere *Band gap energy:* *BET surface area:* 168.8 m^2 g^{-1}	Methanol 10% (100 mL) Catalyst: 0.2 g/L *Light source:* 300 W Xe-lamp band-pass filter ($\lambda = 365$ nm)	*H_2 production rate:* 56.7 $mmol{\cdot}h^{-1}{\cdot}g^{-1}$, 2.5 times higher than pristine	Song et al., 2017
Reduced TiO_x ($x < 2$) nanoparticles (white, gray, blue, and black) were prepared by reducing P25 TiO_2 (400 mg) with Mg (60…400 mg). Annealing: 600°C, 4 h, Ar.	*Phase:* $TiO_{0.89}$, TiO_2 anatase TiO_2 rutile, D ≈24 nm (as pristine) *Morphology:* core-shell	*Light source:* solar-simulated light irradiance at an intensity of 1000 W m^{-2} (1 Sun).	*Solar thermal conversion efficiency*: Black TiO_x: 50%	Ye et al., 2017

(Continued)

TABLE 1 | Continued

Materials		Applications		References
Synthesis	**Characterization**	**Experimental**	**Photocatalysis efficiency**	
		Organic molecules reduction		
TiO_{2-x} hydrothermal synthesis: L-ascorbic acid (0, 0.3 g and 0.7 g), 70 mL DI water, 3.1 mL of $TiCl_3$, NaOH solution (1 mol/L) to pH=4. The mixture was transferred to a 100 mL Teflon-lined stainless steel autoclave and heated at 180°C for 12 h.	*Phase:* Anatase D=10…50 nm *Morphology:* core 10…50 nm *Band gap energy:* 1.0 eV *BET surface area: 64.56 (white), 188.75 (brown), 263.95 m^2 g^{-1} (black), respectively*	Methylene blue (MB) 20 mg/L (V=40 mL) Phenol 10 mg/L Photocatalyst 0.5 g/L *Light source:* 300 W Xenon lamp, UV cut-off filter (λ > 420 nm)	*Degradation efficiecy:* MB 90% (black TiO_{2-x}), 70% (brown TiO_{2-x}), 50% (white TiO_{2-x}), 5% (pristine), after 100 min Phenol 100% (black TiO_{2-x}), after 80 min	Wajid Shah et al., 2015

atmosphere, up to 300°C and held for 5–120 min. When the temperature increase to 350°C, the black titanium oxide was obtained in 60 min. The colored powders from light blue to black were washed with deionised water and ethanol several times to remove unreacted $NaBH_4$ and dried at 70°C (Tan et al., 2014).

Xu et al. obtained black TiO_2 powders in a dual-zone quart tube furnace using titanium oxide synthesized of $TiCl_4$ and ethylene glycol at 150°C for 6 h in a Teflon-lined stainless-steel autoclave with $NaBH_4$ as reductant agent (**Table 1**). The reduction was carried out in an argon atmosphere, between 200 and 500°C for 1 h. The presence of Ti^{3+} and oxygen vacancy defects significantly increased the intensity of the band absorption in the visible spectrum range (Xu et al., 2019).

Metal Reduction

In recent studies, active metals such as magnesium, lithium, aluminum and zinc were used for the synthesis of black TiO_2 with oxygen-deficient metal oxides (Zu et al., 2019).

Ou et al. developed a room-temperature lithium reduction strategy removing oxygen, and generating oxygen vacancies into the titanium dioxide nanoparticles lattice. Lithium metal with a high reductive capacity can reduce a significant number of metal oxides at room temperature (TiO_2, ZnO, SnO_2, CeO_2). TiO_2 Degussa P25 and lithium powders (0.....5% wt%) were mixed with a dispersant (dimethyl carbonate), then washed with diluted hydrochloric acid to remove lithium oxide, centrifugate and washing. The dried powders appear in different colors ranging from blue to black, and shift with the increase in lithium content (Ou et al., 2018).

The aluminum reduction of titanium oxide produces black TiO_2 in two ways: (i) reduction approach in an evacuated two-zone vacuum furnace, low temperature (300–600°C) for TiO_2 and high temperature (800°C) for aluminum and (ii) thermal treatment of a mixture of TiO_2 and aluminum powder (**Table 1**) (Wang et al., 2013). The black TiO_2 nanotube arrays have been used as a photoanode of photoelectrochemical cells for water-splitting, which was about 5 times higher than that of pristine (Cui et al., 2014).

Song et al. Herein prepared the black TiO_2 nanoparticles through subsequent Al reduction, with hollow nanosphere morphology, high crystallinity, small grain size (∼8 nm), and high surface area (168.8 $m^2 \cdot g^{-1}$) for photocatalytic hydrogen generation (56.7 mmol $h^{-1} \cdot g^{-1}$) 2.5 times higher than pristine TiO_2 nanostructures. The aluminum reaction was performed for 6 h in an evacuated two-zone furnace, pristine TiO_2 hollow nanospheres were placed in the low-temperature zone (400….600°C), and the aluminum powder was placed at 800°C (**Table 1**) (Song et al., 2017).

Sinhamahapatra et al. report in 2015 a magnesiothermic reduction under a 5% H_2/Ar atmosphere followed by acid treatment to synthesize reduced black TiO_2 nanoparticles with improved optical absorption in the visible and infrared region for enhanced photocatalytic hydrogen production in the methanol-water system in the presence of Pt as a co-catalyst (Sinhamahapatra et al., 2015).

Nanoparticles with different colors were synthesized by Ye et al. (2017) using Mg as a reductant (**Table 1**). Commercial P25 TiO_2 nanoparticles were mixed with Mg powder into wt. ratio 20:3, 10:3, 5:3, and 1:1, before being purged with argon for 15 min and calcined at 600°C under an Ar atmosphere for 4 h. The TiO_x (x<2) nanoparticles with different Ti/O ratios increased with the increasing addition of Mg in the reaction (Equation 9) and colors (turned gray, blue-gray, light black, and dark black, respectively). The nanoparticles are material for converting solar energy to the thermal energy for evaporation of water.

$$TiO_2 + (2 - x)\,Mg \rightarrow TiO_x + (2 - x)\,MgO \tag{9}$$

Organic Molecules Reductant

Seok et al. synthesis Ti^{3+} self-doped TiO_2 using the sol-gel route: 5 g of $TiOSO_4$, 250 ml distilled water, 1.5 g urea as a dispersant, NaOH was added (pH=7), and precursors annealed under an oxidative atmosphere at 350°C for 6 h in the presence of 2-methylimidazole and HCl when the Ti^{4+} was reduced to Ti^{3+} which resulted in lower internal resistance and improved electronic conductivity with application in Li-ion batteries as anode materials with a capacity retention of 88% at 50°C (Seok et al., 2016).

A facile hydrothermal approach, described in **Table 1**, has been developed by Wajid et al. to prepare defective TiO_{2-x} high surface nanocore using ascorbic acid as a reductant, established theoxygen vacancy concentration and tunable band-gap by setting the amount of ascorbic acid (Wajid Shah et al., 2015).

The synthesis methods of black TiO_2 changed the phase and crystallinity, morphology, band-gap and BET surface area, essential elements in photocatalysis as described in **Table 1**. The experimental conditions (pollutants and catalysts concentration, light irradiation and intensity) influence the pollutant degradation efficiency and H_2 production rate by photocatalysis (**Table 1**).

The synthesis techniques to obtain black TiO_2 and defective TiO_{2-x} follow four strategies: introducing surface disorders, Ti^{3+} defects, oxygen vacancies, Ti-OH and Ti-H groups to narrowing the band-gap for photo-related applications (Liu et al., 2017; Yan et al., 2017).

Chemical reduction is associated with a change in the oxidation state of Ti^{4+} with the formation of Ti^{3+} species responsible for the electronic conductivity, essential for many applications of TiO_2, especially photocatalysis (Di Valentin et al., 2009). The surface Ti^{3+} species are unstable and can be quickly oxidized by oxygen in air or water, developing a method to synthesize black TiO_2 materials that with improved visible-light photocatalytic activity is a challenge (Zheng et al., 2013).

A FUNDAMENTAL PROCESS IN PHOTOCATALYTIC ACTIVITY OF BLACK TIO_2

In the past years, black titanium oxide has attracted attention in different fields, such as photocatalytic pollutants degradation (Chen et al., 2011; Li et al., 2019; Plodinec et al., 2019), photocatalytic hydrogen production through water splitting (Wang et al., 2017; Pan et al., 2019), photocatalytic CO_2 reduction (Qingli et al., 2015; Zhao et al., 2016; Gao et al., 2020), solar–thermal material (Ye et al., 2017), supercapacitor (Zhi et al., 2016; Huang et al., 2018), photoanode in Dye-Sensitized Solar Cells (Ullattil et al., 2017), Lithium-ion batteries (Kim et al., 2017) (Yang et al., 2018), and medicine (Ni et al., 2017; Mazare et al., 2019).

The principle of the semiconductors photocatalysis consists of the following components: photon absorption, carriers separation, carrier diffusion simultaneously with carrier transport, catalytic efficiency and mass transfer of reactants and products (Takanabe, 2017).

Photon absorption: if the semiconductor has energy equal to or greater than E_g and consequent excitation of electrons (e^-) to the CB leaving positively charged vacancies, holes (h^+), in the VB (**Figure 1**)

Carriers separation: the heterojunction between nanoparticles can better band gap arrangement, to improve the separation of photo-generated charge carriers (**Figure 1**), which is advantageous of improving the photocatalytic performance. The oxygen vacancy defects and Ti^{3+} centers on the surface of TiO_2 favor the separation of charge carriers (electrons and holes) and can trap the hole.

Carrier diffusion simultaneously with carrier transport. The photo-generated electrons can initiate the reduction processes, including O_2 reduction to superoxides, H_2 generation, and CO_2 reduction to methane, methanol, or formaldehyde (Wen et al., 2015). The electron transfer is significant for the knowledge of the fundamental concepts of photocatalytic processes and to have an opinion about design and industrialization of the photocatalytic process (Mohamed and Bahnemann, 2012).

The transfer of electron/hole pairs to the interface initiates the redox reaction. The lifetime of the photo-generated charge carrier determines the efficiency of photocatalytic processes (Takanabe, 2017). Hence, increasing the efficiency of charge separation/transport in semiconductor nanoparticles is one of the major problems in photocatalysis to be addressed by the black TiO_2.

The presence of oxygen vacancies in TiO_2 can efficiently *extend the visible light absorption range of titania* because the localized oxygen vacancy states are located at 0.75 to 1.18 eV below the conduction band of TiO_2 (Asahi et al., 2001) (**Figure 1**). The hydroxyl radicals (HO•) can be formed when hydroxyl anions (HO^-), and adsorbed water trap the holes, which are capable of degrading the organic pollutants in wastewater.

SUMMARY AND OUTLOOK

The current review focuses on the investigation of the chemical reduction synthetic route for black TiO_2 nanomaterials, and their applications related to the environmental application such as photodegradation of organic pollutants and photocatalytic water splitting.

Since 1972, when Fujishima and Honda (Fujishima and Honda, 1972) reported about the water-splitting process using a TiO_2 electrode under UV irradiation, photocatalysis has attracted attention. The solar-driven applications of TiO_2 have been limited due to its band-gap (around 3.2 eV). A remarkable step in solar-driven photocatalysis was presented in 2011 by Chen and co-authors when black TiO_2 enhanced the photocatalytic activity of TiO_2. In the last years, many studies have focused on the synthesis and explanation of different properties of black-TiO_2 to improve the activity of the photocatalyst under visible irradiation. An important drawback is the synthesis requirements such as long annealing treatments (a few days), and the high pressure of hydrogen atmosphere, up to 20 bar.

The colored TiO_2 can turn from white to yellow, blue, brown or black, due to the change in optical properties (modification of its band-gap), and defects in the surface layers that enhanced solar light adsorption and photocatalytic reactions. Among the colored forms, black TiO_2 has been one of the most investigated because it can get excellent optical, chemical and electronic properties due to at least one of these characteristics: the presence of Ti^{3+} ions, oxygen vacancies undetectable in white TiO_2 and usually present in black TiO_2, structural disorder/defects in the surface, Ti-OH groups, Ti-H groups, and modifications of the valence band edge. The colored TiO_2 has rich oxygen vacancies and Ti^{3+} defects, which conduct to better conductivity for electron transfer, increased visible absorption and higher conduction band

potential. The oxygen vacancies and Ti^{3+} defects can act as traps for reducing the recombination of e^-/h^+ pairs and enhancing the photocatalytic activity.

The chemical reduction methods include the reduction of TiO_2 with active hydrogen species such as H_2, H_2/Ar or H_2/N_2 gases, using high temperatures with active metals such aluminum, magnesium and zinc powders, or the reduction of TiO_2 in solution with $NaBH_4$ and organic molecules such as imidazole and ascorbic acid can effectively lead to the color change of TiO_2 into black color. The color change of TiO_2 depends on the synthesis conditions, such as pressure, temperature, time, and the reducing agent, featuring different structural (lattice changes or disordering), chemical (formation of Ti^{3+}, oxygen vacancies, Ti-H, Ti-OH), physical properties (such as optical properties), and photocatalytic activities in both hydrogen generation and organic pollutant removal. The thermal treatment changes the color of the samples between yellow at 300–350°C, brown at 400°C and black above 450°C, the crystal structure has no major changes due to hydrogenation.

Black titanium oxide is a versatile photocatalyst with an extended absorption spectrum into the vis light range of the solar spectrum. From both a material and a chemical reaction perspective, this may provide new opportunities in efficiently utilizing the visible-light region of the spectrum to finally improve the efficiency of black TiO_2 nanomaterials for practical photocatalytic applications.

AUTHOR CONTRIBUTIONS

LA planned the content and wrote the manuscript. AE contributed to the photocatalysis chapter. All authors contributed to the article and approved the submitted version.

FUNDING

This work was supported by a grant of the Romanian National Authority for Scientific Research and Innovation, CCCDI-UEFISCDI, Project number 114/2019 ERANET-M.-TESTIMONIES, within PNCDI III.

REFERENCES

Asahi, R., Morikawa, T., Ohwaki, T., Aoki, K., and Taga, Y. (2001). Visible-light photocatalysis in nitrogen-doped titanium oxides. *Science* 293, 269–271. doi: 10.1126/science.1061051

Bi, X., Du, G., Sun, D., Zhang, M., Yu, Y., Su, Q., et al. (2020). Room-temperature synthesis of yellow TiO_2 nanoparticles with enhanced photocatalytic properties. *Appl. Surf. Sci.* 511:145617. doi: 10.1016/j.apsusc.2020.145617

Chen, X., Liu, L., and Huang, F. (2015). Black titanium dioxide (TiO_2) nanomaterials. *Chem. Soc. Rev.* 44, 1861–1885 doi: 10.1039/C4CS00330F

Chen, X., Liu, L., Yu, P. Y., and Mao, S. S. (2011). Increasing solar absorption for photocatalysis with black hydrogenated titanium dioxide nanocrystals. *Science* 331, 746–750. doi: 10.1126/science.1200448

Cui, H., Zhao, W., Yang, C., Yin, H., Lin, T., Shan, Y., et al. (2014). Black TiO_2 nanotube arrays for high-efficiency photoelectrochemical water-splitting. *J. Mater. Chem. A* 2, 8612–8616. doi: 10.1039/C4TA00176A

Di Valentin, C., Pacchioni, G., and Selloni, A. (2009). Reduced and n-type doped TiO_2: nature of Ti^{3+} species. *J. Phy. Chem. C* 113, 20543–20552. doi: 10.1021/jp9061797

Fang, W., Xing, M., and Zhang, J. (2014). A new approach to prepare Ti^{3+} self-doped TiO_2 via $NaBH_4$ reduction and hydrochloric acid treatment. *Appl. Catal. B Environ.* 160–161, 240–246. doi: 10.1016/j.apcatb.2014.05.031

Fujishima, A., and Honda, K. (1972). Electrochemical photolysis of water at a semiconductor electrode. *Nature* 238, 37–38. doi: 10.1038/238037a0

Gao, J., Shen, Q., Guan, R., Xue, J., Liu, X., Jia, H., et al. (2020). Oxygen vacancy self-doped black TiO_2 nanotube arrays by aluminothermic reduction for photocatalytic CO_2 reduction under visible light illumination. *J. CO2 Util.* 35, 205–215. doi: 10.1016/j.jcou.2019.09.016

Haider, A. J., Jameel, Z. N., and Al-Hussaini, I. H. M. (2019). Review on: titanium dioxide applications. *Enrgy. Proced.* 157, 17–29. doi: 10.1016/j.egypro.2018.11.159

Hamilton, J. W. J., Byrne, J. A., Dunlop, P. S. M., Dionysiou, D. D., Pelaez, M., O'Shea, K., et al. (2014). Evaluating the mechanism of visible light activity for N,F-TiO_2 using photoelectrochemistry. *J. Phys. Chem. C* 118, 12206–12215. doi: 10.1021/jp4120964

Hu, Y. H. (2012). A highly efficient photocatalyst-hydrogenated black TiO_2 for the photocatalytic splitting of water. *Angew. Chem. Int. Ed.* 51, 12410–12412. doi: 10.1002/anie.201206375

Huang, C. H., Meen, T. H., Ji, L. W., Chao, S. M., Wu, T. L., Tsai, J. K., et al. (2018). Effects of TiO_2 nanoparticle doping in coconut-shell carbon on the properties of supercapacitor. *Sens. Mater.* 30, 645–653. doi: 10.18494/SAM.2018.1769

Isac, L., Cazan, C., Enesca, A., and Andronic, L. (2019). Copper sulfide based heterojunctions as photocatalysts for dyes photodegradation. *Front. Chem.* 7:694. doi: 10.3389/fchem.2019.00694

Jayashree, S., and Ashokkumar, M. (2018). Switchable intrinsic defect chemistry of titania for catalytic applications. *Catalysts* 8, 1–26. doi: 10.3390/catal8120601

Jedsukontorn, T., Ueno, T., Saito, N., and Hunsom, M. (2017). Facile preparation of defective black TiO_2 through the solution plasma process: effect of parametric changes for plasma discharge on its structural and optical properties. *J. Alloys Compd.* 726, 567–577. doi: 10.1016/j.jallcom.2017.08.028

Kang, Q., Cao, J., Zhang, Y., Liu, L., Xu, H., and Ye, J. (2013). Reduced TiO_2 nanotube arrays for photoelectrochemical water splitting. *J. Mater. Chem. A* 1, 5766–5774. doi: 10.1039/c3ta10689f

Kim, D. S., Chung, D. J., Bae, J., Jeong, G., and Kim, H. (2017). Surface engineering of graphite anode material with black TiO_{2-x} for fast chargeable lithium ion battery. *Electrochim. Acta* 258, 336–342. doi: 10.1016/j.electacta.2017.11.056

Lee, K., Mazare, A., and Schmuki, P. (2014). One-dimensional titanium dioxide nanomaterials: nanotubes. *Chem. Rev.* 114, 9385–9454. doi: 10.1021/cr500061m

Leshuk, T., Linley, S., and Gu, F. (2013). Hydrogenation processing of TiO_2 nanoparticles. *Can. J. Chem. Eng.* 91, 799–807. doi: 10.1002/cjce.21745

Li, G., Lian, Z., Li, X., Xu, Y., Wang, W., Zhang, D., et al. (2015). Ionothermal synthesis of black Ti^{3+}-doped single-crystal TiO_2 as an active photocatalyst for pollutant degradation and H_2 generation. *J. Mater. Chem. A* 3, 3748–3756 doi: 10.1039/C4TA02873B

Li, Z., Bian, H., Xiao, X., Shen, J., Zhao, C., Lu, J., et al. (2019). Defective black TiO_2 nanotube arrays for enhanced photocatalytic and photoelectrochemical applications. *ACS Appl. Nano Mater.* 2, 7372–7378. doi: 10.1021/acsanm.9b01878

Liu, L., Yu, P. Y., Chen, X., Mao, S. S., and Shen, D. Z. (2013). Hydrogenation and disorder in engineered black TiO_2. *Phys. Rev. Lett.* 111:065505. doi: 10.1103/PhysRevLett.111.065505

Liu, Y., Tian, L., Tan, X., Li, X., and Chen, X. (2017). Synthesis, properties, and applications of black titanium dioxide nanomaterials. *Sci. Bull.* 62, 431–441. doi: 10.1016/j.scib.2017.01.034

Mazare, A., Park, J., Simons, S., Mohajernia, S., Hwang, I., Yoo, J. E., et al. (2019). Black TiO_2 nanotubes: efficient electrodes for triggering electric field-induced stimulation of stem cell growth. *Acta Biomater.* 97, 681–688. doi: 10.1016/j.actbio.2019.08.021

Mohamed, H. H., and Bahnemann, D. W. (2012). The role of electron transfer in photocatalysis: fact and fictions. *Appl. Catal. B* 128, 91–104. doi: 10.1016/j.apcatb.2012.05.045

Naldoni, A., Altomare, M., Zoppellaro, G., Liu, N., Kment, Š., Zboril, R., et al. (2019). Photocatalysis with reduced TiO_2: from black TiO_2 to cocatalyst-free hydrogen production. *ACS Catal.* 9, 345–364. doi: 10.1021/acscatal.8b04068

Ni, W., Li, M., Cui, J., Xing, Z., Li, Z., Wu, X., et al. (2017). 808 nm light triggered black TiO_2 nanoparticles for killing of bladder cancer cells. *Mater. Sci. Eng. C* 81, 252–260. doi: 10.1016/j.msec.2017.08.020

Ou, G., Xu, Y., Wen, B., Lin, R., Ge, B., Tang, Y., et al. (2018). Tuning defects in oxides at room temperature by lithium reduction. *Nat. Commun.* 9:1302. doi: 10.1038/s41467-018-03765-0

Pan, J., Dong, Z., Wang, B., Jiang, Z., Zhao, C., Wang, J., et al. (2019). The enhancement of photocatalytic hydrogen production via Ti^{3+} self-doping black TiO_2/g-C_3N_4 hollow core-shell nano-heterojunction. *Appl. Catal. B* 242, 92–99. doi: 10.1016/j.apcatb.2018.09.079

Plodinec, M., Grčić, I., Willinger, M. G., Hammud, A., Huang, X., PanŽić, I., et al. (2019). Black TiO_2 nanotube arrays decorated with Ag nanoparticles for enhanced visible-light photocatalytic oxidation of salicylic acid. *J. Alloys Compd.* 776, 883–896. doi: 10.1016/j.jallcom.2018.10.248

Qingli, W., Zhaoguo, Z., Xudong, C., Zhengfeng, H., Peimei, D., Yi, C., et al. (2015). Photoreduction of CO_2 using black TiO_2 films under solar light. *J. CO2 Util.* 12, 7–11. doi: 10.1016/j.jcou.2015.09.001

Rajaraman, T. S., Parikh, S. P., and Gandhi, V. G. (2020). Black TiO_2: a review of its properties and conflicting trends. *Chem. Eng. J.* 389:123918. doi: 10.1016/j.cej.2019.123918

Ren, R., Wen, Z., Cui, S., Hou, Y., Guo, X., and Chen, J. (2015). Controllable synthesis and tunable photocatalytic properties of Ti^{3+}-doped TiO_2. *Sci. Rep.* 5:10714. doi: 10.1038/srep10714

Schlesinger, H. I., Brown, H. C., Finholt, A. E., Gilbreath, J. R., Hoekstra, H. R., and Hyde, E. K. (1953). Sodium borohydride, its hydrolysis and its use as a reducing agent and in the generation of hydrogen. *J. Am. Chem. Soc.* 75, 215–219. doi: 10.1021/ja01097a057

Seok, D., Il, W.u, M., Shim, K. B., Kang, Y., and Jung, H. K. (2016). High-rate performance of Ti^{3+} self-doped TiO_2 prepared by imidazole reduction for Li-ion batteries. *Nanotechnology* 27, 1–5. doi: 10.1088/0957-4484/27/43/435401

Sinhamahapatra, A., Jeon, J. P., and Yu, J. S. (2015). A new approach to prepare highly active and stable black titania for visible light-assisted hydrogen production. *Energy Environ. Sci.* 8, 3539–3544. doi: 10.1039/C5EE02443A

Song, H., Li, C., Lou, Z., Ye, Z., and Zhu, L. (2017). Effective formation of oxygen vacancies in black TiO_2 nanostructures with efficient solar-driven water splitting. *ACS Sustain. Chem. Eng.* 5, 8982–8987. doi: 10.1021/acssuschemeng.7b01774

Su, J., Zou, X., and Chen, J. S. (2014). Self-modification of titanium dioxide materials by Ti^{3+} and/or oxygen vacancies: new insights into defect chemistry of metal oxides. *RSC Adv.* 4, 13979–13988. doi: 10.1039/C3RA47757F

Takanabe, K. (2017). Photocatalytic water splitting: quantitative approaches toward photocatalyst by design. *ACS Catal.* 7, 8006–8022. doi: 10.1021/acscatal.7b02662

Tan, H., Zhao, Z., Niu, M., Mao, C., Cao, D., Cheng, D., et al. (2014). A facile and versatile method for preparation of colored TiO_2 with enhanced solar-driven photocatalytic activity. *Nanoscale* 6, 10216–10223. doi: 10.1039/C4NR02677B

Tian, M., Mahjouri-Samani, M., Eres, G., Sachan, R., Yoon, M., Chisholm, M. F., et al. (2015). Structure and formation mechanism of black TiO_2 nanoparticles. *ACS Nano* 9, 10482–10488. doi: 10.1021/acsnano.5b04712

Ullattil, S. G., Narendranath, S. B., Pillai, S. C., and Periyat, P. (2018). Black TiO_2 nanomaterials: a review of recent advances. *Chem. Eng. J.* 343, 708–736. doi: 10.1016/j.cej.2018.01.069

Ullattil, S. G., Thelappurath, A. V., Tadka, S. N., Kavil, J., Vijayan, B. K., and Periyat, P. (2017). A sol-solvothermal processed 'Black TiO_2' as photoanode material in dye sensitized solar cells. *Sol. Energy* 155, 490–495. doi: 10.1016/j.solener.2017.06.059

Wajid Shah, M., Zhu, Y., Fan, X., Zhao, J., Li, Y., Asim, S., et al. (2015). Facile synthesis of defective TiO_{2-x} nanocrystals with high surface area and tailoring bandgap for visible-light photocatalysis. *Sci. Rep.* 5:15804. doi: 10.1038/srep15804

Wang, B., Shen, S., and Mao, S. S. (2017). Black TiO_2 for solar hydrogen conversion. *J. Materiomics* 3, 96–111. doi: 10.1016/j.jmat.2017.02.001

Wang, C. C., and Chou, P. H. (2016). Effects of various hydrogenated treatments on formation and photocatalytic activity of black TiO_2 nanowire arrays. *Nanotechnology* 27, 1–9. doi: 10.1088/0957-4484/27/32/325401

Wang, Z., Yang, C., Lin, T., Yin, H., Chen, P., Wan, D., et al. (2013). Visible-light photocatalytic, solar thermal and photoelectrochemical properties of aluminium-reduced black titania. *Energy Environ. Sci.* 6, 3007–3014. doi: 10.1039/c3ee41817k

Wen, J., Li, X., Liu, W., Fang, Y., Xie, J., and Xu, Y. (2015). Photocatalysis fundamentals and surface modification of TiO_2 nanomaterials. *Chinese J. Catal.* 36, 2049–2070. doi: 10.1016/S1872-2067(15)60999-8

Xin, X., Xu, T., Yin, J., Wang, L., and Wang, C. (2015). Management on the location and concentration of Ti^{3+} in anatase TiO_2 for defects-induced visible-light photocatalysis. *Appl. Catal. B* 176–177, 354–362. doi: 10.1016/j.apcatb.2015.04.016

Xu, J., Zhang, J., Cai, Z., Huang, H., Huang, T., Wang, P., et al. (2019). Facile and large-scale synthesis of defective black TiO_{2-x} (B) nanosheets for efficient visible-light-driven photocatalytic hydrogen evolution. *Catalysts* 9, 2–9. doi: 10.3390/catal9121048

Yan, X., Li, Y., and Xia, T. (2017). Black titanium dioxide nanomaterials in photocatalysis. *Int. J. Photoenergy* 2017:8529851. doi: 10.1155/2017/8529851

Yang, Y., Shi, W., Liao, S., Zhang, R., and Leng, S. (2018). Black defect-engineered TiO_2 nanocrystals fabricated through square-wave alternating voltage as high-performance anode materials for lithium-ion batteries. *J. Alloys Compd.* 746, 619–625. doi: 10.1016/j.jallcom.2018.02.309

Ye, M., Jia, J., Wu, Z., Qian, C., Chen, R., O'Brien, P. G., et al. (2017). Synthesis of black TiO_x nanoparticles by Mg reduction of TiO_2 nanocrystals and their application for solar water evaporation. *Adv. Energy Mater.* 7:1601811 doi: 10.1002/aenm.201601811

Zhang, K., and Park, J. H. (2017). Surface localisation of defects in black TiO_2: enhancing photoactivity or reactivity. *J. Phys. Chem. Lett.* 8 199–207 doi: 10.1021/acs.jpclett.6b02289

Zhao, J., Li, Y., Zhu, Y., Wang, Y., and Wang, C. (2016). Enhanced CO_2 photoreduction activity of black TiO_2-coated Cu nanoparticles under visible light irradiation: role of metallic Cu. *Appl. Catal. A Gen.* 510, 34–41. doi: 10.1016/j.apcata.2015.11.001

Zheng, Z., Huang, B., Meng, X., Wang, J., Wang, S., Lou, Z., et al. (2013). Metallic zinc- assisted synthesis of Ti^{3+} self-doped TiO_2 with tunable phase composition and visible-light photocatalytic activity. *Chem. Commun.* 49, 868–870. doi: 10.1039/C2CC37976G

Zhi, J., Yang, C., Lin, T., Cui, H., Wang, Z., Zhang, H., et al. (2016). Flexible all solid state supercapacitor with high energy density employing black titania nanoparticles as a conductive agent. *Nanoscale* 8, 4054–4062. doi: 10.1039/C5NR08136J

Zhu, G., Shan, Y., Lin, T., Zhao, W., Xu, J., Tian, Z., et al. (2016). Hydrogenated blue titania with high solar absorption and greatly improved photocatalysis. *Nanoscale* 8, 4705–4712. doi: 10.1039/C5NR07953E

Zu, D., Wang, H., Lin, S., Ou, G., Wei, H., Sun, S., et al. (2019). Oxygen-deficient metal oxides: synthesis routes and applications in energy and environment. *Nano Res.* 12, 2150–2163. doi: 10.1007/s12274-019-2377-9

Conflict of Interest: The authors declare that the research was conducted in the absence of any commercial or financial relationships that could be construed as a potential conflict of interest.

frontiers in Chemistry

MINI REVIEW
published: 30 November 2020
doi: 10.3389/fchem.2020.606044

A Mini Review on Yolk-Shell Structured Nanocatalysts

Xiaohuan Sun, Jie Han and Rong Guo*

School of Chemistry and Chemical Engineering, Yangzhou University, Yangzhou, China

Yolk-shell structured nanomaterials, possessing a hollow shell and interior core, are emerging as unique nanomaterials with applications ranging from material science, biology, and chemistry. In particular, the scaffold yolk-shell structure shows great promise as a nanocatalyst. Specifically, the hollow shell offers a confined space, which keeps the active yolk from aggregation and deactivation. The inner void ensures the pathway for mass transfer. Over the last few decades, many strategies have been developed to endow yolk-shell based nanomaterials with superior catalytic performance. This minireview describes synthetic methods for the preparation of various yolk-shell nanomaterials. It discusses strategies to improve the performance of yolk-shell catalysts with examples for engineering the shell, yolk, void, and related synergistic effects. Finally, it considers the challenges and prospects for yolk-shell nanocatalysts.

Keywords: yolk-shell, nanocatalyst, size selective, tandem catalysis, yolk-in-shell

OPEN ACCESS

Edited by:
Mario J. Muñoz-Batista, University of Granada, Spain

Reviewed by:
Alain Rafael Puente Santiago, The University of Texas at El Paso, United States
Guohong Wang, Hubei Normal University, China
Qin Li, South-Central University for Nationalities, China

****Correspondence:***
Jie Han
hanjie@yzu.edu.edu

Specialty section:
This article was submitted to Catalysis and Photocatalysis, a section of the journal Frontiers in Chemistry

Received: *14 September 2020*
Accepted: *05 November 2020*
Published: *30 November 2020*

Citation:
Sun X, Han J and Guo R (2020) A Mini Review on Yolk-Shell Structured Nanocatalysts. Front. Chem. 8:606044. doi: 10.3389/fchem.2020.606044

INTRODUCTION

Core-shell nanomaterials have received enormous attention owing to their unique structure related properties and the broad variety of ways in which they can be applied in energy storage (Xie et al., 2015; Lu et al., 2019), sensing (Gong et al., 2019), cancer therapy (Wang et al., 2018b; He et al., 2020), and in particular, catalysis (Gawande et al., 2015; Das et al., 2020; Salvatore et al., 2020). By tuning the intrinsic properties of the core or shell, a variety of nanocatalysts, with active centers that are properly shielded by permeable shells, are ready to be designed and fabricated (Murugesan et al., 2020; Wang et al., 2020). Noveron et al. originally developed a green and sustainable methodology with metal nanoparticles encapsulated in tea leaves (Ahsan et al., 2020a) or tissue papers (Ahsan et al., 2020b,c). After carbonization, core-shell nanocatalysts with excellent electrocatalytic performance were prepared. In comparison with the other nanocatalyst systems, such as metallic nanoparticles or surface coating hybrids, the creation of a core-shell nanostructure significantly improved instability by keeping the active center from coalescence (Zhang et al., 2013). Though the stability issue was greatly enhanced, the surface area of the catalytic core was largely blocked by the shell, therefore, there is still space for the development of nanocatalysts with superior performance.

The yolk-shell nanostructure, which as an exterior hollow shell and interior movable core, has received increasing attention since it was first reported (Yin et al., 2004). Compared with core-shell, yolk-shell has an extra void space with an excellent catalytic performance in several ways. Among these benefits, the yolk-shell scaffolds can provide a field of catalysis, with three major aspects that should be highlighted: (1) the total exposure of the active center inside the shell is to some degree balanced by the contradiction of catalytic efficiency and stability; (2) the presence of void largely expands the space for the occurrence of catalytic reaction and mass transfer; (3) the manipulation of shell, yolk, void, or a combination of these enables the flexible and dynamic modulation of the

catalytic efficiency, stability, recyclability or even synergistic effect induced multifunction. In this minireview, we briefly introduce synthetic methods for creating yolk-shell nanomaterials. We then discuss recent strategies for optimizing the catalytic performance of a yolk-shell nanocatalyst and explore the structure-property relationship.

METHODS FOR THE PREPARATION OF YOLK-SHELL NANOMATERIALS

Through the flexible manipulation of basic physiochemical principles, several methods have been developed to prepare yolk-shell nanomaterials. These include hard template, soft template, swelling and shrinkage, swelling and evaporation, ship-in-a-bottle, hydrothermal and solvothermal methods, among others, which can be categorized as the template-assisted and template-free methods (Li et al., 2019a). Taking advantage of alternative methods, yolk-shell nanomaterials with various features, which boosted the field of catalysis in different perspectives, were synthesized. In this section, we introduce the typical methods that allow the design, preparation, and modulation of the yolk-shell nanomaterials. By summarizing the pros and cons that each method owns, we anticipate providing an instructive guide for the desired preparation of yolk-shell nanocatalysts.

TEMPLATE-ASSISTED METHODS

Template-assisted methods are usually performed according to the mechanism of layer by layer assembly and, due to the simplicity of this synthetic strategy, are widely employed in the preparation of yolk-shell nanostructures (Liu et al., 2014). Among the versatile template-assisted methods that have been developed to date, the hard template method is one of the most commonly adopted approaches. Typically, the method primarily involves synthesizing core-shell structures with a sacrifice inner shell. After the removal of the sacrifice layer, hollow spheres with an interior core are obtained. Fan et al. (2018) developed the standard procedure of yolk-shell fabrication, taking advantage of this method (**Figure 1A**). In this example, pre-prepared AuNPs were capped by SiO_2 shells through the hydrolysis of tetraethyl orthosilicate (TEOS), resulting in Au@SiO_2. Subsequently, polymerization of dopamine occurred on the surface of the Au@SiO_2, after which Au@SiO_2@polydopamine was obtained. Then, the materials were carbonized to convert the polymer shell into a carbon sphere. In the end, the SiO_2 layer was etched with NaOH and Au@C yolk-shell structured nanomaterials were prepared. In this method, SiO_2 was employed as a sacrifice layer due to its low cost and the simplicity with which it can be removed. Carbon sphere (Zhang et al., 2015) and polymers (Joo et al., 2016) are also commonly used as a sacrifice layer. To avoid the preparation of an extra template shell, selectively etching of the shell (Liang et al., 2017) or core (Lee et al., 2008) of a core-shell nanostructure provided alternative ways to fabricate yolk-shells with a tailored interior cavity and a controllable size of the active core.

Although yolk-shell nanomaterials can be elaborately designed and synthesized, the hard template method exhibits several disadvantages, such as the tedious nature of the procedure, the harsh conditions for template etching, a necessity for surface functionalization, and the fact that it is also time-consuming (Fan et al., 2012; Guiet et al., 2015). To circumvent the above-mentioned problems, the soft template method was developed. In this method, a mixture of surfactants, which can easily form micelles or vesicles, were employed to encapsulate core materials. Then, with the replication of the morphology formed by the surfactant, a hollow sphere encapsulated with the desired core can be synthesized in a relatively simple way. Wu et al. have presented a method for preparing the yolk/silica materials, taking advantage of the soft template strategy (**Figure 1B**) (Wu and Xu, 2009). In their strategy, core materials were first dispersed in a mixed solution consisting of zwitterionic (lauryl sulfonate betaine, LSB) and anionic surfactant (sodium dodecyl benzenesulfonate, SDBS). Then, with the addition of 3-aminopropyltriethoxysilane (APS), the formation of vesicles with a movable core was promoted. Besides being a vesicle-inducing agent, APS can also interact with the surface of the vesicle through electrostatic attraction, acting as the costructure-directing agent. The hydrolysis of APS and TEOS led to the direct formation of a hollow SiO_2 shell along the surface of the vesicle. Interestingly, the shells formed were adaptive to the size and shape of the core through self-adjustment. The template can be easily removed by washing or calcination depending on the intrinsic nature of the shell, core, and template. This methodology provides a general principle for the relatively simple preparation of various yolk-shell nanomaterials. This method is particularly productive since, by repeating the soft template driven process, yolk-multishell nanomaterials can also be designed (Wu and Xu, 2010).

TEMPLATE-FREE METHODS

Even though template-assisted methods are a productive approach for the preparation of yolk-shells, their application is largely limited due to the multistep reaction and consumption of the template (Yu et al., 2019). Thus, template-free methods with a simpler procedure have stimulated intensive attention. Various strategies have been developed based on the above consideration and the related synthetic mechanisms were focused on an external trigger induced volume variation, Ostwald ripening, or Kirkendall effect.

A template-free method inspired by the cell plasmolysis phenomena in nature was developed for yolk-shell preparation by Yue et al. (**Figure 1C**) (Yue et al., 2017). The mechanism of this strategy lies in the fact that the low cross-linking resorcinol-formaldehyde resin with loose morphology can undergo volume swelling and shrinkage upon being soaked in or extracted from a specific organic solvent. The strategy developed by Yue et al. primarily synthesized Fe_3O_4 NPs

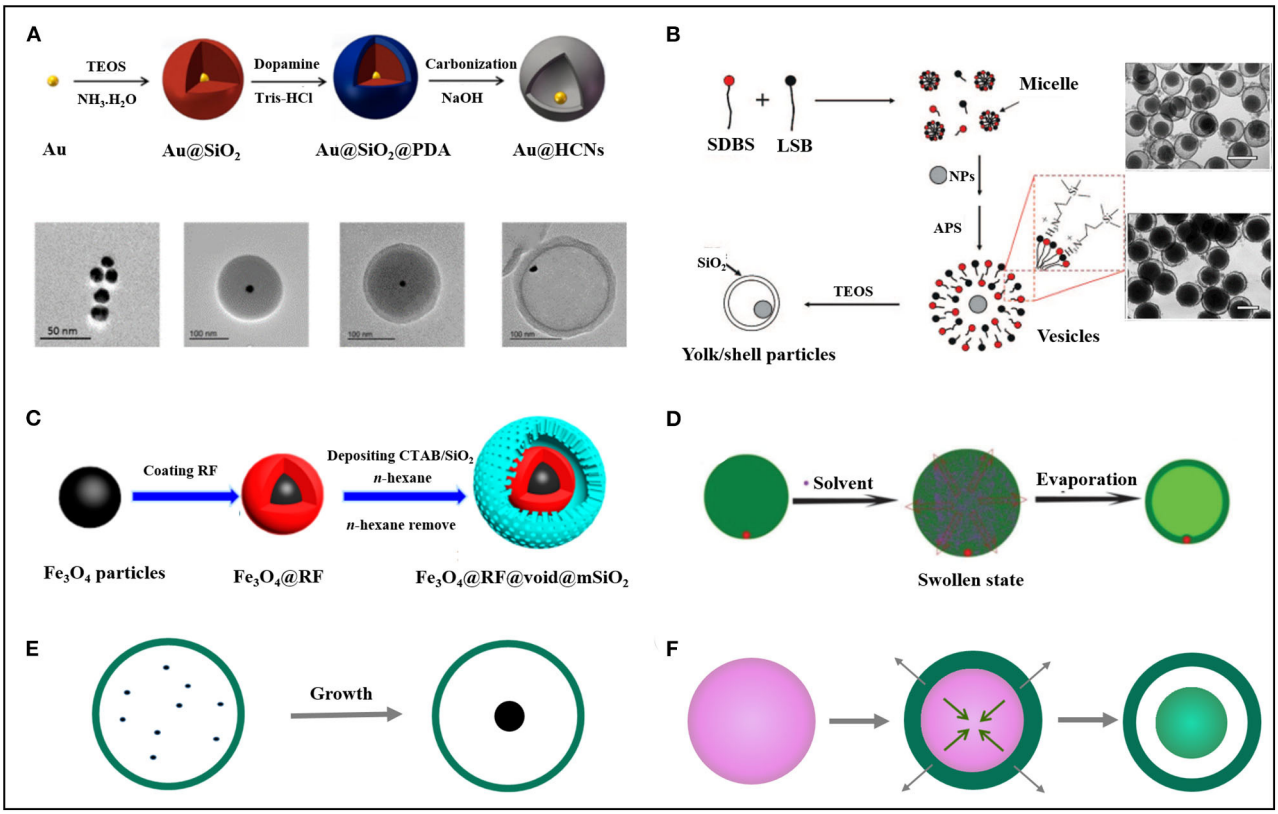

FIGURE 1 | Illustration of the methods for the preparation of yolk-shell nanomaterials. **(A)** Hard-template method. Reprinted with permission from Yin et al. (2004). Copyright 2018 American Chemical Society. **(B)** Soft-template method. Reprinted with permission from Lee et al. (2008). Copyright 2009 American Chemical Society. **(C)** Plasmolysis inspired method. Reprinted with permission from Wu and Xu (2009). Copyright 2017 American Chemical Society. **(D)** Swelling-evaporation method. Reprinted with permission from Yu et al. (2019). Copyright 2014 Royal Society of Chemistry. **(E)** Ship in a bottle method. **(F)** Hydrothermal/solvothermal method. TEOS, tetraethyl orthosilicate; SDBS, sodium dodecyl benzenesulfonate; LSB, lauryl sulfonate betaine; RF, resorcinol-formaldehyde; CTAB, cetyltrimethylammonium bromide.

coated with resorcinol-formaldehyde (RF). Then, an SiO_2 shell was deposited on the swollen surface of Fe_3O_4@RF in a mixed solvent of n-hexane/H_2O. After the extraction of the solvent by the above system, the Fe_3O_4@RF sphere shrank and spherical Fe_3O_4@RF@void@mSiO_2 yolk-shell nanostructures with uniform dispersion were obtained. It is worth noting that yolk-shell structures achieved in this way can reversibly transit between the compact core-shell and spacious yolk-shell by repeating the swelling and shrinkage process, which offer a unique flexibility of the as-prepared nanomaterial. Another example presented by Niu et al. also (Niu et al., 2019) demonstrated the feasibility of this principle. In their case, the yolk-shell nanostructures were fabricated via the modulation of the repulsive interaction between polystyrene-b-poly(acrylic acid) (PS-b-PAA) and CTAB by solvent extraction, which further directed their morphology transformation, leading to the cell plasmolysis like behavior induced yolk-shells formation.

Controllable tuning of the relative position between the exterior shell and interior yolk can modify the yolk-shell interaction. Meanwhile, the migration of the yolk close to the shell will enhance its contact probability with the external substrate, which represents a significant improvement in catalytic efficiency. Taking this into account, our group reported a yolk-in-shell synthetic strategy with the swelling-evaporation method (**Figure 1D**) (Han et al., 2007, 2014). In our method, asymmetric Au-poly(*o*-methoxyaniline) (POMA) core-shell was prepared with the proper modulation of the addition point of Au NP during the polymerization of *o*-methoxyaniline (OMA). After dispersing the Au@POMA core-shell into ethanol, the POMA shell underwent volume expansion due to the entering of the solvent. When ethanol was eventually evaporated, the polymer chain of POMA together with ethanol moved outward, enabling the transformation of the solid core-shell into a hollow sphere with a single AuNP embedded in the shell.

The starting point for the design and preparation of yolk-shell nanostructures is to create a confined microenvironment where the core material can maintain both its activity and stability. For the above mentioned synthetic methods, each displayed unique advantages, however, they all are limited by the fact that the core material has to be prepared in advance and, unavoidably, suffers from the harsh conditions during processing, such as high temperature and highly acidic or alkaline environments, which may have an adverse effect on the physiochemical properties of the core (Zhou et al., 2019). To address these problems, methods

known as "ship in a bottle" (Xiao et al., 2012) have attracted recent attention. This approach involves preparing hollow shells in advance and seeding initiators of the core through diffusion. With the addition of appropriate reduction agents, the core material can grow in the preexisting hollow shell, without the risk of being exposed to the harsh conditions that are employed during the template removal (**Figure 1E**) (Goebl and Yin, 2013).

In the "ship in a bottle" method, the yolk material successfully avoided the harsh conditions for template removal, however, this synthetic procedure is a complex way of preparing the hollow sphere. The hydrothermal and solvothermal methods offer a one pot synthetic approach. In this approach, the precursors were dissolved in hot water (hydrothermal method) or organic solvent (solvothermal method) under high pressure in autoclave. In these conditions, the precursors grow into yolk-shell morphology with the mechanism of Ostwald ripening or Kirkendall effect (**Figure 1F**) (Wang et al., 2018a,c). Besides the simplified procedure, the formation of homo yolk-shell is also an advantage provided by this method. However, this method is only suitable for the fabrication of metal or metal oxide based yolk-shell architectures (Li et al., 2019a).

STRATEGIES TO OPTIMIZE YOLK-SHELL MATERIAL AS NANOCATALYST

Yolk-shell structured nanomaterials, with a unique hollow shell and interior core, have gained increasing attention in the field of catalysis due to the dual or multiple combination of components, which induce synergistic effect that provide the possibility for high performance catalysis. For the initial study of the yolk-shell scaffold as a catalyst, the shell was designed as a protecting agent to prevent the active metal yolk from aggregation and deactivation. Yin et al. reported the preparation of Pt@CoO in 2004 and confirmed its activity in the ethylene hydrogenation reaction, which, to the best of our knowledge, is the first yolk-shell based nanocatalyst (Yin et al., 2004). Afterwards, alternative yolk-shell materials were elaborately designed by tuning the categories of yolk and shell components. Lee et al. fabricated the Au@SiO_2 yolk-shell nanomaterials, since Au is catalytically active and SiO_2 shell is mesoporous and can be easily deposited on the nanosurface (Lee et al., 2008). Catalytic investigations have shown that the Au@SiO_2 exhibits high efficiency toward the reduction of *p*-nitrophenol. Although modulation of the shell and active center significantly enhanced both the stability

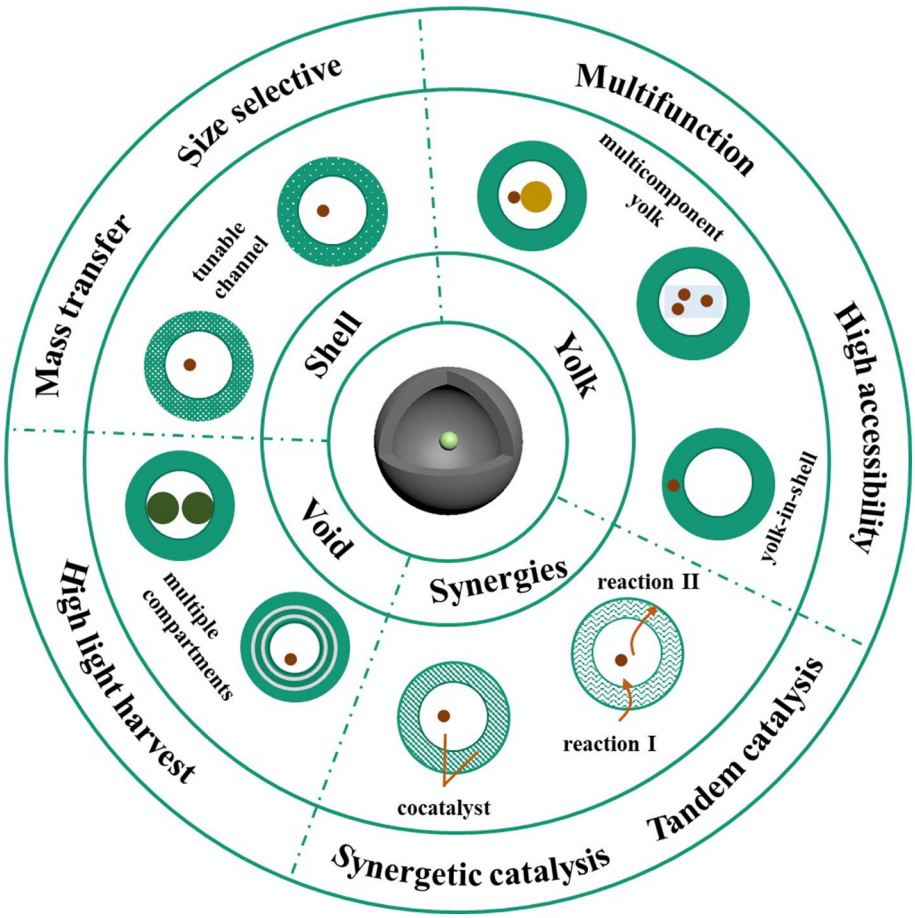

SCHEME 1 | Schematic illustration of the structure related optimization of yolk-shell nanomaterials in catalysis.

and efficiency of the as-prepared catalysts, the construction of superior catalysts is still challenging. In recent decades, novel methods have used flexible modulation of the shell, yolk, and void or a combination of them, to maximize catalytic efficiency. This section discusses the strategies employed to improve the performance of yolk-shell based materials as a robust catalyst (**Scheme 1**).

MODULATION OF SHELL

The shell layer of the yolk-shell catalyst plays an important role in the catalytic process. Even though the shell provides a physical barrier that keeps the active cores from aggregation, it also in some ways hinders the entering of the reactants into the existing products. Therefore, the appropriate modulation of the porosity of the shell can increase the contact probability between substrates and the active center. With a more elaborate design, the shells with specific pore range can offer the yolk-shell structured catalysts intrinsic selectivity (Hofer et al., 2018; Das et al., 2020). Jia et al. (2015) developed a method of preparing Au NPs, which are encapsulated in a hollow styrene shell, in which the size of the pores embedded is <0.8 nm. To investigate the size selective permeation of the yolk-shell, they studied the chemical transformation of benzaldehyde and its sterically crowded analog, 3, 5-di-tert-butyl benzaldehyde. The results showed that the conversion ratio for benzaldehyde is more than 70%, while the conversion ratio for 3, 5-di-tert-butyl benzaldehyde is <10%. Additionally, when cross-linked polymers were employed as the hollow shell, the pore size can be adjusted by solvents with various polarities due to the differential in swelling degree (Xu et al., 2019), which also leads to size selective catalysis.

MODULATION OF YOLK

The interior yolk of a yolk-shell nanostructure acts as an active center where the reagents can undergo a chemical transformation. In principle, looking for highly efficient catalysts and embedding them into a well-designed hollow shell could be a feasible way to improve the catalytic performance of yolk-shell nanomaterial. Meanwhile, in terms of addressing catalyst limitations, there are other promising approaches such as the design of dual or multiple functional yolks. Our group synthesized the yolk-shell with dumbbell-like Pt-Fe_3O_4 encapsulated in the N-doped carbon hollow nanospheres (Sun et al., 2019). With the investigation of the reduction of 4-nitrophenol and oxidation of β-ionone to the epoxide, the as-designed yolk-shell exhibits highly improved catalytic efficiency due to the presence of the heterojunction interface, which largely benefits electron transfer. Moreover, the catalyst can be easily recycled by exploiting the magnetic field thanks to the intrinsic magnetic property of Fe_3O_4. Further studies have shown that with six successive cycles, the catalyst maintained its catalytic performance, indicating the high stability of the yolk-shell based catalyst.

It is well known that catalysts with a smaller size exhibit superior performance. However, most conventional yolk-shells are composed of a single core with a relatively large diameter, to prevent unwanted aggregation. Chen et al. reported a facile method for the preparation of Co@C-N yolk-shell, featured with Co cores embedded in N-doped carbon (C-N) nanosheet and a porous C-N shell (Chen et al., 2018). In this novel scaffold, the nanosheet encapsulated inside the hollow shell can anchor multiple tiny Co NPs, playing an important role in the enhancement of the catalytic efficiency and simultaneously preventing the deactivation of the catalytic centers. Owing to the multi-core and porous shell characteristics, the hollow Co@C-N nanoreactors were highly efficient in the aerobic oxidation of alcohols in neat water under atmospheric pressure in air and base-free conditions. Moreover, due to the intrinsic magnetic nature of Co NPs, the Co@C-N catalyst can be easily recycled by a magnet without significant loss of catalytic activity.

Although the yolk-shell scaffolds already render the active yolk high accessibility to the substrates, catalytic efficiency is still limited due to the relatively large distance between the substrates and the catalytic center. Taking the abovementioned problem into consideration, a feasible way to improve the catalytic performance of the yolk-shell nanocatalyst is to migrate the movable interior yolk into the shell. With this in mind, our group fabricated the Au-POMA yolk-in-shell nanomaterials by elaborately modulating the addition time of AuNP to the polymerization mixture of OMA (Han et al., 2014). Catalytic experiments demonstrated that in the reduction reaction of 4-nitrophenol to 4-aminophenol, the catalytic efficiency of Au-POMA yolk-in-shell is two times higher than that of the Au-POMA core-shell. The comparison between yolk-shell and yolk-in-shell catalysts was also investigated (Hu et al., 2020). The Au@C yolk-shell and Au@C yolk-in-shell were prepared with a single Au nanoparticle located inside the hollow cavity and encapsulated in the shell, respectively. The Au@C yolk-in-shell revealed much higher catalytic efficiency toward the 4-NP catalytic reduction and β-ionone catalytic oxidation compared to the Au@C yolk-shell. Interestingly, the relationship between the thickness of the shell and size of Au NP has a significant effect on the catalytic performance of the Au@C yolk-in-shell. The above examples illustrate how both the decoration and migration of yolk material can endow the yolk-shell nanocatalysts with a better performance.

MODULATION OF VOID

The existence of a void in the unique structure of the yolk-shell material is vital and functions in several ways, such as by providing an isolated space for confined catalysis, offering a high surface to volume ratio, promoting the reflection and scattering of light, and enhancing light absorbance efficiency and therefore, improving photocatalytic performance (Ren and Yu, 2019; Xiao

et al., 2019). Considering the abovementioned feature of voids, the creation of multi-level voids has emerged as an efficient approach to optimizing the performance of yolk-shell catalysts. Liu et al. prepared a $ZnFe_2O4$ double shelled material with a facile solvothermal method (Liu et al., 2017). The shells were mesoporous and the double-shell $ZnFe_2O_4$ was confirmed to possess the surface area of 126.7 m^2 g^{-1}. Due to the high surface area and scattering enhancement induced strong absorption of visible light, the kinetic constant of double-shell $ZnFe_2O_4$ toward the photocatalytic degradation of gaseous *o*-DCB is 1.46 and 1.82 times as high as that of yolk-shelled spheres and solid spheres. Another typical example method of creating multi-level voids is reported by Wang et al. (2012), who prepared a unique ZnO hollow sphere with double-yolks. Compared with the double-shelled architecture, the nanomaterials with double yolk-shelled morphology provide three interior compartments, which may significantly enhance light reflection and scattering in light harvesting. This was confirmed by photocurrent measurements. The photocatalytic ability was investigated by examining the degradation of Rhodamine B. The highest activity was achieved by the double yolk-shelled ZnO, compared with the single yolk-shelled ZnO and single-shelled hollow spheres of ZnO.

MODULATION OF YOLK@VOID@SHELL SYNERGETIC EFFECT

Besides the engineering of one component, another common and efficient approach to improving the activity of the yolk-shell catalyst is to enhance the synergistic effect between the shell and yolk. One of the typical examples is Au@TiO_2 yolk-shell material. Li et al. reported the Gold Nanoparticle@TiO_2 and Gold Nanorod@TiO_2 yolk-shell nanostructures for photocatalytic reaction (Li et al., 2015). The design of this scaffold is based on the fact that TiO_2 shows low activity in solar light and the combination of it with the plasmonic metal would significantly expand the solar light absorption range and favor visible light catalysis. As expected, the Au@TiO_2 yolk-shell shows higher efficiency for the oxidation of benzyl alcohol. An examination of this mechanism showed that when irradiated with light, the electron generated from Au migrated to the conduction band of TiO_2, leaving positive charges on the Au core. The generation of charge separation caused by the synergistic function of Au and TiO_2 greatly benefits the oxidation reaction upon visible irradiation. To further improve the photocatalytic efficiency based on Au@TiO_2 yolk-shell material, our group introduced graphene as the inner shell (Wang et al., 2015). In this case, graphene facilitates electron transfer from Au to TiO_2, thus suppressing the recombination of the electron-hole pair. When used for H_2 production under visible light, the H_2 evolution rate of Au@r-GO/TiO_2 hybrids is 1.8 times higher than that of Au@TiO_2, confirming an enhanced synergistic effect.

The electrochemical water splitting reaction is a promising way of converting and storing renewable energy. With an elaborate design, this yolk-shell nanostructure provides several advantages in water splitting catalysis (Mei et al., 2018; Zhang et al., 2020). Tan et al. synthesized Au NP @ $Ni(OH)_2$ nanomaterials and investigated their catalytic performance for oxygen-evolution reactions (OER) (Cai et al., 2020). They found that the introduction of Au core improved the OER activity of hollow Ni $(OH)_2$. Further study indicated a strong electronic interaction between Au and Ni $(OH)_2$ for Au NP @ $Ni(OH)_2$ and the valence state of Ni $(OH)_2$, which shifted to positive, indicating the production of a larger amount of active sites for OER. The above example illustrates that the synergistic effect of the yolk-shell nanostructure can be favorable for the electrocatalysis of water splitting reaction.

The synergistic effect provided by the unique structure of yolk-shell offered a promising application in the catalysis of tandem reaction. Liu et al. prepared Pd@Al-$MSiO_2$ yolk-shell for the chemical transformation of glucose to 1, 2-propylene glycol (Lv et al., 2020). In this well-designed scaffold, the mesoporous SiO_2 shell is doped with Al, which mainly exists in the form of 4-coordinate, provided the Lewis acid microenvironment and facilitated by the isomerization of glucose to fructose. The isomerization of glucose is the first rate-determining step for the conversion to 1, 2-propylene glycol. Then the resulting fructose underwent retro-aldol condensation in the voids and hydrogenation at the interface of the Pd nanoparticle. With this design, the undesired reaction routes were greatly suppressed. The catalytic transformations processed in the different compartment of yolk-shell make them excellent catalysts for performing tandem catalysis.

SUMMARY AND OUTLOOK

This minireview has summarized methods for the preparation of a yolk-shell nanocatalyst, illustrating the advantages and disadvantages of each method. We also discussed strategies that were recently adopted to improve the catalytic efficiency, stability, and recyclability in the regulation of shell, yolk, voids, and related synergistic effects. These examples demonstrate the promising potential application of yolk-shell structured nanomaterial as catalysts.

One pot synthetic methods, which are suitable for general materials, represent a promising way of further boosting this area of research in the future. Another direction lies in the minimization of the size of the active core, which will undoubtedly optimize the catalytic performance of yolk-shell nanocatalysts. Pickering microcapsule (Wang et al., 2018d) with proper encapsulated inner material, exhibit yolk-shell like structure and may provide a promising alternative for efficient catalysis due to their high interfacial activity (Shi et al., 2018; Li et al., 2019b). Moreover, more control over the tuning of the catalytic performance may bring new dynamic benefits. In terms of practical applications, the scaled-up preparation of yolk-shell catalysts deserves more attention. Additionally, the integration of low-cost and energy clean components could decrease the production price and facilitate the development of more sustainable options.

AUTHOR CONTRIBUTIONS

XS contributed to writing this review. JH and RG established the concept. JH supervised the review. All authors contributed to the article and approved the submitted version.

FUNDING

This work was supported by the National Natural Science Foundation of China (21922202 and 21673202) and the Priority Academic Program Development of Jiangsu Higher Education Institutions.

REFERENCES

Ahsan, M. A., Imam, M. A., Puente Santiago, A. R., Rodriguez, A., Alvarado-Tenorio, B., Bernal, R., et al. (2020a). Spent tea leaves templated synthesis of highly active and durable cobalt-based trifunctional versatile electrocatalysts for hydrogen and oxygen evolution and oxygen reduction reactions. *Green Chem*. 22, 6967–6980. doi: 10.1039/D0GC02155E

Ahsan, M. A., Puente Santiago, A. R., Hong, Y., Zhang, N., Cano, M., Rodriguez-Castellon, E., et al. (2020b). Tuning of trifunctional NiCu bimetallic nanoparticles confined in a porous carbon network with surface composition and local structural distortions for the electrocatalytic oxygen reduction, oxygen and hydrogen evolution reactions. *J. Am. Chem. Soc*. 142, 14688–14701. doi: 10.1021/jacs.0c06960

Ahsan, M. A., Puente Santiago, A. R., Sanad, M. F., Mark Weller, J., Fernandez-Delgado, O., Barrera, L. A., et al. (2020c). Tissue paper-derived porous carbon encapsulated transition metal nanoparticles as advanced non-precious catalysts: carbon-shell influence on the electrocatalytic behaviour. *J. Colloid. Interface Sci*. 581, 905–918. doi: 10.1016/j.jcis.2020.08.012

Cai, R., Jin, H., Yang, D., Lin, K.-T., Chan, K., Sun, J., et al. (2020). Generalized preparation of Au NP @ $Ni(OH)_2$ yolk-shell NPs and their enhanced catalytic activity. *Nano Energy* 71:104542. doi: 10.1016/j.nanoen.2020.104542

Chen, H., Shen, K., Mao, Q., Chen, J., and Li, Y. (2018). Nanoreactor of MOF-derived Yolk–Shell Co@C–N: precisely controllable structure and enhanced catalytic activity. *ACS Catal*. 8, 1417–1426. doi: 10.1021/acscatal.7b03270

Das, S., Perez-Ramirez, J., Gong, J., Dewangan, N., Hidajat, K., Gates, B. C., et al. (2020). Core-shell structured catalysts for thermocatalytic, photocatalytic, and electrocatalytic conversion of CO_2. *Chem. Soc. Rev*. 49, 2937–3004. doi: 10.1039/C9CS00713J

Fan, C. M., Zhang, L. F., Wang, S. S., Wang, D. H., Lu, L. Q., and Xu, A. W. (2012). Novel CeO_2 yolk-shell structures loaded with tiny Au nanoparticles for superior catalytic reduction of p-nitrophenol. *Nanoscale* 4, 6835–6840. doi: 10.1039/c2nr31713c

Fan, L., Xu, X., Zhu, C., Han, J., Gao, L., Xi, J., et al. (2018). Tumor catalytic-photothermal therapy with yolk-shell Gold@Carbon nanozymes. *ACS Appl. Mater. Interfaces* 10, 4502–4511. doi: 10.1021/acsami.7b17916

Gawande, M. B., Goswami, A., Asefa, T., Guo, H., Biradar, A. V., Peng, D. L., et al. (2015). Core-shell nanoparticles: synthesis and applications in catalysis and electrocatalysis. *Chem. Soc. Rev*. 44, 7540–7590. doi: 10.1039/C5CS00343A

Goebl, J., and Yin, Y. (2013). Ship in a Bottle: *in situ* confined growth of complex yolk-shell catalysts. *ChemCatChem* 5, 1287–1288. doi: 10.1002/cctc.201300129

Gong, Y., Wu, X., Chen, J., Li, W., Han, N., Zhang, D., et al. (2019). Enhanced gas-sensing performance of metal@ZnO core–shell nanoparticles towards ppb-ppm level benzene: the role of metal–ZnO hetero-interfaces. *New J. Chem*. 43, 2220–2230 doi: 10.1039/C8NJ04621B

Guiet, A., Göbel, C., Klingan, K., Lublow, M., Reier, T., Vainio, U., et al. (2015). Hydrophobic nanoreactor soft-templating: a supramolecular spproach to Yolk@Shell materials. *Adv. Funct. Mater*. 25, 6228–6240. doi: 10.1002/adfm.201502388

Han, J., Song, G., and Guo, R. (2007). Fabrication of polymer hollow nanospheres by a swelling–evaporation strategy. *J. Polym. Sci. A* 45, 2638–2645. doi: 10.1002/pola.22023

Han, J., Wang, M., Chen, R., Han, N., and Guo, R. (2014). Beyond yolk-shell nanostructure: a single Au nanoparticle encapsulated in the porous shell of polymer hollow spheres with remarkably improved catalytic efficiency and recyclability. *Chem. Commun*. 50, 8295–8298. doi: 10.1039/C4CC01532K

He, X., Peng, C., Qiang, S., Xiong, L. H., Zhao, Z., Wang, Z., et al. (2020). Less is more: silver-AIE core@shell nanoparticles for multimodality cancer imaging and synergistic therapy. *Biomaterials* 238:119834. doi: 10.1016/j.biomaterials.2020.119834

Hofer, C. J., Grass, R. N., Schneider, E. M., Hendriks, L., Herzog, A. F., Zeltner, M., et al. (2018). Water dispersible surface-functionalized platinum/carbon nanorattles for size-selective catalysis. *Chem. Sci*. 9, 362–367. doi: 10.1039/C7SC03785F

Hu, J., Li, R., Han, J., Sun, J., Wang, Y., Yu, L., et al. (2020). Yolk–shell or yolk-in-shell nanocatalysts? A proof-of-concept study. *J. Mater. Chem. A* 8, 10217–10225. doi: 10.1039/C9TA13390A

Jia, Y., Shmakov, S. N., Register, P., and Pinkhassik, E. (2015). Size-selective yolk-shell nanoreactors with nanometer-thin porous polymer shells. *Chemistry* 21, 12709–12714. doi: 10.1002/chem.201501968

Joo, J. B., Liu, H., Lee, Y. J., Dahl, M., Yu, H., Zaera, F., et al. (2016). Tailored synthesis of C@TiO2 yolk–shell nanostructures for highly efficient photocatalysis. *Catal. Today* 264, 261–269. doi: 10.1016/j.cattod.2015.09.008

Lee, J., Park, J. C., and Song, H. (2008). A nanoreactor framework of a Au@SiO_2 Yolk/Shell structure for catalytic reduction of *p*-nitrophenol. *Adv. Mater*. 20, 1523–1528. doi: 10.1002/adma.200702338

Li, A., Zhang, P., Chang, X., Cai, W., Wang, T., and Gong, J. (2015). Gold Nanorod@TiO_2 Yolk-shell nanostructures for visible-light-driven photocatalytic oxidation of benzyl alcohol. *Small* 11, 1892–1899. doi: 10.1002/smll.201403058

Li, A., Zhu, W., Li, C., Wang, T., and Gong, J. (2019a). Rational design of yolk-shell nanostructures for photocatalysis. *Chem. Soc. Rev*. 48, 1874–1907. doi: 10.1039/C8CS00711J

Li, Q., Zhao, T., Li, M., Li, W., Yang, B., Qin, D., et al. (2019b). One-step construction of Pickering emulsion via commercial TiO_2 nanoparticles for photocatalytic dye degradation. *Appl. Catal. B Environ*. 249, 1–8. doi: 10.1016/j.apcatb.2019.02.057

Liang, Y., Yu, K., Xie, J., Zheng, Q., and Wang, T. J. (2017). High hiding power and weather durability of film-coated titanium dioxide particles with a yolk-shell structure. *Colloids Surf. A* 520, 736–742. doi: 10.1016/j.colsurfa.2017.02.046

Liu, B., Li, X., Zhao, Q., Hou, Y., and Chen, G. (2017). Self-templated formation of $ZnFe_2O_4$ double-shelled hollow microspheres for photocatalytic degradation of gaseous o-dichlorobenzene. *J. Mater. Chem. A* 5, 8909–8915. doi: 10.1039/C7TA02048A

Liu, R., Qu, F., Guo, Y., Yao, N., and Priestley, R. D. (2014). Au@carbon yolk-shell nanostructures via one-step core-shell-shell template. *Chem. Commun*. 50, 478–480. doi: 10.1039/C3CC47050D

Lu, W., Guo, X., Luo, Y., Li, Q., Zhu, R., and Pang, H. (2019). Core-shell materials for advanced batteries. *Chem. Eng. J*. 355, 208–237. doi: 10.1016/j.cej.2018.08.132

Lv, M., Zhang, Y., Xin, Q., Yin, D., Yu, S., Liu, S., et al. (2020). Pd@Al-containing mesoporous silica Yolk–Shell-structured nanospheres as high performance nanoreactors for the selective hydrogenolysis of glucose to 1,2-propylene glycol. *Chem. Eng. J*. 396:125274. doi: 10.1016/j.cej.2020.125274

Mei, G., Liang, H. F., Wei, B. B., Shi, H. H., Ming, F. W., Xu, X., et al. (2018). Bimetallic MnCo selenide yolk shell structures for efficient overall water splitting. *Electrochim. Acta*. 290, 82–89. doi: 10.1016/j.electacta.2018.09.062

Murugesan, K., Chandrashekhar, V., Kreyenschulte, C., Beller, M., and Rajenahally, J. (2020). A general catalyst based on cobalt-core-shell nanoparticles for hydrogenation of N-Heteroarenes including pyridines. *Angew. Chem. Int. Ed*. 59, 17408–17412. doi: 10.1002/anie.202004674

Niu, D., Jiang, Y., He, J., Jia, X., Qin, L., Hao, J., et al. (2019). Extraction-induced fabrication of yolk-shell-structured nanoparticles with deformable micellar cores and mesoporous silica shells for multidrug delivery. *ACS Appl. Biol. Mater*. 2, 5707–5716. doi: 10.1021/acsabm.9b00759

Ren, H., and Yu, R. (2019). Hollow multi-shelled structures for energy conversion and storage applications. *Inorg. Chem. Front*. 6, 2239–2259. doi: 10.1039/C9QI00634F

Salvatore, K. L., Deng, K., Yue, S., McGuire, S. C., Rodriguez, J. A., and Wong, S. S. (2020). Optimized microwave-based synthesis of thermally stable inverse catalytic core-shell motifs for CO_2 hydrogenation. *ACS Appl. Mater. Interfaces* 12, 32591–32603. doi: 10.1021/acsami.0c06430

Shi, M., Yang, R., Li, Q., Lv, K., Miron, R. J., Sun, J., et al. (2018). Inorganic self-assembled bioactive artificial proto-osteocells inducing bone regeneration. *ACS Appl. Mater. Interfaces* 10, 10718–10728. doi: 10.1021/acsami.8b00385

Sun, J., Hu, J., Han, J., Yuan, G., and Guo, R. (2019). Dumbbell-like Pt-Fe_3O_4 Nanoparticles encapsulated in N-doped carbon hollow nanospheres as a novel Yolk@Shell nanostructure toward high-performance nanocatalysis. *Langmuir* 35, 12704–12710. doi: 10.1021/acs.langmuir.9b02237

Wang, A., Zhu, Q., and Xing, Z. (2020). Multifunctional quaternized chitosan@surface plasmon resonance Ag/N-TiO_2 core-shell microsphere for synergistic adsorption-photothermal catalysis degradation of low-temperature wastewater and bacteriostasis under visible light. *Chem. Eng. J.* 393:124781. doi: 10.1016/j.cej.2020.124781

Wang, B., Yu, Q., Zhang, S., Wang, T., Sun, P., Chuai, X., et al. (2018a). Gas sensing with yolk-shell LaFeO3 microspheres prepared by facile hydrothermal synthesis. *Sens. Actuat. B Chem*. 258, 1215–1222. doi: 10.1016/j.snb.2017.12.018

Wang, C., Xu, C., Xu, L., Sun, C., Yang, D., Xu, J., et al. (2018b). A novel core-shell structured upconversion nanorod as a multimodal bioimaging and photothermal ablation agent for cancer theranostics. *J. Mater. Chem. B* 6, 2597–2607. doi: 10.1039/C7TB02842C

Wang, J., Chen, M., Yan, X., Zhou, C., Wang, Q., Wang, D., et al. (2018c). A facile one-step hydrothermal synthesis of carbon–MoS2 yolk–shell hierarchical microspheres with excellent electrochemical cycling stability. *J. Appl. Electrochem*. 48, 509–518. doi: 10.1007/s10800-018-1184-4

Wang, M., Han, J., Xiong, H., and Guo, R. (2015). Yolk@Shell Nanoarchitecture of Au@r-GO/TiO_2 hybrids as powerful visible light photocatalysts. *Langmuir* 31, 6220–6228. doi: 10.1021/acs.langmuir.5b01099

Wang, X., Chen, L., Sun, G., and Liu, R. (2018d). Hollow Microcapsules with controlled mechanical properties templated from Pickering emulsion droplets. *Macromol. Chem. Phys*. 220:1800395. doi: 10.1002/macp.201800395

Wang, X., Liao, M., Zhong, Y., Zheng, J. Y., Tian, W., Zhai, T., et al. (2012). ZnO hollow spheres with double-yolk egg structure for high-performance photocatalysts and photodetectors. *Adv. Mater*. 24, 3421–3425. doi: 10.1002/adma.201201139

Wu, X., and Xu, D. (2009). Formation of yolk SiO_2 shell structures using surfactant mixtures as template. *J. Am. Chem. Soc*. 131, 2774–2775. doi: 10.1021/ja808452r

Wu, X. J., and Xu, D. (2010). Soft template synthesis of yolk/silica shell particles. *Adv. Mater*. 22, 1516–1520. doi: 10.1002/adma.200903879

Xiao, M., Wang, Z., Lyu, M., Luo, B., Wang, S., Liu, G., et al. (2019). Hollow nanostructures for photocatalysis: advantages and challenges. *Adv. Mater*. 31:e1801369. doi: 10.1002/adma.201801369

Xiao, M., Zhao, C., Chen, H., Yang, B., and Wang, J. (2012). "Ship-in-a-Bottle" growth of noble metal nanostructures. *Adv. Funct. Mater*. 22, 4526–4532. doi: 10.1002/adfm.201200941

Xie, Z., Ellis, S., Xu, W., Dye, D., Zhao, J., and Wang, Y. (2015). A novel preparation of core-shell electrode materials via evaporation-induced self-assembly of nanoparticles for advanced Li-ion batteries. *Chem. Commun*. 51, 15000–15003. doi: 10.1039/C5CC05577F

Xu, Y., Yao, Y., Yu, H., Shi, B., Gao, S., Zhang, L., et al. (2019). Nanoparticle-encapsulated hollow porous polymeric nanosphere frameworks as highly active and tunable size-selective catalysts. *ACS Macro Lett*. 8, 1263–1267. doi: 10.1021/acsmacrolett.9b00490

Yin, Y., Rioux, R., Erdonmez, C., Hughes, S., Somorjai, G., and Alivisatos, A. (2004). Formation of Hollow nanocrystals through the nanoscale kirkendall effect. *Science* 304, 711–714. doi: 10.1126/science.1096566

Yu, L., Pan, P., Zhang, Y., Zhang, Y., Wan, L., Cheng, X., et al. (2019). Nonsacrificial self-template synthesis of colloidal magnetic yolk-shell mesoporous organosilicas for efficient oil/water interface catalysis. *Small* 15:e1805465. doi: 10.1002/smll.201805465

Yue, Q., Li, J., Zhang, Y., Cheng, X., Chen, X., Pan, P., et al. (2017). Plasmolysis-inspired nanoengineering of functional yolk-shell microspheres with magnetic core and mesoporous silica shell. *J. Am. Chem. Soc*. 139, 15486–15493. doi: 10.1021/jacs.7b09055

Zhang, Q., Lee, I., Joo, J., Zaera, F., and Yin, Y. (2013). Core shell nanostructured catalyst. *Acc. Chem. Res*. 46, 1816–1824. doi: 10.1021/ar300230s

Zhang, Q., Liu, B., Ji, Y., Chen, L., Zhang, L., Li, L., et al. (2020). Construction of hierarchical yolk-shell nanospheres organized by ultrafine Janus subunits for efficient overall water splitting. *Nanoscale* 12, 2578–2586. doi: 10.1039/C9NR08802D

Zhang, W., Lin, X. J., Sun, Y. G., Bin, D. S., Cao, A. M., and Wan, L. J. (2015). Controlled formation of Metal@Al_2O_3 yolk-shell nanostructures with improved thermal stability. *ACS Appl. Mater. Interfaces* 7, 27031–27034. doi: 10.1021/acsami.5b09791

Zhou, M., Wang, T., He, Z., Xu, Y., Yu, W., Shi, B., et al. (2019). Synthesis of yolk–shell magnetic porous organic nanospheres for efficient removal of methylene blue from water. *ACS Sustain. Chem. Eng*. 7, 2924–2932. doi: 10.1021/acssuschemeng.8b01807

Conflict of Interest: The authors declare that the research was conducted in the absence of any commercial or financial relationships that could be construed as a potential conflict of interest.

Advantages of publishing in Frontiers

OPEN ACCESS
Articles are free to read for greatest visibility and readership

FAST PUBLICATION
Around 90 days from submission to decision

HIGH QUALITY PEER-REVIEW
Rigorous, collaborative, and constructive peer-review

TRANSPARENT PEER-REVIEW
Editors and reviewers acknowledged by name on published articles

Frontiers
Avenue du Tribunal-Fédéral 34
1005 Lausanne | Switzerland

Visit us: www.frontiersin.org
Contact us: frontiersin.org/about/contact

REPRODUCIBILITY OF RESEARCH
Support open data and methods to enhance research reproducibility

DIGITAL PUBLISHING
Articles designed for optimal readership across devices

FOLLOW US
@frontiersin

IMPACT METRICS
Advanced article metrics track visibility across digital media

EXTENSIVE PROMOTION
Marketing and promotion of impactful research

LOOP RESEARCH NETWORK
Our network increases your article's readership